Radiation in Art and Archeometry

Editors: D. C. Creagh and D. A. Bradley

ELSEVIER

Radiation in Art and Archeometry

This Page Intentionally Left Blank

Radiation in Art and Archeometry

Edited by

D.C. Creagh

Faculty of Information Science and Engineering
Division of Management and Technology
University of Canberra
Canberra
Australia

and

D.A. Bradley

School of Physics
University of Exeter
Exeter
United Kingdom

ELSEVIER
2000
Amsterdam - Lausanne - New York - Oxford - Shannon - Singapore - Tokyo

ELSEVIER SCIENCE B.V.
Sara Burgerhartstraat 25
P.O. Box 211, 1000 AE Amsterdam, The Netherlands

First edition 2000

Library of Congress Cataloging in Publication Data
A catalog record from the Library of Congress has been applied for.

ISBN: 0 444 50487 7

♾ The paper used in this publication meets the requirements of ANSI/NISO Z39.48-1992 (Permanence of Paper).
Printed in The Netherlands.

Preface

The cover of this book shows an example of Australian Aboriginal rock art from the Kimberley region of Western Australia, and is reproduced here by courtesy of Graham Walsh of the Takarakka Rock Art Research Centre. The paintings were first reported by the explorer Joseph Bradshaw (1891). Because they are unusual and the details are unique there has been some speculation as to their origin. And because these paintings have no direct connection with the traditional owners of the land they have not been retouched as part of tribal ceremonies as is often the case. They are deteriorating as the rock substrate ages and organic binders and pigments oxidize and polymerize, which demands that some conservation measures be initiated for their preservation for future generations.

The rock art paintings illuminate the twin aims of this book: the use of archaeometry to determine the age, and perhaps some of the forensic details about the artefacts under examination; and the use of scientific techniques of analysis to determine the most appropriate strategy for their conservation.

In this book we have assembled twenty chapters covering a wide range of research in the fields of scientific conservation of art and archaeometry. The common thread is the use of radiation in these analyses. And the term "radiation" is used in its widest possible sense. The book encompasses the use of electromagnetic radiation in its microwave, infrared, visible, ultraviolet, x ray and γ ray forms ($E = h\nu = hc/\lambda$), and the use of particulate forms such as electrons, neutrons, and charged particles for which the Planck's Law relation ($\lambda = h/p$) applies. In many cases there is an interplay between the two forms: for example, proton induced x ray emission (PIXE), secondary ion mass spectrometry (SIMS).

As far as was possible the chapters have been arranged in order of ascending particle energy. Thus it commences with the use of microwaves and finishes with the use of γ rays.

The authors were chosen on the basis of their expertise as *practitioners* of their particular field of study. This means that, for example: the mature fields of study such as the IR and UV study of paintings have been written by very senior researchers, whereas for the emerging fields of synchrotron and neutron techniques the chapters have been written by talented researchers at the commencement of their careers.

A variety of systems for citing references are used throughout this book. This followed a deliberate decision by the editors. Because this book is intended for a readership which includes upper level undergraduates and early career researchers it was thought that exposure to a variety of referencing techniques would be useful from a didactic point of view.

In ***Chapter 1*** **Professor Lawrence Conyers** of the School of Archaeology of the University of Denver, USA, discusses the use of ground-penetrating radar (GPR) for the non-invasive study of buried archaeological features. In the past excavation of sites has been the

cause of considerable damage to the sites. Furthermore: because of restricted budgets the mapping of sites by conventional techniques is not feasible. He gives practical insights into the strengths and weaknesses of the GPR.

In *Chapter 2* **Dr Paola Letardi** of the Istituto per la Corrosione Marina dei Metalli, of the CNR, Genova, Italy, introduces a new technique for the study of the integrity of protective wax coatings on the surface of bronze, and other materials. This technique was brought into use by the Australian group (Otieno-Alego,V, Heath, G.A. Hallam, D.L. and Creagh, D.C., (1998) *Electrochemical Evaluation of the Anti-Corrosion Performance of Waxy Coatings for Outdoor Bronze Conservation.* In proceedings of the ICOM Conference, METAL98. Draguignan, France. 27 to 29 May 1998. [Ed. W. Mourey.. James and James. (Science Publishers), London: ISBN 1-873936-82-6] pp309-515). They have used it extensively for characterizing the wax coatings on bronze statues and monuments in the custody of the Australian War Memorial. This is a low frequency (<1 MHz) AC technique in which the impedance of an electrochemical cell, one electrode of which is the waxed surface, is measured. The variation of impedance with applied frequency gives a measure of the integrity of the wax coating. Paola gives a detailed account of the testing processes for cells to be used in field tests on bronze statues.

The next two chapters relate to a mature, but interestingly rapidly evolving fields of infrared (IR) and ultraviolet (UV) examinations of paintings, books, manuscripts, *et cetera.* These techniques are necessarily linked to the appearance of the artefacts in visible light. It is the change in appearance in the artefacts under stimulus by infrared or ultraviolet radiation which gives valuable information on the works of art being examined.

The advent of CCD devices and vidicon tubes, the universal availability of great computing power in small packages, and modern image analysis software packages has greatly enhanced the usefulness of these macroscopic techniques of analysis. The broad-band spectral response of digital cameras coupled to the use of a variety of sources of illumination enables pixel-by-pixel studies of the detail of artworks. **Emeritus Professor Franz Mairinger** of the Institute for Colour Science and Colour Chemistry of the Academy of Fine Arts, Vienna, Austrai, gives us the benefit of his very considerable experience in the fields of the IR and the UV examination of paintings in his contributed chapters (Chapter 3 (IR) and Chapter 4 (UV)).

Chapter 3 outlines the mechanics of undertaking IR examinations of materials. It discusses the properties of IR and the interaction of IR with materials. It gives practical details of radiation sources lenses, detectors and filters. Tables of appropriate sources, filters and detectors are listed, as is the change of colour of many artists' materials under IR illumination.

The UV and fluorescence study of paintings and manuscripts is discussed in ***Chapter 4.*** As in the IR case a discussion of the properties of UV radiation is followed by a detailed discussion of available UV sources, filters, and photographic materials. Their application in both reflected UV and the UV fluorescence studies is discussed, and the colour changes of pigments due to fluorescence is tabulated. Illustrations of the effects of the various possibilities of examination are given.

Recent advances in the analysis of scattered infrared, visible, and ultraviolet radiation using optical spectroscopic techniques have provided researchers with an extremely valuable tool for the analysis of all types of materials of interest to museum curators and conservators, and

archaeologists. The technique described by **Dr Vincent Otieno-Alego** of the Raman Microscope Unit, University of Canberra, Australia, the Raman technique, has been widely used by museums, forensic scientists and geologists, and is an integral part of the training of students, both undergraduate and graduate, in the Conservation of Cultural Heritage Materials. In ***Chapter 5*** he outlines the principles of operation of a Raman microscope. As well, he gives a comparison of the strengths of Raman microscopy *vis a vis* other analytical techniques in the study of pigments in manuscripts and paintings, and in the examination of paint flakes form objects. The use of the Raman technique to map areas to establish paint and ink overlays is also discussed.

Professors Ladia Musilek (Czech technical University, Prague, Czech Republic) and **M. Kubelik** (Technical University of Vienna, Austria) discuss the use of thermoluninescence dating (TD or TLD) in ***Chapter 6***. They discuss both the physical principles underlying the technique and how the technique is used to establish the dates of manufacture of objects which have been fired, ceramics, pottery, bricks and the like. They give an excellent exposition of the assessment of errors (random, systematic and context) in the establishing of the age of fired objects. The reader is directed the Chapters 12, 19 and 20 which deal with the problems of archaeological dating.

The use of synchrotron radiation (*sr*) sources by materials scientists is still comparatively new. It is only in the last decade that *sr* sources have been dedicated to the study of materials have existed. Prior to that their use was the exclusive use of high energy physicists. There has been a rapid growth in their use by materials scientists, to the extent that more than thirty *sr* sources worldwide. Synchrotrons which generate energy in the x ray region (the region used in most structural analyses) typically have energies greater that 2 GeV. For example: the Photon Factory at the Japanese Institute for High Energy Research, Tsukuba, Japan, operates with a circulating current of electrons (400mA at 2.5 GeV) and produces useful maximum x ray energies for a bending magnet of about 20 keV; the Advanced Photon Source at Argonne, USA operates at 6 GeV and produces useful maximum x ray energies of 80 keV). Synchrotron radiation sources are classified by the size of the spot which emits the radiation: values of about 40 nm rad are typical of a Second Generation machine; 20 or less are characteristic of a Third Generation machine.

Whatever the energy to which the charged particle is accelerated the principles underlying the production of x rays is the same. When a charged particle is accelerated (as it is when it is deflected by a magnetic field) it radiates energy in the form of electromagnetic radiation the maximum energy of which is determined by the energy of the particle and the applied magnetic field. The higher the particle energy and the stronger the magnetic field strength, the higher the maximum photon energy, or put another way, the shorter the critical wavelength ($\lambda_c = 18.64/(BE^2)$; where λ_c is in Angstrom, B in Tesla, E in GeV). See for example: U. Arndt (1992) *The generation of x rays.* In International Tables for Crystallography Volume C (Ed. A.J.C. Wilson: Kluwer, Amsterdam) Section 4.2, 172-175.

The principal properties of synchrotron radiation are as follows:

- high intensity, especially if auxiliary bending devices such as wigglers and undulators are used (typically more than 10^6 more intense than a conventional laboratory source)
- emission over a broad spectral range (from IR to x ray energies; "white" radiation)

- high directionality (because of relativistic effects (typically less than2 mrad vertically)
- linearly polarized in the plane of the orbit.

For the experiment described in Chapter 7 "white" radiation was used and the photon energies were separated using energy dispersive analysis techniques. In Chapters 14 and 16 monochromatic radiation has been used. The production of monochromatic radiation and techniques for focussing the already highly collimated, high intensity beams has been described by Creagh (D.C. Creagh (1999). *Monochromators and Filters.* In International Tables for Crystallography Volume C Second Edition (Ed. E. Prince: Kluwer, Amsterdam) Section 4.2.5).

In ***Chapter 7*** **Drs. Sally Colston, Andrew Jupe and Paul Barnes** of the Industrial Materials group, Crystallography Department, Birkbeck College, London, UK, introduce the new techniques of synchrotron radiation energy dispersive diffraction (SR-EDD) and synchrotron radiation energy dispersive diffraction imaging (SR-EDDI).. They give an outline of the theory underlying the techniques and the use of the technique for the study of a neolithic bronze tool and building materials. The interior of objects can be studied as a function of composition using tomagraphic techniques. Attention is given to the important question of data quality. Note that a variant of this technique (using conventional, rather than *sr* sources) is in use at major airports for the examination of passenger baggage, looking especially for explosive materials.

Another approach to the study of solid objects using x ray techniques was adopted by **Dr. Mic Farquharson** of the Department of Radiography, City University, London, England, and **Dr. M. Brickley**, Department of Ancient History and Archaeology, The University of Birmingham, England. They are interested in establishing a protocol for the proper estimation of bone mineral density (BMD) in bones, especially those of archaeological interest. In ***Chapter 8*** they outline the principles of radiography, single (SPA) and double energy x ray analysis (DEXA), and energy dispersive x ray diffraction (EDXRD). One of their projects of topical relevance is a study of osteoporosis, then and now. Comparisons are made between populations in East London in the 18^{th} century and those prevailing now. They studied the BMD of the fourth lumbar vertebra of the human skeleton. Details of their results are given.

Chapter 9 is the first of the chapters which use particulate radiation for the study of museum and archaeological objects. In this chapter **Dr. Mieke Adriaens** of the Department of Chemistry, University of Antwerp, Belgium, discusses the principles of Secondary Ion Mass Spectrometry. In this technique a finely collimated beam of ions is used to probe the surface of the sample. The secondary ions sputtered from the surface are characteristic of the composition of the surface layer. These are analyzed using a mass spectrometer. Hence the surface composition can be determined. As the ion beam eats into the surface a depth profile of the composition of the material can be generated. Numerous applications to the conservation of materials, dating and determining the provenance of materials are given. The reader should refer also to *Chapter 18* on Proton Induced X ray Emission (PIXE) and *Chapter 19* on Accelerator Mass Spectrometry (AMS).

The use of a variety of scanning electron microscope techniques for the study of paintings is given in ***Chapter 10*** by **Dr. Aviva Burnstock**, Department of Conservation and Technology, Courtauld Institute of Art, London, England, and **Dr. Chris Jones**, Electron Microscope Unit,

Department of Mineralogy, The Natural History Museum, London, England. The chapter focuses on the imaging of the materials used in easel paintings, rather than using x ray techniques for the chemical analysis to study compositions. Examples of experimental studies of cleaning, paint surface defects, and bio-degradation of painting materials are given. A compilation of images of selected artists' materials is given to illustrate a number of SEM techniques. Further relevant discussion is contained in *Chapter 11* (Transmission Electron Microscopy) and Chapter 5 Raman Microscopy.

The use of transmission electron microscope techniques for the identification of pigments taken from easel paintings is discussed in ***Chapter 11*** by **Shaun Bulcock** of the Electron Microscope Unit, University of Sydney. He outlines the principles underlying the formation of transmission electron microscope patterns, in particular the selected area diffraction (SAD) and convergent beam electron diffraction (CBED) patterns. He then proceeds to give examples of studies made on small paint fragments from two artworks in which CBED was used in conjunction with energy dispersive x ray analysis (EDAX or EDS) to determine the mineral composition of the fragments. In particular comparisons should be made with the results of Raman microscopy (*Chapter 5*).

The second of the archaeological dating techniques to be reported in this book is radiocarbon dating (^{14}C dating). In *Chapter 12* **Drs. Tom Higham** and **Fiona Petchey**, Radiocarbon Dating Laboratory, University of Waikato, Hamilton, New Zealand, discuss the physical principles of radiocarbon dating and its use in archaeometry. They give a detailed outline of error assessment and they stress the requirements for quality assurance. They discuss matters of sample selection, sample provenance, and sample contamination in the context of archaeological research in Australia and New Zealand. *Chapters 19 and 20* also discuss the strengths and weaknesses, successes and failures of radiocarbon dating.

In ***Chapter 13*** **Dr Marco Ferretti** of the CNR-Istituto per le Tecnologie Appiacate ai Beni Culturali discusses the use of X ray Fluorescence Analysis (XRF) for the study of works of cultural heritage significance. He reviews the literature on this subject and outlines the criteria which must be fulfilled if accurate analyses are to be made using this technique. Results for metals, pottery, glass and paintings are given.

Professor Pauline Martinetto, Dr. G. Tsoucaris, Dr. P. Walter (Laboratoire de recherche des musees de France, Paris, France), **Dr. M. Anne** (Laboratoire de Cristallographie-CNRS, Grenoble, France), and **Eric Dooryhee** (European Synchrotron Radiation Facility, Grenoble, France) have used the technique of synchrotron radiation to study the composition of Egyptian cosmetics of the pre-dynasty, New-, and Old-Kingdoms. In ***Chapter 14*** they describe the use of monochromatic synchrotron radiation to study the structure of the components of the cosmetics, using a focussed beam to illuminate particles as small as 10 μm. The technique of Rietveld analysis has been used to determine the composition of mixed phase samples.

Professor Peter Yu of the Department of Physics and Materials Science, City University of Hong Kong, P.R. China, is an expert in the attribution of provenance of Chinese blue and white porcelain. In ***Chapter 15*** he outlines some of the problems and challenges in the study of these ceramics. He discusses: the feasibility of using ratios between elemental concentrations for the attribution and the feasibility of using for our criteria some elements characteristic of the

colorant (such as Mn and Co) which in theory lies too deep beneath the glaze to be measured; the soundness of calibration sources; the need to use multivariate analysis instead of contents for individual chemical elements; the properties of antique blue and white porcelains other than those of the Qing dynasty, in particular those of the Ming dynasty; the properties of antique blue and white porcelains of the Qing dynasty (separated from the porcelains of the Republic period) and those in different periods of the Qing dynasty, and comparison between Qing and Ming porcelains; properties of antique blue and white porcelains from different main sites of production, including those from the most studied site of Jingdezhen.

Dr. Winfreid Kockelmann (ISIS Facility, Rutherford Appleton Laboratory, Chilton, England), **Dr. Manolis Pantos** (SRS Facility, Daresbury Laboratory, Warrington, England), and **Professor A. Kirfel** (Mineralogisch-Petrologisch Institut, Universitat Bonn, Germany) have used both time-of-flight neutron and synchrotron X-ray diffraction were used for fingerprint determinations and quantitative mineral phase analyses of archaeological objects. In ***Chapter 16*** they discuss the advantages and drawbacks of both techniques in archaeological research. Neutron diffraction allows non-destructive analysis of complete and unprepared objects. Synchrotron X-ray diffraction can be used for fast and high-resolution data collection on small amounts of powder samples, surfaces or thin sections. Their paper concentrates on the introduction of the white-beam neutron diffraction technique to the study of pottery from ancient Greek, Russian and German sources.

In ***Chapter 17*** **Dr Maria Guerra** of the CNRS-Centre Ernest-Babelon, Orleans, France, gives a general description of a wide range of radiation techniques (activation techniques using neutrons (NAA) and protons (PAA), proton induced x ray emission (PIXE) and x ray fluorescence spectroscopy (XRF) can be used for determining the provenance of metals, and developing an understanding of the manufacture technology of metallic objects in ancient times. The main properties and differences for the most used techniques are given. Some, used to complement radiation techniques and used in the later examples, are also considered.

She gives several examples, most of them on coinage, for the most important non-ferrous metals and alloys used in the past. These cover a large but far from complete number of fields of research. She demonstrates that provenance may sometimes be determined by using trace elements patterns. However, for more accurate results a good knowledge of trace elements present as well the geological context is required. To understand the fabrication of an object we need in general to couple both analytical and metallurgical data.

A large number of examples illustrate the questions posed for metalwork. For each main metal, after some geological, smelting and purification considerations, application of the radiation techniques to the manufacture technology and the provenance of the ores were considered to answer a number of particular historical questions.

The *Mössbauer effect* has been used with some success to solve problems associated with archaeology and conservation. Mössbauer spectroscopy makes use of low energy γ-rays emitted by nuclei for studying the properties of solids. In Mössbauer studies of works of art and archaeological ceramics, the 14.4 keV γ-rays of ^{57}Fe are used in most cases, although other Mössbauer isotopes, like ^{119}Sn and ^{121}Sb, can also be used, for instance, for studies of bronzes or

glazes containing tin or antimony, while ^{197}Au has recently been used for studying Celtic gold coins. In ***Chapter 18*** by **Professors Ursel and Fritz Wagner, Dr. W. Hausler and Dr. I Shimada** of the Physics Department, Technical University of Munich, Garching, Germany, only ^{57}Fe Mössbauer spectroscopy and its application to studies of ceramics is discussed. The ceramics discussed in this context are mainly pottery, but also building materials such as fired bricks and tiles as well as parts of kilns and furnaces or even soil or mud-plaster heated in fires.

In ***Chapter 19*** a different approach to radiocarbon dating from that of *Chapter 12* is introduced by **Drs. Claudio Tuniz, Ugo Zoppi** and **Marco Barbetti** of the Australian Nuclear Science and Technology Organization, Sydney, Australia. As mentioned in *Chapter 12* radiocarbon (^{14}C) dating provides an absolute time scale for human history over the last 50,000 years. Accelerator Mass Spectrometry (AMS), with its capacity to analyse ^{14}C in sub-milligram carbon samples, has expanded enormously the applicability of this dating method. Specific molecular compounds extracted from ancient bones, single seeds and other microscopic carbon-bearing substances of archaeological significance can now be dated, increasing the sensibility and reliability of the chronological determination. Thanks to the very limited invasiveness of AMS, rare artefacts can be sampled for dating without undue damage. The state of the art in AMS dating of objects significant for archaeology, history and art is reviewed with examples from some recent applications such as Australian rock art, the Shroud of Turin, the "iceman" mummy, and Charlemange's crown.

Chapter 20 introduces techniques for dating of materials which complements and extends the capabilities of techniques described in *Chapters 6, 12, and 19*. In it **Professor Rainer Grün** of the Research School of Earth Sciences, Australian National University, Canberra, Australia describes how dating can be extended beyond the limits of radiocarbon dating. The U-series and trapped charge dating methods he describes can be applied for the establishment of chronologies well beyond the radiocarbon dating barrier. His chapter gives a short introduction into these methods and illustrates their potential with the dating of the Lake Mungo 3 skeleton. The determination of the age of this skeleton is of importance for the assessment of theories concerned with the manner in which Australia was inhabited.

One invited chapter, mailed but not received at the time this book needed to go to press, was that by **Dr L Ciancabilla and Dr G. Maino** of Facolta di Conservazione dei Beni Culurali, Universita di Bologna, Ravenna, Italy on ***The Study of Art and Archaeological Artefacts using Ion Beam Analysis, PIXE and Reflectography.*** The authors have a formidable reputation for the quality of their research on a wide range of objects of cultural heritage significance. The possibility of its being published in the journal *Applied Radiation and Isotopes* will not be overlooked.

D.C. Creagh and D.A. Bradley

This Page Intentionally Left Blank

TABLE OF CONTENTS

Radiation in Art and Archeometry
D.C. Creagh and D.A. Bradley (editors)

The use of ground-penetrating radar in archaeology

Lawrence B. Conyers

Department of Anthropology, University of Denver, 2130 S. Race Street, Denver, CO 80208

Ground-penetrating radar is a geophysical method that can accurately map buried archaeological features in three-dimensions. Data are collected when radar waves are transmitted from a surface antenna into the ground and reflected off buried archaeological features and stratigraphic horizons. The reflected waves are recorded back at the surface and the transmission time is measured, which can then be converted to depth in the ground. Digital data acquisition allows reflection profiles to be filtered and enhanced in order to produce high quality two-dimensional images. The spatial mapping of reflected wave amplitudes within a grid can be used to accurately map buried sites in three-dimensions.

1. INTRODUCTION

In today's climate of rescue archaeology, cultural resource management and the prevalent ethic of site conservation, non-invasive methods of subsurface exploration and mapping are becoming increasingly important. With many archaeological excavation budgets severely restricted, and strict political and conservation considerations that must be considered, it is often not feasible or is undesirable to excavate large areas or randomly dig test excavations in the hope of finding buried archaeological sites. New computer enhanced geophysical methods, including ground-penetrating radar, are being developed for site identification, mapping and analysis, which can non-invasively gather massive amounts of data from buried sites without having to dig. Archaeologists who are only familiar with the traditional methods of gathering data by the shovel and trowel method are being increasingly marginalized in this changing environment.

Increasingly sophisticated ground-penetrating radar (GPR) acquisition and processing methods can be employed to gather important subsurface information in un-excavated areas including the location, depth and orientation of important buried features and artifacts, precluding the time consuming and costly process of digging. Maps and images produced from the GPR data can not only identify buried features for possible future excavation but also interpolate between excavations into the unknown, projecting archaeological knowledge into areas that have not yet been, or may never be excavated.

2. THE GROUND-PENETRATING RADAR METHOD

Ground-penetrating radar equipment is very portable, consisting of paired surface antennas, radar system and computer with monitor and keyboard (Figure 1). Power is supplied to the system by batteries, electrical generator or normal AC current.

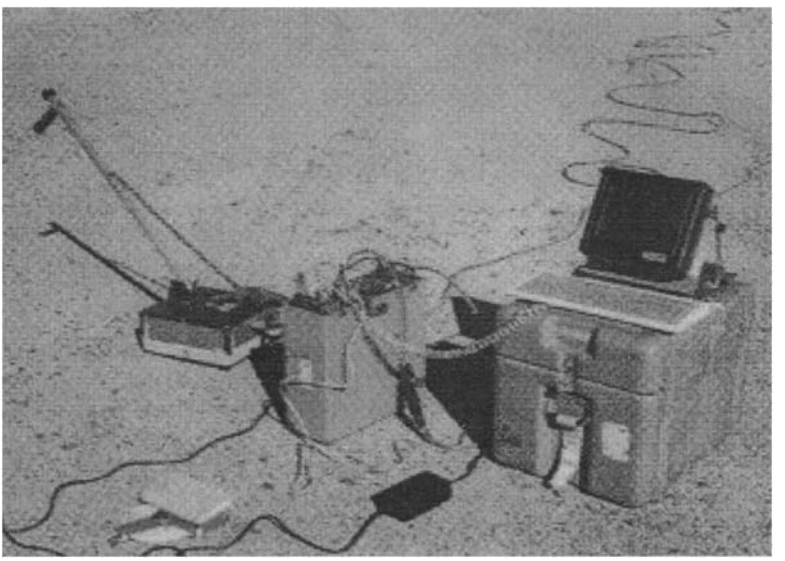

Figure 1. Ground-penetrating radar equipment including a 500 MHz antenna (with handle), radar generation system and hard drive, and computer monitor.

Data are acquired by reflecting radar waves, created by pulses from a surface antenna, off subsurface objects, features or bedding contacts. Reflections that are generated from buried features or stratigraphic changes are detected and recorded at a receiving antenna on the ground surface (Conyers and Goodman, 1997: 23 [1]). The elapsed time between when the pulse was sent and when a series of reflections, from progressively deeper in the ground, are received back at the surface is then measured and recorded.

Any change in the electrical or magnetic properties of features in the ground will cause a portion of the transmitted radar pulse to be reflected back to the surface. When the travel times of the energy pulses are measured, and their velocity through the ground can be determined, distance (or depth in the ground) can be accurately measured (Conyers and Lucius, 1996 [2]).

Reflection data are collected as both surface receiving and transmitting antennas are moved along the ground surface in tandem, while collecting a series of reflections in a linear transect. Each series of reflections recorded at one location on the ground is called a trace. When many

traces along a transect are stacked vertically, they can be viewed as two-dimensional vertical reflection profiles of the subsurface stratigraphy and other buried features (Figure 2).

Different antenna frequencies, ranging from about 80 to 1200 MHz are typically used in archaeological mapping (Conyers and Goodman, 1997: 40 [1]). The lower the antenna frequency, the longer the wavelength of energy transmitted into the ground. These longer radar wavelengths can penetrate quite deeply in the ground, but are only capable of resolving fairly large buried features. For instance, 80 MHz antennas may be able to transmit and then receive energy back at the surface from a depth of 3 meters or more, but

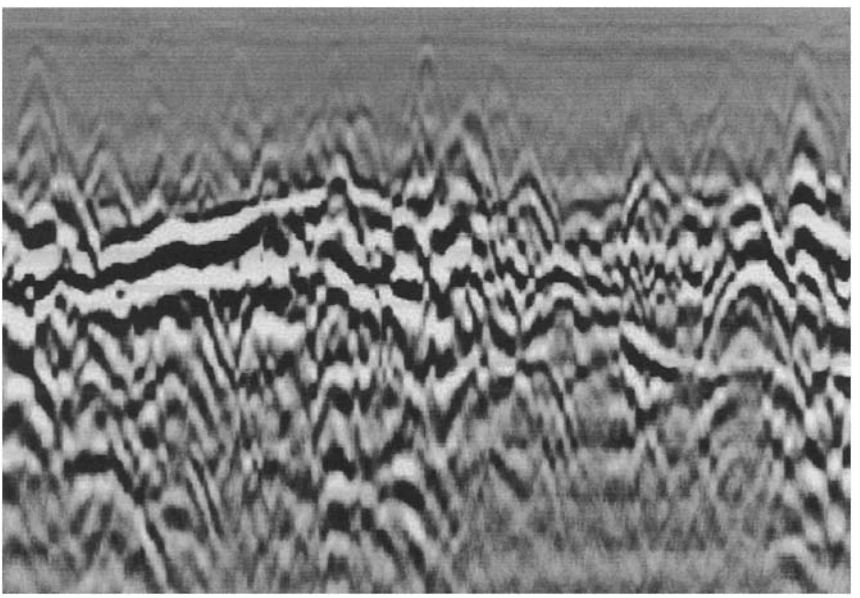

Figure 2. Ground-penetrating Radar Profile showing a buried living surface on the left side of the profile, which has been disturbed by anthropogenic disturbance on the right side of the profile. High amplitude reflections are dark black while areas of little reflection are gray.

are incapable of resolving features smaller than a few meters in diameter. In contrast, a 1,000 MHz antenna can transmit radar energy to at most 50 centimeters depth, but the resulting reflections can resolve objects as small as a few centimeters in diameter.

Some ground conditions are favorable for radar energy transmission, such as dry sand, volcanic ash or dry soils. The media most conducive for radar transmission are electrically resistive materials with little magnetic permeability (Conyers and Goodman, 1997: 53 [1]). In contrast, wet clay and any other material that is highly electrically conductive will readily attenuate radar waves as they penetrate into the ground and most energy will be lost near the ground surface, irrespective of antenna frequency or power.

As large data sets are acquired in a regular series of parallel and perpendicular transects within a grid, and the reflections derived in many two-dimensional profiles are correlated and processed, accurate three-dimensional maps of buried features and associated stratigraphy can be constructed. The physical and chemical changes of the buried materials can also be mapped because digital data measured in this three-dimensional volume of reflections includes the amplitudes of those reflected waves, which are indicative of the variations within the buried materials (Conyers and Goodman, 1997: 149 [1]). The higher the amplitude of the reflected waves, the greater the electrical and magnetic contrast that exists at the contact between contrasting materials in the ground. For instance, a very high amplitude reflection would typically be generated at the boundary between dry sand and wet clay, because they have very different electrical and magnetic properties. Often similar high amplitude reflections are generated at contacts between archaeological features, such as buried floors, and the surrounding materials.

3. THE HISTORY OF GPR DATA PROCESSING AND INTERPRETATION IN ARCHAEOLOGY

Ground-penetrating radar has been traditionally used as a method for identifying the presence or absence of buried archaeological features. Throughout the 1970s and 1980s its use was almost always as an exploration tool, with limited given to detailed subsurface mapping of those features or analysis of the surrounding stratigraphy. Only a limited amount of data processing was done, mostly because of the difficulty in processing and interpreting large GPR data sets that might contain many thousands of individual reflections, most of which were printed out as paper records in the field. In addition the complexity of radar reflections that can occur in the ground, the difficulty in identifying important reflections, and the massive amounts of data that are typically collected usually impeded any sophisticated data interpretation. In addition, the reflection profiles were usually un-processed "raw" data that contained an abundance of "noise", which could be extraneous reflections from surface objects and even from people moving about in the vicinity of the antennas, complicating two-dimensional images. Fortunately, even in these types complex and "busy" data sets, significant reflection "anomalies" could usually be visually correlated with other similar reflections in adjacent profiles. In this type of rudimentary data analysis most archaeological features were identified visually, based only on what buried archaeological features were "thought" to look like. If buried reflection surfaces were extensive enough, reflections could sometimes be correlated from profile to profile within a grid, but often the abundance and complexity of detectable reflections precluded accurate correlation. In addition, without extensive testing and confirmation of the discovered features, little could actually be determined about the origin and spatial orientation of many reflections, and therefore most interpretation was usually quite subjective.

A huge breakthrough in GPR processing occurred in the late 1980s as digital recording methods allowed for post-acquisition data processing, filtering and manipulation of reflection records (Annan and Davis, 1992 [3]). These post-acquisition processing methods allowed background "noise", a common problem in all GPR records, to be routinely removed from the

recorded data (Conyers and Goodman, 1997: 77 [1]). Background noise, which produces the horizontal banding common in typical un-processed GPR profiles, is caused by noise inherent in GPR systems, "ringing" within antennas and multiple recorded reflections that occur as radar energy is repeatedly bounced between the antennas and the ground surface (Conyers and Goodman, 1997: 78 [1]). Multiple reflections can also occur within the housing of radar antennas and sometimes between surface features and the antennas. Computers can easily remove these horizontal bands by arithmetically averaging all recorded waves that were recorded at the same times within all the traces collected in a transect. This "average wave" can then be subtracted from each trace, leaving only those reflections that are non-horizontal and presumably those that were generated from important geological or archaeological features in the ground.

A second form of post-acquisition data processing that also became common with the advent of digital data was the removal of portions of selected frequencies from the recorded signal. These data enhancement processes, sometimes called high and low-pass filters, remove extraneous noise that can be associated with FM radio, cellular phone, television and other electromagnetic transmissions. They can be applied either during data acquisition, or in post-acquisition processing of digital data (Conyers and Goodman, 1997: 74 [1]).

4. TIME-DEPTH CONVERSIONS

A significant aid in the reflection identification process is being able to convert the time at which reflected waves were recorded to their approximate depth in the ground. All GPR reflections are measured in two-way time, which is the elapsed time between when a radar pulse is sent from the surface antenna, travels into the ground, and then is reflected back to the surface and measured. Time is measured in nanoseconds, or billionths of a second. To convert time to depth, the velocity of the radar energy travel in the ground must be determined.

Radar energy travels at almost the speed of light in air, but as it enters the ground, it begins to slow. Usually radar wave velocity decreases with depth as soils, sediment and rock become more compact and progressively more water saturated. However, velocity can also increase, if it enters a void space, or other medium of higher velocity.

The simplest way to convert measured travel time to depth is to directly measure the depth of reflections that are visible in reflection profiles. Many times objects, such as plastic or metal pipes, rocks or other "point source" objects will generate visible hyperbolic reflections in profiles (Figure 3). Hyperbolas are produced from point sources because radar energy travels into the ground from the surface antenna in a conical shape, with the apex of the cone at the surface antenna. Radar energy spherically spreads out from the antenna as it travels into the ground and therefore reflections will be recorded from an object before the antenna is directly on top of it, and will continue to be recorded as it passes away. The result is a hyperbolic shaped reflection, with the apex denoting the actual location of the reflection source.

When point source reflections are visible in profiles, their exact locations on the ground can be identified. If its exact depth below the ground is known or can be measured using a soil probe, post hole digger, or other tool, the average velocity of radar waves traveling through the ground can be calculated (Conyers and Lucius, 1996 [2]). An estimate of radar velocity can also be made by

analyzing the shape of the hyperbola arms. In general, the lower the velocity, the greater the spread in the arms of the reflection hyperbola.

5. REFLECTION MODELING

Two-dimensional reflection profiles do not typically "look like" what one thinks a feature "should look like" in cross-section because of the complex reflection, refraction and multiple reflections of radar waves in the subsurface. Synthetic radar profiles, produced on the computer, that can model how radar reflections are produced in the ground can be of great benefit in feature identification and analysis (Conyers and Goodman, 1997: 83 [1]). These two-dimensional models can be computer-generated if the approximate geometry of target features is input and the electrical and magnetic properties of the geological and archaeological layers are known (Goodman, 1994 [4]). Varying frequencies of radar data can then be passed through the modeled features and geological layers, producing a two-dimensional model of the generated reflections (Figure 4). These synthetic GPR profiles can then be compared to actual GPR profiles collected in the field as an aid in feature identification. They can also be prepared prior to data acquisition in order to study the potential resolution of suspected features, if geological and archaeological parameters are known in advance.

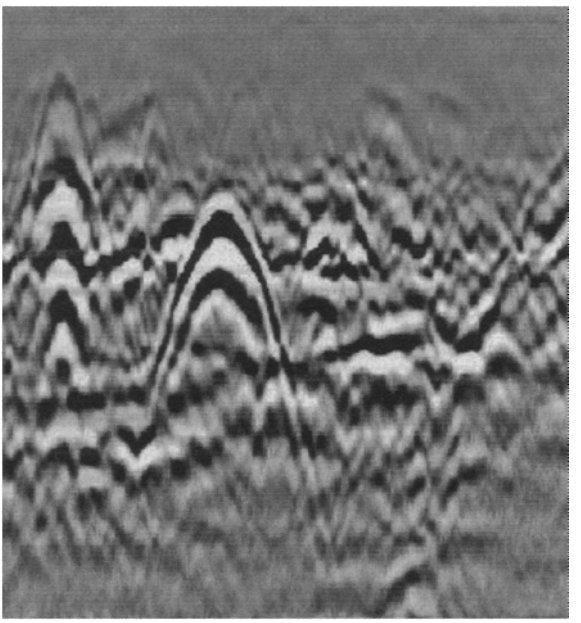

Figure 3. Hyperbolic reflection produced from a buried metal pipe.

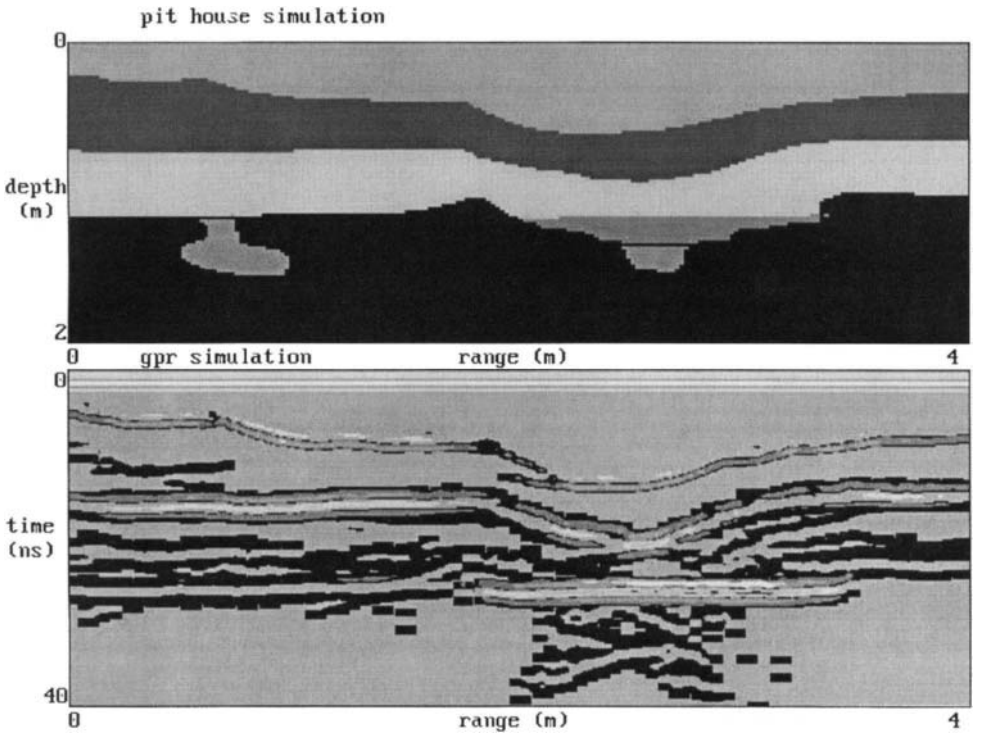

Figure 4. Two-dimensional GPR simulation of a pit-structure with a fire hearth in the floor, using a 500 MHz antenna. A storage cistern is modeled on the left side of the model. An ancient living surface is buried by two stratigraphic units of differing composition. The resulting reflection model shows that the cistern and the hearth in the floor of the pit-house would not be visible in a two-dimensional profile. The house floor would be the most visible feature in two-dimensional profiles.

6. THREE-DIMENSIONAL AMPLITUDE ANALYSIS

The massive amount of GPR data collected, the complexity and abundance of the reflections recorded and the length of time it takes to identify visually and then manually correlate reflections in order to produce valuable maps can still be a daunting task. An extremely valuable data processing tool that can quickly process large quantities of reflection data is the amplitude slice-map method (Conyers and Goodman, 1997: 149 [1]; Goodman et al., 1994) [5]). This

technique analyzes the relative amplitudes of reflections recorded at specific depths within a grid of data. Amplitudes of reflected waves are primarily a function of the contrast in electrical and magnetic properties between buried materials. The greater the contrast, the larger the amplitude of reflected waves is produced as radar energy crosses that boundary.

The slice-map method analyzes reflection amplitudes at defined depths and then correlates them throughout a grid. The computer can then produce maps of the spatial extent of resulting amplitudes at specific depths in the ground. In this way GPR reflection amplitudes can be analyzed in three-dimensions, by viewing progressively deeper slices in the ground. The spatial distribution of amplitudes can then be color coded and adjusted according to the relative strength of the reflections. If the buried archaeological materials produce significantly different amplitudes compared to the surrounding materials, their exact depth and dimensions can be mapped.

At some archaeological sites, where buried features have very distinct physical properties and the surrounding matrix is relatively uniform, the production of amplitude slice maps may be enough to accurately map the site. For instance, in an area where pit-house floors or burial chambers are surrounded by fine-grain sand and silt, a high amplitude reflection will be generated at the floor, but few if any other reflections will be produced. Amplitude slices-maps in these cases can be used to quickly map all significant archaeological features. However, if the stratigraphy of the media surrounding archaeological features is highly variable, high amplitudes can be produced from many non-archaeological elements, producing a potentially very complex and possibly misleading set of maps. This phenomenon can be accentuated if stratigraphic layers are lying at an angle to the slice orientation. If this were the case, when a time-slice crossed a stratigraphic horizon, a high amplitude anomaly would be produced, also leading to possible misinterpretations.

7. EXAMPLES OF GPR SUCCESSES FROM THE AMERICAN SOUTHWEST

The American Southwest is an excellent environment for GPR mapping, but one where traditional archaeological techniques have mostly been used to the exclusion of geophysical methods. Only recently has GPR been successfully applied to a number of site identification and buried feature mapping problems that typically confront archaeologists in this area. This high plateau and desert area of Colorado, Utah, New Mexico and Arizona is an area of abundant buried remains, including pit houses, kivas (semi-subterranean circular pit features used for ceremonial activities) and storage pits. The climate and geological processes active in this area produces an abundance of dry sandy sediments and soil, an excellent medium for radar energy penetration.

Traditional archaeological exploration and mapping methods used for the discovery of buried sites include visual identification of artifacts in surface surveys, random test pit excavation and analysis of subtle topographic features, all of which may indicate the presence of buried features. While these methods can sometimes be indicative of buried sites, they are extremely haphazard and random, often leading to misidentification or non-identification of features.

At a site near Bluff, Utah, a local archaeologist used some of these techniques to map what he considered to be a large pit house village. The area is located in the floodplain of the San Juan

River, an area that was subjected to repeated floods during prehistoric time, often burying low lying structures in fluvial sediment. In a grid that was roughly 50x30 meters in diameter, surface surveys had located 4 or 5 topographic depressions that appeared to be subtle expressions of pit houses in what was presumably a small buried village. Lithic debris from stone tool manufacture as well as abundant ceramic sherds were found in and around these depressions, further enhancing this preliminary interpretation.

A GPR survey was conducted over this prospective area, using paired 500 MHz antennas, which transmitted data to a maximum depth of about 2 meters (Conyers and Cameron, 1998 [6]). While data were being acquired, reflection profiles were viewed on a computer monitor, as well recorded digitally. A preliminary interpretation of the raw data in the field showed no evidence of pit house floors in the areas containing the depressions. Surprisingly, a large distinct floor was located in one corner of the grid, an area not originally considered prospective. Velocity information, obtained in a nearby pit being dug for a house foundation, was used to convert radar travel time to depth.

An amplitude time-slice map was then constructed in a slice from about 1.2-1.5 meters depth, a slice that would encompass the pit house floor and all sub-floor features. A map of the high amplitudes in this slice shows an irregular shaped floor with a possible antechamber and an entrance at opposing sides of the pit structure (Figure 5). In order to confirm this interpretation, derived only from the GPR maps, nine core holes were dug on and around the feature. All holes dug within the mapped feature encountered a hard-packed floor covered with fire-cracked rock, ceramic sherds and even a small bone pendant, at exactly the depth predicted from the GPR maps. Those cores drilled outside the pit house, and in the area of the shallow depressions originally thought to be the location of the houses, encountered only hard, partially-cemented fluvial sediment with no archaeological remains.

This GPR survey demonstrates the advantages of performing GPR surveys in conjunction with typical surface topography and artifact distribution mapping. The standard methods of site exploration indicated the presence of nearby pit houses, but both the artifact distributions and the subtle depressions pointed to the wrong area. If only these indicators were used as a guide to subsurface testing, it is doubtful any archaeological features would have been discovered. Only when used in conjunction with the GPR data was the pit house discovered. It is not known at this time what may have created the subtle depressions that were originally interpreted as pit houses. The artifact and lithic scatters noticed on the surface were likely produced by rodent burrowing, which brought these materials from depth and then concentrated them randomly across the site.

A cautionary lesson about how changing conditions can affect GPR mapping was learned at this site when a second GPR survey over the known pit house was conducted a few months later after a large rain storm. This survey produced no significant horizontal reflections in the area of the confirmed pit house, but many random non-horizontal reflections throughout the grid, none of which looked like house floors. These anomalous reflections were probably produced by pockets of rain water that had been differentially retained in the sediments.

At a well known archaeological site, also near Bluff, Utah, a second GPR survey was performed in an area where a distinct surface depression indicated the presence of a Great Kiva, a large semi-subterranean structure typical of Pueblo II sites in the American Southwest (Conyers and

Cameron, 1998 [6]). A 30x40 m^2 GPR survey using both 300 and 500 MHz antennas was conducted over this feature, to be used as a guide to future excavation. Individual GPR profiles of both frequencies showed only a bowl shaped feature, which appeared to be filled with homogeneous material with no significant reflection (Figure 6). There were no discernable features within the depression that would correspond to floor features or possible roof support structures.

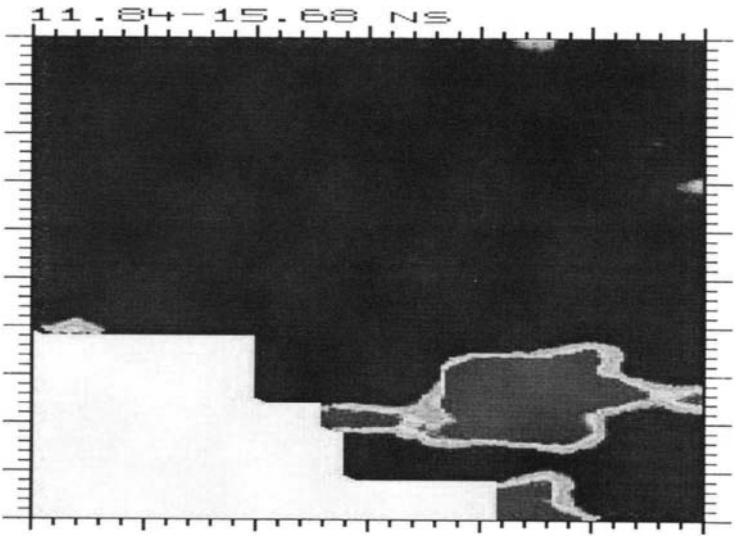

Figure 5. Amplitude slice map showing a square pit-structure with an entrance and possible anti-chamber.

Amplitude time-slice maps were then produced for the grid in the hope that subtle changes in amplitude, not visible to the human eye in normal reflection profiles, might be present in the data. When this was completed, the slice from 1.33 to 1.54 meters in depth (Figure 7) showed a square feature deep within the depression, which was later found in two excavation trenches to be the wall of a deeper feature within the depression (Conyers and Cameron, 1998 [6]).
The origin and function of this feature is not yet known. What can be concluded from this exercise in GPR data processing is that the computer is capable of producing images of subtle features that cannot be readily processed by the human brain. Without this type of GPR processing, this deep feature would most likely not have been discovered or excavated.

Near Tucson, Arizona, a well documented Hohokam Period village has been partially excavated on a gravel terrace above the Santa Cruz River (Conyers and Cameron, 1998 [6]). Known archaeological features at the site include pit structures, large storage cisterns and ceremonial ball courts. The archaeological site is covered by sheet wash and wind blown sediment, burying most features under more than a meter of sediment. The usual method for identification of

subsurface remains in this area is by excavating long trenches using a mechanized backhoe. This method can be quite effective in locating features, as long as they are in the path of the trench, but often, significant structures are destroyed during discovery. In addition, little can be discerned about the exact orientation of the buried features encountered, and nothing at all can be determined about the areas between the trenches.

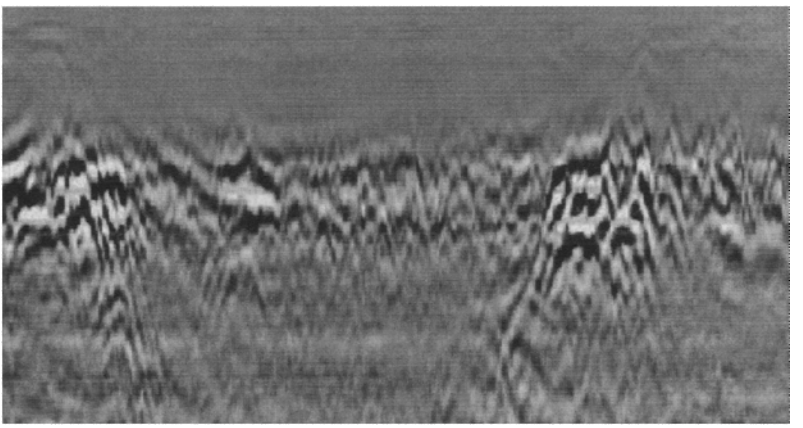

Figure 6. Reflection profile across a Great Kiva. The walls of the kiva are the high amplitude reflections, while the interior of the kiva is filled with wind blown sand, which reflects little radar energy.

To map the known features , found in previous trenching operations, more accurately, and to prospect for possible other remains between trenches, a 30x40 meter grid of 500 MHz GPR data was acquired. The initial results were very disappointing. The radar profiles visible on the computer screen during acquisition were so "noisy" as to be indecipherable (Figure 8). In fact, it appeared from first glance that the survey would be a total failure. The noise that was obscuring any reflections from within the ground appeared to have been created by radio and television transmissions common in the city.

In an attempt to filter out the extraneous frequencies and remove background noise, a low-pass filter that removed all frequencies above 800 MHz was applied to all reflection data after returning from the field. This filtering process effectively removed the interference from the radio transmission in the band width that include UHF Television and FM radio, leaving only those reflections of importance (Figure 9).

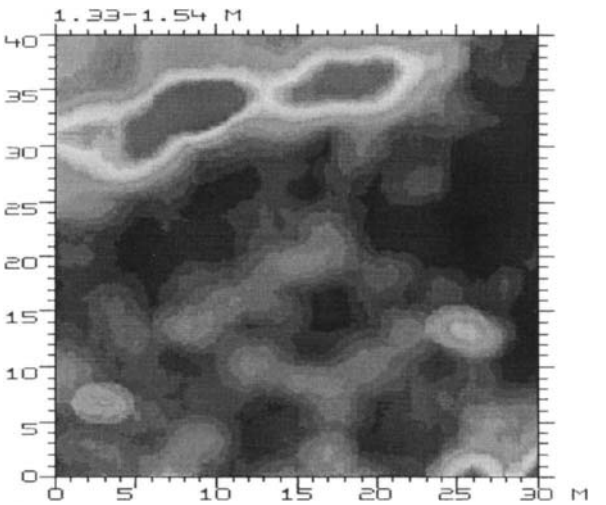

Figure 7. Amplitude slice from 1.33-1.54 meters depth showing a subtle square feature within the Great Kiva.

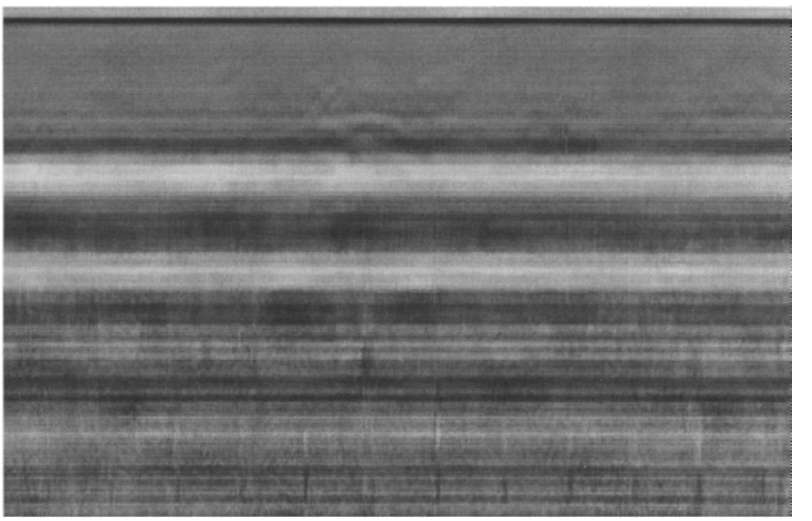

Figure 8. Unprocessed reflection data over a pit-structure in southern Arizona. This image is totally obscured by background noise.

When this was accomplished, reflection profiles within the grid were capable of mapping eleven of the buried archaeological features that were known from the trenching operation (Conyers and Cameron, 1998 [6]). Ten other features were discovered between the trenches, which would probably not have been detected in any other way. The GPR amplitude slice-maps were also capable of producing maps of the exact dimensions of all features and using velocity conversions, their exact depths in the ground were also determined (Figure 9).

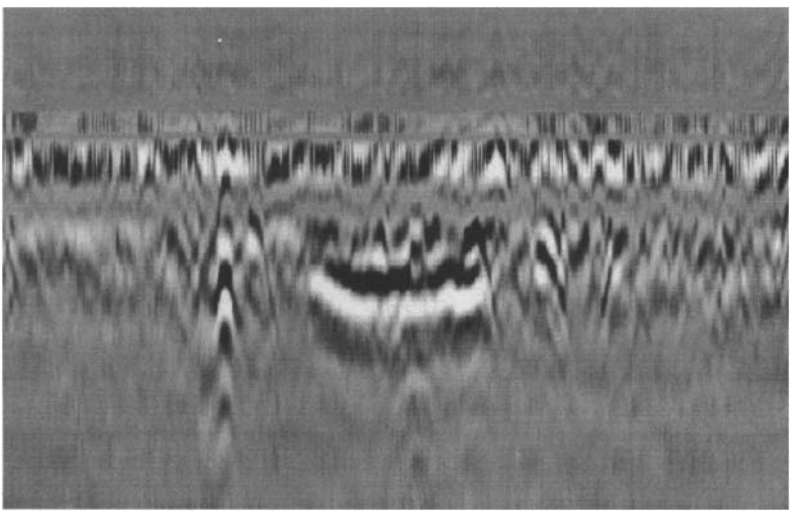

Figure 9: Processed reflection profile from the same data shown in Figure 8. Background noise was removed, frequencies were filtered to enhance reflections from within the ground and the remaining reflections were amplitude enhanced

8. CONCLUSIONS

Ground-penetrating radar surveys can be of tremendous value for the rapid, nondestructive determination of the number, character and orientation of subsurface features at archaeological sites. The GPR mapping method can be used to produce maps that are a far more complete picture of a site than is possible using excavation alone. Furthermore, where buried features are known to exist, GPR surveys conducted prior to excavation can delineate the location and approximate depth of features of interest. Excavation strategies can then be formulated to efficiently test only targeted features, preserving others.

REFERENCES

[1] L.B. Conyers and D. Goodman, Ground-penetrating Radar: An Introduction for Archaeologists. Walnut Creek, CA: Altamira Press.(1975)

[2] L.B. Conyers and J. E. Lucius, Archaeological Prospection 3 (1) (1996) 25-38.

[3] A.P. Annan. and J.L. Davis,"Design and Development of a Digital Ground- penetrating Radar System," in J.A. Pilon, ed., Ground penetrating radar. Geological Survey of Canada, (1992)Paper 90-4, 49-55.

[4] D. Goodman., Geophysics 59 (1992) 224-232.

[5] D. Goodman, Y. Nishimura, and J.D. Rogers, Archaeological Prospection 2 (1995) 85-89.

[6] L.B. Conyers and C. M. Cameron, Journal of Field Archaeology, 25, 4 (1998) 417-430.

Radiation in Art and Archeometry
D.C. Creagh and D.A. Bradley (editors)

Electrochemical impedance measurements in the conservation of metals

P.Letardi

CNR - Istituto per la Corrosione Marina dei Metalli, via De Marini 6, 16149 Genova, Italy

Electrochemical Impedance Spectroscopy (EIS) has proved a useful technique in corrosion science, in the field of protective coatings characterisation especially.

Until recently this technique has been rarely applied to metal conservation problems. The application to cultural heritage protection requires special attention to a number of particular aspects. The development of the technique for field measurement on outdoor monuments is of interest, and the classical method must be adapted to fulfil the special requirements of field measurement.

This paper presents a short overview of the EIS technique and applications to the field of cultural heritage field which are still largely under development. A specially designed measurement methodology is described for field application on outdoor bronzes. This development work is still in progress.

1. INTRODUCTION

Metals and alloys have a tendency to interact with their environment forming oxides and other compounds, which are more stable. In some cases the new compounds form a uniform, adherent and stable layer on the metal surface, preventing the metal from interacting further. In other situations the product formed is either porous and or flakes away easily, leading to a continuous loss of metal. Studies of these types of interaction lie in the field of corrosion science. The corrosion behaviour of metals and alloys is due to a complex interaction of several factors related to both the metallurgical properties of the metal (composition, structure, etc.) and to environmental factors (humidity, pollution, biological aspects, etc.). In the case of atmospheric corrosion the alternation of the different weather conditions (humidity/dry, hot/cold, cloudy/sunny, windy/steady air) and the composition of atmospheric pollutants play a key role. In its initial, polished state, metal surfaces are particularly reactive. They can develop a more or less protective layer according to the metal properties and the initial environmental exposure conditions. For example: chlorine could be present both in marine environment and as a salt spray. Its effect is strong due to its small ion size, which allows for its easy migration in the metal lattice. This creates strong potential gradients which in turn may prevent the formation of well-adhering and homogeneous oxide layers (patinas).

Several studies addressing the environmental damage to bronze monuments have been made to enlighten their corrosion behaviour (see for example [1-4] and references therein). The important role of sulphuric compounds in polluted areas has been pointed out as a driving force for the degradation of outdoor monuments, along with the synergistic effect of different

pollutants, such as NO_x and O_3 [2,6]. Nevertheless an overall comprehension of the problems and a well-established conservation approach have yet to be established.

In the field of Metal Conservation, the approach to corrosion protection is different from that that normally used in material engineering (which seeks a cost-effective solution): aesthetic aspects are the prime consideration. The concern is principally to save a masterpiece for future generations. Every artwork is the result of the overlaying of human interventions and environmental factors for long periods of time, times which are long compared to the industrial time-scale. Thus artworks are often a unique cases for which it is difficult, if not impossible, to ignore their specific requirements: general solutions and generic treatments are not possible.

Although there are metals which are more easily subject to corrosion (such as zinc) and others which are generally resistant (noble metals like gold or platinum), the corrosion resistance it is not merely an intrinsic property of a material. It concerns the *relation* of that material with a particular environment. Bronze, used since ancient times for artistic production, was generally resistant to corrosion in the weather conditions of past centuries. However environmental changes caused by the industrial era changed the behaviour of bronze with respect to atmospheric corrosion, in a manner which was different from the previous history of the art work.

In the restoration and conservation of art works both aesthetic and corrosion protection must be taken into account. These two aspects may be in conflict and it is necessary to find a right point of balance between them. Knowledge from materials science, properly applied to fulfil the peculiar requirements of conservation, can be of great assistance in formulating strategies to find innovative conservation techniques. In particular, knowledge and methods normally applied in the fields of corrosion science and protective coating technology can offer new evaluation tools for conservation and restoration of bronzes, and they can prove valuable for the characterisation of innovative protection methodologies, once they have been adapted to fulfil peculiar conservation requirements. The aim of this paper is to present one of these possible applications, namely the development of impedance measurements for corrosion characterisation, describing the state of the art of a project still under development.

For the sake of simplicity, we will focus on the conservation of outdoors bronze statues. Several of the concepts and methods we deal with may be directly applied or straightforwardly extrapolated to other metal objects of artistic interest.

1.1 Corrosion of Metals

A general description of the theory of metal corrosion is outside the scope of this paper, and several textbooks exist on the argument (see, for example [7,8] and references therein). Here after, only some basic aspects are reported, in order to enlighten the fundamental principles impedance spectroscopy is based on.

Metallic corrosion is electrochemical in nature. From a general point of view, we can consider ***oxidation***

$$M \rightarrow M^{n+} + ne^-$$

in which a metal (M) has an anodic behaviour and it undergoes a *dissolution* process, and ***reduction***

$$M^{n+} + ne^- \rightarrow M$$

in which there is a cathodic behaviour with a *deposition* process. In the atmospheric corrosion of metals the main cathodic reaction is the oxygen reduction:

$$\frac{n}{2}O_2 + nH_2O + 2ne^- \rightarrow 2nOH^-$$

which may follow a complex mechanism due to the environment and the metal. Oxidation and reduction reactions cannot take place separately: they are only partial reactions (electrode reactions), which should proceed in a way that the electrons produced by the first one are consumed by the second. In the case of metal dissolution in an aerated environment the full process will be:

$$2M + \frac{n}{2}O_2 + nH_2O \rightarrow 2nOH^- + 2M^{n+}$$

More generally anodes and cathodes can form on a single piece of metal because of local differences in the metal or in the environment.

For the sake of simplicity we limit our discussion here to the simpler description in which oxidation and reduction occur on separated areas. More refined models exist to take into account situations where it is not possible to identify well-separated anodic and cathodic zones. For the reaction to proceed there should be an electrical link between anodic and cathodic area to allow for an electron flux (current density) to exist. Furthermore that areas should be connected through an electrolyte which allows for the migration of ionic species. The flow of current through the cell is proportional to the amount of metal that corrodes. In the absence of an electrical link no current will flow, and an electric potential difference ΔE will exist between anodic and cathodic areas. One can arbitrary assign a zero value to the potential of a chosen electrode reaction, and define the potential E of any other electrode reaction as the potential energy difference with respect to the reference electrode one. As the cell voltage is linked to the Gibbs Free Energy associated with the reaction, it can be shown that a metal will corrode (will behave as the anode) if a cathodic process is available so that $E_{an} < E_{cat}$. The bigger the difference, the bigger the corrosion rate, in the absence of kinetic slowing factors. Conventionally the hydrogen reduction reaction

$$2H^+ + 2e^- \rightarrow H_2$$

(at 25 C, 1atm, pH=0) has been assigned the zero potential energy. One can than order the metals according to the value of their electrode reaction potential in standard conditions E^o (electrochemical series) which will roughly indicate their higher or lower easy to play as the anode (i.e. to corrode). Several other aspects play a key role in electrode potential, such as pH [9], activity and solubility of the ions in the electrolyte [8].

When an electrochemical interface is displaced from its equilibrium condition by using an external energy supply, permanent charge and mass changes appear. This is due to (i) electrochemical reactions responsible for charge transfer, (ii) gradients of electrical and chemical potentials responsible for the transport of reacting species. Both thermodynamic and

kinetic factors determine the electrode reaction evolution. The behaviour of the corresponding current density as a function of the difference between the equilibrium potential and the actual potential (over-voltage) is due to particular polarisation effects arising at a specific electrode area. Several polarisation effects may occur. The simpler one is due to the finite resistance to charge migration in the metal and electrolyte, so that to a current flow corresponds to a voltage fall iR. If the current is interrupted, this voltage drop disappears immediately. Concentration polarisation is determined by the evolution of a species as the electrode reaction proceeds, with ion migration and build up of reaction products resulting in the development of a back electromotive force. When the current is interrupted, this concentration polarisation will decay with a half-life whose value is linked to the activation energy of the process (diffusion, chemical reaction, etc.). To the microscopic behaviour correspond electrical components such as resistance and capacitors. It is thus possible to get information on the thermodynamic and kinetic process occurring at a specific metal/electrolyte interface by studying its electrical behaviour.

Corrosion rate and its morphology depend both on the equilibrium potential energy differences and on the particular processes developing in the specific anodic and cathodic zones.

1.2 The Electrochemical Impedance Spectroscopy

Electrochemical Impedance Spectroscopy (EIS) has been recognised from the middle of the twentieth century as a powerful tool in coating research mainly. Two major obstacles were to be faced for successful implementation: insufficiently fast and accurate instrumentation and the interpretation of measured spectra. The rapid development of electronics and the widespread diffusion of more and more powerful Personal Computers have largely contributed to overcome those difficulties and to a growth in the application of this technique in corrosion science.

Several review papers and textbook on EIS are available [10-16]. In this paragraph a short introduction to the main principles of the technique will be provided. Only potentiostatic measurements at open circuit potential will be considered, as these are of interest for non-destructive measurements on art works.

Even though the overall current-voltage behaviour of corroding systems is not linear, it is possible to apply a small enough perturbation voltage so that linear-response approximation is valid. EIS measurements consist of the recording of the response current produced by the system under study to the application of a small voltage perturbation around the equilibrium potential. As the relaxation properties of electrochemical systems play a key role, one should consider the time response of the system. In the linear approximation range, the response to a sinusoidal perturbation ***voltage*** of frequency f ($\omega = 2\pi f$):

$$V(t) = V_0 \cos(\omega t) \tag{1}$$

is a sinusoidal ***current*** with the same frequency:

$$I(t) = I_0 \cos(\omega t - \phi) \tag{2}$$

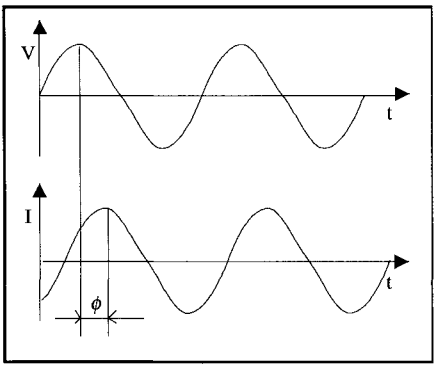

Figure 1. Relationship between sinusoidal Voltage excitation and response Current for a linear system

The current I is shifted by a phase ϕ determined by the relaxation processes (Figure 1). The system response function is the impedance, defined as:

$$Z = \frac{E(t)}{I(t)} = \frac{V_0 \cos(\omega t)}{I_0 \cos(\omega t - \phi)} = Z_0 \frac{\cos(\omega t)}{\cos(\omega t - \phi)} \tag{3}$$

and measured in Ohm. From the above expression it is clear that for each frequency impedance should be described by two associated quantities, i.e. it is represented by a complex number; thus impedance is a complex function of frequency. In an EIS spectrum acquisition, Z is measured for a number of frequencies ranging from a few mHz up to 100 kHz. According to standard complex function representation, impedance can be described as a real and an imaginary part:

$$Z(\omega) = Z_{re}(\omega) + j\, Z_{im}(\omega) \tag{4}$$

(where j is defined as the -1 square root) or as a modulus and a phase:

$$Z(\omega) = |Z|\,(\omega) \exp[j\, \phi(\omega)] \tag{5}$$

where:

$$|Z| = \sqrt{Z_{re}^2 + Z_{im}^2} \tag{6}$$

$$\phi(\omega) = \arctan\,(Z_{im}(\omega)/Z_{re}(\omega))$$

Accordingly two classical graphical representations of the impedance are used which are called Nyquist and Bode plot respectively (Figure 2). Nyquist plots are usually helpful in recognising the kind of processes. In a Bode plot the modulus is plotted on a logarithmic

scale, and this could be particularly useful when processes on quite different time scale are present.

The usual electrochemical cell for EIS measurement (Figure 3) consists of a sample of the metal under study eventually coated with a protective treatment (the Working Electrode WE), immersed in an electrolyte containing vessel together with a piece of an inert metal (a platinum mesh or a graphite rod usually), named the counter electrode (CE), and a reference electrode (REF), whose property should be to have a negligible contact potential regardless of the environment in which it is placed. (The most common lab references are the Saturated Calomel Electrode (SCE) and the Silver/Silver Chloride (Ag/AgCl)). Often the electrochemical cell is obtained sticking a cylinder on the sample with some sealing system and filling it with the test solution, the CE and the REF electrode). The reference electrode allows the measurement of the WE equilibrium potential at open circuit E_{oc}. The electrochemical reactions being studied occur at the working electrode. The current that flows into the solution via the working electrode leaves the solution via the counter electrode.

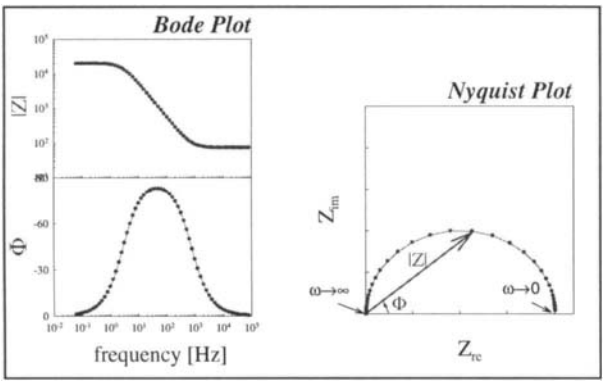

Figure 2. EIS spectra of a bare metal/electrolyte system as Bode and Nyquist

Commercially available measurement instrumentation consists of a potentiostat and a Frequency Response Analyser. The former is an electronic device that controls the voltage difference between REF and WE and allows measuring the cell current; the latter generates the sinusoidal excitation signal sweeping through the frequency range and performs the vector analysis to compute the impedance. Several computer programs are available for spectra acquisition and data analysis. EIS spectrum measurement takes time (hours, perhaps days). The system being measured must be at a steady state throughout the time required to measure the EIS spectrum. In practice a steady state may be difficult to achieve. The cell can change through adsorption of solution impurities, growth of an oxide layer, build up of reaction products in solution, coating degradation, temperature changes, to list just a few factors.

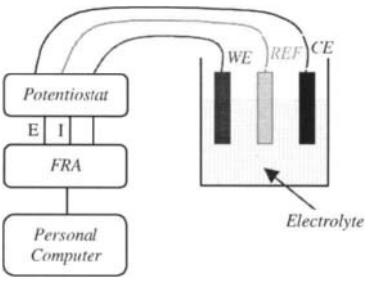

Figure 3. Schematic representation of classical EIS measurement setup (electrochemical cell-Instrumentation)

For a bare metal, ions that are absorbed at the metal solution interface create a charged double layer, which behaves like a leaky capacitor, while the bulk of the solution acts as a resistor. The impedance measured on such a system could thus be modelled like the electrical circuit shown on Figure 4: impedance measured on the electrochemical cell and the one produced by the electrical circuit are the same, once the circuit parameter values R_s, R_{ct} e C_{dl} are properly chosen.

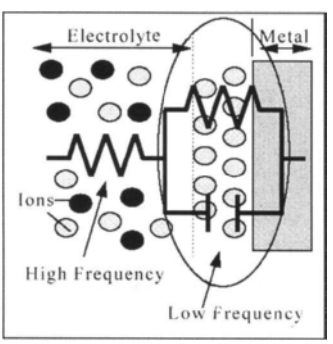

Figure 4. Electrical circuit model for a bare metal/electrolyte system. The corresponding EIS spectra is shown in Figure 2.

In general it is possible to describe the processes at a metal- (coating-) electrolyte interface with equivalent circuit elements. Analysis of EIS spectra is usually performed in terms of equivalent circuit model. The model involves the type of electrical components and their interconnection, in order to produce the correct spectrum shape, and the numerical values of the model's parameter, so as to fit the size of each feature in the spectrum. Although there is a general agreement on equivalent circuit application to EIS data analysis, their physical interpretation is often subject to discussion. When dealing with equivalent circuit caution should be used in drawing conclusions, as there is not a unique equivalent circuit that describes an impedance spectrum [15].

The equivalent circuit elements more widely used are reported in Table 1, with a brief physical interpretation and their typical impedance spectrum. A short description of the basic equivalent circuit used is given in Table 2.

The impedance measured on an electrochemical system depends on the surface involved. In order to compare results impedance for unit surface is usually considered (Ohm*cm^2).

Impedance measurement on good protecting coating implies the measurement of very low currents, and this could cause problems with the instrumentation if its input impedance is not well-matched to the cell. In this case measurement drawbacks increase with lowering the measuring surface [13].

EIS has been applied to a wide range of metal substrates and coating cycles [17]. It has provided a remarkable insight into the protective properties of organic coatings, as well as of the corrosion degradation phenomena occurring under the coating [12].

Other electrochemical techniques can be efficaciously applied to cultural heritage problems [18-22], which are outside the scope of the present paper.

Some of the advantages of AC impedance techniques are the use of only very small signals which do not disturb the electrode properties to be measured and the possibility of studying corrosion reactions and the measurement of corrosion rates in low conductivity media were traditional DC methods fail.

2. ELECTROCHEMICAL IMPEDANCE MEASUREMENTS FOR ART OBJECTS

EIS measurements have been scarcely applied in the cultural heritage field; quite recently one can note an increasing attention [23-26]. Apart from classical laboratory study, field measurement could be of interest as a tool for corrosion characterisation of outdoor bronze statues, as not many techniques are available in this field [27,28]. The development of a measuring method directly applicable on art works is therefore highly desirable. To this end several requirements must be fulfilled: measurement must be performed in a non-destructive way; appropriate electrochemical cells, suitable for application on the particular work of art, must be developed; widely applied electrolyte (for example: sodium chloride or sodium sulphate solutions) should be avoided to prevent the contact of dangerous ions on the surface of the art work. It seems useful therefore to design a measurement method especially devoted to cultural heritage applications. Several issues have to be addressed: how to build up an "electrochemical probe" to be safely applied on a statue surface; how small the area involved in the measurement could be, which could be the most suitable electrolyte. A research project has been developed to this aim [29].

The design adopted is schematically reported in Figure 5, and will be described in Section 2.3.2. It derives from the probe developed for polarisation resistance measurements [18-20], modified to take into account the different measurement requirements. This kind of *contact probe* can be easily applied on a measuring surface and no meaningful traces would be left (as perhaps it might be with gel or sealing tools). All the used materials are easily available and low cost.

To validate the new developed EIS measurement method, the spectra obtained should be checked for stability range, possible experimental drawbacks, and so on. A detailed analysis may be exceedingly too time-consuming, because of the several factors possibly affecting the

electrochemical systems of interest. Therefore an iterative refinement method has been shown in Figure 2.

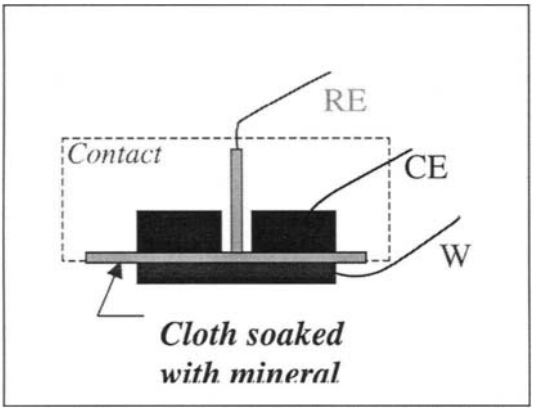

Figure 5. Schematic design for the contact cell adopted for EIS Measurement.

At first EIS measurements with a rough version of the contact probe has been performed to test the general validity of the spectra obtained. Then further refinements have been made on the cell construction and on the measurement details to improve spectral quality. Section 2.2 deals with the rough check of the general validity of EIS spectra obtainable with the contact probe. A detailed description of the measurement method developed is postponed to section 2.3.

To compare the influence of the several parameters investigated, we found it useful to focus on the low frequency limit of the Impedance modulus |Z| [25,30,31]. The variation on the $|Z|_{f=63mHz}$ has been used as a first comparison tool to evaluate the effects of the several factors possibly affecting measurement results. We define a spread factor V as the ratio between the maximum and minimum value obtained. It should be noted this is just a very rough method for validating the system.

2.1 Experimental details

At first [29], samples have been prepared with an easy available 85-5-5-5 bronze (B4). A disk 2cm diameter has been polished with metallographic paper up to grit 1200, degreased in an ultrasonic bath, rinsed with de-ionised water and dried in air. These samples were produced in a limited numbers (sample label beginning with "D"). Later other samples have been prepared from a cast ingots (nominal composition Cu 90%, Zn 8%, Pb 2%) (B3) following the same procedure. We were given the B3 bronze in two trances. The first (B3I) – for which we had only a small amount - had a fairly high level of defects and porosity from which coupons 2x5 cm have been obtained (sample label beginning with "L"). The second (B3II) had better properties and coupons 3x3 and 6x6 cm have been obtained (sample label beginning with

"Q"). Colleagues have made a few other bronze 3.5x2.5 cm samples available (sample label beginning with "F"), aged in climatic chamber [32], and showing a dark-brown patina.

As test coating we have chosen Soter (a mixture of micro-crystalline waxes with benzotriazole), which has been already tested with traditional methods [33,34]. At present waxes seem the more appreciated protective coating for bronze art works because of their reversibility and aesthetic appearance. This wax characterisation is also required as a first step in the analysis of the more complex double coatings systems that has been recommended [33-35]. The coating of the samples with Soter 201 LC has been performed by a conservator. At this stage only B4 and B3I samples have been waxed. The small samples dimension could lead to a poor quality of the coating film. Initially this was not a problem, as the principal aim was the testing of the measurement method. Better samples are necessary when focussing on the characterisation fo the properties of the coating.

Natural weathering has been performed in a marine exposure site, according to a standard procedure. At present, unexposed samples and B4 samples after 3, 12 and 16 months have been characterised. XRD and reflection FT-IR spectra have been recorded on these samples in order to identify main patina components and the modification of the coatings [36].

EIS measurements have been made with a Gamry apparatus (femtostat, with CMS100/CMS300 V3.02 software © 1989-98 Gamry Instruments, Inc.), which is suitable for field operation.

2.2 General approach test

To establish the suitability of the measurement configuration developed for field application on art objects, we have analysed spectra obtained on bronze and waxed bronze, both in laboratory condition and after natural weathering in a marine-urban environment [29]. Even though initial measurements (Figure 6) are prone to a remarkable spread, it is possible to identify main spectral feature and make the following statements [29,36,37].

* The qualitative behaviour of measured spectra is quite similar in shape and order of magnitude to classical EIS measurements on similar systems. In particular one can observe an almost Randles-like behaviour for polished bronze, while the |Z| on waxed bronze ranges roughly from 10^3 to 10^7 Ohm*cm^2 through the frequency range considered. This is the same range obtained for poor quality wax with a classical EIS measurement method [24], which could be considered to be reasonable considering the suspected poor quality of our waxed samples.

* The EIS spectra obtained on the different systems under investigation (bronze, waxed bronze, weathered bronze, weathered waxed bronze) are clearly distinguishable: The EIS spectra differ in shape and the low frequency |Z| values differ by orders of magnitude.

This allows stating the validity of the measurement scheme adopted and its possible application as a monitoring tool for outdoor bronzes. Based on these results a more refined study on the measurement details has been undertaken.

2.3 Measurement configuration

The measurement conditions should be similar as possible to that existing in the environment of the work of art. For outdoor bronzes this could be difficult. In particular measurements require a wet condition while real exposure is characterised by wet/dry alternation.

Figure 6. Initial measurements on B4 bronze (A) [bottom] and waxed bronze (B) [top] after exposure to weathering.

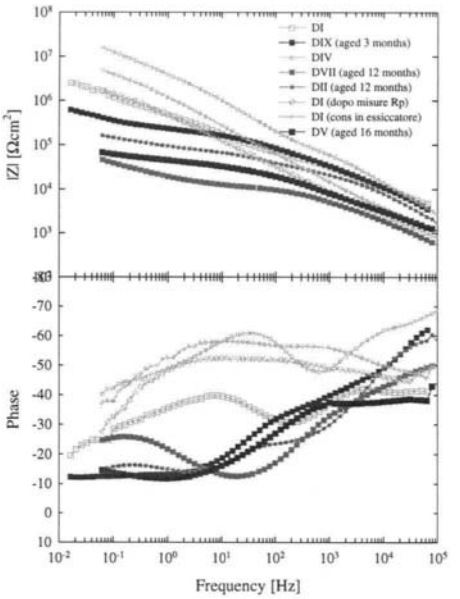

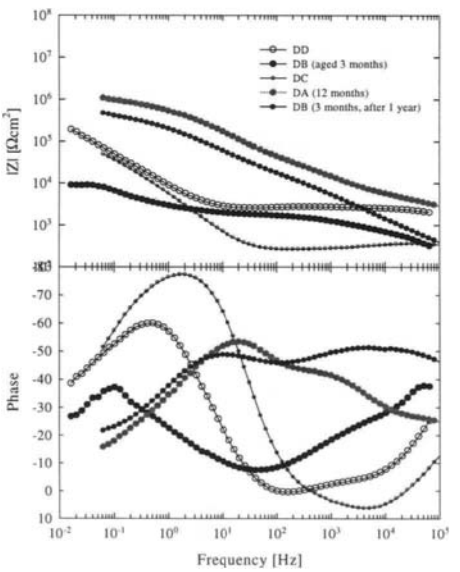

Suitable measurement conditions should:

- create a wet condition similar to the wet phase of the atmospheric exposure;
- produce repeatable and reliable measurements;
- cause no damage the artwork (the measurement effects should be in the range of natural condition fluctuation).

Correlation between measured corrosion rate (all wet condition) and real ones (wet/dry), may then be established with a proper technique of investigation.

2.3.1 Electrolytes

The electrolyte applied in the EIS measurements should provide a good enough conductivity between electrodes and it should be the same medium as occurs in the natural corrosion process under study. For outdoors bronzes the "*natural*" electrolytes are rain, atmospheric humidity with their associated pollutants dissolved in them [2]. Practical considerations demand the use of simple and easily available solutions. Several choices may be considered.

- Standard chloride or sulphate solutions are widely applied in coating characterisation for marine and industrial applications. They are undesirably aggressive and do not seem suitable for cultural heritage applications.
- Town water supplies are subject to uncontrolled chlorinating, which is undesirable both for the variability in the water composition and for the possibly not negligible presence of dangerous chlorine ions;
- Natural mineral waters have several appealing characteristics. They have a fairly well defined composition and, at least in Italy, their chemical and physical properties are reported on the commercial label. They are usually readily obtainable and cheap, and a wide choice is available, with electrical conductivities ranging from as low as 80 $\mu S/cm^2$ up to 2000 $\mu S/cm^2$. Based on the experience on R_p measurements, a mineral water with 200 $\mu S/cm^2$ have been chosen.
- Natural or artificial rain would be an interesting choice but acquiring stocks of this is not as straightforward as using a bottle of well-characterised mineral water. Thus its application has not been considered in the initial stage.

Tests on bronze with a mineral water with 262 $\mu S/cm^2$ and a slightly different ionic composition (Figure 7) showed negligible differences at present refinement status (spread factor$\approx$1.1).

To simulate an electrolyte layer, a cloth soaked with the mineral water has been used to keep the electrolyte between the sample and the contact probe. A commercial glass cleaning cloth has been chosen for its smooth surface and macroscopically homogeneous structure. Several tests have shown the behaviour of this cloth to be somewhat unsatisfactory because a fairly wide spread in measurements results through its use. Some improvement has been obtained by careful washing in deionised water before use, and at least two hours soaking in a vessel with the mineral water before cell assembling (cloth conditioning). The behaviour of the cloth has not yet been fully investigated. Further tests are in progress to better define operation rules to improve measurement repeatability.

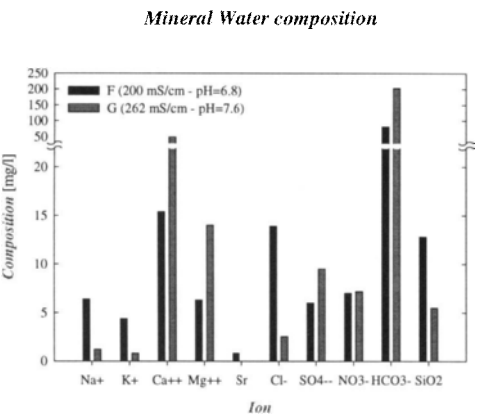

Figure 7. Composition of the mineral waters used for measurements, as stated by the producers.

2.3.2 Cell design

So far, our different prototype contact probes have been tested. All of them are based on the generic scheme already shown in Figure 5. Differences consist of electrodes metal choice, method applied to keep together CE and REF and to connect the cell cables to them, and cell size (i.e. measurement area). The experimental data are summarised in Table 3.

Prototype CV was used initially. It is a very rough version, which can not be considered for use in field applications. Nevertheless it has proved quite useful for a first characterisation of the contact probe for EIS measurement.

Prototypes D15, D20 have then been tested. They have been made with the same technique applied for Rp probe [19]. Their compact design makes them suitable for use in practical applications. Unfortunately measurements obtained with that probes showed severe deficiencies at high frequency (Figure 8). The poor dielectric properties of the resin and cell lead connection and placement are possible reasons why the high frequency performance is poor. It must be stresses that some investigations of the construction have clearly shown the electrical connection with CE and REF to be quite critical. The comparison of EIS spectra obtained with D15 and D20 - distinguished by the size only – do not show any significant differences. Thus one can state - at the present degree of refinement – that a surface area as small as 1.77 cm^2 is suitable for EIS measurements.

For ST15 probe, the CE and REF have been mechanically inserted in Teflon (PTFE), which is a quite common insulating material in electronics applications and it is a recommended material for use in electrochemical cell construction also [16]. AISI 316 Stainless Steel has been chosen for the CE for its quite good corrosion performance in the environment in which measurements are going to be performed. The same material has been used for REF also, as it is cheaper than platinum and comparable performance have been achieved using it. Th connection of the leads has been made -through a pin plug (CE) and a banana socket (REF) - so that CE and REF leads can approach the cell from orthogonal

directions. EIS spectra measured on polished metal with that probe show an almost ideal resistive behaviour at high frequency, as expected (Figure 8). Some discrepancies still remain at higher frequencies. It should be noted that the low frequency behaviour of EIS spectra is almost the same for all the prototypes. (A spread factor of 1.2 exists in this case).

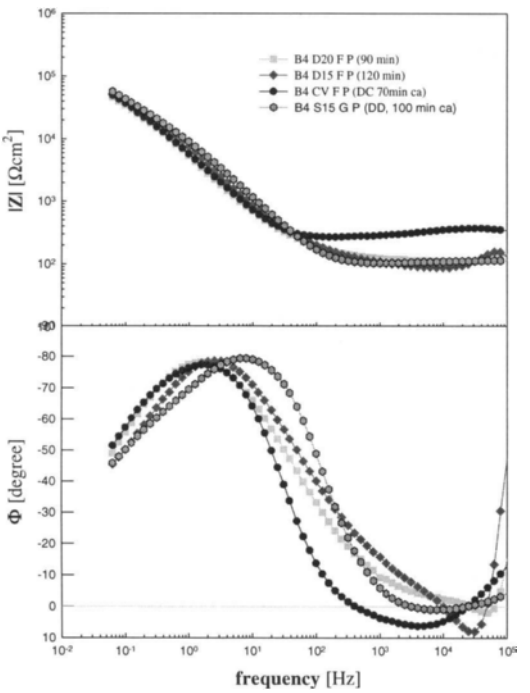

Figure 8. Comparison of EIS spectra obtained on polished bronze B4 with the different prototype contact probes tested.

2.3.2 Data acquisition

Measurements in the high frequency region are interesting for high quality coating characterisation. Because very low frequency measurements require a prohibitively long measurement time a frequency range 100KHz - 63mHz has been selected. With this range spectrum acquisition time with our instrumentation is about twelve minutes. When the contact probe is fitted on the sample, its equilibrium condition is altered because of the surface wetting. Although one would like to make a measurement as soon as possible, it is necessary to wait enough time for the system to reach an equilibrium condition. More practically it seems reasonable to wait until the variation of E_{oc} is not greater than the excitation voltage V_o. An excitation voltage amplitude V_o=10mV has been adopted for measurements. Larger values

would not be suitable as deviation from linearity and non-destructiveness could arise. Spectra with a well-conditioned cloth have been measured on different samples at 3 to 4 equilibration times in the range 10→140 minutes. The E_{oc}.vs.time monitoring utility in the Gamry software has proved quite useful because it allows better control the equilibration evolution sample by sample. Generally the first 10→30 minutes show the most remarkable E_{oc} variations (Figure 9), which usually occur and stay small in the 30→90 minutes range. Sometimes the slope shows a new increase at longer equilibration times.

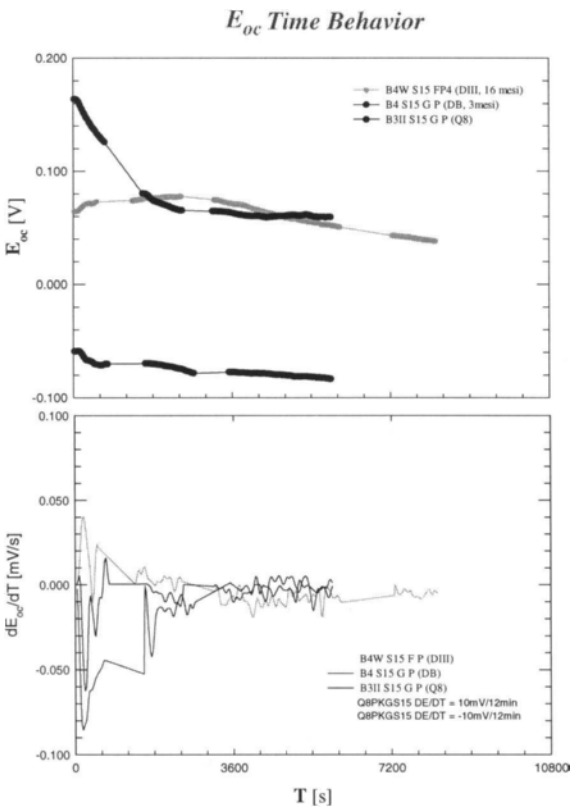

Figure 9. Open Circuit Potential. vs. Vref (AISI 316 Stainless Steel) evolution with elapsed time from cell mounting (A) and its derivative (B). Lack of points on plot (A) correspond to the EIS acquisition and new measurement start times. The grey reference lines correspond to a variation of 10 mV (equal to the EIS measurements applied potential) in 12 minutes, which is the approximate spectrum acquisition time.

A more detailed analysis has not been undertaken, because field measurements will take advantage of short equilibration times. The EIS spectra in the considered time range show

small smooth modifications (Figure 10), with a spread factor ≈ 1.6→1.8, which reduces to 1.1→1.3 if we discard the ten minute measurements. Repetition of spectrum acquisition on polished bronze allows to state measurements made at the same equilibration time are almost the same (Figure 11), with a spread factor 1.2 for 10 minutes equilibration time and 1.1 for longer ones.

A sodium chloride deposit was identified by XRD on 12-month weathered B4 samples, which have been dissolved and mainly removed during EIS measurement (CV prototype). The small amount of low conductivity water that is used for the contact probe EIS measurements results in a relatively strong variation of the actual electrolyte conductivity because of dissolution of highly soluble salts. This produces uncontrolled alteration of measurement conditions. For this reason 16-month weathered B4 samples have been softly washed, by dropping 50cc of deionised water on each sample. Spectra using a well conditioned cloth have been measured on three waxed samples weathered 16 months with prototypes CV, D20 and D15. As obtained on polished bronze, prototypes D20 and D15 gave poor results at higher frequencies, while at lower one the three spectra are comparable, with a spread factor 1.6. Repetition of spectra acquisition on those samples showed a significant increase of impedance value, with a spread factor 13.8 between the first and the fourth measurement. Several other measurements have been repeated on one of these samples showing a slowing down increase, with a global spread factor ≈ 30. This suggests that a better analysis technique is needed for weathered samples so that a well-established procedure for measurements comparison and non-destructiveness can be established.

2.4 Measurement : Non-Destructive Testing

Applying EIS measurements on artworks non-destructiveness is our prime aim and we test to determine that this is indeed the case. In principle measurements at E_{oc} should not produce any damage. Nevertheless a drift of potential during measurement could shift the system into the anodic zone. Moreover we have to consider measurement requirements for surface wetting, which will in general cause an alteration of the equilibrium condition. In evaluating possible traces left by measurements, it is safe enough to allow for measurement effects in the range of possible "natural" fluctuations on artworks, such those induced by weather conditions variations.

The measurements performed to analyse the EIS spectra evolution with equilibration time allow the acquisition of some information on measurement effects also. The E_{oc}.vs.t curves do not show relevant discontinuities before and after EIS spectrum acquisition (Figure 9A), which means measurement does not alter the electrode equilibrium.

On polished bronze samples, a slight darkening on the measurement area appears, analogous to the stain left by drop of waters. A similar darkening is observed, after polishing, on samples left to laboratory atmosphere, and it is due to surface oxidation. No such halo has been observed after measurement on climatic chamber aged samples, for which the dark-

brown patinated surface is not so reactive as polished metal one. Measurements on unexposed waxed samples showed neither visual alteration nor relevant spectra modification.

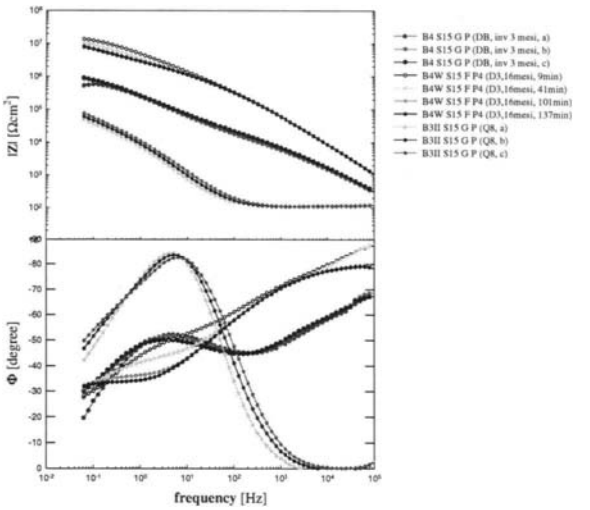

Figure 10. EIS spectrum evolution with the elapsed time between cell mounting and measurement for the same samples shown in Figure 9.

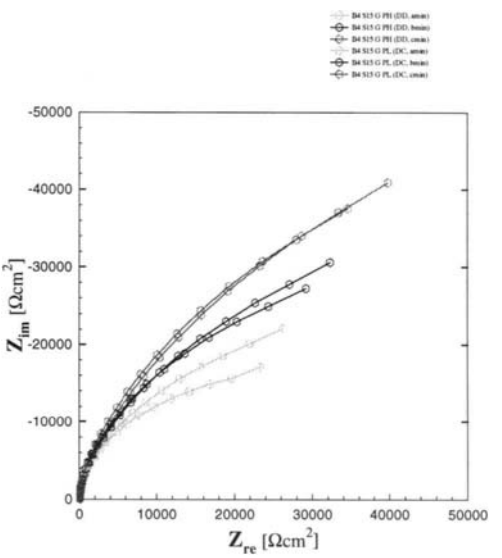

Figure 11. EIS spectra obtained on two different polished bronze samples

Measurements on weathered samples are the most relevant for field application on outdoor monuments. As previously pointed out, soluble salts are possibly present at the surface of weathered samples. Some thought is advisable before undertaking measurement on an unwashed surface. For softly washed samples repetition of measurement on weathered samples has shown an increase in impedance value, which poses no threat at all. Nevertheless a little caution seems advisable, as it is essential that the possible effect of local modifications on the surface should be considered before measurement.

2.5 Coating characterisation

The classical EIS measurement method has been adopted for the comparison of the protective properties of six commercial waxy coating for outdoor bronze sculpture [24]. A study on samples with three different artificial patination has been performed also [25], which shows that the wax which protects a patinated surface best is not the same for all but varies with the underlying patina. These works point out quite effectively the strongly potentiality of EIS for the evaluation of the different conservation strategies on metal artworks.

The application of the contact probe EIS measurement methodology to laboratory studies on protective coatings for application on art objects might be of interest:

- in principle the measurement scheme should be more similar to actual service conditions (wet layer activating ions on the surface [2])
- the protective coating characterisation data, such as equivalent circuits and correlation between measurement parameters values with long term behaviour, which are obtained in laboratory study would be directly usable for the monitoring of restored artworks by field measurements.

Lack of samples and their small size prevented a thorough study from being made. Nevertheless a few spectra collected in a sufficient similar way with the CV probe was selected for a first analysis. The Nyquist plot for the twelve-month weathered sample clearly shows three processes are needed to describe the spectra (Figure 12). The equivalent circuit shown in Figure 13 has been adopted.

Constant Phase Elements must be used in the analysis instead of capacitors to fit experimental data correctly. The first time constant can be linked with some confidence to the electrical and barrier properties of the wax coating. However the physical interpretation of the second and the third are less straightforward, even though the third one can be generically ascribed to processes at the metal interface [17].

The fits obtained are quite good (Figure 14) for all the spectra. Some trial with different circuits provided less satisfactory fits. The evolution with weathering of the circuit's resistances and capacitance (Figure 15) indicate little degradation of the coating, with the deterioration of the corrosion resistance to be ascribed principally to the evolution of processes at the metal interface. This is in agreement with the FTIR results, which showed negligible modification in the wax structure, apart from the up-take of water (36) which is consistent with the obtained Coating Capacitance increase. A few of the spectra obtained repeating EIS measurement on a sixteen-months weathered sample have been fitted also. The behaviour of the fitted resistances and capacitance shows the opposite response with measurement repetition when compared to the one obtained with weathering, in a way compatible with the hypothesis that removal of soluble salts from the surface occurred. Measurements using a more refined technique and on a larger number of samples is clearly required to analyse in detail the wax protective behaviour. bronze so that the operating

conditions for the cloth may be defined more precisely more precisely. These results will be applied in evaluating performances of possible different cloth or sponge as well. A closer **3.**

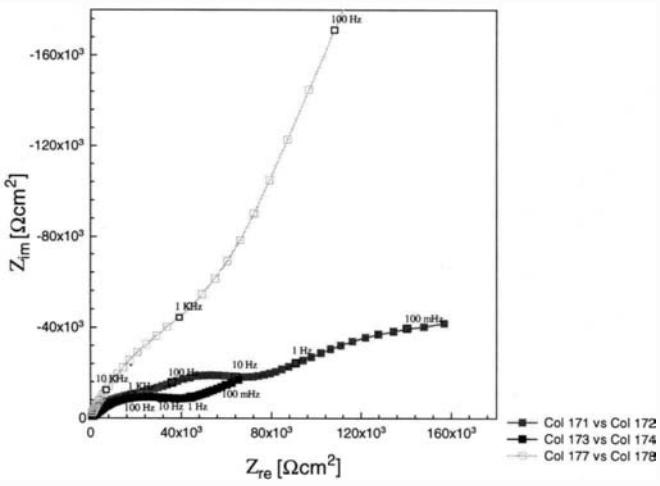

Figure 12. Nyquist plot of the EIS spectra obtained with the CV probe on waxed samples both unexposed and after 12 and 16 months' weathering.

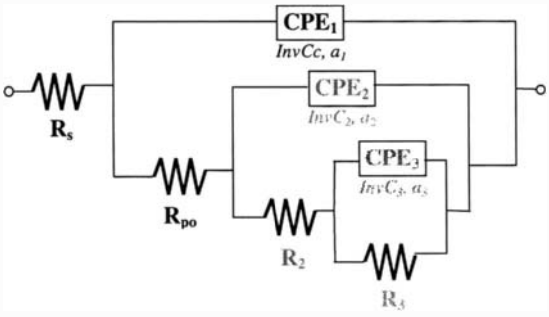

Figure 13. Equivalent electrical circuit applied for analysis of EIS spectra of waxed bronze.

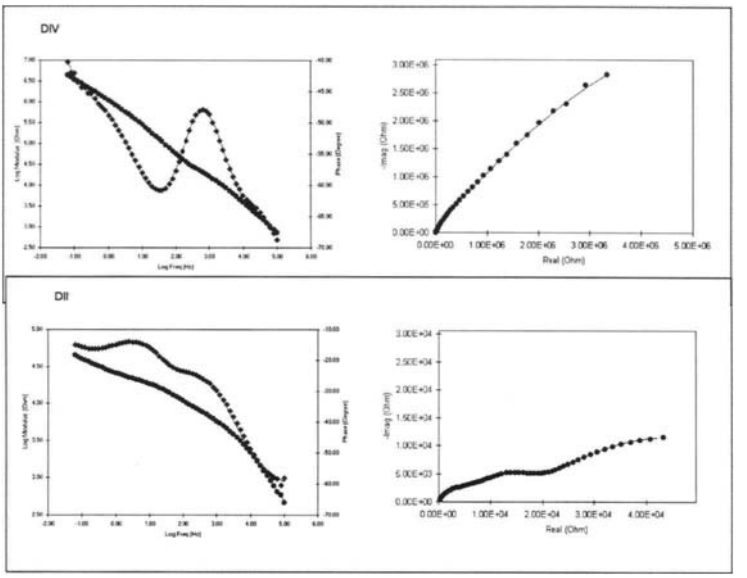

Figure 14. Fitting (lines) of EIS spectra (dots) for waxed bronze: unexposed sample (A); 1 year weathered sample (B).

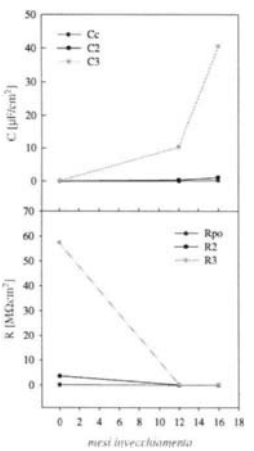

Figure 15. Trend capacitance and resistances with weathering, as obtained by fitting the equivalent circuit in Figure 13 to the spectra in Figure 12.

4. FUTURE DEVELOPMENT

The results obtained so far on the contact probe EIS measurement method are reasonably satisfying. For a full exploitation especially devoted to practical application for field measurement some further technical refinements are in train. Tests with the ST probe without cloth and a different assembly for water containment are in train - both on bronze and waxed examination of measurement method effects on weathered samples will be carried out. The identification of a procedure for well-defined repeatable measurements would be satisfying for application to laboratory study on outdoor bronzes problems. A check on procedure non-destructiveness is required to take advantage of the contact probe EIS technique on artworks directly.

Several aspects relating to corrosion behaviour and conservation treatments effectiveness for outdoor bronzes would benefit from EIS investigation.

The more easy and appropriate application would be the characterisation of protective treatments. The surface preparation prior to coating application should be considered [25]. Polished surfaces are the less interesting than rough surfaces for practical purposes, but they may provide useful information for the understanding of EIS results on more complicated systems. Artificial patination is quite often applied on artworks, and the effect of different protective coatings on them can be effectively analysed. Artificial reproduction of naturally occurring patinas should be carefully considered, as different patina layer conducting properties may be obtained [38]. Recent results on an extended study for artificial reproduction of naturally occurring cuprite and sulphate patinas on copper and bronze samples [39] open up new possibilities for laboratory study of treatments in a configuration more closely linked to actual application ones. Laboratory analysis and comparison by EIS measurements on corrosion resistance and corrosion mechanism for a number of treatments relevant for cultural heritage may be suggested:

- the examination on artificial patina/coating interaction should be further developed;
- the comparison of performances of different waxes [23,24] could be extended, with the evaluation of benzotriazole and/or pigment addition; comparison with other applied protective coatings (such as Paraloid, Incralac, and so on) and multiple coatings application (Incralac + wax) [35] would be interesting for practical and economical evaluation;
- the different application methods - such us hot/cold, brush/spray, etc. - possibly relevant role has not been analytically characterised yet;

These laboratory characterisation on EIS spectra on systems relevant for outdoor bronzes for a number of weathering condition will provide the basic knowledge for relevant factors identification and will open the way to the application for the analysis of (generally more complicated) real systems. A careful analysis on equivalent circuit model, supported by other surface analytical techniques, would possibly lead to proper identify performance parameters for the systems of interest for cultural heritage protection [30]. This would allow for quick assessment of performance, which is of particular interest for field monitoring development.

4. SUMMARY

Although the EIS contact probe we developed allows us to make satisfactory measurements further improvements are still being made. An extensive characterisation of measurement

dependence on several parameters has been performed in order to check possible applications and to easy transfer to use by museum conservators. The factors relevant for conservation (treatment, ageing) give a modification an order of magnitude greater than others do. The specially designed EIS measurement method can be directly applied to examine cultural heritage artefacts. Even though more refinement are still in progress, contact probe EIS measurements could easily become a tool for the testing of conservation treatments during restoration and for maintenance cycles.

Measurements made on a (bronze + microcrystalline wax) system allows the characterisation quantitatively of the evolution of the corrosion resistance during ageing. Several EIS applications for the characterisation of coatings to be applied on bronze art works could be suggested, which can effectively support research on more effective corrosion protection treatments.

AKNOWLEDGEMENTS

Dr Anna Beccaria provided a fundamental assistance for the project development. Dr Maurizio Marabelli support is gratefully acknowledged.

This work has been financially supported by PROGETTO FINALIZZATO BENI CULTURALI - Subproject No. 2.

Dr. Renza Trosti-Ferroni is kindly acknowledged for providing climatic-chamber-weathered samples. With Dr Cecilia Bartuli (Rome University) I had useful discussions on materials for cell design. Mr Giacomo Gaggero (CNR-ICB) made the Teflon-Stainless Steel probe S15.

REFERENCES

1. E.D. Verink Jr, *Bronze and other copper alloys: introduction to corrosion behavior* in DIALOGUE/89 - The conservation of bronze Sculpture in the outdoor environment: a dialogue among conservators, curators, environmental scientists, and corrosion engineers, NACE, Houston, (1992), 87-102.
2. H. Strandberg, *Perspectives on Bronze Sculpture Conservation - Modelling Copper and Bronze Corrosion,* Doctoral dissertation in Environmental Science - Department of Inorganic Chemistry - Goteborg University (1997).
3. B. Stockle, S. Fitz, M. Mach, G. Pohlmann, R. Snethlage, *Die atmosphärische Korrosion von Kupfer und Bronze im Rahmen des UN/ECE-Expositionsprogramms. Zwischenbericht nach 4-jähriger Bewitterung,* Werkst.Korros. 44 (1993), 48-56.
4. B. Stockle, A. Kratschmer, C. Gruber, G. Pohlmann, *Results from the exposure of patinated and waxed bronze,* Report N. 32 - UN/ECE ICP on Effects on Materials, Including Historic and Cultural Monuments, Bavarian State Conservation Office, Munich (1998).
5. *New conservation methods for outdoor bronze sculptures,* (H. Roemich editor), Report N. 3 - Protection and Conservation of European cultural heritage, European Commission, Brussels (1996).

6. H. Strandberg, L.G. Johansson, *Role of O_3 in the atmospheric corrosion of copper in the presence of SO_2,* J.Electrochem.Soc. 144 (1997), 2334-2342.
7. J.T.N. Atkinson, H. VanDroffelaar, *Corrosion and Its Control - An Introduction to the Subject,* NACE, Houston (1982).
8. P.J. Gellings, *Introduction to corrosion prevention and control for engineers,* Delft University Press, Rotterdam (1976).
9. M. Pourbaix, *Electrochemical corrosion and reduction* in Corrosion and Metal Artifacts - A dialogue between conservators and archaeologists and corrosion scientists, NACE, Houston, (1977), 1-16
10. F. Mansfeld, *Electrochemical Impedance Spectroscopy (EIS) as a new tool for investigating methods of corrosion protection,* Electrochim.Acta, 35 (1990), 1533-1544.
11. C. Gabrielli, M. Keddam, *Contribution of Electrochemical Impedance Spectroscopy to the investigation of the electrochemical kinetics,* Electrochim.Acta, 41 (1996), 957-965.
12. U. Rammelt, G. Reinhard, *Application of electrochemical impedance spectroscopy (EIS) for characterizing the corrosion-protective performance of organic coatings on metals,* Prog.Org.Coat. 21 (1992), 205-226.
13. M. Kending, J. Scully, *Basic Aspects of electrochemical impedance application for the life prediction of organic coatings on metals,* Corrosion, 46 (1990), 22-29.
14. *Potentiostat Primer,* http://www.gamry.com/G2/Appnotes/Reference/RefElect/Potentiostat_primer.htm.
15. *EIS Theory,* http://www.gamry.com/G2/Appnotes/Reference/EISTheory/Theory/EIS_Theory.htm
16. *EIS on coatings,* http://www.gamry.com/G2/Appnotes/Reference/EISTheory/painteis.htm
17. P.L. Bonora, F. Deflorian, L. Fedrizzi, *Electrochemical Impedance Spectroscopy as a tool for investigating underpaint corrosion,* Electrochim.Acta, 41 (1996), 1073-1082.
18. M. Bartolini, B. Colombo, M. Marabelli, M. Marano, C. Parisi, *Non-destructive tests for the control of ancient metallic artifacts* in Proc. Metal 95, Semur en Auxois (France) (25-28 september 1995), (I.D. MacLeod, S.L. Pennec, L. Robbiola editors), James & James (Science Publishers) Ltd (1997), 43-49.
19. M. Bartolini, R. Cigna, B. Colombo, G. D'Ercoli, M. Marabelli, M. Marano, *Capillary condensation measurements and electrochemical tests for conservation of artistic metals* in Proc. ART96 - 5th International Conference on Non-Destructive testing and Microanalysis for the diagnostics and Conservation of the Cultural and Environmental Heritage, Budapest (Hungary) (24-28 sept 1996), (1996), 117-130.
20. C. Bartuli, S. Angelucci, S. Lanuti, *Polarization Resistance measurements for the monitoring of the corrosion rate of protected copper alloy sculptures* in Proc. ART99 - 6th International Conference on Non-Destructive testing and Microanalysis for the diagnostics and Conservation of the Cultural and Environmental Heritage, Rome (Italy) (17-20 may 1999), (1999), 1343-1359.
21. L. Robbiola, N. Pereira, K. Thaury, C. Fiaud, J.P. Labbé, *Decuprification phenomenon of Cu-Sn alloys in acqueous solution at nearly neutral pH conditions* in Proc. Metal98, Draguignan (France) (26-26 may 1998), (W. Mourey, L. Robbiola Editors), James&James (1998), 136-144.
22. E. Angelini, P. Bianco, F. Rosalbino, F. Zucchi, *A comparative study of methods for the assessment of recovery techniques for aged copper,* Science and Technology for Cultural Heritage, 4 (1995), 1-10.

23. C. Price, D. Hallam, G. Heath, D. Creagh, J. Ashton, *An electrochemical study of waxes for bronze sculpture* in Proc. Metal 95, Semur en Auxois (France) (25-28 September 1995), (I.D. MacLeod, S.L. Pennec, L. Robbiola Editors), James & James (Science Publishers) Ltd (1997), 233-241.
24. V. Otieno-Alego, G. Heath, D. Hallam, D. Creagh, *Electrochemical evaluation of the anti-corrosion performance of waxy coatings for outdoor bronze conservation* in Proc. Metal98, Draguignan (France) (26-29 may 1998), (W. Mourey, L. Robbiola Editors), James&James (1998), 309-314.
25. V. Otieno-Alego, D. Hallam, A. Viduka, G. Heath, D. Creagh, *Electrochemical impedance studies of the corrosion resistance of wax coatings on artificially patinated bronze* in Proc. Metal98, Draguignan (France) (26-29 may 1998), (W. Mourey, L. Robbiola Editors), James&James (1998), 315-319.
26. E. Guilminot, C. Degrigny, X. Hiron, F. Dalard, *Protection d'un cuivre archeologique par le benzotriazole (BTA) en milieu aqueux de polyéthylène glycol (PEG)* in Proc. Metal98, Draguignan (France) (26-29 may 1998), (W. Mourey, L. Robbiola Editors), James&James (1998), 234-241.
27. A.Salnik, W. Faubel, H. Klewe-Nebenius, A. Vendl, H.-J. Ache, *Photothermal studies of copper patina formed in the atmosphere,* Corros.Sci. 37 (1995), 741-767.
28. W. Faubel, H. Klewe-Nebenius, P. Misaelides, B. Pichler, A. Vendl, *Non-destructive Surface Control of Atmospherically Corroded Copper and Bronze Objects* in Proc. ART99 - 6th International Conference on Non-Destructive testing and Microanalysis for the diagnostics and Conservation of the Cultural and Environmental Heritage, Rome (Italy) (17-20 may 1999), (1999), 233-246.
29. P. Letardi, A.M. Beccaria, M. Marabelli, G. D'Ercoli, *Application of Electrochemical Impedence measurements as a tool for the characterization and protection state of bronze works of art* in Proc. Metal98, Draguignan (France) (27-29 may1998), (W. Mourey, L. Robbiola Editors), James & James (Science Publishers) Ltd (1998), 303-308.
30. J.A. Grandle, S.R. Taylor, *Electrochemical Impedance Spectroscopy of Coated Aluminum Beverage Containers: Part1 -Determination of an Optimal Parameter for Large Sample Evaluation,* Corrosion, 50 (1994), 792-803.
31. J.A. Grandle, S.R. Taylor, *Electrochemical Impedance Spectroscopy as a Method to Evaluate Coated Aluminum Beverage Containers - Part 2: Statistical Analysis of Performance,* Corrosion, 53 (1997), 347-355.
32. M.C. Squarcialupi, A. Atrei, G.P. Bernardini, R. Trosti-Ferroni, *Preliminary treatments of artificial ageing of a bronze alloy in a climatic chamber for corrosive gases* in Proc. Metal98, Draguignan (France) (27-29 May 1998), (W. Mourey, L. Robbiola editors), James&James (1998), 271-274.
33. M. Marabelli, G. Napolitano, *Nuovi sistemi protettivi applicabili su opere o manufatti in bronzo esposti all'aperto,* Materiali e Strutture - problemi di conservazione, 1 (1991), 51-58.
34. A.Giavarini, M.L. Santarelli, *Gli studi per la protezione del Marco Aurelio,* Materiali e Strutture - problemi di conservazione, 3 (1996), 137-144.
35. L.B. Brostoff, E. René de la Rie, *Research into protective coating system for outdoor bronze sculpture and ornamentation* in Proc. Metal 95, Semur en Auxois (France) (25-28 september 1995), (I.D. MacLeod, S.L. Pennec, L. Robbiola Editors), James & James (Science Publishers) Ltd (1997), 242-244.

36. P. Letardi, A.M. Beccaria, M. Marabelli, G. D'Ercoli, *Applicazione delle misure di Impedenza Elettrochimica per la Caratterizzazione dei rivestimenti applicati nel campo della conservazione di bronzi artistici* in Proc. Giornate Nazionali sulla Corrosione e Protezione dei Materiali Metallici, Genova (Italia) (14-15 aprile1999), AIM (1999), 267-272.
37. P. Letardi, A.M. Beccaria, M. Marabelli, G. D'Ercoli, *Non-destructive Electrochemical Impedance measurements: application to the corrosion characterisation on bronze works of art* in Proc. ART99 - 6th International Conference on Non-Destructive testing and Microanalysis for the diagnostics and Conservation of the Cultural and Environmental Heritage, Rome (Italy) (17-20 may 1999), (1999), 313-319.

Radiation in Art and Archeometry
D.C. Creagh and D.A. Bradley (editors)

The infrared examination of paintings

Franz Mairinger

Institute for Colour Science and Colour Chemistry, Academy of fine Arts Vienna

The properties of Infrared Radiation, its generation , detection and interaction with materials are discussed, as are a wide range of practical apects of the use of IR to study materials. How IR is employed in the study of paintings is discussed in some detail.

1. INTRODUCTION

Infrared examinations reveal, like ultraviolet investigations, object states which the naked eye cannot see. Whereas UV radiation is readily absorbed or scattered already in the surface layers of objects, infrared radiation penetrates quite often opaque strata. This property makes IR to helpful instrument in many fields of research concerned with history of art, archaeology and conservation of works of art. For these purposes IR radiation can be used in two ways.

1. Many substances reflect or absorb in the near IR region frequently quite differently from the visual range. So two materials (e. g. pigments) which look optically alike, are rendered dissimilar in infrared recording.
2. Some opaque materials, especially turbid media like fog, haze or paint layers, even human skin, transmit IR and gain transparency in this region. This valuable ability permits e. g. the detection of under drawings made immediately on the ground of paintings.

Depending on the wavelength, this invisible radiation can be recorded by photographic or electronic means. For *infrared photography*, films sensitized for IR must be employed. The electronic recording can be accomplished by video cameras with infrared sensitive detectors, which provide access to the rang around 2.0 μm. According to a proposal of VAN ASPEREN DE BOER [1], this method is called *infrared reflectography.*

In the following sections a discussion of properties of IR, the choice and the handling of suitable instruments and the scope of this method in art and archaeology is offered. The detection and application of thermal radiation in the range of 3 – 10 μm (*thermography*) is not discussed.

2. INFRARED RADIATION

The invisible infrared radiation, it was discovered 1800 by the astronomer WILLIAM HERSCHEL, extends in increasing wavelength beyond the red end of the visible spectrum. It comprises the wavelength range from 0.78 μm to 1 mm. The upper end of this region merges continuously into the microwave band. According to PLANCK's law [$E = hc/\lambda$] IR photons

have less energy than visible light. Thus they excite in molecules vibrational or rotational states only, no electronic transitions occur. So special detection methods have to be applied.

The IR spectrum is usually divided arbitrarily in 4 bands (Figure 1).

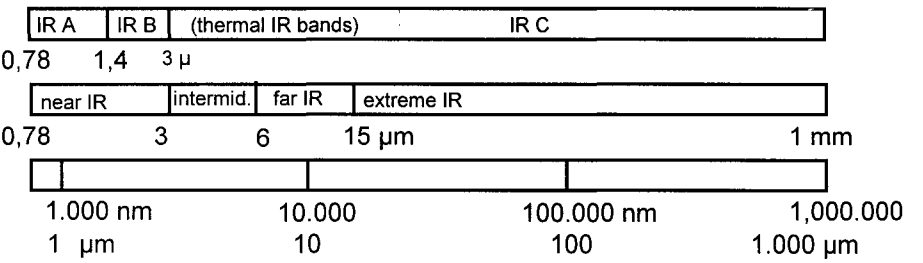

Figure 1. The spectrum of infrared radiation

1. ***Near infrared*** (NIR) encompasses the region from 0.78 – 3 µm. It is produced by incandescent objects such as the sun or tungsten lamps. This range is of great practical importance, since the region near to the visible (up to 1.35 µm) can be recorded photographically. Specially sensitised emulsion must be used. The 1.4- 3 µm range can be detected by electronic image converters.
   Near IR is used for examinations of works of art and archaeological objects.
2. ***Intermediate infrared*** extends from about 3 – 6 µm. It is produced by hot non-incandescent objects at temperatures between 200 – 400° C. This thermal radiation, the thermal bands expand up to 15 µm, is perceived by receptors of human skin as heat. Water and many organic molecules (e.g. binding media in paintings) absorb strongly in this region. Intermediate infrared can also be recorded electronically. It is used in surveillance systems
3. ***Far infrared*** expands from 6 – 15 µm. It is radiated by bodies at room temperature and slightly above. The maximum emission of the human body occurs about 9 µm (starting at 3µm). A lot of organic substances have absorption bands in this region of radiation. This range can be recorded by special electronic cameras. They can be applied for imaging the heat flux in objects like buildings. This technique is called *thermography*.
4. ***Extreme infrared*** extends in wavelength from 15 µm to 1mm. It is generated by either microwave oscillators, lasers, or incandescent sources. Since the range between 18 – 23 µm is readily absorbed by many materials, even by human tissue, it is widely used in industry especially in precision cutting. In medicine the IR laser beam makes an effective scalpel.

Another division of the infrared range is used also: *IR-A* (0.78 – 1.4 µm), *IR-B* (1.4 – 30 µm) and *IR C* (3 µm – 1mm). See Figure 1.

3. THE INTERACTION OF INFRARED RADIATION WITH TURBID MEDIA

In a turbid medium small particles are dispersed in a homogeneous, transparent matrix, that can be a gas, a liquid or a solid. Examples for this kind of systems are fog, smoke, paints and colloidal liquid and solid solutions (like ruby glass). The interactions of infrared radiation with these systems are intrinsically the same as with light. They are governed by (diffuse) reflection resp. remission, refraction, dispersion, scattering and in case of coloured substances specific absorption of certain spectral regions. Scattering and specific absorption are the determining factors for the transmittance of such systems.

For example the hiding power of white paint layers is (apart from the thickness of the layers,) solely due to scattering, while in a paint layer of Prussian blue specific absorption is the dominating factor.

Scattering can be described quantitatively by specific scattering coefficients of the dispersed particles (KUBELKA – MUNK theory [2]). They depend in a complicated way on the wavelength of the incident radiation, on the geometry of the particles (diameter, shape) and on the difference of the refraction indices of pigment and medium. So generally speaking, a white paint layer becomes more transparent:

- the greater the wavelength of the incident radiation
- the smaller the thickness of the paint layer
- the smaller the number of particles in the layer (pigment/volume concentration)
- the lesser the difference of refractive indices of pigment and medium

VAN ASPEREN[1] showed in his thesis, that for many pigments a maximum of transmittance occurs in the near infrared region between 1.8 and 2.2 μm. At greater wavelength the (organic) media start to absorb and the layers are less transparent and the contrast ratio is diminished.

The spectral range around 2 μm is inaccessible to photographic emulsions, but it can be detected by video cameras with appropriate electronic image converters. This technique is applied successfully for the detection of under-drawings of paintings.

3.1 Infrared Luminescence

Visible luminescence (fluorescence) excited by UV radiation is well known. The phenomenon of invisible infrared luminescence, stimulated by blue-green light, is less familiar. Although the intensity is very low, it can be recorded by IR photography. The first paper on this subject was probably publishes by DHÉRÉ [1]. He reported 1936 the fluorescence of chlorophylls a and b at a wavelength of 820 nm. There are many other inorganic and in organic materials which exhibit luminescence in the near infrared: wood, natural resins, leather, parchment, minerals, pigments, dyes. BRIDGEMAN and GIBSON[2] have published examinations of artists pigments by this method.

3.2 Radiation Sources for Infrared Recording

As mentioned above mainly the near infrared range (0.78 – 3.0 μm) is used for examination of this type in art and archaeology. All hot bodies with temperatures above 500° C can serve as efficient radiation sources in this region. Thus any incandescent lamp (tungsten filament, halogen) can be used for infrared photography and reflectography. For the latter it is not necessary to operate the lamps at full mains voltage. The voltage reduction can be accom-

plished by a resistor, transformer or a voltage regulator of the thyristor type. This will protect the subject from unnecessary radiant heat and it will reduce the strain on the bulbs.

An efficient source for infrared photography are *electronic flash* discharge tubes. With appropriate filtering, they provide a high intensity in the IR A region. Whereas other discharge lamps like fluorescent tubes are very poor IR sources.

The lamps are used normally with appropriate reflectors. Slide projectors are also good sources for directed light, if the heat (absorbing) filter is removed. They give a very even illumination of objects. For indoor infrared colour photography the electronic flash illumination is the best choice.

For the irradiation of smaller objects *IR light emitting diodes* (IR-LED's) can be employed. They emit IR radiation in fairly narrow bands in the range of 0.9 – 1.3 µm. The intensity is fairly low, but there are cluster lamps commercially available, where many LED's are mounted on a small board. This source is of interest, when heat sensitive objects like illuminated manuscripts are examined.

3.2 Filters for infrared photographic and electronic recording

Since nearly all IR recording devices have a fairly high sensitivity in the visual range, images in both regions, the infrared and the visual, will be recorded equally. They are superimposed. In IR photography the result is very similar to a normal panchromatic recording. To separate these images, filters must applied, which absorb the visible part of the spectrum and transmit the IR part. For this purpose gelatine and glass (absorption) filters with different absorption edges and optical densities are produced by several manufacturers. Table 1 shows the data of some IR filters.

For infrared photography the filter must be chosen that corresponds with the sensitization of the emulsion. The spectral sensitivity of commercially available infrared films end about 900 – 920 nm, the maximum sensitivity is at 820 nm. Hence the cut-on wavelength of the filter should be about 800 nm or less. The WRATTEN filters # 87 and 87 C are perfectly suited for this purpose. But even red filters (e.g. WRATTEN # 25, 29 and 70) can be used quite successfully.

Table 1
Infrared filters

Manufacturer	Designation	Cut-on wavelength	Remarks
KODAK WRATTEN	# 87	740 nm	Gelatine
KODAK WRATTEN	# 87 C	800 nm	Gelatine
KODAK WRATTEN	# 88 A	730 nm	Gelatine
SCHOTT	RG 780 (3 mm)	780	Glass
SCHOTT	RG 1000 (3 mm)	1000 nm (1µm)	Glass

The appropriate choice of filters for *IR reflectography* can be more critical. In most cases the WRATTEN # 87 C or the SCHOTT RG 1000 give good results. But in some instances, if the cut-on wavelength of the filter is too high, some materials become completely transparent, drawn lines or inscriptions vanish.

A completely different type of filtering must be employed for the *IR colour film*. For this emulsions only the violet and blue part of the visible spectrum must be blocked out by using a dense yellow filter. (e. g. WRATTEN # 12).

3.3 Lenses

Optical glass normally transmits IR radiation up to 2.7 μm, depending on its chemical compostion,. Thus common camera lenses can be used for infrared photography and reflectography. For IR reflectography the use of macro lenses is advantageous.

The correction of common camera lenses is optimised for the visual range (450 – 650 nm) and declines in the infrared (and ultraviolet) region, the imaging quality is less. Since the refractive index (of glass) is a function of the wavelength, it gets smaller with increasing wavelength, the focal length and the chromatic aberrations increase with wavelength. Thus the resolving power in the infrared region between 0.78 – 2.2 μm is impaired.

This deterioration of the resolving power doesn't play an important role in *infrared photography*, since merely the range of 0.78 – 0.9 μm is used. Only the focal length and the image distance is slightly increased (0.2 – 0.3%). Since the image focused visually, it is somewhat defocused in the IR region. This can be corrected easily by closing diaphragm two steps below the maximum aperture. If the focusing is done with a red filter (which must be replaced afterwards by the IR filter) the focus difference is also diminished.

Some lenses have a red dot or an "R" on the focusing scale to indicate an average correction for IR photography.

In *IR reflectography* the detector picks up the whole IR region between 1.0 and 2.2 μm. This generates appreciable chromatic aberrations, a cause for blurred images. It can be reduced by use of appropriate IR line filters (with a substantial loss in intensity).

Another difficulty arises from the (multilayered) antireflection coatings of modern lenses. They eliminate unwanted reflections of glass surfaces in the visual range by destructive interference. In another wavelength region like IR a reverse effect can take place. The coatings reflect strongly and diminish the transmittance of the lenses, moreover the stray light reduces the image contrast considerably. WALMSLEY et al.[3] measured the transmittance of several macro lenses (Nikon, Pentax) in the range from 0.4 – 2.1 μm. At 1 μm the spectral transmission is only 50 % of the value near 0.6 μm. Much better results can be obtained with (expensive) fluorite and quartz lenses which are manufactured by ASAHI, NIKON and ZEISS. They have a good correction in the range between 0. 22 – 1.5 μm, so they can be used for UV recording and IR reflectography.

3.4 Infrared Recording Methods

For infrared examinations of works of art two categories of detecting techniques are available: *photographic* and *electronic* recording. *Film recording* utilizes photographic emulsions sensitized to infrared radiation. Common cameras can be used. It is also employed to record luminescence in the infrared region. *Electronic recording* makes use of video cameras equipped with IR sensitive electronic image converters.

3.4.1 Photographic materials for infrared recording

Silver halides have a natural sensitivity in the ultraviolet, violet and blue sections of the spectrum, they are "blind" for green and red light and for the near IR, because spectral range is not absorbed. But it is possible to extend the sensitivity of emulsions to 1.25 μm by using *sensitizing dyes* (mostly Carbocyanine dyes).

Until about 1970 a variety of infrared films in all common forms were available. Nowadays the choice is very limited. Only two black-and-white and one infrared colour emulsions

are available in Europe. Two manufacturers, KODAK and KONICA, produce such materials. For spectroscopic investigations (in astronomy) infrared emulsions on films and glass plates are offered by KODAK.

3.4.2 Infrared black-and white films

Common panchromatic films cannot be used for infrared recording. Only special emulsions sensitized for infrared can be applied. These emulsions also have a fairly high sensitivity for UV (down to 300 nm) and for the visible spectrum, only in the green region they are less sensitive than panchromatic films.

KODAK offers the *High Speed Infrared Film Type 4143* in sheets (4x5") and 35 mm. The spectral sensitivity curves are given in Figure 2. Its sensitivity ends near 920 nm with a flat maximum at 820 nm. The maximum resolution is about 80 lines/mm. For recording the infrared image only, a red or infrared filter must be used over the lens (or light source). WRATTEN red filters # 25, 29, 70, and the infrared filters 87, 88A and 87C are suitable. It is not possible to give exact speeds, since the ratio of visible to infrared depends on the light source used and the common exposure meters respond not or differently to infrared radiation. So test exposures have to be done. For infrared recording of paintings with halogen lamps (600 W) and a Wratten 87C filter a speed of ISO 24/200 gave correct exposures.

Figure. 2(a)

Figure. 2(b)

Figure 2. H. Bosch: "The last judgment", tryptich, Paradise wing. 164cm X 60 cm, oil tempura on wood (oak).

(a) **normal** recording: (Kodak Ektachrome).
(b) **infrared** recording: Kodak Ektachrome infrared film, type 2236 filter: WRATTEN #12; electronic flash.

KONICA produces the *Infrared 750 Black & White Film*. It is not a genuine infrared emulsion. It should be better called a deep red film, since the its sensitivity ends at 750 nm. So only the use of a red filter (e.g. Wratten # 25) is permissible.

Infrared film should be stored at low temperature in a refrigerator or even in a deep-freeze unit, otherwise fogging by the thermal radiation at room temperature occurs. Loaded sheet film holders or 35 mm cassettes should not be left in a warm room for a longer time. The 35 mm film has a black opaque leader strip, so three blank frames must be made. Exposed films should be developed immediately, at least on the same day.

3.4.3Infrared Colour Film

An interesting (contrasty) material is the KODAK *Ektachrome Infrared Type 2236*. It is a "false" colour daylight type reversal film sensitized to infrared (up to 900 nm). It was originally produced for aerial cameras to detect camouflage of military objects. Unlike normal colour films with 3 layers sensitized to blue, green and red, the image layers of this film are sensitized to green, red and infrared. Since all three layers are sensitive to blue, a yellow filter, WRATTEN # 12 is recommended, must be used on the lens to withhold the blue and violet part of the spectrum. The film has only a latitude of about ½ stop. Its reciprocity failure shows up already at exposure times longer than 1/25 s, the speed goes down and colour correction filters must be used. So the best light source is an electronic flash. With the WRATTEN filter # 12, the exposure meter should be set to ISO 21/100.

Upon processing the green sensitive layers forms a positive yellow image, the red sensitive records a positive magenta and the infrared a positive cyan image.

Since this film adds an infrared component to the visible light record, green or red colouring matters with equal or similar chroma in the visible range are rendered in different hues, if they have dissimilar infrared absorption or reflection. Blue pigments appear black, if they absorb infrared and red if they reflect infrared. A general synopsis of the resulting modified rendition of object colours is given inTable 2.

Practical examples for the colour rendition of some pigments used in paintings are given in Table 3, but it should be kept in mind that the tabulated "false" colours are also (slightly) influenced by the media (e. g. drying oils, distemper, animal glue) and by varnish layers.

Table 2
Modified object colour rendition of *Ektachrome Infrared* film

Object Colour	***Rendition (no IR reflection)***	***Rendition (with IR reflection)***
Red	Green	Yellow
Green	Blue	Magenta
Yellow	Cyan	White
Blue	Black	Red
Infrared	-	Red

This modified colour rendition makes this emulsion a valuable tool for the examination of works of art and artefacts and for problems of conservation. Later additions in paintings like retouches or overpaintings, which were applied in equal hues, but executed with different pigment, show up in many cases quite clearly in this type of infrared recordings. An

example of this behaviour is given in Figure 2, which shows a section of the Paradise wing of the altar-piece "The last judgement" by H. BOSCH. The green meadow, painted with green earth, shows a bright purple spot caused by a retouch executed with a green chromium pigment of the same hue. The red vestment of the archangel Gabriel is rendered in a reddish yellow, since madder was used as a pigment. This emulsion can be applied for the examinations of dyed textiles, painted pottery and porcelain and in graphic arts for the discrimination of inks and pencils.

Table 3
Ektachrome infrared colour rendition of some pigments

Pigment	***False Colour Rendition***
Cobalt Blue	Bright Red
Blue	Lavender
Ultramarine	Dark Purple
Chromium Oxide Green	Purple
Green earth	Bright Blue
Emerald Green	Bright Purple
Madder	Warm Yellow
Verdigris	Dark Blue

3.5 Photographic Techniques

As already mentioned, there is no need to use special cameras for infrared photography. Only specially sensitized emulsions and barrier filters for the visible part of the spectrum must be applied. But it is necessary to say a few words about indoor lighting techniques. Subjects can be illuminated by *direct* or *diffuse lighting*. The camera records the light reflected by the specimen. An important factor for success in infrared photography of any type of subject is *flat* lighting. That implies that more than one light must be employed, all must be of the same wattage and be placed at equal distance from the object. As far as backgrounds are concerned, it should be kept in mind that many materials are rendered in a different colour or shade than their visual appearance. The choice however is only critical for infrared colour photography.

Diffuse lighting is strongly recommended for three-dimensional subjects. It can be accomplished by means of light tent or a cubicle made of (flame-proof) white textile sheets. They are illuminated by (electronic flash) lamps in appropriate lighting angels.

An interesting technique for infrared photography is *transmission lighting*, since thin sections or layers of various materials like paper, parchment, wood (up to 5 mm), minerals, rocks, paintings (on canvas) that are opaque in the visible range, become transparent in the near infrared region. For the set-up the specimen must be placed over a (light tight) opening of the enclosure for the light. The room must be darkened to prevent any stray light. The intensity of the transmitted infrared radiation is quite low, so the most convenient way is infrared photography, making use of the light cumulating ability of photographic emulsions. The determination of exposure time is difficult. A series of test exposures is necessary.

The application of this technique for the examination of paintings is described in detail by LAZZARINI[3] and KUSHEL[4]. Examinations of sedimentary rocks by this method were performed by RHOADS and STANLEY[4]4.

For the photographic rendering of *infrared luminescence* blue-green light is mostly used for excitation. The IR radiation of the illuminating light source (tungsten or flash) must be filtered out. This can be accomplished either by glass cells filled with an aqueous solution of copper sulphate (13 %) or less clumsy with glass filters. Two filters must be used, a blue-green (e. g. CORNING # 9780 or WRATTEN 39) and heat absorbing filter (CORNING # 3966 or SCHOTT BG 38). The filters are fitted tight on the lamp house. The heat absorbing filter must be located between the light source and the blue-green filter. For B&W recording an IR filter (WRATTEN # 87) is placed on the camera lens, the room must be darkened. The approximate exposure is determined by measuring the intensity of the blue-green light and multiplying the reading with 20.000. For further information consult the KODAK Technical Publication M-28[5].

3.6 ELECTRONIC RECORDING OF INFRARED RADIATION (IR Reflectography)

It has been stated that the spectral range of infrared photographic recording with commercially available emulsion is limited to about 920 nm. In this region many materials, like paint layers, are not penetrated, they behave like opaque strata. It was already discussed, that the range of optimal transmittance for these visually opaque layers is located in the region around 2 μm, which is only accessible by special electronic devices like video cameras equipped with IR sensitive image converters. After a proposal of VAN ASPEREN DE BOER [1] this technique is called *Infrared Reflectography* (IRR). The infrared image can be viewed immediately on a monitor, with a frame grabber digitised and stored in a computer respectively on a CD. This is a great advantage compared with photographic recording. The disadvantage is the much lower resolution of these cameras. It is overcome by recording only small sections of the object.

3.6.1 Electronic Infrared imaging devices

Two systems of imaging devices are used: *video cameras* equipped with tubes of the *vidicon* type and cameras based on special semiconductor devices (CCD or focal plane arrays). Both are based on the photoelectric effect, i.e., the ability of photons to separate electrons from atoms.

The camera lens projects an optical image on a photosensitive layer, where it is transformed by the photoelectric effect into a charge image, which is read out, amplified and made visible on a monitor screen.

3.6.2Video Cameras with (Vidicon) Tubes

Vidicon camera tubes with a lead oxisulfide (PbS/PbO) target (i.e., the photosensitive layer on the front end of the tube) have an intrinsic sensitivity up to 2.4 μm with a maximum response around 1.9 μm. This corresponds with the region of highest transmittance of pigment layers. Such systems are therefore used for the examination of paintings. Infrared vidicons with different spectral response are manufactured by HAMAMATSU, HEINEMANN and TELTRON The spectral response of the HAMAMATSU IR vidicon N 2606-06 is shown in Figure 3.

The photo-surfaces of vidicons have several disadvantages. One of it is the inability to record moving objects at low levels of illumination. An other is the "lag". If the light is instantaneously turned off , the image on the target will take some time to vanish. This happens also, when the camera is directed for a longer time on the same object, especially if the illumination level is high, "blooming" occurs, the image may even "burn in". This is particularly cumbersome, when reflectograms of larger paintings are produced, since when taking a new frame, one must wait till the old image has vanished.

Moreover the production of targets with a uniform sensitivity over the whole area and without any blemishes is technically quite difficult. Faults cause shading effects (radiometric distortions) and black spots in the image.

An other problem is the loss of image contrast, when the camera is switched on for a longer time. The heat produced by the filament warms up the target and the camera "sees" its own thermal radiation.

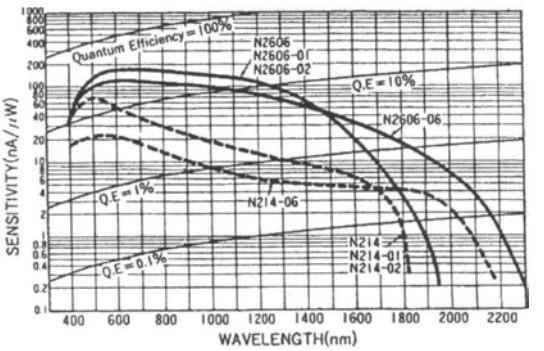

Figure 3. Spectral response of the infrared vidicon type N 2606 (Hamamatsu)

Camera control units for IR vidicons are produced by several manufacturer e. g. HAMAMATSU (C 2400), GRUNDIG (FA 70), IKEGAMI (ITC 62) or QUANTEX (QVC 2500). The time base of scanning generator should be very stable, otherwise geometric distortions may arise, which make the production of image mosaics difficult.

Semi-professional control units have many auxiliary electronic circuits, which are quite convenient for a better image quality. The sensitivity of the vidicon is controlled by a potentiometer which regulates the target voltage. By the *contrast enhancement circuit* the image contrast can be optimised manually (gain and Offset). The *video booster* circuit changes the slope of the gradation of the image. Nearly all cameras have an automatic gain control (AGC) which provides a constant amplitude of the video signal. For objects with high contrasts there should be a possibility switch the AGC off, otherwise the dark areas are void of any details.

3.7 CCD CAMERAS

In the last few years nearly all tube cameras have been replaced by cameras with semiconductor image converters, based on silicon CCD chips. These new detectors have many advantages compared to camera tubes.

Their dimension is much smaller, so more compact cameras can be built. No heating filaments are necessary, so no warming-up period is required and much less heat is generated, which means a better thermal stability and a better signal-to-noise ratio. The latter can be improved further by (electronic cooling) of the chip. The light sensitivity is much higher than that of high speed photographic emulsion (by two orders of magnitude). Since no scanning electron beam is necessary, no geometric distortions arise. No blooming or lag occurs.

But CCD sensors used in home and semi-professional camcorders have also a grave disadvantage, their spectral response ends at 1.3 – 1.4 μm, a region, not far above the photographic range, where many pigments are still opaque. Monochrome CCD cameras with an increased IR sensitivity (up to 1.3 μm) are manufactured by HAMAMATSU (C 5999) SONY (XC 77) or ORIEL.

For common colour video cam-corders the sensitivity of the sensors in the near infrared range is quite inconvenient, since it causes a erroneous colour rendition. So IR barrier filters are built in. Therefore these camcorder can't be used for IR examinations. But SONY has constructed cameras (High 8, Mini DV, D8) where these filters can be removed mechanically, this feature is called "night shot". For IR illumination two IR LED's are incorporated. With an IR filter over the lens this camera is valuable tool for a quick inspection of paintings in galleries and museums. With a capture card and a computer the stored information can be processed and printed with fairly good quality. An example of such an application is given in Figure 4. The under-drawing of a detail in an Italian painting "Circumcision of Jesus" shows up quite clearly.

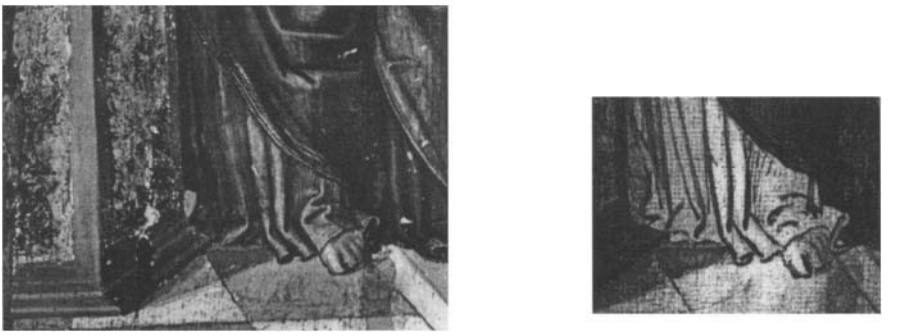

Figure 4. G. Campi. " The Presentation of Christ", oil-distemper, detail.
(a) normal recording
(b) infrared recording with SONY DRV 9 (digital camcorder), "night shot"-recording IR Filter B+W 092. Processed with SONY DV Still Image Capture Board DVBK-2000E.

3.8 FOCAL PLANE ARRAY (FPA) CAMERAS

Half a decade ago new types of infrared semiconductor sensors (for non-military applications) became available: platinum silicide (PtSi) and gallium arsenide (GaAs) detectors.

As early as 1973 SILVERMAN et al. [6] proposed a new IR sensor on the basis of PtSi focal plane (photodiode) array (FPA). The spectral response of this new detector was in the range between 1.0 and 5.7 μm. It was used mainly for military purposes. Thermal images of subjects at a temperature around 30° C could be recorded.
1993 WALMSLEY et al.[6] tested successfully such cameras manufactured by EASTMAN KODAK and MITSUBISHI for use in infrared reflectography of paintings. The handling of the Kodak camera was not quite easy, since the sensor had to be cooled by liquid nitrogen to – 196° C, while the Mitsubishi used thermoelectric Sterling cooling. This cameras, configured for the 1.5-2.0 μm region, offered a dramatic improvement in penetration of paint layers and resolution, whereas a configuration in the 2.2 - 5.0 μm range gave less satisfying results. The price for this cameras was very high. A light weight camera of this type (256x256 pixels) with sterling cooling is now manufactured by INFRAMETRICS USA, MA (InfraCAM).

A very promising material for IR focal plane arrays is *gallium arsenide*, sensitive in the 0.9 to 1.7 (2.5) μm band. Its quantum efficiency exceeds 70% and the detector can be operated at 18°C. A camera of this type with a 320x240 pixel focal plane array is manufactured by SENSORS UNLIMITED, USA. (Model SU320-1.7RT). The costs are much lower than for a PtSi camera. (Outside USA an export licence is necessary.)

There is an other very attractive FPA on the basis of a $HgCdTe/Al_2O_3$ semiconductor[7] manufactured by ROCKWELL Intern. (USA) with a cut-off wavelength near 2.5 μm. Since the price is excessive it has yet not been tested.

3.9 APPLICATIONS OF IR EXAMINATIONS

IR investigations play an important role in many fields of research and conservation of works of art and artefacts. Only a few characteristic applications will be discussed.

3.9.1 Graphic arts

Since infrared photography and reflectography are non-destructive methods of examination, they have found numerous application for works of graphic arts like drawings on paper and parchment, illuminated manuscripts, prints, illegible manuscripts resp. documents, palimpsests and papyri.

An important fact is that inks and pigments that appear identical to the eye are frequently rendered differently by infrared techniques. The behaviour of writing fluids in the near infrared was studied at an earlier time by MITCHELL[7] and THOLL[8]. The intricate discrimination of brownish inks like sepia, bistre or iron gall ink can be accomplished by infrared colour photography [9,10].

Texts which are illegible by dirt, deterioration, charring, obliteration, chemical bleaching or mechanical erasure can be made visible again by infrared reflection and luminescence techniques. Especially for soot inks these techniques were applied successfully.

Transmission techniques are useful when parts of an infrared transparent object are coated with paper or (thin) cardboard.

A combination of infrared methods with UV is recommended. UV-fluorescence photography is always worthwhile.

When infrared reflectography is applied for such investigations, the choice of the appropriate filter is critical. Drawings executed with iron gall ink will completely vanish at wavelength longer than 1.3 μm, bark inks even at 0.9 μm, whereas inks containing soot remain visible up to 2.2 μm [11]. This behaviour can be employed to discern the different types of

inks used for drawings. Interference filters of the band pass type should be used, they transmit only a very narrow range of wavelengths.

3.9.2 Paintings

Much work has been done in the infrared examination of paintings. Two main goals can be archived:

- the *detection of alterations* and later *additions* like over-paintings and retouches. This is mainly the domain of infrared (colour) photography. Differences in the spectral behaviour between original and later added materials are detected. Such information is of special interest for conservators and restorers.
- Another feature is also important. Since infrared rays penetrate discoloured varnish layers quite easily, old retouches, located under such coatings, can be detected. They are often nor perceived by UV-fluorescence, because they are masked by the strong luminescence of the varnish. This is illustrated by Figure 5, which shows the infrared photograph of a Dutch painting of a Madonna with the Child. It should be compared with the UV fluorescent record shown in the section on UV examinations. Apart from the under-drawing additional (old) retouches are revealed.

Figure 5. Follower of Rogier van der Weyden: "Madonna with the Child". Oil-distemper on wood (oak); 38., X 29.0 cm. Gallery of the Academy of Fine Arts Vienna, Austria. Inv- # A2, Infrared recording: KODAK High Speed Infrared, Type 4143; 4" X 5";
filter: WRATTEN 87C.

The revealing of underdrawings.

Since mediaeval times artists made a drawing to define form and composition on the ground of paintings with pencil, pen or brush. For white grounds, used until the end of the 16.c. and then again at the beginning of the 19.c., black colouring matters like charcoal, natural black chalk or bone black (and sometimes red ochre) were used. During the execution of the painting these underdrawings were covered by the (opaque) paint-layers.

These sketches are untouched by later hands, so art historians use them for attributions of paintings. Sometimes parts of the under-drawing can be observed with the naked eye or more clearly by infrared photography, but under blue (exception: natural ultramarine) and green paint layers the lines of the drawing remain invisible. In those cases infrared reflectography (in the spectral range around 2.0 μm) is applied [12]. This is demonstrated in Figure 6. The azurite layer of the blue kerchief is not penetrated by IR photography, whereas in the reflectogram the under-drawing is visible.

The resolution of infrared video cameras is fairly low, so only small, overlapping sections of paintings are recorded (with the aid of a positioning system). The single frames are digitized by a frame-grabber and then, after correction of geometric and radiometric distortions, assembled to a mosaic by the aid of computers. Appropriate mosaic programs were published by WECKSUNG et al.[12], BILLINGE et al. [13] and MAIRINGER [14].

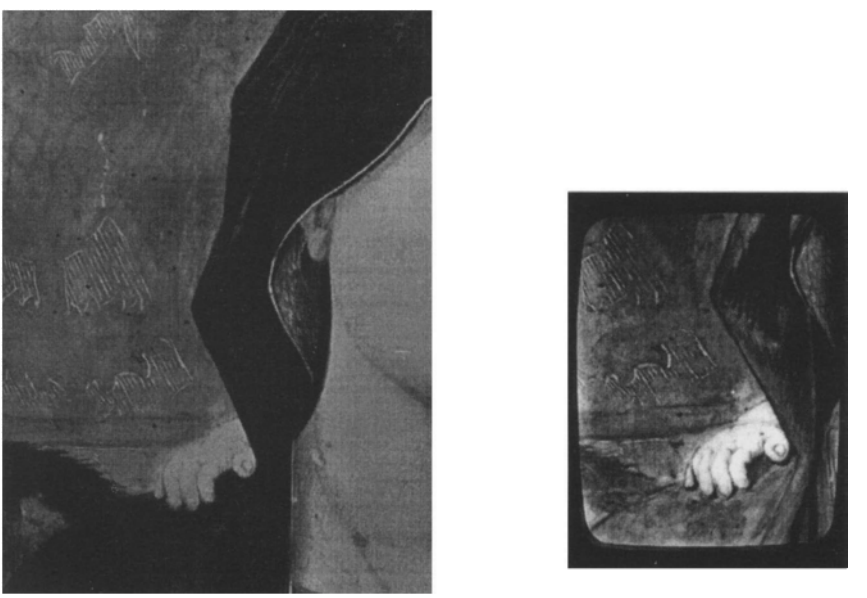

Figure 6. Italian painter 16th c. (After mantenega). "Sacra conversatione" . Didtemper on wood (poplar) 189 X 119 cm. Detail.
(a) IR photograph. KODAK High Speed Infrared. Type 4143. Filter: WRATTEN 87C
(b) IR reflectogram. MAMMAMATSU C2400 with vidicon type N 2602-06.
Filter. WRATTEN 87C (screen shot).

3.9.3 Other works of art and artefacts

Similar applications as discussed for graphic objects and paintings can be utilized for dyed textiles. Restorations on tapestries can be detected because of different IR luminescence and reflectances of natural and synthetic dyes.

Design on pottery fragments, invisible to the eye can be revealed by infrared examinations. In many cases patina, saline incrustations and resinous crusts are penetrated by infrared radiation. This can serve for the detection of inscription made with carbonaceous materials and encrusted wall paintings.

REFERENCES

[1] C. DHERE et O. BIERMACHER, „Spectrochimie biologique." Compt. Rend. 203 (1936) 412-414.

[2] C.F. BRIDGEMAN and H.L. GIBSON, Infra-red Luminescence in the Photographic Examination of Paintings and other Art Objects. Stud. Conserv. 8 (1963) 77-83.

[3] L. LAZZARINI, "Studio technico-scientifico di un dipinti di Giuseppe Porta detti Il SalviatiNotizie da Pallazzo Albani" (Univ. Urbino) Anno *III*, N 2/3 (1974) 38-47.

[4] D.C. RHOADS and D.J. STANLEY, "Transmitted Infrared Radiation:A Simle Methodfor Studying Sedimentary Structures." J. Sedimentary Petrol., 36 (1966) 1144-49

[5] "Applied Infrared Photography " Kodak Technical Publication M-28 (1968)

[6] WALMSLEY, E., METZGER AND C. DELANEY, J.K.: *„Evaluation of Platinum Silicide Cameras for Use in Infrared Reflectography"*. ICOM Comm. Conserv. 10th Triennial Meeting, Washington D.C., 22.-27. Aug. 1993, Pre-prints 57 - 62.

[7] C.A. MITCHELL, „The Use of Infra-Red Rays in the Examination of Inks and Pigments." Analyst. 60 (1935) 454-461.

[8]J. THOLL, Infrared Photography of documents. J. Phot. Soc. Am.17B, Part I, 10-13, Part II (1951) 34-39.

[9] A. BURMESTER und K. RENGER, "Neue Ansätze zur Erforchung von Handzeichnungen. Untersuchungen der "Münchner Rembrandt-Fäschungen." im nahen Infrarot." Maltechnik-Restauro 92/3, 9(1986).

[10] A. BURMESTER, „The Study of Drawings in the Near Infrared" in: *Analysis and Examination of an Art Object by Imaging Technique*, Tokyo Nat. Res. Inst. of Cultural Properties (1991) 61-81.

[11] R. TEPEST, "Der Einsatz von Filtern in der IR-Reflektographie." Catalogue of the Exhibition "*Unsichtbare Meisterzeichnungen auf dem Malgrund – Cranach und seine Zeitgenossen.*" Wartburg/Eisenach Feb. 1998,

[12] WECKSUNG, G., EVANS, R., WALKER, J., AINSWORTH, M., BREALY, J. and CARRIVEAU, G.: *„Assembly of infra-red Reflectograms by digital processing using a portable data collecting system"*. ICOM Comm. Conservation. 8th Triennial Meeting Sidney (1987) 107 - 109.

[13] BILLINGE, R, CUPITT, J. DESSIPRIS, N. and SAUNDERS, D.: *„A note on an improved procedure for the rapid assembly of infrared reflectogram mosaics"*. Stud. Cons. 38 (1992) 92-98.

[14] MAIRINGER, F. und PAPST, A.: „*Die Erstellung von Infrarot-Reflektogrammen von Kunstwerken mittels des Programmpakets IREÏKON*". 4th Intern. Conf. on Non-Destructive Testing of Works of Art, Berlin 3. - 8- Oct. 1995, 175-182.

Radiation in Art and Archeometry
D.C. Creagh and D.A. Bradley (editors)

The ultraviolet and fluorescence study of paintings and manuscripts.

Franz Mairinger

Institute for Colour Science and Colour Chemistry, Academy of fine Arts Vienna

The properties, methods of generation and detection are given for Ultraviolet radiation. Practical advice is given on the use of UV radiation for the study of paintings and inks in manuscripts.

1. INTRODUCTION

Ultraviolet and fluorescence examinations are invaluable tools in many aspects of scientific research and conservation of works of art and archaeological objects. For these purposes UV-radiation can be used in two different ways:

1. to record the invisible UV reflected by the object either by photographic or electronic means
2. to excite visible fluorescence, which can be photographed.

In both cases surface states of objects, invisible to the naked eye, can be recorded. The techniques involved are fairly simple to handle. UV- and fluorescence photography uses the same equipment as ordinary photography, no elaborate gear is necessary. Only the radiation sources are different. In the following sections the practical aspects as the selection of suitable radiation sources, filters, photographic materials, ordinary and video cameras and their handling are described. Then the scope and the limitations of these methods are discussed.

2. ULTRAVIOLET RADIATION

This invisible portion of the electromagnetic spectrum extends in decreasing wavelength from the violet end of the visible spectrum at 400 nm to the range of soft x-rays at 10 nm. Ultraviolet radiation was discovered 1801 by J.W. RITTER (1776-1810) by its photochemical action.

The ultraviolet spectrum is arbitrarily divided into 4 bands (Figure 1).

1. ***Near*** or ***long wave ultraviolet*** extends from about 320 – 400 nm. The range between 340 – 400 nm is transmitted by regular optical glass of which most of the photographic lenses are made. Therefore this range is of most practical importance in ultraviolet photography. It also posses the ability to excite visible fluorescence in many inorganic and organic materials.
2. ***Middle ultraviolet*** comprises radiation from about 280 – 320 nm. Part of this band (295 – 320 nm) is present in sunlight and exhibits the tanning (and sunburn) action on human skin. It is emitted from mercury vapour lamps. Middle ultraviolet radiation is not trans-

mitted by regular optical glass. To produce a photographic image in this range quartz or fluorite lenses must be used.

3. ***Far*** or ***Short wave ultraviolet***: is considered to extend from 200 – 280 nm. It is known for its germicidal action and is very dangerous for unprotected eyes and skin. It induces photoluminescence in many minerals and gems, which is not or only weakly excited by long wave ultraviolet radiation. It is also used for photographing chromatograms.
4. **Vacuum ultraviolet** extends from 200 nm down to about 10 nm, where the range of soft x-rays begins. This radiation is strongly absorbed by air and can be handled only in vacuum. sorbed by air and can only be handled in vacuum. The region around 190 nm is used for photo –lithography of semiconductor devices and is of scientific interest in UV-spectrometry.

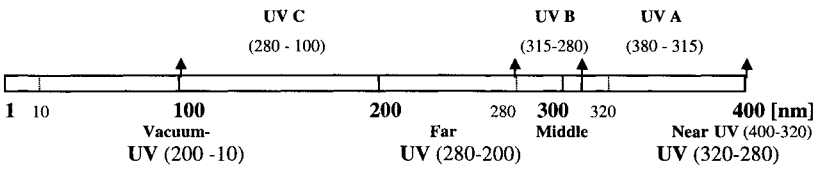

Figure 1. The spectrum of ultraviolet radiation

Another division of the UV range is also frequently used: ***UV A*** (400 – 310 nm), ***UV B*** (310 – 280 nm) and ***UV C*** (280 – 100).

3. ULTRAVIOLET RADIATION SOURCES

Although *sunlight* is a strong source of ultraviolet radiation it is not a very practical one, because the intensity depends on atmospheric conditions and the position of the sun, therefore it is difficult to determine the proper exposure

Other powerful sources are *carbon* and *metal* (e.g. iron or cadmium) *arcs*, but they not very convenient, since they give off noxious fumes and produce a lot of heat.

The most preferable artificial sources are *gas discharge lamps* like mercury high and low pressure lamps, fluorescent tubes, metal halides lamps and Xenon arcs. They are stable sources and constant in intensity. They come in compact units, which are easy to obtain and to handle.

3.1 Mercury vapour discharge lamps

Mercury vapour, when electrically excited, emits many strong lines in the visible and ultraviolet region. The emission spectrum is shown in **Figure 2**. The spectral intensity distribution depends on vapour pressure and temperature. If the pressure is low, the intensity of short wave UV at 253.7 nm is emitted with high intensity. When the pressure increases, an

arc in the gas is established and mainly the long wave UV at 365 nm is emitted, also the luminous efficiency in the visible range increases strongly. So two lamp types are commercially available: *low-pressure* and *high-pressure lamps*. Most manufactures produce both types, so does e.g. PHILIPS. Its production palette is taken as representative example.

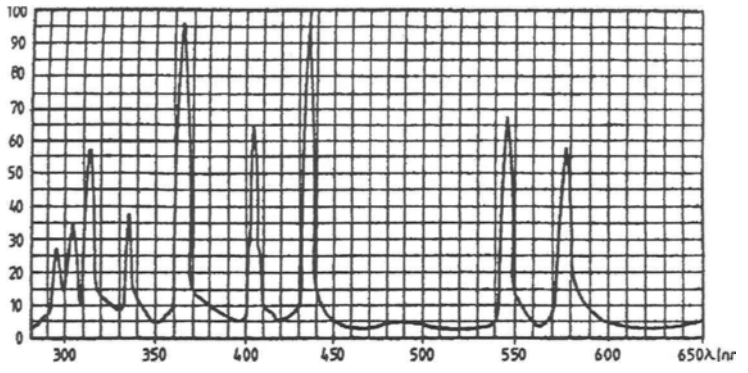

Figure 2. Spectral lines of mercury vapour

3.2 High Pressure Mercury Vapour Lamps

Short arc high pressure mercury discharge lamps emit visible light and ultraviolet radiation in the 340 – 380 nm range. The burner of PHILIPS HPW high pressure lamp has an outer envelope made of dark Wood's glass, which acts as a barrier for the visible radiation. The main output in the UV is at 365 nm. There are no hazards involved for eyes and skin. The spectral power distribution is shown in Figure 3.

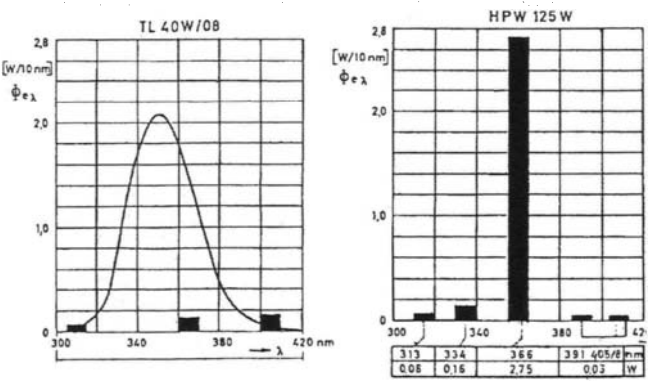

Figure 3 Spectral power Distribution of Philips HPW lamp.

The HPW lamp has an ordinary E 27 base like domestic lamps and there are no restrictions in burning position. It is operated at 220 V (mains voltage) via a choke. The wattage is 125 W. It takes about 2 –3 minutes run-up time to reach the full output. The lamp will ignite

only in cold condition. If it is switched off, it must cool down at least for 5 – 8 minutes before re-ignition is possible. This relatively small, intense source is advantageous for small objects. To illuminate larger areas at least 4 lamps are necessary to establish an even illumination.

There are also *metal halide lamps* (Philips HPA) available, which have a very high radiant efficiency and are used for reprography. They are single enveloped and optimised for the UV-A radiation, but the spectrum contains also some UV-B, which is harmful to eyes and skin. For use in fluorescence work a filter which absorbs the visible part of the spectrum must be used.

3.3 Low Pressure Mercury Vapour Lamps

The low pressure mercury vapour discharge lamps produce mainly short wave UV radiation at 253,7 nm. These tubular lamps are well known as *fluorescent tubes.* The tube wall is internally coated with a fluorescent powder (phosphor), which converts the short wave radiation into long wave ultraviolet radiation in the range of 350 –395 nm with a maximum at 360 nm. The *Philips TL(D)/08 fluorescent tubes* have a dark blue glass envelope, which transmits the UV-A radiation and only a minimum visible radiation in the blue range. They are operated on AC mains supply via a ballast and a starter. The tube length, which varies between 14 – 120 cm, can be chosen to suite the size of the objects. The length determines also the wattage. There are no restrictions as far as burning position or switching is concerned. The useful life is over 2000 hours. These "black light" fluorescent tubes are therefore the most convenient UV-source for larger objects.

When low pressure lamps have clear tubes(special glass or quartz) and a filter which absorbs the visible range, they are excellent sources for short wave ultraviolet radiation with an emission peak at 253,7 nm (UV-C). The Philips TUV lamps have tubular envelopes made of special glass, which filters out the 185 nm ozone-forming line. Their wattage ranges from 4 – 115 W (TUV4W, TUV115W). They are mainly used for disinfection of water, air and surfaces and also for exciting fluorescence of minerals and for curing of lacquers.

3.4 Electronic Flash lamps - Xenon Arc lamps

Electronic flash lamps contain a mixture of the noble gases xenon, krypton and argon. They are primarily designed for photography in the visible range, but they have also an fairly intense output in the near UV (and in the infrared region). The actual spectral distribution depends on the gas mixture. Tubes containing a high percentage of krypton or argon emit more long wave UV (and blue) than one with a high percentage of xenon. Some lamps are covered with yellowish lacquer layer, which reduces the UV output. These types are less suitable UV-sources.

When flash lamps are covered with a filter which absorbs the visible part of the spectrum, they are convenient sources of long wave UV for fluorescence and reflected UV photography after the working conditions have been established by test exposures. If one flash is not enough for the proper exposure, several flashes in a darkened room with open camera shutter (multi-flash technique) are ignited. This technique can also be used for recording the fluorescence light. Of course for the preliminary visual observation of fluorescence phenomena a continuous source is necessary, in the short time of the flash the fluorescence cannot be seen.

High-pressure xenon continuos arc lamps with a high wattage are also commercial available. They have a sun-like spectrum and are used for colour measurements. Compared

with mercury vapour lamps they are much more expensive and less efficient sources in the UV region.

4. FILTERS

In reflected ultraviolet and fluorescence photography two different types of filtration are applied.

1. ***Filters with a high percentage transmittance of long wave ultraviolet and no visible light transmittance.*** This type is known as *exciter filter.* They are used either in front of UV sources to remove the visible components, when recording the visible fluorescence or for (reflected) UV photography in front of the camera lenses to block out the visible light. In this case the filter must be optically polished.
2. ***Filters which transmit visible fluorescence and remove any residual reflected or scattered UV radiation***, which would also affect the photographic emulsions. They are called *(UV-) barrier filters.*

Occasionally other filters, such as colour compensating or conversion filters, are used in combination with barrier filters. They are especially helpful when colour films are exposed or in case of black-and-white films to enhance contrast between colours of similar or equal brightness.

4.1 Exciter Filters

The most common exciter filter, used with the radiation source, are made of Woods' glass, whose exact composition varies. It is a special barium-sodium-silicate glass, which is tinted with about 9 % nickel oxide, their transmittance is limited to long wave UV region. This is not a disadvantage in UV photography since the transmittance of camera lenses is also limited to this region. There are no gelatine filter suitable for this type of filtration.

For some fluorescence applications (e. g. minerals) medium wave and short wave ultraviolet radiation is necessary for excitation, than tinted quartz filters must be used. Some UV sources include exciter filters, attached to the lamp house or incorporated in the (tinted) glass envelope (Philips HPW or TL types). There are several manufacturers for this type of filters. Data of some of these species are given in Table 1.

Table 1 UV
Exciter Filters

Manufacturer	Designation	Transmission range (nm)	Remarks
KODAK	18 A (2 mm)	310 - 400	Transmits Infrared
CORNING GLASS # 5840	CS 7-60 (2 mm)	310 - 400	
CORNING GLAS 9863	CS 7-54 (5mm)	250 - 380	
SCHOTT	UG 1 (2mm)	310 - 400	Transmits infrared
SCHOTT	UG 5	240 -480	Transmits infrared

As can be seen in Figure 4, most of the filters have also a high transmittance in the infrared region. This fact is of importance only, if infrared sensitive films are used.

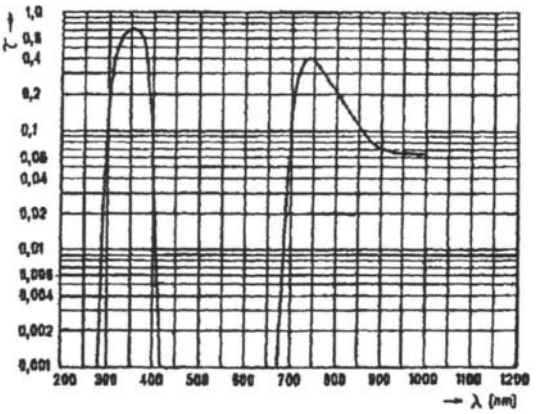

Figure 4 Transmittance of SCHOTT UG 1 exciter filter (2mm)

4.2 Barrier filter

The exciter filter transmits the radiation, which excites fluorescence, but not all of this radiation is used up in this process. There will be an appreciable amount, which is reflected, transmitted or scattered by the object. Since the brightness of fluorescence is usually very low, this residual radiation will cause more exposure than the fluorescence, this would degrade fluorescence recording. So in front of the camera lens a filter must be used , which acts by absorption as a barrier to the UV radiation.

So a barrier filter must absorb all radiation transmitted by the exciter filter and transmits only the wavelengths of the generated fluorescent light. If the exciter filter passes UV and some of the short visual blue (up to 420 nm), then the barrier filter must absorb in this region also.

The *selection* of a suitable *barrier filter* depends not only on the spectral distribution of the exciting radiation, but also upon the wavelengths of the fluorescent light. This is only a problem, when the object exhibits a blue fluorescence, which is the same or near to the wavelength of blue light transmitted by the exciter filter. In this case either the exciter filter must be substituted by a filter, which has no blue transmittance or when the wavelength of the fluorescence light is longer than the transmitted blue, than a barrier filter of the interference type (long pass filter) can be used.

If no fluorescence in the blue region occurs or the blue fluorescence should be suppressed, the selection of filters is very simple, any of the (cheap) yellow gelatine filter which absorb UV can be used (e. g. WRATTEN gelatine filters Nos. 9, 12, 15). These filters transmit freely green, yellow, orange and red. If the fluorescence occurs in the infrared region, the

Wratten filter No. 87 is an effective barrier filter. For this purpose an infrared sensitive film must be used.

An other difficulty may arise from the fact, that some of these filters show a bright fluorescence, they seem to glow when irradiated with UV. This would lead to a severe degradation of the fluorescence record. To avoid that, a filter which absorbs only UV (e. g. Wratten 2A or 2B) is placed in front of yellow filter.

It should also be kept in mind, that the dyes used for gelatine UV filters are not very stable, so the filters should be replaced from time to time.

In Table 2 the data of some barrier filters with different absorption edges are summarised.

Table 2
Data of UV Barrier Filters

Manufacturer	Designation	Transmission starts at nm	Remarks
KODAK	Wratten 2B	395	Pale Yellow
KODAK	Wratten 2A	410	Pale Yellow
KODAK	Wratten 2E	420	Pale Yellow
KODAK	Wratten 9	480	Yellow
KODAK	Wratten 12	510	Deep Yellow
SCHOTT	GG 420	420	Pale Yellow (Glass)
SCHOTT	GG 495	495	Yellow
SCHOTT	LP 400	400	Interference filter
SCHOTT	LP 430	430	

5. PHOTOGRAPHIC MATERIALS

5.1 Reflected ultraviolet photography

For long wave ultraviolet photography any film or plate can be used, in view of the fact tat all photographic emulsions which contain silver halides are inherently sensitive to blue and ultraviolet. Only black-and-white materials will be considered, since colour films have no advantage.

The exposure determination has to be done by test exposures since the sensitivity of common photographic materials in the ultraviolet region is very often less than the rated speed. This is due to the fact that the gelatine of the emulsions absorbs UV. So KODAK states for the TRI-X Pan Film (ISO 27/400) in the long wave UV region an effective speed about 10 ASA.

Most of the conventional exposure meters (for incident light) have a (reduced) sensitivity to UV. If the window of the meter is covered with an ultraviolet filter (e.g. Wratten 18 A or Schott UG2) an indication of ultraviolet intensity is obtained. If the source contains an ultraviolet filter (Philips HPW), the room is darkened and the intensity of fluorescence is low, no filter is necessary in front of the meter. From a test series with varying exposure times the

actual speed of the film can be calculated. There are also specially designed meters for UV measurement commercially available.

A similar procedure can be applied for the determination of exposure with electronic flash lamps. An ultraviolet filter is placed in front of the lens and a test series with constant shutter speed and varying *f*-numbers is made. If the exposure of one flash is not enough, the shutter is opened and additional flashes are fired.

5.2 UV-fluorescence photography

Since fluorescence light is in the visible range, common black-and white materials and colour films can be used to record fluorescence. As already mentioned all photographic emulsions are sensitive to blue and ultraviolet, therefore a barrier filter which absorbs the reflected UV, must be used always.

5.3 Colour Films

Colour films are the first choice in recording fluorescence, because it allows a differentiation between colours of equal inherent brightness (e.g. red – green) which a black-and-white film would render with equal grey tones. The spectral composition of fluorescence light resembles to daylight. So for a correct colour rendition a daylight type colour film is recommended. But the subject brightness of fluorescing objects is usually very low, so the exposure time becomes excessively long (up to 10 minutes). At that low levels the film speed goes down by the failure of the reciprocity law:

$$E = I \cdot t$$

where E means the exposure, I the illuminance and t the time. This effect is usually not a serious disadvantage for black-and-white films, but is very important for daylight type colour films, because the three emulsions have different reciprocity failure characteristics. Therefore the colour balance is altered and a erroneous colour rendition occurs. The effect can be compensated with appropriate colour compensating filters indicated on the data sheet of (professional) films. If the exposure time is appreciably longer than one second, the contrasts of the three images are also different. This effect cannot be corrected by colour compensating filters.

To solve this problems two ways are possible: (a) the use of a high speed daylight type colour film in order to minimise exposure time or (b) the use of a colour film balanced for tungsten illumination. This film is designed for long exposure times, but it has a very high blue sensitivity which must be compensated by the use of a conversion filter (e.g. Wratten 85B) which alters the colour balance of the exposing light. To prevent the fluorescence of this filter, a barrier filter (Wratten 2B or 2E) should be placed in front.

To give an example for recording the fluorescence of paintings by colour photography : As UV-source 4 fluorescent tubes Philips TL40W at a distance of 1m were used, WRATTEN 2E + 85B as filters, and KODAK Ektachrome 320T film at f/4, the exposure time was varied between 8 and 30 seconds depending on the intensity of the fluorescence.

5.4 Black-and-white films

There are many applications for which a black-and-white film is perfectly satisfactory for recording fluorescence. It should have panchromatic sensitivity and high speed. In any

case a barrier filter for UV must be used. Since all colours are recorded as grey tones, it can be difficult to differentiate between colours of different hue but equal luminosity. Contrast can be achieved by use of colour compensating filters (covered with the barrier filter).

For black-and-white films the reciprocity failure in case of very long exposure times is no problem, since the loss in speed is simply compensated by increase of exposure times. For professional films the necessary corrections are tabulated.

6. CAMERA LENSES

There are no restrictions for fluorescence photography, common lenses made of optical glass can be used, since visible light it recorded.

For the recording of reflected UV several problems can arise. It must be kept in mind that that the recording range for optical glass is limited to 340 nm. So only long wave ultraviolet radiation will be recorded.

All modern camera lenses are covered with antireflection coatings. Some of these layers exhibit a strong fluorescence when irradiated by UV. This would severely degrade the UV recording. This possible fluorescence can be easily determined beforehand by holding the lens in the beam of the UV source. If fluorescence occurs, the lens can't be used.

The chromatic correction of camera lenses pertains only to the visible range. The refraction index of glass for UV radiation is greater than for the visible range, so the focal length is shorter when UV is used. That means that an image in sharp focus visually may not be quite so sharp in the UV region. This can be compensated by decreasing the lens aperture to obtain a greater depth of field. At least two steps down below the maximum aperture will be adequate.

To avoid this problem and to extend the recording range below 340 nm, lenses made of quartz or fluorite must be used. They are corrected in the range between 220 – 1.000 nm. NIKON (UV-Nikkor 4,4/105mm) and ZEISS (UV-Sonar 4,3/105mm) make this type commercially available (at a high price).

7. ELECTRONIC RECORDING DEVICES FOR EXAMINATIONS IN REFLECTED UV

Most of the video cameras (respectively camcorders) with camera tubes of the Vidicon type or CCD-chips have an appreciable sensitivity in the near UV range and can therefore be used for preliminary examinations. The result can be seen immediately on a monitor. If the result is positive, a photographic recording (with better resolution) can be made. There are also special UV-Vidicons with a sensitivity range of 200 – 720 nm (e. g. HAMAMATSU N 983) available.

8. APPLICATIONS OF UV-FLUORESCENCE PHOTOGRAPHY

Since many inorganic and organic substances exhibit a characteristic coloured fluorescence this method can be applied to differentiate materials. But it should be kept in mind, that this is a very sensitive method. Even traces of active impurities can generate strong fluores-

cence. So minerals of the same chemical composition but of different deposits show completely different fluorescence. An example is the colourless calcite, its fluorescence colours may vary from red or orange to blue. The same holds for natural chalk.

On the other hand certain substances can quench the fluorescence of other materials, for example, verdigris, which was used as a green glaze in gothic paintings, quenches the fluorescence of natural resins like mastic or dammar. The same holds for certain ochres, umbers and sienna earths. So the identification of materials on the base of a specific fluorescence colour is very unreliable.

For paintings, it should be kept in mind that paint layers mostly are complex mixtures of pigments and binding media, which are very often covered by varnish layers of aged natural resins and that UV radiation has no significant penetration ability. Almost always it is strongly absorbed in the top layer. Only in case of water-colours, tempera and wall paintings the primary fluorescence of pigments can be observed. This holds also in some cases for the polychromy of sculptures.

Some inorganic and organic pigments exhibit a characteristic primary fluorescence. Examples for pure pigment powders are given in Table 3. The samples were taken from the collection of the Institute. A filtered long wave UV source (Mineralite, Ultraviolet Products, Inc.) was used for excitation.

Some of the binding media used in easel paintings (natural resins, gums, animal glue) exhibit also a characteristic fluorescence. The intensity and the colour of their fluorescence depend strongly on their age. Young varnishes show often only a light blue, whereas older resins give a strong green fluorescence, the intensity depending on their age.

In most cases later additions like retouches or over-paints appear as more or less dark spots or areas on the greenish fluorescence of the varnish layer. This behaviour gives a possibility to judge the state of preservation of a painting. But with increasing age these additions begin also to fluoresce, so after 80 – 100 years it is very difficult to recognise them. So a perfectly uniform fluorescence is no reliable indication of a perfect state of preservation, other methods like infrared or x-ray examinations have to be applied.

The normal and the fluorescent colour photos of the painting "Madonna with Child" attributed to a follower of Rogier van der Weyden, shown in Figure 5a and 5 b, should serve as an example for the mentioned phenomena. The state of preservation and the locations of damages can be seen quite clearly on the fluorescence record.

There is an uneven greenish fluorescence of the varnish layer, especially on the gilded background. The border zones (especially on the right side), which were covered by the frame, exhibit a bluish tint, an indication that light and the oxygen of the air influence the ageing of the varnish. The red undergarment of the Madonna shows a blunt red fluorescence, which is an indication that vermilion (art.) or cinnabar (nat.) was used. The black vertical line on the right side is a crack in panel, which has been retouched. There are many smaller retouches in the flesh parts of the Madonna and the child. The are over-paints in the white cloth and the hair of the child which show different brightness, indicating different age. There is fluorescence quenching in the hair of the Madonna, due to the umber, which was used as pigment. Of course this UV fluorescence recording tells just the location of the later additions and doesn't reveal the true extent of damages. Only a thorough comparison with the x-ray photograph and a microscopic examination gives a final clue.

Table 3.
Fluorescence of pigments

BLUE PIGMENTS

Egyptian Blue	purple
Azurite, natural	dark blue
Blue Verditer (Blue Bice)	dark purple
Cerulean Blue	lavender blue
Phtalocyanine Blue (ICI)	no fluorescence
Indigo	dark purple
Cobalt Blue	red
Prussian Blue	no fluorescence
Smalt	light purple

GREEN PIGMENTS

Viridian	bright red
Green earth	bright blue
Verdigisn	no fluorescence
Phtalocyanine Green	no fluorescence
Chrome Green	dark red

ROTPIGMENTE

Cadmium Red	red
Madder (root-)	yellow
Madder (Alizarin)	no fluorescence
Red lead	dark red
Red Ochre, red Bole	no fluorescence
Vermillion	red

WHITE PIGMENTS

White lead	brownish pink
Lithopone (ZnS-Pigments)	orange to yellowish orange
Zinc white	light green
Chalk, natural	dark yellow
Chalk precipitated	no fluorescence
Gypsum	violet
White Bole	reddish violet

YELLOW PIGMENTS

Orpiment	light yellow
Chrome Yellow	red
Cadmium Yellow	light red
Yellow Ochre	
Naples Yellow	light red
Zinc Yellow	bright red

Figure 5. Follower of Rogier van der Weyden: "Madonna with Child", Tempera on Wood (Oak), 38,5x29,0 cm, Inv.-# A 2, Gallery of the Academy of Fine Arts Vienna/Austria

(a) normal colour recording

(b) UV Fluorescence, Kodak Ektachrome 320 T/120, WRATTEN 2B + 85 filters, 4 PHILIPS HPW lamps

(c) Reflected UV recording, 2 PHILIPS HPW lamps, SCHOTT UG 5 filter, 2 mm

Another important use of fluorescence is the examination of signatures or datings on paintings. If the original inscriptions are under old varnish layers they can't be seen in fluorescence. If they show up clearly (in black), they must lie on top of the varnish layer and are added or gone over by a restorer. Even local cleaning procedures (with organic solvents) in these areas are easily recognised.

There are many other fields of application of UV fluorescence examination. It can be applied for the investigation of dyed textiles, since many natural and synthetic dyestuffs have characteristic fluorescence colours. Later additions or restored damages of amber objects can be recognised quite easily.

Quite often metal sculptures or gilded parts of wooden sculptures are coated with (dyed) varnish layers which cannot to be seen by the naked eye. They show up in the fluorescence quite clearly.

An example of the application of secondary fluorescence by using fluorochromes, is the documentation of minute cracks in metal objects (e. g. sculptures). Cracks, extremely small in breadth, can be impregnated by capillary action with a liquid penetrant (organic solvent or water) containing a fluorescent substance. The excess liquid is carefully removed with a suitable solvent and the object is subjected to UV radiation. Even the smallest cracks will be visible, because the fluorescent substance will remaining in the clefts.

An other well known application is the investigation of faded inks and paints on graphic documents (paper or parchment). Iron gall inks absorb long wave UV quite strongly without showing fluorescence, whereas the fibres fluoresce brightly. Mechanical erasures or chemical bleaching will also alter this fluorescence. For erased soot inks infrared photography is the better choice.

9. APPLICATIONS OF UV-PHOTOGRAPHY

Compared with UV fluorescence, there are less applications for reflected UV photography. In the case of faded iron gall inks this method may bring better results than fluorescence. An example is shown in Figure 6. On page 246 of a French Bible moralisée (around 1250) the margin bears an inscription, which is barley readable. One pair of lines is written with blue ink, the following pair with red ink. To make this (Latin) text more readable several methods were applied (fluorescence, infrared, x-ray). Only the recording with reflected UV showed new details.

For the investigation of the state of preservation of paintings reflected UV photography can be utilised in a similar way as fluorescence. Areas which absorb UV (with or without visible fluorescence) show up as black spots, whereas regions which reflect the incident UV, appear bright on a photograph. An example of these phenomena is shown in Figure 5c. The retouches in the flesh parts which show up in the fluorescence as black spots are rendered very bright in the UV recording, an indication, that the radiation is reflected and not absorbed. There is also a further differentiation in the varnish layer (right of the head of the Madonna), which is difficult to explain.

In general can be stated, that the UV recording is more difficult to read than the fluorescence.

Figure 6 shows photographs of detail in a Bible moralisée (French, ~ 1250), Austrian National Library,Vienna, Codex 1179, folio 246 (watercolours on parchment).

Figure 6(a) Recording in normal light.

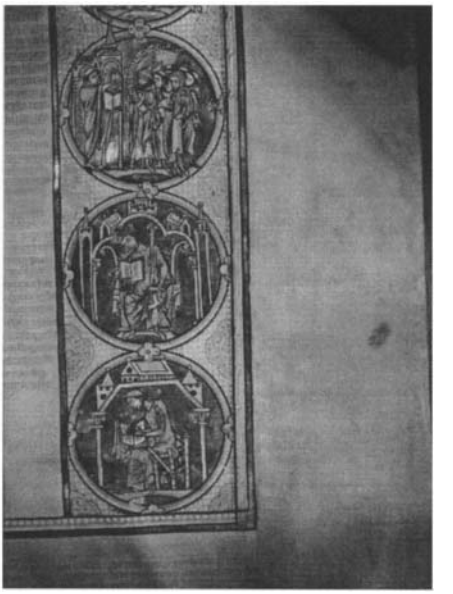

Figure 6(b) Infrared recording (KODAK Infrared High Speed, filter: WRATTEN #87C

Figure 6 (c) UV fluorescence recording, 2 PHILIPS HPW lamps, filter: WRATTEN # 2B

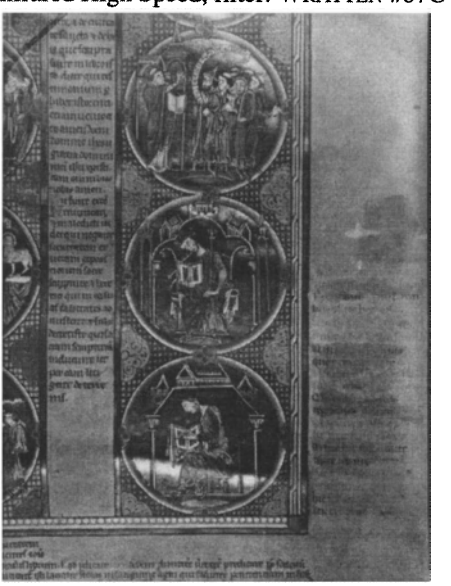

Figure 6(d) reflected UV recording 2 PHILIPS HPW lamps filter: SCHOTT UG 1

REFERENCES

Following is list of general references, in alphabetical order, on the topic of ultraviolet and fluorescence examination of artworks.

Aulmann, H., "Die technischen Methoden der Gemäldeuntersuchung im Museum. "Fest schrift zur Eröffnung des Kunstmuseums in Basel (1936) (Sonderdruck)

Aulmann, H., "Gemäldeuntersuchungen mit Röntgen-, Ultraviolett- und Infrarotstrahlen zum Werk des Konrad Witz" Basel (1958), Hans Holbein Verlag

Autenrieth, H.P., A. Aldrovandi, and P. Turek, "Die Praxis der UV-Fluoreszenzfotografie" Z. Kunsttechnologie und Konservierung 4 (1990) Heft 2, 215-234.

Bandow, F., "Lumineszenz. Ergebnisse und Anwendung in Physik, Chemie und Biologie. " Wiss. Verlagsgesellschaft, Stuttgart (1950)

Bather, F.A., "Ultraviolet rays, an aid to museums work" The Museums Journal 28 (1929) 189-193.

Beutel, E. and A. Kutzelnigg, "Beiträge zur Lumineszenzanalyse I." Mh. f. Chem. 55 (1930) 158.

Beutel, E. and A. Kutzelnigg, "Beiträge zur Lumineszenzanalyse II: Über die Lumineszenz der weißen Malerfarben und die Anwendung der Lumineszenzanalyse zur Untersuchung von Gemälden." Mh. f. Chem. 57 (1931) 9.

Beutel., E. and A. Kutzelnigg, "Beiträge zur Lumineszenzanalyse IV. Zur Kenntnis des Fluoreszenz des Zinkoxids." Mh. f. Chem. 61 (1932) 69.

Brandmayer, C., "Neue Methoden zur Untersuchung alter Gemälde. "Die Kunstauktion 4 (1930) 9.

Brandmayer, C., "Neue Methoden zur Untersuchung alter Gemälde." Weltkunst 4, Nr. 34 (24. Aug. 1930) 24

Brandt, W., "Fotostaffelei für Gemäldeaufnahmen." Maltechnik 68 (1962) 37-45.

Brandt, W., "Fluoreszenzaufnahmen farbig." Maltechnik 70 (1964) 2, 46-48.

Brandt, W., "Photographische Dokumentation im Bereich der unsichtbaren Strahlen." Nachrichtenblatt der Denkmalpflege in Baden-Würtemberg 10 (1967) 68-75.

Celerier, J.F., "Die wissenschaftlichen Methoden im Gebrauch bei Gemäldeuntersuchungen. "Mouseion 13/14 (1931) 3.

Dake, H.C. and. J. De Ment, "Fluorescent Light and its Applications"New York (1941).

Dake, H.C. and. J. De Ment, "Ultraviolet Light and its Applications." New York (1942).

Danckwort , P.W., "Die Bedeutung der Lumineszenz-Analyse für die Lack- und Farbenindustrie." Abstract: Tech. Stud. 1 (1933) 214-215.

Danckwortt, P.W. and J. Eisenbrand, "Die Lumineszenzanalyse im filtrierten Leipzig; 5. Aufl. 1942, 1956 7. Aufl. 1964.

De la Rie, E.R., "Ultraviolet Radioation Fluorescence of Paint and Varnish layers" in: PACT 13 (1986). 91-108 (Scientific Examination of Easel Paintings)

De la Rie, E.R., "Fluorescence of Paint and Varnish Layers" Part 1: Stud. Cons. 27 (1982), 1-7 (1), Part 2: 27 (1982), 65-69 (2), Part 3: 27 (1982), 102-108 (3).

De Ment, J., "Fluorochemistry" Chem. Publ. Co. Brooklyn (1945).

De Ment, J., "Fluorescent Chemicals and its Applications" New York (1942).

De Ment, J., "Handbook of fluorescent gems and minerals: An exposition and catalogue of the fluorescent and phosphorescent gems and minerals including the use of ultraviolet light in the earth sciences"Portland 15, Ora, Mineralogist Pub. Co. (1949).

Déribéré, M., "Die Unterscheidung zwischen Elfenbein und seinen plastischen Nachahmungen" Res. gen. Matières plastiques 11 (1935), 311, Abstract: Ch. Z. B. 1936 I. 3029.

Déribéré, M., "L'application des phénomènes de fluorescence à l'étude des pigments"La Chimic des peintures 5 (1942), 137-141, Abstract: Cem. Z.B. (1942) II 2646.

Iwase, E. and T. Kuronuma," Zur Lumineszenz des Calzit I. Das Fluoreszenzspektrum Japanischen Calzits im ultraviolettem Licht." Bull. chem. Soc. Japan 11, Nr. 8 (1936) Abstract: Chem. Z.B. 1937 I. 3112.

Iwase, E. and Kuronuma, T."Zur Lumineszenz des Calzits II. Thermolumineszenzspectra Japanischer Calzite"Bull. chem. Soc. Japan 11, Nr. 8 (1936), 523 Chem. Z. B. 1937 I. 3112.

Iwase,E. and T. Kuronuma, "Zur Lumineszenz des Calzits III. Änderung der Fluoreszenz-spektren von Calziten durch vorheriges Erhitzen"Bull. chem. Soc. Japan 11, Nr. 8 (1936)Chem. Z.B. (1937) I. 3112.

Eibner, A., "Lichtwirkungen auf Malerfarben VII: Die Lumineszenz-forschung im Dienste der Bilderkunde und Anstrich-technik" Chemiker-Zeitung 55 (1931), 395; 593-604; 614-615; 635-637; 655-656.

Eibner, A., "Lichtwirkungen auf Malerfarben VII: Die Lumineszenz-forschung im Dien ste der Bilderkunde und Anstrich-technik" Chemiker-Zeitung (1931), 593-604; 614-615; 635-637; 655-656.

Eibner, A., "Zum gegenwärtigen Stand der naturwissenschaftlichen Bilduntersuchung." Angew. Chem. 45 (1932) 301-307.

Eibner, A., "Les rayons ultraviolets appliqués à l'examen des couleurs et des agglutinants"Monseion, Bd. 7, 21/22 (1933), 32-69.

Eibner, A., "Les rayons ultraviolets appliqués à l'examen des couleurs et des agglutinants" Mouseion 21/22 (1933) 301-307 Abstract: Tech. Stud. 2 (1934), 232-233.

Eibner, A., L. Widenmayer and A. Stois, "Zur Möglichkeit der Beurteilung anorganischer Farbstoffe im Dunkelfelde der Analysen-Quarzlampe." Farbenzeitung 31 (1926) 2399-2400.

Elenbaas, W., "Light Sources" Philips Techn. Library, London (1972).

Engel, C.E., "Photography for the Scientist" London (1968).

Feller, R.L., "Artist's Pigments. - A handbook of their history and characteristics"Vol 1, Washington Cambridge (1986).

Filatov, V.V., and V. N.Bobkov, "Recent Research of Church Painting of 1408 in the Cathedral of the Assumption at Vladimir in Ultra-Violet Rays" ICOM Comm. f. Cons., 5th Triennial Meeting Zagreb 1978/15/11; 78/15/11, S. 1-8

Fink, C.G., "Chemistry and Art" Ind. Engeneering Chem. 26 (1934), 234 Abstract: Chem. Z. B 1934 I. 3095

Garlick , G.F.J., "Luminescence" Handbuch der Physik, Encyclopedia of Physics, XXVI. Bd, Licht und Materie, Light and Matter, Flügge S. Ed., Springer Berlin (1958) 1-128.

Garlick, G.F.J., "Photoconductivity" Flügge's Handbuch der Physik, Bd. IX (1956).

Gilgendorf, I.N., "Study and restoration of lost ancient inscriptions on the dry plaster by

the method of infrared and ultraviolet photography“ ICOM Comm. f. Cons., 4th Triennial Meeting Venice (1975), Preprints 1, 75/4/8, 1-9.
Goulinat, J.G., "Beitrag zu den wissenschaftlichen Verfahren bei der Restaurierung von Gemälden." Mouseion 15 (1931) 47.
Grant, J., "Die Anwendung ultravioletter Strahlen in der Fluoreszens-analyse: Verfahren zur Prüfung und Kontrolle von Pigmenten"Paint Colour Oil Varnish Ink Laquer Manuf. 7, 340; Manuf. Chemist pharmac. fine chem. Trade 8 (1937), 387; Chem Z.B. (1938) I. 1231
Grant, J., "Fluoreszenzanalyse von Anstrichstoffen"Amerc. Paint J. 22, 15; Paint, Oil Chem. Rev. 99, 64; Nat. Paint, Varnish Laquer Ass. Sci. Sect. Circular Nr. 546 (1937) 279; Ch ZB (1938) I. 1473.
Guilbault, G.G., "Practical Fluorescence" New York (1973).
Haitinger, M., "Sammelreferat: Methoden der Fluoreszenzanalyse."abs: T. S. 1 (1933) 165.
Hallström, B., "The Use of UV-Reflectograms for the Examination of Paintings" ICOM Comm. f. Cons., 4th Triennial Meeting Venice (1975) 75/VI/10
Hansell, „Ultraviolet and Fluorescence Recording"in: Engel, Ch. E.: "Photogr. for the Scientist" Academic Press, London, N.Y. (1968) (3. p. 1969), Chapter 8: 363-382.
48. C. S. Holliday,"The Application of Ultra-Violet Light to Prehistoric Rock Art"in: SAMAB 7 (1961), 179-184.
49. A. A. Hopkins, "Art restauration and frauds detected by use of UV-radiations"Scient. American 146, 4 (1932), 220-221
50. M. Hours-Miedan, "A la découverte de la peinture par les méthodes physiques"Paris (1957) Arts et Métiers Graphique
51. D. Jakobs and H. F. Reichwald, "Untersuchungsergebnisse und Maßnahmen der jüngsten Restaurierung von St. Georg Reichenau-Oberzell " Z. f. Kunsttechnik und Konserv. 4 (1990) 291-332
52. H. Kaufmann, und P.Vogelmann "Über die Wirkung des Lichtes auf die Autoxidation von Fetten I.: Bleichung, Fluoreszenz und Vergilbung“. Fette, Seifen, Anstrichmittel 61 (1959) 206-210.
55. J. Kiefer, "Ultraviolette Strahlen" Berlin, New York (1977).
56. J. King, "The examination of porcelain etc. by ultraviolet light." Apollo 58 (1953) 74
57. Kodak (Eastman),"Ultraviolet and Fluorescence Photography"Eastman Kodak Co., Rochester, N.Y. (1968).
58. Kodak (Ed.),"Ultraviolet and Fluorescence PhotographyKodak Adv. Data Book M 27, Rochester (1972).
59. Kodak (Ed.),"Infrared and Ultraviolet Photography"Kodak Adv. Data Book M3 (1963) Rochester
60. G. R. Kögel, "Die Palimpsestphotographie"(in: Encyclopädie der Photographie Bd. 95) Halle (1920)
61. L. R. Koller, " Ultraviolet Radiation"2. Aufl. New York (1965).
62. G. Kostka,"Der Ultraviolett-Detektor als Hilfsmittel zur Unterscheidung des echten Bernsteins von seinen Imitationen" Chem. Ztg. 53 (1929) 117; 138.
63. Sr Kreutz, "Über die Lumineszenzeigenschaften der Calzite. (Mit besonderer Berücksichtigung der polnischen Lagerstätten)" Bull. int. Acad. polon. Sci. Lettres, Ser. A (1935) 486; Abstract: Chem. Z. B. 1936 II. 1692.
64. H. Kühn, "Fluoreszenzaufnahmen von griechischen Grabstelen" Internat. Photo Technik

H. 2(1970) 2-4, 52-55.
65. H. Kühn, "Möglichkeiten und Grenzen der Untersuchung von Gemälden mit Hilfe naturwissenschaftl. Methoden." Maltechnik 80 (1974) 149-162.
66. G. F. Kunz and Ch. Baskerville, "Die Einwirkung von Radium-, Röntgenstrahlen und ultraviolettem Licht auf Mineralien"Chem. News 89 (1904), 1; Abstract: Chem. Z.B. (1904) I. 399.
67. A. Kutzelnigg, "Zur Lumineszenz der Zinkverbindungen" Z. anorg. all. Chem. 208 (1932) 29.
68. Landoldt-Börnstein, "Lumineszenz" Neue Serie, Gruppe 4; Springer Berlin (1967)
68. A. P Laurie,."Alte Meister und moderne Fälschungen" Analyst 59 (1934) 657; (Ch ZB (1935) I., 307)
69. Lyon, R. A(rcadius),"Ultra-Violet rays as aids to restorers"Tech. Stud. in the Field of the Fine Arts 2 (1934) 152-157.
70. F. Mairinger, "Untersuchung von Kunstwerken mit sichtbaren und unsichtbaren Strahlen"Wien (1977).
71. F. Mairinger and T. B Newton, "Die Anwendung der UV-Reflektographie in der Papier-Restaurierung" Maltechnik-Restauro 82, 1 (1976) 33-39.
72. B. Marconi, "Application of UV-Fluorescence Photography, UV and IR experiments in application of autoelectronography to the examination of mural paintings"Zagadniema techn. 26-40.
73. M.Matteini, ed A. Moles, "Scienza e Restauro" - Metodi di IndagineFirenze (1984) 2. Aufl. (1986) Dt.: Naturwissen-schaftl. Untersuchungsmethoden in der Restaurierung, München (1990).
74. R Maurer, "Neue Methode zur Feststellung von Übermalungen an Kunstwerken und eine Neuerung auf dem Gebiete der Restaurierung derselben" Phot. Korrespond. 64 (1928) 200.
75. R. Maurer, "Heutige Gemäldeforschung "Umschau 33 (1929) 998.
76. R. Maurer, "Die Echtheitsprüfung von Gemälden" Umschau 34 (1930) 683.
77. L. Meunie and A. Bonnet, "Über die Fluoreszenz der pflanzlichen Farbstoffe" Comp. Rend. Acad. Sci. 181 (1925), 465 Abstract: Chem. Z. B. 1926 I., 591.
78. H. A. E. Meyer und E. O. Seitz, "Ultraviolette Strahlen" - Ihre Erzeugung, Messung und Anwendung in Medizin, Biologie und Technik, Berlin (1949).
79. F. Müller-Skjold,, H. Schmitt, und K. Wehlte, "Gemäldephotographie im Licht verschiedener Wellenlängen" Z. angew. Photographie 1 (1939) 125-140.
80. W.C Naylor, and A. Surfleet, "Prüfung der Kreidearten unter ultraviolettem Licht." Pharm. Journ. 136, Nr. 4 (1936) 82, 261; Abstract: Chem. Z. B. (1936) I., 4941.
81. E. H. Newton, "History of Luminescence (1900)"Am. Phil. Soc., Philadelphia (1966).
82. H.L Nickel, "Fotografie im Dienste der Kunst" Halle/S. (1959).
83. K. Nicolaus, "Gemälde. Untersucht, entdeckt, erforscht" Braunschweig (1979).
84. K. Noack, "Verzeichnis der fluoreszierenden Substanzen, nach der Farbe des Fluoreszenzlichts geordnet mit Literatur-hinweisen." Marburg (1887).
85. Passwater, R(ichard),."Guide to fluorescence literature" (1950-1964) New York (1967).
85. H. J. Plenderleith, "Application of Modern Physics for the Examination of Paitings." Nature (London), 147 (1941), 165; Abstract Chem. Z.B. (1941) II. 2739.
88. F. Preusser, , V. v. Graeve, und Ch Wolters."Malerei auf griechischen Grabstelen. Techn. und natur-wissenschaftl. Aspekte eines aräologischen Materials. "Maltechnik-

Restauro 87 (1981) 11-34.
89. J. A .Radley, "The Fluorescence Analysis of Waxes" Abs: Tech. Stud. 1 (1933), 220.
89. J. A. Radley, and J. Grant, "Fluorescence Analysis in Ultraviolet Light"New York (1959); 4. Aufl. London (1954), New York, 3.Ed. (1939).
90. J. Rawlins, "Wissenschaftliche Methoden in der Konservierung von Gemälden" Endeavour 7 (1948), 104.
91. N. Riehl, (Hrsg.), "Einführung in die Lumineszenz" K. Thiemig, München (1971).
92. H. Rinnebach, "Die Lumineszenzanalyse im Dienste des Kunsthistorikers und Restaurators." Techn. Mitt. f. Malerei 47/5 (1931), 54-55; 47/6 (1931), 64-66; 47
93. H. Rinnebach, "Die Lumineszenzanalyse im Dienste der Museumskunde" Museumskunde, N. F. 3 (1931) 5
93. R. Robl, "Untersuchungen mit der Analysenlampe. Lumineszenzanalyse" Z. angew. Ch. 39 (1926) 609-611.
94. J.J. Rorimer, "Ultraviolet Rays and their Use in the Examination of Works of Art" New York (1931); Metropolitan Museum of Art Techn. St. F. F. A. 1 (1932), 36.
95. J.J. Rorimer, "Ultraviolet Rays and their Use in the Examination of Works of Art"New York (1931).
96. J.Rubner, „Ultraviolette Strahlen und unsichtbare Geheimschriften." Techn. Mitt. f. Malerei 47, Nr. 6 (1931), 63-64; Archiv f. Kriminologie 79, Heft 4.
97. I. Sandner, "Untersuchung von Gemälden mit Ultraviolett-, Infrarot- und Röntgenstrahlen." Hochsch.Bild. KÜnste Dresden Abt. Restaurierung, Dresden (1987) 37 S.
100. K. Schmidinger, "Die Verwendungsmöglichkeiten der Analysenquarz-lampe in der arben- und Lackindustrie. "Farben-Zeitung 31 (1926) 2451-2453.
101. K. Schmidt-Thomsen, "Fluoreszenzbilder an Westfälischen Wandmalereien" Westfalen-Hefte f. Geschichte, Kunst und Volkskunde 37 (1959) 301-308.
102. M. J. Schoen, und J. Rinse, "Die Unterscheidung von Farbpigmenten im ultravioletten Licht." Chem. Weekbl. 26 (1929), 321; Z.B. (1929) II. 799.
103. Schott, "Transmission of Coloured Glasses and Filters", Handb. Chem. Phys. 3052-84 (Schott, Wratten)
104. P. Schreiber, und G. Ott, "Schutz vor ultravioletten Strahlen" (Schriftenreihe der BA f. Arbeitsschutz, Sonderschrift 14); Bremerhaven (1984).
105. G. Schwendt, "Fluorimetrische Analyse" Weinheim (1981).
106. L. J. Spencer, "Fluorescence of minerals in ultraviolet light." Americ. Mineralogist 14 (1928), 33 Ch. Z. B. (1929) I. 1557.
107. G. Spitzing, "Infrarot- und UV-Fotografie" - Grenzbereiche der Fotogr.München (1981), 2. Aufl. (1989).
108. G.G. Stokes, D. Brewster and J. Perschel "On the Change of Refrangibility of Light" Phil. Transactions Roy. Soc. London (1852) 463-562.
109. S.Strugger, "Fluoreszenzmikrokopie und Mikrobiologie"Hannover (1949).
110. W. Summer, "Ultraviolet and Infrared Engineering"London (1962).
111. C. Traunecker, and A. Bellod, "Wandmalereien aus den Krypten der Tempel von Karnak"Arbeitsbl. f. Restaurat. 7 (1974) H.1, 23-29.
112. H. Trillich, "Die Ultra-Violett-Bestrahlung im Dienste der Maltechnik" Techn. Mitt. F. Mal. 47, Nr. 10 (15.5.1931), 111-114.
113. H. Trillich, "Die Ultra-Violett-Bestrahlung im Dienste der Maltechnik." Tech. Mitt. f.

Mal. (1931) 109.
114. C. P. Van Hoek,"Die Weißpigmente und ihr Verhalten gegenüber ultra-violetten Strahlen"Farben-Zeitung 34 (1929) 833.
115. G. Wehlte, "Fluoreszenzuntersuchungen von Gemälden" Maltechnik 63 (1957), 34-40.
115. E. L. Wehry, *(Ed.)*"Modern Fluorescence Spectroscopy" Vol. 1, 2 and 4; New York, London (1976-81).
116. C.E. White and R Argauer, *J.*"Fluorescence Analysis. A practical approach" New York (1970).
117. H. Wolff, und W. Toeldte, "Leinöl im Ultraviolettlicht der Analysenquarzlampe" Farbe und Lack 31 (1926) 509.
118. H. Wolff, und W. Toeldte, "Zur Fluoreszenz-Analyse der Öllacke" Farbenzeitung 31 (1926) 80-81.
119. H. Wolff, und W. Toeldte, "Ein Beitrag zur Kenntnis und Prüfung der Harze" Farbenzeitung 31 (1926), 2503-2505
120. H.Wolff, und W.. Toeldte, „Leinöl im Ultraviolettlicht der Analysenquarzlampe" Farbe und Lack 31 (1926) 509.
121. H. Wolff, und W. Toeldte, "Ein Beitrag zur Kenntnis und Prüfung der Harze" Farbenzeitung 31 (1926) 2503-2505.
122. C. Wolters, "Eine bemalte attische Grabstele unter der Quarzlampe" Münchner Jahrbuch d. bild. Kunst, 3. Folge, 11 (1960) 11-13
123. C. Wolters, "Naturwissenschaftliche Methoden in der Kunstwissenschaft" in: Enzyklopädie der Geisteswissenschaftlichen Arbeitsmethoden, 6. Lieferung, 69-91, Oldenburg Verlag. München, Wien (1970).
124. R. W Wood."Physical Optics"New York (1905) 3. Aufl. (1936).
125. M. Zander, "Fluorimetrie"(Anleit. chem. Lab. Praxis 17), Berlin (1981).

Radiation in Art and Archeometry
D.C. Creagh and D.A. Bradley (editors)

Raman Microscopy: A useful tool for the archaeometric analysis of pigments

V. Otieno-Alego

Raman Microscopy Unit, Division of Science and Design, University of Canberra, Canberra, ACT 2601, Australia.

Raman microscopy is now established as a major technique for the rapid identification of pigments on archaelogical artefacts. This chapter reviews some of the recently published work in this regard. A brief background to the technique is presented as well as the different experimental procedures. A comparison is made between Raman microscopy and the other common analytical methods used for pigment identification. Relevant examples are included in the discussions to show the versatility of this technique.

Keywords: Raman microscopy, Pigment identification, Archaeometry, Artefacts

1. INTRODUCTION

Identification of pigments on archaeological objects by Raman microscopy has developed progressively, even explosively within the last decade. A stream of papers have been published in which analysis and identification of pigments (both organic and inorganic) have been conducted on a range of artefacts [1-50]. Today, the technique has emerged as one of the analytical methods that satisfies most of the important criteria for the archaeometric analysis of pigments on artefacts [1,3,39]. In several respect, Raman microscopy is well-suited for this task. Firstly, it combines the required attributes of being non-destructive, reliable, sensitive and largely immune to interference from other materials within the matrix (e.g. other pigments, binders). Secondly, the microscope attachment to the Raman spectrometer facilitates the study of very small amounts of material, or even domains within materials, with high spatial resolution (# 1 μm), an important feature if the particular pigments to be identified are on a color made from a mix of pigments. Thirdly, the technique can be applied in-situ which makes it possible to study valuable artefacts for which sampling is forbidden [3,19,41].

Detailed knowledge of pigments on archaeological objects offers the restorer, conservator, art historian and authenticator a wealth of information relevant to their practice [39]. For example, if pigments of known susceptibilities are identified on an object, then the conservator can decide on the appropriate conditions for their storage and display. Incase where deterioration has already occurred, identification of the decomposition products would enable the conservator to consider treatments that would halt or reverse the process. For the art historians and curators, comparison between pigments on different objects can provide interesting insights into the early trading patterns of pigments, as well as clarifying the technological evolution associated with their manufacture. Similarly, identification of a synthetic pigment whose dates of introduction is well documented can be used by the authenticator to shade light on the date of the artefact and hence on its authenticity. For example, titanium white, introduced in the 20th century, should not appear

on a genuine pre-19th century painting [42].

This chapter provides an introduction to Raman microscopy as an analytical tool to archaeologists (and for archaeology students, in particular) who may want to use this technique in their research work. The chapter is organised in four main sections. Firstly, a brief literature review covering the use of Raman microscopy in archaeometric analysis of pigments is given. This is followed by a description of Raman effect, Raman microscopy and the associated experimental procedures. Finally, a comparison is made between this technique and the other common analytical methods used for pigment identification. Examples are given to illustrate the versatility of Raman technique in archaeometry.

2. BRIEF LITERATURE REVIEW

Over the past few years, analysis of archeological objects by Raman microscopy has rapidly increased, and the following brief review is intended only to highlight the breath of this analytical technique in archaeology. In particular, I acknowledge the important contributions made by both Clark and Edwards Research Groups[ϕ] in this regard. A number of reviews have appeared focused on the use of Raman microscopy as a sensitive technique for pigment identification on medieval manuscripts and other artefacts [3,5,41,42]. Other excellent reviews have also been published in the past five years relating to the general analytical applications of Raman spectroscopy [43-45]. These later reviews are recommended for any reader who is not fully acquainted with the potential applications of this technique. It is worth noting at this stage that there is no fundamental difference between Raman microscopy and Raman spectroscopy. The former term merely identifies the sampling technique in which a research grade optical microscope coupled to a Raman spectrometer is used for micro sampling.

In the past, only a paucity of information about pigments on medieval manuscripts existed in comparison with pigments from other works of art such as easel paintings. This is because pigment analysis of manuscripts was hindered by the inappropriateness of the established analytical techniques, most of which required samples to be removed from the manuscripts [40]. Today, the nondestructive, in-situ capability of Raman microscopy has been exploited and significant advances in the analysis of pigments in manuscripts has been achieved. This is evident in the volume of published work describing pigments used to illuminate medieval manuscripts from both the Western and Eastern worlds. The Western manuscripts studied to date include, among others; a 14th century Spanish choir book [4], a Paris Bible (c.1275) [41], a 13th century North Italian choir book [40], a 16th century German choir book [40], Three 15th centutry Latin manuscripts [32], the 15th century manuscript A*Concessione di Francesco Sforza alla Certosa di Pavia. Cimeli. 1450 settembre 20, Milano*@ [7], Three 15th century German manuscripts [31], the 18th century A*Flora Danica*@ - the unique Danish catalogue of plants of the Scandinavian region [17], and The Skard copy of the Icelandic Book of Law (c.1360) [46]. The Eastern manuscripts studied include; two Persian manuscripts A*Anatomy of the Body*@ (19th century) and A*Poetry in Praise*@ (16th century) [47], a 16th century Qazwini manuscript [48], sections of a 13th century Qur=ran [49], 13th century Byzantine/Syriac Gospel lectionary [21], manuscript fragments from Dunhuang, China (10th century) [50], as well as 19th century Thai and Javanese manuscripts [14].

[ϕ]1. R.J.H. Clark, Department of Chemistry, University College London, London, UK.
2. H.G.M. Edwards, Chemical and Forensic Sciences, University of Bradford, Bradford, UK.

Some of these studies have identified substances arising from the degradation of labile medieval pigments. For example, the presence of pararealgar (yellow pigment, a polymorph of realgar, As_4S_4) in a Italian Renaissance masterpiece by Tintoretto has been attributed to the light-induced degradation of the original orange pigment, realgar (arsenic (II) sulphide, As_4S_4) [37]. Likewise, in-situ Raman studies have shown that the serious blackening of Byzantine Gospel lectionary is due to the transformation of the white lead pigment ($2PbCO_3.Pb(OH)_2$) to black lead (II) sulphide [24,29].

Another area that is attracting considerable attention is the characterization of pigments present on medieval wall painting [6,11-13,34]. For example, Raman microscopy has recently been used to identify pigments from the 1891 tomb (first century Early Roman Empire) at Kertch, Ukraine, displaying the pigments cuprorivaite , amorphous carbon and minium [13]. The discovery of minium at this site is significant as it is one of the earliest known locations of its use. The non-destructive study of the dark-blue pigment present in post-mediaeval glazed tiles from a standing historic building at Bottesford in Leicestershire, UK, have also been reported [9].

Studies have also been conducted to examine pigments on pottery shards, faience and glazes therein from various archaeological sites e.g. Bancun (Henan, China c. 4000 - 5000 B.C.)[21], Village of Castel Fiorentino (Foggia, South Italy, c. 13th century) [36], El-Amarna (Nile Valley, Egypt, c. XVIIIth Dynasty) [35] and Xishan (Henan, China c. 4300 - 2800 BC) [2]. Studies on shards from Xishan revealed, for the first time, that the white pigment anatase was in use from nearly 5000 years ago [2]. Notable also is the first identification of lapis lazuli in the blue decorations on the pottery fragments from South Italy [36]. This blue pigment has now been established as a characteristic of this pottery class. Differentiation of the common red decoration on shards of medieval pottery from many archaeological sites in Italy have been achieved and the pigments have been identified as being either red orchre, venetian red or Indian red [25].

Other types of historical artefacts already investigated by Raman spectroscopy include the identification of pigments on prehistoric rock paintings [8,20] and rock art in caves [1], decorated stained glass [22], illuminated papyri [3], water colours [51], lithographic prints [42] and oil-based paintings such as the Titian and Veronese paintings at the National Gallery, London [38].

A list of some of the common pigments identified on archaeological objects by Raman microscopy is given in Table 1. The extensive studies conducted using genuine artefacts has led to the generation of valuable reference databanks of Raman spectra. For example, a Raman spectral database (60 pigments) of both natural and synthetic pigments known to have been used before 1850 AD has been compiled and published [26]. A computer searchable Raman spectra of geomaterials and biomaterials of interest in archaeology (ARCHAEORAMAN[8]) has also been published [52]. This wealth of information forms a basis for the authentication and possible dating of artefacts. On a wider perspective, comparison of the pigments from different archeological sites can be used as a means of establishing early trade routes for the artefacts [40].

Table 1[Ψ]
Some common pigments already identified by Raman spectroscopy

Colour	Common Name	Chemical Composition
Black	ivory black	C, contains $Ca_3(PO_4)_2$
	lamp black	C
	Magnetite	Fe_3O_4

[Ψ]Compiled from references [21,26,41]

Table 1[Ψ] *continued*
Some common pigments already identified by Raman spectroscopy

Colour	Common Name	Chemical Composition
Green	Atacamite	$CuCl_2.3Cu(OH)_2$
	Chromium oxide	Cr_2O_3
	Cobalt green	$CoO.nZnO$
	Emerald green	$Cu[C_2H_3O_2].3Cu[AsO_2]_2$
	Malachite	$CuCO_3.Cu(OH)_2$
	Scheele=s green	$Cu(AsO_2)_2$
	Terre-verte	Variations of $K[(Al^{III},Fe^{III})(Fe^{II},Mg^{II})]$, $(AlSi_3,Si_4)O_{10}(OH)_2$
	Verdigris (raw)	$Cu(CH_3COO)_2$
	Verdigris (no.1)	$[Cu(CH_3COO)_2]_2.Cu(OH)_2.5H_2O$
	Verdigris (no.2)	$Cu(CH_3COO)_2.Cu(OH)_2$
	Viridian	$Cr_2O_3.2H_2O$
Yellow	Barium yellow	$BaCrO_4$
	Berberine	$[C_{20}H_{18}N_1O_4]^+$ plus sulphate or chloride anion
	Cadmium yellow	CdS
	Chrome yellow	$PbCrO_4$
	chrome yellow - deep	$PbCrO_4.PbO$
	Chrome yellow - orange	$PbCrO_4.PbO$
	Cobalt yellow	$K[Co(NO_2)_6].xH_2O$
	Gamboge	$C_{38}H_{44}O_8$ and $C_{29}H_{36}O_6$
	Indian yellow	$MgC_{19}H_{16}O_{11}.5H_2O$
	Lead tin yellow type I	Pb_2SnO_4
	Lead tin yellow type II	$Pb_2Sn_{1-x}Si_xO_3$
	Mars Yellow	$Fe(OH)_3$
	Massicot	PbO
	Naples yellow	$Pb_2Sb_2O_7$
	Orpiment	As_2S_3
	Pararealgar	As_4S_4
	Saffron	$C_{20}H_{24}O_4$
	Strontium yellow	$SrCrO_4$
	Yellow ochre	$Fe_2O_3.H_2O$ + clay + silica
	Zinc yellow	$ZnCrO_4$
Orange/Brown	Mars orange	Fe_2O_3
	Cadmium orange	Cd(S,Se)
	Ochre (goethite)	$Fe_2O_3.H_2O$ + Clay

[Ψ]Compiled from references [21,26,41]

Table 1[Ψ] *continued*
Some common pigments already identified by Raman spectroscopy

Colour	Common Name	Chemical Composition
Blue	Azurite	$2CuCO_3.Cu(OH)_2$
	Cobalt blue	$CoO.Al_2O_3$
	Lazurite (from lapsi lazuli)	$Na_8[Al_6Si_6O_{24}]S_n$ (n = 2,3)
	Prussian blue	$Fe_4[Fe(CN)_6]_3.14\text{-}16H_2O$
	Cerulean blue	$CoO.nSnO_2$
	Egyptian blue	$CaCuSi_4O_{10}$
	posnjakite	$CuSO_4.3Cu(OH)_2.H_2O$
	smalt	$CoO.nSiO_2$
	Indigo	$C_{16}H_{10}N_2O_2$
Red	Cadmium red	CdSe
	Litharge	PbO
	Realgar	As_4S_4
	Red lead (minium)	Pb_3O_4
	Vermilion (cinnabar)	HgS
	Mars red	Fe_2O_3
	Purpurin	$C_{14}H_{18}O_5$
	Red earth/red ochre	Fe_2O_3 + clay + silica
	Kermesic acid	$C_{16}H_{10}O_8$
White	Anatase	TiO_2
	Barytes	$BaSO_4$
	Bone white	$Ca_3(PO_4)_2$
	Chalk (calcite, whiting)	$CaCO_3$
	Gypsum	$CaSO_4.2H_2O$
	Kaolin	$Al_2(OH)_4Si_2O_5$
	Lead white	$PbCO_3$
	Lithopone	$ZnS + BaSO_4$
	Rutile	TiO_2
	Zinc white	ZnO

[Ψ]Compiled from references [21,26,41]

3. DESCRIPTION OF RAMAN MICROSCOPY

3.1. The Raman Effect

The Raman effect was first predicted in 1924 by Smekal and demonstrated experimentally by Sir C.V. Raman in 1928, for which he was awarded a noble price [53]. The classical concept of Raman scattering is shown in Figure 1. In the basic Raman experiment, a sample is irradiated by a high energy monochromatic light source (usually a laser) of known frequency. Most of this incident radiation (approximately 99%) collide with the molecules in the sample and are scattered

with the same frequency (or energy) as the incident beam. This is called elastic or Rayleigh scattering. However, a small part of the incoming radiation (approximately 1 part in 10^{10}) interacts with the sample and is scattered inelastically (Raman scattering) re-emerging with a different frequency due to a subtle change in energy. This difference in energy can be accounted for by considering the changes in molecular motion (i.e. changes in vibrational states) within the sample. The frequency changes produced as a result of Raman scattering, therefore, contains information about the energies of molecular vibrations, and these depend on particular atoms or ions that comprise the molecule, the chemical bonds that connect them, and the physico-chemical environment where they reside. Thus in a Raman experiment, the Raman spectrometer analyses the difference between the frequency of the incident radiation and that of the Raman scattered radiation to give a vibrational spectrum (Raman spectrum). The particular combination of the Raman bands provides identification of the inorganic or organic species present on the sample by means of comparison of the band characteristics of the unknown species with those of standard materials stored in a database.

Figure 1. Schematic diagram showing classical concept of Raman scattering when a beam

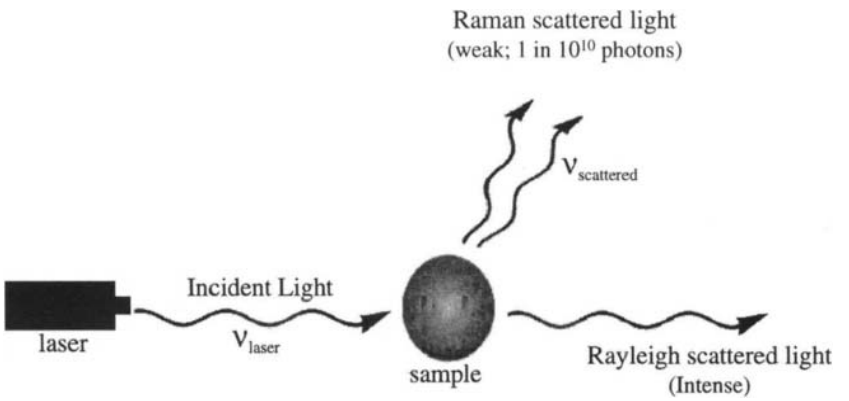

$$\nu_{laser} - \nu_{scattered} = \Delta\nu_{Raman}$$

interacts with the sample. The frequency difference ($\Delta\nu_{Raman}$) between the incident light (ν_{laser}) and Raman scattered light ($\nu_{scattered}$) directly relates to properties of the illuminated sample.

Raman spectroscopy, is therefore, very similar to the more frequently used infrared spectroscopy in that both spectroscopies provide information on molecular vibrations. In fact, the two techniques are complementary. That is: vibrations which are strong in a Raman spectrum are usually weak in an infrared spectrum and vice versa. Qualitatively, antisymmetric vibrational modes and vibrations due to polar bonds (such as O-H, N-H, C=O) generally exhibit prominent infrared bands, while Raman tends to emphasise vibrations involving more symmetrical bonds (such as C=C, C-C, S-S)[53].

To the analyst, Raman spectroscopy offers many benefits in comparison to infrared spectroscopy, the most important being the ease of sample preparation, sampling through glass and plastic, and the ability to analyse aqueous samples. Furthermore, Raman technique is

compatible with fibre optics allowing for remote sampling. Raman spectroscopy, however, suffers a major drawback in the problem of fluorescence. In some instances, when the sample is irradiated (particularly with visible laser sources), the impacted energy sufficiently excites the sample such that it starts to radiate its own light (or energy). This process is termed *fluorescence.* Whenever this process occurs, a tremendous background is superimposed on the Raman spectrum which often obscures the useful vibrational information. In extreme cases, the Raman signal is completely swamped. The problem encountered with fluorescence has been reduced significantly by using low energy near-infrared lasers. Not surprisingly, the high energy laser sources used for excitation can also cause the photodegradation of liable samples.

3.2. The Raman microscope

A Raman microscope (sometimes called Raman microprobe or Ramascope) is a very specialised optical microscope. As mentioned earlier, it is constructed by coupling a normal research grade optical microscope to a Raman spectrometer. The coupling of the microscope to the spectrometer makes it possible to achieve a very high spatial resolution, allowing individual particles as small as 1 μm to be studied [44]. A schematic diagram of such a microprobe is shown in Figure 2.

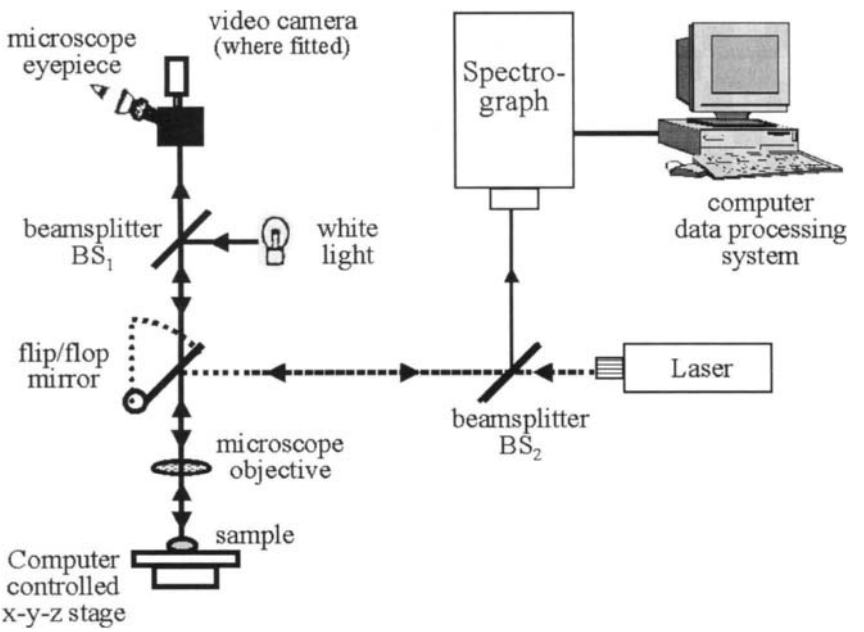

Figure 2. Schematic diagram of a Raman microscope

Typically, a flip/flop mirror is used to shut off the laser and open the white light path, and vice versa. With the white light path opened, a sample placed on the microscope stage can be viewed and the individual particles to be analysed pinpointed by focusing on them as in a normal

conventional microscope. This white-light observation can be facilitated by displaying the image via a video camera attached to the microscope. With the target in focus (under the cross-hair of the microscope objective), the laser beam is introduced via a 50% transmitting beamsplitter (BS_2) and is automatically focused onto the sample by following the same path as the white light beam. The laser interacts with the target and 180° back scattered Raman radiation retraces the path of the incident laser beam as far as the BS_2, where half of the radiation is directed to the Raman spectrometer. The beam entering the spectrometer is filtered to eliminate the Rayleigh scattered light before passing into a frequency dispersing unit, and then onto a detector for final measurement. The detector signal is digitised and sent to the computer where the final presentation is in the form of a normal Raman spectrum. As mentioned earlier, interpretation of the Raman spectrum from an unknown pigment is facilitated by comparing its Raman trace with published spectra of standard materials. Such reference spectra are now readily available in the literature or computer databanks of most Raman laboratories.

4. EXPERIMENTAL PROCEDURES

A variety of experimental procedures can be used with a Raman microscope in order to analyse pigment on an archaeological artefact. These procedures can be grouped into two main categories namely; (i) in situ analysis and (ii) micro sampling (e.g. chips, flakes, cotton swabs) from the object. The choice between the two procedures is largely dictated by the uniqueness of the artefact as well as the general agreement between the curators/conservators and the analyst.

4.1. Direct in situ pigment identification

Raman examination can be performed directly on artefacts because the technique (in good hands) is nondestructive. Artefacts that are small enough are simply placed on the microscope stage and the pigments of interest targeted and analysed. Special microscope stages can also be designed to accommodate medium sized or specialised objects. For example, a special translational microscope stage shown in Figure 3 was used to support the rare and valuable (more than US$ I million) Byzantine/Syriac Gospel lectionary (13^{th} century) illuminated manuscript [29]. With this arrangement, the inks and pigments used to illuminate this lectionary were simply positioned under the microscope and analysed. The Raman micro analysis revealed five pigments - white lead, vermilion, lapis lazuli, orpiment, realgar and pararealgar [24,29]. This was the first identification of pararealgar (a light-induced transformation product of realgar) on an illuminated manuscript. In this instance, however, there was sufficient evidence to suggest that the artist deliberately applied pararealgar rather than the natural realgar, which appears as an impurity. The artist mixed pararealgar and orpiment to generate the different shades of yellow as shown in Figure 4. This study also revealed that the serious blackening of many hues that affected most of the illuminations was caused by the degradation of lead white to lead (II) sulphide. The polluted London atmospheres of the late 19^{th} century and the town-gas lighting used by the British museum in the early eighteen hundreds has been mentioned as the most likely sources of the polluting sulphur [29].

Figure 3. A special translational microscope stage used to support a manuscript during an in situ Raman microanalysis of pigments thereon. The special weight on page holds it firmly allowing good focus at high magnification. (Reproduced by permission of Elsevier Science Publishers from R.J.H. Clark, J. Mol. Struct. 481, (1999) 15).

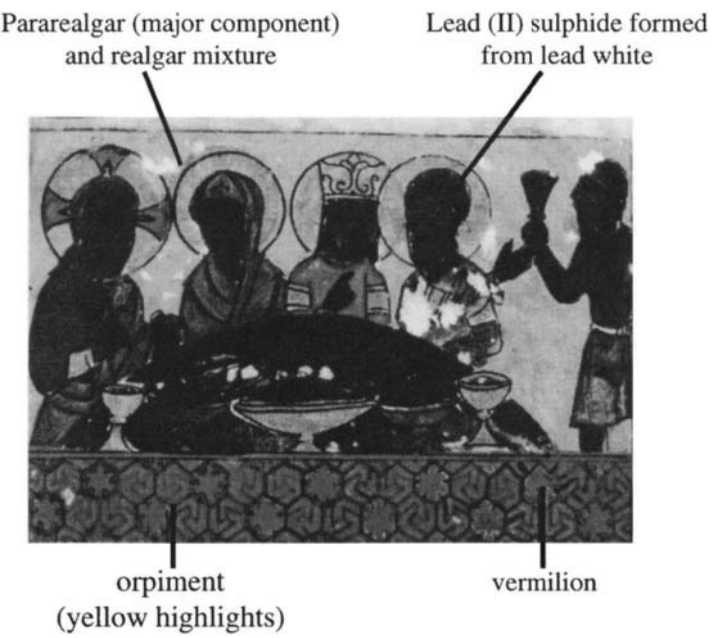

Figure 4. A detail of illumination from Byzantine lectionary (13th C) showing different shades of yellow and blackening of white lead (especially on faces). Spectrum from blackened areas confirmed presence of lead (II) sulphide. The yellow hues were due to the pigments pararealgar, realgar and orpiment. (Reproduced by permission of Elsevier Science Publishers from R.J.H. Clark and P.J. Gibbs, Chem. Commun. (1997) 1003.)

4.1.1. Confocal Raman microscopy

Raman microscopes can be adjusted to obtain very high spatial resolution and depth discrimination (confocal setting) [44]. Confocal mode is beneficial in archaeometric analysis of pigments because it allows for their noninvasive identification through transparent medium such as glass, glazes and adhesive protective films. For example, the Raman spectra for pigments on post-medieval glazed tiles in Leicestershire, UK, (mentioned previously in Section 2) were recorded by scanning through the glaze [9]. Similarly, spectra of nine pigments present on the portrait miniature of Elizabeth I (popularly known as the *Amanda Jewel*) have successfully been collected by focusing the laser beam through the amorphous glass cover [15]. This non-invasive approach is also ideal for studying pigments on pastel, which are often protected by glass, and whose removal can damage the fragile drawings [44].

Confocal arrangement of a Raman microprobe ensures very *tight* focus which can allow, where favourable, the recording of spectra at different depths. This depth profiling ability is exemplified by our laboratory's study of a late 19th century Chinese painting on pith paper (Figure 5). Under the microscope, the yellow shirt worn by the middle person (labelled D) appears to consist of grains of a white pigment covered by a yellowish film. With the help of a motorised XYZ microscope stage, both the film and the pigment layers were analysed by collecting Raman spectra at different micro depths. The results are shown in Figure 6. Except for the band at 1050 cm^{-1}, the spectrum recorded for the uppermost layer (mainly film) matched well with that of standard gamboge. The spectrum collected from the greatest depth (laser beam fully focused on the pigment layer) was significantly different from that of the top, showing only a single Raman band at 1050 cm^{-1}, which is typical of lead white. Thus, the thin sectioning of these two layers allowed the positive noninvasive identification of the film (gamboge) as well as the underlying white pigment (lead white). This type of study can be extended to investigate other transparent medium such as oil layers or coats of vanish commonly used as protective films on paintings.

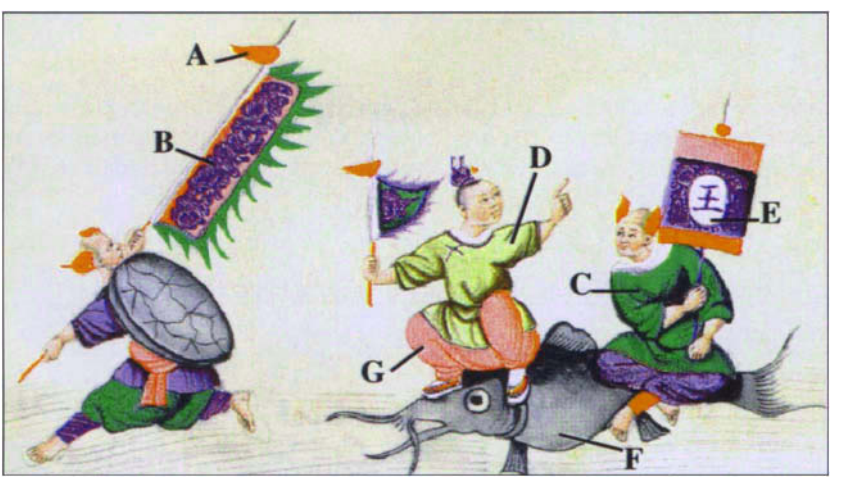

Figure 5. Late 19th century Chinese painting on pith paper. In situ Raman microanalysis unambiguously identified eight out of nine pigments used on the painting.

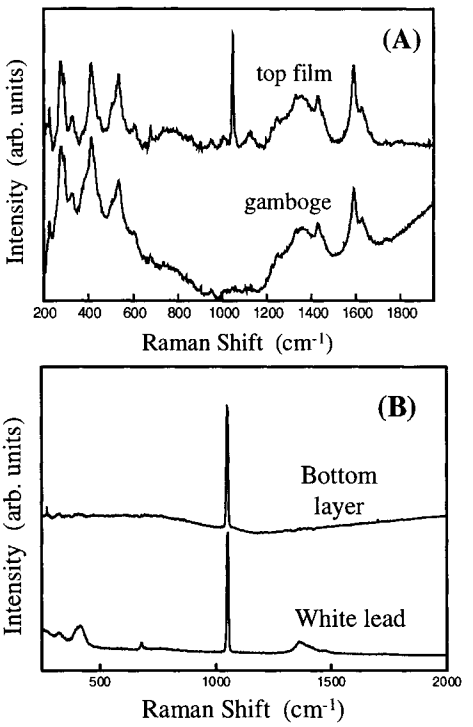

Figure 6. Raman spectra recorded from the yellow shirt by (a) focusing on top surface of yellowish film and (b) focusing deep into the film; with a x50 microscope objective. Reference spectra for gamboge and lead white are included for comparison.

Eight of the nine pigments used on this painting were also identified in situ and are summarised in Table 2. Typical identifying spectra are shown in Figure 7. The Raman trace from the red section (labelled LR) did not match any of our reference spectra and is yet to be characterised.

Table 2
Pigments identified in situ on a late 19th century Chinese painting.

Label on Figure 5	Colour	Pigment/s Identified
A	Dark red	Mixture of vermilion and red lead
B	Blue	Ultramarine
C	Green	Emerald green
D	Yellow	Mixture of gamboge and lead white
E	White	Lead white
F	Blue/grey	Mixture of prussian blue and lamp black
G	Red	?? Mixture of some red pigment/dye and lead white

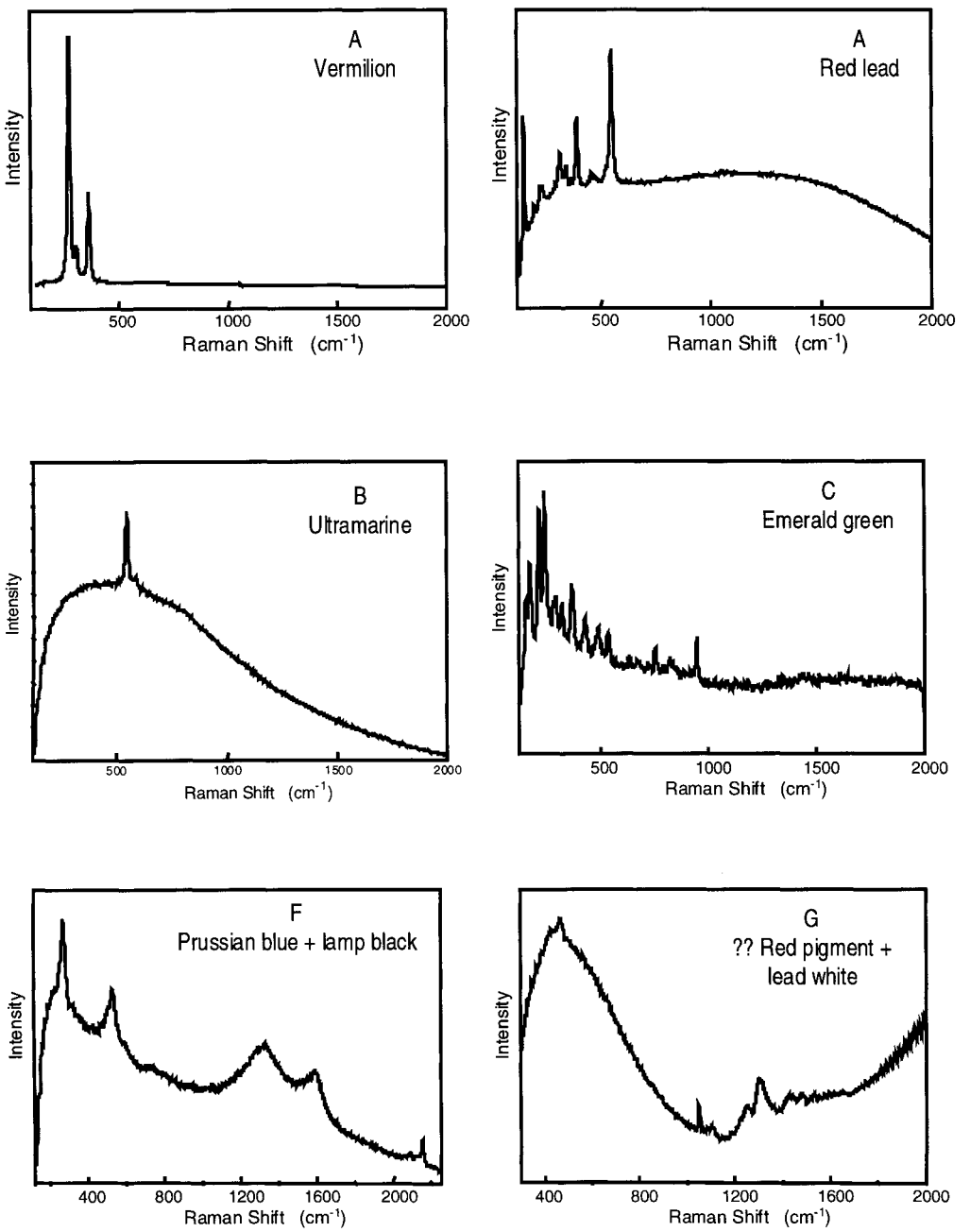

Figure 7. Raman spectra of the pigments used on the Chinese painting. Pigments identified include vermilion, red lead, ultramarine, emerald green, gamboge, lead white, prussian blue, lamp black and some unidentified ??red pigment/dye (spectra for gamboge and lead white given in Figure 6).

4.1.2. Mobile Raman microscopes

In case of very large objects such as wall paintings or statues, or precious objects which must remain in special safe places within the museum, portable Raman spectrometers with fibre optic cables of up to 500 m long can be used for remote in situ sampling. For example, recent archaeological studies conducted on several priceless sculptures of the Musée de l=Homme in Paris used such a remote sampling Ramascope [19]. The principal conditions for the analysis were; (i) that the works must not leave their security room, and (ii) that they must not be touched by any sampling tool, except fingers for purposes of movement only [19]. These extreme restrictions meant that most micro analytical techniques could not be used. This study characterised the mineral species present on a number of the statues in addition to the identification of three pigments; cinnabar on a B.C. Tsimshian mask, Indigo on Aztec statuette, and phthalocyanine blue on Totonaque sculpture. Identification of the 20^{th} century synthetic phthalocyanine blue on this sculpture was *very* interesting because this sculpture is nearly 1000 years older than the pigment [19].

4.2. Micro sampling

Whenever micro sampling is possible, the requirement is that it should be conducted without mutilating the object in anyway. The sample size needed for Raman micro analysis is in the order of 1 μm and this is compatible with this requirement. Samples are collected from features of interest. They are usually removed from the artefact by the help of a tungsten needle under a microscope (typical of micro sampling procedure for pigments on drawings, pastels, and manuscripts) or by use of surgical scalpels in case of flakes on large oil paintings [44]. The micro sample is directly placed on a microscope slide (usually secured in place by a microscope cover slip) and its Raman spectrum directly recorded. In cases where the Raman signal is swamped by fluorescence from the matrix, the problem can often be overcome by confocal setting of the microscope, which helps discriminate the scattering from the fluorescent surrounding [41]. Alternatively, the medium can be disrupted with a suitable solvent (e.g. deionised water for water colors or dichloromethane for oil paintings) allowing the sample to be spread thinly on the microscope slide. In this way, the individual "lean" pigments can easily be targeted and their fluorescence free Raman spectrum recorded [42]. It is noteworthy that the micro samples analysed in this way are not destroyed and can be re-examined by some other micro-analytical techniques.

During examination of paint flakes or paint layers, it is a common practice to mount them in some kind of resin which is then polished to expose the cross section. Embedded or microtomed paint layers are easily analysed by the Ramascope. The samples is simply placed on a microscope slide and the pigments on each section or layer can then be analysed by laser scanning across the specimen. In the following example, a paint stratigraphy was sampled from a German World War II 8.8cm Flak 36 anti-aircraft gun [54]. This is a large artefact with multiple exchangeable components. The gun was captured in North Africa (c.1942) and has undergone a number of contemporary painting restorations, current and post-discard. A study was thus undertaken to try and reconstruct its history based on a number of physical evidence such as graffiti, manufacturing marks and the relative chronology of the paint layers.

Figure 8 shows a typical white light micrograph of a cross section that was subjected to Raman micro-analysis. This particular paint flake was considered contemporary to the object at the time of sampling. In this investigation, each paint layer was analysed with an expanded (defocused) laser beam (using x 50 microscope objective) in order to sample from the bulk of the paint layer. The corresponding Raman traces for the different paint layers are presented in Figure 9, with a summary of the identified pigments in Table 3.

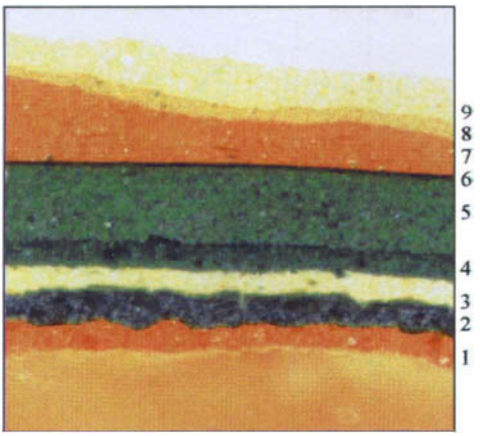

Figure 8. White light micrograph (using x40 microscope objective) of a paint stratigraphy sampled from a German World War II 8.8cm Flak 36 anti-aircraft gun (1 = bottom layer, 9 = top layer at time of sampling).

Table 3
Identification of paint sampled from a World War II 8.8 cm Flak 36 gun [54]

Paint Layer (label)	Identification / Comments
Red (1,7)	mars red - synthetic iron (III) oxide (Fe_2O_3)
Grey (2)	mixture of lamp black (C) and barytes ($BaSO_4$)
Yellow (3)	mars yellow - synthetic iron (III) hydroxide ($Fe_2(OH)_3.H_2O$), barytes and lamp black
Light Green (5)	a mixture of prussian blue ($Fe_4[Fe(CN)_6]_3$), chrome yellow ($PbCrO_4$), lamp black and barytes
Dark Green (4)	a mixture of prussian blue ($Fe_4[Fe(CN)_6]_3$), chrome yellow ($PbCrO_4$), lamp black and barytes. Based on comparison of peak areas for chrome yellow and carbon, the lighter green appear to be brought about by a higher proportion of chrome yellow.
Black (6)	lamp black (C)
Tropical Green (8)	??Unknown and could not be identified from databank
Light Yellow (9)	modern paint, contains a mixture of chrome yellow ($PbCrO_4$), mars red (Fe_2O_3), rutile (TiO_2) and ??some unidentifiable organic matrix.

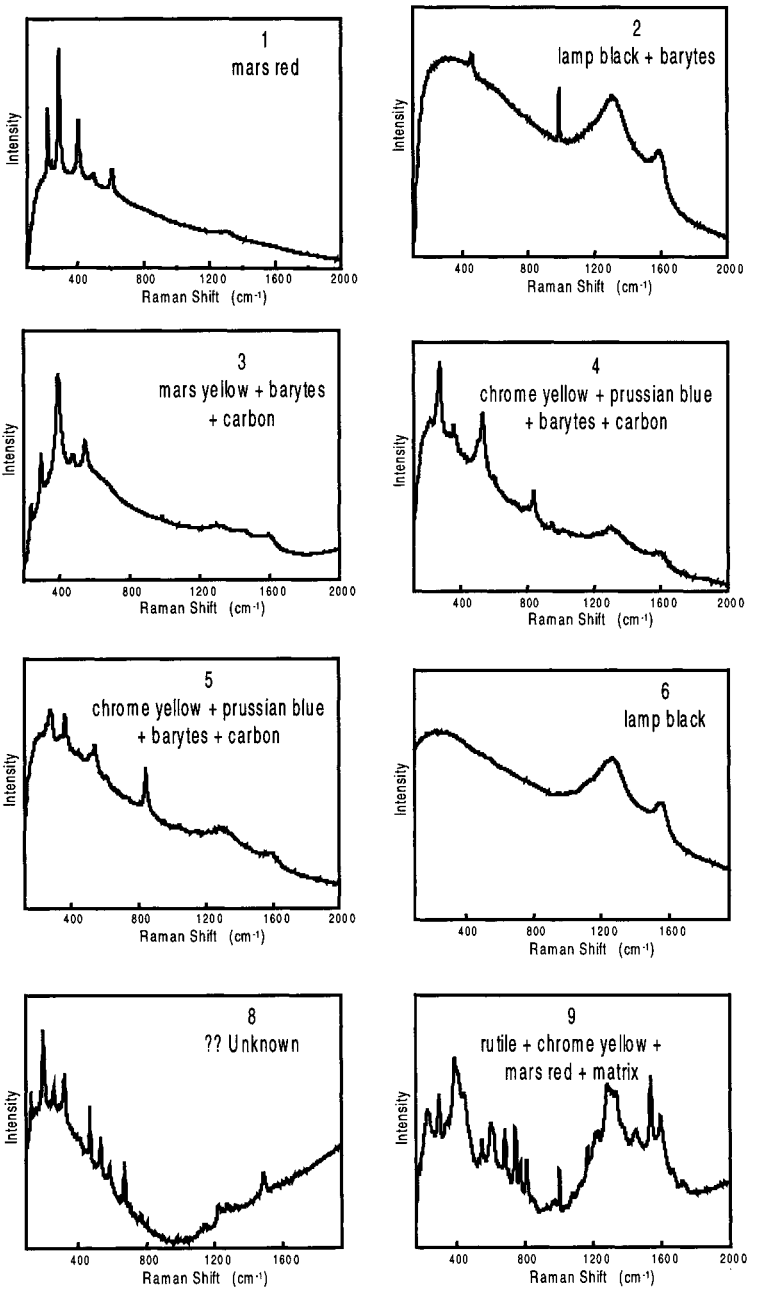

Figure 9. Raman spectra of paint layers from a World War II 8.8 cm Flake 36 gun. A defocused laser beam (x50 microscope objective) was used to sample from bulk rather than focus on individual pigments.

In addition to Raman technique being able to identify pigments present in the paint layer, the particular combination of the Raman bands present on the spectrum acquired from the bulk of the paint sample is specific to its composition (i.e. combination of pigments, binder and fillers) [55]. This is also true for the same batch of paint that has experienced the same history. In this study, for example, the grey paint layer contained black carbon and barytes (Figure 9). The peak areas were computed and the area ratios for the barytes band at 987 cm^{-1} to that of lamb black at 1584 cm^{-1} (after deconvolution) was found to be constant for all the spectra collected at different spots within this paint layer. This barytes-carbon peak *ratio* was thus used as an indicator for this particular grey paint batch and was tested against the other grey layers sampled from different parts of the gun. The same ratio strongly suggested the same paint source, possibly applied on the object at the same time. Such layers were matched and it was possible to establish a relative chronology based on the stratigraphical sequence of the identical paint layers. Accordingly a relative chronology was established for the many exchangeable components of the gun [54]. It should be noted that the ratios of any specific Raman bands typical of the paint layer (whatever the chemical species the peaks may represent) could be used for this type of comparison. This was the case with the more complex tropical green and light yellow paint layers. The more Raman bands considered in the analysis, the more reliable are the matched samples.

4.3. Raman imaging

4.3.1. Direct 2-D imaging

Like the optical microscope which gives contrast of mixed pigments based on their refractive index or reflectivity, a Raman microscope can also offer a selective two dimensional (2-D) Raman image of a given molecular species. Direct Raman imaging is useful for rapidly establishing the presence of a given chemical species (e.g. pigment) in a sample. The technique relies on the use of special filters and a 2-D detector (such as charge coupled devices). Typically, the laser beam is expanded (defocused) to fill the field of view of the microscope objective. Better Raman images are obtained using higher microscope objective (e.g. x50, with typical fields of view of 10 - 200 μm). The Raman scattered light from the illuminated part of the sample is filtered except for *one* selected band (wavelength) characteristic of the constituent to be imaged. This characteristic band must be known before hand. The filtering of the scattered light gives an instant black and white 2-D image on the detector. Bright regions on the 2-D Raman image confirms the presence and distribution of the selected Raman band (and hence the selected species) within the microscope's field of view [44].

The following hypothetical example explains the concept of 2-D imaging. Two pigments rutile and anatase were mixed in the ratio 10:1, respectively, and thoroughly mixed to serve as a model for a "white paint" patch. After mixing, it was impossible to visually isolate the two pigments. A Raman image was then constructed at 145 cm^{-1} (band typical for anatase) to highlight the presence of anatase (see Figure 10). The direct 2-D Raman imaging rapidly identifies and localises anatase within the illuminated area of the white paint. Raman 2-D imaging is fast and can be used to rapidly determine the presence or absence of a suspected pigment on an artefact.

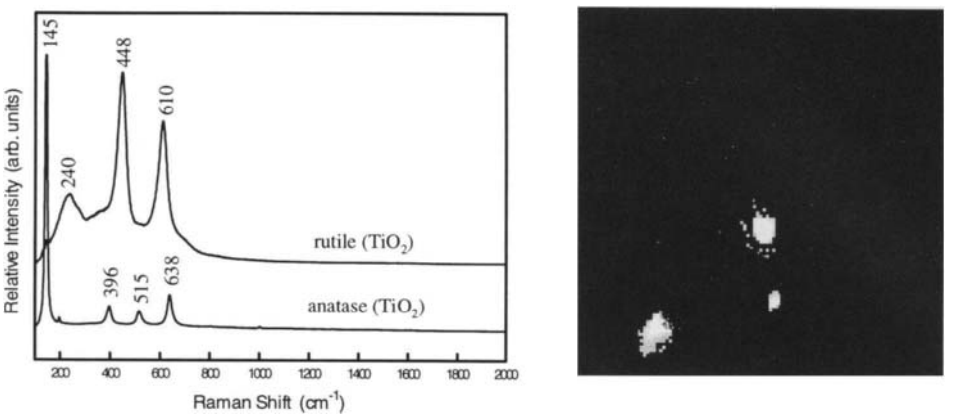

(A) (B).

Figure 10. (a) Raman spectrum of anatase and rutile. The strongest anatase band at 145 cm^{-1} was selected for imaging. (b) 2-D Raman image showing the presence and distribution of anatase within the microscope=s (x50) field of view.

4.3.2. Raman mapping (point-to-point mapping)

Another area of interest is Raman mapping. Likewise to Raman imaging, this technique has not significantly been exploited in archaeological studies of pigments. By surface scanning of a defined area on a sample, the Raman microscope has the ability to provide both the chemical information and the spatial distribution (or map) of a selected chemical species. This technique is comparable to elemental mapping in scanning electron microscopy. A computer-controlled motorised stage is a prerequisite accessory for Raman mapping. The motorised stage permits the fine distance movements during the acquisition of Raman spectra in lines, areas and volumes on the sample to be mapped.

The example presented in Figure 11 [56] was obtained from pigments embedded in a polished thin section. The point-to-point scans require the surface to be flat to ensure that adequate focus is maintained during the scans. Alternatively, some Raman microscopes are equipped with an autofocus facility which allows scans on not so planar surfaces. In practice, the sample is placed on the motorised stage and an XY grid is defined for analysis (e.g. 20 μm x 20 μm, as in the example, Figure 11). The white light photomicrograph of this grid can be documented on a video camera (where such accessory is present). A number of Raman spectra are then collected at micro distances to cover the whole area. The resolution of the components in the sample is determined by the number of sampling spots within the grid, i.e. density of the grid.

From the array of the spectra collected, a Raman band unique to the chemical species to be mapped is then selected and the appropriate computer software is used to generate a black-and-white contour plots of this band on the grid. The changes in thickness of the contour lines represents the changes in intensity of the selected band, thickest line corresponding to the strongest band intensity. The final plot gives information on the relative concentration and distribution of the selected chemical species within the analysed grid. The Raman map can be

related to the physical features documented on the white light micrograpgh (captured on video camera, where this is fitted).

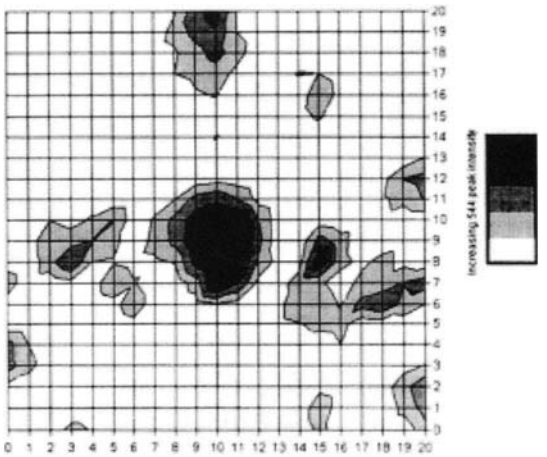

Figure11. Raman mapping for ultramarine band (545 cm^{-1}) on a polished thin section. The darker sections correspond to the strongest band intensity i.e. higher concentration of ultramarine. (excitation source - 514.5 nm) (Figure reproduced by permission of The AICCM (Inc), Canberra, Australia from L. Mathieson and K.W. Nugent, AICCM Bulletin, 21 (1996) 3).

Some limitations of the mapping technique include the time required to collect the data, which could take up to *days* depending on the grid size, resolution and the Raman scattering tendencies of the sample. Appropriate software experience is also necessary to be able to generate proper Raman maps, more so incases where the Raman signals are weak, or when there is a closely interfering bands (to the selected one) or other background effects. Quantitative analysis is also very poor. These limitations are the most probable cause for the demise use of the mapping technique in a number of analytical sciences.

5. Raman microscopy versus other methods used in pigment analysis

Many analytical techniques have been used to identify pigments on archaeological artefacts with varying degrees of success [40]. These techniques are either specific to the elements (e.g. energy dispersive x-ray (EDX), x-ray fluorescence (XRF), electron microprobe, particle-induced x-ray emission (PIXE), inductively coupled plasma (ICP), atomic absorption spectroscopy (AAS) and particle-induced γ-ray emission (PIGE)) whilst others are capable of identifying the chemical groups or compounds present in the pigment material (e.g. infrared spectroscopy, x-ray diffraction (XRD), Raman spectroscopy, secondary ion mass spectrometry (SIMS), uv-visible diffuse reflectance (UV-VIS), optical microscopy, gas chromatography coupled with mass spectrometry (GC-MS) and high pressure liquid chromatography (HPLC)). A detailed analysis of the strengths

and weakness of a number of these analytical techniques for pigment identification has been made and the results are summarised in Table 4 [24,41]. The following five criteria were considered: (i) ability to perform in situ measurements, (ii) specificity, (iii) spatial resolution, (iv) sensitivity, and (v) immunity to interference. Raman microscopy scored high in all the criteria and was considered the best single technique for pigment identification [41].

Table 4
Strengths and weakness of the common analytical techniques used in pigment identification [24]

Technique	In situ	Specificity (elemental or molecular)	spatial resolution	Sensitivity	Immune to interference
Raman microscopy	yes	excellent (molecular)	excellent	excellent	good[a]
XRD	no	good (molecular)	poor	fair[b]	poor
SEM-EDX[ϕ]	no	good (elemental)	excellent	good	good
XRF	yes[c]	good (elemental)	good	good[d]	good
PIXE/PIGE	yes	good (elemental)	poor	good[e]	good
IR[Ψ]	yes	good (molecular)	fair	good	bad
Uv-Vis	yes	poor (molecular)	fair	good	fair
Optical microscopy	yes[f]	moderate (elemental & molecular)	good	fair	good

[ϕ]SEM-EDX - scanning electron microscope coupled with Energy dispersive x-ray analysis
[Ψ]IR - Infrared reflectance microscopy/diffuse reflectance spectroscopy
[a]Fluorescence can be an interference (Section 2.1).
[b]Increases with atomic number.
[c]With appropriate modifications, in situ studies can be performed, but with a loss of spatial resolution.
[d]Typically elements heavier than sodium are analysed.
[e]Simultaneous analysis of all elements with atomic number > 9; Li, Be, B and N can also be detected with high sensitivity.
[f]Polarization studies require samples to be removed.

. Similar to Raman microscopy, a number of the analytical techniques listed in Table 4 (e.g. PIXE, PIGE, XRF, IR) are non-destructive and can be used in situ. However, these techniques cannot conveniently analyse pigments below surfaces such as glass or transparent films. The Ramascope ' s capability in this regard was demonstrated by the many examples given in Section 4.1. Raman analysis can also be achieved for pigments contaminated with water since the latter is a weak Raman scatterer. Unlike XRF where in situ measurements are carried out in an atmosphere of helium [42] or PIXE/PIGE which require beam time on a particle accelerator, there are no such restrictions for Raman measurements which can be conducted anywhere using the

now readily available Ramascopes. In situ Raman studies have also been facilitated by the recent advent of portable Ramascopes with long fibre optic cables for remote sampling. Instead of the usual procedure of sampling *from* the artefact, the spectrometer can now easily be *taken to* the sampling site. This provision has opened a whole new avenue for studying almost all kinds of artefacts securely placed in the museums and galleries. Moreover, samples for Raman studies are often analysed without any sample preparation.

Most of the analytical methods used for pigment identification are element specific and can unambiguously identify pigments with different chemical compositions. For example, the yellow pigments - cadmium yellow (CdS) and chrome yellow ($PbCrO_4$), can easily be differentiated by EDX or PIXE. These element specific techniques cannot, however, discriminate between compounds of exactly the same formula, but different crystalline structures (polymorphs). This is often not a problem when the pigments in question have different colors. For example, EDX will reveal the presence of lead (and possibly oxygen) in both litharge (PbO) and massicot (PbO), but the two pigments can easily be distinguished because the former pigment is red whilst the latter is yellow. The same is not true for the pair of white pigments anatase (TiO_2) and rutile (TiO_2), or calcite ($CaCO_3$) and aragonite ($CaCO_3$). Raman scattering is sensitive to lattice vibrations and as such it can be used to distinguish polymorphic compounds. In case of these white pigments, each compound has a unique Raman spectrum (Figure 12) that allows for their unambiguous identification.

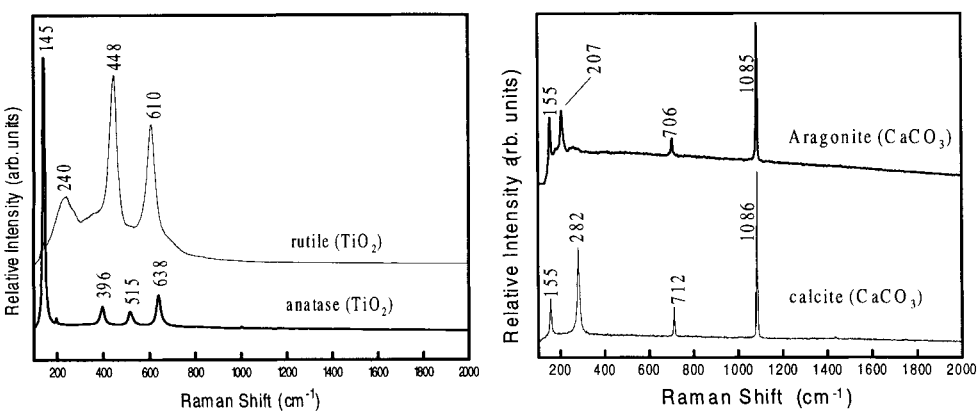

Figure 12. Unambiguous identification of polymorphs by Raman microscopy. (a) Characteristic spectra for anatase and rutile; (b) Characteristic spectra for calcite and aragonite.

Like Infrared (IR) spectroscopy, complete compound identification is possible with Raman microscopy. IR technique is more suitable for organic pigments [42] but not the common inorganic pigments since their spectrum occur in the far infrared region which require that special detectors be added to the IR spectrometer. XRD also gives a complete compound identification

as long as the material is a crystalline solid. Raman=s specificity to compounds (in addition to differentiating polymorphic compounds) is shown by the following examples. It can distinguish compounds of comparable chemical composition (e.g. chrome yellow – deep ($PbCrO_4.PbO$) and chrome yellow-orange ($PbCrO_4.PbO$) (see Figure 13), compounds with varying degrees of hydration (e.g. $CaSO_4$ (anhydrite) and $CaSO_4.2H_2O$ (gypsum) [26], neutral lead carbonate ($PbCO_3$) from basic lead carbonate ($2PbCO_3.Pb(OH)_2$) [56], azurite and malachite [56], verdigris (no.1) and verdigris (no.2) [26], and in some instances, natural from synthetic pigments e.g. Egyptian blue [57].

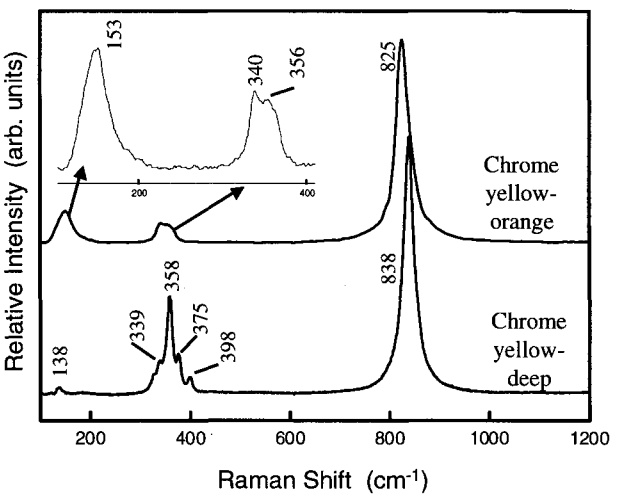

Figure 13. Distinct Raman spectrum observed for two closely related chrome yellow pigments ($PbCrO_4.PbO$). Each compound can easily be identified from the characteristic Raman signals.

The Raman microscope has excellent spatial resolution. Using the microscope attachment, analysis can be achieved by focusing on a sample as small as 1 μm. The technique is one of the very few microanalytic method available by which it is possible to characterise small particles of micrometer dimensions in situ [41]. Such a particle size could also be sampled easily from an artefact with minimum damage. Some x-ray techniques (e.g. XRD) requires an amount of material which may be unacceptable for removal from the artefact. The Raman microscope's high spatial resolution is important when analysing mixtures of pigments which can easily be discerned for individual identification. In cases where the pigment is embedded in some matrix, the high spatial resolution also enables good focus on the pigments thereby reducing the collection of interfering signals from the surrounding matrix. As mentioned earlier in Section 4.2, the ability of Raman microscopy to perform depth profiling of thin transparent films is dependent on this high spatial resolution.

6. LIMITATIONS OF RAMAN MICROSCOPY

The application of Raman microscopy in pigment identification (and in other analytical applications as such) can severely be restricted by laser-induced fluorescence. As earlier explained in Section 3.1, extreme cases of fluorescence can completely mask the Raman spectrum. This problem is most common when visible laser lights (400 - 700 nm) from either argon ion, helium-neon or krypton ion sources are used to excite the samples, especially organic pigments, binders and vanishes. Fluorescence can arise from the matrix on which the pigment is embedded or sometimes the colouring pigments themselves fluoresce. In the former situation where the fluorescence is localised, this problem can usually be minimised by using the technique's excellent spatial resolution to choose within the sample, regions which exhibit minimum fluorescence. In cases where sampling is allowed, the matrix can be disrupted by a suitable solvent (see Section 4.2) to expose the "lean" pigments. In some instances, exposure of the sample to the laser radiation for a long period of time can also burn out the fluorescence emission (process commonly known as photo-bleaching) [44]. This burn out can significantly reduce the interfering fluorescence to allow the detection of useful Raman bands. Alternatively, if the fluorescence is due to the pigment itself, the most effective solution is to change the excitation source to a longer wavelength (i.e. low frequency or low energy). The use of near infrared (NIR) lasers (750 - 1064 nm) has been exploited in this regard. This is because the energy of the light quanta within this spectral range is too low to excite fluorescence spectra in most samples. The use of NIR laser has enabled the collection of good Raman spectra of a wide range of common natural pigments (e.g. saffron, β-carotene, astaxanthin, ovorubin and malvidin) as well as synthetic organic pigments (e.g. pigments containing the triarylmethane group, perylenes, aryl amides and quinacridones, and organometallic pigments) [41].

Photodegradation of labile pigments under laser illumination is another problem that can occur whilst analysing pigments using Raman microscopy. For example, red lead (Pb_3O_4) decomposes readily when sufficiently heated with an argon ion laser (514.5 nm) to massicot [41]. Such transformations can lead to incorrect pigment identification. The problem of laser overheating is overcome by the placement of neutral density filters on the laser path allowing the power of the laser to be toned down accordingly. It is important, however, that one should watch closely for any spectral changes during data collection involving photosensitive pigments.

Whereas techniques based on x-ray detection systems (e.g. XRF, XRD, EDX, PIXE) can yield precise quatitative data on chemical elements present on a pigment, Raman microscopy is intrinsically non-quantitative and cannot be used to accurately determine the concentrations of the different chemical species within the sample. However, relative intensities of the different species can be inferred from the Raman bands. In Raman mapping, for example, distribution of the species of interest is determined based on the relative intensity of the associated Raman band. In common with the other spectroscopic techniques, complete Raman identification of unknown compound relies heavily on having a perfect match from a set of spectra for standard compounds. At the present moment, most reference databases are in-house generated and are not very comprehensive. Thus a pigment yielding a good Raman spectrum may be unidentifiable due to lack of a spectral match from the incomprehensive spectral database. This is especially true for the many synthetic organic pigments whose unambiguous identification in modern paintings has remained difficult. It is for these same reasons that the most recent paint layers on the World War II 8.8 cm Flake 36 gun (tropical green and light yellow) (Section 4.2) could not be identified with certainty.

A search through the literature also shows that some pigments fail to give an identifiable Raman spectrum either because they are poor Raman scatterers, or because their particles are too small, or because they have no Raman active modes [5,19].

7. CONCLUSIONS

Raman microscopy, with its unique versatility and special advantages which combines the attributes of no sample preparation, excellent sensitivity, specificity, high spatial resolution (~ 1 μm) with those of being nondestructive, noninvasive and reasonable immunity to interference, is now established as the *best* single analytical technique for studying pigments on archaeological artefacts. This notion is supported by the many published work reviewed in which successful pigment identification has been achieved on manuscripts, paintings, ceramics, frescoes and other artefacts. In particular, *in situ* studies have been facilitated with the recent development of portable Raman microprobes. Micro sampling is soon becoming a thing of the past since the spectrometer can now be *taken* to the sample, instead of the opposite. These portable microprobes have opened a whole new window of opportunity to study priceless artefacts in storage inside special holdings in our museums and galleries.

The major limitation of Raman technique is fluorescence. This problem has significantly been reduced by the use of NIR lasers. These low power lasers can also be used to study most photosensitive pigments. It is also anticipated that more comprehensive (and commercially available) computer searchable Raman catalogue for pigment standards (both inorganic and organic) will soon become available to facilitate the identification of unknown pigments.

Raman microscopy has a definite practical use in archaeometric analysis of pigments, and with the cost of such instruments becoming reasonable, it is anticipated that its use in archaeological realms will expand further in future. In some instances, however, Raman microscopy cannot answer all the questions about a pigment (even worse if the pigment gives no readable Raman signal). In such circumstances, other analytical methods should be used to complement the weakness of the technique.

Acknowledgments

The author wishes to acknowledge the contributions of D. Wise (Lecturer, Painting Conservation, University of Canberra, Australia) for the provision and discussions on the Chinese painting on pith paper. I also wish to thank D. Pearson (Australian War Memorial, Canberra, Australia) for allowing the use of examples from his Thesis.

REFERENCES

1. D.C. Smith, M. Bouchard and M. Lorblanchet, J. Raman Spectrosc., 30 (1999) 347.
2. J. Zuo, C. Xu, C. Wang and Z. Yushi, J. Raman Spectrosc., 30 (1999) 1053.
3. R.J.H. Clark, J. Mol. Struct., 481, (1999) 15.

4. H.G.M. Edwards, D.W. Farwell, F.R. Perez and S.J. Villar, Appl. Spectrosc., 53 (1999) 1436.
5. R.J.H. Clark, An arts/science interface: medieval manuscripts, pigments, and spectroscopy, Proc. R. Inst. G.B. 69 (1999) 151.
6. J. Zuo, C. Wang, C. Xu, P. Qiu, G. Xu and H. Zhao, Spectrosc. Lett., 32 (1999) 841.
7. S. Bruni, F. Cariati, F. Casadio and I. Toniolo I., Spectrochim. Acta., 55A (1999) 1371.
8. H.G.M. Edwards, L. Drummond and J. Russ, J. Raman Spectrosc., 30 (1999) 421.
9. C.J. Brooke, H.G.M. Edwards and J.K.F. Tait, J. Raman Spectrosc., 30 (1999) 429.
10. H.G.M. Edwards, D.W. Farwell and S. Rozenberg, J. Raman Spectrosc., 30 (1999) 361.
11. F.R. Perez, H.G.M. Edwards, A. Rivas and L. Drummond, J. Raman Spectrosc., 30 (1999) 301.
12. H.G.M. Edwards, D.W. Farwell, F.R. Perez and S.J. Villar, J. Raman Spectrosc., 30 (1999) 307.
13. D.C. Smith and A. Barbet, J. Raman Spectrosc., 30 (1999) 319.
14. L. Burgio, R.J.H. Clark and P.J. Gibbs, J. Raman Spectrosc., 30 (1999) 181.
15. A. Derbyshire and R. Withnall, J. Raman Spectrosc., 30 (1999) 185.
16. B. Wehling, P. Vandenabeele, L. Moens, R. Klockenkamper, A. Von Bohlen, G. Van Hooydonk and M. De Reu, Mikrochim. Acta., 130 (1999) 253.
17. L. Burgio, R.J.H. Clark and H. Toftlund, Acta Chem. Scand., 53 (1999) 181.
18. P. Vandenabeele. B. Wehling, L. Moens, B. Dekeyzer, B. Cardon, A. Von Bohlen and R. Klockenkamper, Analyst. 124 (1999) 169.
19. D.C. Smith, Mineralogigal Society Bulletin, London, No.125 (1999) 3.
20. H.G.M. Edwards, L. Drummond and J. Russ, Spectrochim. Acta., 54A (1998) 1849.
21. J. Zuo, C.S. Wang and C.Y. Xu, Spectrosc. Lett., 31 (1998) 1431.
22. H.G.M. Edwards and J.F.K. Tait, Appl. Spectrosc., 52 (1998) 679.
23. G. Vanhooydonk, M. Dereu, L. Moens, J. Vanaelst and L. Milis, Eur. J. Inorg. Chem., (1998) 639.
24. R.J.H. Clark and P.J. Gibbs, Anal. Chem., 70 (1998) 99A.
25. R.J.H. Clark and M.L. Curri, J. Mol. Struct., 440 (1998) 105
26. I.M. Bell, R.J.H. Clark and P.J. Gibbs, Spectrochim. Acta., 53A (1997) 2159.
27. H.G.M. Edwards, E.R. Gwyer and J.K.F. Tait, J. Raman Spectrosc., 28 (1997) 677.
28. L. Bussotti, M.P. Carboncini, E. Castellucci, L. Giuntini and P.A. Mando, Stud. Conserv., 42 (1997) 83.
29. R.J.H. Clark and P.J. Gibbs, Chem. Commun., (1997) 1003.
30. R.J.H. Clark, M.L. Curri and C. Laganara, Spectrochim. Acta., 53 (1997) 597.
31. L. Burgio, D.A. Ciomartan and R.J.H. Clark, J. Mol. Struct., 405 (1997) 1.
32. L. Burgio, D.A. Ciomartan and R.J.H. Clark, J. Raman Spectrosc., 28 (1997) 79.
33. R.J.H. Clark, P.J. Gibbs, K.R. Seddon, N.M. Brovenko and Y.A. Petrosyan, J. Raman Spectrosc., 28 (1997) 91.
34. H.G.M. Edwards, C.J. Brooke and J.F.K. Tait, J. Raman Spectrosc., 28 (1997) 95.
35. R.J.H. Clark and P.J. Gibbs, J. Raman Spectrosc., 28 (1997) 99.
36. R.J.H. Clark, L. Curri, G.S. Henshaw and C. Laganara, J. Raman Spectrosc., 28 (1997) 105
37. K. Trentelman, L. Stodulski and M. Pavlosky, Anal. Chem., 68 (1996) 1755.
38. R.J.H. Clark, L. Cridland, B.M. Kariuki, K.D.M. Harris and R. Withnall, J. Chem. Soc., Dalton Trans., (1995) 2577.
39. R.J.H. Clark, J. Mol. Struct., 347 (1995) 417.
40. R.J.H. Clark, Chem. Soc. Rev., 24 (1995) 187.
41. S.P. Best, R.J.H. Clark and R. Withnall, Endeavour. 16 (1992) 66.

42. R. Davey, D.J. Gardiner, B.W. Singer and M. Spokes, J. Raman Spectrosc., 25 (1994) 53.
43. L.A. Lyon, C.D. Keating, A.P. Fox, B.E. Baker, L. He, S.R. Nicewarner, S.P. Mulvaney and M.J. Natan, Anal. Chem., 70 (1998) 341R
44. G. Turrell and J. Corset., (eds.), Raman Microscopy: Developments and Applications, Academic Press, New York, 1996.
45. J.A. Pezzuti and M.D. Morris, Anal. Commun., 34 (1997) 5H.
46. S.P. Best, R.J.H. Clark, M.A.M. Daniels, C.A. Porter and R. Withnall, Stud. Conserv., 40 (1995) 31.
47. D.A. Ciomartan, R.J.H. Clark and J. Braz, Chem. Soc., 7 (1996) 395.
48. R.J.H. Clark and P.J. Gibbs, J. Archaeolog. Sci., 25 (1998) 621
49. R.J.H. Clark and K. Huxley, Science and Technology for Cultural Heritage, 5 (1996) 95.
50. R.J.H. Clark and P.J. Gibbs, J. Raman Spectrosc., 28 (1997) 91.
51. B.W. Singer, D.J. Gardiner and J. Derow, Pap. Conserv., 17 (1993) 13.
52. D.C. Smith and H.G.M. Edwards, A Wavenumber Searchable Tabular Indexed Catalogue for >ARCHAEORAMAN[8]: Raman Spectra of Geomaterials and Biomaterials of Interest in Archaeology (sensu lato), in ICORS Capetown, 1998, A.M. Heyns (ed.), John Wiley, Chichester, (1998) 510.
53. B. Schrader, (ed.), Infrared and Raman Spectroscopy, VCH Publishers Inc., New York, 1995.
54. D. Pearson, Display and Power: An Archaeological Analysis of a German 8.8cm Flak Gun, Honours Thesis, Department of Archaeology and Anthropology, Australian National University, Canberra, Australia, 2000.
55. A.H. Kuptsov, J. Foren. Sci., 39 (1994) 305.
56. L. Mathieson and K.W. Nugent, AICCM Bulletin, 21 (1996) 3.
57. P.V. Huong, J. Vib. Spectrosc., 11 (1996) 17.

Radiation in Art and Archeometry
D.C. Creagh and D.A. Bradley (editors)

Thermoluminescence Dating

L. Musílek[a] and M. Kubelík[a+b]

[a]Czech Technical University in Prague, Faculty of Nuclear Sciences and Physical Engineering, Behová 7, CZ-115 19 Praha 1, Czech Republic

[b]Technical University Vienna, Institute for the History and Theory of Architecture and Historic Building Survey. Karlsplatz 13/251, A-1040 Wien, Austria

This chapter describes the physical principles underlying the phenomenon of luminescence on which the technique of thermoluminescence (TL) is based. It discusses such practical issues as instrumentation, the determination of dose-rate, and describes the thermoluminescence technique as it is applied in archaeometry. It discusses, sampling, the TL response curve, and error assessment (random, systematic, and context). Examples are given if the use of the technique in the dating of pottery and architecture.

1. PHYSICAL PRINCIPLES OF THERMOLUMINESCENCE

The phenomenon of thermoluminescence (TL) was possibly seen even by prehistoric man, and with certainty observed by Sir Robert Boyle in 1663 and published in 1664 [1]. The word "thermoluminescence" was introduced by Wiedeman and Schmidt in 1895 [2], and mentioned in the doctoral thesis of Marie Curie in 1904. However, the theoretical explanation using the model of electron traps in crystals was given much later, in 1945, by Randall and Wilkins [3]. The beginnings of its practical use in dosimetry are connected to the name of F. Daniels and his co-workers, who were also the first authors suggesting a possible application of TL for age determination in archaeology and geology [4]. The first dating results of ceramics and bricks were published by Houtermans and his co-authors in 1960 [5].

Since then TL has become one of the most useful and widespread methods for dose determination, not only for the purposes of radiation monitoring and protection, but also for dating of both man-made fired artefacts like ceramics and bricks and natural materials like sediments, dunes, igneous rocks or meteorites. The bibliography of TL is extensive and only a selection of the monographs describing the principle, theory and use of TL can be given here [6-12].

The mechanism of radiation induced TL is complex and its explanation will here be restricted to the qualitative description of the basic principle. Details (and also problems) of

the theory of TL can be found in specialised monographs cited above. The energy band diagram (Fig 5.1) shows that the forbidden gap in an ideal crystal does not contain any energy levels and all radiation caused electron transitions between the valence and conduction bands and back, are direct. Real crystals always contain some lattice defects - vacancies, dislocations or impurities. These defects can lead to an appearance of local energy levels of various types in the forbidden gap. From the point of view of TL three types of levels play an important role: electron traps E, hole traps H and luminescence centres L.

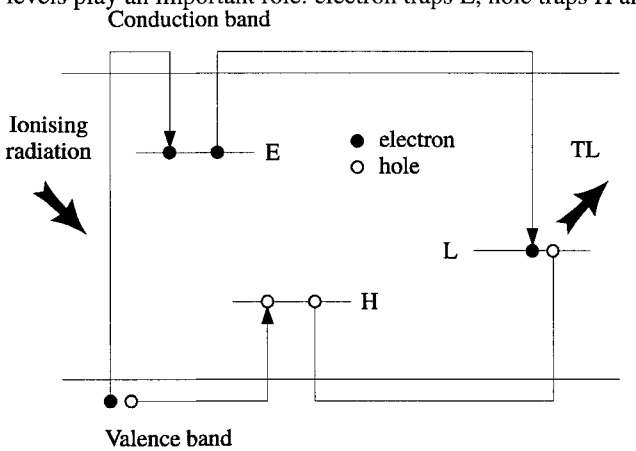

Figure 1. Energy band diagram and transitions leading to TL

Ionising radiation produces free electrons, transferred from the valence band to the conduction band. They move through the crystal and return to the conduction band, where they recombine with holes. However, if traps are present (as E in Figure 1), they can be captured. The same is true for holes in the conduction band, which can be trapped in hole centres H.

If the traps are energetically deep enough, the trapped electrons will remain there until they acquire sufficient energy to be released. This can, e.g. be thermal energy when the material is heated. The released electrons again move through the conduction band and on their return to the valence band they can recombine with holes in luminescence centres L. This recombination is accompanied by the emission of electromagnetic radiation, usually in the visible or ultraviolet range of wavelengths. This effect is called thermoluminescence and can serve as a measure of the dose accumulated in the material, as the number of radiation induced electron trappings is proportional, within a wide range of doses, to the radiation dose.

Usually, there are more types of traps in the material. When the temperature rises, electrons are gradually released from increasingly deeper and deeper traps and maxima, which correspond to the release of electrons from particular types of traps (TL peaks), can be observed on the curve of emitted light vs. temperature (the "glow curve"). The shape of the glow curve therefore reflects the number of lattice defects and impurity atoms of various types in the material lattice and is characteristic for a given material. An example of such a glow curve for quartz is in Figure5.2. Electrons in shallow traps can be released at room

temperature, if they obtained sufficiently high energy in the random redistribution process of thermal energy. This slow emptying of traps is called fading, and, of course, minimal fading is needed both for TL dosimetry and dating - i.e. relatively deep traps must be used.

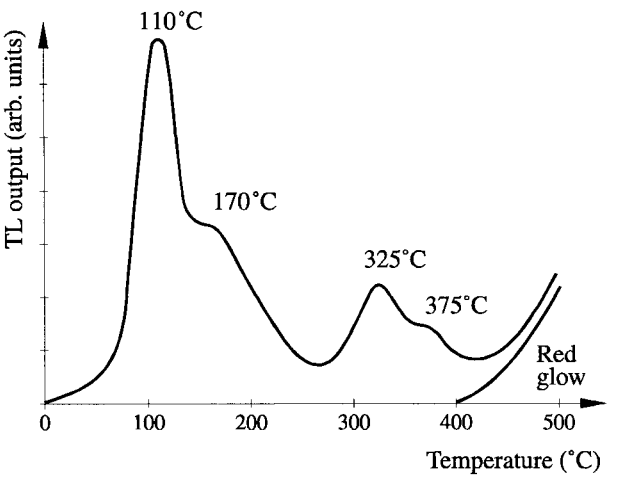

Figure 2. Glow curve of quartz (after [13]).

An instrument for TL measurement - TL reader - must ensure the following functions:

a) heating the sample of TL material in a well defined and reproducible way,
b) collecting quantitatively the emitted light,
c) converting the light signal into an electrical one and measuring it,
d) recording and displaying the result in the form of glow curve or an integral of the whole curve or a predefined part of it.

Most commonly ohmic heating is used, i.e. the TL sample is placed on a readout tray, which is heated either by directly passing electrical current through it or indirectly by contact with an electrically heated element. The regulation of the heating rate is controlled by means of a thermocouple connected to the tray. Other possibilities are: heating by hot nitrogen, heating by an induced current produced in the tray by a radio-frequency induction heating coil or heating by the radiant energy from an infrared heating element.

The light collection and detection system must be designed in such a way as to collect the TL light with maximum efficiency and to have a low sensitivity to any other optical radiation (e.g. infrared thermal glow from the heating tray). It converts an optical signal into an electrical one (current, integrated charge or single voltage pulses), which is then measured and recorded. The most obvious device for light detection used for TL measurements is a photomultiplier system. It is necessary to select it from the point of view of the spectral sensitivity of the photocatode, which must be well fitted to the spectral emission of the most

often measured TL material. Thus, the selection of a photomultiplier for dating, where quartz and feldspar are the most frequent TL materials, is conditioned by the need to measure electromagnetic radiation spectra near the blue-green end of the visible range and to suppress the red background incandescence of the heating tray. Extension of sensitivity to the ultraviolet region by a quartz window is advantageous. Cut-off or band pass filters are used to provide spectral discrimination between the measured light emission and unwanted thermal radiation background. The typical scheme of a TL-reader is on Figure 3.

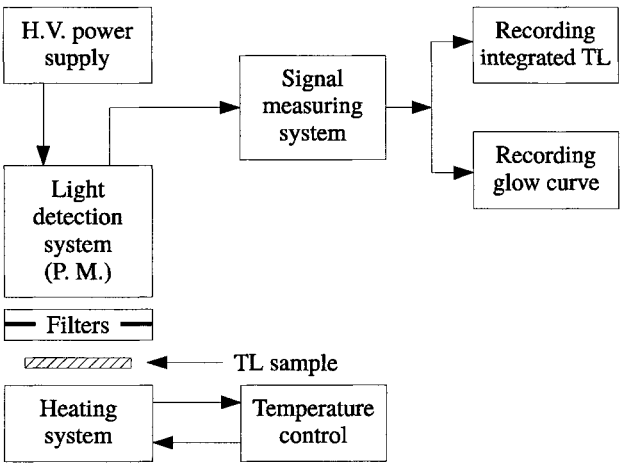

Figure 3. Typical scheme of a TL-reader

Commercially available TL-readers for dating have been available for about thirty years. Initially they were designed for a single sample, which had to be removed for artificial irradiation. Today various semi-automated machines can be purchased for routine TL-dating, which allow the artificial irradiation and measurement of a sufficient large number of samples to be carried out. For special applications it is still advisable to build a machine to suit the specific requirements.

2. THE IMPORTANCE OF ACCURATE DATING OF HISTORIC ART AND ARCHITECTURE

Accurate dates are important in the evaluation of art objects, archaeological finds and historic architecture for a variety of different reasons:

a) The method is today routinely used for authentication of valuable ceramics. This has a clear economic factor, and often forms the key point in appraisals and valuations.
b) In archaeology, art and architectural history the method is used to varying degrees to allow a correct historical interpretation of the object itself, its positioning in an absolute

or relative chronology within its art form, its type etc.

c) In preservation of historic architecture the method is still used far to rarely. More often than not, fundamental decisions in the adaptation, revitalization, restoration and reconstruction of historic architecture, need to be made with regard to the relative or absolute chronology of the whole of, or parts of the historic fabric.

3. BASIC PRINCIPLES OF TL DATING

The basic idea of TL dating is simple. Practically all materials around us contain small amounts of natural radionuclides. The most important ones are the radionuclides of the natural decay series and ^{40}K. Cosmic rays also contribute to the radiation field on Earth. Therefore, an absorbed dose is accumulated in any material. This dose is proportional to the dose rate in this natural radiation field and to time. There are two necessary conditions for TL dating: the object of which the age is to be determined must contain a TL capable component, and all relevant TL traps must have been emptied at the moment in time which is to be dated. Then the TL signal emitted by a sample of the TL-capable material extracted from the object *(NTL)* is proportional to the TL sensitivity S of the sample (TL response per unit of dose), and to the dose D, and the dose is proportional to the life-time of the object from the zero point T and to the dose rate $\dot{D}$ inside the sample during its life-time.

Then the age of the object is given by the simple equation:

$$T = \frac{D}{\dot{D}} = \frac{(NTL)}{S\dot{D}}. \tag{1}$$

The two conditions mentioned above are fulfilled by ceramic materials like pottery or bricks which were fired at the very beginning of their "life" and which usually contain quartz and feldspars as TL-capable materials. Some other materials, like meteorites, quaternary sediments, sand dunes and even biological materials (especially teeth) have also been successfully dated by TL.

For actual dating, Equation (1) cannot be directly used, as it does not distinguish between the specifics of various types of radiation. The natural radiation field on the Earth's surface is formed by particles α, β, photons γ, and a mixture of particles from cosmic radiation (where electrons, photons and muons are the most important). TL sensitivity is the same for all weakly ionising radiation, i.e. β, γ and cosmic radiation, but it is different (usually smaller) for α particles. It is therefore necessary to calculate with two TL sensitivities S_α and S_β. Thus Equation (1) changes to:

$$T = \frac{(NTL)}{S_\alpha \dot{D}_\alpha + S_\beta (D_\beta + D_\gamma + D_c)}, \tag{2}$$

where D_α, D_β, D_γ and D_c are partial contributions to the total dose D from α, β, γ and cosmic radiation. Equation (5.2) can be rewritten, defining a factor $k = S_\alpha/S_\beta$ and an equivalent dose from β radiation $D_e = (NTL)/S_\beta$, as:

$$T = \frac{D_e}{k\dot{D}_\alpha + \dot{D}_\beta + \dot{D}_\gamma + \dot{D}_c}. \tag{3}$$

This means that the dose rates from α and other types of radiation must be determined separately, which can be done by analysing the content of natural radionuclides in the measured material and its surroundings (e.g. the soil in which a piece of pottery was found in an archaeological excavation) and an estimate of the cosmic ray contribution (which does not exceed a few percent) at the sampling location. Experimental determination of the sensitivity S_α of the material to α radiation, and S_β to β, γ and cosmic radiation must also be carried out by irradiation with artificial α and β doses. TL dating, therefore, becomes a complex procedure, consisting of sampling and sample preparation, the determination of dose rates, the determination of TL sensitivities, the measurement of natural TL, the calculation of age and the evaluation of the error of the calculated TL date.

4. DOSE RATE DETERMINATION

Contributions to the dose rate in pottery or bricks are mostly due to radiation of natural radionuclides in the fabric itself and in its surroundings (e.g. for archaeological shards, soil in which the artefact was buried). As mentioned above, the main sources of radiation fields are nuclides from the uranium and thorium decay series, ^{40}K, and a small contribution from cosmic radiation. The data for the cosmic ray component is given, e.g. in [14]. Apart from the contribution from these sources, there are other natural radionuclides, but their contribution is usually negligible for TL dating purposes. Typical dose rates in pottery dating are summarised in Table 1 (after [15]). The values correspond to pottery and soil having 1 % potassium, 0.005 % rubidium, 10 ppm natural thorium and 3 ppm natural uranium. For the effective α dose rate the value of 0.15 is assumed for the coefficient k from Equation (3).

Table 1.
Dose rates in TL dating for typical pottery and soil (in Gy/ka)

Source	α	Effective α	β	γ	Effective total
Potassium	-	-	0.83	0.24	1.07
Rubidium	-	-	0.02	-	0.02
Thorium	7.39	1.11	0.29	0.51	1.91
Uranium	8.34	1.25	0.44	0.34	2.03
Cosmic	-	-	-	0.15	0.15
Total	15.73	2.36	1.58	1.24	**5.18**

The standard procedure for the determination of the dose rates from the ^{238}U series and ^{232}Th series is the measurement of α activity, most commonly by a zinc sulphide scintillator in contact to a layer of the sample, which is thicker than the range of α particles. Typically, a count rate of about 1000 counts per day is measured for a scintillator with a diameter of 42 mm, which is fully covered by a layer of the sample. β and γ dose rates from the radionuclides of the natural decay series can also be derived from this α count measurement, however, the variation in the ratio of the thorium to the uranium content cannot be determined this way, and this leads to a systematic error in the dating result (see later). It is also possible to determine the thorium and the uranium content by an analytical method

sensitive to their traces, e.g. by activation analysis. Various analytical methods are sufficiently sensitive for the measurement of the potassium content, such as activation analysis, atomic absorption methods, X-ray fluorescence. Conversion factors from K, Th and U concentrations to annual dose rates, based on the radio-nuclide data from ICRP Publ. 38 [16] are given in [17].

To avoid an error in the determination of the β dose rate, introduced by the unknown thorium to uranium ratio, it is possible to measure the β dose rate directly by TL dosimetry. A very sensitive TL dosimetry phosphor is needed for this purpose (e.g. fluorite or calcium sulphate activated by dysprosium). An apparatus for such a measurement, using about 1.5 g of sample material and fluorite mixed with silicone resin as a dosimeter is described in [18]. The measurement period (i.e. irradiation time of the dosimeter) for each sample is a few weeks.

Similarly the γ component of the dose rate can be measured by TL dosimetry in situ. The same types of very sensitive phosphors in special capsules are buried in the sampling location. Irradiation time can be one year or more - such a long period has the advantage not only in obtaining an accurately measurable TL signal, but also in averaging the influence of the seasonal climatic variations.

Another much quicker option is the use of a portable γ–spectrometer for in situ measurement. The evaluation of the measured spectra allows the determination of the individual contributions of potassium and the thorium and uranium decay series. It also offers an indication of possibly present artificial radionuclides (e.g. ^{137}Cs from the Chernobyl accident), leaching effects in the soil and the rate of disequilibrium in the radioactive series due to the radon escape. The size of the γ–spectrometric gauge is the main disadvantage of this technique.

Both the *in situ* conditions and the equipment available to the laboratory carrying out the TL dating influence the choice of the method used. For reliability, it is advisable to determine dose rates by two independent means. Nevertheless, some uncertainties remain, e.g. the varying moisture content over time, which influences the radiation field of the sample, as water acts as a radiation absorber.

5. TL DATING TECHNIQUES

Various techniques, based on the specific properties of the material to be investigated, have been developed. Neither pottery nor bricks are homogeneous materials from the point of view of their internal composition. They usually consist of a fine grain clay matrix with a particle size typically less than 10 μm in diameter, in which larger coarse grains of various minerals are embedded, quartz being the most common and most important one. The majority of natural radionuclides are contained in the clay matrix (concentrations being typically in the order of magnitude of ppm of uranium and potassium and above 10 ppm of thorium). Clay is relatively homogeneous both from the point of view of composition and distribution of natural radioactive elements. Thus radiation fields within the clay matrix are also homogeneous. In comparison, the quartz inclusions only have a negligible content of radioactive elements and a their dose originates from outside radiation, i.e. from the clay matrix and surrounding materials up to a distance of a few tens of cm, depending on their properties. On the other hand, they are much more TL sensitive than the matrix. The short

range of α particles means that they only influence the surface layer of quartz grains, and taking into consideration the attenuation of β radiation, the dose distribution inside these grains is inhomogeneous and depends on the grain size. Zircon is another mineral which has coarse inclusions, especially in pottery. In contrast to quartz it usually has a high content of natural radionuclides (uranium in concentrations in the order of magnitude of a few tens to a few hundreds ppm). It has high TL sensitivity, but it usually varies significantly from one grain to another.

Based on this varied composition of the material, two major techniques have been developed for TL dating, using different grain sizes: the fine-grain technique and the quartz inclusion technique. Less common is the use of some other techniques: the zircon inclusion, the subtraction , the pre-dose and the photo-transfer techniques.

5.1 Fine-grain technique (fg)

The fine-grain technique was developed by D.W. Zimmerman [19,20] as an alternative technique to the slightly older quartz inclusion technique. It is one of the options for avoiding inhomogeneities caused by non-uniform radiation fields inside larger grains. Only grains that are small enough are used, so that, even if they happen to be crystalline with low radioactivity, the alpha dose attenuation inside them is negligible. The size of such grains is typically of the order of magnitude of micrometers. It is necessary to avoid breaking large grains and mixing them with the fine grains during sampling. Under these circumstances it is possible to assume that the absorbed dose is uniform and consists of the full contributions from α and all weakly ionising radiation. The TL sensitivity is tested by irradiating the sample with both α and β artificial doses.

5.2 Quartz inclusion technique (QI)

Many quartz grains in the clay matrix are substantially larger (100 - 200 μm) than the maximum range of α particles. As quartz grains contain only negligible radioactivity and there is therefore no dose from α particles inside these grains deeper than the α particle range. The contribution of these particles coming from the clay matrix appears only in the outer layer. Removing this surface layer by etching (usually in hydrofluoric acid) means that only those part of the grains which were irradiated exclusively by more penetrating weakly ionising radiation, are left. Therefore no α dosimetry is needed. This is the main advantage of the quartz inclusion technique (e.g. [21, 22]), high TL sensitivity of quartz being the other. The disadvantage of the technique is the necessity of a correction for the attenuation of β particles in the grains, which introduces a correction factor for the mean grain size, and the higher dependency of the technique on assessing correctly the outer conditions and the dose rate from the surroundings, which is due to the exclusion to the α contribution.

5.3 The Subtraction technique

The subtraction technique was developed on the basis of fine-grain and the quartz inclusion techniques, to avoid the influence of γ–radiation from the surroundings of the sample [23]. The symbols *A*, *B* and *G* are used for the individual components of the archaeological dose in the sample due to α, β and environmental radiation (the last one including a small contribution of cosmic-rays) and *F* and *I* for the total archaeological fine-grain and quartz inclusion accumulated dose. Factor *f* takes β radiation attenuation due to

grain size into account. The annual dose rates from α (α) and β (β) radiation can be obtained from radioactive analysis of the pottery clay. This means that $A = \alpha T$ and $B = \beta T$, where T is the measured age. Then:

$$F = A + B + G, \tag{4}$$

is valid for the fine-grain technique, and:

$$I = fB + G. \tag{5}$$

for the inclusion technique. Moreover it is evident that independently of the age T:

$$A:B = \alpha:\beta. \tag{6}$$

Hence:

$$F - I = A[1 + (1 - f)\frac{\beta}{\alpha}] \tag{7}$$

and

$$T = \frac{A}{\alpha} = \frac{F - I}{[\alpha + (1 - f)\beta]}. \tag{8}$$

The main complications of the method are the necessity of carrying out measurement by two techniques, which leads to an increased error, and the influence of water content variations. The need of a large value for $F - I$ also brings a serious limitation of this technique.

5.4 Zircon inclusion technique

The technique is based on the work of Zimmerman [24] and Sutton and Zimmerman [25]. Zircon inclusions with dimensions ranging from less than 10 μm to about 200 μm are less common than quartz inclusions in pottery, bricks, etc., but they appear to a limited extent in most objects. They are interesting for TL dating due to their high content of uranium and thorium (tens to hundreds of ppm). Because of their high natural radioactivity the doses absorbed in the grains are so large that the contribution from other sources outside the grains can be neglected and therefore the influence of wetness is also negligible. In practice this means that even shards from museum collections excavated long ago can be dated. On the other hand, the technique is rather difficult. Uranium and thorium content varies within orders of magnitude from grain to grain and the same is valid for TL sensitivity. Large single grains are therefore used for measurement, and even within an individual grain well-pronounced spatial inhomogeneity can be observed. Selection of uniform grains can be done by measuring the spatial uniformity of cathodoluminescence. Accurate measurement of uranium and thorium content is needed. This is made possible by detecting fission tracks from uranium after irradiation with thermal neutrons (the natural isotopic ratio of $^{235}U/^{238}U$ is taken into account) and fission tracks from thorium (plus uranium) after irradiation with 30 MeV ^{3}He particles.

5.5 Pre-dose technique (p-d)

The techniques discussed above are based on electron capture in deep "archaeologically stable" traps. The pre-dose technique uses a different property of quartz: the sensitisation of the TL peak at 110 °C (see Figure 2) by a radiation dose [26]. This low-temperature peak has a short lifetime of about one hour and is therefore not present in the natural glow curve of an archaeological sample. However, it appears after irradiation of a sample by an artificial test dose, which can be so small (between 10 and 100 mGy) that it is insignificant compared to the natural dose. The initial TL sensitivity S_0 of this peak must be measured using the test dose in the first step of the dating procedure. The sensitisation can then be measured by the following treatment of the sample. It is heated up to 500 °C, which depletes the natural TL, and the TL sensitivity of the 110 °C peak is measured again using a small test dose. The value obtained, S_n, is higher than S_0, the difference being due to the sensitisation by the natural dose. Repeating this procedure leads to the value S_n', which, under regular conditions, is approximately equal to S_n, as the test dose contributes negligibly to the sensitisation, and no increase of sensitivity is expected as a result of the heating alone. The calibration dose (pre-dose) D_c of several Gy of β radiation is then applied to the sample, it is again heated to 500 °C and the sensitivity $S_{n+\beta}$ is measured. The sensitivity enhancement $(S_{n+\beta} - S_n')$ corresponds to the calibration dose D_c. Hence the natural dose D_n is given as:

$$D_n = \frac{S_n - S_0}{S_{n+\beta} - S_n'} D_c . \tag{9}$$

A modification of this procedure uses two portions of quartz extracted from the sample, optimally of equal mass. The pre-dose D_c from β radiation is applied to one of them, both portions are heated to 500 °C and sensitivities S_N and $S_{N+\beta}$ are measured. The sensitivity enhancement p is defined as:

$$p = \frac{S_{N+\beta} - S_N}{S_0} \frac{1}{D_c} \tag{10}$$

and the natural dose D_n is therefore:

$$D_n = \frac{S_N - S_0}{pS_0} . \tag{11}$$

The saturation of the sensitivity enhancement at a few Gy limits the range of this method to relatively young samples, not more than about ten or fifteen hundred years. It also should be added that not every quartz grain extracted from fired materials exhibits the effect of sensitivity enhancement by the pre-dose.

5.6 The phototransfer technique

Some TL materials including quartz exhibit phototransferred thermoluminescence (PTTL). In this process electrons from deep ("stable" and therefore archaeologically significant) traps are transferred into shallow traps, when the material is irradiated with

ultraviolet light [27]. Deep traps act as donors, shallow traps as acceptors of charge carriers. The TL glow peak corresponding to the shallow traps, which had been previously thermally bleached, then appears again. Phototransfer is possible over a broad range of UV wavelengths, the maximum efficiency depending of the TL material; e.g. from the peak at 375 °C to the peak at 110 °C for quartz appears at about 260 nm. Though the majority of electrons excited from the deep traps are lost by immediate de-excitation or caught by other types of traps, the sensitivity of the 110 °C peak is so high that even the efficiency of phototransfer of about 5 percent is sufficient for measuring the effect. In a subsequent heating, the signal from the shallow traps (i.e. the 110 °C peak in quartz) is proportional to the electron population of the deep traps. This means that it can be used for determining the "archaeological" dose and consequently also the age [28]. Zircon and some other minerals show a similar effect.

5.8 Further observations

The above review summarises only basic information about the various techniques of TL dating and refers only to the fundamental publications on the topic. Hundreds of papers on TL dating have appeared over the last three decades. The journal *Archaeometry*, published by the Research Laboratory for Archaeology and the History of Art, Oxford University, and *PACT* and the *Journal of the European Study Group on Physical, Chemical and Mathematical Techniques Applied to Archaeology* should be mentioned as the important sources.

Thermoluminescence is not the only method using minerals from man made fired artefacts as "dosimeters" for doses from natural radiation, which are then used for authenticity testing and dating. Similar principles are applied in electron spin resonance (ESR) dating, for the first time systematically described by Ikeia [29], and optically stimulated luminescence (OSL) dating, pioneered by Huntley et al. [30]. Both methods lie outside the scope of this chapter, butwill be addressed in other chapters of this book.

6. SAMPLING AND SAMPLE PREPARATION

A careful survey of the artefact or building is necessary, so as to optimally choose the critically relevant positions for sampling, both from the historical and the physical point of view. Although different quantities of material are needed for the different goals of a TL-analysis, certain general considerations apply for all purposes:

1. Sampling historic artefacts should occur in such a way that no visible damage to the historically valuable substance occurs: e.g. ceramic vases should be sampled on the underside, reliefs from the rear, glazed objects where the glaze is already damaged, and brick walls not through frescoes, but if possible, where the plaster has been damaged or fallen off.
2. Caution needs to be taken not to overheat the object during the sampling process, so as not to interfere with the TL-signal; a temperature of about 60° C should not be surpassed at the point of the drill bit.
3. Samples cannot be taken from artefacts damaged by fire, unless complex factors are taken into account, as it is possible that in such instances the date of the fire, and not the date of the object manufacture will be obtained.

Ideally a chunk of material should be removed, which would allow certain peripheral measurements (e.g. H_2O saturation) to be carried out to a very high degree of precision. But as this would cause undue damage to the artefact, it is common practice to remove powder from a certain depth by drilling.

For archaeological shards and ceramic artefacts samples must be taken from a depth greater than 2mm (to avoid an external β dose). For authentication purposes a few milligrams are necessary: for dating as much as can be reasonably extracted must be used. It is advisable to take samples from more than one location.

Additionally in brick dating the following factors should be considered when sampling in order to obtain optimal results.

1. Samples should always be removed from a location above the influence of ground water.
2. Brickwork should be visually homogeneous in an area with a radius of 24 cm around the sampling point.
3. A brick-wall should optimally be at least 48 cm thick. As this is not always the case, thinner brick-walls can be dated, but it should be realised, that the error of the individual sample, and thus also the context-error of a sample group, will be statistically increased (see later).
4. Sampling on the outside of a building should not occur during rain, and at such points a minimal sampling depth (dependant on local climatic conditions) must be observed.

Due to the many parameters involved in both the age and the error calculation a careful and detailed protocol must be kept.

Sample preparation must be carried out in such a way, that the cleanest and purest possible quartz grains (or other minerals which have TL-capabilities) are obtained in the right fraction size. For the fine-grain technique this objective is usually achieved by chemical cleaning and sedimentation. The obtained quartz fraction is then deposited in thin grain layers on small circular metal sample holders. An even distribution is obtained by pipetting the dispersed powder in acetone and allowing the acetone to evaporate. For quartz inclusion separation is carried out by sieving, liquid separation, magnetic separation [31], and other mineralogical techniques, e.g. individual grain extraction under a microscope (especially for single grain dating). The grains are then placed on small U-shaped circular sample holders. For this technique a relatively large quantity of material is needed to obtain enough grains for dating.

7. GENERAL PROBLEMS CONNECTED WITH THE TL RESPONSE CURVE

Equation (3) represents, unfortunately, only an approximation of the real situation. It presumes that the dose-response curve is linear in the whole range of measured ages and that an electron, once trapped, remains captured in the TL centre without any change up to the moment the sample is heated in the laboratory. None of these assumptions are sufficiently accurate and therefore a more complicated response curve needs to be considered.

At very high doses the TL response of the material extracted from the fired object can be significantly supralinear until it finally saturates. This supralinearity can be corrected in the follwowing way. Several samples of the material are irradiated to different values of an

"artificial" dose. The curve obtained crosses the ordinate of the graph in Figure 4 at the point corresponding with the TL response to the natural dose (curve 1). The linear extrapolation to the abscissa gives the value corresponding with the natural dose D_{nl} if the response-dose curve were linear. Irradiation by artificial doses and readings on a series of samples of the same investigated material which have been heated and read out before this irradiation leads to the curve 2, which shows a lower response when compared with curve 1. The difference between both curves corresponds to the natural dose. The extrapolation of the linear part of this curve intercepts the abscissa in the point corresponding with the correction for supralinearity D_c. The sum of D_{nl} and D_c gives the "true archaeological" dose D_n. If the curves 1 and 2 are not parallel because of increasing sensitivity caused by a high dose and the supralinearity correction for both curves is different, a further complication arises. Examples of such behaviour and possible ways of dealing with it can be found, e.g. in [31].

With the exception of the pre-dose technique, TL centres will keep electrons trapped for centuries, i.e. they will exhibit only negligible fading. This is not valid for all traps and therefore the glow curve for artificial irradiation has a different shape compared with the natural glow curve. It has the same peaks corresponding to deep traps which are emptied at high temperatures, but it also possesses lower energy peaks corresponding to shallower traps. These traps are not able to retain electrons without escape for archaeologically significant times and therefore they cannot be used for TL dating purposes. This can be seen in Figure 5 (according to [15]), where the curve N is the glow curve for natural TL and the curve N+β for the sample of the same material with an artificial dose of β radiation added. The so-called plateau-test for the determination of the temperature above which the signal can be used for dating is based on the ratio of both TL-responses (the dashed curve). The plateau on the plot of this ratio against temperature usually starts somewhere above 300 °C. This corresponds to the energy levels of traps where the captured electrons have lifetimes, at room temperature, substantially longer than the age of the sample, and fading during the period between two firings is negligible. The temperature range used for TL dating is shifted to higher temperatures compared with the application of TL for dosimetry in, e.g. radiation protection, and the background thermal incandescence radiation plays a much more significant role.

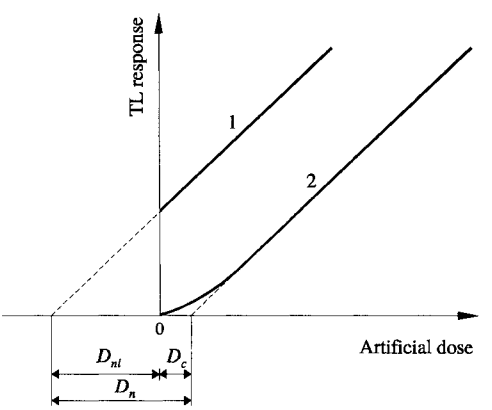

Figure 4: Correction for supralinearity .

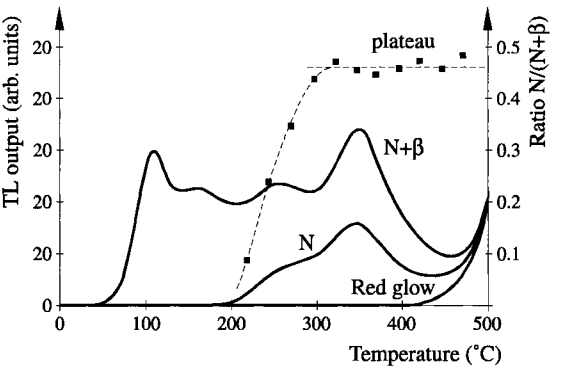

Figure 5: The plateau-test. N is the glow-curve of natural TL of the sample, N+β the glow curve of another portion of the same sample with the artificial dose added, the dashed curve shows the ratio of both.

Absence of a plateau indicates the occurrence of some disturbance. It can be caused by contamination of the sample during sampling or preparation. Another possible reason is spurious TL, which usually influences more markedly the glow-curve of natural TL than the artificial one and hence the plateau is destroyed and the ratio of natural and artificial TL continues to increase. The firing at low temperature, or no firing at all of the object to be investigated during manufacture, can cause the absence of a plateau. Another complication can be caused by anomalous fading exhibited by some minerals, especially feldspars [32], [33]. The measured rate of fading of high-temperature peaks on the glow-curve cannot be explained by the probability of thermal release of electrons governed by the thermal distribution of their energies and is probably due to quantum mechanical tunnelling. An appropriate thermal or optical pre-treatment can help to obtain reliable ages even in this case [34].

8. ERROR ASSESSMENT

No TL date is complete without information about the uncertainty with which it is determined. Only this will avoid over- or under-estimation of the method and historical misinterpretations. Assessment of an error in TL dating is not straightforward due to the complex character of the measurement, where numerous quantities enter into the calculation, and where not all uncertainties are quantifiable. The method was originally introduced into historical disciplines in archaeology, and all considerations, particularly those in regard to the error calculation, were concentrated on the sort of problems encountered there. The "standard" procedure for error assessment for pottery dating from the quantifiable

uncertainties was established early on in the development of TL as a dating method [35], [36]. The experience has proven that this procedure leads to relevant error values.

It considers random and systematic errors separately. Random errors originate in the process of measurement of both the TL glow-curve and the annual dose rate and are specific for each measurement. Systematic errors, on the other hand, are given entities, which can, however, vary, originating in the uncertainties related to the to the radioactive sources and machines used, with the specifics of the sampling location. They derive from the general background of the method and influence the results of all samples in a similar way. This means that the overall random error can be reduced by dating a larger number of samples. But this is ***not*** the case when dealing with the systematic error.

8.1 **Random error**

The random error consists of two main components: σ_1 expresses the uncertainty in the glow curve analysis and includes the error in the determination of the equivalent dose D_e, of the supralinearity correction D_c and of the α-radiation efficiency k, and σ_2 corresponds to the uncertainty of the dose rate determination at the sampling location and includes the error of the radioactive analysis of the sample, and of the β and γ dose rate measurements. Therefore four combinations of dosimetry options must be considered: a) radioactive analysis only, b) radioactive analysis and β dosimetry, c) radioactive analysis and γ dosimetry, and d) radioactive analysis and both β and γ dosimetry.

If δD_e, δD_c and δk are estimates of errors of corresponding quantities and all standard deviations are quoted as a percentage, than:

$$\sigma_1^2 = \{100(1-f_\alpha)\frac{\delta D_e}{D_e}\}^2 + \{\frac{100\delta D_c}{D_e + D_c}\}^2 + \{100 f_\alpha \frac{\delta k}{k}\}, \qquad (12)$$

and for the various options of dosimetry:

$$(\sigma_2)_a^2 = 25[(f_\alpha + f_{\beta,Th,U})^2 + f_{\beta,K}^2 + f_{\gamma,Th,U}^2 + f_{\gamma,K}^2], \qquad (13a)$$

$$(\sigma_2)_b^2 = 25[f_\alpha^2 + f_{\gamma,Th,U}^2 + f_{\gamma,K}^2] + \{100 f_\beta \frac{\delta D_L}{D_L}\}^2, \qquad (13b)$$

$$(\sigma_2)_c^2 = 25[(f_\alpha + f_{\beta,Th,U})^2 + f_{\beta,K}^2] + \{100 f_\gamma \frac{\delta D_p}{D_p}\}^2, \qquad (13c)$$

$$(\sigma_2)_d^2 = 25 f_\alpha^2 + \{100 f_\beta \frac{\delta D_L}{D_L}\}^2 + \{100 f_\gamma \frac{\delta D_p}{D_p}\}^2. \qquad (13d)$$

In these equations, f_α is the fraction of the total annual dose rate due to α radiation, similarly f_β and f_γ for β and γ radiation, which can be further divided into the fraction due to the radionuclides from the uranium and thorium series and due to ^{40}K. D_L is the β dose rate

derived from the dosimetry measurement for the sample in dry conditions and D_p the dose rate measured by the TL dosimeter. Both random errors of α-counting and potassium content determination are considered to be ±5 %.

The resulting random error is the sum of both components:

$$\sigma_r^2 = \sigma_1^2 + \sigma_2^2. \tag{14}$$

If the soil in which the shard is buried is very inhomogeneous and contain stones, an additional term needs to be added:

$$\sigma_3^2 = r f_\gamma \left(\frac{D_1 - D_2}{D_\gamma}\right).100, \tag{15}$$

where D_1 and D_2 are the γ dose rates in soil and stone and r is the weight fraction of stones.

8.2 **Systematic errors**

The uncertainties contributing to the systematic error originate from various sources. The first source of the systematic error is the calibration of the α source, the β source, the α counter, the potassium content measurement, the β measurement and the γ measurement. Assuming that each of these uncertainties is ±5 %, then, for the various versions of dosimetry, the error terms are:

$$(\sigma_4)_a^2 = 25\{f_\alpha^2 + (1 - f_\alpha)^2 + (f_\alpha + f_{\beta,Th,U} + f_{\gamma,Th,U})^2 + (f_{\beta,K} + f_{\gamma,K})^2\}, \tag{16a}$$

$$(\sigma_4)_b^2 = 25\{f_\alpha^2 + (1 - f_\alpha - f_\beta)^2 + (f_\alpha + f_{\gamma,Th,U})^2 + f_{\gamma,K}^2 + f_\beta^2\}, \tag{16b}$$

$$(\sigma_4)_c^2 = 25\{f_\alpha^2 + (1 - f_\alpha - f_\beta)^2 + (f_\alpha + f_{\beta,Th,U})^2 + f_{\beta\gamma,K}^2 + f_\gamma^2\}, \tag{16c}$$

$$(\sigma_4)_d^2 = 25\{2f_\alpha^2 + f_\beta^2 + f_\gamma^2\}. \tag{16d}$$

Due to the observed discrepancy between the calculated (from radioactive analysis) and measured (by TLD) γ dose rates, which is estimated to ±10 %, an additional error term needs to be added:

$$\sigma_5 = 10 f_{\gamma,Th,U}. \tag{17}$$

The second source of the systematic error arises from the uncertainty of the ratio between the uranium and thorium series. The measurement by α counting gives no information about this ratio, and converting the α count-rates to dose rates depends on it, as the energy of β and γ radiation emitted per α particle differs between both series. For the uncertainty in this ratio ±50 % is assumed and it is used for various options of dosimetry:

$$(\sigma_6)_a^2 = 15 f_{\beta,Th,U}^2 + 10 f_{\gamma,Th,U}^2, \tag{18a}$$

$$(\sigma_6)_b^2 = 10 f_{\gamma,Th,U}^2 , \tag{18b}$$

$$(\sigma_6)_c^2 = 15 f_{\beta,Th,U}^2 , \tag{18c}$$

$$(\sigma_6)_d^2 = 0. \tag{18d}$$

Another problem is given by the fact, that both uranium and thorium series contain one of the isotopes of radon as a member. Possible escape of this gas can influence the dose rate and can be evaluated by the measurement in a gas cell, where only particles from escaped radon are detected by a scintillator. This technique is described in [37]. However, the estimate of the escape measured in the laboratory does not necessarily correspond to the real escape rate at the sampling location. Assuming that the uncertainty of the value g_s, which expresses the lost α counts for the conditions of the sample, is ±25 %, then we obtain the error term:

$$(\sigma_7)^2 = (g_s / 4\alpha_B)^2 (f_\alpha + f_{\beta,Th,U})^2 + (g_w / 2\alpha')^2 f_{\gamma,Th,U}^2 , \tag{19}$$

where α_B is the α count rate corrected for radon escape and the second term refers to radon escape in the soil, α' being the corrected α count rate from the soil and g_w the lost counts for the soil sample (having the same wetness as in the ground).

The last important source of the systematic error is given by the uncertainty δF of the fractional water uptake F. The value of δF must be estimated from the knowledge about the conditions (rainfall, drainage, etc.) on site. This error can be approximated by:

$$\sigma_8 = (\delta F / F)\{W(1{,}5 f_\alpha + 1{,}25 f_\beta) + W'(1{,}15 f_\gamma)\} . \tag{20}$$

W and W' is the saturation wetness of the sample and the soil, respectively, expressed as the ratio of the saturation weight minus the dry weight and the dry weight in percent.

The overall systematic error is a combination of the contributions discussed above, i.e.:

$$\sigma_s^2 = \sigma_4^2 + \sigma_5^2 + \sigma_6^2 + \sigma_7^2 + \sigma_8^2 , \tag{21}$$

and the overall error for the sample is given by the combination of random and systematic errors as:

$$\sigma^2 = \sigma_r^2 + \sigma_s^2 . \tag{22}$$

8.3 Context error

For obtaining a more accurate age with a smaller quotable error margin it is always useful to date more objects from a given historic context. The system of context error determination deals with such instances and only with those sources of error which are known to be present and where their magnitude can be assessed. Some other possible sources of error may appear in a particular case of dating. The age for the context containing n samples can be calculated as:

$$T_0 = \frac{\sum_{j=1}^{n} T_j / \sigma_j^2}{\sum_{j=1}^{n} 1/\sigma_j^2}. \tag{23}$$

The standard error of this value is:

$$\sigma_0^2 = \{\frac{\sum_{j=1}^{n} (\sigma_j)_s / \sigma_j^2}{\sum_{j=1}^{n} 1/\sigma_j^2}\}^2 + \frac{1}{\sum_{j=1}^{n} 1/(\sigma_j)_r^2}. \tag{24}$$

Thus the value:

$$a = \frac{\sigma_0 A_0}{100} \tag{25}$$

is the standard error of the age of the given context in years.

Systematic uncertainties represent the limit for reducing the overall error, which for pottery is typically in the range of ±7 - 10 % (1σ) of the age, only under very advantageous circumstances about ±5 % (1σ) can be reached. Moreover, the TL characteristics of pottery materials vary a great deal, and in some instances they are so problematic that it is impossible to obtain a reliable date. The situation is different in the dating of brick architecture, where lower errors can be reached.

In architecture, that is in brick dating, some of the above mentioned parameters have to be reconsidered: for example, a weak TL-signal due to the relatively short time since the material was fired, the potentially low quartz content and the possibility of high spurious light levels. These factors are, however, minimised by the fact that very much larger quantities of material can be removed for analysis from bricks, than is possible from pottery and that more bricks can be sampled from one historic context. The fact that a brick wall can be defined, on a macroscopic level, for TL purposes as a homogeneous medium [38], redefines certain factors in the uncertainty of some of the random errors in the dating calculations.

a) **Gamma dose rate**: The assumption that the actual sample remained *in situ* from the time of the erection of the brick wall to the moment of sampling (if the dating analysis is to have any historical value), makes the surroundings of the sample both constant over time and homogeneous in material. Taking the volumetric distribution of mortar joints, the size of the bricks, and the fact that γ rays are attenuated in a layer after approx. 24 cm in bricks to such an extent, that their contribution to the total dose rate is negligible, into account, it is possible to establish a revised mathematical model which will allow a calculation of the γ dose rate directly from the α count values. The accuracy of this calculation is dependent on sufficient homogenous wall depth (> 48 cm) and sufficient sampling depth (> 24 cm) and is usually smaller than for pottery [39]. Sampling a thinner wall and at shallower locations is possible, although this will increase the error margin.

b) **Fluctuation of the water content**: Instead of operating with an assumed error margin within the extremes of dryness and saturation, it is possible in brick walls to insert an actual fluctuation variable into the error calculation, for both the random and systematic

errors. Although the variable of the systematic error has to be established for each climatic zone with a relatively complex simulation on whole brick samples of the type to be dated and then a lengthy statistical calculation, a generalisation is possible [40], except in extreme climatic zones, providing the sampling depth is sufficient. In most instances sampling depths greater than 8 cm provide minimal fluctuations of the in situ water content. The actual statistical measurement error, the random component, is, in such cases, substantially larger than the systematic error, which has to be taken into account by revising the corresponding system of equations from (12) to (20) [38].

The number of samples that may be taken and the possible quantity of such samples, is directly responsible for the reduction of context error of a statistically and historically significant sample group, i.e. samples from different bricks within a historically uniform structure. Using the traditional error calculation, with the above mentioned corrections, and inserting typical individual sample errors, the optimal context error for the group reduces itself to a theoretically calculated value of about ±3%.

In cases where a sufficient number of samples could be considered as one historically and statistically significant group, the actual deviation between TL mean date and known building date has been shown to lie in the region of ±1 % or below [38]. It must be stressed that this accuracy is empirically obtained, and cannot be presumed for the interpretation of other TL-dates for which the actual date of construction is unknown. On the other hand it is essential to point out the importance of the fact that the actual historical error is usually smaller than the physically and statistically calculated context error. It can therefore be presumed that in those cases where the actual construction date is obtained through TL, this construction date will be within the margin established by its context error.

Results are commonly quoted by one of the published formats, of which the one suggested by Fleming [41] is the most detailed:

Date BC/AD (+/-p, +/-a, laboratory and site reference) (TL-technique),

where: p is the standard error (1σ) of the group of samples in years, a is the error (1σ) of a single sample or context error (1σ) of a group of samples in years, and where the site reference should include all sample numbers used to form the context.

Furthermore it is suggested that a detailed list of "factors considered" be added, which could include, among others: saturation and assumed fractional uptake of H_2O, supralinearity correction, correction for radon emanation, fading check, contribution of α, β and external γ radiation in the total annual dose rate, etc.

9. INTERPRETATION PROBLEMS

The date obtained by TL is the last firing date of the object. Although in most cases this is the historically relevant date, this cannot be automatically assumed:

1. The TL result is a time span (usually quoted as the TL date ±1 σ) within which the specific object was last fired. Although this time span can be reduced for various objects (e.g. bricks) by successfully grouping historically (but not physically) connected parts and carrying out a statistical context calculation, the time span offered by TL, may not always be sufficiently small to answer a detailed historical question.
2. The TL date is valid only for that object, and if an analysed work contains more than

one part (e.g. a terracotta frieze composed of various plates; a brick wall, obviously built from numerous bricks), the date obtained is valid only for the part dated, and it cannot be automatically presumed that the whole object was fired in the same period.

3. If the object underwent a subsequent fire, TL may date this fire, and not the manufacture of the object. In most instances the object will show such damage, so that a dating campaign need not be carried out, unless, the date of the fire is of historic interest. In architectural dating, due to the volume of a brick wall, both the date of the fire (by sampling closer to the surface of the wall), and the original date of manufacture of the brick (by deeper sampling) may be obtained. In these cases, the depth of influence of the fire on the TL signal should be checked by ensuring that the signal remains constant over a certain depth. Empirically it has been shown that this occurs after about 6 cm [42]. This is a shallower sampling depth than is necessary to ensure a minimal fluctuation in the water content and being able to disregard the influence of the external gamma dose.
4. In architectural dating a further problem is encountered, namely that the historically relevant date is not the manufacture of the brick, but the construction of the wall (or building), which the brick is part of. Before correlating the date obtained by TL with the construction date of the building, certain factors have to be considered:

    a) The customary time, or, if possible, documented time frame between the manufacture of the brick and its use in that particular region and in that historic period.

    b) The possibility that the brick was reused from an older building on the same or nearby site.

On the other hand, when dating a brick wall or building, samples from numerous different bricks can be taken, which offers a far greater accuracy for 1 σ, but before grouping the bricks into one historically relevant time, certain considerations have to be made.

a) The bricks grouped into one context have to come from, architecturally and historically speaking, a united structure.

b) The grouped bricks have to be similar, if not identical, in their manufacturing process. This can usually be done visually, by checking size, colour, texture etc., but sometimes a chemical analysis or the TL response can be helpful.

10. EXAMPLES

10.1 Pottery authentication and dating

Pottery is the most widespread application of the TL dating method. Some dating campaigns can be found for nearly each geographic region and period of civilisation. Only a few randomly selected examples can be presented here to demonstrate the scientific and historic potential of the method. The examples chosen cover a variety of different types of artefacts, different regions and different periods.

P.D. Shaplin [43] deals with the St Louis Art Museum's collection of three-dimensional ceramic sculptures, popularly known as urns (their function is not yet fully understood), originating in the Zapotec culture, which flourished in southern Mexico *circa* AD 200-800. These urns are cylindrical vessels conceived of as anthropomorphic or theriomorphic figures

with costumes and attributes of social and cosmological importance. Thousands of such urns are now in museums and private collections all over the world, often without the known archaeological context, many of them are suspected to be forgeries.

Authenticity testing of one hundred and seventeen urns from the St. Louis collection was carried out, the primary test being based on the fine-grain technique. For authenticity tests relatively small samples can be used, in this case it was 3-5 mg of bulk ceramic scraped with a dental tool from an inconspicuous area of the urn. Presumably because of the large content of feldspar, the TL response was good. Even the sample with the lowest natural dose gave a signal to noise ratio in natural TL of about 10 : 1. Good plateaux were obtained in the ~350 to ~425 °C region for all except one sample. For that urn a larger sample was taken and satisfactory TL measurement was obtained from separated large mineral grains.

Before the TL campaign sixteen urns were selected which were believed to be forgeries on the basis of the following criteria:

a) unusual material or surface treatment,
b) manufacturing technique, form or size inconsistent with other variables,
c) iconographic motifs not previously encountered elsewhere and not consistent with the urn's assumed date or iconographic category,
d) apparent stylistic similarity to known or strongly suspected forgeries,
e) qualities that would tend to increase the urn's commercial value, such as extreme rarity, extreme beauty or appeal to tastes promulgated by mass media ("cuteness").

However, TL measurement showed that these criteria needed to be re-considered. Only 6 % were forgeries instead of the suspected 13.7 % of the collection. And, moreover, only two pieces suspected to be fakes really were, 14 urns looking like fakes were genuine, but on the other hand five pieces looking genuine were forgeries. The difference in the TL response between ancient and modern urns was well pronounced, the natural doses measured in modern urns were between 0.04 and 0.25 Gy, for ancient urns they were in the range of units of Gy, a few pieces exceeding even 10 Gy.

Because of the high content of feldspar, especially plagioclase, possible influence of anomalous fading was also investigated, with the result that this effect would not invalidate the results. Three of the urns, whose origin in antiquity was most surprising from the point of view of their style, were further tested by the zircon inclusion technique to avoid the possibility that they were modern. If they had been irradiated with an artificial dose by a modern forger, then the dose in zircon grains would be comparable with the dose in the bulk material. If the urns were ancient, the dose in the zircon grains would be many times higher due to the high content of radionuclides in zircon. The authenticity of the three most suspicious pieces was so confirmed with the highest possible degree of credibility.

Wang and Zhou [44] compared results of TL dating of Chinese pottery of various ages and from various regions with radiocarbon ages. The results agreed within the range of experimental error. Some of their objects were dated both by fine-grain and quartz inclusion techniques. Unfortunately, only for one sample of Zengpiyan pottery all three dates can be found in their paper, however the agreement is very satisfactory: fine-grain technique gave the age of 8080±540 years BP, quartz inclusion technique 7750±570 years BP and ^{14}C dating 7680±150 years BP.

Comparison between TL and radiocarbon dating was also carried out for the archaeological sites of El Kadada and El Ghaba near Shendi in Central Sudan [45]. Both these archaeological sites are from the neolithic period, their first chronology was obtained by

radiocarbon dating of calcium carbonate from the water shells found in the sepultures. However, this is the kind of material which is not the best from the methodological point of view, and therefore the results were a bit doubtful. For instance, the initial ratio of ^{14}C in the carbon reservoir within which the shell was growing could be influenced by the presence of fossil carbon in the Nile river, and a carbonate ion exchange during burial was possible. As the chronology of neolithic cultures in the Sudanese Nile Valley was mainly based on ^{14}C shell dating, the problem was of more general interest, and not limited only to El Khadada and El Ghaba.

Therefore the TL dating campaign was carried out, using ceramic samples extracted during the archaeological excavations in both sites. The fine grain technique was used, the plateau region in which the TL signals were integrated was usually between 350 °C and 450 °C. The internal radiation doses were determined from the analysis of the content of K, Th and U by various analytical techniques (AE ICP, energy dispersive XRF, neutron activation analysis) and for some samples also by γ–spectrometry with a Ge-Li detector. The external component was evaluated by *in situ* measurements using a gamma detector with a plastic scintillator, additional information was obtained by laboratory measurement of samples of surrounding sediment.

Two kinds of ceramics could be distinguished by their composition, one of them was "quartz-rich" and had a low level of radioactivity, the other was "K-feldspar rich" and had higher K as well as Th and U contents. The first group was found to be very suitable for TL dating, the second one exhibited significant fading, especially on the feldspar inclusions. The possible inhomogeneity of the α and β radiation fields due to the presence of zircon and monazite grains had to be taken into consideration. Therefore, only the first group was used for comparison with radiocarbon dates.

The chronology deduced from the TL and radiocarbon dates showed a high correlation. At the KDD 98/3 grave in El Kadada, e.g. the average TL date was 3630±200 BC, the date range for radiocarbon was 3695-3535 BC. This confirmed that significant errors in the radiocarbon chronology are not probable.

Both TL and ^{14}C dates show that the most ancient sepultures in El Ghaba were built during the fifth millenium BC and the necropolis was in use for about 1500 years (all dates belong to the period from 4800 to 3300 BC, which overlaps the so called Khartoum neolithic period). At El Kadada the occupation started later, at about 4200 BC, and ended around 3000 BC. This shows that El Kadada is more recent than most other neolithic sites in Central Sudan.

To mention at least one investigation carried out in the Mediterranean, as the treasury of archaeology, the dating of prehistoric pottery sherds from Milena, Sicily [46] will be mentioned. The samples originated from a wide range of periods, from the Middle Neolithic to the Bronze Age. For the Bronze Age it was possible to correlate the TL data with a precise stratigraphy. TL dating was combined with petrographical and mineralogical analyses, aiming not only to identify the main constituents of the pottery, but also to formulate a hypothesis regarding the specific manufacturing techniques in different periods. The dates obtained were generally in agreement with the chronology established by archaeologists on the basis of style and typology.

Ancient bronzes and other metalwork are also sometimes objects of TL dating or authentication. Such analysis cannot be carried out on the metal itself, as it does not possess TL properties, but on the remnants of the ceramic-like casting core, which can be found in

10.2 Dating in architecture

The architectural manifestation of the tower of the Villa Gonzato in Pozzoleone (Figure 6) [47-49], is a typical feature of the Venetian countryside. Most probably such towers served originally as a defence against raiding troops and outlaws. On 30 June 1520 the Venetian Senate passed a law expropriating all *torre e fortezze* on the Venetian mainland [50]. A rigorously enforced law, it was still in use in the late 17th century. The tower of the Villa Gonzato in Pozzoleone is a typical example of the successful attempt to escape expropriation by altering its function to that of a dovecote. A dating analysis using dendrochronology showed that the carpentry of the tower of the Villa Gonzato stems from two distinct periods:

- the beams on the lower floors were made of trees felled between 1378 and approximately 1390;
- the frame of the pitched roof was, however, built of trees felled between 1525 and approximately 1545 [48], [49].

Figure 6: Pozzoleone (Italy), Tower of the Villa Gonzato.

This proves that in the years immediately after the passing of the above-mentioned law a roof was added to the tower. The obvious assumption to be drawn from these dates was that the battlements would have been bricked in, with openings left only for the pigeons to fly

in and out, and that the roof was added. These alterations successfully changed the function from a defensive one to a peaceful one.

The TL-date of

AD 1532 (+/- 15.4, +/- 9.2, RFTL-VV 5/3;12) (fg), [38]

confirms this alteration, but allows significant additional deductions to be drawn. This is possible by analysing the location of the samples. Sample locations which give the 1532 context-date are situated in parts of the structure hitherto presumed to have formed part of the older building, i.e. from the parts used for defensive purposes. These samples were removed from one of the Ghibelline battlements and from the dog-tooth brick moulding running below. This result implies that the battlements themselves were reinforced at the same time that the function was ostensibly altered. What was evidently done was a camouflage operation that concurrently satisfied the Venetian lawmakers and improved the defensive potential for times of need. It would have only taken a short time to remove the roof and replace the openings of the battlement. Although bricks of only this one tower were analysed by TL, and the results obtained are therefore definitive only for this one building, the political implications of such a custom are far reaching. The facts seem to indicate that the landowners on the *terra firma* were preparing further actions against Venetian domination even after the various treaties which ended the wars of the League of Cambray, and which confirmed the Venetian domination of these lands.

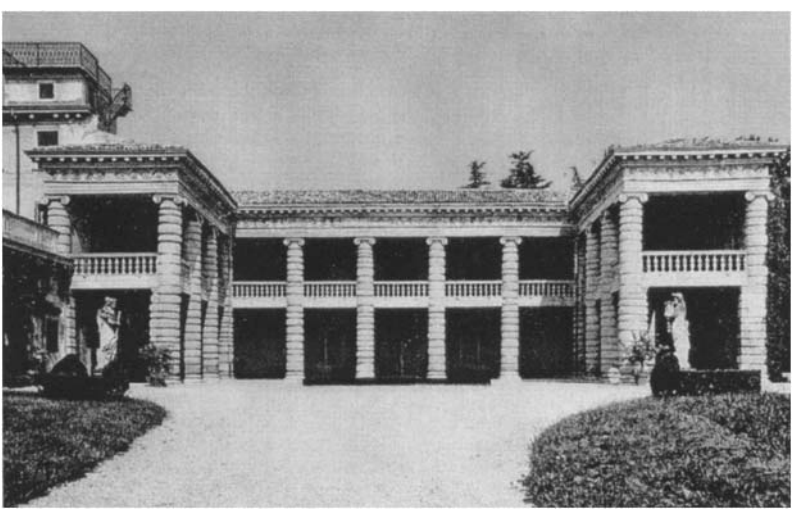

Figure 7: Santa Sofie die Pedemonte, Villa Sarego.

The dating of the Villa Sarego at Santa Sofia di Pedemonte [38] (Figure5.7), most probably designed by the architect Andrea Palladio (1508-1580), was, until its dating by TL,

one of the most controversial ones in this important architects oeuvre. Suggestions based on circumstantial documentary and stylistic evidence produced dates ranging from 1541-1569, in other words spanning most of Palladio's active career. Because the material chosen for construction is, in contrast to the usually employed material, brick, and the heavily rusticated columns at the Villa Sarego are made of stone, and because of the necessity to preserve the decoration in the lower floors, all samples for TL were taken in the attic level of the building. In this particular case this procedure actually proved of assistance in the interpretation of the dates, because the results support the earliest hitherto made proposal for the building of the villa, and thus indicate that even at that height of the construction, work must have been in progress at such an early time. The TL-date of

AD 1534 (+/- 8.5, +/- 9.2, RFTL-VV 12/12;13;14) (fg) [38]

gives as the latest probable firing date of the bricks the year 1543. This evidence overlaps Cevese's suggestion [51], based on stylistic criteria, of 1541-1547, and might suggest a period of construction of about 1541-1543. TL does not however answer the question of authorship, and the narrowing down of the construction date through the overlap with Cevese's suggestion is only then valid, if the Villa is by Palladio. The only deduction TL in itself allows, is the probability, that the bricks of this part of the building were fired between 1525 and 1543. Should therefore the possibility of building activity in the 1520is or 1530is by others than Palladio be substantiated through other means at a later date, the interpretation of the TL-date would need to be looked at again.

The central supporting wall, however, is substantially older, with a TL-date of

AD 1384 (+/- 14.5, +/- 12.8, RFTL-VV 12/11) (fg) [38]

and proves the existence of an older building on the site as indicated by documents. The Sarego family had owned these lands since 1381 and received the investiture of the chapel of Santa Sofia in 1388. The TL-date lies exactly in between these dates and proves that the Sarego family built their first villa on the site immediately upon ownership. Parts of this earlier Villa, which was built in the late 14th century, were incorporated into the 16th century building.

The two examples mentioned above are part of a larger TL dating campaign of Venetian Villas carried out in the late 1970s and early 1980s; the largest research project of this type to date [38]. It included further such famous buildings as Palladios Villa "La Rotonda" near Vicenza and his Villa Foscari, better known as "La Malcontenta" in Mira. Other examples of fundamental TL-dating campaigns in architecture dealt with civic and ecclesiatic architecture in Lübeck [52], the dating of various structures in the Roman town Carnuntum [53], and, most recently, the medieval architecture in Liguria, Italy [54].

11. OTHER MATERIALS

Pottery and fired bricks are not the only materials datable by TL. Burnt flint and other stones, volcanic lava, unburnt sediments or stalagmitic calcite, sand dunes and even some biological materials can also be successfully dated, though in some of these materials the

complete zeroing of TL at the beginning of their "life" is problematic. Only the main problems connected with dating of these materials will be briefly mentioned.

Flint is a form of quartz and therefore its TL properties are usually good for dating. On the other hand, its low content of radionuclides causes a high contribution of external γ radiation to the radiation field inside, therefore the error in the measured TL date is strongly dependent on the knowledge of the environment. It is also even more important than in pottery dating to remove approx. 2 mm from the outer layer, to avoid the influence of β radiation from the soil. Flint implements of Paleolithic men were sometimes heated, accidentally or intentionally placed in a fire. The plateau test will show, if the heat was sufficient to zero the "geological" dose. The lower limit of measurable dates is conditioned by the low radioactivity of flint and therefore the low dose rate and it is in the order of magnitude of thousands of years. The upper limit is given by saturation and is usually between one and five hundred thousand years, exceptionally for flints and soil with a very low radioactivity even more.

No generalisation can be made for the other types of stones from ancient fireplaces, used as pot-boilers for cooking or heated during fires. They contain a variety of minerals and hence their TL properties differ. Problems with inhomogeneity of radiation fields is quite often caused by the appearance of large grains. On the other hand, these grains can, under certain circumstances, be used for dating (as, e.g. feldspar with high potassium content in [55]).

Volcanic lava has primary importance for geology, but occasionally can give relevant information for archaeologist - in instances when some cultural strata was buried between two layers of lava or when a volcanic eruption destroyed a human habitation. Lava usually does not contain quartz, but it can be dated using other minerals like plagioclase feldspar [56]. Other volcanic products or soil and rock over which the glowing lava flowed can also be used for dating.

The TL dating of sedimentary rocks is mostly of geological importance. Such rocks usually contain TL capable minerals like calcite, quartz, dolomite, aragonite or magnesite. On the ground these minerals are zeroed mainly by exposure to UV radiation and surface heating of rocks by the sun. When they are buried under the subsequent layers of sediment, this influence ceases and the TL signal starts to accumulate. Therefore, the last exposure to sunlight is dated. The same principle can be used for dating sand dunes. The depth profile of the dose in the sediment or in the dune is a source of information about the formation of the rock or the dune. The key problem is the completeness of zeroing during the exposure to sunlight. This is valid especially for waterborne sediments, where UV radiation is filtered by the water layer. The question of zeroing is important also in dating calcite in stalagmites in paleolithic caves, when the moment of crystal formation is dated. The usefulness for archaeology is similar as in the case of volcanic lava.

TL was also observed in fossil bones, teeth and marine shells (e.g. [57], [58]), although ESR dating appears to be the better and the preferably used dating method for these materials. The main TL sensitive mineral in these materials is hydroxyapatite, which has the TL peak at 70 °C. Therefore, the pre-dose technique must be used.

REFERENCES

1. R. Boyle, Experiments and Considerations upon Colours with Observations on a Diamond That Shines in the Dark, Henry Herringham, London, 1664.
2. E. Wiedeman and G.C. Schmidt: Ann. Phys. Chem. Neue Folge, 54, 1895, 604.
3. J.F. Randall and M.H.F. Wilkins, Proc. Roy. Soc., A184, (1945), 366, 390.
4. F. Daniels, C.A. Boyd and D.F. Saunders, Science, 117, (1953), 343.
5. F.G. Houtermans, N. Grögler and H. Staufer, Helvetia Physica Acta, 33, (1960), 595.
6. J.R. Cameron, N. Suntharalingham and G.N. Kenney, Thermoluminescence Dosimetry, Univ. of Wisconsin Press, Madison, 1968
7. M. Oberhofer, A. Scharmann, Applied Thermoluminescence Dosimetry, Adam Hilger, Bristol, 1981.
8. A.F. McKinlay, Thermoluminescence Dosimetry, Adam Hilger, Bristol, 1981.
9. Y.S. Horowitz (ed.), Thermoluminescence and Thermoluminescent Dosimetry, Vols 1-3, CRC Press, Boca Raton, 1983.
10. S.W.S. Mc Keever, Thermoluminescence of Solids, Cambridge University Press, Cambridge, 1985.
11. K. Makesh, P.S.Weng and C. Furetta, Thermoluminescence in Solids and its Application, Nuclear Technology Publishing, Ashford, 1989.
12. S.W.S. Mc Keever, M. Moskovitch and P.D. Townsend: Thermoluminescence Dosimetry Materials: Properties and Uses, Nuclear Technology Publishing, Ashford, 1995.
13. R. Boeckl, Nature, 236, (1972), 25.
14. J.R. Prescott and J.T. Hutton: Nucl. Tracks Radiat. Meas., 14, (1988), 223.
15. M.J. Aitken: Science-based dating in archaeology, Longman, London and New York, 1990.
16. Radionuclide Transformations: Energy and Intensity of Emissions (ICRP Publ. No. 38), Annals of the ICRP, 11-13, (1983).
17. K.S.V. Nambi and M.J. Aitken, Archaeometry 28, (1986), 202.
18. I.K.Bailiff, PACT, 6, (1982), 72.
19. D.W. Zimmerman, Archaeometry, 10, (1967), 26.
20. D.W. Zimmerman, Archaeometry, 13, (1971), 29.
21. S.J. Fleming, Archaeometry, 9, (1966), 170.
22. S.J. Fleming, Archaeometry, 12, (1970), 133.
23. S.J.Fleming and D. Stoneham, Archaeometry, 15, (1973), 229.
24. D.W. Zimmerman, Science, 174, (1971), 818.
25. S.R. Sutton and D.W. Zimmerman, Archaeometry, 18, (1976), 125.
26. S.J. Fleming, Archaeometry, 15, (1973), 13.
27. I.K. Bailiff, S.E.G. Bowman, S.F. Mobbs and M.J.Aitken, J. Electrostatics, 3, (1977), 269.
28. S.E.G. Bowman, PACT, 3, (1979), 381.
29. M. Ikeya, Nature, 255,(1975), 48.
30. D.J. Huntley, D.I. Godfrey-Smith and M.L.W. Thewalt, Nature, 313, (1985), 105.
31. S.J. Fleming, Thermoluminescence Techniques in Archaeology, Clarendon Press, Oxford 1979.
32. A.G. Wintle, M.J. Aitken and J. Huxtable, Abnormal Thermoluminescence Fading Characteristics, In: Proc. 3rd Int. Conf. Lumin. Dosim., Risö Report 249, (1971), 105.

33. A.G. Wintle, PACT, 2, (1978), 240.
34. R.H. Templer, Radiat. Prot. Dosim., 17, (1986), 493.
35. M.J. Aitken, M.C. Alldred, Archaeometry, 14, (1972), 257.
36. M.J. Aitken, Archaeometry, 18, (1976), 233.
37. V.S. Desai and M.J. Aitken: Archaeometry, 16, (1974), 95.
38. C. Goedicke, K. Slusallek and M. Kubelik, Thermolumineszenzdatierungen in der Architekturgeschichte, dargestellt an Hand von Villen im Veneto, Berliner Beiträge zur Archäometrie, 6, (1985).
39. C. Goedicke, M. Kubelik and K. Slusallek, PACT, 6, (1982), 45.
40. C. Goedicke, M. Kubelik and K. Slusallek, Application of TL in Architectural History: Assessment of Water Error of Brick Specimens, 21st Symposium for Archaeometry, Brookhaven National Laboratories, Upton, N.Y., 18-22 May 1981.
41. S.J. Fleming, MASCA Journal, 1, (1978), 12.
42. C. Goedicke, M. Kubelik and K. Slusallek, PACT, 9/I, (1983), 245.
43. P.D. Shaplin, Archaeometry, 20, (1978), 47.
44. W. Wang and Z. Zhou, Archaeometry 25, (1983), 99.
45. P.Guibert, C. Ney, F. Bechtel, M. Schvoerer and F. Geus, Radiat. Meas.,23, (1994),393.
46. S.O. Troja, A. Cro, A.M.Gueli, V. LaRosa, P. Mazzoleni, A. Pezzino and M. Romeo, Archaeometry,38, (1996), 113.
47. R.Cevese, A. Canova and F.Rigon, Le Colombare, Comune di Breganze and Biblioteca Civica, Breganze 1982
48. M.Kubelik Die Villa im Veneto, Zur typologischen Entwicklung im Quattrocento, Deutsches Studienzentrum in Venedig, Studien 1, Süddeutscher Verlag, Munich 1977.
49. M. Kubelik, Saggio introduttivo: Le villa sotto la dominazione della serrenissima, in, R. Schiavo, C. Guerrieri and B. Chiozzi, Ville del Vicentino, Traverso, Vicenza 1995, pp. 5-46.
50. Archivio di Stato, Venice, Senate Terra, reg.21 (1519-1520), 129r.& v.
51. R. Cevese, Palladio, Catalogo della mostra, Vicenza 1973
52. C. Goedicke and J.C. Holst,Thermolimineszenzdatierung an Lübecker Backsteibauten, Probleme und Entwicklungen, in, R.Hammel-Kiesow, Wege zur Erforschung städtischer Häuser und Höfe, Karl Wachholtz, Neumünster, (1993), 251.
53. R. Erlach and N. Vana, Nucl.Tracks Rad. Meas., 14, (1988), 295.
54. C. Chiavari, T. Mannoni, M. Martini, E. Migliorini and E. Sibilia, TL Dating in architecture: Historical Monuments in Liguria (NW Italy). LED99 - 9th Int. Conf. on Luminescence and Electron Spin Resonance Dating, Rome, 6-10 September 1999.
55. V. Mejdahl, PACT, 9, (1983), 351.
56. G. Guerin and G. Valladas, Nature, 286,(1980), 697.
57. M. Jasinska and T. Niewiadomski, Nature, (1970), 1159.
58. L. Benko and L. Kozorus, Nucl. Instrum. Meth., 175, (1980), 227.

Radiation in Art and Archeometry
D.C. Creagh and D.A. Bradley (editors)

Synchrotron Radiation Tomographic Energy-Dispersive Diffraction Imaging

S. L. Colston, A. C. Jupe and P. Barnes

Industrial Materials Group, Crystallography Department, Birkbeck College, Malet St., London WC1E 7HX, United Kingdom

A description of the synchrotron energy-dispersive x-ray powder diffraction method and its particular advantages is given first. Example applications are illustrated with data collected from various samples, including archaeological objects.

1. INTRODUCTION

The ability of x-rays to 'see into' solid objects was their first observed property, and of course it is still the most widely known. X-ray photographs give excellent spatial resolution, but they only show changes in absorbance, and give no explicit information about sample composition. Our aim in developing x-ray diffraction tomography is to combine spatial resolution with the crystalline phase information available from diffraction data. For several reasons, conventional laboratory x-ray sources are not suitable for this technique, and we must turn to synchrotron sources instead.

The world's first dedicated synchrotron radiation source was built at Daresbury, UK and became operational in the early 1980's, and today such facilities are to be found in every continent. Synchrotrons have several significant advantages over traditional laboratory x-ray sources. These are in essence, that the beam contains a continuous spectrum of wavelengths, is highly collimated, and is many orders of magnitude more intense than that obtained from a sealed tube source. The impact of synchrotron radiation on the application of the powder diffraction method has been immense in many respects. An excellent example of this is the energy-dispersive diffraction (EDD) method, which has emerged as a powerful tool for time resolved studies of chemical reactions such as zeolite synthesis and cement hydration. More recently, we have been exploiting the rapidity and unconventional geometry of EDD, developing a spatially resolved diffraction technique, which we refer to somewhat loosely as tomographic energy-dispersive diffraction imaging, or TEDDI. TEDDI has several features of particular interest for the characterisation of archaeological objects.

1. It can probe a selected small volume element or series of volume elements within a sample, *i.e:* it can give spatially resolved information. The sample volume element for each diffraction pattern is selected by positioning the sample appropriately in the x-ray beam.
2. The radiation is intense and penetrating, so even relatively bulky samples can be analysed.
3. It is a non-destructive method (provided that beam damage does not occur) and it requires no special sample preparation.
4. As a powder diffraction method, it is essentially equivalent to conventional laboratory diffractometry in that it gives data from which we can make reliable mineral phase identifications.

5. Data sets can be acquired rapidly (within seconds or minutes depending on the sample) so a relatively large number of volume elements can be probed in a reasonable time.

'Small volume element' here means typically a needle-shaped region about 0.5 mm in cross-section and a few millimetres in length. These dimensions vary from one experiment to another, but in general we can easily obtain good enough spatial resolution to distinguish, for instance, weathering products in the outer layers of a piece of masonry, or crystalline kiln firing products in a ceramic artefact. As far as we can tell, most mineral samples are neither chemically nor mechanically affected by exposure to the beam, but certain materials (*e.g.* glasses, and halides such as common salt) may undergo objectionable discoloration. This effect can be minimized or eliminated where it occurs by using short data collection times, or by attenuating the damaging low-energy radiation by placing a sheet of aluminium in the incident beam.

1.1 Theory of EDD

EDD was first demonstrated by Geissen and Gordon [1]. It is perhaps most readily understood by comparison with the angle-dispersive Debye-Scherrer camera method, in which a powder sample in a glass capillary is encircled by a radiation sensitive film. The sample is irradiated with a monochromatic (single-wavelength) beam, and scattered x-rays are registered by the film at all angles ,2θ, in the plane normal to the capillary axis. The EDD set-up may be seen as the inverse of this, in that the sample is irradiated with a 'white' beam (containing a continuous range of wavelengths), the scattered radiation being measured at only a single angle. The EDD experimental setup is distinctive in two respects.

1. The speed of data collection is not limited by moving parts within the apparatus.
2. The diffraction pattern is not acquired systematically as in a conventional diffractometer, but is allowed to accumulate for some chosen period of time.

A schematic representation of an EDD diffractometer is given in Figure 1. The diagram is by no means drawn to scale! The important points are:

1. the beam passes completely through the sample, which is placed between source and detector;
2. only x-ray photons scattered through a chosen angle are allowed to enter the detector. This angle (2θ) is selected by the collimator. Typically the spacing between the molybdenum collimator plates is 0.1 mm or less, and the distance from sample to collimator is 200–500 mm, so that 2θ is quite sharply defined. This is important if we are to obtain reasonably well-resolved diffraction peaks, since the greater the collimator plate separation, the broader the peaks will become, especially at the low 2θ settings (about 2–8°) which are commonly used.
3. Only a defined portion of the sample contributes to the diffraction pattern. This is the volume contained by the intersection of the incident beam with the 'line of sight' of the collimator. If the sample is translated (since we cannot move the synchrotron) a different part of it will be 'seen' in the diffraction data. This is the principle of spatially resolved TEDDI.

Clearly, EDD data collection requires a detector that not only measures the diffracted beam intensity, but also its wavelength spectrum. A detector that not only counts photons but also measures their energies will serve, since we can convert between photon energy

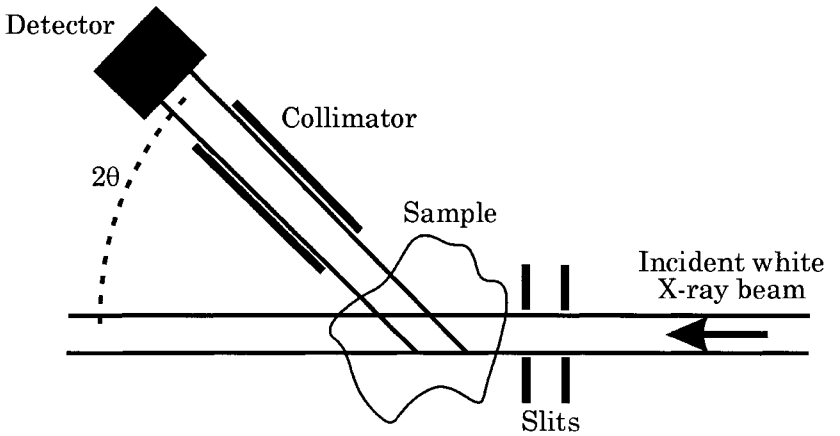

Figure 1. Schematic diagram of an energy-dispersive diffractometer. The intersection of the incident and diffracted beams defines the diffracting volume or 'needle'.

distribution and wavelength spectrum using the Planck-Einstein photon energy relation $E=hc/\lambda$ where h and c are Planck's constant and the speed of light respectively. The authors of [1] used a lithium-doped Si crystal detector of the type used for fluorescence microprobe analysis in scanning electron microscopy, but the intrinsic Ge crystal detector is now universally preferred for its greater efficiency in detecting the higher energy photons which are of interest for EDD. As an example, the range of detection for the EDD instrument at the Daresbury SRS is chosen to be about 6–113 keV. Owing to the ≈6 keV lower limit, fluorescence lines from elements below Fe in the periodic table are excluded from the data. Note, however, that this is of little practical importance, since generally we are only interested in Bragg reflections and the information they give us about which crystalline phases are present in the sample.

How do we use diffraction data to identify crystalline phases? A complete and coherent exposition of the theory of x-ray diffraction by crystals would require a whole chapter in itself. Such chapters are to be found in all of the many textbooks on x-ray crystallography, but it is appropriate to give at least a very brief outline of the principles involved, in order to highlight the equivalence between EDD and convention angle-scanning diffraction (ASD).

A crystal consists, by definition, of an orderly array of building blocks known as unit cells, each unit cell containing an identical arrangement of atoms. Thus a well-crystallised material such as quartz can be described as a periodic array of atoms: this is why crystals are able to diffract x-rays. The crucial point is that in practice, the size and shape of the unit cells, and thus the periodicity of the crystal, are unique to any one crystalline compound. X-ray diffraction enables us to quantify the periodicity (the separation or d spacing of crystal planes) from which we are able to identify each phase present in the sample. In other words, every crystalline material has its own 'signature' in a diffraction pattern.

The periodicity actually extends to more than three directions. For any crystal, there are numerous, though prescribed, directions along which the arrangement of atoms repeats itself regularly. The periodicity in each of these directions can be characterised by a d spacing corresponding to that direction, and each peak in a diffraction pattern corresponds to a d spacing characteristic of some component of the sample, the positions of the peaks being determined by the d spacings. The x-ray diffraction patterns of tens of thousands of inorganic phases have been measured, and collected into a database by the International Centre for

Diffraction Data (ICDD). Each entry lists peaks according to their corresponding *d*-spacings and relative intensities. Regardless of which experimental set-up we choose for data collection, if we can assign a *d* spacing to each peak in the diffraction pattern obtained, we should be able to use the database to help interpret what we see.

With conventional angle-dispersive diffraction, the traditional Bragg equation

$$\lambda = 2d\sin\theta \qquad (1)$$

is used to convert a scattering angle 2θ to a *d* spacing, since the fixed radiation wavelength λ is known in advance. This can be recast into a more convenient form for EDD with the help of the photon energy relation $E=hc/\lambda$. Combining this with equation (1) (and using appropriate units for the physical constants *h* and *c*) we get

$$Ed\sin\theta = 6.19926 \text{ keV}\cdot\text{Å} \qquad (2)$$

This gives us a simple relationship between *d* and the photon energy *E* at which Bragg reflection takes place, since owing to the fixed detector angle, sin• is now constant.

Figure 2 shows two datasets collected in 5 minutes from a sample of gypsum, (thickness 8 mm), with a 0.5×0.5 mm incident beam. For the data shown in Figure 2(a), the detector angle was set to 5.1°. Substituting this value into equation (2) and rearranging a little gives

$$d = 6.19926/(E\sin\theta) = 6.19926/(E\times\sin(5.1/2)) = 6.19926/(E\times\sin(2.55)) = 139.34/E \qquad (3)$$

For this reason, the plots in Figure 2 have dual *x* axes, with an energy scale below and a $10/d$ scale above.

Table 1 shows the strongest peak positions and their corresponding *d* spacings. The peak intensities can be seen to be very high, and indeed the collection time could have shortened (to 1 or two minutes, say) without significant loss of data quality. Although the peaks are positioned as expected, the relative intensities differ from those in the ICDD database. The main reason for this is that the synchrotron white beam is not equally intense for all photon energies. This is why, for instance, the peak at 18.33 keV is much weaker than expected compared to the peak at 45.5 keV, where the beam is much more intense. At the Daresbury SRS we expect a similar weakening of intensities above about 70 keV. Provided that we bear these factors in mind, however, the discrepancies are not so great as to seriously impede phase identification. This is particularly true when (as usually) we have some prior knowledge of the sample composition. The effect of changing the detector angle can be seen clearly from a comparison of Figures 2(a) and 2(b).

Table 1
Details of EDD peaks from gypsum ; $2\theta=5.1°$

Energy (keV)	Calculated *d* spacing	Reflection *hkl*	2θ for Cu K_α (ASD)
18.33	7.60	020	11.59°
32.53	4.28	021	20.72°
45.46	3.06	041	29.11°
48.50	2.87	-221	31.10°

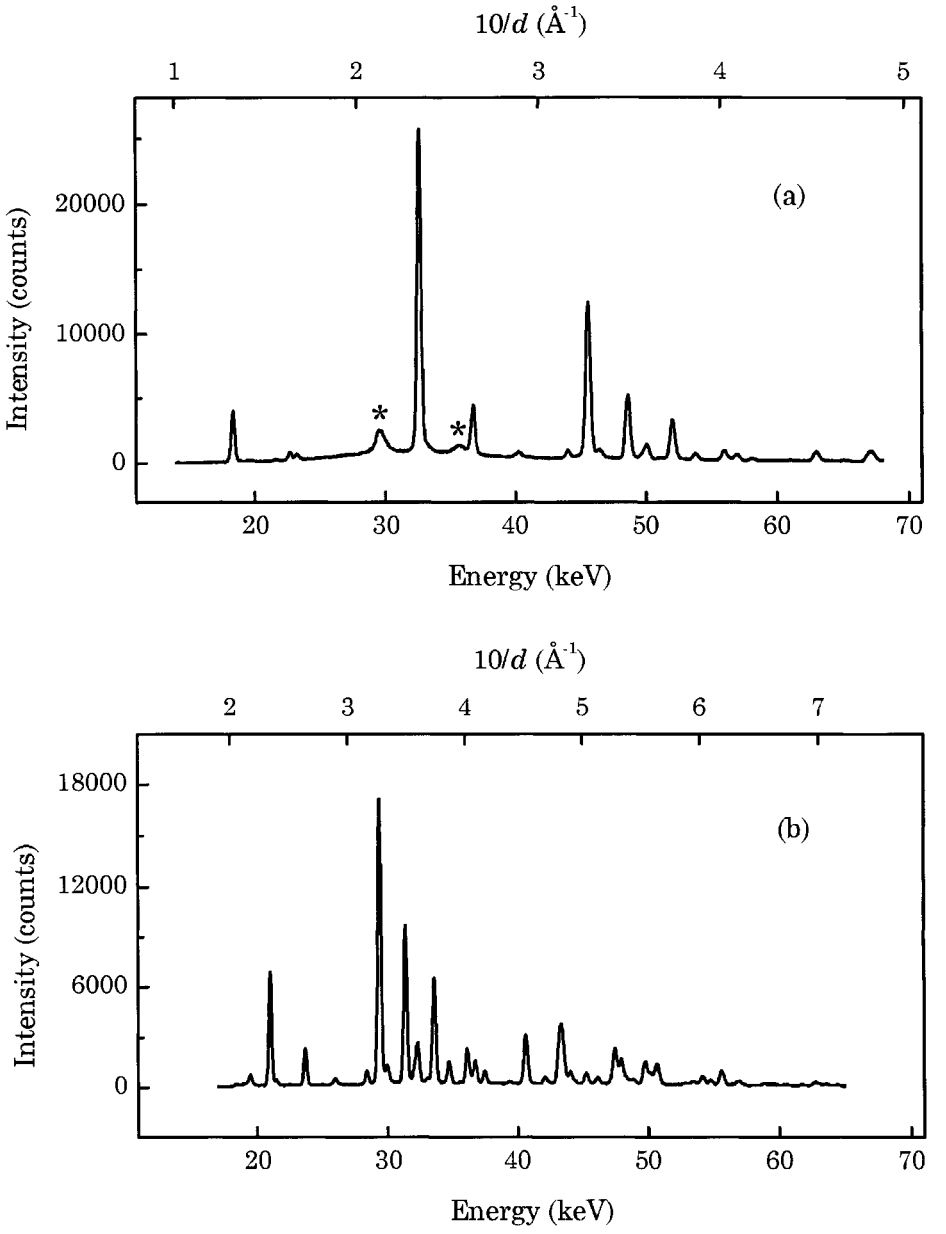

Figure 2. EDD data from a sample of gypsum. 2θ settings were 5.1° in (a) and 7.9° in (b). The peaks marked (*) in (a) are due to the PEEK sample holder. The *x* scales show photon energy below and 10/*d* above. Note the more condensed 1/*d* scale in (b), and the correspondingly greater density of peaks with respect to the energy scale.

Figure 2(b) shows data again from a gypsum sample, but with 2θ set to 7.9°. It is immediately apparent that the density of peaks is greater at the higher angle. EDD is a relatively low-resolution diffraction technique, so ideally we would like to maximise the separation between adjacent peaks, and so avoid peak overlap. Overlaps between peaks may make weaker peaks more difficult to identify, and generally hampers the precise determination of individual peak intensities. Choosing a lower detector angle in EDD is equivalent to choosing a longer wavelength in conventional diffraction. In both cases peaks are shifted further apart and upwards in energy (EDD) or 2θ (angle-dispersive). This is not the only, or even the primary consideration, to be made when the detector angle is chosen, however, because our main aim is to capture as many strong peaks as possible from such phases as may be present in our sample. A fuller account of the theory of EDD can be found in [2], which also contains a copious list of further references.

Figure 3 [3] shows the relative intensity of the incident beam as a function of photon energy. There is a clear maximum at about 38 kV, although the reduced flux at the high-energy end of the spectrum is offset by the enhanced sample penetration of the higher energy radiation. As the useful energy range is essentially fixed, the range of *d* spacing coverage is determined by the detector angle; for larger *d* spacing, we need a lower angle. Table 2 shows the observable range for several 2θ settings, assuming a useful energy range of 30–100 keV.

What is the best range to select? Fortunately, there *is* a reasonably general answer to this question; the ICDD database shows that nearly 80% of known inorganic crystals give strongest Bragg reflections in the 5–2 Å range. Thus a detector angle of about 4.7° would seem to be a reasonable choice in general. We should, however, qualify this by pointing out that with this setting some clay and zeolite minerals with strong reflections at longer *d* spacings (to 10 Å or greater) may be difficult to detect. At the Daresbury SRS this limitation is surmounted by the use of an array of three detectors, collecting data simultaneously at three angles; this is not universal practice. (Note that the choice of a lower detector angle is

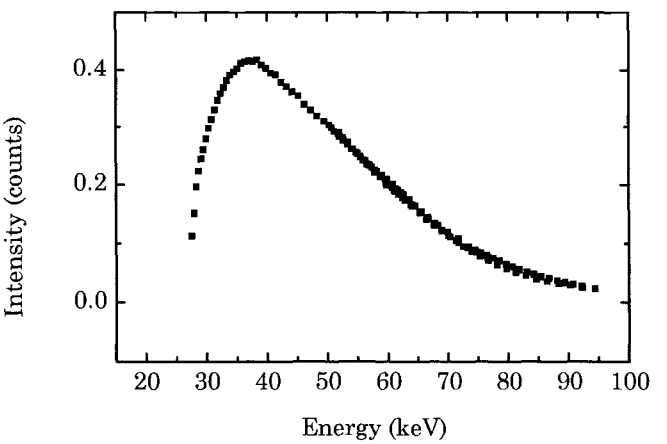

Figure 3. Relative beam flux from beamline 16 at SRS Daresbury, as a function of energy. The points are based on experimentally determined values.

Table 2
d-spacing ranges

2θ detector angle	lower d-spacing (Å) (at 30keV)	upper d-spacing (Å) (at 70keV)
2.0	4.4	17.7
5.0	1.8	7.1
8.0	1.11	4.4

equivalent to the choice of a longer x-ray in ASD. However, EDD is not a substitute for small angle-dispersive diffraction techniques as *d*-spacings longer than about 20 Å are difficult to measure, and the *d*-spacing resolution is probably not adequate for this purpose.

The detector angle crucially determines the shape of the diffracting volume within the sample. This is a very important where spatial resolution is a primary objective.

1.2 The Diffracting Needle

To get the best spatial resolution, clearly we would like the diffracting volume to be as small as possible. The synchrotron beam is very intense and has a very small angle of divergence, so we can make the incident beam cross-sectional area quite small (*i.e.*, 0.1×0.1 mm) to minimise the volume in directions transverse to the beam. Unfortunately, we have less control over the length of the diffracting volume along the beam direction. This length depends on the detector angle and the width of the diffracted beam collimator, as well as on the size of the incident beam, but with these set to useable values, the length of the diffracting volume is typically several millimetres. If we assume that both incident and diffracted beams are parallel (which is a reasonable assumption as long as the diffracted beam collimator is narrow enough) the length of the diffracting volume L is given by

$$L = W_I/\sin\theta + W_D/\tan\theta \qquad (4)$$

where W_I is the collimator plate separation, and W_D is the vertical size of the incident beam. In the range of 2θ commonly used, $\sin\theta \approx \tan\theta \approx \theta$ (θ in radians), and to a good approximation, $L \propto 1/\theta$; as we would expect, the diffracting volume elongates along the beam axis as 2θ is

Table 3
Diffraction needle lengths

Detector 2θ	Beam size (mm)	Diffraction needle length (mm)
2	0.1	4.30
2	0.2	7.16
2	0.5	15.75
5	0.1	2.29
5	0.2	3.43
5	0.5	6.86
8	0.1	1.43
8	0.2	2.14
8	0.5	4.28

lowered. Typically, L is 5–15 mm, and the diffracting volume resembles a compass needle when viewed from the side, rather than the lozenge shape seen in Figure 1, and we refer to it as the diffraction 'needle'. Clearly, spatial resolution is much more limited in the direction parallel to the incident beam than in directions perpendicular to it. Table 2 lists calculated needle lengths for some typical 2• settings, beam sizes and collimator plate separations.

We have yet one other constraint to consider. We need to sweep out a certain (usually relatively large) volume of our sample within a limited time period, while obtaining diffraction data of adequate quality. From this point of view, reducing the diffracting volume is disadvantageous in two ways. Firstly, we need to collect more data sets, and secondly, we will need to spend more time collecting each set, because the smaller diffracting volume will result in lower diffracted intensities. In all, we can deduce that as a rule-of-thumb, the overall data collection time requirement is proportional to V/v^2 where V is the overall sample volume to be traversed, and v is the diffracting volume, for a given peak-to-noise ratio in the data. Because of this, we can sensibly argue that if spatial resolution is required in only one or two directions, the extension of the diffraction needle along the beam axis is actually an advantage. It enables more rapid data collection (provided that the needle is fully contained within the bulk of the sample object). Applications such as probing for surface weathering products can benefit from this diffraction needle geometry. For true three-dimensional imaging, we could in principle collect a second matrix of data sets after turning the sample through 90° about a vertical axis and collating all of the data appropriately. The applicability of computed tomography techniques to TEDDI data has yet to be investigated.

The time requirement for each data set collection is determined largely by the thickness and absorbance of the sample object (assuming that all or most of the sample components are crystalline). It varies quite widely. In favourable cases 30 seconds per data set may be sufficient, whereas for, say, a concrete block 5 cm in thickness 3–5 minutes may be required. It is especially important that we allow adequate time for each data acquisition if we are looking to locate minority components in the sample, since otherwise the main features of interest in the data may be too indistinct to be of real use. The subject of count statistics and data quality needs to be addressed here, particularly as it tends to be neglected in the synchrotron EDD literature dealing with less severe applications, where satisfactory count statistics can safely be taken for granted.

1.3 Data Quality

By 'data quality' we primarily mean the peak-to-noise ratio as observed in the diffraction pattern (as opposed to the detector signal-to-noise ratio, which affects peak widths). Noise is an intrinsic feature of all diffraction patterns. Strictly speaking we can never eradicate it, but by acquiring data for long enough we can aim to average out the noise over the data acquisition period. The problem here is that this effect may be difficult to attain with the weakest peaks in the pattern, which can be a serious limitation on the detection of minority phases in the sample. Despite the great intensity and penetration of the synchrotron beam, we need to remember that TEDDI is a particularly demanding application, and maintain a certain realism about statistical limitations.

Figure 4 is intended to illustrate the problems that may arise when the presence of noise is combined with peak overlap. In plots (a) to (c), the solid lines show the results of adding simulated 'Poisson noise' to the sum of two calculated, overlapping Gaussian peaks; in Figure 4(d) no noise has been added, in order to show the ideal combined profile. The noise has been generated to simulate the condition that each observed datum y_n(obs.) composed from

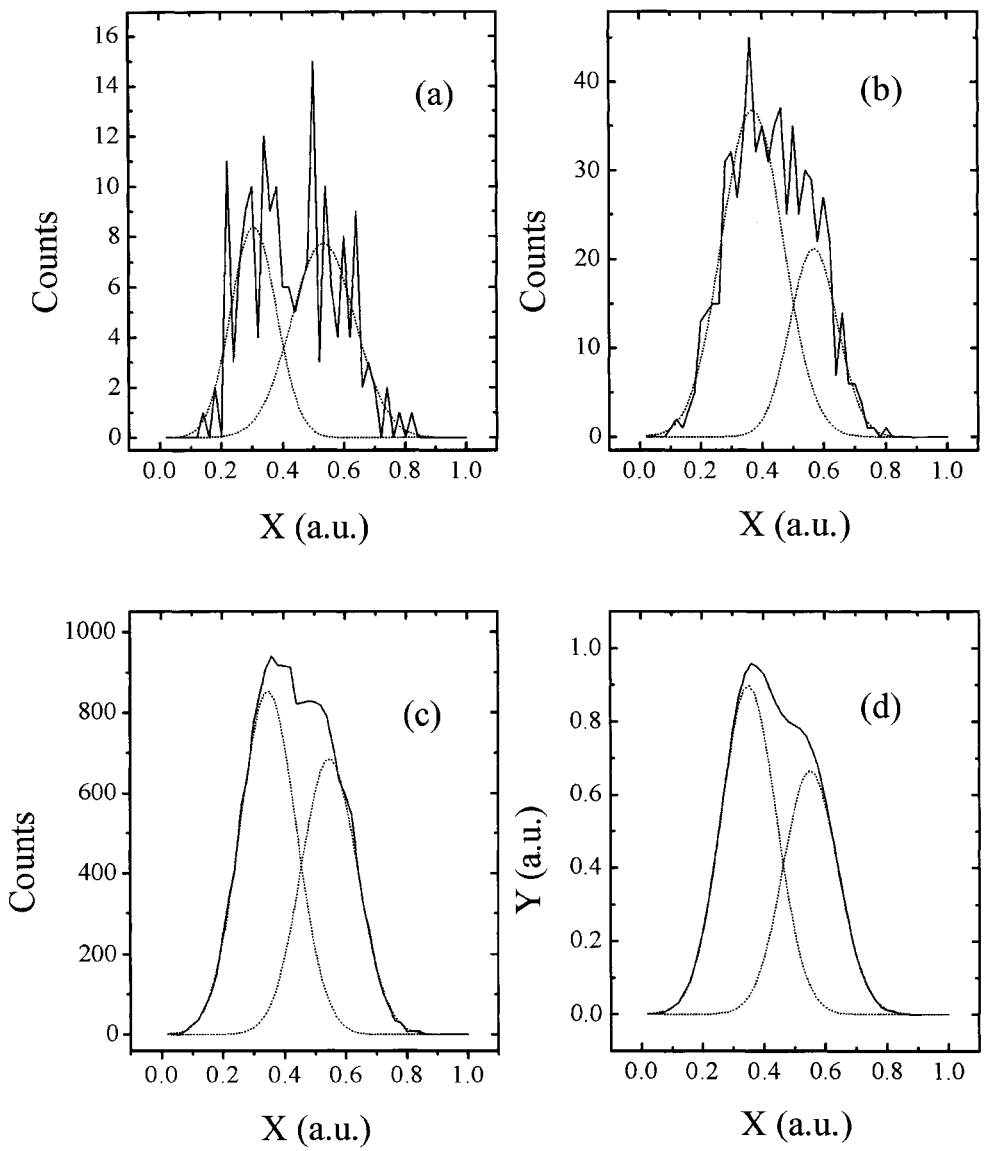

Figure 4. Simulated Poisson noise added (plots (a), (b) and (c)) to calculated gaussian peaks shown in (d). The signal-to-noise ratio depends on the intensities of the peaks, as indicated by the different vertical scales. Dotted lines show the 2-gaussian least-squares fit results for each case.

y_n(ideal)+y_n(noise) is an estimate of y(ideal) with an estimated standard deviation (esd) of $\sqrt{y}$(ideal). Plots (a), (b) and (c) in Figure 4 show the typical effects of Poisson noise on progressively more intense peaks. Taking the relative esd $\sqrt{y}/y=1/\sqrt{y}$ as a reasonable measure of peak-to-noise ratio, we would expect the noise to be less and less significant as peak

intensities increase, and the plots show clearly that this is indeed so. Unfortunately, we must also expect to spend n^2 times as long acquiring data to obtain a general n-fold improvement in peak-to-noise ratio. We would have to increase data collection time by a factor of 100 to see a profile as well defined as in Figure 4(c) in place of that in Figure 4(a). On the other hand, by quadrupling the nominal intensity time we have already the noticeable improvement seen in Figure 4(b). There is a law of diminishing returns regarding data quality with respect to collection time, as with many other experimental methods.

The noise problem becomes still more evident when we apply least squares fitting to the noisy data, to obtain a measure of the apparent peak intensities and positions. Our aim is to recover the two noiseless Gaussian distributions from the data. The actual results of this procedure are plotted as dotted curves in Figure 4. Ideally, the fitted peaks should be centred on 0.35 and 0.55 respectively on the arbitrary x axis, with equal widths of 0.2 and an intensity ratio of 4:3, as shown in Figure 4(d). Not surprisingly, the procedure is not particularly successful in case (a), where the noise has misled the least-squares algorithm into assigning too much width to the second peak. The intensity ratio obtained here is about 3:4, far from the original value, and furthermore, position errors are about 25% of the full-widths-at half maxima (FWHM), which is too inaccurate for reliable phase identification to be made. In case (b) the situation is significantly better, in that the first peak is now measured as more intense than the second, and positions are determined to within 5% of the FWHM. Here again, though, peak width estimation is rather poor, giving an exaggerated intensity ratio of 9:4. In case (c), excellent agreement with expected values is obtained from the fitting process. In designing a TEDDI experiment, we aim to have at least the stronger peaks as well defined as in Figure 4(c), if not better. Weaker peaks as in 4(b) may give useful phase identification provided we have some prior knowledge of possible components in the sample. Very weak peaks such as shown in 4(a) can be given only speculative interpretations at best, unless they can be linked to other stronger peaks in the same pattern. As so many parameters are involved in any given experimental case, it is difficult to derive a lower limit of detection in terms of phase concentration within the diffraction needle, from a limit in terms of diffraction peak height. Experience suggests, however, that about 1% by weight is a reasonable estimate of attainable sensitivity. The relationship between statistical data quality and accuracy of d-spacing measurement is at least as important as that between d-spacing measurement and peak width, a fact not always made clear in the literature. In practice, we can sometimes obtain more reliable position and width information on the weaker peaks by summing a number of spectra in which they occur, and using this information when treating the individual data sets. Even then, the resulting intensity data may be of little use if the phase is widely diffused through the sample. For very demanding applications some trial and error may be necessary to find the best experimental parameters, but of course this is likely to entail a considerable expense of synchrotron beamtime.

The typical EDD peak FWHM is about 0.3 keV, though this can be greater if the crystallites are very small [4]. Thus the Bragg equation (2) can be used to predict the degree of overlap which may be expected between the peaks from a given mixture of phases. (For instance, there are some unfortunate overlaps between the peaks from two of the commonest minerals, quartz and calcite, though this is usually not disastrous if we choose the well-resolved peaks for analysis.)

Ideally the relative intensities of the peaks due to any given sample phase should reasonably resemble those tabulated in the ICDD database. To understand why we cannot place too much reliance on this, we need to consider in more detail the effect of sample characteristics on the data we obtain.

2. MATERIALS CONSIDERATIONS

The TEDDI experimental set-up is quite different to that of ASD. Whereas the latter looks at relatively small volumes of samples sitting on a variety of sample stages the TEDDI experiment non-destructively collects diffraction information from real, intact objects. Of course there has to be a limit on the size of object we can investigate and the size of the image we can collect. These limiting factors are tied in with the sample composition, phase distribution, crystalline character, synchrotron radiation characteristics and the time restraints on synchrotron experiments. The sample and materials concerns that we address in the following section should help in deciding if TEDDI is the best technique to apply to a given problem or in designing a TEDDI experiment. The discussion is based on both theoretical and empirical studies.

2.1 Texture and Sampling

To obtain a usable powder diffraction pattern, one that allows phase identification and quantification, there must be a large number of randomly oriented crystallites in the diffraction volume. This gives an unbiased 'powder average' in which all orientations are equally represented. As with ASD, the occurrence of texture in the samples and its effect on the diffraction data is a concern in the interpretation of TEDDI data. In TEDDI, however, we are looking at intact objects, and there is no opportunity to reduce the grain sizes by grinding, or to improve poor sample packing. Also, spinning the sample to improve particle statistics is only rarely an option in the sort of experiments we are concerned with here. To exacerbate the problem, a wide range of grain sizes and large inclusions often occur in the metal or rock objects that are being investigated. As the grain size of the powder increases so the numbers of crystallites decreases until there are too few of them for the powder averaging condition to be properly realised. Diffraction patterns from samples like this suffer from poor particle statistics and often no longer provide the material's characteristic 'signature'. (A crystallite is the same as a grain only if the grain in question is a small single crystal; since this is not always the case, the term 'grain' is used for the sake of generality).

The TEDDI probe is a long thin needle-like volume with linear dimensions in the range 0.1–0.5 mm in the plane normal to the incident beam, and several mm in length along the direction of the beam. This makes calculating the number of crystallites available for diffraction somewhat difficult. Given its needle-like shape, the diffracting volume in a 'real' sample with a distribution of grain sizes could contain many more crystallites than a simple volumetric calculation would predict. This is because a significant proportion of the larger crystallites might be only partially contained in the needle.

Table 4
Diffracting needle volumes and crystallite numbers for a range of different grain sizes

Square beam size (mm^2)	Needle volume* (mm^3)	Number crystallites
0.01	0.028	224
0.04	0.115	920
0.25	0.716	5728

*assuming a solid specimen with no voids
†detector 2θ angle = 2°, linear dimension of grains=50 μm

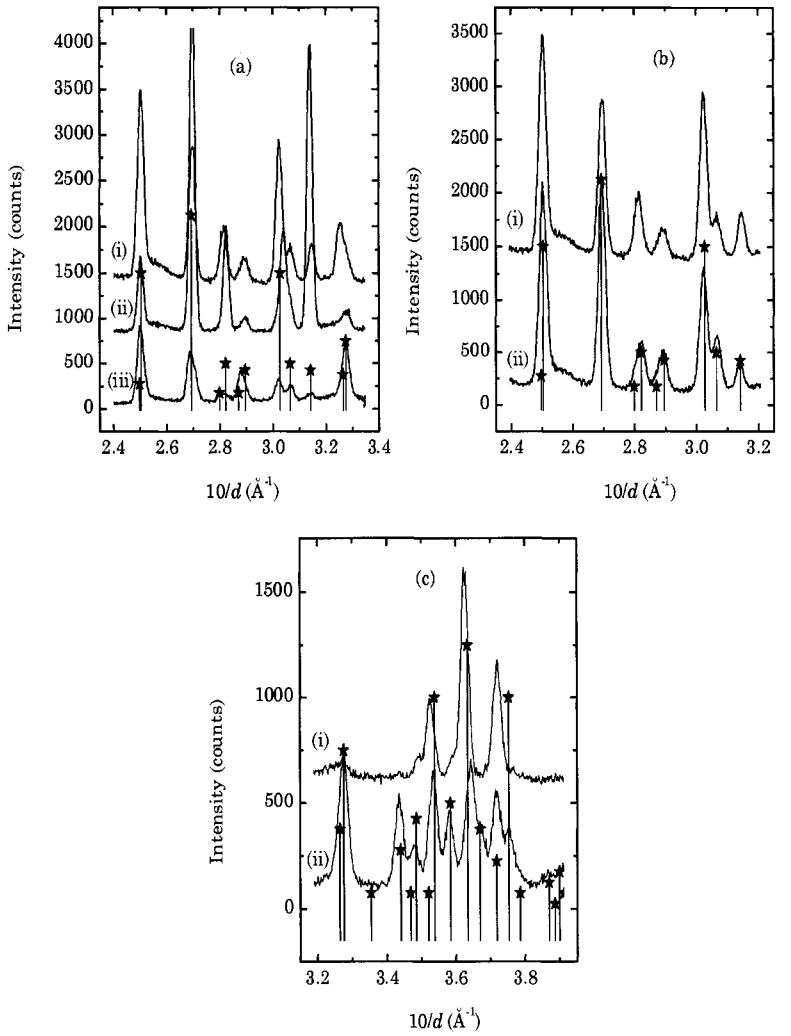

Figure 5. These diffraction spectra were collected from $CuSO_4.H_2O$ ground and sieved to a range of grain size distributions. (a) (i) has grains size x. $x < 38$ μm; (ii) 75 μm< x <100 μm; (iii) 180 μm< x< 600 μm. (b) Grain size less than 38 μm (i) stationary; (ii) spinning (60rpm). (c) Grain size 180 μm< x< 600 μm (i) stationary, (ii) spinning (60rpm). The stick plots are the ICDD peak positions for $CuSO_4.H_2O$ the lines have been scaled to reflect the intensity ratios in the diffraction file. The plots have been offset for clarity and only a section of the complete spectra are shown.

Table 4 gives theoretical values for the volume of the diffracting needle and the minimal estimate of the number of crystallites intersecting this volume.

Figure 5 illustrates the effect of texture with real data collected on Station 16.4 at SRS Daresbury. In this experiment diffraction spectra were collected from $CuSO_4.5H_2O$ powders that were ground and sieved to a range of crystallite sizes. EDD spectra were then collected over 180 seconds for each grain size. In Figure 5(a) we see how the intensity of the spectrum increases as the grain size decreases, since then the number of diffracting crystallites increases. For the smallest grain size used (<38 μm) all the expected reflections are present, and their relative intensities match closely those tabulated in the ICDD database. From such data, phase identification would be straightforward. With larger grains (between 180 and 600 μm) the relative intensities are skewed. From data such as shown in Figure 5(a)(iii) phase identification would be fairly easy given some prior knowledge of the sample, but less assured otherwise.

The datasets in Figure 5(a) were obtained with a spinning sample. In the majority of the kinetic experiments using EDD the sample cells are spun to improve the particle statistics. In TEDDI experiments such spinning around any axis perpendicular to the beam direction would have a very deleterious effect on the spatial resolution, but these are the only axes along which it is relatively easy to introduce spinning. The ideal axis for spinning, which would not introduce any loss of spatial resolution, is along the direction of the beam, but this would be mechanically very difficult to achieve such a motion with the necessary precision. Figure 5(b) shows that for small grain sizes (less than 38μm) there is no significant advantage to be gained by spinning the sample. However, Figure 5(c) shows that where the sample is stationary, larger grain sizes (between 180μm and 600μm) lead to poor particle statistics, resulting in loss in intensity, absent reflections and anomalous relative intensities. The effect of oscillating the sample about a vertical axis passing through the centre of the diffracting needle has been investigated. This motion improves the particle statistics by 'sweeping' more crystallites into the diffracting volume, but it also changes the volume sampled to a bow-tie shape. Although this is preferable to full rotation, it still significantly degrades spatial resolution. For example, a 2° oscillation would smear a 100 μm wide beam to 250 μm.

Investigating materials with large inclusions and/or large grain sizes will be problematic for *ab-initio* phase identification. One aid in this process is to use the spatial correlations that become apparent in scanned datasets. From correlated changes to groups of reflections it is possible to associate them and perform database searches. Search and match software routines specifically for EDD data have not been devised, as far as the authors are aware.

2.2 Composition and X-ray Absorption

In transmission geometry the absorption of both incident and diffracted beams determines the size limits of objects that can be investigated and the length of time for data collection. The more absorbing the material (*i.e.*, the higher the density and average atomic weight) the longer the count times required to collect enough diffracted photons to produce a good quality pattern. We can obtain data from very thick samples because the synchrotron provides a high flux of hard x-rays. The flux distribution with respect to photon energy at any white beam station is determined by the current and electron energy in the synchrotron storage ring, and the insertion devices used to boost/generate more flux.

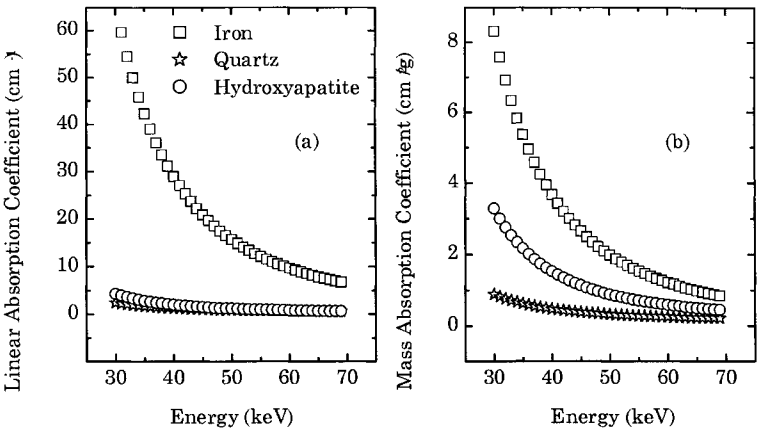

Figure 6. Linear absorption (a) and mass absorption (b) coefficients respectively over the 30-70keV x-ray photon energy range for materials: iron, quartz and hydroxyapatite.

We can estimate the thickness of material that a synchrotron x-ray beam can penetrate using standard tables and known densities to calculate the linear absorption coefficients [5]. For materials of interest such as iron, quartz and hydroxyapatite we can calculate the mass absorption coefficient as a function of photon energy using an empirical equation with parameters tabulated in the International Tables for X-ray Crystallography. The linear absorption coefficient μ is the product of the mass absorption coefficient and the sample density. The effect of beam absorption can be quantified as

$$I=I_0\exp(-\mu t) \tag{5}$$

where I is the resultant beam intensity, I_0 the incident beam intensity and t the thickness of material. For a given x-ray wavelength (*i.e.* energy) the total linear absorption coefficient (μ cm^{-1}) is characteristic of the absorbing material. In Figure 6 the linear and mass absorption coefficients for iron, quartz, and hydroxyapatite have been plotted for the x-ray energy range 30-70 keV. This energy range is typically the region with the highest flux for a synchrotron white beam station (see Figure 3). The softer x-rays (lower energy) are much more strongly absorbed than the harder x-rays and the metal is more highly absorbing than the minerals. Hydroxyapatite has a higher mass absorption coefficient than quartz. It is informative to plot the photon transmittance of these materials (I/I_0), as in Figure 7. At the hard x-ray end of the spectrum the beam will have 50% penetration through 12 mm of mineral material but only 3 mm of metal. At the soft x-ray end of the spectrum the x-ray beam is almost completely absorbed by 1 mm of iron, and by 10 and 16 mm of hydroxyapatite and quartz respectively.

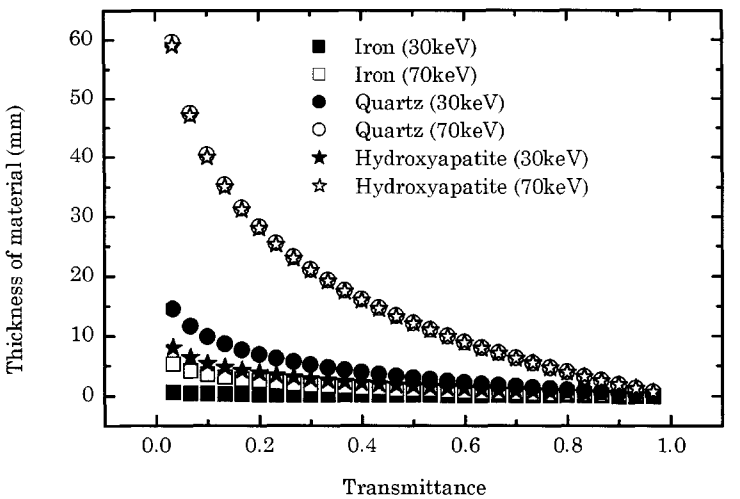

Figure 7. Calculated transmittance for photons with energy range 30-70 keV through iron (density 7.87 g/cm^3), quartz (density 2.65 g/cm^3) and hydroxyapatite (density 1.3 g/cm^3).

The general effect of absorption on a pattern is to impose an overall intensity envelope onto the diffraction spectra, in addition to that already imposed by the incident beam energy spectrum. In the case of a highly absorbing and/or thick object this would mean lower intensities in the 'softer' low energy x-ray region. A study of a bronze agricultural tool (C11th) illustrates the severity of absorption for metallic objects. The work was done on Station 9.7 at SRS Daresbury. Figure 8(a) shows a photograph of the bronze tool which is approximately 200mm in length and, whilst hollow, is 30mm in thickness. The enlargement of the tip of the tool in Figure 8(b) shows the x-ray sensitive paper over the region investigated. The scan was obtained by scanning the tool perpendicular to the beam in 21 incremental steps of 1mm and in a mutually perpendicular direction in 10 steps at 0.5 mm intervals. The individual dot marks along the 0.5mm scan cannot be resolved but most of the 21 lines indicating where the beam entered the sample are clearly visible. Each dataset was collected over 60 seconds. The diffraction pattern in Figure 8(c) shows the peaks that have been identified in a single dataset that is the summation of all the datasets along a single line as in Figure 8(b). Figure 8(d) is a 2D contour map illustrating the change to the spectra as the tool is moved transverse to the beam direction. At point 0 mm in the traverse the beam is not intersecting the tool. There is slight background intensity in the lower energy region, which is due to air scatter and secondary scatter from the edge of the tool. As the tool moves to intersect the beam the strongest peaks in the pattern at this point are the Sn $K\alpha_1$ and $K\beta_1$ fluorescence lines at 25.272 and 28.491 keV respectively and Cu $K\alpha_1$and $K\beta_1$ lines at 8.048 and 8.905 keV. (The detected x-ray fluorescence originates from, not only the diffracting volume but also from along the diffracted beam path.) Where the beam intersects the tip of the tool the first diffraction peaks appear. These are three reflections from malachite at 5.93Å (I_{84}), 5.01Å (I_{96}), and 3.67Å (I_{100}), (subscripts refer to the intenities tabulated in the ICDD database, normalised to 100) and these, along with the fluorescence peaks grow in intensity as the traverse continues into the tool.

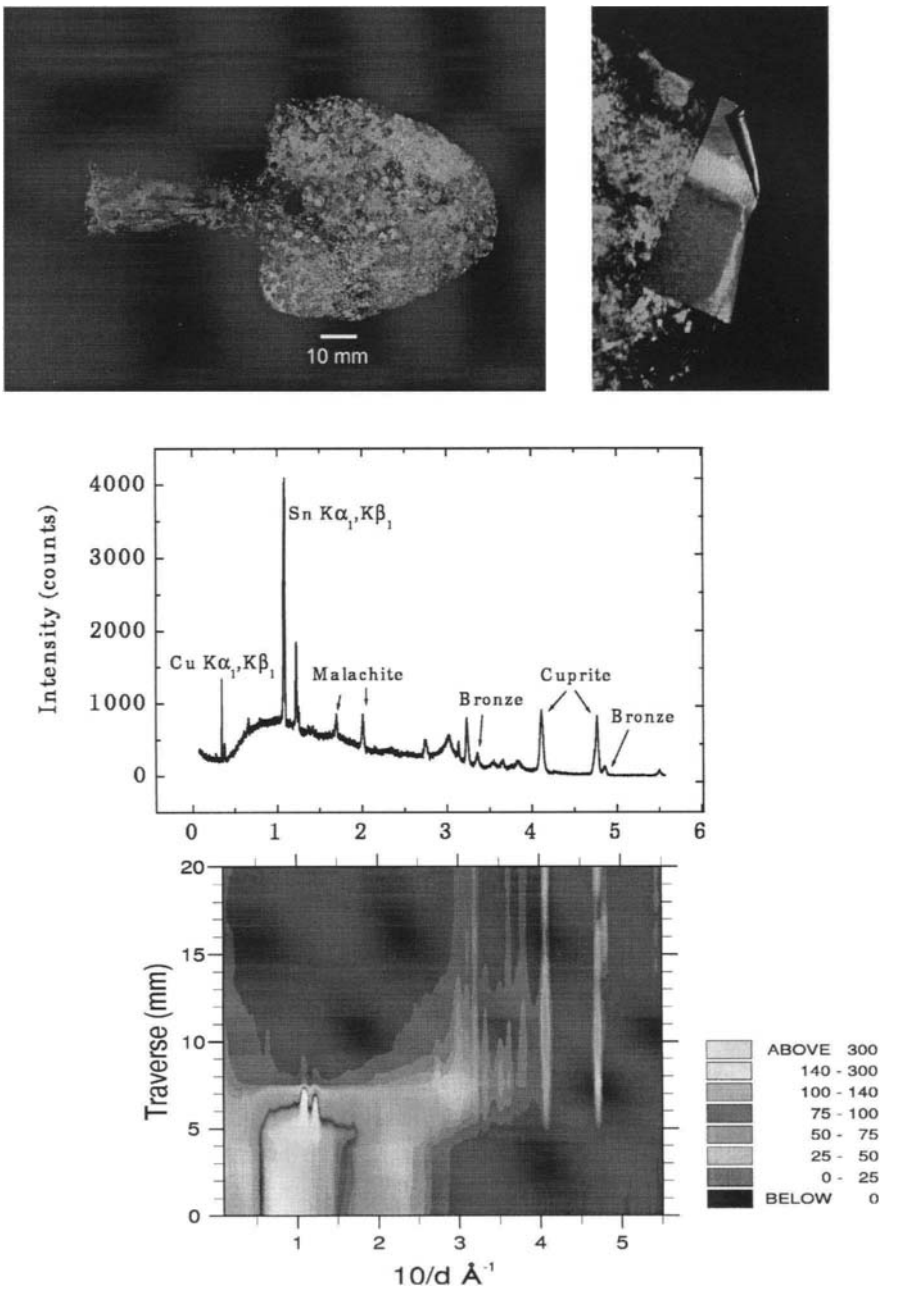

Figure 8. The photograph of the bronze tool in (a) has been enlarged in (b), where it shows the x-ray sensitive paper which marks the beam entry points on the tip of the tool. The plot in (c) shows the sum of 20 datasets taken along a 1D traverse of 20 mm. The 2D contour map (d) shows this data spatially resolved.

The edge of the tool has a wedge shape and as the thickness of material increases so there is a gradual loss in the signal in the soft x-ray region as these x-rays are absorbed. Once the thickest region of the tool (30mm) is in the diffracting volume (the diffracting needle is nominally 23mm in length and hence completely contained within the tool) so only x-rays in the high-energy x-ray region can penetrate the bronze tool. The high-energy region of the diffraction pattern has reflections from cuprite and bronze phases. By examining both the individual spectra and the correlations between spectra at different points on the traverse, it is fairly straightforward to identify and differentiate between surface phases, bulk phases. With more complex multi-phase materials, such as ceramics, phase identification and mapping requires prior knowledge of the material and accurate *d*-spacing values, as well as spatial information.

As absorption has a marked effect in determining the pattern profile so this physical effect can mask the contributions to the patterns from the materials chemistry. It is important to bear this in mind during the analysis. Also peak identification in diffraction patterns of alloys and minerals is also complicated by the possibility that peak positions have shifted due to variations in crystallographic unit cell dimensions caused by solid solution effects. In some instances the phase identification may need to be supported with higher resolution ASD or microscopy.

An experiment looking at the growth of minor mineral phases around rock aggregates in a concrete block illustrates the penetrating power of the beam on Station 16.4, SRS Daresbury. The block was rectangular (77x78x42 mm) with limestone and dolomitic aggregates in a cement/quartz matrix. The density of concrete is similar to that of quartz although it is a stronger x-ray absorber because of the quantities of higher atomic weight elements in the composition, especially calcium, and iron.

The aggregate pieces ranged in size from sub-millimetre dimensions to over 15mm. The concrete block was positioned to overlap with the entire diffraction needle (13mm in length) and to contain, as far as could be guessed, a mix of aggregate and matrix phases. The rectangular block was placed in 3 orientations and a diffraction spectrum collected in each one. Details are given in Table 5. The quality of the patterns can be seen in Figure 9(a), obtained through the thinnest section of the block (37.5mm) has the greatest number of peaks with contributions from the aggregate and the matrix. A minor cement hydrate phase, ettringite (less than 1% by weight) is also detected.

Through the thickest dimension (77.5mm), Figure 9(c), we see that the number of strong peaks has greatly decreased. As the strongest two peaks are from the same phase and this is an aggregate phase, we may deduce that the needle was positioned almost entirely within a single piece of aggregate. This could be confirmed with a 2D/3D traversed data collection, which would produce a map of the area around this point. An example of this type of map is given later.

Table 5
Diffraction spectra obtained through a concrete block, Figure 14

Plots	Thickness of concrete (mm)	Data collection time (seconds)	Height of calcite I_{100} reflection (counts)
(a)	37.55	300	328
(b)	47.55	300	168
(c)	77.46	300	54
(d)	47.56	120	28

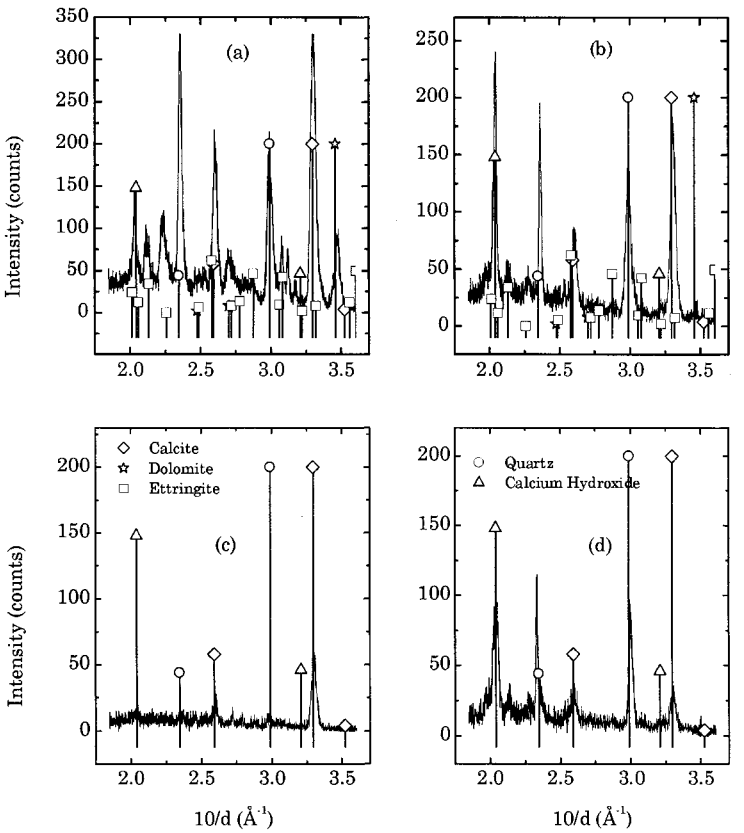

Figure 9. Diffraction patterns collected through various thickness of concrete. See Table 5 for details.

Comparison of Figure 9(b) and (d) clearly shows the advantage of longer count times. Figure 9(b), which was collected in over twice the time of Figure 9(d) has a better peak to noise ratio and overall intensity.

2.3 Resolution

Without the use of computed tomography techniques and reconstruction algorithms, the spatial resolution of the TEDDI technique is compromised by the high aspect ratio of the diffracting volume. The smallest dimensions of the needle are determined by the beam slits pre- or post-sample and these dimensions can be as small as 10 microns. Using the smallest beam dimensions then has the associated problem of low photon count rates. The limits on the step size for translating the object are determined by the engineering restraints on the stage. In the simplest linear traverses of the stage it is driven either in mutually perpendicular directions to the beam direction or along the beam direction. In the latter cases the step dimensions can be set to be similar to the slitted-beam width. Where the step size is the same as the needle width then the limit of resolution is the needle width. Where the step size is smaller than the beam width then the limiting factor of resolution is the step size and the

image obtained is a convolution of the signal from the object and the needle width. An example of a 2D traverse perpendicular to the beam is given in Figure 10. The sample shape, in this case, lent itself favourably to the needle shape of the diffracting volume. It is a cement micro-engineering structure with 120x120 μm high and wide channels that were of the order of a few millimetres in length. The sample was aligned face-on to the incident beam and moved in 25 μm steps along the width of the channels (range 2.5mm) and 100 μm steps along the height of the channels (range 0.4mm). The beam width was set at 100 μm. The point of interest in this study was the distribution of a particular mineral addition, mordenite, to the cement, between the base and the channel features. The analysis of the complete diffraction spectra, of which there were 200, involved extracting the diffraction information on the mordenite, calcium hydroxide (a cement hydrate) and tricalcium silicate (a cement-starting phase). The 2D diffraction contour maps in Figure 10 reveal the crystalline content of the channels and provide semi-quantitative information on the distribution of these phases between the channel and the bulk of the material. In this case TEDDI has reproduced the shape of the object, and provided information on its microcrystalline content with a spatial resolution better than 100μm.

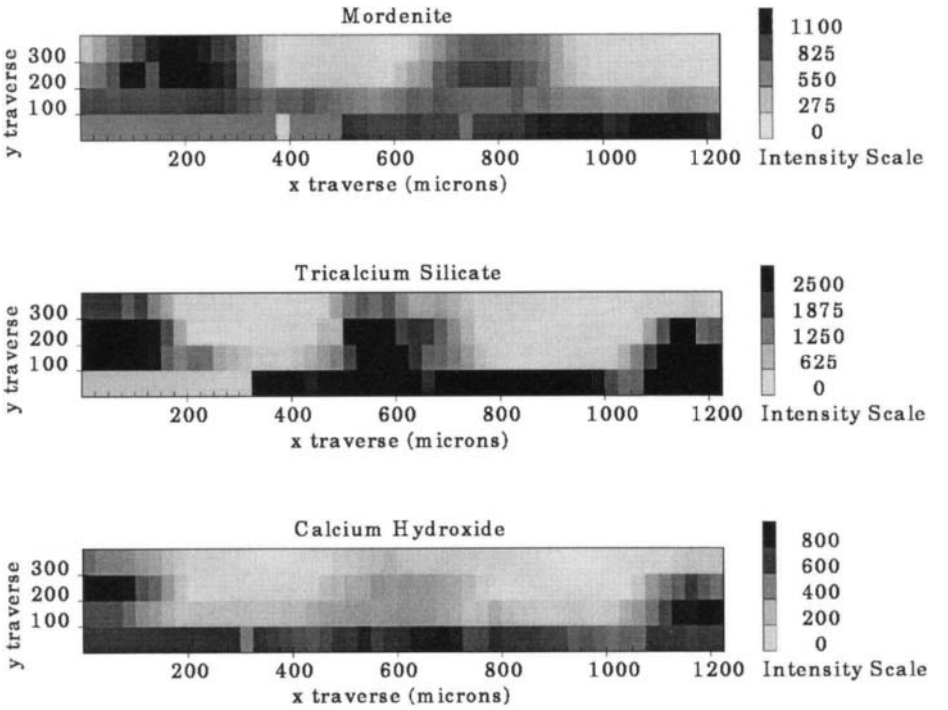

Figure 10. 2D phase maps of a cement micro-engineering structure showing the distribution of the crystalline phases; calcium hydroxide, tricalcium silicate and mordenite through the 100 μm wide channels. The area of low intensity marks the void space between the channels.

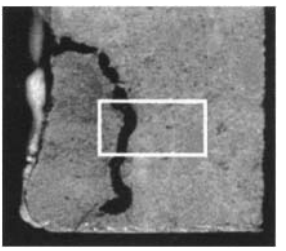

Concrete rock sample (8×2.5 mm box inset.)

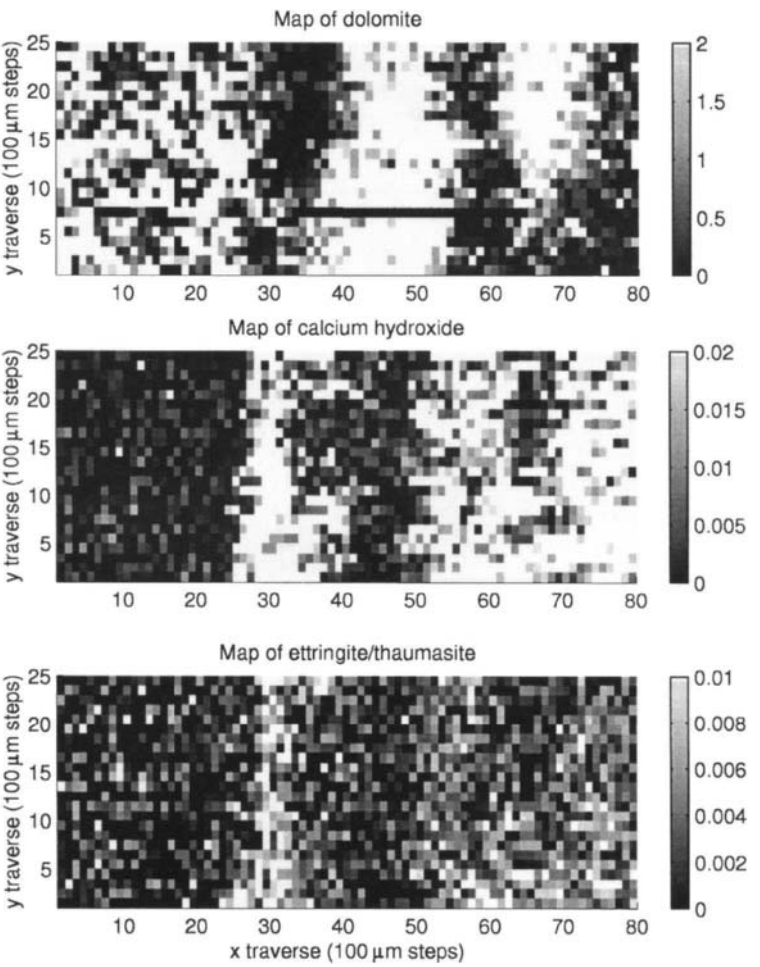

Figure 11. The photograph at the top of the page is of the concrete block. The depth of the block along the beam path was 4 cm and diffraction volume was several millimeters inside the block. The 2D phase maps above show the distribution of the cement phases around the aggregate (dolomite).

A similar TEDDI investigation was made of the interior of a larger object, a concrete block. In this case the feature of interest is the aggregate/cement interface and the occurrence of particular phases at this interface. Figure 11 shows the concrete block and similar 2D contour maps for this work. In this experiment the diffracting volume was completely inside the concrete block but the volume under investigation was selected with reference to large aggregates on the surface. In interpreting these data it is important to remember that the 2D pixellated representation is the projection of the phase information along the length of the diffracting needle (approximately 3.8 mm). This could explain the left-hand region of the map where there is a strong but not continuous signal from the aggregate and a dispersed signal from the cement phases. Here the diffracting volume may, along its length, have intersected with both cement and aggregate phases. A 3D scan, *i.e.,* a depth traverse along the length of the beam, would have fixed the position and size of this piece of aggregate. Yet despite this resolution handicap we are still getting spatial resolution on a 100 μm scale. We cannot expect to distinguish spatially between the microcrystalline phases of calcium hydroxide and ettringite, but we can see the distribution of these phases around the larger aggregate. What is really exciting about these images is that they were collected from the interior of a 4 cm block of concrete!

These two examples of work done on industrial materials have demonstrated a spatial resolution down to the order of 100 μm for the technique. An early piece of work at the European Synchrotron Radiation Facility (ESRF) on test objects [6] has shown that with a small beam size, small step size and suitably sized sample, spatial resolution down to the order of a few microns is possible.

There have been other applications of TEDDI to archaeological objects which highlight all the good points that we have already discussed; investigation of weathering on a temple frieze from Ankor Wat, Cambodia [7], a Grecian ceramic pot sherd [8]. Each of these studies has non-destructively revealed the interior crystalline character of these objects. These experiments discussed above were both performed on 'real' samples, *i.e.* solid 'as-found' objects rather than powders or prepared surfaces.

In conclusion we can say that TEDDI has unique capabilities for the characterisation of solid objects.

1. It is non-destructive.
2. It reveals details of the internal phase composition of even relatively bulky sample objects.
3. It has potential for high spatial resolution.

As has been pointed out, the technique has certain specific limitations, but it is hoped that there will be many applications for which TEDDI will be a new and exciting tool.

REFERENCES

1. B.C. Giessen and G.E. Gordon, Science, 159 (1968) 73.
2. Buras and L. Gerward, Prog. Cryst. Growth Char., 18 (1989) 93.
3. S.D.M. Jacques, PhD thesis, London University (1999).
4. L. Gerward, S. Mørup and H. Topsøe, J. App. Phys. 11 (1976) 137.
5. D.C. Creagh and J.H. Hubbell. *X-ray absorption (or attenuation coefficients).* In International Tables for Crystallography Volume C (Ed. A.J.C. Wilson. Kluwer: Dordrecht). Chapter 4.2.4. (1992) pp189-206.
6. C. Hall, P. Barnes, J. K. Cockcroft, S. L. Colston, D. Hausermann, S. D. M. Jacques, A. C. Jupe, M. Kunz, Nucl. Inst. Meth. Phys. Res. B 140, (1998) 253-257

7. P. Barnes, S. Colston, A.C. Jupe, S Jacques, J. Cockcroft, A. Bennet, C. Hall, Proc. Eur. Cryst. Com. Prague, (1998) in press.
8. E. Pantos, C.C. Tang, E.J. Maclean, K.C.Cheung, R.W. Strange, P.J. Rizkallah, M.Z. Papiz, S.L. Colston, B.M. Murphy, S.P. Collins, D.T. Clark, M.J. Tobin, M. Zhilin, K. Prag and A.J.N.W. Prag, Synchrotron Radiation in Archaeometry, Proc. EMAC99, 5th Eur. Meeting on Ancient Ceramics, Athens (1999).

Radiation in Art and Archeometry
D.C. Creagh and D.A. Bradley (editors)
2000 Elsevier Science B.V.

The use of X-ray techniques for bone densitometry in archaeological skeletons

M.J.Farquharson [a] and M.Brickley [b]

[a] Department of Radiography, City University, Rutland Place, Charterhouse Square, London, EC1M 6PA.
[b] Department of Ancient History and Archaeology, The University of Birmingham, Edgbaston, Birmingham, B15 2TT.

The following pages introduce the reader to various x-ray techniques which can be applied to the examination of archaeological bone. A brief explanation of the anatomy and physiology of bone is given and the basic radiation physics needed to understand the techniques described is outlined. A range of techniques for measuring the bone mineral density (BMD) of archaeological bones is introduced and examples of use given. A recent study is presented showing the use of a particularly novel technique for measuring the trabecular bone density of archaeological bone.

1. INTRODUCTION

In recent years, there has been a growing interest amongst researchers investigating archaeological bone in the study of bone mineral density (BMD). One of the primary reasons for the increase in studies seeking to investigate BMD has been a growing appreciation of the problems that conditions characterised by low BMD, such as osteoporosis, produce in the present population. Knowledge of the morbidity and mortality currently caused by osteoporosis related fractures has prompted researchers to ask whether individuals in the past were similarly affected.

The study of BMD has also been important for archaeozoology, the study of (non-human) animal remains in archaeology. Clearly, when seeking to reconstruct the activity of humans and other animals through the analysis of faunal remains it is important to have an understanding of the differential survival of various skeletal elements (Lyman 1994). It has been appreciated for some time that the structural density of bones will be a key factor for survival (Brain 1969). Photon absorptiometry/densitometry has been used in several studies to determine the BMD of various skeletal elements in a number of species (Lyman *et al.* 1992, Kreutzer 1992).

One of the first techniques to be applied to the study of BMD in archaeological bone was dual energy X-ray absorptiometry (DEXA), a widely used clinical diagnostic tool. Perzigian (1973 a and b) used DEXA in a study of two native American groups to determine

relative levels of health between the groups. Differences in bone loss between males and females were also reported. Since the studies by Perzigian, there have been a number of other studies that have used DEXA to address a range of problems associated with BMD, Nelson (1984), Sambrook *et al* (1988), Frigo and Lang (1995), Bennike and Bohr (1990), Raptis (1992), Lees *et al.* (1993), Molleson *et al.* (1993), Mays *et al.*(1998), Kneissel *et al.* (1994), Brickley (1998). However, only in the last two studies listed above is any serious consideration given to the effect that post mortem (diagenetic) changes might have on bone.

Diagenetic change is a term used to describe all changes occurring in bone after death. It includes all processes that affect degradation and remineralisation, both in and out of the ground, but excludes the effects of high temperature and pressure (Lapedes 1978, Pate and Brown 1985). Many possible factors influencing the appearance and survival of archaeological bone have been discussed in the literature, including soil chemistry and chemical weathering (Pate and Hutton 1988), the nature and composition of bone itself (Henderson 1987) and fungal or bacteriological activity (Douglas *et al.* 1987, Hackett 1981, Marchiafavia *et al.* 1974, White and Hannus 1983). However, at present such changes are not fully understood. The presence of diagenetic change is not necessarily detectable from the outward appearance of bone, and bones that appear well preserved may have undergone many changes (Bell 1990, Bell *et al.* 1993, Hanson and Buikstra 1987, Stout and Simmons 1979).

Recently researchers have become aware that structural and compositional changes may affect interpretations made about the age, health status or diet of individuals being examined (Bell 1990, Lambert *et al.* 1985, Thompson 1980). Clearly, such changes have serious implications for the study of bone density. As a result of the nature of diagenetic change, analysis of archaeological bone by non-invasive techniques, where bone mineral density is assessed, may be particularly prone to misinterpretation.

The use of x-ray techniques for the determination of bone density in archaeological material is required as such changes cannot be determined from simple examination of the external surfaces of bones. In the study of osteoporosis for example, although evidence of fractures associated with the condition can be looked for with the naked eye, this approach will not enable a full assessment of levels of age-related bone loss and osteoporosis to be determined. Not all bones that have undergone significant loss and structural changes within the trabecular region which makes the individual prone to osteoporotic fracture, will do so during the individuals lifetime (Jayasinghe 1991). Therefore, in order to gain a complete picture of bone loss in past populations or assess the density of different skeletal elements from animals and their likelihood of survival, techniques such as those outlined in this paper must be employed.

Techniques such as DEXA were developed for clinical use. As a result, there are problems involved in their application to archaeological bone. As mentioned above, the possibility that diagenetic changes may have taken place should always be addressed when undertaking non-invasive studies of bone. Non-invasive techniques such as DEXA calculate a Figure for the physiological 'bone mineral' (mostly hydroxylapatite) content of the object being scanned, but the equipment cannot distinguish between different minerals. If a volume of a relatively high atomic number was scanned, the equipment would calculate this as a density of hydroxylapatite in the scanned object.

1.1 Bone Structure.

Bone is a connective tissue which is made rigid by the deposition of minerals and can be split into two categories, cortical bone and trabecular bone. The anatomy of the femoral head and neck, which is typical of a long bone is shown in Figure 1. Cortical bone is a dense bone tissue that is found on the exterior of all bone and is generally thicker in the diaphysis than the epiphysis. Trabecular bone contains many spaces between bony struts which make a rigid network of bone and constitute most of the bone in short, flat, irregular shaped bones e.g. vertebrae and the calcaneus, and is found in the epiphysis of long bones, for example the head and neck of the femur. The irregular latticework of trabecular bone is made up of thin plates called trabeculea which provide a large surface area and are the most metabolic part of the skeleton. Trabeculea are typically 100-200 μm thick and enclose spaces which are 600-1000 μm across. Figure 2 shows a slice of bone taken through the neck of the femur. The outer cortical bone and trabecular bone are clearly visible.

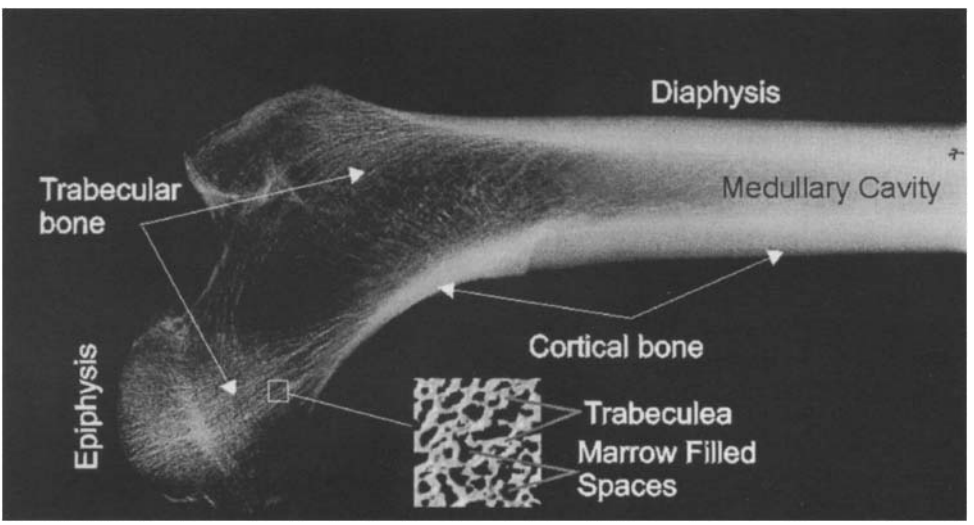

Figure 1. The anatomy of the femoral head and neck, typical of a long bone.

Bone fibres consist of a protein called collagen, which is encrusted with a crystalline mineral or bone salt. Mature bone mineral is hydroxylapatite, formed from calcium carbonate and calcium phosphate. As well as calcium and phosphorous, bone contains magnesium, sodium, potassium, carbon, chlorine, hydrogen and oxygen.

2. Basic Physics of Radiography

X-rays are electromagnetic radiation and are part of a range of electromagnetic energy known as the electromagnetic spectrum. X-rays can be produced in an x-ray tube and they

can be highly penetrating, hence we can use them to look 'inside' objects. When x-ray or gamma (γ) ray photons are incident on any form of matter, some are transmitted through the matter and some are not, i.e. the incident beam of photons is attenuated by the medium. The removal of the photons from the primary beam can be through absorption of photons, or scattering of photons from the incident angle.

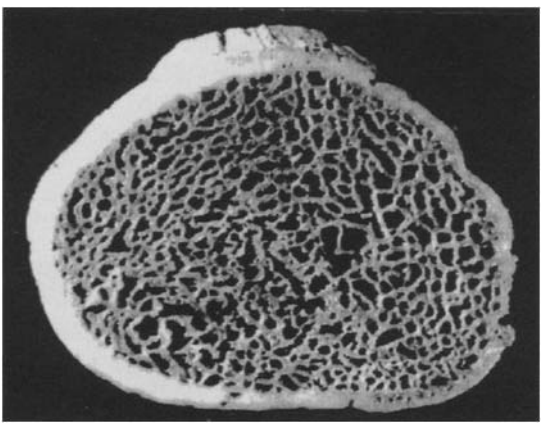

Figure 2. Slice of bone 5.0 mm thick taken through the neck of the femur showing the outer cortical ring and the trabecular structure.

Consider the experimental set up shown in Figure 3. It consists of a source of photons that are monoenergetic, are highly collimated via small apertures into a pencil beam, and are directed towards a suitable kind of photon detector.

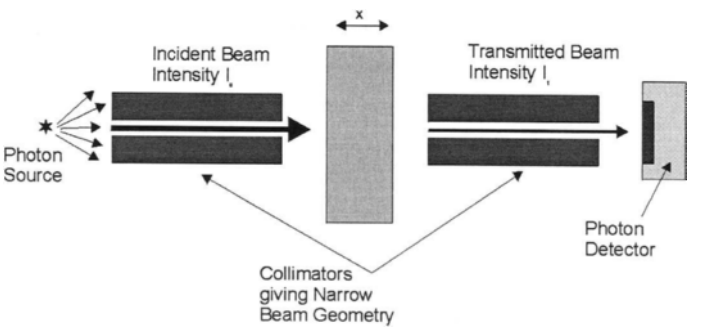

Figure 3. Representation of an experimental setup to measure the attenuation of a beam of photons passing through a material of thickness x.

A photon can either be totally absorbed by the material, scattered from its path by the material or a mixture of both, i.e. some of the photon energy is absorbed and some is scattered. The number of photons removed from the primary beam is proportional to the thickness of the material through which it has passed hence:

$$\frac{-\Delta I}{I} = \mu \Delta x \qquad [1]$$

where $-\Delta I$ are the photons removed from the primary beam which has an intensity I, Δx is the thickness of the material through which the beam is passing and μ is a constant of proportionality. For an elemental thickness of the material dx, and letting the primary intensity be I_0 i.e. when the thickness of material $x = 0$, integrating Equation [1] gives

$$I_t = I_0 e^{-\mu x}. \qquad [2]$$

The linear attenuation coefficient, μ, is normally quoted in units of cm^{-1} and is dependent on the physical density of the attenuating medium. A more fundamental coefficient is the mass attenuation coefficient, μ_m, which is independent of physical state and is given by dividing the linear attenuation coefficient by the density, ρ, of the attenuating medium

$$\mu_m = \mu / \rho. \qquad [3]$$

Attenuation coefficients vary depending on the attenuating material that is in the path of the primary beam of photons, and the photon energy. The probability of a photon being removed from the primary beam is given the term cross section per atom or molecule. The total cross section, σ_{tot}, is made up from the cross sections of the individual processes that occur in the attenuation of the primary beam. For the energies used in the measurement of bone mineral density discussed in this study we are concerned with three interaction processes that contribute to the attenuation process, namely photoelectric absorption, Compton scatter and coherent scatter.

The total linear attenuation coefficient is dependent on the total cross section of the atoms or molecules in the medium and the number of sites at which an attenuation process can occur i.e.

$$\mu = N\sigma_{tot} \qquad [4]$$

where N is the number of attenuating sites per unit volume. Figure 4 shows the linear attenuation coefficients for cortical bone as a function of the photon energy of the primary beam for a typical energy range used in techniques discussed in this study.

2. INTERACTION PROCESSES

2.1 Photoelectric absorption

A photon of incident energy E_I interacts with one of the atoms in the attenuating medium and ejects a bound electron from one of the inner shells of the atom, usually the K, L or M shell. The ejected electron, called the photoelectron, is given kinetic energy which is equal to the incident energy less the energy that holds the electron in its orbit around the atomic nucleus, called the binding energy (E_{BE}). This is shown in Figure 5. The vacancy resulting in the shell by the emission of the photoelectron is quickly filled by an electron from another shell which can result in a characteristic x-ray being emitted as shown in Figure 6.

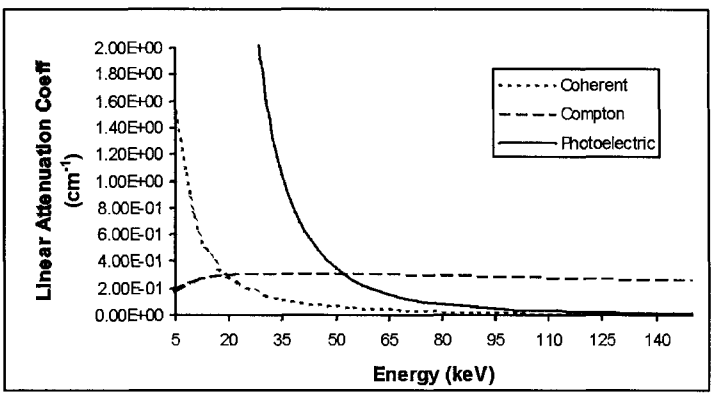

Figure 4. Linear attenuation coefficients for Incoherent scattering, Compton scattering and photoelectric absorption for cortical bone.

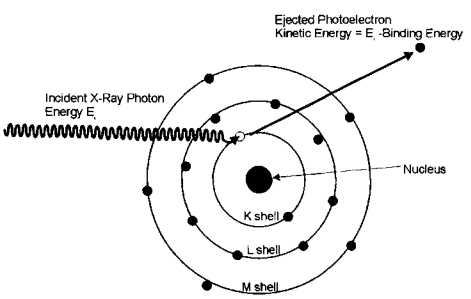

Figure 5. The process of photoelectric absorption: the incident photon ejects an inner shell electron from the atom.

As a result of a photoelectric interaction the incident photon is completely absorbed. The photoelectric mass attenuation coefficient, τ_{PE}^{Mass} varies as a function of incident photon

energy as $\tau_{PE}^{Mass} \alpha\ 1/E^{-3}$ (see Figure 4). The effect of this energy dependence results in low energy photons being preferentially absorbed. There is also a dependence on the atomic number of the attenuating medium and varies approximately as Z^4, a fact that needs to be kept in mind when measuring bone density in samples that may have been contaminated with other materials.

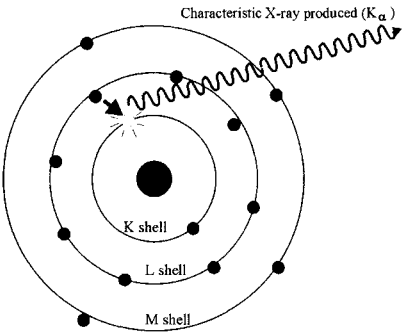

Figure 6. The process of photoelectric absorption can result in the emission of characteristic x-rays.

2.2 Compton (incoherent, inelastic) scattering

A Compton interaction is one between an electron of an atom and the incident photon. The electron is assumed to be a free electron i.e. the binding energy is ignored which is reasonable for the outer shell electrons. The incident photon interacts with an electron and gives up some of its energy to it, which consequently gains kinetic energy leaving the scattered photon with lower energy. The process is shown diagrammatically in Figure 7. The electron is given most kinetic energy when the photon is completely back scattered i.e. $\theta = 180°$. It is given a minimum kinetic energy when the photon scatter angle is small i.e. when $\theta \cong 0°$.

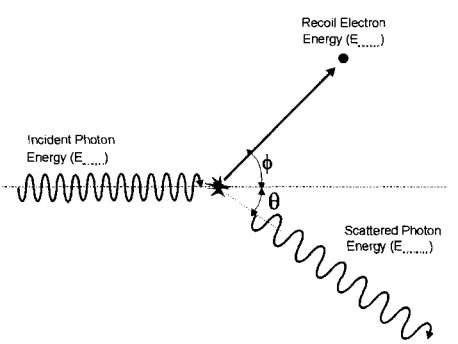

Figure 7: Diagrammatic representation of a Compton scattering event.

By the conservation of energy we can write:

$$E_{incident} = E_{scattered} + E_{electron} \quad [5]$$

The energy of the scattered photon can be calculated by

$$E_{scattered} = E_{incident} \frac{1}{1 + \frac{E_{incident}}{m_0 c^2}(1 - \cos\theta)} \quad [6]$$

where $E_{incident}$ and $E_{scattered}$ are the energies of the incident and scattered photons, m_0c^2 is the rest mass energy of the electron equal to 511 keV and θ is the photon scattering angle.

The Compton mass attenuation coefficient, $\sigma^{Mass}_{Compton}$, is dependent on energy i.e. $\sigma^{Mass}_{Compton} \alpha\ 1/E$ but is not dependent on the atomic number, Z, of the material. A Compton event results in a mixture of scattering and absorption of the incident photon.

2.3 Coherent (Rayleigh, elastic) scattering

This mechanism involves the interaction between a photon and an atom in the material. It results in a change of direction of the incident photon, but no change in energy. It is therefore a scattering process only. The wavelength of the incident and scattered photon remain the same since the wavelength defines the energy through the equation $E = hc/\lambda$ where h and c are constant and λ is the wavelength. However, due to interference phenomena, the amplitude of the scattered wave is reduced. The energy of the incident photon must be low such that ionisation of the atom (i.e. the removal of an electron) does not take place. A diagrammatic representation of the process is shown in Figure 8. The coherent mass attenuation coefficient σ^{Mass}_{Coh} varies with the atomic number, Z, of the material with which it interacts and also with the energy of the incident photon in the following manner,

$$\sigma^{Mass}_{Coh}\ \alpha\ Z^2 \quad \& \quad \sigma^{Mass}_{Coh}\ \alpha\ \frac{1}{E}$$

i.e. the higher the atomic number the more probably a coherent scatter event will occur for a given energy. However, as the energy of the incident photons is increased the probability of a coherent scatter event occurring will reduce (see Figure 8).

3. THE RADIOGRAPH

The most frequently used clinical radiographic procedure is the conventional 'x-ray' or radiograph, and is used in some of the bone densitometry techniques described in this study. Radiography has been applied to the study of archaeological human remains since the technique was developed. The first application of such techniques to the study of archaeological bone is thought to date back to 1900, just five years after Röntgen discovered x-rays (Fiori and Nunzi 1995).

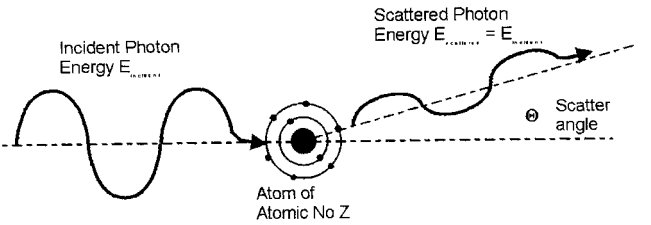

Figure 8. Diagrammatic representation of the coherent scattering process.

The most common way to obtain an x-ray image is to use a type of film that is sensitive to x-rays as a detecting medium. If x-rays fall on such a film then it darkens and the more x-rays that reach the film the darker it will become. If a film is exposed to x-rays it will darken uniformly across the film as shown in Figure 9a.

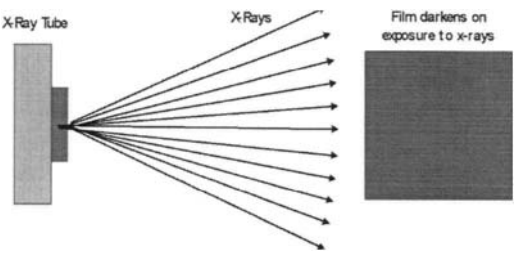

Figure 9a. A film exposed to an x-ray source will darken uniformly.

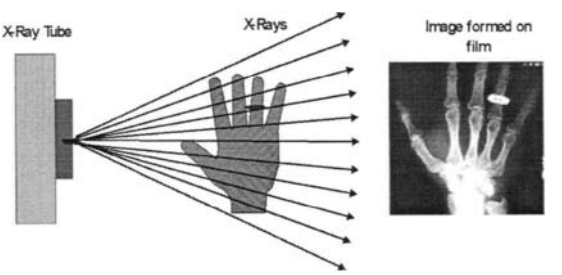

Figure 9b. An object placed in the x-ray beam will cause non-uniform darkening.

If an object is placed in the path of the x-rays we get differing shades of darkening on the film which produce the image as seen in Figure 9b. This occurs because some of the photons interact with the object in the path via the mechanisms described above. If the object

consists of materials of different atomic number, Z, then there will be differential attenuation leading to different amounts of darkening of the film.

A number of factors need to be kept in mind in order to obtain a correctly exposed radiograph. X-ray photons are produced in a tube by accelerating electrons onto a target material. The area on the target where the x-rays are produced is known as the focal spot. The x-rays will have a range of energies (spectrum) depending on the applied voltage that is selected. A typical x-ray tube spectrum is shown in Figure 10. As an example, if we apply a voltage of 70 kV_P across the tube the maximum x-ray photon energy (peak energy) will be 70 keV, but the average energy will be approximately 38 keV. Increasing the voltage applied to the x-ray tube increases the average photon energy.

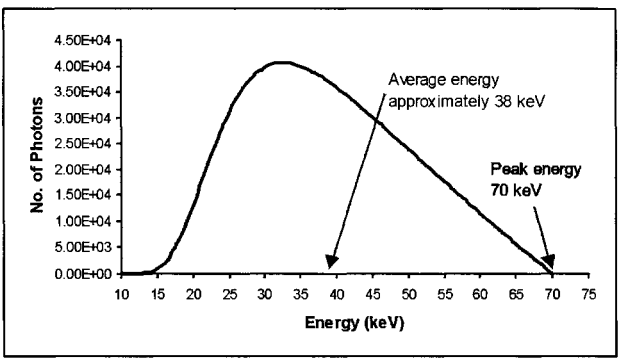

Figure 10. Photon spectrum from a tungsten target x-ray tube with applied voltage of 70 kV_p.

Selecting the correct kV_P is important because this determines the energy of the photons that form the image. From the discussion on attenuation above it can be seen that higher energy x-ray photons will be more penetrating than low energy photons. A kV_P needs to be chosen such that the average energy of the beam will penetrate the densest component of the object being imaged. If the energy is too low, all the photons will be absorbed by the object, and none will reach the film. If the energy is too high there will be little attenuation of the beam by all the components in the object resulting in most of the photons reaching the film producing an image of low contrast.

A further consideration is the distance between the focal spot of the x-ray tube and the film (FFD). The focal spot in the x-ray tube is a finite size, typically 3x3 mm for a large focal spot and 0.3x0.3 mm for a small spot. X-rays are produced over the entire area of the focal spot and spread out in a cone from each discrete point on the spot. Figure 11 shows how this affects the blurring of an image which is known as geometric unsharpness or penumbra. It is clear that penumbra can be minimised by increasing the FFD and this is important when the image has been produced to take measurements of, for example, cortical thickness as described in section 4.

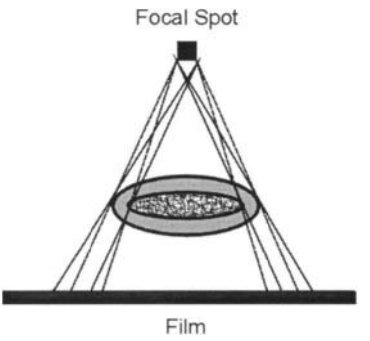

Figure 11: Geometry of penumbra or geometric unsharpness.

There are limits on increasing the FFD because the x-rays diverge from the focal spot, hence the same number of photons are spread over a larger area as the FFD is increased. To compensate for this the number of photons must be increased by exposing the film for longer times, and/or increasing the current, (mA), applied to the tube. The value of mA determines the number of photons that are produced at the focal spot but will not alter the energy spectrum.

One advantage of radiographing archaeological bones is that the radiation dose does not have to be considered. This means that the choice of film used is very wide and that slow film with good resolution can be used to optimise image quality. Plain x-rays have also been used to assess bone loss through the application of the Singh Index. Details of this technique were first published in 1970 (Singh *et al.*) as a way of assessing trabecular bone loss and osteoporosis from radiographic images. Six stages of bone loss, based on the visibility of the five main groups of trabecular structures present in the Ward's triangle region were defined. A series of diagrams illustrating each of the stages of trabecular loss were produced with accompanying descriptions to allow other workers to use the technique. In theory, this should be a simple technique to apply to archaeological bone, as it is non-invasive and utilises inexpensive and widely available equipment.

However, a pilot study (Brickley 1998) found that there were high levels of inter and intra observer error involved in the scoring of trabecular bone loss. Variations in the scores awarded were particularly apparent for scores in the middle of the sequence. Another problem encountered was that the region over which observations should be made is large and archaeological bone is often fragmentary or damaged. Any damage to the observation area makes accurate observation and scoring impossible. Therefore, in many studies there would be a large number of bones that could not be analysed using this technique. These observations demonstrated that even when repeatable scores could be obtained from undamaged sample material, there was not a clear correlation between these and age at death of individuals analysed, or bone loss recorded using other techniques. ***Consequently, the Singh Index is not a technique recommended for use on archaeological bone material.***

Plain x-rays are also very important in aiding the diagnosis of pathological conditions encountered in the study of archaeological bone and this is probably their most common use on archaeological bone material. Analysis of plain x-rays often enables internal bone

changes to be observed, greatly adding to information on which a differential diagnosis might be based. Importantly, it is often possible to make comparisons between x-rays of archaeological bone and modern cases. As this application of x-rays is so widespread, there is a large quantity of literature that deals with the practical application and interpretation of plain x-rays of archaeological bone (Ortner and Putschar 1985, Aufderheide and Rodríguez-Martín 1998).

However, as with all types of study of archaeological bone, care must be taken that diagenetic changes do not lead to misinterpretation, for example ingress of soil into bones, or uptake of minerals by bones. One case in which bones were found to have been altered by soil ingress was a study of material from Christchurch Spitalfields (Molleson and Cox 1993). Radiographic images of the bones of some infants and juveniles, buried in lead coffins, appeared very opaque and analysis revealed that this was due to uptake of lead by bones.

3.1 The Microradiograph

Microradiographs are obtained by embedding bone before making a plane parallel section (Armelogos *et al.* 1972). Sections are normally between 10 and 15 microns thick (Roberts 1991), and are placed on x-ray film to obtain contact radiographs. The resulting image should enable the different levels of mineralization to be analysed. However, this technique has been largely superseded by the use of a back-scattered imaging mode in scanning electron microscopy (SEM). One advantage of using SEM techniques is that blocks of embedded bone can be analysed rather than obtaining a thin section, which can be very difficult in archaeological bone.

Figure 12 shows an image of archaeological bone obtained using back-scattered imaging (SEM). Variation in levels of mineralization can be seen, more highly mineralised areas appear lighter than less well-mineralised areas. Areas of diagenetic change can also be observed. In this case, they appear as small holes with highly mineralised edges.

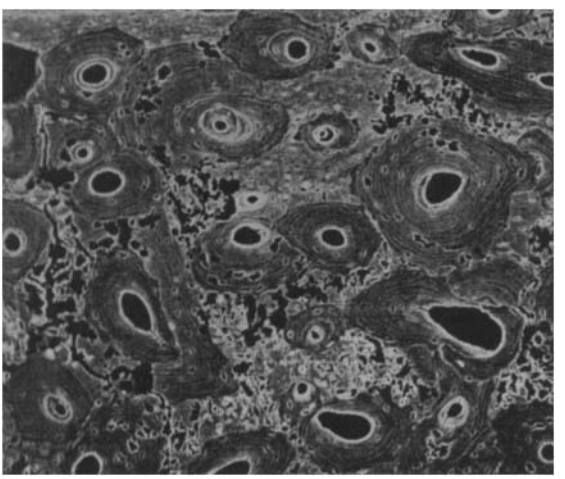

Figure 12. Variation in levels of mineralization seen on an image obtained using back-scattered imaging in a scanning electron microscope (SEM).

4. RADIOGRAMMETRY

Radiogrammetry is a technique that allows the quantity of bone present to be determined via a measurement of the thickness of cortical bone from plain radiographs. Cortical bone loss occurs mainly due to resorption at the endosteal surface between the cortical bone and the medullary cavity which causes an increase in the width of the medullary space and a consequent decrease in the thickness of the cortex.

The method was devised as a way of monitoring bone loss in a clinical environment nearly forty years ago (Barnett and Nordin 1960). A standard methodology for the technique would be to produce a postero-anterior radiograph of the second metacarpal of the left or right hand. Measurements are then made on the radiograph (Dequeker 1976) as shown in Figure 13.

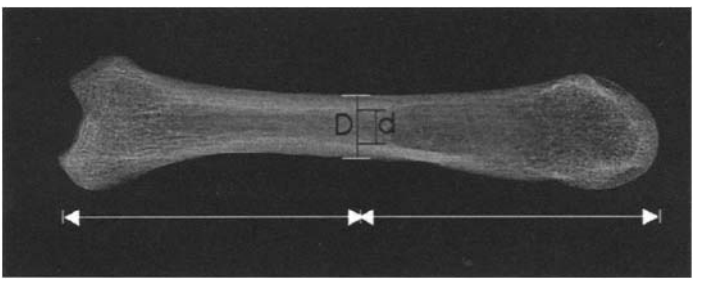

Figure 13. Measurements made on a radiography of the second metacarpal bone in radiogrammetry.

The midpoint of the bone is found using a rule, which has been shown to be accurate to ± 1.0 mm (Naor *et al* 1972). A measurement is now taken at the outer diameter (D) and the width of the medullary space (d). It should be noted that these measurements need to be as accurate as possible and should be taken with a vernier calliper with pointed tips. The cortical thickness (D-d) and the cortical area $\pi/4\left(D^2 - d^2\right)$ can now be calculated.

Radiogrammetry has some distinct advantages for use with archaeological bone. It is simple to carry out, is cheap and requires the use of ordinary x-ray equipment. It is non destructive requiring no sectioning of the bone. As mentioned above, the clinical site chosen for this technique is the second metacarpal and this should be the bone of choice from the archaeological skeleton if direct comparisons of bone density are to be made. One such study has been carried out by Mays (1996) on bone from 83 males and 71 females. A measure of cortical thickness was used using the cortical index that gives the percentage of bone width occupied by the cortex and is defined as,

$$\textit{cortical index} \quad = \quad [(D-d)/D]\times 100 \qquad [7]$$

A further study by Mays *et al* (1998) used the technique to find the cortical index in the mid-shaft of the femur.

Another study was carried out on humeri and femora obtained from three collections of Native American material (Ericksen 1976). Measurements were taken from the mid-shaft of femur and from the region immediately below the tuberosity of the humerous and corrections for body size were applied. From the results obtained it was stated that bone loss in the humerous and femur was observed to begin in middle age (30-50 years). Females were seen to lose more bone than males and for the loss to begin at an earlier age.

Users of this technique should be aware of possible sources of error. Two sources of error inherent in the method are intra-observer measurement and the error associated with the radiography. The former is due to the precision of the measuring apparatus being used and the latter is the difficulty in defining the edges of the cortical bone due to poor film quality and/or using incorrect exposure values. Further sources of error can occur when applying the technique to archaeological samples, e.g. post depositional factors which can affect the cortical thickness via the erosion of bone.

5. PHOTODENSITOMETRY

Radiogrammetry has some limitations in the study of bone mineral density in archaeological samples. Firstly, it is restricted to certain skeletal areas i.e. the mid shaft of long bones and if direct comparison with modern data is required, then the second metacarpal should be used. Associated with this limitation is the uncertainty of how cortical thinning in the metacarpal correlates with bone loss in other parts of the body. Another limitation is that the measurement is unable to quantify any change in the trabecular component of bone. A method that allows a measure of both the cortical and trabecular component of bone is photodensitometry. A radiograph is taken of the sample of interest which is placed next to a calibration stepwedge made of a suitable bone mineral equivalent material (see Figure 14).

The radiograph is processed and optical density readings taken from the stepwedge to produce a calibration curve. Further optical density measurements can be made on the sample enabling the bone density at any chosen point to be given as an equivalent thickness of the step-wedge material. This method shares some of the advantages of radiogrammetry in that it is cheap and the equipment is readily available. However one disadvantage is that each film needs to be calibrated to a step-wedge which is time consuming.

Care should be taken as diagenetic changes may produce erroneous results. The technique requires the use of plain x-rays and these can be examined for signs of changes such as soil ingress, but simple examination of such images may not be sufficient to detect all such changes. However, a study undertaken on bone material that had not been diagenetically altered found that very good results could be obtained from archaeological bone using this method (Farquharson *et al* 1997).

6. SINGLE PHOTON ABSORPTIOMETRY (SPA)

This technique is essentially a measure of the attenuation of a beam of radiation as it passes through the whole bone, i.e. both cortical and trabecular components. The method relies on the exponential law of attenuation discussed in Section 2. A beam of radiation is highly collimated into a small pencil beam and directed at a suitable detector, usually a NaI

crystal scintillation detector or a germanium solid state crystal detector. A radiation source that is commonly used is the isotope iodine-125 which produces photons with an energy of 27.4 keV. Each photon that reaches the detector causes an electrical pulse to be generated which is then sent to a counting device. The set up is shown in schematic form in Figure 15.

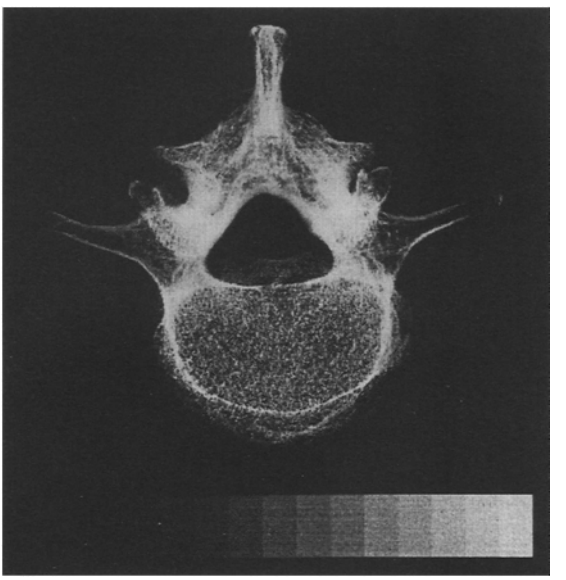

Figure 14. Photodensitometry. A radiograph is taken of the bone in conjunction with a step wedge.

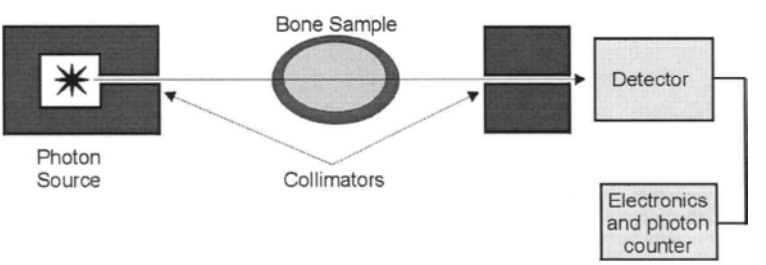

Figure 15. Schematic representation of the experimental setup for single photon absorptiometry.

It can be seen from Figure 15 that it is a straightforward task to count the number of photons that reach the detector in a given time along a given path, with and without the bone sample in place. The bone mineral, m_b, that is present in the path of the beam can be determined using,

$$m_b \alpha \frac{\rho_b \ln\left(I_0 / I_t\right)}{\mu_b} \qquad [8]$$

where I_0 is the intensity of photons reaching the detector with no sample in place, I_t is the number of photons reaching the detector after being transmitted through the bone sample, ρ_b is the physical density of bone and μ_b is the appropriate linear attenuation coefficient of bone for the energy of the photons being used. Note this technique satisfies the requirement for equation [2] to be valid i.e. the use of a monoenergetic photon source and narrow beam geometry. To obtain the bone mineral content the sample should be scanned over a region of interest and a summation performed over all values of m_b.

It is important to understand that photon absorptiometry is a measure of all of the material that is in the path of the beam, which includes both cortical and trabecular bone and also any other material which has found its way into the trabecular spaces e.g. ground soil etc. Diagenetic change within the bone will also cause errors in calculating the bone mineral density because the atomic number of the material changes hence the physical density and the attenuation coefficient used in the calculations will be incorrect.

7. DUAL PHOTON ABSORPTIOMETERY AND DUAL ENERGY X-RAY ABSORPTIOMETRY (DEXA)

In the clinical environment, a major disadvantage of single photon absorptiometry is that the site of the bone must be placed in a tissue equivalent surrounding, normally a water bath, in order for the attenuating material to have the same path length. An improvement of this method was developed using two photon energies, dual photon absortiometry (DPA), which allows both bone and soft tissue to be measured without knowing the thickness of material, hence removing the need for the water bath. The method is similar to that of SPA but two monoenergetic photon sources are used, commonly 44 keV and 100 keV. The amount of bone, M, is calculated using an equation of the form;

$$M = \frac{\left[\ln\frac{I_0(E_1)}{I_t(E_1)} - \frac{\mu_s(E_1)}{\mu_s(E_2)}\ln\frac{I_0(E_2)}{I_t(E_2)}\right]}{\left[\mu_b(E_1) - \frac{\mu_s(E_1)}{\mu_s(E_2)}\mu_b(E_2)\right]} \qquad [9]$$

where $I_0(E_1)$ and $I_0(E_2)$ are the intensities of the photon beams with the energies E_1 and E_2 with no sample in the beam, and $I_t(E_1)$ and $I_t(E_2)$ are the transmitted intensities of the beams through the sample containing soft tissue and bone. The constants μ_s and μ_b are the mass

attenuation coefficients for soft tissue and bone respectively. As with SPA, to obtain the bone mineral content the sample should be scanned over a region of interest and a summation performed over all values of M. The value of M can be divided by the area of bone scanned and this bone mineral density (BMD) is given in units of g/cm^2. Note this is not a true density, but the amount of bone corrected for the area over which the measurement was made.

The technique has been extended further and uses an x-ray tube source which emits spectra of two kV values obtained via filtering the output from the x-ray tube or by rapidly switching between the two kV energies typically 40 keV and 70 keV. This technique is known as Dual Energy X-ray Absorptiometry (DEXA) and is the most commonly used technique in the clinical environment for non-invasive assessment of bone-state (Njeh *et al* 1996). The use of the x-ray tube source rather than the gamma source used in DPA gives a much higher photon flux resulting in better image resolution, shorter scan times, better precision and a reduction in radiation dose to the patient per scan. Clinical measurements can be made at sites that are otherwise inaccessible.

It must be remembered that clinical DEXA machines are designed to work on living patients with varying amounts of soft tissue surrounding the bone, and marrow inside the trabecular cavities. Care must be taken to compensate for this when measuring archaeological bone particularly when wishing to compare data with modern populations. There are a number of manufacturers of DEXA equipment, and each brand of machine will have a range of scanning options. The equipment used by the authors in tests using DEXA on archaeological bone was the Lunar DPX-L (Lunar Corporation, Madison, Wisconsin) (Farquharson *et al.* 1997). Advice was sought from the Applications Department at Lunar Corporation for the best methods to employ the Lunar DPX-L on the sample material available. The Lunar Corporation recommended that the 'forearm option' was used when performing scans for all bone specimens as it can be used in air providing the tissue equivalent platform made of delrin is included in the scan. Delrin (Acetal/Celcon) is a homopolymer material.

An example of the application of the clinical DEXA technique to archaeological bone material is the analysis of a vertebra, found at Pella in Jorden, that displayed evidence of a crush fracture (Sambrook *et al* 1988). The figure obtained for the bone mineral density was considered to be very low in comparision to modern clinically derived data, whatever the age and sex of the individual. It was stated that "bone density measured by dual photon aborptiometry in dried, marrow free vertebrae appears to be directly comparable to measurements performed in living subjects". However, this is certainly not the case and measurements derived from archaeological bone material cannot be directly compared to clinical data.

A DEXA analysis of skeletal material from the crypt at Christchurch Spitalfields, London (Lees *et al* 1993) concluded that women in London during the time period under study (A.D. 1700-1850) had a higher bone density than modern day women and did not start to lose bone until a later age. It was suggested that one factor that may have contributed to these results may have been higher levels of physical activity in past populations. The fact that the results obtained for bone mineral density obtained form archaeological bone were not suitable for comparison to data obtained from living patients was realised. In order that an idea of the levels of bone loss taking place within the population could be gained, the results were expressed as a percentage of the mean value found in the young normal subjects from each

group. However, no consideration was given to the possibility that bone from some individuals may have undergone diagenetic change despite the fact that the site publication reported that the same skeletons had been contaminated by metal elements from coffins in the crypt (Molleson *et al* 1993). When looking at lead levels in bone as part of a study of diet "evidence for the post mortem uptake of heavy metal emerged" (*ibid* p.17). Other metals were also observed to have been taken up by the bones: there were "high levels of iron indicated by the spectra for an infant" (*ibid* p.18). Only infants and juveniles produced anomalous radiographic images, but this does not rule out the possibility that adult bones were also contaminated to a lesser extent.

8. ENERGY DISPERSIVE X-RAY DIFFRACTION (EDXRD)

All of the above techniques assess bone density by measuring cortical bone or both cortical and trabecular bone. It has already been stated that bone loss may be accelerated more in the trabecular region of the bone, consequently it may be an important part of a study into osteoporosis that a measure of trabecular bone be made in isolation from the cortical component. Energy Dispersive X-Ray Diffraction (EDXRD) can be used to detect and perform quantitative analysis on the components of the sample being measured (Luggar *et al* 1996, 1993, Luggar and Gilboy 1994, Kosanetzky *et al* 1987). The technique has been applied to bone (Farquharson and Speller 1998, Royle and Speller 1991, 1995) and in particular to samples of human archaeological bone (Farquharson *et al* 1997).

The technique relies on the fact that diffraction of x-ray photons occur from crystalline materials resulting in an energy dispersive diffraction spectrum which is unique to the material under investigation. Diffraction effects can most readily be observed from materials with a high range order i.e. crystalline materials. A crystal can be defined as a solid that is made up of atoms arranged at points in a periodic pattern in three dimensions known as a lattice. The simplest crystals are ones that have a single atom of one element associated with each point in the lattice and many metals crystallise in this way forming body centred cubic and face centred cubic structures. More complex structures arise when two or more identical atoms are associated with each lattice point and again this is common to many metals resulting in a hexagonal close packed structure. The structure of compounds are also built up on the sites of the lattice e.g. CsCl and NaCl. Materials of such high range structural order give rise to diffraction, which is a consequence of the phase relationship between photons scattered from the atoms in a crystal lattice. Photons are electromagnetic waves and if two waves of equal amplitude are completely in phase and are superimposed on one another the resultant wave will have an amplitude of twice the original. In such a case complete constructive interference is said to have occurred. If two waves are completely out of phase then the resultant amplitude will be zero and complete destructive interference is said to have occurred. If the two waves are somewhere in between these two extremes then partial interference occurs. In a regular array of periodic atoms such as in a crystal, there will be certain directions of scatter such that the path difference between waves, scattered from different lattice points, is an integral number of wavelengths, thus constructive interference will result. This is known as Bragg diffraction as is illustrated in Figure 16.

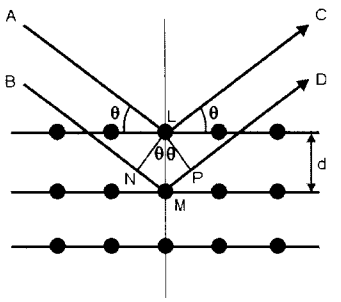

Figure 16. Bragg diffraction from a periodic crystal.

Consider a crystal consisting of parallel planes of atoms spaced a distance d apart with a monoenergetic source of x-ray photons incident on it at an angle θ. Consider photons along **A** and **B** which are scattered by sites **L** and **M**. It is only in directions **C** and **D** that the scattered beams are in phase and hence constructive interference occurs. The path difference between the two planes travelled by the incident and scattered waves is NM + MP = $d\sin\theta$ + $d\sin\theta$, and if this path difference is an integral number of wavelengths then the scattered beams will be in phase i.e.

$$n\lambda = 2d\sin\theta \qquad [10]$$

Equation 10 is known as the Bragg Law. For a given material there will be a set of planes each of which will each have one specific angle that satisfies the Bragg law for a given photon energy.

EDXRD is a technique which can be configured to take a measurement from the trabecular region of the bone in isolation from the cortex. A polyenergetic source of photons from an x-ray tube is collimated using lead slits, which leads to a ribbon beam of photons being incident on the bone sample being investigated. A second pair of lead slit collimators is arranged at a chosen scattering angle to the incident beam. This collimator arrangement allows a measuring volume to be defined within the sample, which in the case of bone can consist of the trabecular component. Depending on the molecular structure of the material, certain wavelengths of photons in the incident beam will satisfy the Bragg condition of Equation 10 for constructive interference to occur. The resulting scattered spectrum will be a unique signature characteristic of the material being investigated, the intensity of which will be dependent on the amount of material within the scattering volume. The scattered beam is detected using an energy dispersive detector of suitable resolution, and the signal processed using a multi channel analyser (MCA). Figure 17 shows a schematic diagram of the experimental set up.

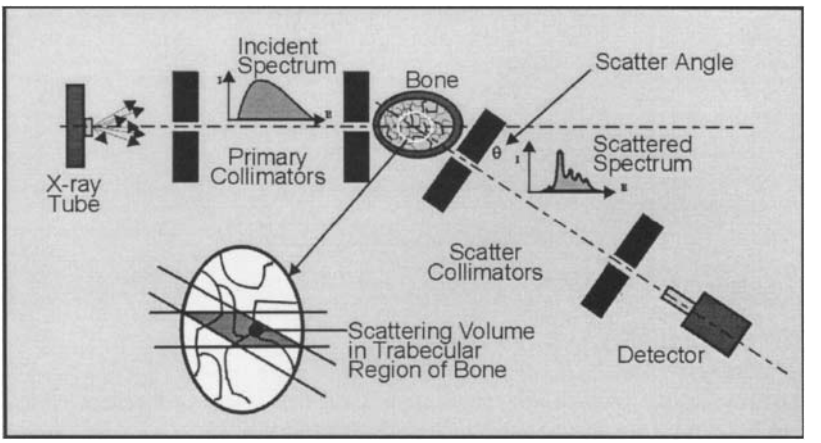

Figure 17. Schematic representation of the EDXRD equipment.

A typical diffraction spectrum obtained from archaeological bone material is shown in Figure 18. The geometry for this measurement was a scatter angle of 5 degrees with the primary and scattered collimator slits set at 0.5 mm and slit separation distances of 300 mm. The x-ray tube voltage was 70 kV. The spectra are presented as an intensity/momentum transfer plot where momentum transfer, x, is defined as:

$$x = \frac{1}{\lambda} \sin\left(\frac{\theta}{2}\right) \qquad [11]$$

where λ is the wavelength of the photon and θ the scattering angle.

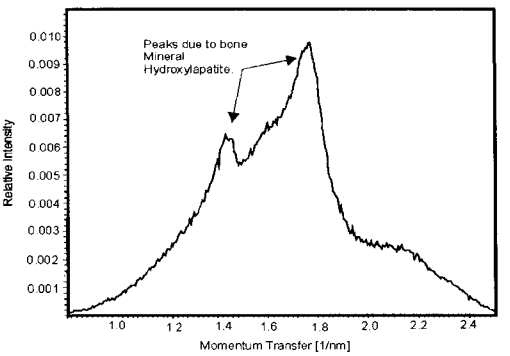

Figure 18. A typical diffraction spectrum for bone material showing peaks characteristic of hydroxylapatite.

Figure 18 clearly shows two peaks that are characteristic of the bone mineral hydroxylapatite. It is the intensity of these peaks that are important as they represent the number of scattering centres, i.e. the amount of bone material, that is in the scattering volume.

When making estimates of bone disease by any technique it is normal to compare the test case against a matched population sample distribution. However, comparative measurements from EDXRD spectra cannot be made directly in their raw form because the bone, through which the incident and scattered photons must pass, leads to attenuation of the measured spectra. Some of the photons are photoelectrically absorbed while others may be scattered from their original direction hence not reach the detector. These processes have been described in section 2. The cortical bone plays a particularly significant role in this as shown in Figure 19. In this example, the parameters for each measurement were the same, the only difference being the removal of the cortical bone around the measurement site. It can be seen that the lower energy peaks are preferentially absorbed, and some information may be lost completely. A correction for this must be made to the spectra and two methods will be described here.

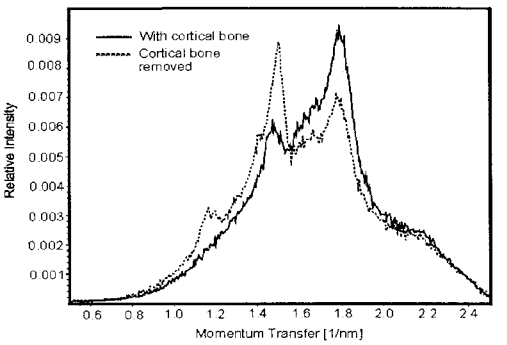

Figure 19. Attenuation of the measured spectrum due to the surrounding cortical bone.

The first method involves taking a radiograph of the bone sample alongside a suitable calibration step wedge usually made from a bone equivalent material or aluminium. Once the radiograph has been developed, the EDXRD measurement site is analysed using an optical densitometer and given an equivalent thickness of aluminium taken from optical density measurements made on the image of the step wedge (see section 5). To correct for attenuation, each momentum transfer (hence energy) intensity value in the spectrum is corrected individually using Equation [2] with the appropriate linear attenuation coefficient, μ, for the energy of each channel, and the equivalent thickness of aluminium for x. This method of attenuation correction is time consuming and requires resources i.e. taking a radiograph and finding an equivalent thickness of step wedge material. An alternative method uses the relative attenuation of two peaks of the same material within the measured spectrum. It can be seen from Figure 19 that the lower energy peak of the hydroxylapatite is attenuated preferentially to the higher energy peak when the cortex is present. The ratio of the number of photons in these two peaks can be used as a representation of the transmission thickness, x, in equation [2].

8.1 EDXRD and Diagenesis.

One way of examining diagenetic change is to use conventional x-ray diffraction and microprobe techniques, that will determine the mineral constituents and elemental composition of bone. These are useful tools but both require preparation of the bone sample.

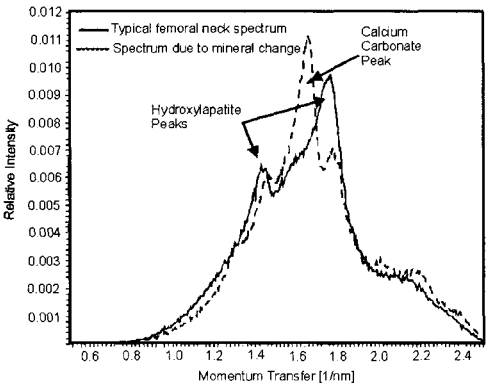

Figure20. Scattering signatures for the two bone samples, one showing features expected of bone; the other evidence of the presence of calcium phosphate.

X-ray diffraction requires part of the sample to be finely powdered and the microprobe requires a thin slice of bone, which is set in methylmethacrylate. Pilot work has been undertaken to employ EDXRD to determine mineral composition of bone in a non invasive manner (Farquharson and Brickley 1997). Figure 20 shows two EDXRD signatures from bone samples taken from Redcross Way in the parish of St. Saviours, Southwark, London. The solid line is the typical spectrum we expect from the hydroxylapatite in the bone. The dashed line showed a variation that occurred in some of the samples due to calcium carbonate being present which it is believed may have been deposited in the trabecular region from contact with ground water.

The technique could be extended to look for other minerals caused by diagenetic change or contamination of soil etc. This could be an important non invasive method of checking the integrity of bone samples before subjecting them to some of the bone mineral measuring techniques described above. Any technique that measures the attenuation of a beam of photons is dependent on the composition of the absorbing medium and hence should be accurately known.

9. A STUDY TO MEASURE THE TRABECULAR BMD OF 4TH LUMBAR VERTABRAE

This piece of work was part of a study to try to establish if osteoporosis was present in the population of East London in the 1700's. One aspect of this determination is the measurement of the trabecular bone content of the 4th LUMBAR vertebra. The bones were

excavated from two sites, one set being from the Redcross Way burial ground in the borough of Southwark, London, and were approximately 200 years old with an age range of individuals from 16 to over 45 years. Measurements were made on twenty-five 4^{th} LUMBAR vertabrea from this site. A second set of bones were from a burial site in Farringdon St. London, and were also approximately 200 years old with a large range of individual ages. Measurements were made on 18 samples from this site. The 4^{th} LUMBAR vertebra was chosen for this part of the study because the measurement site could be chosen in the body of the vertebra which consists mainly of trabecular bone.

DEXA measurements were made on each sample from the Redcross Way site on a Lunar DPX-L scanner. The scanner has various scanning options depending on the site of the body being used. After consultation with the manufacturers, the forearm option was chosen as the software used in the processing assumes no soft tissue surrounding the bone. This meant no soft tissue substitute material needed to be supplied, the option only requires the use of the tissue equivalent platform, made of delrin, which is placed such that the forearm of the patient rests on the platform. A high resolution scan was used which is recommended for measurements with a small region of interest. Two measurements were made of each sample, one being rotated 180° relative to the other. Regions of interest were set over the predetermined measurement volume and two bone mineral density readings recorded that were then averaged.

An estimation of the precision of the DEXA measurements was made by recording ten bone mineral density readings of a chosen bone sample over the same region. This was repeated for a number of samples with varying density values and the mean and standard deviation of the readings calculated. Two standard deviations were expressed as a percentage of the mean for the value of the precision and plotted as a function of the mean bone mineral density. The plot can be seen in Figure 21. From this curve the precision of the BMD for each sample could be estimated. It can be seen that the precision is poor particularly with low density samples. The precision of normal DEXA readings on calibration phantoms is approximately 1% (Mazess et al 1998) which would indicate that, although using the forearm option on the machine, the software routines in the analysis of the attenuation data may not be suitable for low bone mass archaeological samples. Some of the very low bone mass samples did show a zero bone density reading using DEXA which is described later.

EDXRD measurements were then made on the samples from the Redcross Way site. The exposure factors used were 70 kV and 20 mA incident spectrum from a tungsten target continuous operation x-ray tube. The scatter angle used was 5°. The collimator geometry was a 0.5 mm slit width and a collimator aperture separation distance of 300 mm which gives an acceptable photon count rate. Each sample was positioned in the diffractometer such that the predetermined measurement volume within the vertebral body matched, as closely as possible, that measured using the DEXA machine. Each measurement was carried out for 1000 seconds which gave good counting statistics for all of the samples being measured such that the error in each of the peaks of interest was approximately 1%. The raw EDXRD data was then corrected for attenuation using both the optical densitometry method and the peak ratio method described in Section 8.

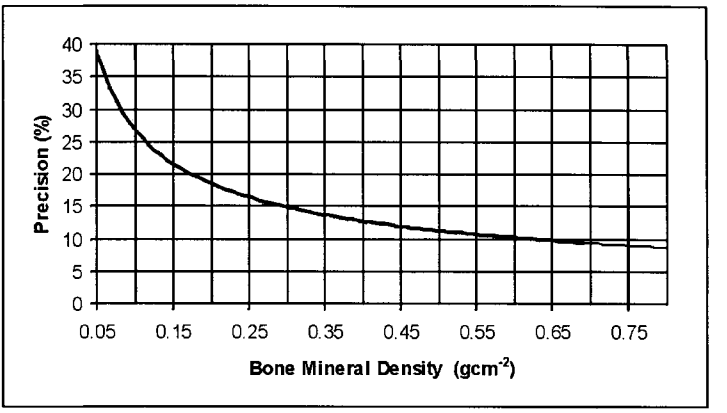

Figure 21. Estimated precision for DEXA measurements as a function of bone mineral density.

The final stage of the experimental procedure for the Redcross Way samples was to physically remove the measurement volume from the vertebral body. The density was then determined by calculating the exact volume and measuring the mass. This procedure enabled a direct measurement of the bone density to be made and could be used as reference data to compare with DEXA and EDXRD.

The total of the measurements made from each of the three modalities were all normalised to unity and then compared. Figure 22 shows scatter plots comparing the reference data and DEXA data. Figure 23 shows a similar plot for the EDXRD data with both methods of attenuation correction.

The R^2 values for the DEXA data is 0.74. It can be seen that the EDXRD technique has the better correlation with the reference data with R^2 values for the photodensitometry attenuation correction and peak ratio correction of 0.93 and 0.92 respectively. Several of the DEXA readings were recorded as zero, suggesting there is a lower limit to which the DEXA clinical system is sensitive enough to detect any bone mass.

If EDXRD is to be used for measuring bone mineral density, a calibration model is needed from which to predict the density from the attenuation corrected scattered spectrum. In order to carry this out, a least squares regression model was carried out on the measurements made on the Redcross Way samples i.e. mapping the EDXRD data to the known reference data. EDXRD measurements were now made on the samples from the Farringdon St. site, each sample had 10 spectra recorded. The data was corrected for attenuation using the peak ratio method. The BMD could now be predicted from the EDXRD data using the calibration model. The mean and standard deviation of the 10 predicted BMD values from each sample was calculated. The predictions were tested by omitting the measurement volume and obtaining the true BMD as described above.

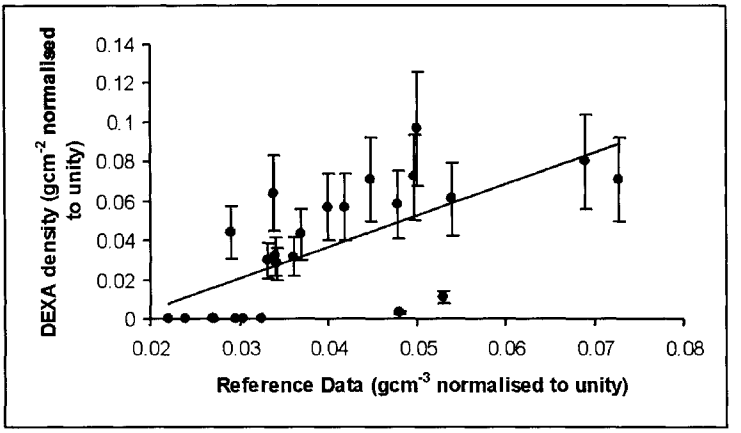

Figure 22. Scatter plot of reference data and DEXA bone mineral density.

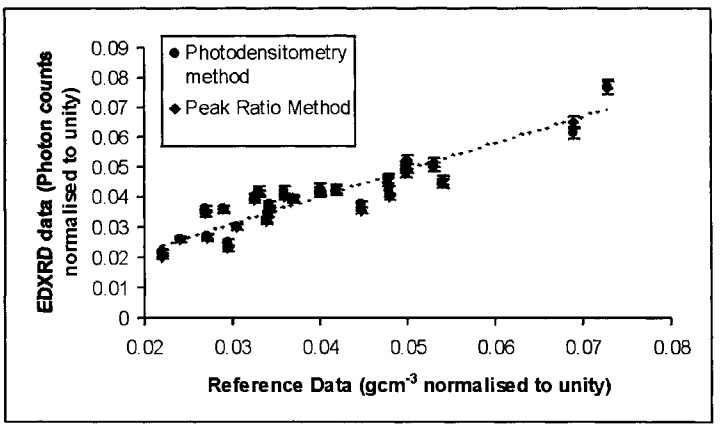

Figure 23. Scatter plot of reference data and EDXRD data.

Figure 24 shows the predicted BMD values obtained from the calibration model with the error bars being the estimated precision as describe above. The predictions from the calibration model were accurate to within approximately 2% and the precision was estimated to be approximately ±5%.

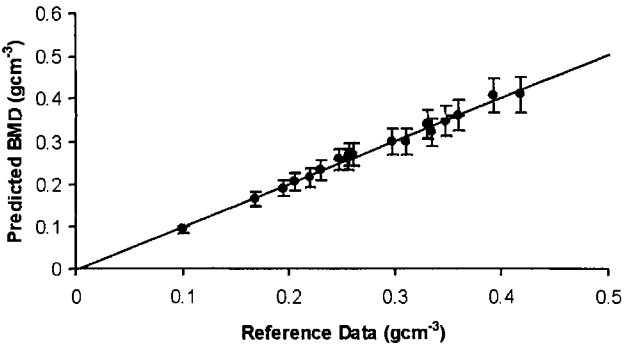

Figure 24. Predictions of BMD made using the calibration model.

10. SUMMARY

There are several methods that can be used to make an estimate of BMD in archaeological bone. Indeed there are others not covered in this paper including quantitative computerised tomography, Compton scatter densitometry, and neutron activation analysis. The method you choose should be based around an understanding of the technique and understanding the specific measurement you wish to make. One problem in examining bone density in archaeological bone is a lack of comparability between the results obtained from the various studies undertaken. Comparability between results is essential in order that a better understanding of possible time, geographical, or culturally related differences between 'populations' can be gained. Such an understanding would be of considerable value in the light of what is known about osteoporosis in modern populations, and contribute greatly to understanding the evolution of human disease.

References

Armelagos, G.J. Mielke, J.H. Owen, K.H. Van Gerven, D.P. Dewey, J.R. Mahler, P.E. 1972. Bone growth and development in prehistoric populations from Sudanese Nubia. *Journal of Human Evolution*

Aufderheide, A.C. Rodríguez-Martín, C. 1998. *The Cambridge Encyclopedia of Human Paleopathology.* Cambridge: Cambridge University Press.

Barnett E. and Nordin B.E.C. 1960 The radiological diagnosis of osteoporosis: a new approach. *Clin. Radiol.* **11** 166-174

Bell L.S., Wong F.S., Elliot J.C., Boyde A. and Jones S.J. 1993 Post mortem changes in buried human bone. *Journal of Anatomy* **183** 196

Bell LS 1990. Palaeopathology and diagenesis: An evaluation of structural changes using backscattered electron imaging. *Journal of Archaeological Science* 17:85-102.

Bennike P. and Bohr H. 1990 Bone mineral content in the past and Present. In C.Christiansen and K. Overgaard, *Third international Symposium on Osteoporosis.* Copenhagen: Osteopress 89-91

Brain, C.K. 1969. The contribution of Namib Desert Hottentots to an understnding of australopithecine bone accumulations. *Scientific Papers of the Namib Desert Research Station* 39: 13-22.

Brickley, MB 1998. Age-Related Bone Loss and Osteoporosis in Archaeological Bone: A study of two London collections, Redcross Way and Farringdon Street. Ph.D. Thesis Uinversity of London.

Dequeker J. 1976 Quantitative radiology: radiogrammetry of cortical bone *Br. J. Radiol.* **49** 912-920

Douglas B, Hanson JE, Buikstra 1987. Histomorphological alterations in buried human bone from the Illinois Valley: Implications for paleodietary research. *Journal of Archaeological Science* 14:549-563.

Ericksen M.F. 1976 Cortical bone loss with age in three Native American populations. *American Journal of Physical Anthropology* **45** 443-452

Farquharson M.J. and Speller R.D. 1998 Trabecular bone mineral density measurements using Energy Dispersive X-Ray Diffraction (EDXRD) *Radiat. Phys. Chem.* **51** 607-608

Farquharson M.J., Brickley M. and Speller R.D. 1997 Measuring bone mineral density in archaeological bone using energy dispersive low angle x-ray scattering techniques *Journal of Archaeological Science* **24** 765-772

Farquharson, M.J. Brickley, M. Speller, R.D. 1997 Measuring Bone Mineral Density in Archaeological Bone using Energy Dispersive Low Angle X-Ray Scatting Techniques. *Journal of Archaeological Science* 24: 765-772.

Fiori, M.G. Nunzi, M.G. 1995. The earliest documented applications of X-rays to examination of mummified remains and archaeological materials. *Journal of the Royal Society of Medicine* 88: 67-69.

Frigo P, Lang C 1995 Osteoporosis in a woman of the Early Bronze Age. *New England Journal of Medicine* 333:1468.

Hackett CJ 1981 Microscopical focal destruction (tunnels) in exhumed human bones. *Medicine Science and the Law* 21:243-265.

Hanson D.B. and Buikstra J.E. 1987 Histomorphological alteration in buried human bone from the lower Illinois valley: Implications for palaeodietary research. *Journal of Archaeological Science* **214** 549-563

Henderson J 1987 Factors determining the state of preservation of human remains. In (Boddington A, Garland AN, Janaway RC, Eds.). *Death Decay and Reconstruction. Approaches to Archaeology and Forensic Science.* Manchester: Manchester University Press pp.43-54.

Jayasinghe J.A.P. 1991 A study of change in human trabecular bone structure with age during osteoporosis. PhD. Thesis UCL London

Kneissel M., Boyde A., Hahn M., Treschler-Nichola M., Kalchhauser G. and Plenk H. Jr. 1994 Age and sex dependent cancellous bone changes in 4000y BP population. *Bone* **15** 539-545

Kosanetzky J., Knoerr B., Harding G. and Neitzel U. 1987 X-ray diffraction measurements of some plastic materials and body tissues. *Medical Physics* **14(4)** 526-532

Kreutzer, LA. 1992. Bison and deer bone mineral densities: comparisons and implications for the interpretation of archaeological faunas. *Journal of Archaeological Science* 19:271-294.
Lammbert JB, Simpson SV, Szpunar CB, Buikstra JE 1985 Bone diagenesis & dietary analysis. *Journal of Human Evolution* 14:477-482.
Lapedes DN (Ed.) 1978 *Mc Graw-Hill Encyclopaedia of the Geological Sciences.* Mc Graw-Hill Inc: New York pp.153-155.
Lees B, Molleson T, Arnett TR, Stevenson JC 1993 Differences in proximal femur bone density over two centuries. *The Lancet* 341:673-675.
Luggar R.D. and Gilboy W.B. 1994 Application of Rayleigh scattered photons to substance identification. *Nuclear Instruments and Methods in Physics Research.* **A353** 650-653
Luggar R.D., Horrocks J.A., Farquharson M.J., Speller R.D. and Lacey R.J. 1996 Real time analysis of scattered x-ray spectra for sheet explosive detection. SPIE **2936**
Lyman, RL Houghton, LE. Chambers, AL. 1992 The effects of structural density on marmot skeletal part representation in archaeological sites. *Journal of Archaeological Science* 19:557-573.
Lyman, RL. 1994 *Vertebrate Taphonomy.* Cambridge: Cambridge University Press.
Marchiafavia V, Bonucci L, Ascenzi A 1974 Fungal osteoclasia: A model of dead bone resorption. *Calcified Tissue Research* 14:195-210.
Marchiafavia V., Bonucci L. and Ascenzi A. 1974 Fungal osteoclasia: a model of dead bone resorption. *Calcified Tissue Research.* **14** 195-210
Mays S., Lees B. and Stevenson J.C. 1998 Age-dependent bone loss in the femur in a medieval population *International Journal of Osteoarchaeology* **8** 97-106
Mays S.A. 1996 Age-dependent cortical bone loss in a medieval population *International Journal of Osteoarchaeology* **6** 144-154
Mazess R.B., Sorenson J.A., Hanson J.A., Collick B.D. and Smith S.W. 1988. Dual Energy X-ray Absorptiometry (DEXA) In: Osteoporosis and bone mineral measurement, IPSM
Molleson, T. Cox, M. 1993 *The Spitalfields Project Volume 2 – The Anthropology. The Middling Sort.* Council for British Archaeology Research Report 86.
Naor E., Di segni V., Robin G., Makin M. and Menczel J. 1972 Intra-observer variability in the determination of the metacarpal cortical index *Br. J. Radiol.* **45** 213-217
Nelson DA 1984 Bone density in three archaeological populations. *American Journal of Physical Anthropology* 63:198.
Njeh C.F., Apple K., Tempertion D.H. and Boivin C.M. 1996 Radiological assessment of a new bone densitometer-the Lunar EXPERT *The British Journal of Radiology.* **69** 335-340
Ortner, D.J. Putschar, W.G.J. 1985 *Identification of Pathological Conditions in Human Skeletal Remains.* Smithsonian contributions to anthropology, number 28. Washington: Smithsonian Institution Press.
Pate (F) D, Brown KA 1985 The stability of bone strontium in the geochemical environment. *Journal of Human Evolution* 14:483-491.
Pate F.D. and Hutton J.T. 1988 The use of soil chemistry data to address post mortem diagenesis in bone mineral. *Journal of Archaeological Science.* **15** 729-739
Perzigian AJ 1973a. Osteoporotic bone loss in two prehistoric Indian populations. *American Journal of Physical Anthropology* 39:87-96.

Perzigian AJ 1973b The antiquity of age-associated bone demineralization in man. *Journal of the American Geriatrics Society* 21:100-105.
Raptis G 1992 Paleopathological investigation of osteoporosis with dual energy X-ray absorptiometry. Validation of bone mineral content determination in ancient specimens. *Orvostorteneti Kozlemenyek, Communicationes De Hisioria Artis Medicinae* 1-8:133-140.
Roberts, C. A. 1991 Scientific methods in paleopathology: past present and future. In P. Budd, B. Chapman, C. Jackson, R. Jannaway & B.O'Haway eds.) *Archaeological Sciences 1989: Proceedings of a Conference on the Application of Scientific Techniques to Archaeology*. Oxford: Oxbow Books. 373-385.
Royle G.J. and Speller R.D. 1991 Low angle x-ray scattering for bone analysis. *Phys. Med. Biol.* **36** 383-389
Royle G.J. and Speller R.D. 1995 Quantitative x-ray diffraction analysis of bone and marrow volumes in excised femoral head samples. *Phys. Med. Biol.* **40** 1487-1498
Sambrook PN, Browne CD, Eisman JA, Bourke SJ 1988 A case of crush fracture osteoporosis from late Roman Pella in Jordan. *OSSA* 13:167-171.
Singh M, Nagrath AR, Maini PS 1970 Changes in the trabecular pattern of the upper end of the femur as an index of osteoporosis. *Journal of Bone and Joint Surgery* 52a: 457-67.
Stout S, Simmons DJ 1979 Use of histology in ancient bone research. *Yearbook of Physical Anthropology* pp. 228-249.
Thompson DD 1980 Age Changes in Bone Mineralisation, cortical thickness, and Haversian canal area. *Calcified Tissue International.* 31:5-11.
White E.M. and Hannus L.A. 1983 Chemical weathering of bone in archaeological soils. *American Antiquity* **48** 316-322

Radiation in Art and Archeometry
D.C. Creagh and D.A. Bradley (editors)

The role of SIMS in understanding ancient materials

A. Adriaens

University of Antwerp, Department of Chemistry, Universiteitsplein 1,
B-2610 Antwerp, Belgium

The role of Secondary Ion Mass Spectrometry (SIMS) in the study of mediaeval stained glass, buried glass, and stone and ceramic objects is discussed. Also discussed is its use for dating of obsidian and teeth, and the determination of the provenance of metallic objects.

1. INTRODUCTION

As the field of archeological science or archaeometry keeps expanding, more analytical techniques become available to provide invaluable information in the interpretation of art objects and archaeological artefacts. Among them, secondary ion mass spectrometry (SIMS), which belongs to the most powerful analytical techniques for the compositional information of surfaces, has gained a growing interest.

SIMS is a technique in which bombardment of energetic primary ions on a solid specimen removes particles by sputtering. The emitted particles are partially ionized and are directed into a mass analyzer, where they are separated and detected as a function of their mass. The main advantages of using SIMS include its capability of performing in-situ analyses with a high sensitivity (ppb-ppm range) and a high mass resolving power. In particular its possibility to depth profile and to image elemental distributions on a μm scale has made SIMS into a notably popular tool.

On the whole SIMS contributes to three main areas within archaeometry: conservation science involving the study of decay processes, dating methods to acquire absolute or relative chronologies, and third artefact studies which provide information on provenance, technology and usage.

This paper will give an overview of the present day investigations that are conducted to study ancient materials using secondary ion mass spectrometry and will be grouped according to the three above-mentioned categories. Its capabilities and limitations will be addressed to illustrate its role within this interdisciplinary field. Reading through the various examples however, it should be kept in mind that in general hardly any applied analysis depends on the application of a single analytical tool. Very often it is by the application of a wide range of techniques and the synergy of answers that complex problems can be solved. And even

though it is not always explicitly mentioned in this paper, as a rule SIMS is indeed usually used to complement information from other methods.

2. BASIC CONCEPTS OF SIMS

Secondary ion mass spectrometry (SIMS) is an analytical technique which is based on the mass spectrometric analysis of ions that are generated by the interaction of a primary ion beam (keV range) with a solid sample. The ion beam (Ga^+, Ar^+, Cs^+, O^-, SF_5^+, ...) penetrates the solid material and sets of a cascade of atomic collisions, which can eventually transfer enough momentum in the backward direction to result in the ejection of surface particles. Some of this sputtered material is emitted either as positive or negative ions. These so-called secondary ions are accelerated into a mass analyzer, where they are separated according to their masses.

2.1. Operational regimes

A distinction is made between two operational regimes in SIMS, each of which yields fundamentally different information and analytical features. The "dynamic SIMS" technique rapidly erodes the surface with an intense beam of ions and is mainly used for depth profiling and inorganic trace analysis. "Static SIMS", on the other hand, is less destructive as it uses a lower ion flux of primary ions. Each molecular micro-environment is hit by only one primary ion and as a result, only the outer monolayer at the surface is analyzed. This technique is primarily used for obtaining organic and inorganic information on the uppermost surface monolayer. Unless otherwise mentioned, the studies discussed in this paper use dynamic SIMS.

Figure 1 shows a detailed setup of the Cameca IMS 3f / 4f (Cameca, France), which is a commercial dynamic SIMS instrument. Since the instrument is well known and has been discussed repeatedly, the reader is referred to the literature on this subject (Benninghoven et al., 1987). Only a brief overview will be given here.

The instrument can schematically be subdivided into two separate parts. The primary ion beam system includes the ion sources and the primary beam optics, while the secondary ion beam system basically consists of an electrostatic sector, a magnetic sector and the detector systems. The primary ions are generated in the duoplasmatron source (O_2^+, Ar^+, O^-) or by the Cs^+ ion source. Both sources are held at a potential in the order of kV and an ion beam is extracted by a conical lens, which is fixed at ground potential. The beam is deflected and mass filtered by an electrostatic deflector and by a primary magnet, which serves to provide a clean ion beam. It then passes through a series of electrostatic lenses, deflectors and apertures. The purpose of these ion optics is to control the intensity, size and shape of the ion beam, finally focusing it onto a spot on the sample surface. Typical ion current densities in this instrument are of the order of μAcm^{-2}.

The secondary ion beam system contains three functional components: the ion extraction system, the mass spectrometer and the detectors. A series of electrostatic lenses is configured

so that ions emitted from each point on the sample surface converge in a corresponding image point, thereby forming a real magnified image of the sample surface. In the magnetic sector, the ion image is filtered with respect to a particular mass-to-charge ratio. The filtered image is displayed on a fluorescent screen or the ion beam is measured using an electron multiplier or a Faraday cup.

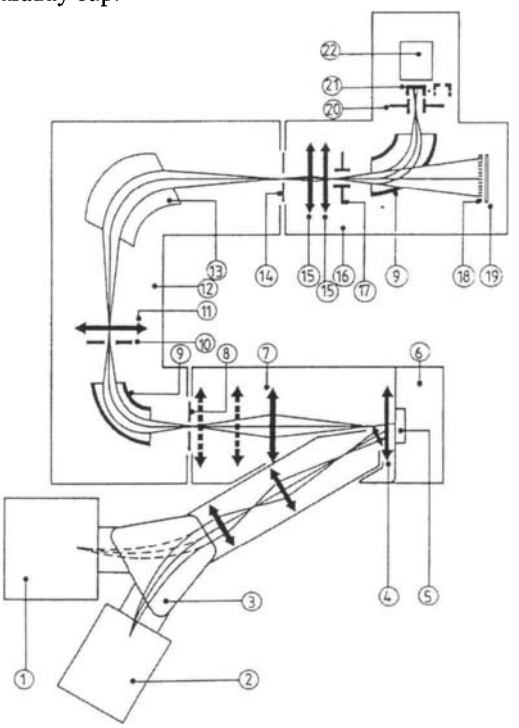

1. Duoplasmatron source
2. Cs source
3. Primary mass filter
4. Immersion lens
5. Sample
6. Sample chamber
7. Transfer optics
8. Entrance slit
9. Electrostatic sector
10. Energy slit
11. Spectrometer lens
12. Mass spectrometer
13. Secondary mass filter
14. Exit slit
15. Projection lenses
16. Projection, display and detection unit
17. Deflector
18. Microchannel plate
19. Fluorescent screen
20. Deflector
21. Faraday cup
22. Electron multiplier

Figure 1. Schematic representation of the Cameca IMS 3f/4f dynamic SIMS.

2.2. Types of information which can be obtained

The SIMS technique can be operated in different ways depending on the type of data that have to be obtained from the analysis. Three different modes are distinguished: mass spectra, images and depth profiles. They are shown schematically in Figure 2.

Mass spectra yield compositional information on a specific point or area of the sample. The detected signal is plotted as a function of mass and elements from the entire periodic system, starting with hydrogen, can be detected with detection limits in the order of ppb-ppm. As the beam can raster a specific area of the surface, SIMS enables to provide distributional information allowing two-dimensional element-mapping or imaging of the surface. Under

suitable conditions, the ion beam removes the surface of the sample as an on layer-by-layer basis. Signals can then be detected as a function of the bombardment time or depth. This mode of operation is called depth profiling and is very useful for instance for the investigation of diffusion processes. The time to depth conversion is done by measuring the total depth of the sputtered crater with a profilometer, while assuming a constant sputter rate. Ion yields are sensitive to the chemical composition of the sample and the conversion of the detected signals to concentrations is in practice done by calibrating against standards of known composition.

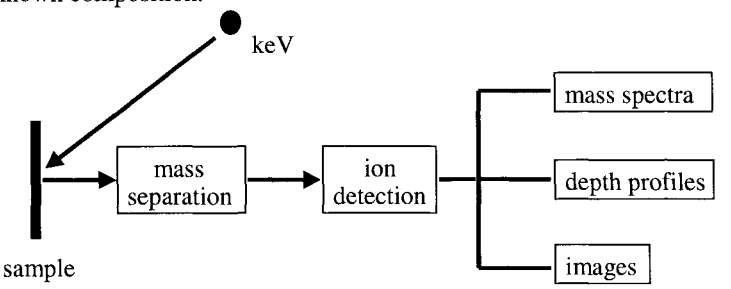

Figure 2. Different types of analytical information available using the SIMS technique.

2.3. Sample properties and preparation

The sample preparation for SIMS is not very elaborate as analyses are done directly on the solid sample. A few limitations apply however. One of them is the sample size. Depending on the instrument type this may vary but in general the sample size is in the order of maximum 25 mm in diameter and 5 mm in height. Second the sample needs to be flat and should be mounted in parallel to the extraction electrode. Not meeting these conditions may result in non-uniform sputtering which will hamper the interpretation of the results. Third it is necessary that the samples are conducting. As primary ions are implanted into the sample, it is very likely that the surface potential of non-conducting samples, such as ceramics and glasses, will change drastically which may disturb the experiments in several ways. The emission of ions from the surface can be lowered or even stopped and ultimately the primary ion beam can be deflected away so that sputtering will stop. Charge compensation techniques exist which can overcome these problems. Commonly applied methods are electron flooding or coating the surface with a very thin layer of gold (the latter only in dynamic SIMS).

3. CONSERVATION

3.1. Medieval glass paintings

One of the areas in which the SIMS technique has up to now been frequently used is the deterioration study of glass objects. Investigations have shown that the exposure to a moist environment causes the glass to deteriorate, including both chemical and structural changes. The initial stage of attack is a process which involves ion exchange between the alkali ions which are present in the silicate structure of the glass, such as Na, K, and hydrogen from the environment (Doremus, 1973) as is shown in equation (1).

$$\sim Si\text{-}O^- M^+ + H^+ \Leftrightarrow \sim Si\text{-}OH + M^+ \quad (1)$$

This leads to the formation of a leached layer or so-called "gel layer" in which alkaline elements are depleted. Provided the glass is in continuous contact with water, the attack will eventually lead to a complete breakdown of the silicate structure. In case of atmospheric attack, the leached ions will interact with components from the ambient atmosphere such as carbon dioxide and sulfur dioxide which will lead to a crust formation including products such a calcite ($CaCO_3$) and gypsum ($CaSO_4.2H_2O$) (Doremus, 1973). The backscattered electron image in Figure 3 shows the layered structure of a corroded glass object.

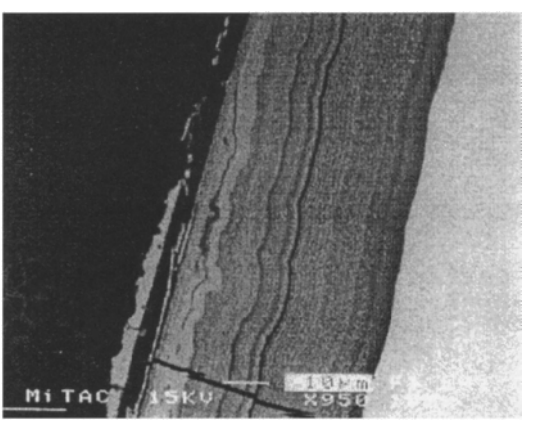

Figure 3. Backscattered electron image of the corrosion layer of a glass object. Magnification 950. Reproduced from Aerts (1998).

Figure 4. Medieval glass painting. Reproduced from Schreiner (1991) with the permission of Springer-Verlag.

It is presumed that Medieval glass paintings in particular are very sensitive to atmospheric attack or weathering due to their high content of potash and therefore also due to a much lower silica content than for instance modern glasses (Schreiner et al., 1984). The attack reduces their thickness and influences the transparency due to the crust formation.

In a study by Schreiner (1991), SIMS is used to characterize the deterioration process on a Medieval glass painting (Figure 4) from the Heiligenkreuz, a monastery near Vienna in Austria. The aim existed in determining the quantitative depth resolution of the elements in the glass. The sample was coated with a thin layer of gold before analysis to minimize the charging. Figure 5 shows the depth profile on a piece of glass painting that is rich in K, Ca and Pb.

The time scale has been converted into a depth scale by measuring the crater depth. Signals were converted to concentrations (at %) using relative sensitivity factors, which were determined by analyzing a glass standard.

From the depth profile it can be seen that elements such as K, Ca and Ba are heavily depleted in the leached layer in comparison to the bulk, while Na on the other hand seems to be quite constant or is even slightly increased. At the same time the incorporation or replacement by hydrogen can be observed in the leached layer. All elements however are enriched in the outer layers where the crystalline corrosion products have formed.

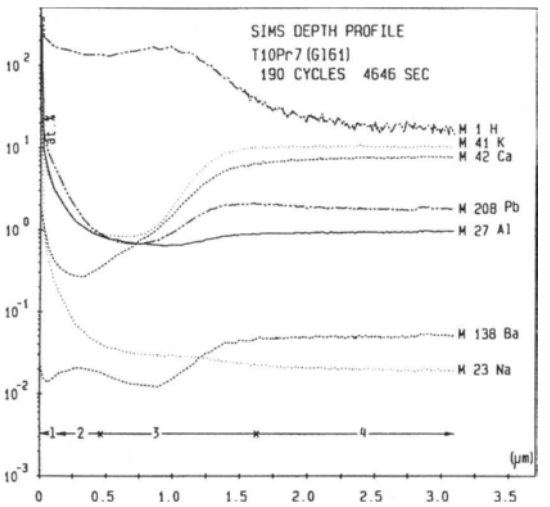

Figure 5. Quantitative depth distribution of a Medieval glass painting measured by SIMS: layer 1 is the gold layer, layer 2 is the outermost region with corrosion products, layer 3 is the leached layer and layer 4 is the bulk material. Reproduced from Schreiner (1991) with the permission of Springer-Verlag.

In general it could be concluded that not only alkaline elements but also earth alkaline elements, such as Mg and Ba, leach from the bulk. In addition the experiments have shown that SIMS is a very suitable technique to study the ion exchange process which occurs during weathering. Especially the possibility to detect hydrogen, makes SIMS into a very useful tool in these type of studies.

3.2. Simulation burial experiments with model glasses

One way of learning more about the factors which determine the alteration of glass in damp soil is to perform a series of controlled laboratory experiments in which the burial of glass objects is simulated. A systematic and detailed laboratory study was performed at the University of Antwerp in Belgium together with the Fraunhofer-Institut fur Silikatforschung in Bronnbach, Germany (Aerts, 1998). Their idea was to carry out a series of controlled corrosion experiments. In these, a number of fast-corroding glass types would be brought in contact with damp soil to investigate the importance of parameters such as the composition of the glass and the soil, the pH, the water content in the soil, the temperature and the exposure time. The corrosion layer was then in a second stage characterized using scanning electron microscopy (SEM) and SIMS.

In their experiments three compositions were made from analytically pure oxides and carbonates. The selected compositions were restricted to a particular three component system SiO_2-K_2O-CaO, which is very sensitive to attack by water and humidity. The composition of the samples is shown in Table 1. M1.0 is the most sensitive one as it contains the highest K_2O / Si_2O ratio. Composition MIII is to be the least sensitive one.

The model glasses were brought into a series of controlled environments in the laboratory. Soil was put into plastic boxes which were hermetically closed from the surroundings. As a reference, one box was kept at room temperature. Nothing was added to the soil. For the other boxes water or CaO (to change the pH) was added and were kept either at lower or higher temperature than the reference box. Table 2 summarizes the conditions.

After the so-called excavation of the glasses from the various test environments, cross sections were made, which were embedded in resin. SEM measurements were performed to determine approximately the thickness of the corrosion layer and showed that time is an important factor: corrosion is much more extensive after 6 months in comparison to 3 months, but the correspondence does not follow a linear behavior and eventually reaches a maximum. The corrosion occurs much faster when the glass is exposed to damp soil in comparison to the atmosphere. In addition a faster corrosion is observed with higher temperatures and a higher pH. The latter conclusion should however be interpreted with some care as the pH range was limited plus was changed by adding CaO, which means in fact that the composition of the soil also changes.

Table 1
Composition of the model glasses used in the simulation burial experiments (mol %).

	M1.0	M2.0	MIII
SiO_2	59.8	61.2	62.3
CaO	20.0	23.4	27.8
K_2O	20.2	15.4	9.9

Reprinted from Aerts (1998).

Table 2
Conditions used in the simulation burial experiments.

	Parameter values
Humidity / water content	1x, 2x, 3x, 4x, saturated
pH	5.6, 7.6, 8.5, 8.8, 9.1
Temperature	-10 °C, RT, 50 °C
Glass-soil exposure time	3 months, 6 months

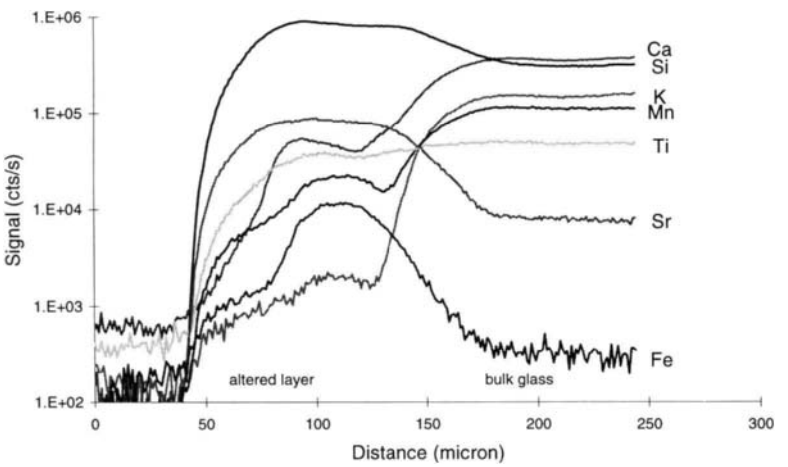

Figure 6. SIMS line profile of the major and minor elements in model glass M1.0. The conditions were saturated water, RT, and pH=5.6. Reproduced from Aerts (1998).

To obtain data on the leaching behavior and the distribution of the major, minor and trace elements, SIMS line profiles were made across the cross section of the glass samples. In these experiments, the bombarding ion beam is moved across the sample in distinct steps of a few μm. At each ion beam position compositional data of the sample are acquired. Figure 6 shows the results for the major and minor elements and shows that both K and Ca have leached out of the glass. The distribution of the trace elements on the other hand shows a more complicated behavior (not shown here), and indicates the formation of sub-layers encountered in the leached layer. Figure 6 is representative for all the measurements and conditions. Some small differences can be seen in the location of the maximum of certain signals but the elemental tendencies are the same. It can therefore be concluded that apart from the thickness of the layer no differences in the composition of the altered layer can be seen, even with different glass compositions.

3.3. Conservation of stone

Investigations to determine the origin and nature of superficial coatings, used to protect building materials from weathering processes, is an important task in building conservation. For several decades organosilicon compounds $RSiX_3$ (R=CH_3, Phe; X=OCH_3, OC_2H_5 or Cl) have proven to be one of the most efficient chemical water repellents. Nevertheless questions of long-term effectiveness of impregnation and degradation phenomena at protective layers have been ignored to a certain extent and demand close attention. In a study by Bruchertseifer et al. (1997) static SIMS was used to investigate the effectiveness and durability of two commercial hydrophobic agents applied to sandstone of the Obernkirchener (Germany). Both propyl / octylsilane as well as a methyl / octylsiloxane mixtures have been used to try to prevent moisture uptake. In general static SIMS is known to be able to provide a wealth of information on polymers (Van Vaeck et al., 1999; Adriaens et al., 1999). Its advantage lies in particular in the capability of obtaining both molecular and organic information. SIMS spectra of both freshly soaked stone slabs as well as on weathered coatings of eight years are able to demonstrate a significant difference in the speed of hydrolysis and polycondensation reactions.

In the framework of the restoration of the "Santa Maria la Vetere" Renaissance church in Militello Val di Catania (Sicily), Ciliberto et al. (1995) carried out investigations to determine the chemical composition of the materials used in the coloration processes of the wall paintings. The goal of their research was to restore the remnants as closely as possible to the original condition, while at the same time controlling the degradation processes. Next to SIMS, the authors used SEM, energy dispersive x-ray microanalysis (EDX), electron spectroscopy for chemical analysis (ESCA) and x-ray diffraction (XRD) to study the most significant elements of the portal. The use of the different techniques proved to be necessary to get an overall view of the layered structure and the composition of the wall paintings and at the same time allowed to determine the chronological development of the technology used. SIMS data in particular contributed in identifying the pigments that were used.

3.4. Patina studies and microstructure of metal objects

The contribution of SIMS for the study of patina studies of metal objects has been shown useful for the rapid qualitative indication of phases and inclusions. In particular the ability to image the distributions of major and minor elements proves to be helpful in understanding the different types of corrosion mechanisms that can occur.

The complexity of corrosion however suggests that no single technique is able to provide a complete picture. In a study of two copper alloys from the Hasse collection, Wouters et al. (1991) used SIMS imaging to complement information from other techniques such as SEM and optical microscopy. Small samples were removed from the objects and were embedded in epoxy resin as cross sections, so that both the patina as well the bulk of the alloy could be analyzed. Based on the observed elemental distributions of silicon, calcium, potassium and chlorine the authors suggested a partly covered concretion growth as well as the presence of pitting corrosion, which has been very clearly initiated by chlorine.

Also in a study by Allen et al. (1995), the authors have made use of imaging and spectra to study a bronze filled bracelet from the Early Iron Age from northern Italy. They showed that the chlorine distribution is mainly confined to the grain boundaries. Figure 7 shows this distribution (white signal) over an analyzed area of 200 x 200 μm^2. The authors could also demonstrate a gradient of the chlorine concentration from the edge of the sample (upper left in Figure 7) to the center (lower right). The combination of these results allowed the authors to identify two sources for chlorine: the external environment in which the object was buried and the starting materials from which the bronze was made.

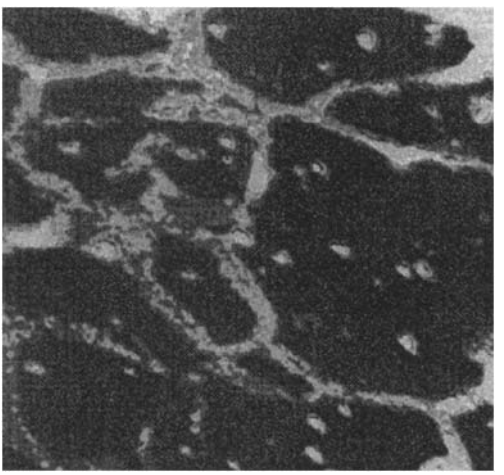

Figure 7. Secondary ion signal of $^{35}Cl^-$. Area of analysis is 200 x 200 μm^2. Reproduced from Allen et al. (1995) with the permission of IM publications.

4. DATING

4.1. Obsidian dating

Over the years several methods have been used to date obsidian artefacts. The most commonly one used is the hydration method (OHD) and is based on the fact that when a fresh surface of obsidian is exposed to the ambient atmosphere, water causes a hydration layer to form just below the surface. The thickness of this hydration layer ranges between less than 1 micron and more than 50 micron depending on the time of exposure and is usually measured using optical microscopy. Though used on a widespread basis, there are quite a few questions with regard to the reliability of this technique.

In a recent study by Anovitz et al. (1999), SIMS was used to investigate the limitations of the OHD method in more detail. The hydration rims of archaeologically recovered obsidian samples as well as natural glass samples were analyzed. The obsidian samples were chosen to represent a variety of environmental conditions and a variety of sources in order to allow to distinguish parameters that may influence the formation of the hydration rim. Signals for alkali elements as well as for H_2O were monitored as a function of depth. From these results the authors could conclude that the standard OHD methodology is insufficient for reliable dating as three main factors are in general overlooked: the water-concentration dependent diffusion, the effect of surface loss due to dissolution and the assumption that the actual diffusion front is sharp. Though these conclusions may sound pessimistic, the authors emphasize the regularity of their SIMS results and are therefore convinced that suitable changes in both measurement and modeling procedures should be able to make obsidian hydration useful for chronometrical purposes.

Other dating methods for obsidian which have been investigated by SIMS include depth profiling of the leached layer, which is in fact similar as in the deterioration studies of glass (see paragraph 3), and profiling of the nitrogen penetration. The latter is based on the fact that nitrogen penetrates the freshly exposed surface as a function of time (Ettinger and Frey, 1976). The determination of the nitrogen depth could then be used to calculate the length of time the surface has been exposed to that environment. Researchers from Oxford University were indeed able to show the presence nitrogen gradients (Hedges and Freeman, 1993). The question of course was whether they could actually be used to date obsidian. In a paper by Patel et al. (1999), the authors have tried to resolve this question using SIMS depth profiling. In their study they used samples from three different archaeological sites with different ages and one freshly cut. Depth profiles were taken over an analyzed area of 250 by 250 micron. Figure 8 shows the results of one of the samples. A nearly constant distribution for elements such as O, Si, Cl and Al can be observed, while there is a significant decrease according to depth for SiN^-. The authors chose to monitor the SiN^- signal over the N^- signal because it ionizes better and it does not have any significant interferences. A more detailed analysis on different spots of the same sample however showed that that the slope of the N signal seemed to correlate with pit-like features (40-120 μm in size) on the surface of the archaeological obsidian samples. The mechanism of their formation is unclear but the authors suggest the

pits to be stress related. They therefore conclude that the nitrogen profiles in aged obsidian are not necessarily due time dependent processes and care should be taken when interpreting.

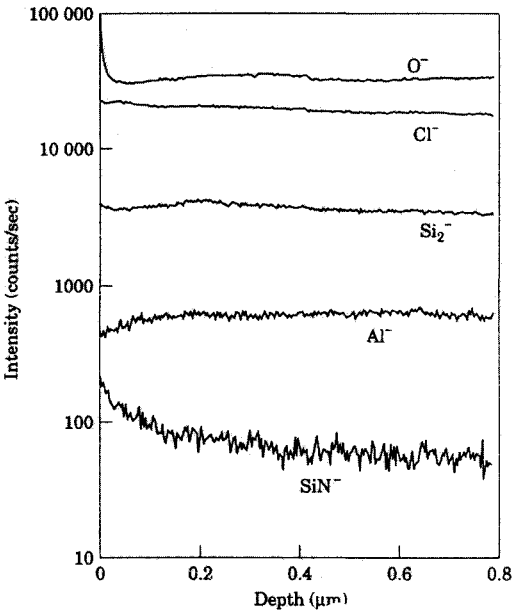

Figure 8. SIMS depth profile measured from a weathered obsidian surface. Reproduced from Patel et al. (1999) with the permission from Academic Press.

4.2. Trace element studies and dating of teeth

Teeth are mainly composed of apatite, a calcium fluoride phosphate, containing numerous impurities and elemental substitutions, which are influenced endogenously as well as by oral fluids. Also postmortem teeth continue to interact with the environment, which may prove to be interesting from an archaeological point of view, in that sense that the question arises whether the distribution of certain elements can give us dating information. Different regions of the teeth (Figure 9) can have varying element information. It is therefore very important to compare data on the same region of teeth, which implies that we need a technique with spatial resolution. In a series of investigations by Fischer et al. (1985, 1989) SIMS is used to explore the possibility of dating teeth by studying the diffusion pattern of specific elements. As a sample preparation each tooth was cut perpendicular to the surface in two parts and was embedded in an epoxy resin. The samples were gold coated to reduce potential charging.

Line scans were performed in which the beam was moved in steps of 5 to 15 μm along a straight line across the cross section of a tooth, thereby going from pulp of the tooth towards the outer surface. Figure 10 shows a line scan in which the concentrations for F, C, Mg, Ba and Pb are plotted. The right hand side of the figure represents the surface of the tooth, the left hand side is the pulp.

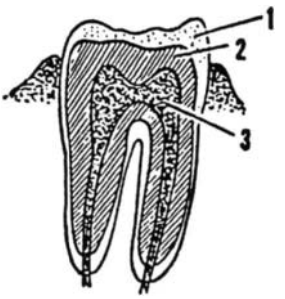

Figure 9. Cross section of a tooth showing the different dental tissues.

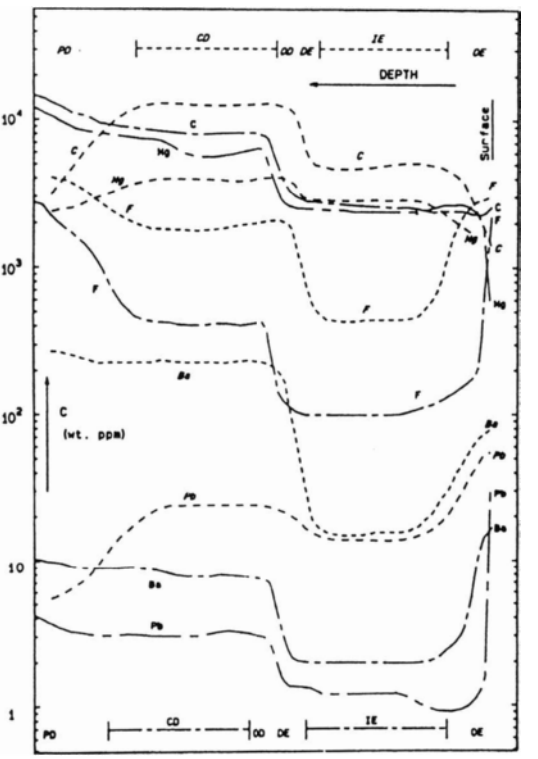

Figure 10. Line scan across the cross section of teeth. The left hand side represents the pulp, the right hand side the surface. The dashed curves are results from a tooth dating back to 1800 BC. The other ones are typical for recently extracted teeth of young adults. Reproduced with the permission of Springer-Verlag.

The broken line (— - —) is a typical profile for a recently extracted adult tooth, while the dashed line (- - -) comes from a young woman buried ca 1800 BC. In general it can be

observed that for each region of the tooth, that is enamel and dentin, the concentration for each element reaches a plateau value, which will make a comparison for a specific dental tissue between teeth easy. When the ancient tooth is compared to the modern tooth, certain elements seem to be enriched (Ba, Pb), other seem to be leached (Mg, C) which is most probably an influence from the geological environment of the burial site.

The fluorine concentration in the enamel can give information on the time of burial. It is known that the fluorine concentration at the outer enamel tends to saturate around 2000 ppm regardless the absolute age of the tooth and independent of the fluorine agent. The fluorine concentration at the inner enamel on the other hand is dependent from age and is zero for young children and max 200 ppm for adults. The dating model proposed by the authors is based on the fact that the fluorine diffuses from the surface, which acts as a reservoir, towards the enamel as a function of time. Provided the diffusion can be described by Fick's first law of steady state diffusion, with a diffusion coefficient of $5x10^{-14}$ cm^2/s, it is possible to plot the concentration as a function of time.

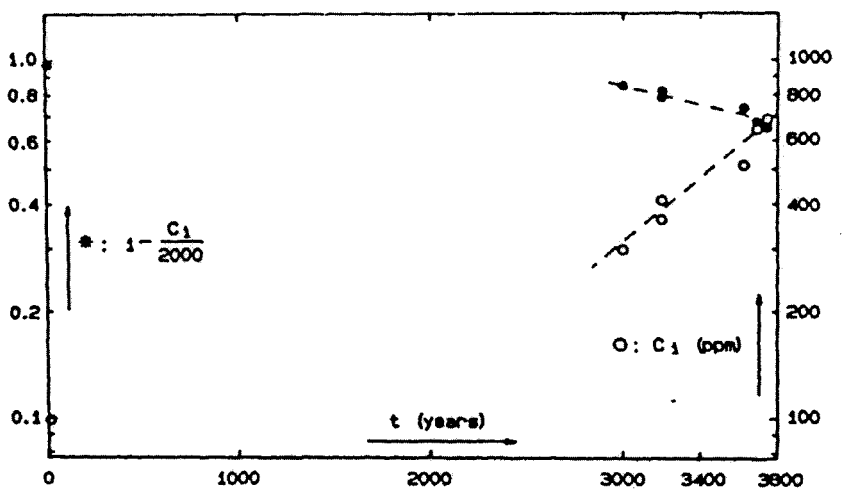

Figure 11. Fluorine concentration as a function of age. The dashed line is the calculation according to Fick's law. Reproduced with the permission of Springer-Verlag.

Figure 11 shows the predicted and the measured values for eight samples and shows a good correlation. To make this plot a few assumptions were made, such as the thickness of

the enamel (~ 3 mm), the reservoir (surface) fluorine concentration (2000 ppm) and the fluorine concentration in the enamel equal to zero at t=0. In addition a site calibration is necessary that takes into account the variations in speed of the diffusion process as a result of different environmental conditions.

5. ARTEFACT STUDIES

Artefact studies represent the second major application of the physical sciences to archaeology. The aims of these studies are to obtain information in the three main areas. First the provenance studies which involve characterizing and locating the natural sources of the raw materials used to make the artefacts and thus establishing the pattern of trade or exchange. Second there are the technological studies which involve identifying the materials and techniques used to make artefacts. And third there are usage studies that involve investigating the ways in which artefacts were used.

5.1. Provenance studies

5.1.1. Metals

An important feature of many ancient copper ingots is their population of nonmetallic inclusions. Type, composition, amount and distribution of these inclusions may provide data about smelting and casting conditions (Rehren and Northover, 1991). In a study by Adriaens and Adams (1996), analyses were concentrated on the selenium and tellurium contents of sulfide inclusions in Late Bronze Age (LBA) copper ingots. The samples originated from Rook Hall in Essex (UK). Se and Te occur as traces together with sulfur in almost all copper ores. The ratio of both depends on the type of deposit. When smelting sulfur bearing copper ore, Se and Te tend to concentrate in the sulfide phases (Rehren and Northover, 1991). The objective of the present analyses was to obtain statistically significant values for the Se:Te ratio using SIMS in a number of samples of the same hoard. The concentrations for Se and Te were too low for electron microprobe x-ray analyses (<0.1 %), and the study therefore formed an ideal application for SIMS. As can be seen in the backscattered electron image of Figure 12, the size of the copper sulfide inclusions ranges from a few micron to several tens of microns.

For this study the samples were embedded in a resin and polished according to standard metallurgical procedures. Secondary negative ions were detected for the elements Se, Te, S and Cu. Signals were obtained from the inclusion area only by setting appropriate apertures. The measurement of the Se/Te ratio was not very straightforward due to many interferences of Cu and S molecular clusters. The less abundant isotopes of $^{78}Se^-$ and $^{125}Te^-$ were measured, which were free of interferences. This of course implied lower signals, which was sometimes a problem in the case of tellurium. The signals for all elements detected were converted to an abundance of 100 %.

Table 3 lists the results for four samples. For each sample, 3 to 5 analyses were performed on different inclusions. The standard deviation for each analysis is below 10% for all

analyses. The Se/Te ratio seems to be quite homogeneous throughout the samples except for RH 9. Nevertheless, the results clearly indicate that there is a wide spread in the Se/Te results within a single hoard of samples. The latter implies that the accumulation of copper represented by these ingots was assembled from a number of different sources. This may indicate that the copper, at least in part, represented a metal surplus and possible a store of wealth (Northover, 1995).

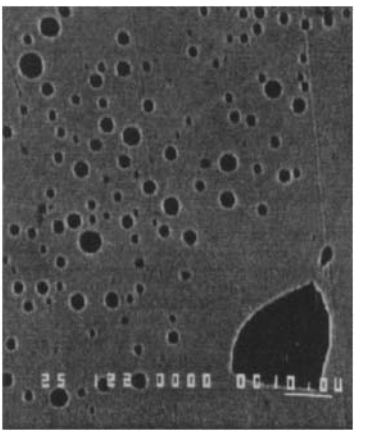

Figure 12. Backscattered electron image of a LBA copper ingot. Magnification 1200.

5.1.2. Flint

In a study by Domanski and Wojtowicz-Natanson (1980) the possibility was studied of using SIMS analyses to discriminate between varieties of flint of different provenance. In their study three flint samples were investigated of known origin and age: samples 1 and 2 from the same location but different age, sample 3 from an entirely different site. To compensate for the inhomogeneity of the samples, mass spectra were taken at several points on their surfaces. The samples were coated beforehand with a thin layer of platinum to reduce charging. In the three samples the same elements could be observed but with different ratios: significant differences could be observed between samples 1 and 2 on one side and sample 3 on the other side.

5.1.3. Ceramics

SIMS mass spectra were found to be very useful for fingerprinting of Cypriot pottery (Fischer, 1993). The aim of the study was to demonstrate the potential of SIMS for the characterization of pottery and to use the information in a later stage for provenance studies.

Table 3
Se/Te ratio for four Essex copper ingots.

	Se:Te ratio	Number of analyses
RH 09	15 ± 7	4
RH 12	501 ± 39	3
RH 13	2.1 ± 0.4	4
RH 14	0.16 ± 0.03	5

Attention was focused on the clay matrix of the samples. For statistical reasons three mass spectra were taken on different spots of each sample, with two analyses per spot. The variability within a single sherd was of the order of 10-20 %. The variability between groups was much larger and indicated the presence of a total of five different groups.

5.2. Technology / usage studies

The question of the used gilding technique of a Buddha statue dated 1720 AD, was addressed in a study by Schreiner and Grasserbauer (1985). On the surface, SEM-EDX analyses could demonstrate the presence of Hg, next to Au, Cu and Zn, which may indicate the technology for fire gilding. Nevertheless buried archaeological objects in contact with the ambient soil can also become contaminated with Hg. To resolve this question SIMS was used to depth profile the concentrations of Au and Hg. The similar depth profile of both elements (Figure 13) confirms that the statue has a fire gilded surface. Contaminants of Hg would show a sharp decrease of the Hg signal.

Blackish staining found on the crowns of teeth from 51 skulls, excavated at the Medieval St. Olav's church in Trondheim (Norway), was investigated to learn about its origin (Stermer et al., 1995). By identifying the elements responsible for this discoloration, the authors wanted to verify whether the staining was caused by oral habits during life time, by conditions in the burial soil or possibly by both. The methods chosen for trace element analysis were SIMS and AAS. A pilot study had already shown that SEM-EDX was not sensitive enough. Line scans were performed across the cross section of four teeth. Many trace elements show an increased concentration in the outer enamel due to an influx from the environment (see also paragraph 4.2.). Manganese, barium and strontium were the only three elements that showed a correlation with the black staining. In particular for manganese, its concentration was much higher than that expected from surface effects and shows the highest degree of conformity with gray scale patterns taken of the teeth. Manganese occurs primarily as oxide salts in nature. Both pyrolusite (manganese oxide) and psilomelane (barium

In a study by Adriaens et al. (1999) SIMS was used for the analysis of ceramic fragments from Göltepe (Turkey). It was strongly held view that the excavated vessels were crucibles in which tin ore from the nearby Kestel mine was smelted (Yener et al., 1989). Using SIMS the intention was to examine whether any remains of tin smelting activities could be found inside the crucibles to resolve the question of whether tin was indeed smelted at the site in Göltepe. Cross sections were embedded in epoxy resin in such a manner that the inside of the material could be analyzed.

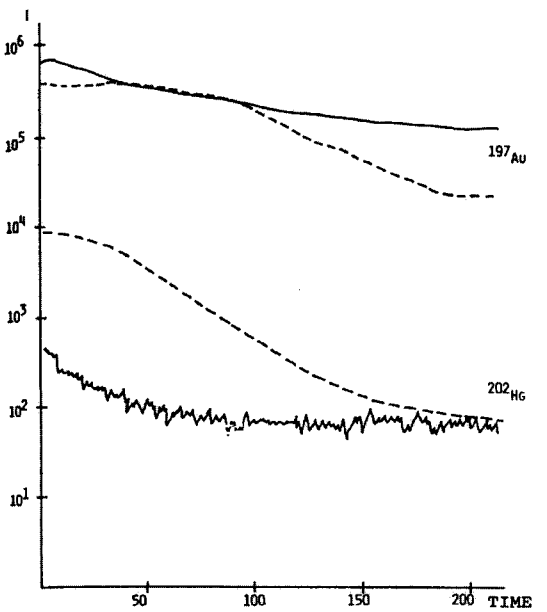

Figure 13. SIMS depth profile of Hg and Au (dashed lines) through the fire gilded surface of the Buddha statue. The solid lines are a result from an Inca mask which demonstrate that a correct answer to the technology used is more questionable. Reproduced from Schreiner and Grasserbauer (1985) with the permission of Springer-Verlag.

Figure 14 shows a line scan across a section of a crucible sample. The left hand side of the figure represents the inner surface of the sample. The right hand side is the bulk of the crucible material. The signals for Ca^+, SiO^+ and Sn^+ are shown. The calcium peak, clearly recognizable at the surface of the crucible, originates from an accretion layer of calcium carbonate. This calcareous encrustation is a result of long-time burial. Analyses on different

areas of the surface of the crucible indicate that this layer does not cover the entire inner surface but is observed at localized areas with a thickness of roughly 200 to 500 micrometer. Silicon is present both in the ceramic material and in the $CaCO_3$ layer. A tin peak can be observed at the interface of the ceramic material and the $CaCO_3$ layer and therefore at the inner surface of the crucible. Reproducible results have been obtained for several crucible samples. Additional SEM-WDS analyses have shown that the tin-bearing layer actually consists of a silicate phase with an average of 40 % of tin.

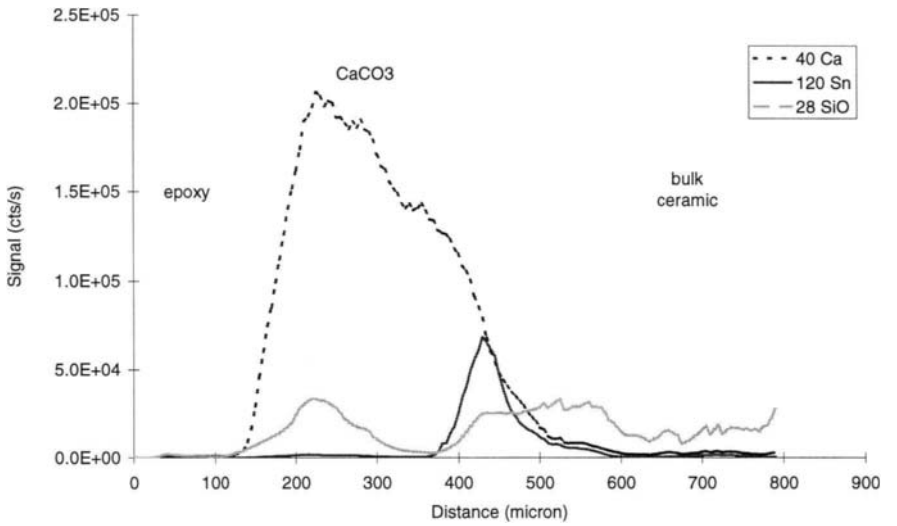

Figure 14. Line scan across a crucible cross section. Reproduced from Adriaens et al. (1999) with the permission from Academic Press.

One of the ceramic crucible samples contained on its inner surface a visible layer (a few square cm) of shiny accretion. This vitreous material was carefully removed from the ceramic, after which it was embedded in epoxy and treated in the above-mentioned manner. The accretion sample was analyzed using secondary ion imaging. The matrix shows the existence of two types of grains, as is demonstrated by the elemental distributions in Figure 15 a-d. The sodium signal (a), which is at least a factor ten higher in the matrix than in the grains, clearly differentiates the grains from the matrix. The quadrangular grains are primarily composed of iron (b) and tin (c) oxides (the tin concentration in the matrix and the quadrangular grains is roughly the same). The average size of these grains is 10 μm^2. The longitudinal grains are tin oxides (c, d), presumably in the SnO_2 form. The longitudinal grains are 0.5-2 μm wide and can be up to 50 μm long. The signal of the SnO_2 molecular cluster was too low in order to acquire a statistically significant image. The fact that the accretion

sample is composed of silicates with different admixtures of oxides and metals shows that it corresponds in composition to a typical metallic tin slag. The observed inclusions are primarily slag minerals originating from the ore and gangue, which have been isolated in the glassy matrix, and which have not been reduced to metal.

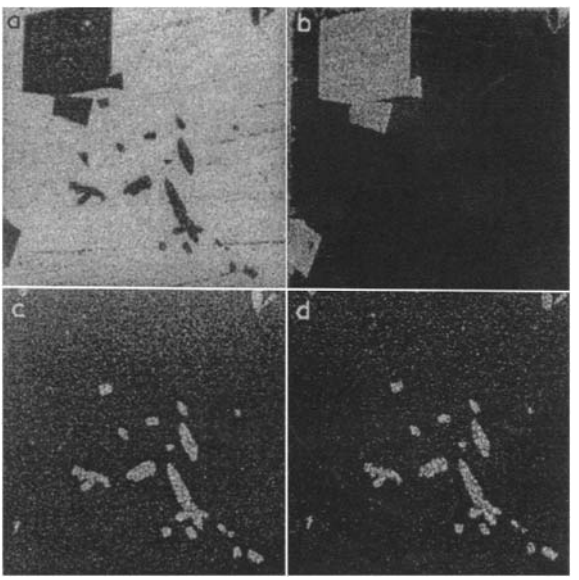

Figure 15. Secondary ion maps of Na^+ (a), Fe^+ (b), Sn^+ (c) and SnO^+ (d) of the crucible accretion. The area of analysis is 40×40 μm^2. Reproduced from Adriaens (1996) with the permission from Springer-Verlag.

6. CONCLUSIONS

The use of analytical methods for the study of art or archaeology related objects knows an increasing amount of attention, both by scientists as by archaeologists. Collaborations between these two groups have been limited in the past, but nowadays the necessity and the relevance of collaborating has become more evident and there is indeed an active search for collaborations.

In this paper the role of secondary ion mass spectrometry for the study of ancient materials has been demonstrated. The principal advantage of using this technique lies in its capability to perform in-situ analyses, eliminating time-consuming sample preparations and therefore also avoiding the possibility of introducing additional systematic errors. In particular the possibility to perform depth profiles with an ultimate depth resolution and the potential of ion

imaging on a μm scale gives SIMS a rather unique position in the field of microanalysis. Its high sensitivity and the possibility to perform analyses at high mass resolving power, for eliminating isobaric interferences, in general makes SIMS a very valuable tool within archaeometry.

REFERENCES

Adriaens, A. (1996) Elemental Composition and Microstructure of Early Bronze Age and Medieval Tin Slags, *Mikrochimica Acta* **124**, 89.

Adriaens, A.; Adams, F. (1996) "The Application of Ion Microprobe Analyses and Other Beam Methods in Archaeological Research" In: *Proceedings of the 7th National Symposium on Mass Spectrometry* (S.K. Aggarwal, Ed.) Mumbai: Indian Society for Mass Spectrometry, pp. 1.

Adriaens, A.; Yener, K.A.; Adams, F. (1999) An Analytical Study Using Electron and Ion Microscopy of Thin-walled Crucibles from Göltepe, *Journal of Archaeological Science* **26**, 1069.

Adriaens, A.; Van Vaeck, L.; Adams, F. (1999) Static Secondary Ion Mass Spectrometry (S-SIMS). Part 2: Applications in Materials Science, *Mass Spectrometry Reviews* **18**, 48.

Aerts, A. (1998) *Microscopic Analysis of Roman Vessel Glass.* Antwerp: University of Antwerp, Dissertation.

Allen, G.; Brown, I.T.; Ciliberto, E.; Spoto, G. (1995) Scanning Ion Microscopy (SIM) and Secondary Ion Mass Spectrometry (SIMS) of Early Iron Age Bronzes, *European Mass Spectrometry* **1**, 493.

Anovitz, L.M.; Elam, J.M.; Riciputi, L.R.; Cole, D.R. (1999) The Failure of Obsidian Hydration Dating: Sources, Implications and New Directions, *Journal of Archaeological Science* **26**, 735.

Bruchertseifer, C.; Stoppek-Langner, K.; Grobe, J.; Deimel, M.; Benninghoven, A. (1997) Examination of Organosilicon Impregnation Mixtures by Static SIMS and Diffuse Reflectance FTIR, *Fresenius Journal of Analytical Chemistry* **358**, 273.

Benninghoven, A.; Rüdenauer, F.G.; Werner H.W. (1987) *Secondary Ion Mass Spectrometry, Basic Concepts, Instrumental Aspects, Applications and Trends.* Chemical Analysis. Vol. 86. New York: Wiley.

Ciliberto, E.; Fragala, I.; Spoto, G.; Di Stefano, C.; Allen, G.C. (1995) Analyzing a Sicilian Renaissance Portal: Microanalytical Techniques Yield Valuable Information about the Materials and Techniques used During Construction of a Renaissance Church. *Analytical Chemistry* **67 (7)**, 249A.

Domanski, M.; Wojtowicz-Natanson, B. (1980) A Possible Application of the SIMS Method to Determine Provenance of Archaeological Objects, *Nuclear Instruments and Methods* **168**, 435.

Doremus, R.H. (1973) *Glass Science.* New York: Wiley.

Ettinger, K.V.; Frey, R.L. (1976) "Nitrogen Profiling: A Proposed Dating Technique for Difficult Artefacts" In: *Proceedings of the Sixteenth International Symposium on Archaeometry and Archaeological Prospection* (E.A. Slater and J.O. Tate, Ed.) Edinburgh, p. 293.

Fischer, P.M.; Norén, J.; Lodding, A.; Odelius, H. (1985) "Quantitative SIMS of Prehistoric teeth" In: *Secondary Ion Mass Spectrometry SIMS V* (A. Benninghoven, J. Colton, D.S. Simons, H.W. Werner, Ed.) Berlin: Springer-Verlag, p. 438.

Fischer, P.M.; Lodding, A.; Norén, J. (1989) "Trace Element and Dating Studies of Teeth by Secondary Ion Mass Spectrometry" In: *Archaeometry* (Y. Maniatis, Ed.) Amsterdam: Elsevier, p. 109.

Fischer, P.M. (1993) "Some Cypriot Pottery Wares Analyzed Using SIMS" In: *Archaeology and Natural Science (ANS).* Volume 1 (P. Fischer, Ed.). Göteborg: Paul Åströms Förlag.

Hedges, R.E.M.; Freeman, S.P.H.T. (1993) "The Possibility of Dating Lithics from Diffused Nitrogen Profiles" In: Stories in Stone (N. Ashton and A. Davies, Ed.), *Lithic Studies Society Occasional Paper 4*, p. 7.

Northover, P. (1995) personal communication.

Patel, S.B.; Hedges, R.E.M.; Kilner, J.A. (1999) Surface Analysis of Archaeological Obsidian by SIMS, *Journal of Archaeological Science* **25**, 1047.

Rehren, Th.; Northover, P. (1991) "Selenium and Tellurium in Ancient Copper Ingots" In: *Archaeometry '90* (E. Pernicka and G.A. Wagner, Ed.) Basel: Birkhauer Verlag, pp. 221.

Schreiner, M.; Stingeder, G.; Grasserbauer, M. (1984) Quantitative Characterization of Surface Layers on Corroded Medieval Window Glass with SIMS, *Fresenius Journal of Analytical Chemistry* **319**, 600.

Schreiner, M.; Grasserbauer, M. (1985) Microanalysis of Art Objects: Objectives, Methods and Results, *Fresenius Journal of Analytical Chemistry* **322**, 181.

Schreiner, M. (1991) Glass of the Past: The Degradation and Deterioration of Medieval Glass Paintings, *Mikrochimica Acta* **II**, 255.

Stermer, E.; Risnes, S.; Fischer, P.M. (1996) Trace Element Analysis of Blackish Staining on the Crowns of Human Archaeological Teeth, *European Journal of Oral Sciences* **104**, 253.

Van Vaeck, L.; Adriaens, A.; Gijbels, R. (1999) Static Secondary Ion Mass Spectrometry (S-SIMS). Part 1: Methodology and Structural Interpretation, *Mass Spectrometry Reviews* **18**, 1.

Wouters, H.J.; Butaye, L.; Adams, F.C. (1991) Application of SIMS in Patina Studies on Bronze Age Copper Alloys, *Fresenius Journal of Analytical Chemistry* **342**, 128.

Yener, K.A.; Özbal, H.; Kaptan, E.; Pehlivan A.N.; Goodway, M. (1989) Kestel: An Early Bronze Age Source of Tin Ore in the Taurus Mountains, Turkey, *Science* **244**, 200.

Radiation in Art and Archeometry
D.C. Creagh and D.A. Bradley (editors)

Scanning electron microscopy techniques for imaging materials from paintings.

Aviva Burnstock[a] and Chris Jones[b]

[a]Department of Conservation and Technology, Courtauld Institute of Art, Somerset House, Strand, London WC2R ORN, United Kingdom.

[b]Electron Microscope Unit, Department of Mineralogy, The Natural History Museum, Cromwell Road, London SW7 5BD, United Kingdom.

ABSTRACT

This chapter reviews a range of techniques of scanning electron microscopy (SEM) and its application to the study of paintings and artists materials. The review focuses on imaging the materials (rather than chemical analysis), and its application to the materials used for and from easel paintings. Examples of published experimental studies of cleaning, paint surface defects, bio-deterioration of painting materials from the conservation and paint manufacturers literature are discussed, with reference to sample preparation and imaging conditions. Images of selected artists materials and materials from paintings examined using conventional high vacuum SEM, low vacuum (variable pressure) SEM and ESEM are given to illustrate comparative techniques.

1. INTRODUCTION

Scanning electron microscopic imaging has been almost universally applied for the surface characterization of materials from art and archaeological objects. Amongst the technical studies of these objects, it is difficult to find a publication that does not include SEM images of some aspect of the material structure, its degradation or conservation additions. This review focuses on the application of SEM imaging techniques specifically for the study of paintings and artists materials.

The SEM, unlike non-invasive methods of analysis, requires a sample be taken. It is a particularly attractive addition to the arsenal of methods for the technical study of paintings because useful information can be gleaned from very small samples. The study of real paintings is limited by sampling opportunities; ethical considerations limit sample taking to the edges of damages or cracks, and paintings in good condition may not offer the opportunity to remove even the smallest flake or fragment of material, which is the minimum necessary for SEM examination. Although instruments with a large sample chamber could theoretically accommodate whole small works, preparation by coating with carbon or metal would not be recommended due to its irreversibility, and has not been attempted. The examination of whole objects and organisms without preparation from natural history collections has been successfully carried out using low vacuum instruments (Barnes 1991) although this has not been applied to whole paintings.

Electron microscopy offers higher magnification combined with significantly better resolution than the light microscope, which has traditionally been used to examine the surface and layer structure of paintings, which at best provides magnifications up to 1000x. The magnification is limited simply by the wavelength of light. The potential for high magnification is advantageous, especially in the examination of problems where illustration of fine topographical features helps to understand gross effects, or in the detection of changes which may occur as the result of a specific treatment that are beyond resolution of the light microscope.

While the use of the light microscope for the examination of paintings has a long history (Raehlmann, 1910; 1914; Plesters, 1954; 1956; Gettens, 1958) the application of SEM for the surface characterisation of materials from easel paintings is relatively recent. Von Ardenne first constructed a modified electron microscope in 1938, adding scan coils to a transmission electron microscope, thus making the first scanning transmission electron microscope (Von Ardenne, M, 1938), and in 1942 Zworykin et al. described a SEM for the examination of thick sections. They recognised that topographic contrast was produced by the excitation of secondary electrons from the sample surface (Zworykin, Hillier and Snyder, 1942). In 1948, Oatley built the first SEM at Cambridge University, which by 1952 could resolve 50nm (Goldstein et al.,1984). Bell (1960) reviewed the use of electron microscopy in the field of commercial paint research from 1944 at the Paint Research Station at Teddington, UK. Since its introduction, SEM has found application in almost all fields of scientific investigation, including biological and materials sciences.

The following section provides an historical review of SEM imaging techniques and instrumentation, and Section 3. introduces examples from literature where SEM imaging has been applied to the study of paintings and artists materials. Section 4. includes a comparative study of a range of materials from, and used for paintings, examined using four different SEM imaging techniques: conventional SEM using a secondary electron detector (SEM/SE),

low vacuum (variable pressure) SEM using a backscattered electron detector (ABT/BSE), field emission SEM using a secondary electron detector (FEG/SE) and environmental SEM using a gaseous secondary electron detector (ESEM/GSE).

2. SEM IMAGING TECHNIQUES AND INSTRUMENTATION

Following the work of the early pioneers of electron microscopy, described above, the first commercial SEM was built in 1965 by Cambridge Scientific Instrument Co. The Cambridge Mark I SEM was built to a design of Zworykin, et al. and formed the basis of modern SEM design, utilising magnetic lenses and an Everhart-Thornley secondary electron detector.

Images produced with a scanning electron microscope give an impression of three dimensions. A spot of electrons from a primary source scans the surface of a sample in a raster pattern. The primary source may be a spot 1(+) nm in diameter when it strikes the sample surface. The primary electrons spread in a tear-drop pattern longitudinally into the sample and interact with its atomic structure until the primary energy has dissipated.

Two types of electron scattering may result from the interaction of the primary beam with the sample's atomic structure: elastic and inelastic scattering (Bozzola and Russell, 1992). Elastically scattered electrons collide with atoms within the sample and change direction, without losing energy or velocity, producing backscattered electrons. Inelastic scattered electrons interact with atoms within the sample and may lose some energy and velocity. The result is the production of secondary electrons, which are scattered at many different angles. Secondary electrons have a lower energy than backscattered electrons, typically having energies less than 50eV. They also represent a shallower sampling depth, due to their low energy. Secondary electrons represent a sampling depth somewhere in the region of one hundred times less than backscattered electron, (Goldstein, et al., 1992). Electrons excited from the surface of the sample are detected and the signal is displayed on a screen, or digitized and displayed on a computer monitor. A range of signals may be detected, including: secondary electrons (SE's), backscattered electrons (BSE's), x-rays, Auger electrons, cathodoluminescence and transmitted electrons. Different detectors may collect these signals.

Secondary electrons are routinely collected using the Everhart-Thornley type photo-multiplier detector (Everhart and Thornley, 1960). Negatively charged secondary electrons are attracted to the detector window by a Faraday cage, charged at -100 to +300V. The electrons collide with a positively charged (+1-10kV) aluminium coated scintillator, producing photons. The photons move along a light guide and the resulting signal is amplified in a photomultiplier. The processed signal is displayed on a screen or computer

monitor. The position of the detector relative to the sample is not critical as the secondary electrons will move in a curved pathway towards the scintillator because of the positive bias applied to the Faraday cage. Backscattered electrons are commonly collected either by a solid state detector or a scintillator detector. The scintillator type backscattered electron detector (Robinson, 1975) utilizes a metal-doped and coated plastic window attached to a light tube. The detector window is placed above the surface of the sample, the closer the better, to maximize the efficiency of signal collection. The sample should be kept normal to the detector window, as any degree of tilt will result in a reduced collection rate as the backscattered electrons are exiting the sample surface at a high angle.

Solid state backscattered electron detectors are designed to detect electrons with energies greater than 5kV. A large angle of collection, close to the sample surface, picks up energies from backscattered electrons using a semi-conductor amplification system. Secondary electrons are not picked-up as their energies (0-50eV) are too low.

The number of elastic scattering events at the surface of a sample increases with atomic number. The heavier elements will give a brighter signal when displayed on screen. A variation in atomic number will be seen as a change in the signal intensity of backscattered electrons. Hence the heavier the element the greater the number of backscattered electrons ejected from the sample.

For most imaging it is necessary to make sure that the sample is electrically conductive. This is not a problem with metallic samples but becomes difficult if objects are insulators. To overcome this problem samples are coated with a thin layer of metal in a vacuum environment, either using an evaporative or sputtering (plasma) technique. Typical metals used for coating samples include carbon, gold, gold/palladium, platinum and chromium. The coating medium selected, and method of coating, will be determined by the type of imaging required. Samples for analysis will usually be carbon coated. Gold coating is adequate for a conventional tungsten filament SEM, and gold/palladium or platinum is used for field emission SEM. Coating thickness must be kept to a minimum as the primary electron beam will only penetrate the surface of the sample by, perhaps, 1 micron, depending on the type of sample and accelerating voltage applied. Typical coating thickness will range from 1-40nm.

2.1 Conventional high vacuum scanning electron microscopes

Conventional high vacuum scanning electron microscopes are the routine tools used for imaging. A typical SEM operates at a pressure of 10^{-2} Pa or better. It is necessary to remove as much air as possible from the microscope column and sample chamber to prevent the primary electron beam being scattered by gas molecules. The presence of gas molecules will also scatter any electrons generated as a result of collisions within the atomic structure of the sample. Electron scattering will result in an overall loss of signal and an increase in noise.

The primary electron beam may be generated from one of a number of sources: thermionic source, Lanthanum hexaboride (LaB_6) or a field emission tip. The thermionic source is usually a V-shaped tungsten filament, chosen because of the high melting point of tungsten (3,653°K). The filament, approximately 0.1mm thick, is heated through the application of a current, and gives off a large number of thermionic electrons (Chescoe, D and Goodhew, P J, 1990). The optimum temperature for tungsten thermionic emission and long filament life (perhaps one hundred hours) is around 2,600°K. Electrons are accelerated through a negatively charged Wehnelt cap and are focused to a crossover point at the anode before accelerating through the electromagnetic lenses and apertures of the column. The intensity of the primary beam is determined by the filament current, the bias on the Wehnelt cap, and the accelerating voltage. The accelerating voltage will usually fall within the range of 1kV-30kV, and its setting will be determined by the sample and the type of imaging required.

A lanthanum hexaboride (LaB_6) source works in the same way as a tungsten thermionic source, although at a lower temperature of around 1,000°K. Despite the lower operating temperature a LaB_6 source produces an electron flux several times greater than tungsten and may last up to one thousand hours. The source consists of a single crystal of LaB_6 with a point source measuring a few microns across. LaB_6 is usually operated at a pressure of 10^{-5} Pa, or better, due to its chemical reactivity when heated.

The third source of electrons is from a field emission gun. The gun utilizes a single crystal of tungsten as the source. The tungsten crystal has been chemically thinned in an orientation to maximize the electron extraction from its crystal lattice by the process of field emission. As opposed to thermionic emission, field emission is achieved by drawing electrons from the tungsten tip through the application of a positive bias to a number of anodes. The resulting electron flux is in the region of one thousand times greater, or 'brighter', than from a conventional tungsten filament. Ultrahigh vacuum is required to maintain a contaminant free path for the electron beam. Pressures in the gun area of a field emission SEM are usually better than 10^{-8} Pa.

The advantages of the different types of electron source are seen in the physical size of the emitting tip and ultimate resolution of the SEM. A tungsten filament source may give an ultimate resolution of around 3.5nm, LaB_6 2.5nm and field emission 1.5nm or better.

2.2 Low vacuum (variable pressure) scanning electron microscopy

Low vacuum or variable pressure, SEM is a technique capable of imaging uncoated samples and has been established for more than twenty years. The technique is known by a number of terms, including: low vacuum, variable pressure and WET SEM, and is particularly suited to applications where samples cannot be coated or are not sufficiently robust to withstand the high vacuum environment within the SEM. Biological material is made up of soft tissue

(cells) and water, neither of which are capable of surviving the high pressures associated with a conventional SEM. Such material is normally imaged after chemical fixation, critical point drying and coating or cryo preparation. Low vacuum SEM enables the examination of this type of material through the application of a differential pressure between the sample chamber and microscope column.

The microscope column and gun areas are pumped to high vacuum by conventional means of rotary and oil diffusion or turbo molecular pumps. The pressure required is dictated by the type of electron source, as described earlier. The microscope chamber is only evacuated by a rotary pump, restricting the achievable pressure in the sample chamber. The differential vacuum achieved between the chamber and column is restricted by a pressure limiting aperture(s) at the base of the pole piece. Gas molecules still present in the chamber ionize the charge that may build up on the surface of uncoated samples. The amount of gas present in the chamber may be varied through the use of a manual or computer controlled needle valve. Most low vacuum SEMs will operate with a chamber pressure between 10^{-1} Pa and 3Pa, and a minimum pressure of 10^{-4} Pa in the gun area.

The disadvantage of low vacuum SEM as a technique is the trade off between chamber pressure and image resolution. Maintaining a sample and chamber at low vacuum, and maintaining a controlled atmosphere of gas molecules will cause a degree of scattering of the primary electron beam. In addition, the electrons that are excited from the sample may also be scattered by the gas molecules before reaching the detector. Thus the signal to noise ratio may be relatively poor. In addition, as a result of signal scattering it is generally only possible to detect the backscattered electron component of the signal. The lower energy secondary electrons do not have sufficient energies to make a pathway through the gas molecules to a conventional secondary electron detector.

The advantages, however, are many and far-reaching. Delicate, valuable or irreplaceable samples can be safely imaged in the low vacuum SEM. Preparation and coating is unnecessary. Flakes of oil paint, non-conducting pigments and ceramics can all be examined with the advantage of the large depth of field offered by the SEM.

2.3 Environmental scanning electron microscopy

An environmental SEM is an extension, and improvement, of low vacuum (variable pressure) SEM and was developed during the mid 1980's. The primary electron beam may be a tungsten filament, LaB_6 or field emission gun source and the gun area is pumped to an appropriate pressure to suit that source. The main difference between conventional SEM, low pressure SEM and environmental SEM is the ability to image samples at a variable range of pressures, temperatures and gas environments. Non-conductive fully hydrated

samples, oils, wet paints, fluorescent or incandescent materials can be imaged without risk of damage or interference.

The gun area is separated from the sample chamber by multiple pressure limiting apertures, enabling a coherent beam of electrons to accelerate into the sample chamber. The chamber, the region between the final two pressure limiting apertures and the column are separately pumped to provide a graduated vacuum. This ensures that the primary electron beam only travels a very short distance through the higher pressure stages before reaching the sample chamber (Robert John Associates, 1996). The graduated vacuum may have a pressure of 10^{-8} Pa, or better, in the gun area and 6000Pa in the sample chamber.

The environmental SEM uses a patented gaseous secondary electron (GSE) detector to collect secondary electrons from the sample. Unlike the conventional Everhart-Thornley detector, the gaseous detector uses a positively biased conical electrode to receive the signal. The incoming secondary electrons collide with gaseous molecules in the vicinity of the detector, creating ionization. As a result of the ionization further secondary electrons and positive ions are produced. Further collisions result in amplification of the secondary electron signal. The positive ions produced are attracted to the surface of the sample and suppress or eliminate any surface charging that may occur. The overall image will also be enhanced by the backscattered electron component of the signal.

As a result of the application of the gaseous secondary electron detector, the environmental SEM is capable of achieving superior resolution in comparison with a low vacuum SEM.

3. SEM IMAGING OF SAMPLES FROM PAINTINGS

Although the popularity of SEM imaging for the study of artists materials is evident in publications from the last ten years, there are a small number of reviews published in the 1970s which describes the traditional SEM instruments available at that time, and their application to the field of art, including the study of pigments and binding media.(See Moll (1976)). The authors of the present review have found no published reviews of SEM imaging specifically for paintings applications. The following introduces selected examples of the use of SEM imaging for the study of aspects of painting materials and techniques, where it has been used to examine deterioration phenomena and in comparative experimental studies of conservation treatments.

3.1 SEM for the study of pigments

Conventional (high vacuum) SEM imaging techniques using secondary electrons (SE's) have been used in studies of artists materials to illustrate detailed topographical features of artists pigments (McCrone (1973), Feller (1972), Gettens et al. (1974a and b), and Winter (1983a). Duval (1985) reviewed the use of SEM for the examination of a range of art objects including pigments from

paintings. A monograph series on artist's pigments edited by Feller (1986), Roy (1993) and West Fitzhugh (1997) contains chapters by a number of authors on the history and characteristics of a selection of pigments, several of the articles include SEM images for pigment particle characterisation. Volume I includes images of cadmium colours, red lead and minium, green earth, lead antimonate yellow, cobalt yellow barium sulphate. Volume II covers azurite and blue verditer, ultramarine blue, lead white, lead-tin yellow, smalt, verdigris and copper resinate, vermilion and cinnabar, malachite and green verditer and calcium carbonate whites. Volume III contains SEM characterization of Egyptian blue, Prussian blue, emerald green and Scheele's green, chromium oxide greens and titanium dioxide whites. In each monograph, conventional high vacuum SEM imaging using a secondary electron detector is employed to produce topographical images, with the exception of the use of TEM for characterization of viridian.

Studies which involved removal of paint medium from samples from paintings (as opposed to pure unbound standard pigment samples) before characterization of pigment particles include Winter's (1975) paper on the examination of chalk/glue grounds using SEM, the Moffatt et al.(1983) study of blue pigments in Chinese wall paintings and a study by Leighton et al.(1987), which included an examination of yellow pigments used by Vincent van Gogh. A study of some pigments used by the Impressionists (Bomford et al.1990) with SEM was also carried out. Harding et al (1989) undertook examination of the drawing materials used for the cartoon for Leonardo Da Vinci's Virgin and Child with S. Anne and S. John the Baptist in the National Gallery, London, and characterized the surface of the work after an attack by a gunman. In this study, SEM was used to characterize the carbon based drawing materials by examination of particle morphology, and to examine the relationship between sub-light- microscopic fragments of glass and the drawing surface. A comparable study of a range of carbon based pigments was carried out by Winter (1983a).

Imaging using SEM was most useful for characterization of pigment particle morphology where the samples examined were free of organic materials associated with paintings such as the binding medium, which has an amorphous surface appearance. Whilst the SEM images of many inorganic pigments have characteristic features, some classes of 19th and 20th century manufactured pigments (for example: some types of chrome yellow (Leighton et al, 1987) titanium and zinc white and others) are similar in appearance, and are better characterized by use in conjunction with another technique (such as elemental analysis). No studies have been found that employ SEM imaging for the characterization of organic pigments, except where the an inorganic extender was present (for example, the characterization of indigo paint containing chalk from a 17th Dutch portrait, Burnstock, 1997).

In experimental studies of pigments, Gutscher et al.(1989) looked at the conversion of azurite to tenorite using SEM to show topographical changes. Martin et al. (1990) used the backscattered electron signal to examine types of

lead-tin yellow pigments from paintings, and Winter (1983) looked at gold on Japanese paintings using secondary electron imaging.

At the National Gallery, London, the SEM has been used to examine the materials of paintings other than pigments. Micrographs have been included in published studies by Dunkerton et al. (1986), Bomford et al. (1988,1989) for the examination of gesso grounds, and by Bomford et al. (1986), Roy (1988), and Leonard et al. (1988) for the identification of canvas fibres from paintings. The grounds of Italian panel paintings have been studied using SEM by Sonoda et al. (1990).

3.2 SEM for characterisation of the surface of samples from paintings

Illustration of paint surfaces using SEM with both SE and BSE imaging has been carried out by Plesters et al. (1982) on samples from a 17th century Dutch landscape by Cuyp, and by Townsend (1994) who examined samples from an unfinished painting by Turner. Stringari (1990) used SEM to illustrate the surface coating on a painting by Vincent van Gogh, and Groen (1997) used SE and BSE images to illustrate the surface topography and composition of samples from paintings by Rembrandt. SE images of selected paint samples from paintings can provide useful qualitative information about surface texture, for example, the nature of the relationship between pigment and binding medium at the surface, fine cracking, paint film drying defects and surface pores. In suitable samples, fractured edges of layered paint fragments can be tilted in the microscope to examine the interfaces between layers and presence of coatings. BSE images provide a rough guide to the atomic number contrast within the sample, and this has become a standard method for imaging paint cross-sections prior to EDX analysis.

The SEM imaging has been applied to study the surface of paintings that suffer from patchy or overall whitening of paint described as "blanching". A study by Groen (1988) utilized SEM for the examination of blanching in French School paintings of the 17th century, and the whitening of the surface of paintings produced by the migration of free fatty acids has been characterized using SEM study of samples from paintings by Stanley Spencer (Burnstock and Caldwell 1995). Although the causes of blanching in paintings is not well understood, it is likely to relate to specific materials and techniques used, their drying, deterioration and the role of environmental fluctuations. In these studies, traditional SEM of samples from paintings were examined, which comprised complex inhomogeneous materials including paint and varnish layers, making interpretation difficult. In the paintings by Spencer, organic degradation products were evident on the surface, which may be partially volatile under ambient conditions, and may be affected by sample preparation or vacuum pressure in the microscope. SEM imaging has been used as the main technique for characterization of blanching in different types in samples from a number of paintings in an unpublished chapter from a Ph.D. thesis by Burnstock (1991).

Many studies of the materials of wall paintings have utilised SEM imaging, for example, Alessandrini et al.(1989) looked at charcoal and gypsum in a Milanese wall painting and Aslam (1990) examined plasters in the Taj Mahal. More numerous are the studies which focus on the deterioration of wall paintings, specifically the formation of salt deposits. While a discussion of these studies is beyond the scope of the present review, recent advances include the application of ESEM, which has provided the opportunity for dynamic studies of salt formation in samples in situ in the ESEM chamber (Doehne and Stulik 1991).

3.3 Cleaning studies

Traditional SEM has been used in a number of experimental studies of the cleaning of paintings, using either prepared paint and or varnish samples (Hedley et al. 1990, Burnstock and Learner 1992, Erhardt and Bischoff 1994, Mansmann, 1998) or simulated painting surfaces (Burnstock and White 1990). Similar imaging techniques have been used to compare the surface of real paintings before and after cleaning treatments (Eipper and Reiss; 1996 White and Roy; 1998), while Burnstock and Kieslich (1996) used low vacuum SEM to detect semi-volatile gel residues. Interpretation of "before and after treatment" surface micrographs of samples from paintings is problematic because paintings are inhomogeneous and because once coated, for imaging, the same sample cannot be re-examined in its original form. Thus there is great reliance on the careful selection of samples that exhibit similar pre-treatment surfaces to the control samples, and to the selection of a characteristic area of the sample for imaging/photography. While the use of low vacuum or ESEM techniques in these studies might allow for re-treatment of samples after an initial examination, the preference for experimental paradigms which closely follow cleaning procedures used by conservators limits this approach. Treatment of a micro-sample does not replicate cleaning with a swab or brush on a larger scale. While there is perhaps more scope for interpretation of general trends in cleaning effects from studies which employ prepared, relatively homogeneous paint films, artificial aging of the samples pre-treatment may not replicate naturally aged paint, introducing further variables to be considered.

3.4 Bio-deterioration of paintings and artists' materials

SEM imaging biodegradation of paintings has been widely used, despite the potential for beam damage or vacuum induced artefacts on biological material. Hallstrom et al. (1974) and Hofmann et al. (1990) used SEM to look at fungal infestation of paintings and paper respectively, and Edmonds (1990) used SEM to examine fungi on polyvinylacetate coatings on Aboriginal paintings. Kuhn (1985) used SEM and other techniques to examine the material from Leonardo's Last Supper fresco in Milan, including fungal deterioration. Petersen (1993) characterized the degradation of synthetic consolidants employed in the restoration of mural paintings exposed to humid conditions.

The relationship between moisture sensitive materials, such as proteinaceous glue size (used to prime canvas or as a binding medium for pigment and ground), and fungal infestation has been widely illustrated using SEM/SE micrography. It is likely that examination of similar uncoated samples, using low vacuum or a water vapour environment in an ESEM, might provide more realistic images and more precise information,(See Section 3).

3.5 SEM imaging studies of surface dirt, coatings, binding media, fibres and other organic materials

In a study using a simulated canvas painting surface as substrate and samples from paintings, Phenix and Burnstock (1990) used SEM to examine the nature of a variety of surface dirt and its deposition on paint and varnish surfaces. SEM/SE images (from gold coated samples) of dirt that comprised a mixture of organic and inorganic material. Imaging was most successful where the dirt fragments were imbibed or partially embedded in the surface of the samples, while loose particles suffered electron beam-induced charging.

Burnstock and Learner (1994) examined a range of artificially aged varnish coatings used for paintings. The surface and paint-varnish interface of a commercially primed canvas coated with traditional varnishes such as egg white, oil, di- and tri-terpenoid resins and selected modern synthetic varnishes were characterised using SEM/SE from gold-coated samples.

Ansell (1994) reviewed the application SEM to the study of coatings, including a discussion of the minimisation of beam damage. Domech-Carbo and Aura-Castro (1999) used traditional high vacuum SEM with fractured cryo-preparations of synthetic polymers (used for varnishing and consolidation of paintings). Samples were exposed to variable relative humidity prior to treatment. Studies which include images comparable to those from paintings include Underhaug et al. (1983) and Zicherman et al. (1972) who looked at coatings on wood, and Woodward (1988) who produced an atlas of SEM images of the surface of organic materials including some polymers used in the conservation of paintings.

Imaging of partially dry organic coatings, such as linseed oil, using conventional high vacuum SEM is problematic. Unaged synthetic varnish coatings which retain solvent and or moisture are particularly prone to electron beam artefacts, even when imaged at low accelerating voltages. Alternative imaging techniques have been used for the surface characterization of organic materials, for example acoustic, confocal and atomic force microscopy. Some of these techniques may find application in the conservation of paintings, varnishes and consolidants (Lange et al 1996).

In an experimental study, Townsend et al. (1998) used SEM imaging and other techniques to look at the composition of 'megilp' (oil and resin) paint binding media. Conventional high vacuum SEM imaging has limited use for the study of organic materials from paintings, due both to similarities in appearance and beam sensitivity of some organic materials. Varnishes and paint binding

media in fresh samples are particularly susceptible to beam and vacuum artefacts due to the retention of volatile components and their subsequent loss during coating or in the microscope chamber during examination.

SEM has long been used to characterize textile fibres (Gay 1972): an atlas of SEM images of paper fibres was published by Parham (1974). More recently, Clements et al. (1998) used similar techniques to identify fibres in rag paper. These studies have aided the identification of fibres from canvas painting supports.

3.6 SEM studies in paint manufacturers' literature

Studies carried out by researchers in the commercial paint-manufacturing field that employed SEM images have been crucial in aiding interpretation of images of samples from paintings. The literature on the application of SEM for the examination of commercial paints which are relevant to studies of artist's materials began in England in 1944 (Bell, 1960) with a study of pigments by the Paint Research Station. A review of the use of electron microscopy in the field of paint technology by Bell (1960) included SEM micrographs of pigments prepared in various ways including pre-coating of samples with metals and carbon. Photographic mosaics of paint cross-sections containing pigment and oil paint were published, and micrographs of crystalline bloom on the surface of alkyd paints were examined by making replicas of the paint surface. This review also discussed the use of SEM in the examination of paint films, their aging, pigment distribution and the effects of moisture on films.

The SEM has been widely used in the study of commercial paints to examine changes in paints due to weathering (Carter et al., 1974, Princen et al., 1974), water transport through paint films (Perera et al., 1971), paint film morphology (Funke et al., 1976), dirt accumulation (Raaschou et al.,1978), micro-void formation (Rosenthal et al., 1973) and paint film defects at the interfaces between layers (Quach 1974). Similar imaging techniques have been applied in the examination of multi-layered materials (Cheever 1986) and pigment volume concentration in linseed oil films (Eissler et al., 1971). This study includes SEM/SE images, which illustrate the relationship of pigment to binder in oil paint films, and shows the formation of a 'skin' of paint medium in medium-rich (fat) paint films. Murley et al., (1970) also used SEM to examine the skin of medium on gloss paint films. Work by Eissler et al., (1974) examined the effects of moisture on paint films, and Kampf et al., (1982) carried out a time lapse SEM study of chalking in paint films. These papers are very helpful in the interpretation of SEM micrographs taken of materials from paintings that are more complicated than the simple test films or layers examined in these studies. Kennedy et al., (1988) studied the effectiveness of various polymers as moisture barriers for paint and the effects of solvents on paint films. Solvent diffusion and drying was examined by Waggoner and Blum (1989), and Bladin et al., (1987) looked at the drying process of single and double layers of paint and coating using SEM to illustrate changes in surface topography. These studies are useful

in interpreting SEM micrographs from paintings where surface coatings such as varnishes are present.

3.7 Application of environmental scanning electron microscopy (ESEM)

In 1990, Doehne and his colleagues at the Getty Conservation Institute, California pioneered the use of environmental electron microscopy (ESEM) in paintings-related applications. The technique has been applied in a variety of conservation related studies, including examination of cleaning swabs from the Sistine Chapel ceiling, corrosion of metals by solvents, dynamic studies of the consolidation of stone, and formaldehyde induced lead corrosion has been introduced by Doehne et al., (1990). The same authors published ESEM (GSE) images of selected samples that posed problems for high vacuum examination in that they were potentially outgassing or intrinsically moist. These included samples from the dead sea scrolls, untreated oak wood, sandstone and a cotton cleaning swab used for cleaning the Sistine Chapel (Stulik and Doehne 1991). A dynamic study of the dissolution and recrystallisation of sodium chloride salt crystals was also carried out using the ESEM (Doehne and Stulik 1991). Scott and Hyder (1993) used the environmental SEM at the Getty Conservation Institute to examine uncoated pigment samples from a Californian rock art site. In 1994, Doehne and his colleagues described the advantages of environmental SEM for conservation applications (Derrick et al., 1994, Bower et al., 1994) and reviewed the methods more fully in a more recent publication (Doehne 1997). The authors of the present review compared duplicate samples of a range of painting materials examined using field emission SEM/SE, low vacuum SEM with backscattered electron detector and ESEM (Burnstock and Jones 1999).

Although the problems associated with conventional high vacuum SEM examination of painting materials which contain volatile materials has been recognised, the relative expense and inaccessibility of environmental SEM to conservation scientists could explain why SEM of coated samples has remained the most widely used technique for the study of paintings.

3.8 Sample preparation

The range of techniques for the preparation of samples for imaging from paintings-related studies is remarkably limited. This is linked with the wide availability of high vacuum SEM instruments in universities and museums to which conservators and conservation scientists have access. Most imaging studies employ coating using an unspecified thickness of a conductive metal such as gold or gold palladium, or if used in conjunction
with elemental analysis, carbon. Apart from the few studies where low vacuum or ESEM were available for the study of uncoated samples (for example, Burnstock and Jones, 1999; Burnstock and Kieslich, 1996; Doehne et al., 1990, 1991; Stulik et al., Scott and Hyder, 1993, Derrick et al., 1994) there are few exceptions. Variations have included preparation of pigment samples from paintings, and of canvas fibres using water, solvents and reagents to remove

organic coatings or binding media. Coating water-sensitive material, such as studies carried out by Jakes and Mitchell (1992) carried out a study of water-sensitive textiles recovered from a deep ocean shipwreck. A number of preparation steps were necessary, including critical point and solvent/vacuum freeze drying and coating prior to study using conventional high vacuum SEM. Although this paper does not fall within the remit of this chapter, the study of textile fibres is directly relevant to the examination of canvases and other textile supports for painting.

4. A COMPARATIVE STUDY OF SELECTED ARTISTS MATERIALS USING FOUR ELECTRON MICROSCOPY TECHNIQUES

Figures 1-30 are images of samples from paintings and selected artists materials using a conventional high vacuum SEM/SE (Hitachi S530), field emission SEM/SE (Philips XL30 FEG), low vacuum (variable pressure) SEM/BSE (ISI ABT55) and ESEM/GSE (Philips XL30 ESEM). The images illustrate the different information that can be obtained using these techniques and, in some instances, the presence of artefacts. Artefacts may occur as a result of sample preparation, cleaning or sample interaction with the electron beam and vacuum pressure in the microscope. Other examples include those relating to particular themes in the study of problems in the deterioration of paint from paintings, or experimental studies in the field. The aim is to illustrate the kind of information that can be provided by SEM imaging and to show its limitations. The sample preparation techniques and equipment employed are described in Section 2.

Figures 1-6 "wet process" vermilion pigment, leanly bound in linseed oil, before and after artificial aging using heat and light. Comparison of the images illustrates the information available using different methods of electron microscopy and signal detection. Also note the effects of aging on the samples.

Figures 1 & 2 taken at a magnification of 20,000x using the ESEM/GSE show a single particle of vermilion before (Figure1) and after aging. The particle from the aged film (Figure2) exhibits darkened spots at the surface, which, where it occurs in particles at the surface of the whole film, produces an optical effect of blackening. A thin film of the binding medium is evident surrounding the upper edge of the unaged particle in Figure1, while at this magnification the electron beam penetrates the organic binder to reveal the particle morphology. This is even more pronounced in the image of the same paint film (Figure3) taken using the ABT55/BSE (1000x magnified), where the relatively high atomic number of the pigment particles renders them in high contrast against the oil binding medium. Complimentary information is available from the FEG/SE image also taken at a magnification of 1000x (Figure4), where the smooth homogeneous coating of oil binder on the surface of the pigment in the unaged film is clearly evident.

Figures 1-8

Figure1 ESEM/GSE. Vermilion in oil, single particle before ageing, 20,000x.
Figure2 ESEM/GSE. Vermilion in oil after artificial ageing, single particle showing dark pits in the surface, 20,000x.
Figure3 ABT55/BSE. Vermilion in oil, unaged 1000x.
Figure4 FEG/SE. Vermilion in oil, unaged, 1000x.
Figure5 ABT55/BSE. Vermilion in oil, artificially aged, 1000x.
Figure6 FEG/SE. Vermilion in oil, after artificial aging, 1000x.
Figure7 FEG/SE. Back of canvas from S. Christopher by William de Morgan (c.1865) 100x.
Figure8 FEG/SE. Size-coated canvas from S. Christopher by William de Morgan (c.1865) 100x.

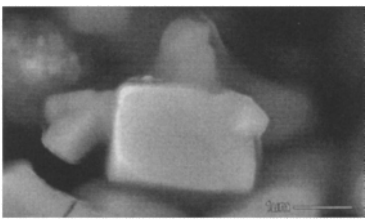

Fig 1

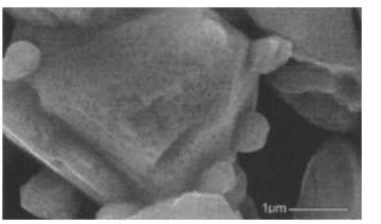

Fig 2

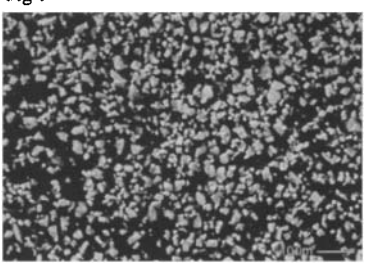

Fig 3

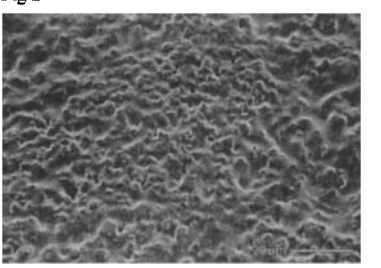

Fig 4

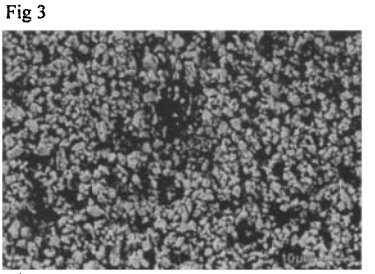

Fig 5

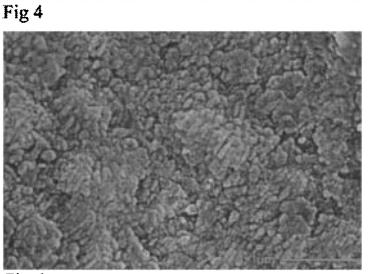

Fig 6

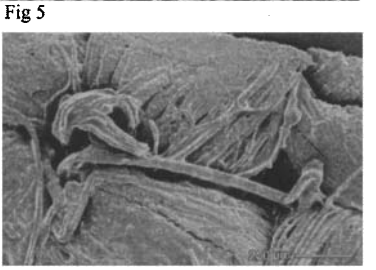

Fig 7

Fig 8

Figures 5 & 6 are directly comparable to Figure 3 & 4, showing the aged film at the same magnification, 1000x. Figure5, taken using the ISI ABT55/BSE illustrates a change in the distribution of the binding medium, suggesting areas of higher and lower concentration of pigment. The FEG/SE image (Figure 6) show a decrease in the overall covering power of the organic binder.

Figure 7-12. Artists' linen canvas

Figures 7-12 are taken using a range of SEM techniques, and show the relationship between proteinaceous size coating and the fibres of linen canvas painting supports. The hygroscopicity of both the cellulose fibres and in particular, the size layer, presents problems for high vacuum SEM/ high kV conditions, and in some images artefacts are evident.

Figures 7 & 8 are samples of canvas from a painting by William De Morgan, dated ca.1865. Both images were taken using the FEG/SE instrument at a magnification of 100x. Figure7 shows an area of the reverse of the canvas, where linen mixed with cotton fibres are imbibed with more than 100 years of dirt. The sample in Figure 8 from the upper surface of the same canvas has a coating of size, which appears as a smooth layer on the surface of the woven yarns. A crack in the layer may be due to embrittlement of the aged protein layer.

Figures 9-11 is of an Ulster linen canvas coated with proteinaceous size, aged naturally for 10 years.

Figure9 illustrates a sample thickly coated with size and imaged using ESEM/GSE. Figure10 from the same sample using ABT55/BSE. The two images provide similar information: both illustrate the marks left by air bubbles that resulted from the size application, and the coating itself appears smooth and unaffected by the electron beam or vacuum. The emphasis on atomic number contrast available using the BSE detector provides more information about the pigment particles on the surface of the size layer. Figure11 is a linen sample with a thin application of size, imaged using the ESEM/GSE and provides greater sub-surface information. It illustrates differences in size thickness (dark pockets where the layer is thinnest) as well as air bubbles. A fine fissure in the size layer is evident in the intersticies of the canvas weave, which is likely to be the result of an electron beam artefact. Figure12 is linen canvas taken from a 19th century painting which suffered flaking loss of paint. The image taken using conventional high vacuum SEM (Hitachi S530/SE) provides a low magnification, tilted view of the surface of the paint, the relationship between paint layers and the size on fibres of the canvas support. The SEM image illustrates an in-focus view with a depth of field unattainable using the light microscope. The image confirmed the hypothesis that the cause of flaking paint in this work is the presence of a moisture responsive layer beneath the paint, of significant thickness beneath the aged, relatively brittle inflexible paint film. Fissures in the size layer are likely to have been produced by the dehydrating effects of the vacuum during coating or examination of the sample.

Figures 13-18. Fungal infestation of artists canvas size and paint

Figures 13-16 show the relationship between fungal hyphae and spores on the hygroscopic proteinaceous size layer and within the paint of samples from S. Christopher by William de Morgan (c.1865). Figure 13 & 14 taken using ESEM/GSE provide information both about the morphology of the fungal infestation and the size and priming below. The hyphae have retained shape during examination, while a small amount of charging is evident in the bright edges of these structures at the higher magnification of 8000x (Figure14). A duplicate sample, uncoated, examined using the ABT55/BSE (Figure15) is limited in its resolution of the hyphae as a result of the chamber pressure in the microscope, c. 3Pa. The image emphasises atomic number contrast, which renders organic structures (hyphae) less visible against a background of organic size. However, the image was recorded using an accelerating voltage of 20kV. The greater beam penetration of the sample gives information about pigment particles in the priming layer beneath the size as well as at the surface of the sample, which is not seen in the ESEM/GSE images recorded at lower voltages.

Figure16, taken at an accelerating voltage of 5kV using the FEG/SE microscope favours surface topography. In the image, taken at a magnification of 50,000x, fungal spores, the largest of which is approximately 250nm diameter, are visible. Suspended fungal hyphae emerge from another spore on the right side of the image. Plates of pigment partly coated by organic size are also evident.

Figure17 illustrates spores on a layer of size, taken using conventional high vacuum SEM/SE (Hitachi S530) and an accelerating voltage of 25 kV. The spores have collapsed in the vacuum, resulting in some compression of their structure. Fissures in the smooth size layer are an artefact caused by both vacuum and electron beam sensitivity of the material.

Figure 18 was taken using a conventional Cambridge Stereoscan 200 SEM with an accelerating voltage of 10 kV. The image shows a well-established network of fungal hyphae on and within the organic binding medium of a paint film. The solid particles of lead white pigment have become poorly bound as the bio-infestation has imbibed the paint binder, and chalking of the paint has occurred.

Figures 9-16

Figure9 ESEM/GSE. Ulster linen, coated thickly with size, 200x.
Figure10 ABT55/BSE. Ulster linen, coated thickly with size, 100x.
Figure11 ESEM/GSE. Ulster linen, coated thinly with size, 100x.
Figure12 SEM/SE Hitachi S530. Tilted view of a sample from a 19th century painting suffering from paint flaking.
Figure13. ESEM/GSE. Fungal hyphae network on the underside of the priming layer from S. Christopher, by William De Morgan (c.1865), 4000x.
Figure14. ESEM/GSE, Fungal hyphae network on the underside of the priming layer from S. Christopher, by William De Morgan (c.1865), 8000x.
Figure15 ABT55/BSE: Fungal hyphae network on the underside of the priming layer from S. Christopher, by William De Morgan (c.1865), 8000x.
Figure16. FEG/SE. Spores and fungal hyphae network on the underside of the priming layer from S. Christopher, by William De Morgan (c.1865) 50,000x.


Fig 9

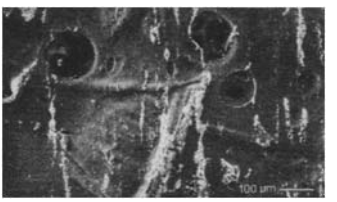
Fig 10

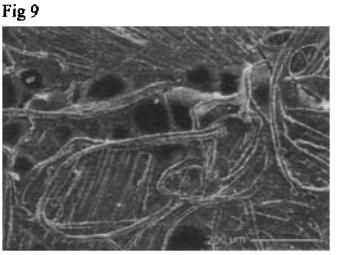
Fig 11

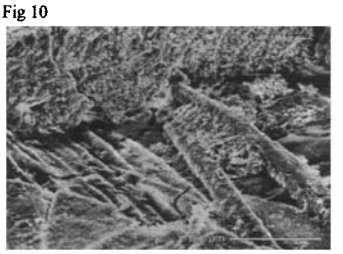
Fig 12

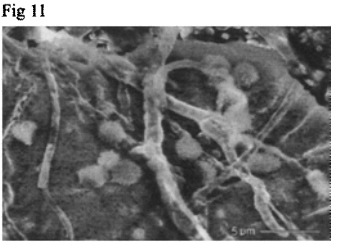
Fig 13

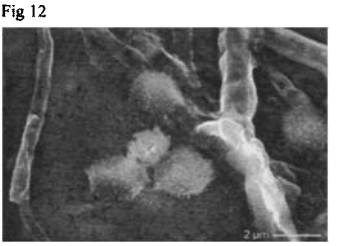
Fig 14

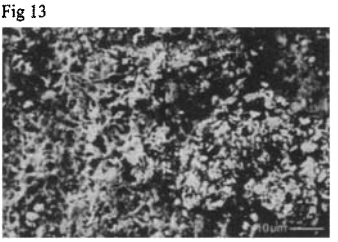
Fig 15

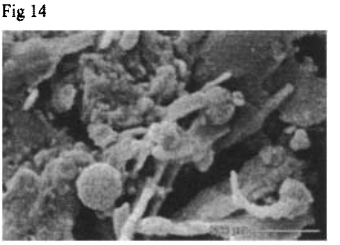
Fig 16

Figure 19-24. Blanching and paint film defects in samples from paintings

Figure 19-24 show images of paint samples taken from areas that appear optically light or white. In each case, close examination of the surface topography of the samples suggests a number of causes of the whitening, or "blanching", of the paint. Figure 19-21 are from the white priming and brown robe of S. Christopher by William de Morgan. On visual examination, all samples exhibit a white patchy surface deposit. Figure19, taken using an ESEM/GSE at 4000x, suggests a disruption in the organic material at the surface and to the pigment particles within and below the surface. Figure20 shows the feather-like organic material on the surface is clearly resolved at 8000x in an image taken using the FEG/SE instrument. The distribution of pigment particles within the film is most evident in the ABT55/BSE image in Figure21, where the inorganic pigment appears bright, in contrast to the binding medium of lower atomic number.

Figure22 illustrates the surface of azurite pigment bound in egg tempera medium after artificial aging using light and heat. The ESEM/GSE image taken at 1000x shows a feather-like organic degradation product on the surface of the paint, which accounts for the visual appearance of light-scattering on the painting.

Figure23 & 24 were taken using conventional high vacuum SEM/SE (Hitachi S530) of samples from paintings, show two different kinds of surface phenomena that result in optical light scattering and a blanched appearance of the painting. The painting sampled for Figure23 had a poorly-wetting synthetic varnish coating, here illustrated by the partial peeling off of the upper layer (varnish) from the undulating paint film below. Figure24 illustrates a sample from an area of brown paint from a 19^{th} century painting and shows rounded cells characteristic of a paint-drying defect produced by the loss of volatile materials from the film, known as hexcell formation. In all cases information about the causes of the light scattering effects was beyond the resolution of the light microscope. The depth of field offered by SEM imaging techniques provided critical evidence for further defining the cause of blanching in these paintings.

Figures 25-30 Cleaning tests using solvent and water swabs on an artificially aged paint film of burnt sienna bound in linseed oil.

The images in Figures 25-30 illustrate a typical experiment conducted using an artificially aged linseed oil paint film pigmented with burnt sienna, before and after treatment by swabbing with solvent or water.

Figures 17-28

Figure17. SEM/SE Hitachi S530. Fungal spores on sized canvas from a 19th century painting.
Figure18. SEM/SE Cambridge Stereoscan 200. Fungal spores and hyphae on the surface of a lead white paint film, 1150x.
Figure19. ESEM/GSE Blanched brown paint from S. Christopher by William de Morgan, 4000x.
Figure20 FEG/SE Blanched priming from S. Christopher by William de Morgan, 8000x.
Figure21 ABT55/BSE Blanched brown paint from S. Christopher by William de Morgan, 500x.
Figure22. ESEM/GSE Azurite pigment bound in egg tempera artificially aged, 1000x.
Figure23. SEM/SE (Hitachi S530) A poorly wetting layer of synthetic varnish on a paint film.
Figure24. SEM/SE (Hitachi S530) Brown paint from a 19thC painting showing a surface paint film drying defect resulting in the formation of "hexcells".

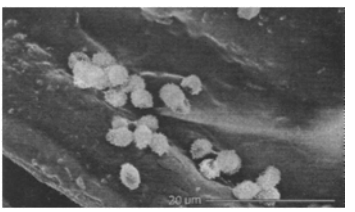
Fig 17

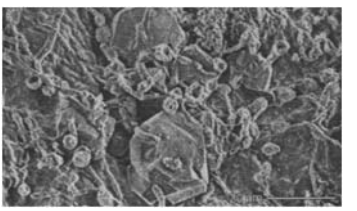
Fig 18

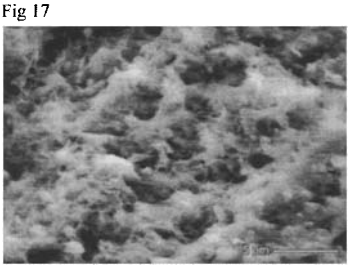
Fig 19

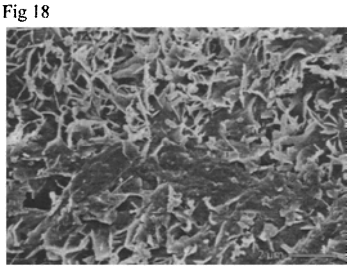
Fig 20

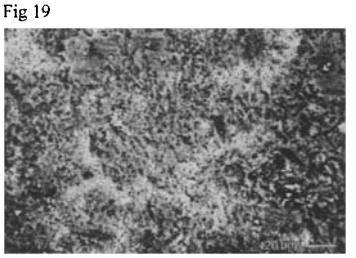
Fig 21

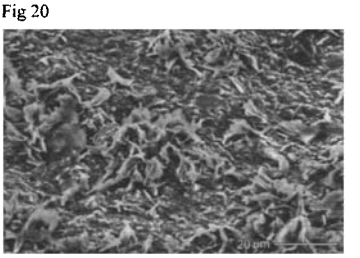
Fig 22

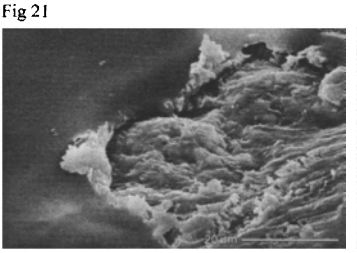
Fig 23

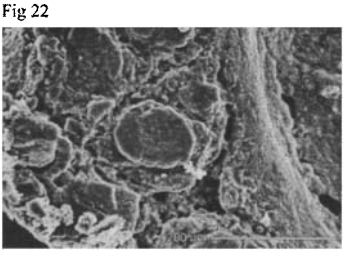
Fig 24

Figures 25-30

Figure 25 ESEM/GSE paint film surface before treatment.
Figure 26 ABT55/BSE paint film surface before treatment.
Figure27 FEG/SE paint film surface before treatment.
Figure28. FEG/SE paint film surface after swabbing with water.
Figure29. FEG/SE paint film surface after swabbing with IMS.
Figure30. ABT55/BSE paint film surface after swabbing with IMS.

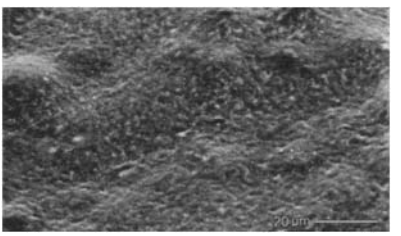

Fig 25

Fig 26

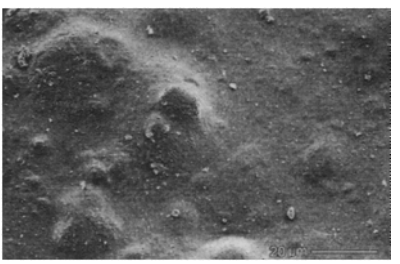

Fig 27

Fig 28

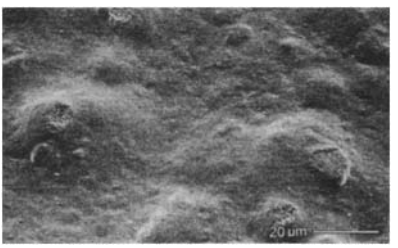

Fig 29

Fig 30

All the micrographs were taken at 1000x magnification, to facilitate scale comparison of samples before and after treatment. Figures 25-27 show the paint film before treatment. The relatively medium rich surface of the paint is most evident in the image taken using the FEG/SE instrument (Figure27), while the ESEM/GSE image (Figure25) combines surface topography with some contrast between pigment and binder beneath the surface. The ABT55/BSE image predictably emphasises the peaks and troughs in the paint, where peaks are created by sub-surface inorganic particles of iron-oxide sienna pigment coated with a thin layer of the darkly contrasting oil medium. Figure 28 taken using the FEG/SE instrument illustrates the surface of the paint after swabbing with water: the oil is slightly swollen, and small particles of dust have lodged in the softened surface. Figure 29 & 30 show the paint surface after treatment with ethanol (IMS), using the FEG/SE and ABT55/BSE respectively. The mechanical swabbing with the solvent has etched, or "topped" the organic binder covering the peaks in the paint film. Both images illustrate this phenomenon showing crater-like areas where the smooth surface of the oil has been disrupted, and in both images a difference between surface topography and the bulk structure of the paint film is suggested. The depth of field shown in the FEG/SE image (Figure 29) confirms that the peaks of the paint medium are the most affected by treatment. This is less clear in the low vacuum image (Figure 30), which provides information about pigment particle (grey patches) and surface particle (brightly contrasting) distribution.

REFERENCES

Alessandrini, G., Bonecchi, R., Burgini, R., Fedeli, E., Ponticelli, I.S., Rossi, G., and Toniolo, L. (1989). Bramante in Milan: the Cascina Pozzobonelli, technical examination and restoration. Studies in Conservation 34, 56-63.

Ansell, P. (1994). Scanning electron microscopy and the study of coatings. JOCCA 32-1, 3, 99-101.

Aslam, M. (1990). Studies on Taj Mahal plasters. Studies in Conservation 35, 102-6.

Barnes S. (1991). Electron microscopy and analysis at the Natural History Museum, Microscopy and Analysis 25, 29-37.

Bell, S.H. (1960). Electron microscopy and paint technology: a survey. JOCCA 43, 406-492.

Bladin, H. P., David, J.C., Verngnaud, J.M., Illen J.P. and Malizewicz, M. (1987). Modelling the drying process of coatings with various layers. Journal of Paint Technology 59, 27-32.

Bomford, D., Kirby, J., Leighton, J., and Roy, A. (1990). Impressionism, The National Gallery, London, in association with Yale University Press, New Haven and London.

Bomford, D., Dunkerton, J., Gordon D., and Roy, A. (1989). Italian Painting Before 1400, National Gallery Publications Ltd., London.

Bomford, D., Brown, C., and A. Roy (1988a). Rembrandt, National Gallery Publications Ltd., London.

Bomford D. and Roy A. (1986). The techniques Dieric Bouts: two paintings contrasted. National Gallery Technical Bulletin 10, 39-57.

Bower, N.W., Stulik, D.C., and Doehne E. (1994). A critical evaluation of the environmental scanning electron microscope for the analysis of paint fragments in art conservation. Fresenius J.Anal. Chem.348, 402-410.

Bozzola, John J. and Russell, Lonnie D. (1992). Electron Microscopy Principles and Techniques for Biologists. John and Bartlett Publishers, Boston.

Burnstock, A. and Jones C. (1999). A comparative study of the surface characterisation of artists paints using conventional, low vacuum and environmental electron microscopy. 6th International Conference on non-destructive testing and microanalysis for the diagnostics and conservation of the cultural and environmental heritage, AIPND Rome,
2,1129-1143.

Burnstock, A. (1997). Scientific examination and the restoration of easel paintings at the Courtauld Institute of Art: case studies. Interface between Science and Conservation, British Museum Occasional Paper Series 16, 47-58.

Burnstock, A. and Kieslich, T. (1996). A study of the clearance of solvent gels used for varnish removal from paintings. ICOM Committee for Conservation, 1, 253-262.

Burnstock, A. (1995). The Deeper Picture. Chemistry in Britain 31, 621-626.

Burnstock, A. (1992). Chemistry beneath the surface of Old Master paintings. Chemistry and Industry 18, 192-195.

Burnstock, A. and Learner, T. (1992). Changes in the surface characteristics of artificially aged mastic varnishes after cleaning using alkaline reagents, Studies in Conservation 37, 165-184.

Burnstock, A. (1991). The application of scanning electron microscopy (SEM) to the examination of painting materials with special reference to cleaning and blanching, PhD thesis, Courtauld Institute of Art.

Burnstock, A. and White, R. (1990). The effects of selected solvents and soaps on a simulated canvas painting. Cleaning, Retouching and Coatings, IIC, London, 111-118.

Carter, O.L., Schindler, A.T., and Wormser, E.E. (1974). Scanning electron microscopy for evaluation of paint film weatherability. Applied Polymer Symposium 23, 13-25.

Cheever, D.C. (1986). Analyses of defects occurring at interfaces in multilayer paint systems on polymeric substrates. Journal of Coatings Technology 58, 25-37.

Clements, G. and Holden, J.R.J. (1988). Report on pilot project to determine whether various processing techniques of paper fibres can be distinguished either visually of experimentally by the scanning electron microscope. Conservation Analytical Laboratory, Smithsonian Institution.

Chescoe, Dawn and Goodhew, Peter J. (1990). The operation of transmission and scanning electron microscopes. Royal Microscopical Society Handbook 20, 1990.
Oxford Science Publications.

Danilatos, G.D. (1988). Foundations of Environmental Scanning Electron Microscopy, Academic Press.

Danilatos, G.D. and Postle, R. (1982). The environmental SEM and its applications. Scanning Electron Microscopy, Vol.1982 I: 1-16.

Derrick, M., Doehne, E.F., Parker, A.E. and Stulik, D.C. (1994). Some new analytical techniques for use in conservation. JAIC 33, 171-184.

Doehne, E. (1997). ESEM development and application in cultural heritage conservation, In-situ Microscopy in Materials Research, P. L. Gai, ed., Kluwer Academic Publishers, 45-62.

Doehne, E. and Stulik, D. C. (1991). Dynamic studies of materials using the environmental scanning electron microscope. Mat.Res.Soc.Symp.Proc. 185, 31-37.

Doehne, E. and Stulik, D. C. (1990). Applications of the environmental scanning electron microscope to conservation science. Scanning Microscopy 4, 275-286.

Domech-Carbo, M. T. and Aura-Castro, E. (1999). Evaluation of the phase inversion process as an application method for synthetic polymers in conservation work. Studies in Conservation 44, 19-28.

Dunkerton, J. and Roy, A. (1986). The technique and restoration of Cima's "The Incredulity of Saint Thomas". National Gallery Technical Bulletin, 10, 4-27.
Duval, A. (1985). Microscopie electronique a balage, Les Methodes Scientifiques dans l'Etude et la Conservation des Oeuvres d'Art, 2nd edition, Ecole de Louvre, Paris.

Edmonds, P. (1990). Fungi and its relationship with Aboriginal painted surfaces containing the PVA emulsion binder "Aquadhere". ICOM Committee for Conservation, I, 151-156.

Eipper, P. B., and Reiss, G. (1996). Comparative examinations of cleaning agents applied to surfaces of paintings. The Picture Restorer 10, 5-10.

Eissler, R. L., Baker, F.L. and Stolp, J. A. (1974). The filler-binder interface in paint films. Applied Polymer Symposium 23, 41-8.

Erhardt, D. and Bischoff, J. (1994). The roles of various components of resin soaps, bile acid soaps and gels and their effect on oil paint films. Studies in Conservation 39, 3-27.

Everhart, T. E., and Thornley, R. F. M. (1960). J. Sci. Instr. 37, 246.

Feller, R.L. (ed.) (1986). Artists Pigments, A Handbook of their History and Characteristics, Vol.1, Cambridge University Press.

Feller, R.L. (1972). Scientific examination of artistic and decorative colorants. Journal of Paint Technology 44, 51-8.

Funke, W. (1976). Preparation and properties of paint films with special morphological structure. JOCCA 59, 398-403.

Gay, M-C. and Monrocq, R. (1972). Identification des fibres textiles naturelles par examen microscopie. Laboratoire de Recherche des Musees de France Annales, 16-22.

Gettens, R.J. and Fitzhugh, E.W. (1974a). Malachite and green verditer. Studies in Conservation 19, 2-23.

Gettens, R.J., Fitzhugh, E.W. and Feller, R.L. (1974b). Calcium carbonate whites, Studies in Conservation, 19, 157-184.

Gettens, R.J. (1958). Identification of pigments and inerts on paintings and other museum objects, Application of Science in Examination of Works of Art. 31-50.

Goldstein, J.I., Newbury, D.E., Echlin, P., Joy, D.C., Romig, A.D., Lyman, C.E., Fiori, C. and Lifshin, E. (1992). Scanning Electron microscopy and X-ray Microanalysis, 2nd Ed. Plenum NY.

Groen, K. (1997). Investigation of the use of the binding medium by Rembrandt. Kunsttechnology und Konservierung 11, 207-227.

Groen, K. (1988). Scanning electron microscopy as an aid in the study of blanching in paints by Claude. Hamilton Kerr Institute Bulletin 1, Ian McClure ed., 48-65.

Gutscher, D., Mulethaler B., Portmann, A. and Reller, A. (1989). Conversion of azurite into tenorite. Studies in Conservation 34, 117-22.

Hallstrom, B. and Goransson, B. (1974). Microbial Environment SEM - examination of the Microbial Environment in Works of Art, Dokumenta Brahegatan 43, 11437 Stockholm.

Harding, E., Braham, A., Wyld, M. and Burnstock, A. (1989). The restoration of the Leonardo Cartoon. National Gallery Technical Bulletin, 13 5-28.

Hedley, G., Odlyha, M., Burnstock, A., Tillinghast, J. and Husband, C. (1990). A study of the mechanical and surface properties of oil paint films treated with organic solvents and water. Cleaning, Retouching and Coatings, IIC, London, 98-105.

Hoffmann, C., Flamm, V., Banik, G. and Messner, K. (1990). Bleaching of foxing stains in Art Nouveau prints, ICOM Committee for Conservation II, 472-477.

Jakes, K.A. and Mitchell, J.C. (1992). The recovery and drying of textiles from a deep ocean shipwreck. JAIC 31, 343-353.

Kampf, G., Papenroth, W., Volz, H.G. and Weber, G. (1982). Time-lapse observation of chalking under the electron microscope. Proceedings of the 16th FATIPEC Congress, Liege 3, 167-74.

Kennedy, V. O. (1988). Polymeric motions detected by wetting measurements at the film/water interface as influenced by conformational changes at the film/substrate interface. Journal of Paint Technology 60, 37-51.

Koestler, R.J., Charola, A.E. and Wheeler, G.E. (1983). Scanning electron microscopy in conservation: the Abydos reliefs. Application of Science in Examination of Works of Art, Museum of Fine Arts, Boston, 225-9.

Kuhn, H. (1985). A scientific examination of Leonardo's Last Supper in Santa Maria dell grazie, Milano. Maltechnik Restauro 4, 24-51.

Lange, J., Andersson, H., Manson, J.A.E. and Hult, A. (1996). Microscopic, stereoscopic and rheological analysis of solvent-free organic coatings. Surface Coatings International JOCCA 79, 486-491.

Leighton, J., Reeve, A., Roy, A. and White, R. (1987). Vincent Van Gogh's "A Cornfield, with Cypresses". National Gallery Technical Bulletin 11, 42-59.

Leonard, M., Preusser, F., Rothe, A. and Schilling, M. (1988). Dieric Bouts's Annunciation, materials and techniques: A summary. Burlington 17-22.
McCrone, W. C. and Delly, J. C. (1973). The Particle Atlas. Ann Arbour Science Publishers, 2nd Edition, Vols.2 and 3.

Mansmann, K. (1998). Oberflachenrienigung mit Ammoniumcitraten. Kunsttechnologie und Konservierung 11, 220-237.

Martin, E. and Duval, A.R. (1990). Les deux varietes de jaune de plomb et detain etude chronologique. Studies in Conservation 35, 117-36.

Moffatt, E., Adair, N.T. and Young, G.S. (1983). The occurrence of oxalates on three Chinese wall paintings, Application of Science in the Examination of Works of Art, Museum of Fine Arts, Boston, 234-37.

Moll, S. (1976). Scanning electron microscopy: a versatile tool. Technology and Conservation 1, 24-28.

Murley, R. D. and Smith, H. (1970). An electron microscope examination of the "clear layer" at the surface of gloss paint films. JOCCA 53, 292-8.

Parham, R.A. and Kaustinen, H.M. (1974). Papermaking Materials: An Atlas of Electron Micrographs, Division of natural materials and systems in the Institute of Paper Chemistry, Graphics Communication Centre, Appleton, Wisconsin.

Phenix, A. and Burnstock, A. (1990). Surface dirt: A review of the literature with a scanning electron microscope study of dirt on selected paintings, U.K.I.C. London, 11-18.

Plesters, J., Roy, A. and Bomford, D. (1982). Interpretation of the magnified image of paint surfaces and samples in terms of condition and appearance of the picture. Science and Technology in the Service of Conservation, Bromelle, N.S and Smith, P. (eds.) IIC London 169-176.
Plesters, J. (1956). Cross-sections and chemical analysis of paint samples. Studies in Conservation II, 110-132.

Plesters, J. (1954). The preparation and study of paint cross-sections. The Museums Journal, London, LIV, 97-101.
Perera, D.Y. and Heertjes, P.M. (1971). Water transport through paint films Part V: Pigmented films. JOCCA 54, 774-94.

Princen, L.N., Baker, F.L. and Stolp, J.A. (1974). Monitoring coatings performance upon exterior exposure. Applied Polymer Symposium 23, 27-40.

Quach, A. (1974). Applications of energy dispersive X-ray spectroscopy in interfacial coating failures. Applied Polymer Symposium 23, 49-59.

Raaschou, H.K., Kornum, L.O. and Saberg, O. (1978). Dirt retention on painted surfaces. Journal of Coatings Technology 50, 69-78.

Raehlmann, E. (1914). Uber die Farbstoffe der Malerei, Seemann, Leipzig.

Raehlmann, E. (1910). Uber die Maltechnik der Alten, George Reiner, Berlin.

Robert John Associates (1996). Environmental Scanning Electron Microscopy. An introduction to ESEM.

Robinson, V. N. E. (1975). SEM/1975, IIT Research Institute, Chicago, Illinois, 51.

Rodriguez Navarro, C. and Doehne, E. (1999). Time-lapse video and ESEM microscopy: Integrated tools for understanding processes in-situ. American Laboratory.

Rosenthal, W.S. and McBane, B.N. (1973). Microvoids as light scatter sites in polymer coatings. Journal of Paint Technology 5, 73-80.

Roy, A. ed., (1993). Artists Pigments. A Handbook of their History and Characteristics, Vol.2, National Gallery of Art Washington DC and Oxford University Press.

Roy, A. (1988). The technique of a Tuchlein by Quinten Massys. National Gallery Technical Bulletin 12, 36-43.

Sonoda, N., Martin, E., Duval, A. and Grimstad, K. (1990). Utilisation des microscopes optique et electronique pour Ietude des preparations blanches de tableaux Italiens sur bois. IIC London, 79-82.

Stringari, C. (1990). Vincent van Gogh's tryptich of Trees in Blossom, Arles (1888) Part 1. Examination and treatment of the altered surface coatings. Cleaning, Retouching and Coatings, IIC London, 126-30.

Stulik, D. and Doehne, E. (1991). Applications of environmental scanning electron microscopy in art conservation and archaeology. Mat.Res.Soc.Symp.Proc. 185, 23-29.

Townsend, J., Carlyle, L., Burnstock, A., Odlyha, M. and Bone, J. (1998). Nineteenth Century Paint Media: the formulation and Properties of Megilps. Painting Techniques History, Materials and Studio Practice, IIC London 205-210.
Townsend, J. (1994). Microscopy and paintings. Microscopy and Analysis 39, 11-13.

Von Ardenne, M. (1938). Z. Phys. 109, 553.

Von Ardenne, M. (1938). Z. Techn. Phys. 19, 407.
Underhaug, A., Lund, T.J. and Kleive, K. (1983) Wood protection - the interaction between substrate and product and the influence on durability. JOCCA 66, 345-350.

Waggoner, R.A. and Blum, F.D. (1989). Solvent diffusion and drying of coatings. Journal of Coatings Technology 61, 51-7.

West Fitzhugh, E. ed. (1997). Artists Pigments A Handbook of their History and characteristics, Vol.3, National Gallery of Art Washington DC and Oxford University Press.

Winter, J. (1983a). The characterization of pigments based on carbon. Studies in conservation 28, 49-66.

Winter, J. (1983b). Gold in Japanese paintings: A case history involving the Kirikane technique. Application of Science to the Examination of Works of Art, Museum of Fine Arts, Boston, 46-54.

Winter, J. (1975). Chalk-glue grounds from paintings for scanning electron microscopy. Studies in Conservation 20, 169-173.

White, R. and Roy, A. (1998). GC-MS and SEM studies on the effects of solvent cleaning on old master paintings from the National Gallery, London. Studies in Conservation 43, 59-76.

Woodward, A.E. (1988). Atlas of Polymer Morphology, Hanser Publishers, New York.

Zicherman, J.B. and Thomas, R.J. (1972). Scanning electron microscopy of weathered coatings on wood. Journal of Paint Technology 44, 88-94.

Zworykin, Hillier and Snyder (1942). ASTM Bulletin 117, 15.

Radiation in Art and Archeometry
D.C. Creagh and D.A. Bradley (editors)

Transmission Electron Microscopy and its use for the study of paints and pigments

S. Bulcock

Electron Microscopy Unit (F09), University of Sydney, Sydney, NSW 2006, Australia

This chapter outlines principles underlying the formation of transmission electron diffraction patterns, in particular the selected area diffraction (SAD) and the convergent beam electron diffraction (CBED) patterns. It then proceeds to give examples of studies taken from small paint fragments from two artworks in which the CBED technique was used in conjunction with energy dispersive x-ray analysis (EDAX) to determine the mineral composition of the fragments.

1. INTRODUCTION

When restoring a work of art conservators are faced with the dilemma of needing to minimise the disfigurement of images, due to fragments missing, while still maintaining the original artist's designs. The ability to positively identify certain paints and pigments, from the smallest extractable samples, is therefore essential, especially in the study or conservation of any art work. For this reason, conservators must be able to analyze ever-decreasing sample sizes. Since the pioneering work of John Haslem, and reported by [1], Jean Chaptal [2] and Sir Humphry Davy [3], where destructive chemical tests were employed in identifying certain compounds, many techniques have been developed with the aim of fulfilling these requirements. These include, optical spectroscopy to identify certain crystals by their distinctive shapes [4], and infrared spectroscopy to analyse paints and binders [5]. Fourier transform infrared spectroscopy (FTIR) has been shown to be useful in distinguishing between different binders [6]. X-ray diffraction (XRD) and x-ray fluorescence spectroscopy (XRF) are also used routinely in archaeology [7].

Other non-destructive techniques such as scanning electron microscopy (SEM) and electron microprobe analysis, which utilise energy dispersive x-ray detectors (EDS) and wavelength dispersive x-ray detectors (WDS), provide sufficient dimensional resolution to detect the inorganic contents of individual layers and are commonly used by conservators. These detectors rely on the analysis of characteristic x-rays emitted by an atom decaying to its ground state after having its bound electrons excited by the incident electron beam to a higher energy orbital.

The transmission electron microscope (TEM), with an EDS detector attached, is another very powerful instrument that has been used in materials science and crystallography for a long time, but it is used surprisingly little in conservation. A search of the literature has found

very few publications where TEM was employed and even fewer cases where electron diffraction was used, authors usually reported using the technique only to obtain very high magnifications of images. One of the few publications where electron diffraction was used is by Kleber et al., [8]. In his paper, he investigated a blue pigment formed by reacting attipulgite with indigo at 190 ^{0}C, which was determined to be "Maya Blue" from its diffraction patterns.

There are many obvious advantages to TEM, mainly its ability to give simultaneous elemental composition using EDS and crystal structure information by selected area diffraction (SAD) or convergent beam electron diffraction (CBED). This approach has been avoided by conservators because of the belief that, with the number of layers usually present in a paint sample, it would be difficult to separate and identify them. Then one question that needs to be asked is: why bother with TEM when SEM and XRD can separately identify the composition of paint layers and their crystal structure. To answer this: with the exception of SEMs specially fitted with "Back Scattered Kikuchi" detectors, the TEM has a unique advantage in that it can do simultaneous composition and crystallographic determination so providing a means of identifying a compound outright. This avoids the problems associated with moving a specimen between two machines, as would have to be done in a combined SEM and XRD study, and relating their respective data.

A second question is then: why do you need electron diffraction anyway? Is not x-ray diffraction sufficient? In answer to this question, data obtained from EDS will often fail to identify a single compound uniquely because of the numerous slight variations in elemental concentrations. To identify a compound properly using EDS solely, one must have well calibrated samples of close composition, with which one can make a comparison. However such standards are usually not available. Finally several compounds exist in more than one crystallographic form (alotrophism), and only by determining the crystal structure can they be identified. Electron diffraction has many advantages over x-ray diffraction in determining crystal structure data. Because x-ray diffraction can be approximated by kinematical scattering events, it obeys "Friedel's law". In simple terms this means that, the intensity of opposing reflections in an x-ray diffraction pattern will be equal (i.e. $I(hkl)$ equals $I(\bar{h}\bar{k}\bar{l})$). This has the effect of limiting the number of crystal types that can be determined by XRD to fifty. With electron diffraction, multiple scattering (i.e. dynamical scattering) of the electron beam as it passes through the specimen, results in a break down of Friedel's law, allowing for the unique identification of all 230 possible crystal types.

The TEM has other advantages over the SEM also, because it generally operates at much higher accelerating voltages, and the samples are generally much thinner, the electron beam suffers less broadening through scattering. So the spatial resolution and effective spot size are a lot smaller, tens of nanometres (nm) for TEMs as opposed to micrometres (μm) for SEMs. This means that for a sample consisting of multiple layers of differing composition, it is easier to distinguish the compositions of these individual layers in a TEM. It might be noted that the spatial resolution of a TEM can be improved by an order of magnitude, by the use of a parallel electron energy loss detector. A discussion of EEL detectors is beyond the scope of this text.

2. PRINCIPLES OF TRANSMISSION ELECTRON MICROSCOPY AND ELECTRON DIFFRACTION.

In this section the topics of transmission electron microscopy and electron diffraction will be discussed, specifically CBED or micro-diffraction. It is however important that some of the background theory to diffraction, in a simplified form, is mentioned as well as the more general technique of SAD used in TEM.

Louis de Brogli.e. [9] first formulated the theory that an electron had wave-like characteristics and a wave length, and that this was much smaller than that of visible light. In 1927 Davisson and Germer [10] and Thompson and Reid [11] independently demonstrated that an electron had a wave-like nature and could be diffracted when passing through a thin crystal. Hans Bethe, in his Ph.D. thesis in 1928, proposed the use of Bloch waves, to explain the observations of Davisson and Germer, and Thompson and Reid. Bethe's theory was later extended to the transmission case by Blackman [12]. In the mean time Knoll and Ruska [13] had built the first electron lenses and demonstrated electron images taken on the instrument.

The resolution limit of a light microscope is described in terms of the Rayleigh criterion.

$$\delta = 0.61\lambda/\mu\sin\beta \tag{1}$$

where μ is the refractive index of the material between the object and the lenses, and β is the semi angle of collection of the magnifying lens. In a TEM, where only very small scattering angles are involved, this criterion can be approximated by

$$\delta = 0.61\lambda/\beta \tag{2}$$

where $\mu = 1$ in a vacuum. It should be noted however that due to lens aberrations, a TEM approaches nowhere near this resolution limit. Based on de Broglie's idea of wave- particle duality, a particle's momentum ρ is related to its wavelength λ by,

$$\lambda = h/\rho \tag{3}$$

h being Planck's constant. In an electron microscope, the kinetic energy (eV) gained by the electron as it is accelerated by the electron gun is equal to the electron's drop in potential energy (V) so that

$$eV = m_0 \upsilon^2/2 \tag{4}$$

And applying this to de Broglie's formula we find that

$$\lambda = h/\left(2m_0 eV\right)^{1/2} \tag{5}$$

This treatment is however too simplistic because it neglects relativistic effects, which are important in electron microscopy since the electrons are accelerated to potentials of typically 100 keV (achieving a velocity of approximately half the velocity of light). Introducing a correction for relativistic effects, the wavelength λ is then,

$$\lambda = h/\left[2m_0eV\left(1+eV/2m_0c^2\right)\right]^{1/2} \tag{6}$$

So as can be seen, increasing the acceleration voltage has a dramatic effect on the wavelength of the electrons and so is critical for resolution.

When an electron beam passes through a specimen, it is either scattered by a variety of processes or remains relatively unaffected by the specimen. This scattering can be described in terms of coherent and incoherent scattering (or as elastic and inelastic scattering). For elastic scattering there is no loss of energy : for inelastic scattering there is a measurable loss of energy. The emerging beam, which has a non-uniform distribution of energies and scattering directions, contains the structural and chemical information about the specimen.

The probability of an electron interacting with an atom as it passes through a sample is described in terms of its "cross section" (σ) and "mean free path" λ, where the mean free path (λ) describes how thin the sample needs to be to avoid or minimize plural scattering. The cross section (σ), when divided by the actual area of the atom, represents the probability that a scattering event will occur. For the simplified case of a specimen of thickness t, which contains N atoms/unit volume, and where effects such as electron cloud screening are ignored, the total probability of scattering an electron as it passes through the sample is

$$Q_T t = N_0\sigma_T(\rho t)/A \tag{7}$$

where N_0 is Avogadro's number, σ_T is the total scattering cross section for an isolated atom (i.e. $\sigma_{elastic} + \sigma_{inelastic}$), and A is the atomic weight of the atoms in the specimen which have a density of ρ and "mass thickness pt, [14].

Alternatively one can describe the probability of an electron scattering in terms of λ. λ represent the average distance that an electron travels between scattering events. The probability of an electron scattering as it passes through a specimen of thickness t is then

$$1/\lambda = N_0\sigma_T(\rho t)/A\,. \tag{8}$$

The total scattering cross section, called Rutherford, or electron- nucleus scattering, is $\sigma_{nucleus} = 1.62\times10^{-24}(Z/E_0)^2\cot^2(\theta/2)$, [15]. The total probability of scattering an electron is then

$$Q_{nuclues}t = (N_0(\rho/A)t)\sigma = 1.62\times10^{-24}(N_0(\rho/A)t)(Z/E_0)^2\cot^2(\theta/2) \tag{9}$$

The differential cross section given by

$$d\sigma/d\Omega = (1/2\pi\sin\theta)d\sigma/d\theta \tag{10}$$

and defines the range of angles thought which the electron can be scattered. Where the solid angle Ω is simple defined as $\Omega = 2\pi(1-\cos\theta)$.

The intensity of this scattered wave, for an isolated atom, is then defined as $|f(\theta)|^2 = d\sigma(\theta)/d\Omega$ where $f(\theta)$ is called the atomic scattering factor. The total amplitude of the scattered wave, summed over all atoms within a unit cell is defined as the structure factor

$$F(\theta) = \sum_i f_i(\theta) e^{i\phi_i} = \sum_i f_i(\theta) e^{2\pi i(hx_i + ky_i + lz_i)} \tag{11}$$

where x_i, y_i, and z_i are the positions of the atoms in the unit cell. The atomic scattering factors for each atom have been multiplied by a phase factor to account for the difference in phases between waves scattered on different planes with Miller indices, (hkl).

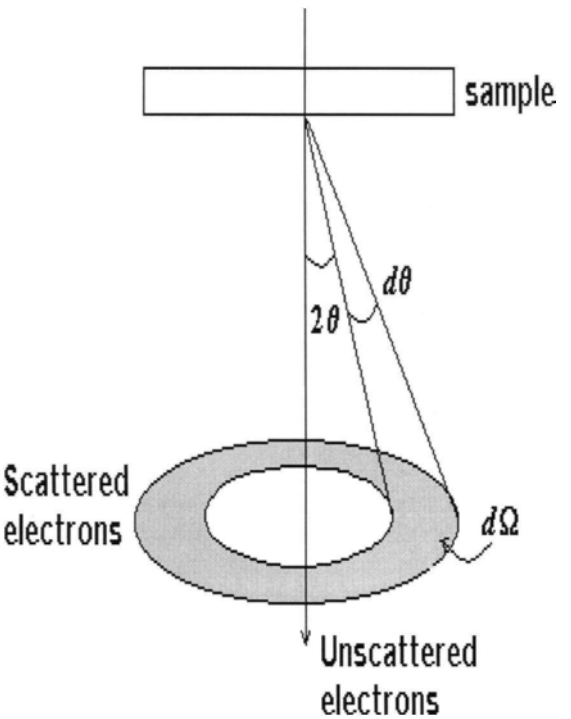

Figure 1. Scattering of an electron by a single atom.

When an electron beam is scattered from atoms within a plane, these atoms act like individual sources of electron wave fronts. These individual wavefronts then interfere with

each other, either constructively or destructively. If we define the wavefront being scattered from an individual atom in terms of wave vector k, a wave vector being perpendicular to the wavefront, by simple vector addition we have $K = k_D - k_I$, where k_D and k_I are the diffracted and incident wave vectors (assuming elastic scattering), and

$$|k_I| = |k_D| = 1/\lambda \tag{12}$$

We can use trigonometry to derive the relationship

$$\sin\theta = |K|/(2/k), \text{ or, } |K| = 2\sin\theta/\lambda \tag{13}$$

in its better known form.

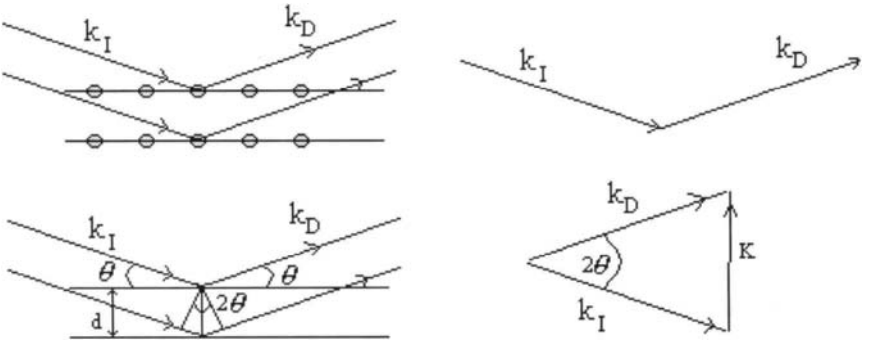

Figure 2. The Bragg description of electron scattering by atom planes.

Extending this to interference by two atoms we find that

$$AC + CD = 2d\sin\theta \tag{14}$$

where $AC + CD$ is the difference in length that the wave vectors travel and d is the length of the vector between the two atoms. Consider now, the case of Bragg angle (θ_B) scattering, i.e. the angle where electron wave interference scattering is constructive, then the difference vector is $|K| = 2\sin\theta_B/\lambda$. The path difference between two planes of atoms is then $n\lambda$ and we get the equation $n\lambda = 2d\sin\theta_B$. For the case of $n = 1$, the magnitude of the vector K is denoted K_B, and becomes $|K_B| = 1/d = g$, where g is often referred to as the diffraction vector.

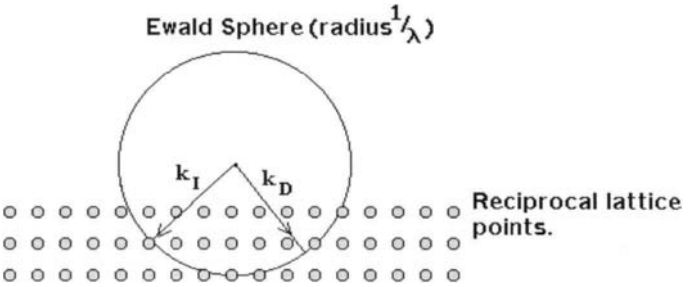

Figure 3. Construction of a Ewald Sphere of reflection.

To determine when a Bragg condition is satisfied, a technique using a sphere of reflection, or "Ewald Sphere" is commonly used. The technique involves firstly drawing a three-dimensional set of reciprocal lattice points. Over this 3D set of lattice points, a sphere of radius $1/\lambda$, the "Ewald" sphere, is drawn, (Figure 3 shows a 2D cross section of this). Wherever the Ewald sphere intersects a reciprocal lattice point, the Bragg condition is satisfied and a diffraction spot results.

It is still possible to get electron diffraction spots generated even when the Ewald sphere does not intersect a reciprocal lattice point, because in a TEM, the much thinner crystals required for TEM observation result in a limited periodicity in the vertical direction. The Fourier transform of this limited periodicity, which can no longer be approximated as being infinite, results in the lattice points being extended into rods. The distance from the Bragg condition, where diffraction beams are still being observed, is represented by the vector s known as the *excitation error*. The diffraction vector K is then ($K = g + s$).

The lattice for a crystal can be represented in two forms, one which describes the arrangements of the units cells of the atoms within the crystal, and the other called a reciprocal lattice, which is the Fourier transform of the lattice. In this case, each point corresponds to a particular set of planes within a crystal. This representation was first described by Gibbs in 1881, and applied by Ewald in 1911-14 to explain observed diffraction. It has since become a very useful method for providing a physical picture for understanding diffraction geometries.

The amplitude of the scattered beam, for a single unit cell, is simply the structure factor, equation (11). By summing this for all unit cells in the specimen, the amplitude of the diffracted beam ϕ_g , in the direction θ , is then given by

$$\phi_g = \left(\pi a i / \xi_g\right) e^{-2\pi i K \cdot r_n} e^{2\pi i k_D \cdot r} \tag{15}$$

where there are n unit cells per unit area on a plane parallel to the crystal surface. The distance between these planes is a and r_n denotes the position of each unit cell. ξ_g is called the

"extinction distance" because, at a thickness of ξ_g, the diffracted beam will have zero intensity (i.e. be extinct).

There are fourteen basic lattice types (see **Figure 4**), which, when combined with other symmetry operators such operators as mirrors planes, glide planes, and screw axes, give rise to a total of 230 possible crystal types. Certain lattices, like body centered cubic (Cubic I) and face centered cubic (Cubic F), have what are known as "kinematically" forbidden reflections. These are reflections where, due to the arrangements of the atoms in the unit cell, the structure factor equation (11) is zero, i.e.

$$F(\theta) = \sum_i f_i e^{i\phi_i} = \sum_i f_i e^{2\pi i(hx_i + ky_i + lz_i)} = 0 .$$

However, they can still be present due to multiple, i.e. dynamical, scattering events.

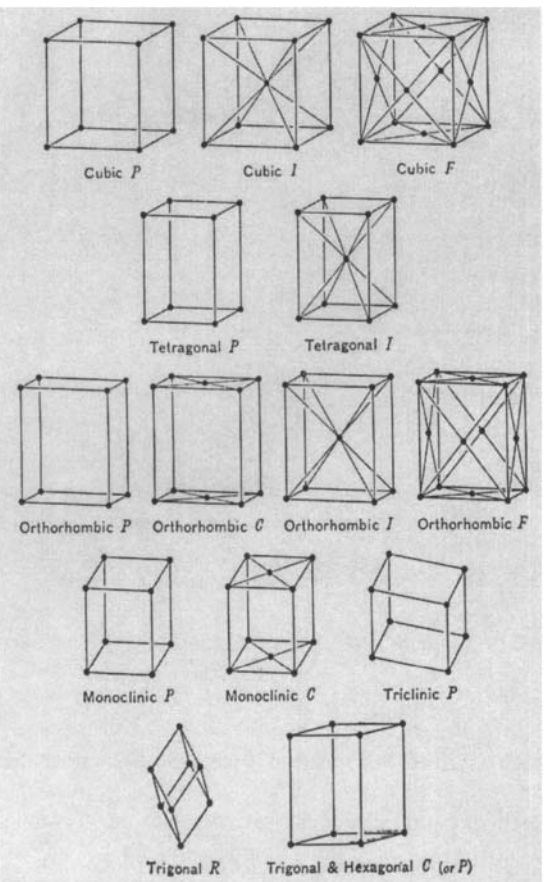

Figure 4. The fourteen basic lattice types.

2.1 Diffraction techniques: Selected Area Diffraction (SAD)

Two methods exist for generating an electron diffraction pattern in an electron microscope. The most common method is the formation of a traditional point pattern (TPP), or SAD pattern, where sharply focused diffraction spots are formed. In this method, developed by [16], the electron beam incident on the sample is enlarged, so as to cover a wide area on the sample, by weakening the condenser lens on the microscope. This means that the electron beam approximates a plane wave incident on the sample. Then by switching to diffraction mode on the microscope, we alter the focus of the projection lenses so as to focus on the back focal plane of the objective lens.

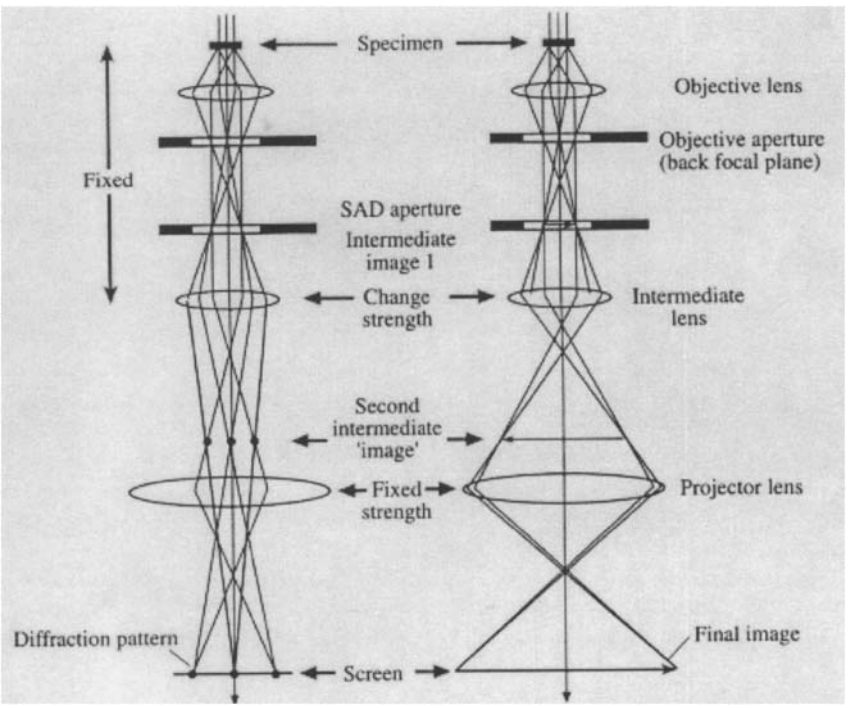

Figure 5. Ray diagram of the lens conditions for the two basic modes of operation of the TEM.

Because the electron beam covers such a wide area of the specimen, an aperture is introduced into the image plane of the objective lens to select an area and so restrict the region which generates the diffraction pattern. This is then called a selected area diffraction (SAD) pattern. This method is ideal for grains larger than $100nm$. Operators should not be tempted to use progressively smaller SAD apertures in an attempt to reduce the size of the area of the sample under examination because this in fact increases the uncertainty of knowing the area of

the sample which is generating the observed diffraction pattern. To be able to reduce the area being examined further, it is recommended that CBED techniques be used.

A common SAD pattern consists of an array of diffraction spots around a central (000) disk, this type of pattern is also known as a zero order Laue zone (ZOLZ) pattern as it is formed by a single reciprocal lattice plane. All *hkl* reflections must satisfy the general Weiss zone law relationship $hU + kV + lW = 0$. The size of the diffraction pattern is determined by the lattice parameters of the crystal and the camera length employed in the TEM. The reciprocal lattice spacings R, measured as the distance from the origin to some diffraction spot, is related to the real crystal spacings d, by

$$d = \lambda L / R \tag{16}$$

where L is the camera length and λL is known as the camera constant.

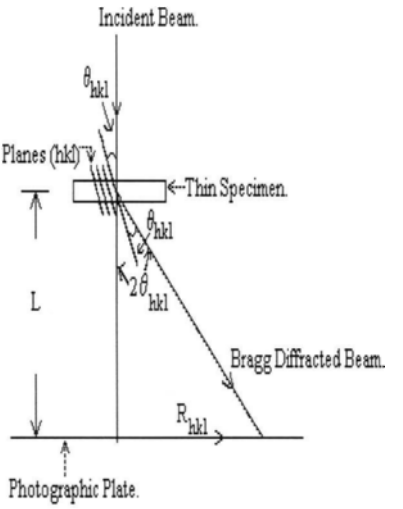

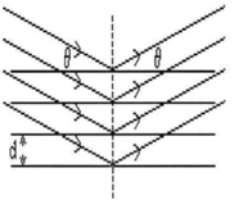

Figure 6. The relationship between the spacings R and the camera length L for diffraction in a TEM.

It is of importance that the camera length, the distance from the specimen to the photographic plate or ccd camera, be accurately known. Otherwise the calculated d spacing could easily be in error, and by as much as 10-20%. Usually this is achieved by ensuring that the specimen is positioned in the "eucentric plane". This is done simply by manually tilting the specimen and adjusting the height of the specimen holder so that the image of the specimen remains stationary.

At higher angles, the Laue conditions is not longer satisfied and so the ZOLZ intensity decreases to zero. However, when the Ewald sphere intercepts the higher order Laue zone planes of reciprocal lattice this intensity returns. The resulting spots, which must satisfy the relationship $hU + kV + lW = n$, where n is an integer, form rings of diffraction intensity named higher order Laue zones (HOLZ). The first of these rings is called the first order Laue zone (FOLZ) because it must satisfy the relationship that $hU + kV + lW = 1$, the second ring, where $n = 2$, is then called the second order Laue zone (SOLZ), and so on. Often the symmetry of the diffraction pattern from the ZOLZ is repeated in the HOLZ patterns, but displaced relative to the ZOLZ because of lattice centering or some other symmetry element requiring no allowed reflections on the zone axis. Figure **7** is an example of this; it clearly shows the ZOLZ with its intensity approaching zero before returning at the FOLZ.

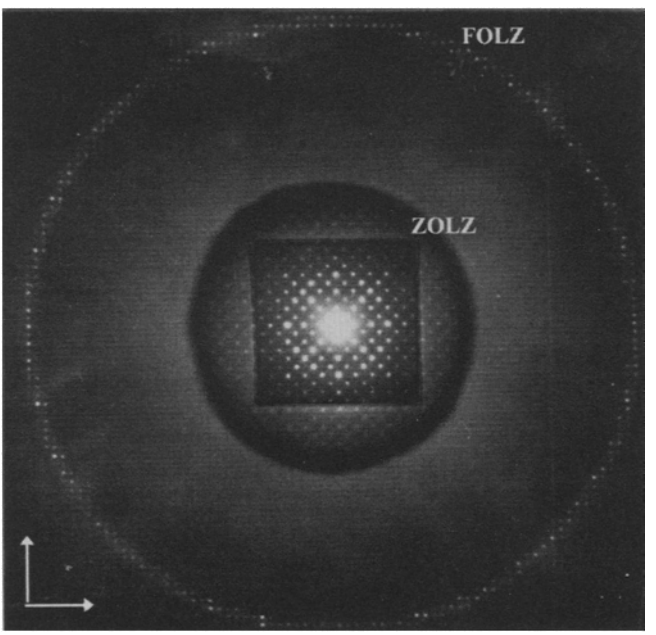

Figure 7. An electron diffraction pattern showing both the ZOLZ and FOLZ.

The radius of the HOLZ rings is defined by the interception of the Ewald sphere with the allowed HOLZ spots of the reciprocal lattice. In the absence of any extinctions due to screw and glide symmetry elements, this radius is a direct measure of the interplanar spacing

of the crystal along the incident beam direction. This interplanar spacing H can be related to the radius of the HOLZ ring r by the approximation

$$H = 2L^2\lambda/r^2 \tag{17}$$

For samples where the grain sizes are less then $\approx 100nm$, the technique of CBED is preferred over SAD. With CBED the size of the region is limited only by the beam size and the beam-specimen interaction volume. This does increase with specimen thickness, but is still much smaller then SAD. The convergent beam concepts have their origin in the discoveries of Kikuchi patterns in 1928, and Kossel patterns in x-ray diffraction in 1937 [see Phys. Status Solidi A, 116, 13 (1989)]. In both cases the patterns can be envisaged as being generated by sources of radiation from atomic sites within the crystal.

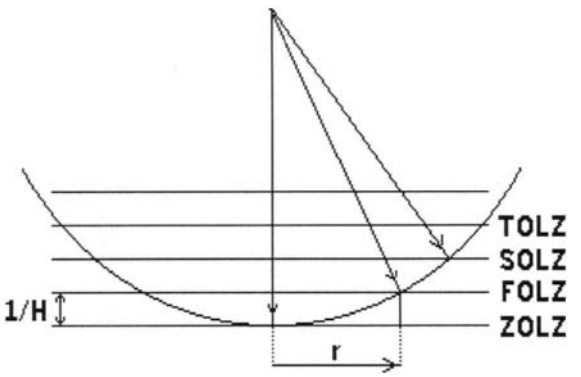

Figure 8. Intersection of a Ewald Sphere of reflection with the HOLZs.

The convergent beam technique was adapted for electron diffraction by Kossel and Möllenstedt in 1939, whose first experiments were to obtain CBED patterns on mica, [17]. The first attempts to measure structure factors, by applying two beam dynamical electron diffraction theory to fit experimental CBED patterns, were performed by MacGillavry in 1940, [18]. Developments on dynamical theory, with emphasis on the symmetry properties of scattering, continued through the 1950s by numerous researchers. In 1965, *Gjønnes* and Moodie, explained the occurrence of forbidden reflection in the presence of strong multiple scattering, [19]. Later it was shown by Uyeda [20] and *Høier*, [21,22] that the position of Kikuchi lines could be used to determine accelerating voltages and lattice parameters. Through the early seventies, systematic procedures were developed for the determination of point and space groups by CBED, (Goodman, [23-26], Moodie, [27,28], Buxton, [29-32].

The method has become so versatile that several microdiffraction techniques have been developed based on the CBED procedures. These include the "nanoprobe" method [33] and the "rocking beam" method as applied on STEMs.

The growth in popularity of this technique can be attributed to the wealth of information provided by CBED which include, lattice parameters, specimen thickness, and 3D crystal symmetry information. The technique of CBED can be performed on any TEM capable

of creating a small (<<1μm) beam with a convergence semi-angle (α) > 10 mrads, [34]. The approach for generating a CBED pattern is opposite to that applied for SAD. In this case a cone of incident radiation is formed by increasing the strength of the condenser lens to produce a small probe which is focused on the surface of the sample. If the beam is defined by a circular aperture (i.e. through the use of a condenser aperture), and the coherence across the width of this aperture is negligible, then each spot in the diffraction pattern is spread out to form a disc. Each point "P" within the condenser aperture, which can be considered an ideally incoherent source, acts like an independent electron point emitter, defining an incident plane wave direction on the sample. Assuming the ideal case of a perfect crystal for simplicity, one such point source "P" gives rise to a set of diffracted beams P' separated by multiples of $2\theta_B$ (twice the Bragg angle). A second point source "Q" within the condenser aperture would therefore define a different incident beam direction and give rise to a different set of points Q' within each disc. So each diffraction disc in a CBED pattern can be thought of as a sum of all allowed diffraction angles within the incident cone.

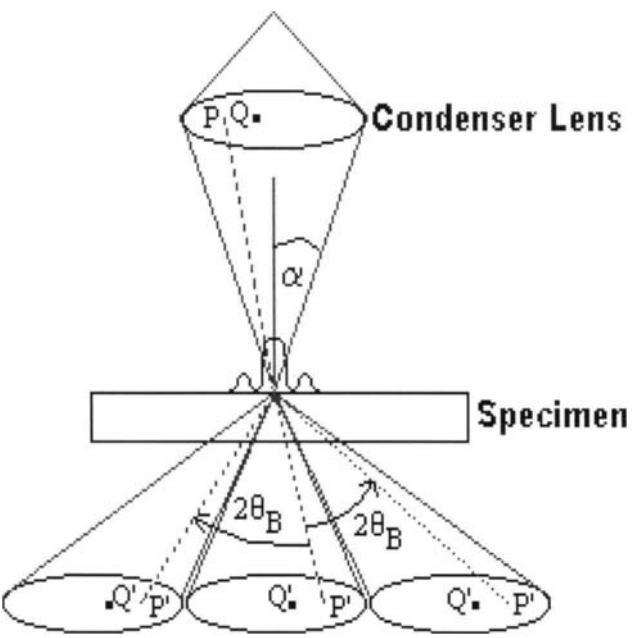

Figure 9. Ray diagram of a CBED construction.

As the condenser aperture dictates the convergence semi angle (α), it is used to control the diameter of the diffraction spots. If the condenser aperture is chosen, so that $2\alpha < 2\theta_B$, the diffraction pattern will consist of non overlapping spots and is called a Kossel-Möllenstedt (K-M) pattern. If a large enough condenser aperture is chosen, such that 2α is so large that the

diffraction disks overlap to the point where any local maxima can no longer be distinguished, then a Kossel pattern is generated.

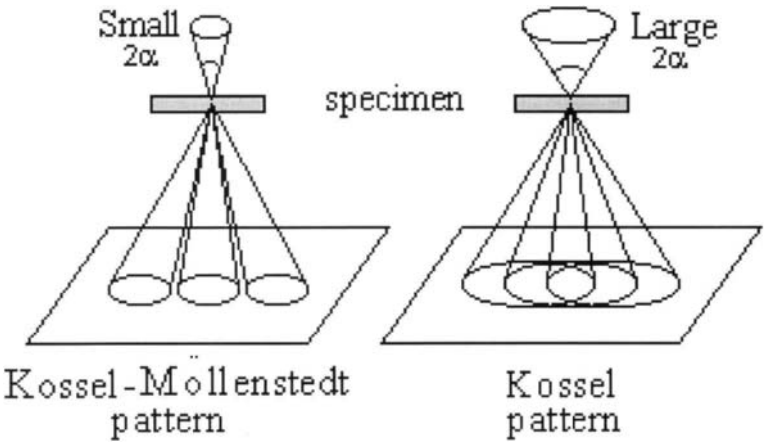

Figure 10. Ray diagram for a Kossel and Kossel-Möllenstedt pattern.

One of real strengths of the CBED technique is that it can easily provide 3D crystal symmetry information from very small grains. In determining the crystal symmetry, one must consider both the symmetry of the zero disk (i.e. the 000 disk) and the symmetry of the whole pattern including any HOLZ reflections and any HOLZ Kikuchi lines. Kikuchi lines are formed when electrons, which have been diffusely scattered within the crystal, are Bragg diffracted by the HOLZ planes of the crystal. The result is two lines being formed at $+\theta_B$ and $-\theta_B$. These lines are unique in that one will be black and the other white, with the black line always closer to the central beam of the diffraction pattern. The methodology for determining the symmetry of a crystal is to first determine accurately the point group and then any Bravais lattice centering. Detail in the ZOLZ of the CBED zone axis pattern can usually be used to determine mirror and rotational symmetry elements. Lattice centering is found by projecting the HOLZ diffraction spots onto the ZOLZ pattern. Finally: to determine the space group, any translational symmetry elements such as glide planes and screw axis must be taken into account. These reflections, which are kinematically forbidden, can occur through double diffraction and result in a line of zero intensity passing through the center of the diffraction disk. These absences are referred to as Gjønnes-Moodi.e. or G-M lines after the early work by Gjønnes and Moodi.e. [35].

There are some general rules which can be applied to determine certain symmetry elements. Rotational axes are seen directly in CBED patterns when the beam is aligned with the rotation axis. Mirror planes of symmetry in the crystal are also seen directly as mirror lines in the CBED pattern, if the beam lies in the mirror plane of symmetry. A vertical glide plane also produces a mirror line in the CBED pattern. A horizontal twofold axis or twofold screw axis in the ZOLZ along g imparts a mirror line of symmetry onto disk g if it is at the Bragg

condition, and this line runs normal to g. Horizontal three-, four-, and six-fold axis produce no useful symmetries. A horizontal mirror plane or glide plane (strictly running through the midplane of the crystal slab) produces a centric distribution of intensity in every CBED disk at the Bragg condition. When there are screw axis or glide plane symmetries present is a crystal system, it is often observed that the resulting forbidden reflection can occur and on occasion, be as strong as the allowed ones. The rules for determining such symmetry elements have been given by Gjønnes and Moodi.e. (1965) and can be loosely summarised as follows. If there is a glide plane parallel to the beam with the relevant axis perpendicular to the beam, the odd order reflections in the direction of this axis will be absolutely forbidden. On the other hand: if there is a screw axis or glide plane for which this is not strictly true, but for which the projection of the unit cell in the beam direction has a symmetry which would give forbidden reflections, then these reflections would not be absolutely forbidden but would certainly be very weak. To test whether a glide plane or screw axis exists, rotate about the axis where every second reflection is forbidden, if the spots remain absent then a screw axis exists.

Although there is a lot more to the CBED technique, and the information that it can provide about a sample (for instance measurements of sample thickness or strain within a crystal lattice) this is beyond the scope of this is chapter. What must be remembered is that SAD and CBED are used to provide information on the lattice spacings, and not trying for a full crystallographic analysis. Also: because the grains are often limited in size and sensitive to the electron beam, it is often not possible to spend the time needed to examine the grains in order to determine certain symmetry elements. The important thing with the SAD, or for smaller grains, micro-diffraction or CBED techniques, is that accurate measurements of the reciprocal lattice spacings in the plane of the zone axis, and if possible the HOLZ, are obtained. Ideally this should be from a low-index high-symmetry zone axis. However this is not always achievable and one must record the diffraction pattern observed. The problem with such patterns is that they could be matched to a number of possible low symmetry- high index zone axes, so increase the likelihood of being matched to more than one compound.

It would also be helpful to obtain a second zone axis pattern, however with the very limited amount of sample typically available in conservation work, this is rarely possible from a single grain. If the sample can be shown to have a mirror plane, rotation axis, screw axis or glide plane, then this is a bonus which will have added weight in identify compounds. By using the EDS data as a guide to rough elemental ratios, databases of known compounds with their crystallographic data can be used to generate a list of possible compounds. Then by comparing the observed electron diffraction pattern taken on the microscope with the crystallographic data listed for the compounds and matching this to possible zone axes, a likely determination can be made.

4. ILLUSTRATIVE EXAMPLES

The rest of this chapter is on examples of this approach being applied. It is based on work done in conjunction with the National Gallery of Victoria [36].

It is an absolute requirement that conservators minimize the damage to art works while still extracting enough sample for accurate analysis. During the period 1992-1994 the School of Physics at the University of Melbourne explored and developed techniques in electron

microscopy and their application to the conservation of objects and paintings of cultural heritage significance. Because of the close proximity of the Melbourne University's Ian Potter Gallery and Conservation Unit to the School of Physics, a collaborative experimental programme was set up. And through this relationship contacts with the conservation department at the National Gallery of Victoria, Australia (NGV) were developed. The first collaboration with the Potter Gallery was on the restoration of an oil sketch by the Australian Rupert Bunny. Following this, an investigation of a 15th century Venetian panel painting, titled "The Garden of Love" was undertaken with the NGV. This painting, is attributed to the studio of Antonio Vivarmi and believed to date from 1465-1470. The painting had been through a number of restorations and required analysis of its material content to distinguish the original material from the restoration. In addition the structure of parts of the painting layer appeared uncharacteristic of the period, especially the foliage. In order to determine the pigments used on some leaves from the foliage, samples were excised from an existing crack using an ophthalmological scalpel. The largest of these samples, shown below, consisted of a needle of approximately 200μm in length and 20μm wide, was prepared for TEM analysis.

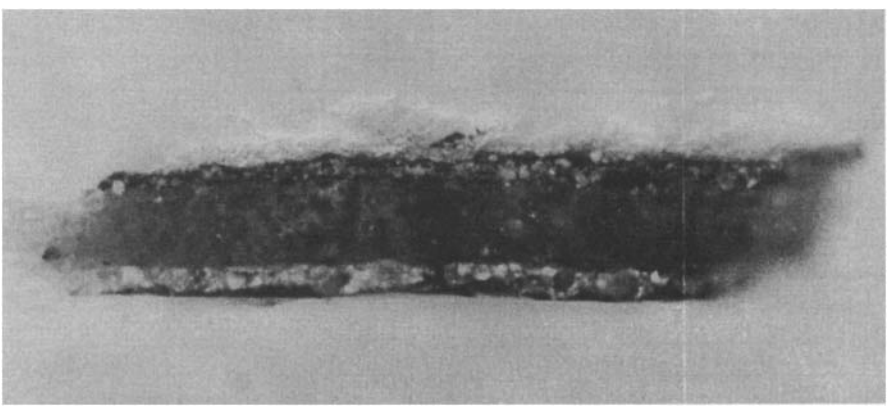

Figure 11. Paint sample excised from "The Garden of Love".

Because the sample was so small, special care needed to be taken to ensue that all the material was deposited onto the TEM grid with none being left behind in the preparation. Normally samples of this nature are crushed in an agate pestle and mortar prior to being deposited on a TEM grid. However this technique usually resulted in remnants of material being left behind on the mortar or pestle. A modified technique that allowed the maximum amount of sample to be retained was developed. This technique involved first transferring the needle to a pyrex glass test tube, then while observing it with an optical microscope, partially crushing it under ethanol using a glass rod. This was done to avoid losing any portion of the needle. The sample was further dispersed in an ultrasonic bath before being deposited on a TEM grid using a drop by drop method where the application of each drop was followed by successive drying in a vacuum oven. The pyrex test tube and glass rod were then examined

under an optical microscope again to verify that no materials were left behind. One problem with this technique is that because of the softness of the glass, a small amount a silica contamination can occur. This usually does not occur with an agate pestle because agate is very much harder than glass. The choice of possible TEM grids is vast with many different forms being offer by suppliers. Copper, aluminium, nickel, and nylon, are just a few examples, with copper being the most common type in use. But because copper is far more common in pigments then nickel, it was decided to avoid the copper grids in preference for the nickel grid instead.

The prepared sample was loaded into a JEOL 100CX TEM and various grains were quickly examined with EDS before attempts were made to tilt the grain so a suitable electron diffraction zone axis pattern could be recorded. After this, the sample was then tilted back to the standard orientation for EDS, and a longer more comprehensive EDS spectra was collected.

4.1 Egyptian blue.

The first grain successfully identified by this approach was "Egyptian Blue". The EDS spectra collected from this grain shows four major peaks at energies of 1.74, 3.69, 7.472, and 8.04 KeV. These were identified as being from Si, Ca, Ni, and Cu respectively, with the Ni being explained as resulting from scattering onto a grid bar. A semi quantitative analysis of this spectra shows a Ca/Cu ration of approximately 1 and a Si/Ca ratio of around 4.

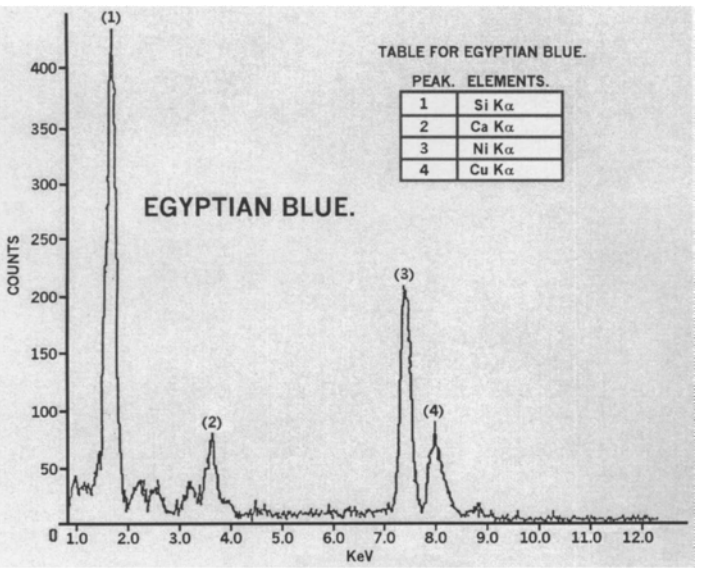

Figure 12. EDS spectrum identified as $CaCuSi_4O_{10}$.

The electron diffraction pattern collected from the same grain shows a square symmetry with identical spacings in both directions. This is an indication of a tetragonal structure (Figure 13).The orthogonal vectors on this pattern were measure and the dimensions were determined to be about 3.6 Å.

Using the "X-ray powder data file", from 1967, (which was the only copy available at the time this experiment was performed), a number of matches were made for compounds containing the elements Ca, Cu, Si, and with or without O. Only one was found to have reflections with a d-spacing close to that measured in the electron diffraction. That compound, card number 12-512, was identified as Egyptian Blue. This is consistent with the blue colour observed in the paint segment. A recent search of the X-ray powder data files JCPDF (Ver 2.0, copyright 1998), on the other hand now lists six compounds with elements Ca, Cu, Si, and O. Three of which have the same chemical formula as Egyptian Blue but with differing structures. The structure of $CaCuSi_4O_{10}$, i.e. Egyptian Blue, was first solved by Pabst [37] , and later refined from Rietveld refinement of powder neutron diffraction data by Chakoumakos et al. [38]. These authors refined the structure as tetragonal, space group P4/ncc, with a=7.3017 Å , c=15.1303 Å .

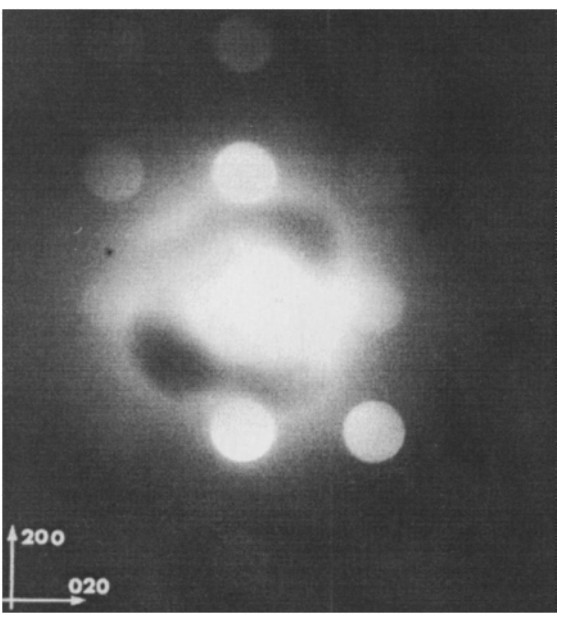

Figure 13. Electron diffraction pattern from Egyptian Blue, showing a square symmetry of spots.

From the information on the card file, the reflections measured from the electron diffraction pattern could be match to the (200) and (020) reflections, with the zone axis therefor as [001]. The (110) reflections which are present in the structure, did not record on the film because of their relative weakness. From the observed symmetry in the diffraction

pattern, we can then conclude that the following reflections conditions apply to this structure, h+k=2n, with h=2n and k=2n reflections much stronger. In simple terms this means that only reflections which follow those conditions are allowed, i.e.: (110), or (200) is allowed, however (100) or (210) are forbidden. These observed reflection rules are consistent with the space group P4/ncc proposed by the authors

3.2 Murdochite

In the next example, we have a grain containing a much more complex chemical structure with ten major peaks and one minor peak being identified in the EDS spectra.

The minor peak, 5, identified as calcium, was judged to be too small to be statistically relevant. The ten remaining peaks can initially be associated with eight possible elements, with these elements being listed on the accompanied table. As with the first example, the nickel peak can be associated with scattering from the grid bar so can be ignored. The remaining elements on the list can in turn be reduced to just four by simply considering the following points.

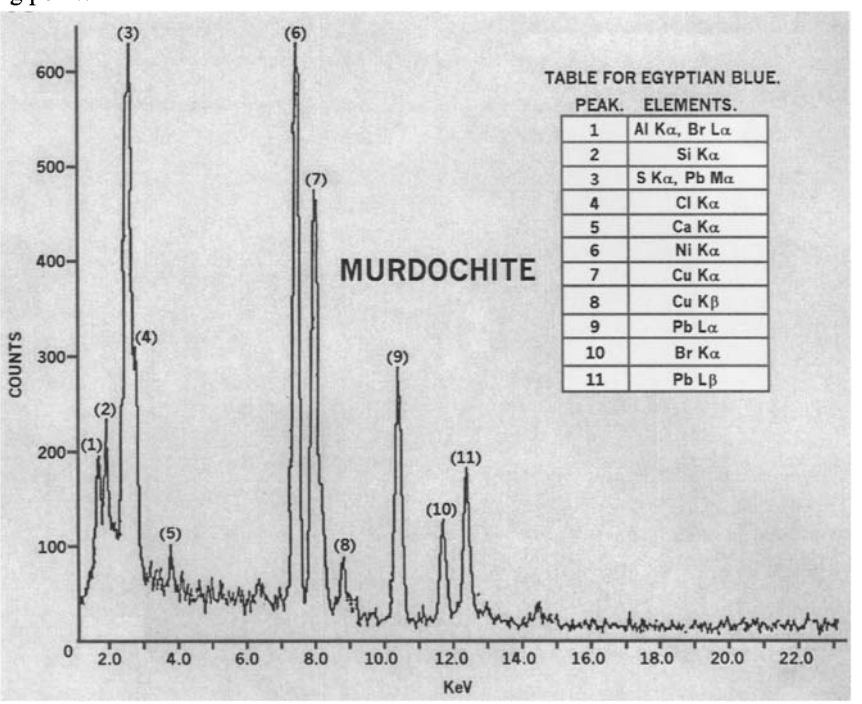

Figure 14. EDS spectrum identified as $Cu_6PbO_{8-x}(Cl,Br)_{2x}$.

As can be seen from the Table, peak 1 (energy = 1.48 KeV) can be attributed to either Al Kα or Br Lα which have energies of 1.48 KeV, and 1.49 KeV respectively. The energy separation of these peaks is beyond the energy resolution of this particular detector, so it is

not possible to distinguish between them. But at higher energies, peak 10 (energy = 11.9 KeV) may be associated with Br Kα. Bearing this in mind, we are led to the conclusion that peak 1 is more likely to be the Br Lα line.

A similar analysis may be performed on peak 3. On this occasion the peak has an energy of 2.3 KeV and can be identified as being from either, sulphur or lead. However, if looking again at the higher energy peaks, peaks 9 and 11, with energies of 10.5 KeV and 12.6 KeV respectively, may be ascribed to the Pb Lα and Pb Lβ lines. So again we can draw the conclusion that peak 3 is more likely to be the Pb Mα line. Peak 2, with an energy of 1.74 KeV, is also a fairly substantial peak, and is identified as silicon. A closer examination of the grain reveals that this peak was the result of a shard of glass deposited with the grain, and is a result of the specimen preparation.

Electron diffraction from the same crystal shows a rectangular symmetry with spacings of 3 Å and 1.6 Å being measured for the orthogonal directions (Figure 15).
Matching possible zone axis to compounds listed in the JCPDF files we come up with four possible compounds:

(i) $3PbO.PbBr_2$;

(ii) 2PbO.PbBrCl;

(iii) $2PbO.PbCl_2$;

(iv) $Cu_6PbO_{8-x}(Cl,Br)_{2x}$ $\quad x<=0.5.$

Of these, the first three compounds can be eliminated because they tend to lose halides during electron beam irradiation. As well, they have to be aligned down unusual zone axis to account for the diffraction pattern. Only $Cu_6PbO_{8-x}(Cl,Br)_{2x}$ (murdochite) is stable under electron beam irradiation, and aligned along a major zone axis. Fahey [39] first proposed the idealised composition $Cu_6Pb_1O_8$ for this rare black mineral. The chemical composition was later refined by Burke et al. [40] from data collected using electron-microprobe analysis. The author observed that naturally occurring murdochite contained significant amounts of chlorine and bromine. This had not previously been reported. The structure of murdochite was eventually solved from x-ray diffraction by Dubler et al., [41] , with these authors reporting it to be have a cubic symmetry, space group Fm3m and unit cell a=9.224 Å .

From structure information provided, the observed reflections can be matched to the (224) and $(2\bar{2}0)$ reflections. The obtained electron diffraction pattern is therefore equivalent to what would be observed along the [11-1] zone axis.

Without the use of CBED, used in conjunction with energy dispersive analysis techniques, it would have been impossible to determine correctly the mineral used in the pigments which were extracted from the paintings. It must be borne in mind that the fragments taken from the sample are microscopic. Burnstock and Jones have described the use of the electron microscope for the study of artworks in an earlier chapter of this book.

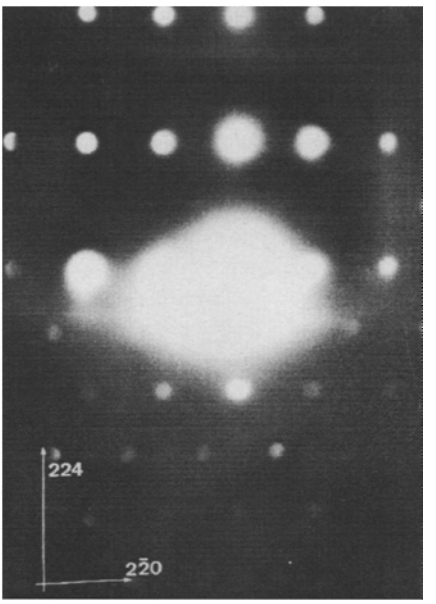

Figure 15. Electron diffraction pattern from Murdochite, showing a rectangular symmetry of spots.

ACKNOWLEDGMENTS

The author is indebted to the late Professor Peter Goodman for his guidance and assistance. He was one of the first electron microscopists to recognize and develop the CBED technique. His links to the Ian Potter Gallery and the National Gallery of Victoria enabled the extension of its use from the mineral and metallurgical field to that of the conservation of cultural heritage materials. As well, he is indebted to Professor David Cockayne for discussions with respect to this chapter.

REFERENCES

General

Williams, D and Carter, C. (1996) Transmission Electron Microscopy. Basic I. New York: Plenum Press.
Williams, D and Carter, C. (1996) Transmission Electron Microscopy. Diffraction II. New York: Plenum Press.
Cowley, J. M. (1975) Diffraction Physics. Amsterdam: North- Holland Publishing Company.
Spence, J. C.H. and Zuo, J. M. (1992) Electron Microdiffraction. New York: Plenum Press.

Specific.

1. Smith, J. T. (1807) Antiquities of Westminster. London.
2. Chaptal, J. (1809) Annales de chimie. 70, 22-31.
3. Davy, Sir H. (1815) Philosophical Transactions of the Royal Society. 105, 97-124.
4. Naumova, M. M., Pisareva, S. A. and Nechiporenko, G. O. (1990) Studies in Conservation. 35, 81-88.
5. Van't Hul- Ehrnreich, E. H. (1970) Studies in Conservation. 15, 175-182.
6. Meilunas, R. J., Bentsen, J. G. and Steinberg, A. (1990) Studies in Conservation. 35, 33-51.
7. Glinsman, L. A. and Hayek, L. C. (1993) Archaeometry. 35. (1), 49-67.
8. Kleber, K., Masschelem-Kleiner, L. and Thissen, J. (1967) Studies in Conservation. 35. (No2), 41-56.
9. de Broglie, L. (1925) Ann. De Physiques 3, 22.
10. Davisson, G. and Germer, L. H. (1927) Phys. Rev. 30, 705.
11. Thompson, G. P. and Reid, A. (1927) Nature 119, 890.
12. Blackman, M. (1939) Proc. Roy. Soc. Lond. A173, 68.
13. Knoll, W. and Ruska, E. (1932) Ann. Phys. 36, 133.
14. Heidenreich, R. D. (1964) Fundamentals of Transmission Electron Microscopy, Interscience, New York.
15. Rutherford, E. (1911) Phil. Mag.21, 669.
16. LePoole, J. B. (1947) Phillips Tech. Rundsch. 9, 33.
17. Kossel, W. and Mollenstedt, G. (1939) Ann.der Phys. 36, 113.
18. MacGillavry, C. H. (1940) Physica 7, 329.
19. *Gjønnes*, J. and Moodie, A. F. (1965) Acta Crystallogr. 19, 65.
20. Uyeda, R. (1968) Acta Crystallogr. A24, 175.
21. *Høier*, R. (1969) Acta Crystallogr. A25, 516.
22. *Høier*, R. (1972) Phys. Status Solidi 11, 597.
23. Goodman, P. (1971) Acta Crystallogr. A27, 140.
24. Goodman, P. (1975) Acta Crystallogr. A31, 793.
25. Goodman, P. (1976) Acta Crystallogr. A32, 793.
26. Goodman, P. (1978) EMAG 1978, Inst. Phys. Conf. Ser., Vol. 41, Institute of Physics, London, 166.
27. Moodie, A. F. (1972) Z. Naturforsch. 27a, 437.
28. Moodie, A. F. (1979) Chem. Scripta. 14, 21.
29. Buxton, B. F. (1976) Proc. R. Soc. London A350, 335.
30. Buxton, B. F., Eades, J. A., Steeds, J. W. and Rackham, G. M. (1976). Philos. Trans. . Soc. London, Ser. A. 281, 171.
31. Buxton, B. and Loveluck, J. E. (1977) J. Phys. C. 10, 3941.
32. Buxton, B. F. and Tremewan, P. T. (1980) Acta Crystallogr. A36, 304.
33. Riecke, W. D. (1962) Proc. 5th Int. Cong. on Electron Microscopy, 1 (Ed. S.S. Breese Jr), p. KK-5, Academic Press, New York.
34. Williams, D and Carter, C. (1996) Transmission Electron Microscopy. Diffraction II, Plenum Press, New York.
35. Gjønnes, J. and Moodie, A. F. (1965) Acta Cryst. 19, 65.

36. Bulcock, S. (1995) *Structure Analysis of Perovskite-Related Compounds and the Investigation of Art Materials.* M.Sc. Thesis. School of Physics, The University of Melbourne.
37. Pabst, A. (1959) Acta Cryst. 12, 733-739.
38. Chakoumakos, B. C., Fernandez-beca, J. A. and Boatner, L. A. (1993) J. Solid State Chem. 103, 105-113.
39. Fahey, J. J. (1955) Am. Mineral. 40, 905-906.
40. Burke, E. A. J. and Maaskant, P. (1970) Neues Jahrb. Mineral. Monatsh, 558-565.
41. Dubler, E., Vedani, A. and Oswald, R. (1983) Acta Cryst. C39, 1143-1146.

Radiation in Art and Archeometry
D.C. Creagh and D.A. Bradley (editors)

Radiocarbon dating in archaeology: methods and applications

Tom Higham and Fiona Petchey*

Radiocarbon Dating Laboratory, School of Science and Technology, University of Waikato, Private Bag 3105, Hamilton, New Zealand.

We discuss the physical principles of radiocarbon dating and its use in archaeometry. A detailed outline of error assessment and quality assurance is given. Correct sample selection, sample provenance, and contamination evaluation procedures are discussed. We give examples of C^{14}dating in the context of Australian and New Zealand archaeology.

1. INTRODUCTION

"Everything which has come down to us from heathendom is wrapped in a thick fog; it belongs to a space of time we cannot measure. We know that it is older than Christendom, but whether by a couple of years or a couple of centuries, or even by more than a millennium, we can do no more than guess."
Rasmus Nyerup, 1802[1].

Nyerup's words illustrate poignantly the critical power and importance of dating in archaeology; to provide an independent means of measuring the age of past events. Radiocarbon dating is one of the most significant discoveries in archaeological research. Oakley[2] suggested its development meant an almost complete re-writing of the evolution and cultural emergence of the human species. Clark[3] wrote that were it not for radiocarbon dating, *"we would still be foundering in a sea of imprecision's sometime bred of inspired guesswork but more often of imaginative speculation"*. Writing of the European Upper Palaeolithic, Movius[4] concluded that *"time alone is the lens that can throw it into focus"*.

It is now fifty years since Willard Libby and his co-workers developed the radiocarbon dating technique. In the intervening years it has become established as the premier method for dating prehistory in the Holocene and Late Pleistocene periods. In addition, there have been significant advances in routine analysis, methodology and instrumentation, while our understanding of the sources of error in archaeological dating has increased. In this chapter, we outline the basis of the method and tackle some of the significant developments. We then consider the basis for archaeological radiocarbon dating and illustrate its use with some archaeological case studies.

2. The method

The underlying principles of radiocarbon dating are well known. Carbon is essential for life on Earth, it is the building block of plants and animals. There are three principal isotopes of carbon on Earth; ^{12}C (98.89% of the global carbon budget), ^{13}C (1.11%) and ^{14}C (0.00000000010%). Each are identical chemically, but ^{14}C is unstable, or radioactive, because it contains extra neutrons in its nucleus. ^{14}C is created in the upper atmosphere through the action of cosmic rays, which impact the Earth, forming thermal neutrons. A secondary effect of this production is an impact upon the isotope ^{14}N that results in the emission of a proton and a particle of ^{14}C:

$$^{14}N + n \rightarrow {}^{14}C + {}^{1}H$$

Very soon after production, ^{14}C is oxidised and becomes ^{14}C-labelled CO_2 (i.e. $^{14}CO_2$). This $^{14}CO_2$ enters plant and animal lifeways via photosynthesis and exchange with Surface Ocean water. ^{14}C is eventually incorporated within all living organisms throughout the biosphere (Figure 1).

The ^{14}C concentration of a plant or animal is maintained in equilibrium during its lifetime with the level of atmospheric ^{14}C. As soon as the organism dies, decaying ^{14}C is no longer replaced and a state of increasing disequilibrium begins. As ^{14}C decays it emits a weak beta particle, or electron ($\beta-$):

$$^{14}C \rightarrow {}^{14}N + \beta-$$

Libby and his collaborators measured the half-life, or period when half the ^{14}C in a given body of carbon could be expected to decay, at 5568 ± 30 years. Libby used this half-life to calculate an exponential decay curve showing predicted ^{14}C levels back through time. The method was tested by dating samples of known-age Egyptian material and dendrochronologically-dated wood, the results of which were within the statistical limits of the curve[5] (Figure 2). It is now known that the so-called "Libby half-life" underestimates the true half-life by ~3%. A more accurate value was later calculated to be 5730±40 years (the so-called Cambridge half-life). Nevertheless, by convention, the Libby half-life is used when computing radiocarbon determinations for the sake of historical continuity. The resulting error is essentially corrected for by the conversion of radiocarbon determinations to calendar years through the application of a calibration curve measured using the same half-life.

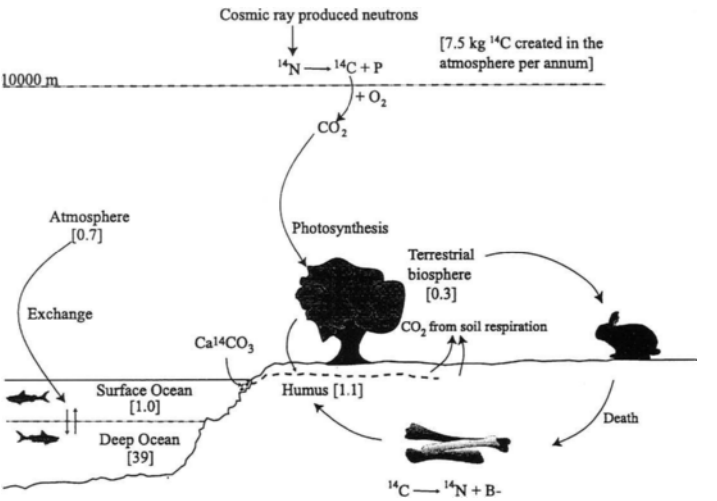

Figure 1. Pathways of ^{14}C in nature. Figures in brackets represent ^{12}C contents in million million tonnes within each of the selected reservoirs[6].

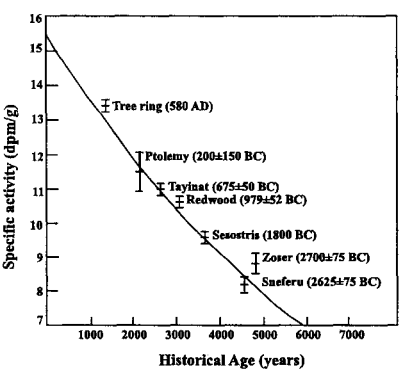

Figure 2. The first check of known-age samples with radiocarbon content, originally published by Arnold and Libby [7]. This is based on Libby[8]. The theoretical curve was calculated using the half-life of 5568 years. The activity is represented in distintegrations per minute per gram carbon (dpm/g).

3. Age calculation

The carbon in the Earth's biosphere forms compounds with many different elements. This means that there is a tremendous range of materials that may conceivably be dated (Table 1). Herein lies one of the principal advantages of the method for dating in archaeology. The task of a radiocarbon laboratory is to determine the ^{14}C concentration of carbonaceous samples of unknown age. This is understandably complex because ^{14}C is a low-level isotope, present at a ratio of 1.5 atoms of ^{14}C for every 1 000 000 000 000 ^{12}C atoms in modern material. The measurement of radiocarbon activity is achieved to routine levels of *ca.* 1.0—0.3% (see below) either radiometrically, by measuring beta decay events (represented by counts per minute per gram of carbon—cpm/g/C) or, using direct ion detection accelerator mass spectrometers (AMS), by measuring ^{14}C concentration ratios.

Table 1
Carbon materials that are commonly radiocarbon dated in archaeology (denoted by *), and some of those which have been dated experimentally. Some samples are only able to be dated using AMS radiocarbon techniques because they are commonly small in size (these are denoted by +) (see below).

Charcoal, wood, twigs and seeds*	Wall paintings and rock art works+
Bone*	Iron
Marine, estuarine and riverine shell*	Avian eggshell
Leather*	Corals *
Peat*	Blood residues+
Coprolites	Textiles and fabrics*
Lake muds and sediments*	Paper and parchment*
Soil*	Fish remains
Pollen+	Insect remains+
Hair+	Resins and glues
Pottery	Antler and horn*
Metal casting ores	

Stuiver and Polach[9] have defined the conventions for the reporting of conventional radiocarbon ages, which are now widely adopted:

1. calculation using the Libby half-life of 5568 ± 30 yr;
2. ages calculated with respect to a modern reference standard whose activity is correlated to wood grown in 1890 AD and normalised for decay to 1950 AD;
3. ages released in years BP ('Before Present'), with 'present' being 1950 AD (the year of the publication of the first radiocarbon determinations by Libby, Anderson and Arnold [10]);
4. a correction for sample isotopic fractionation, with $\delta^{13}C$ normalisation to –25.0‰ with respect to (wrt) the VPDB standard carbonate (Vienna PeeDee Belemnite)[11];
5. assumption that there is constancy in radiocarbon levels during the past.

Laboratories report ages with reference to accepted standards. The *absolute international standard activity* is defined as 95% of the activity of the U.S National Institute of Standards and Technology (NIST) Oxalic Acid 1 (termed HOX 1), in 1950 AD, which is normalised for isotopic fractionation to a $\delta^{13}C$ of -19.0‰ (see below). Declining amounts of Oxalic Acid 1 resulted in the introduction of a new standard, Oxalic Acid II (HOXII)[12].

Absolute measurements are difficult to achieve due to measurement efficiency parameters. Instead, a ratio of the activity of the unknown sample and standard is determined under identical experimental conditions. The measurement is not therefore absolute, but relative. Stuiver and Polach[13] defined the activity ratio as A_{SN}/A_{ON}, where A_{ON} is the modern standard activity measured in the laboratory and normalised for isotopic fractionation, and A_{SN} is the normalised activity of the sample whose age is unknown. The conventional radiocarbon age may then be calculated with reference to the average lifetime of ^{14}C (the average lifetime of ^{14}C is -8033 yr, so 1% of the ^{14}C in a sample of carbon will decay every 80 years), using the radiocarbon decay equation:

$$-8033 \ln\left(\frac{A_{SN}}{A_{ON}}\right)$$

'ln' is the natural logarithm. Since both A_{SN} and A_{ON} are defined with respect to 1950 AD, this measured ratio, and the radiocarbon age from which it is derived, does not change, irrespective of the year of measurement.

The background limit for the ^{14}C method is reached by about ten half-lives (approximately 55 000 years). This limit varies under different laboratory and experimental conditions. Significant reductions to the background limit can be achieved by shielding the measurement system from cosmic radiation. It has been suggested that AMS systems might one day have the potential to extend beyond the effective limit because of enhanced detection efficiencies, but this has yet to eventuate. In practice, a range of post-depositional contamination and system errors effectively limit the potential for dating very old archaeological samples.

Although the decay of ^{14}C is constant, it is also random, which means that repeat measurements of sample activity should cluster around the "true" age of the sample, producing a Gaussian or normal distribution. Radiocarbon ages are therefore expressed with a one standard deviation '±' value, so they comprise an age (y), and a standard error (σ). Consider a radiocarbon age of 2500 ± 200 BP, for instance. This means that the "true" age has a 68% (1 σ) chance of falling between 2300 and 2700 BP. Some archaeologists opt for a more conservative two standard deviation value, which means that the "true" age has a 95% (2 σ) chance of falling between the range (i.e., $y + 2\,\sigma$, $y - 2\,\sigma$, or 2100—2900 BP).

Standard errors are based principally on measurement statistics. In radiometric counting systems, the principal influence on the standard deviation is the length of the measurement time and the number of recorded decay events during that time. Larger fractions of the same carbon sample will produce more counts. High Precision (HP) ^{14}C laboratories therefore utilise longer counting times as well as increased sample sizes[14](Figure 3). Consider a sample which has an activity of 7 cpm/g/C. This sample will produce 10000 counts in 24 hours, and yield a standard deviation of ± 100 yr (where s.d $=\sqrt{}$total counts). The standard error quoted with a radiocarbon determination will therefore be

1%, or ± 80 years. Doubling the sample size will yield twice the counts in the equivalent counting time, so 20000 counts will be obtained, with an equivalent reduction in standard error to 0.7%, or ± 60 years.

In natural biochemical processes, such as photosynthesis, plants preferentially take up $^{12}CO_2$ over $^{14}CO_2$. This 'fractionation' can result in an error of *ca.* 0—400 years in an uncorrected radiocarbon age. Because the depletion in ^{14}C is twice that of ^{13}C, one means to correct for fractionation is to measure the ratio of $^{13}C/^{12}C$ and then correct the measured activity of ^{14}C. The depletion in ^{13}C from the international standard carbonate (VPDB) is termed $\delta^{13}C$ and is expressed in parts per thousand (‰, per mille).

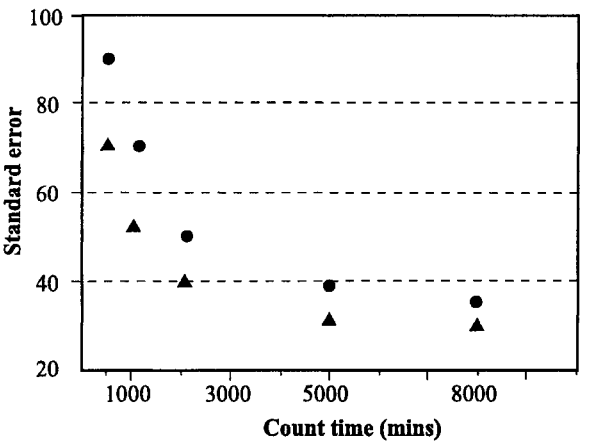

Figure 3. Relationship between measurement time and standard error in 3 (•) and 5 mL (▲) samples of benzene (C_6H_6). Data from the Waikato Radiocarbon Laboratory[15].

In Table 2, the $\delta^{13}C$ values for commonly dated samples are listed. Without correction, there is an age change in an uncorrected radiocarbon age of 16 years, with every 1‰ change in $\delta^{13}C$. The correction is made by using the $\delta^{13}C$ to normalise the sample activity to an agreed base of -25 ‰ wrt VPDB. Problems have arisen for archaeologists where it is unclear whether laboratories have or have not corrected for isotopic fractionation. The $\delta^{13}C$ value for marine shell (*ca.* 0 ‰), for example, is equivalent to *ca.* -400 years, coincidentally the same as the average oceanic reservoir correction *ca.* +400 years, so in the past many laboratories applied no $\delta^{13}C$ or reservoir correction to shell, because they were approximately equal to one another. The majority of laboratories now provide routine $\delta^{13}C$ corrections, or estimate the $\delta^{13}C$ value for the particular sample type and correct on that basis.

Not all radiocarbon samples come from an environment, or reservoir, which is in equilibrium with atmospheric ^{14}C. If they are not they may produce "apparent ages". As described above, marine organisms living in equilibrium with the ocean surface layer, for

example, will yield radiocarbon ages *ca.* 400 years older than contemporary terrestrial organisms[16]. This is known as the 'marine reservoir effect'. Oceanic ages may be corrected once the extent or size of the reservoir effect is known. Other apparent ages are produced from samples of plants growing near volcanic fumeroles[17], lacustrine environments, or gastropods living on limestone deposits[18].

In the modern era, two types of human activities have modified atmospheric ^{14}C concentration. The first is the industrial (or Suess effect)[19] effect which refers to the emission of CO_2 from fossil sources which contain no ^{14}C due to their extreme age. The effect has been to dilute the ^{14}C in the post-1880 AD atmosphere by *ca.* 2%. The second is the nuclear effect. Beginning the mid-1950s[20], there was an increase in ^{14}C in the atmosphere from nuclear testing, peaking in 1963-5 *ca.* 100% above normal levels. Since then, the level of atmospheric ^{14}C has been declining as the 'bomb' carbon enters the biosphere (Figure 4).

Table 2
Variations in $\delta^{13}C$ in nature[21].

Material	**$\delta^{13}C$ ‰ (per mille)**
Marine HCO_3	-1 ± 2
Marine CO_3	0 ± 2
VPDB $\delta^{13}C$ standard	0
Soil CO_2	-5 ± 3
Speleothems	-9 ± 3
Atmospheric CO_2	-9 ± 2
Bone apatite and original carbonate	-12 ± 3
Grains, seeds, maize, millet (C4 plants)	-10 ± 2
Freshwater plants (submerged)	-16 ± 4
Grasses arid zone, sedges	-13 ± 3
Straw, flax	-14 ± 3
Marine organisms (organic)	-15 ± 3
Succulents (cactus, pineapple etc)	-17 ± 2
NIST Oxalic acid 1 standard (HOXI)	-19 ± 1
NIST Oxalic acid 2 standard (HOXII)	-17.6 ± 1
Bone collagen (C3 diet), wood cellulose	-20 ± 2
C3 plants, grains (wheat, etc). Graphite, coal	-23 ± 3
Wood, charcoal (C3 plants)	-24 ± 3
Recent wood	-25 ± 3
Tree leaves, wheat, straw etc	-27 ± 2
Peat, humus	-27 ± 3

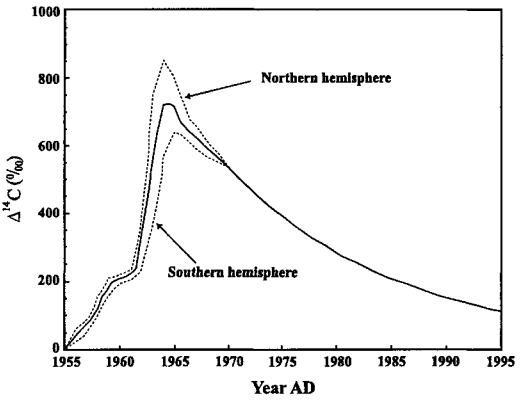

Figure 4: Influence of 'bomb' carbon in the Earth's atmosphere since 1955 AD. Midline represents average mean atmosphere. Note the lag in the uptake of bomb carbon in the Southern Hemisphere and the steady decline in ^{14}C through the last three decades. Based on Peng, Key and Östlund[22]. $\Delta^{14}C$ represents the per mille (‰ parts per thousand) depletion in ^{14}C.

4. MEASUREMENT METHODS

Three methods of measuring residual ^{14}C activity are used today in radiocarbon dating; Liquid Scintillation Spectrometry (LSC), Gas Proportional Counting (GPC) and Accelerator Mass Spectrometry (AMS). LSC and GPC are both conventional, or radiometric techniques which rely on the measurement of ^{14}C decay events. AMS is a direct ion counting technique.

The LSC method involves the conversion of sample carbon to a suitable counting solvent, usually benzene (C_6H_6). Benzene is targeted because it has a high proportion of carbon atoms and excellent light transmission qualities. The measurement of the beta activity ($\beta-$) within the sample benzene is made by addition of an organic compound called a scintillator which, in the presence of ionising radiation, traps emitted beta particles within the benzene and then emits a photon in response. There is a quantitative relationship between the process of beta decay and photon emission. Commercially available LS spectrometers employ photomultiplier tubes which register an electronic pulse proportional to the energy of the beta particle when a photon is detected[23].

GPC was the successor to the modified "solid-carbon" geiger technique, with which Libby had made the first ^{14}C measurements. GPC detects ionising radiation within a gas sample, using electrodes located in a shielded counter. The majority of laboratories utilise CO_2 or acetylene[24], the purity of which is critical. An advantage of GPC systems is their flexibility in terms of gas sizes, from 10 mL to 7.5 L[25]. Mini-counters developed during the

1980s have resulted in the reduction in required sample size to <1 g C, but long count times are required for reasonable precision.

Until recently, archaeologists required samples comprising 2—4 g C for each radiometric measurement, but since the 1970s, AMS has enabled milligram-sized samples to be dated (Table 3) and, therefore, expanded the range of possible radiocarbon sample types. Accelerators operate on the principal that when a stream of atomic particles is deflected from a straight trajectory, those of lower mass will be deflected from their path to a larger extent than those which have higher mass. AMS involves an ion accelerator and powerful magnets, which effectively select and then separate ^{14}C and ^{12}C (or ^{13}C) according to their atomic mass, and measures their ratio. AMS extends the sensitivity of regular mass spectrometers which operate at a typical ^{14}C abundance sensitivity of 10^{-6}—10^{-10}, to ~10^{-15}[26]. This increase is critical when it is remembered that ^{14}C is present in modern atmospheric CO_2 at 10^{-12}.

Table 3
Sample size requirements for typical radiometric and AMS systems. Weights are a guide only, requirements may vary between different laboratories.

	Dry weight		
Material	**Radiometric dating (ideal weight)**	**Radiometric dating (minimum weight)**	**AMS dating**
Wood and charcoal	8—12 g	1 g	5—10 mg
Carbonates	35 g	5 g	15 mg
Peat~	5—10 g	1 g	0.1—1 g
Bone~	100—200 g	20—80 g	1 g
Lake sediment~	30—100 g	10—20 g	1 g

NB: ~ranges reflect varying carbon content (weights approximate).

There are a number of advantages to dating by AMS. Measurement times are significantly shorter (*ca.* 1 hour per sample) because the technique involves direct ion counting (equivalent radiometric measurement times range from about 30-50 hours per sample). AMS also enables poorly preserved or contaminated samples to be more rigorously pretreated and still yield a sufficient sample size, while different fractions of the same sample may be dated to determine the extent of contamination. On the other hand, small samples suitable for AMS dating are sometimes more mobile in archaeological contexts. In addition, radiometric samples are more likely to yield an 'average' age in samples that are contaminated, because exogenous carbon will often be proportionally less concentrated and more homogenised than in a comparable small sample. Milligram-sized AMS samples are also more prone to laboratory-induced contamination during pretreatment and processing due to their small size[27]. Finally, radiometric systems in general continue to produce higher levels of measurement precision, although the lower sample size constraints of AMS systems allow multiple ^{14}C measurements.

Suggestions of a complete dominance of radiocarbon laboratories by AMS systems[28], [29], are yet to come to fruition. The majority of ^{14}C facilities are radiometric, which are much cheaper to construct and maintain. Nevertheless, it is widely recognised that AMS has ushered in another revolution in archaeological dating applications.

5. QUALITY ASSURANCE

One question, which arises in radiocarbon analysis, concerns the reliability and reproducibility of results from different laboratories. The majority of the world's laboratories adhere to generally agreed protocols to ensure Quality Assurance (QA). This involves intercomparison exercises, regular measurement of radiocarbon standards, determination of reproducibility based on replication of QA samples, and set written and database protocols.

A series of international intercomparison exercises amongst the radiocarbon community has been undertaken to enable laboratories to analyse standard samples of varying age[30][31], as well as maintaining in-house programmes of Quality Assurance. The IAEA[32][33] and TIRI[34][35][36] intercomparisons provided a bank of reference samples which were sent to participating laboratories for radiocarbon analysis. The TIRI samples, for instance, included barley (modern), Belfast pine (4500 BP), IAEA cellulose (modern), peat (3800 BP), whale bone (12700 BP) and calcite (background), amongst others. The results are compiled, anomalous determinations are set aside and consensus values determined by the coordinators. These values are then used to determine bias and offsets amongst laboratory results.

These exercises demonstrated that a significant degree of variation was present. In particular, radiocarbon laboratories have tended to underestimate standard errors. This has led to the adoption of a 'laboratory error multiplier' by many laboratories. This value is generated by repeat measurements of standards and used to increase routine standard errors to take into account variations in reproducibility.

6. Archaeological dating

6.1 Sample selection and provenance

Accurate radiocarbon dating depends crucially upon the care and attention attached to both the analytical chemistry performed on carbonaceous samples and the measurement of residual ^{14}C in the laboratory, as well as the rigour of the archaeological investigation (see Table 7 for summary). Precise archaeological dating begins with the careful mapping of the stratigraphic location of the cultural remains, the documentation of the contextual association between material selected for dating, and the inferred cultural activity or archaeological event which is to be dated. In reality, this can be exceedingly complex because of the difficulties often encountered in establishing precisely what is being dated, and how the material relates to that perceived *event*. The misassociation of sample and event is almost certainly the principal source for error in dating archaeological sites which are less than 2-4 half-lives old.

We refer to the event to be dated as the *target event*. This might be, for example, the deposition of a shell midden, the construction of a house, or the manufacture of a spear. A radiocarbon determination may incorporate error because the dated event spans a significant period of time and result in a *pre-event age*. The construction of a large ceremonial structure, for example, might conceivably involve many phases of construction over many years. If the archaeologist is unsure of the sequence of construction and if a single phase is dated with a single radiocarbon determination, there is a strong possibility that the structure may contain a degree of pre-event age. It is the task of the archaeologist to infer the length of time and contextualise the level of offset between archaeological event and scientific date. Similarly,

accurate dating can be affected by *post-event age*, which results in ages that are too young. One example is the reuse of material in archaeological sites[37], or the retouching of rock art.

Table 4
Inferred dating strength in archaeology. Based on Mook and Waterbolk[38].

Strength	Description
1	*Robust determination.* The target event and determined age have no offset or bias because the material *is* that event. These samples comprise "single entities" [39], rather than combined, homogenised samples of possible varying age. Examples: bone with butchery marks in which the date of butchery is sought, rice dated in pottery temper where the date of manufacture of the pot is sought.
2	*Very strong determination.* There is a strong probability that the material dated and the event share the same true age. The relationship is implied strongly by functionality and context. Example: preserved wood within a grave context, charcoal from a hearth.
3	*Strong determination.* While there is no absolute direct relationship between the event and the material to be dated, there is a realistic expectation that they are contemporaneous. Examples: shells from a concentrated feature within an occupation layer of a site, charcoal from a lens within an occupation layer.
4	*Tentative determination:* The material dated is only related to the event on the basis of an interpretation, which may or may not be robust. The radiocarbon determination may be interpreted after the event as reliable or unreliable based upon additional chronological information. Examples: grave fill charcoal which may or may not have been taken in prehistory from pre-event layers, midden shell which has been recently redeposited, disseminated charcoal from agricultural soils which may originate from old pre-existing trees.

Another potential problem is caused by sample constituent errors, including *inbuilt age* [40]. Inbuilt age is defined as the difference in age between the death of the sample and the archaeological event which is to be dated. In the case of wood, it is the combination of *growth age* (the age of old wood in a tree) and *storage age* (the time the tree was lying around before it was used)[41]. Inbuilt age produces non-systematic offsets causing the radiocarbon determination to be too old.

The relative 'strength' of any particular sample to be dated may be ranked (Table 4), so that the greatest confidence is placed on samples such as bone associated with butchery or burial, where the material belongs to an identified archaeological event. The advantages of ranking radiocarbon determinations have been demonstrated by the work of Kuzmin and Tankersley[42] who applied rankings to their analysis of the ^{14}C corpus from Eastern Siberian Palaeolithic sites, which resulted in a clearer understanding of the chronology in question.

6.2 CONTAMINATION

One advantage of dating using ^{14}C is the wide range of available carbonaceous materials. This inherent advantage is compromised to an extent because over time it becomes increasingly unlikely that original carbon will resist contamination by foreign, or exogenous carbon. Contamination results in age shifts from the 'true age' by an amount influenced both by the percentage of the contaminant within the sample and by the age of the contaminant (Table 5). For example, contamination from sources which contain no radioactive carbon (i.e. background) introduce a larger proportional shift in error in young samples, whereas old samples are more significantly affected by young contaminants.

Table 5
The influence of contamination upon a sample of carbonaceous material 900 BP in age.

		% of sample composed of contaminant					
Sample 'true age'	**Age of contaminant**	**0%**	**1%**	**5%**	**10%**	**25%**	**50%**
900 BP	Modern†	900 (0)	890 (1)	850 (5)	810 (11)	670 (26)	440 (51)
900 BP	Background^	900 (0)	980 (9)	1320 (47)	1770 (97)	3280 (264)	6630 (637)

^: contamination with sample which contains no ^{14}C. † : contamination with carbon equivalent to the radiocarbon activity of ^{14}C from 1950 AD. Figures in brackets represent the percentage shift in age from 'true age'. Table adapted from Caughley[43].

A range of routine pretreatment chemistries has been applied to isolate original carbon in dateable materials and remove a majority of non-sample contaminants (Table 6).

Table 6
Routinely applied pretreatments on regularly dated materials.

Sample	Pretreatment
Bone	Exterior surfaces removed with a drill and the sample is crushed. Bone collagen (protein) is isolated after heating with weak acid. A NaOH wash may also be used to remove humic contaminations. Greater purification is achieved by extracting bone gelatin from the collagen.
Charcoal/ wood	Fragments are selected and any adhering surface contamination removed. The sample is crushed and acid washed to remove non-sample carbonates. An alkali treatment is used with samples suspected of soil humic contamination, followed by an acid wash to remove precipitated atmospheric CO_2.
Lake muds/ soil/ peat	Similar pretreatments to charcoal and wood. The isolation of plant macrofossils, fine and coarse fractions may be employed to determine a more reliable age.
Shell/ coral	Exterior surfaces are cleaned. A dilute HCl acid wash may be used to remove areas of further contamination.

Sometimes, more rigorous pretreatments must be applied to samples which originate from problematic environments. In the case of old wood, for instance, resins, lignins and waxes can be removed to isolate cellulose, the carbohydrate fraction of the wood[44]. Bone which is at risk of contamination or degradation may be pretreated to fractions which are specific only to bone, including individual or total amino acids[45].

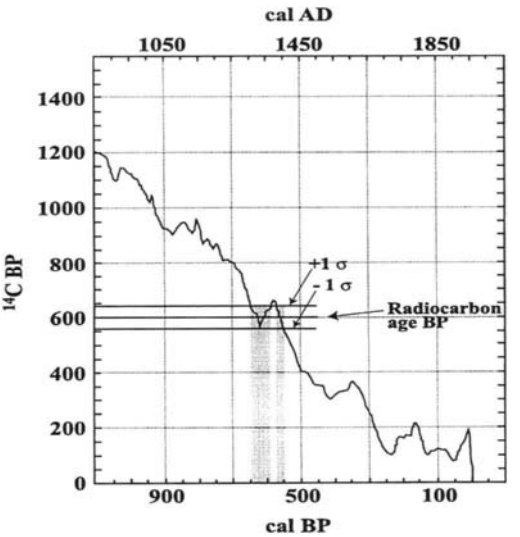

Figure 5. Calibration of a radiocarbon determination of 600 ± 40 BP using the 1998 INTCAL calibration dataset[46]. "Wiggles" in the calibration curve mean that there is a bimodal calendar age range for this radiocarbon determination. The shaded area shows the calendar age ranges which can be read off the *x*-axis. The CALIB computer programme shows that the calendar age at 1 σ is 1300-1370 cal AD (650-580 cal BP) and 1380-1405 cal AD (570-565 cal BP).

7. Calibration

The assumption that the concentration of ^{14}C in each radiocarbon reservoir has remained constant was addressed early in the history of the method and found to be unsustainable[47]. Archaeological sites in Europe and the Mediterranean which had been dated by comparative methods, played a central role in first determining that the relationship between secular time and radiocarbon years was not linear[48]. It is now known that the ^{14}C production rate is influenced by short term variations in the bombardment of the upper atmosphere by cosmic rays[49], a slow long-term increase in the intensity of the geomagnetic dipole over the last 30 000 years, and changes in ocean ventilation patterns during the last deglaciation. This results

in fluctuations or "wiggles" in the concentration of radiocarbon in the biosphere over time (see Figure 5).

Past atmospheric variation in $^{14}C/^{12}C$ production has been reconstructed for the Holocene period using dendrochronologically-dated oak and pine from Europe and North America[50][51]. This has enabled the calibration of radiocarbon determinations to calendar time back to 11 850 cal BP[52]. Beyond this date there is a paucity of suitable wood for extending the calibration curves, so a range of other proxies have been utilised, including corals dated by $^{230}Th/^{234}U$ [53][54] which span the period 11 850—24 000 cal BP[55], and laminated sediments[56]. The 1998 INTCAL dataset integrates these various proxies and covers the period 0—24 000 BP[57]. INTCAL 98 enables the calibration of surface ocean samples using a marine curve, which models the movement of radiocarbon within and into the ocean[58][59].

While the calibration of radiocarbon determinations appears to be a simple process, it is hampered by two factors. The first is that radiocarbon standard errors can make it difficult to distinguish absolutely the corresponding calendar date for a radiocarbon measurement. The second is caused by the "wiggles" in the calibration curve which mean that the calibration of single radiocarbon determinations can result in multiple intercepts along the curve and more than one possible age range. Understandably, this can provide serious interpretive problems for archaeologists. Using a section of the 1998 INTCAL curve a radiocarbon age of 600 ± 40 BP is calibrated by running a horizontal line from 600 BP, to the points which intersect the calibration curve (Figure 5). In this example there are four intercepts. From the intercepts, vertical lines are drawn to the point where they bisect the *x*-axis and the same is done at 1 σ either side of the ^{14}C age to give the corresponding calendar age range. In this example, the "wiggle" in the calibration curve results in bimodal age ranges, either of which could theoretically contain the "true" age. A calibrated radiocarbon age is referred to in "cal AD/BC" or in "cal BP".

A recent approach has been to calibrate radiocarbon data in combination with archaeological evidence. Archaeological information in the form of relative stratification (phases, sequences), historic evidence (coins, written texts), information derived from the boundaries of the event (*termini post* and *ante quem*) and artefactual evidence[60][61] assume importance in the dating of an archaeological site. Bayesian statisticians have incorporated this *a priori* (prior) information along with radiocarbon data to determine calendrical age for archaeological contexts. Computer software programmes, such as OxCal[62] and Date Lab[63], and the Internet-based BCal[64] have made this Bayesian approach to calibration much more accessible to archaeological users.

8.0 CASE STUDIES

To the archaeologist falls the task of interpreting the results generated by the radiocarbon laboratory. Ideally, the task of dating ought to be a collaborative process between laboratory and field archaeologist, with samples chosen on the basis of both archaeological and dating suitability. In this section, we focus upon actual dating problems which impact critically upon archaeological interpretations.

Table 7
Influences on the reliability of archaeological radiocarbon determinations. After Polach[65].

Error source	Direction, size of error	Means to reduce error
Archaeological variables		
Misassociation , *pre-* and *post-* event age	Old or young	Rigorous attention to stratigraphy and geomorphology
Human contamination (hair, petrol, oil, waxes, paper etc)	Old or young	Care during excavation, rigour attached to sample collection and storage
Inbuilt age of wood (growth age)(see text)	Older (non-systematic)	Screening of samples and selection of short-lived twigs/seeds
Inbuilt age of wood (storage age)	Older	Selection of charcoal from species which are not durable
Radiocarbon variables		
Half-life of radiocarbon	Libby half-life is 3% too low	Calibrate results, or multiply Libby age by 1.03
Sample isotopic fractionation	0-450 years (if $\delta^{13}C$ estimated)	Measurement of $\delta^{13}C$
Laboratory induced fractionation	Young or old	Check $\delta^{13}C$ values, rerun if in doubt. Rigorous lab chemistry
Measurement precision	Increases statistical uncertainty	For radiometric samples: increase counting times and sample sizes. In AMS dating: multiple measurement
Distribution of ^{14}C in nature	Surface ocean 300—700 years: too old. deep ocean 1400--1800 years too old	Determine reservoir effect (or ΔR offset) using samples of known age, or marine shell-terrestrial pairs.
Variation in past ^{14}C production rates	±5% <: beyond the limit of calibration curve: error difficult to quantify	Calibration of archaeological samples using established calibration curves
Environmental variables		
Post-depositional contamination	Old or young depending on source	Physical and chemical pretreatment. Experimentation to determine the most reliable fractions
Recrystallisation of CO_3	In closed system — none; in open system — older or younger	X-ray diffractometry of carbonate to check for recrystallisation of calcite
Bioturbation, geoturbation	Old or young	Rigorous attention to stratigraphy and geomorphology.
Hard water effect (marine/lacustrine)	Old	Comparison with paired terrestrial samples
Upwelling effect (marine samples only)	Old	Avoid marine samples, date terrestrial samples only

8.1 Single radiocarbon determination from New Zealand

In the first case study, we shall consider a simple example of a radiocarbon dating exercise, by following the process of dating a single sample from the site, to the laboratory.

At Kawatea, Little Okains Bay, New Zealand, scattered artefacts including a prehistoric fishhook, human hair and trade knives were collected from the surface of a cave in the 1890s. In the 1960s, the cave was excavated. From the cave floor, the stratigraphy comprised 15 cm of cave roof dust, 60 cm of midden remains belonging to the so-called Classic Maori culture (*ca.* 1500—1769 AD), and 13 cm of Archaic phase midden (*ca.* 1250-1500 AD). Moa bone, mussel shells and fire stone chips were excavated from this lower context.

No samples were submitted for radiocarbon analysis after the excavation, but some of the material was stored in the Okains Bay Museum, where many local Maori and European artefacts are held. Museum staff decided to submit a sample of moa bone to date other artefacts found at Okains Bay and to aid the writing of a local history of the area.

A moa leg bone, weighing 127 grams, was brush cleaned at the Museum, and then packed in double polythene bags, which were carefully labelled. The packaged samples were sent to the Waikato Radiocarbon Dating, in New Zealand, along with a completed sample submission form containing information on the sample material, its location, an estimated age, and other relevant data. Upon arrival at the laboratory, the sample was given an accession number, and the submitter was notified that it had arrived safely.

The bone was physically pretreated in the laboratory, by cleaning with a scalpel and dental probe and then washing in an ultrasonic bath. The bone was then crushed to a fine powder and chemically pretreated to isolate a fraction of the original protein. The bone powder was reacted with 2% concentrated HCl, rinsed and dried. This yields acid insoluble "collagen". The sample was then gelatinised, by heating in weakly acidic (pH=3) water at 90° C for 4 hours, rinsed and dried. Finally, the bone gelatin was freeze-dried, weighed and queued in the laboratory for benzene synthesis.

The gelatin was converted from its carbonaceous form, into benzene, a process that takes three days. First it was combusted to produce carbon dioxide. The measured gas was then reacted with molten lithium at 800°C to produce lithium carbide (Li_2C_2). Afterwards, distilled water was added to the Li_2C_2 to produce acetylene (C_2H_2) which was then allowed to sublime onto a vanadium catalyst that converts three acetylene molecules into one molecule of benzene by a process called catalytic trimerisation. The weight of benzene produced was 2.98 grams.

The radiocarbon activity of the benzene was determined using one of the laboratory's LS spectrometers. The sample was counted for 2500 minutes, and produced a total of 66360 counts during that time (26.371±0.1 cpm). This data was compared with a laboratory standard of ANU sucrose measured previously in the same spectrometer in the same glass vial, which recorded an activity of 28.404 cpm. The radiocarbon age was calculated using the radiocarbon decay equation on one of the laboratory computers.

$$
\begin{aligned}
&-8033 \ln\left(\frac{A_{SN}}{A_{ON}}\right) \\
&= -8033 \ln\left(\frac{26.371}{28.404}\right) \\
&= -8033 \ln(0.92842557) \\
&= -8033(-0.074265058) \\
&= 596 \text{ years BP}
\end{aligned}
$$

The calculated age was rounded up to 600 years BP. The standard error was calculated at ± 35 years (a measurement precision of 0.43%), so the conventional radiocarbon age for the moa bone sample from Okains Bay, was 600 ± 35 BP. This radiocarbon age was calibrated using the 1998 INTCAL calibration curves and yielded a bimodal calibrated age range (1285—1305 and 1365—1385 AD at 1 σ). This calendar age was slightly earlier that the estimated age of 1400—1500 AD, which the archaeologist involved in the project, provided, but very similar to the earliest phase of moa hunting identified in the South Island of New Zealand.

8.2 DATING AT THE LIMITS OF THE RADIOCARBON METHOD: AUSTRALIA

The expansion of humans into the "new lands" of the Americas, Australia and the Pacific has been linked to the extinction of a range Pleistocene animals and environmental changes associated with anthropogenic influences[66]. In these regions, dating by ^{14}C assumes central importance to the identification of the earliest cultural evidence and the decipherment of human impacts. In Australia, dating the first humans extends the radiocarbon method to its limits.

One of the problems with archaeological dating in Australia is the lack of unambiguous stylistic and artefactual markers through time, as well as a paucity of clear faunal changes to provide independent chronometers of site age[67]. Developments in dating techniques over the past 40 years have extended the antiquity of humans in Australia from 9000 BP in the 1960s[68] [, to 32000 BP in the early 1970s[69] to *ca.* 40 000 BP since that time[70]. The accuracy of the *ca.* 40 000 BP date is the subject of considerable debate. Jones, Roberts and others[71][72] have argued that these results represent an 'event horizon'[73] caused by the influence of small amounts of contaminants in old samples, rather than being representative of the earliest human presence in Australia as Allen and others have argued[74]. In the early 1990s, the application of TL (Thermoluminescence) and OSL (Optically Stimulated Luminescence) techniques resulted in ages of 50—60 000 years at two sites in northern Australia[75][76] which lent support to a prehistoric chronology which exceeds 40 000 years.

Allen and Holdaway[77] compared the distribution of geological and archaeological determinations from published and unpublished works to determine the robustness of this supposed radiocarbon event horizon (Figure 6). They argued that if the barrier at 40 000 BP were a real phenomenon, then ^{14}C determinations would be affected by it whether they were from archaeological or natural, non-cultural sites. The archaeological data did not challenge the threshold, but the geological data yielded ages which exceeded it. Allen and Holdaway[78] concluded therefore that the radiocarbon barrier had not influenced the

distribution of the radiocarbon results at *ca.* 40-50 000 years BP because if it had, geological determinations would have been similarly affected.

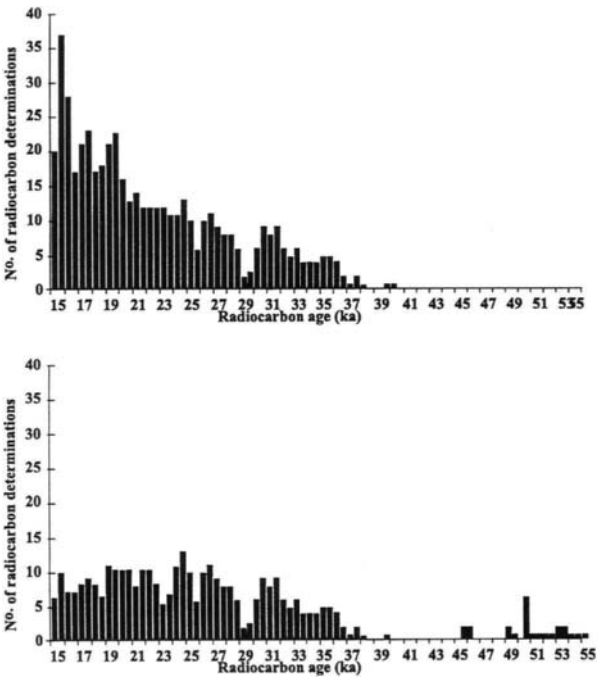

Figure 6. Radiocarbon determinations from Australian archaeological (above) and geological (below) sites which predate 14999BP (from Allen and Holloway [82].

A number of scholars have criticised this approach. Webb[79], for instance, has shown that some of the series of pre-40 000 BP determinations in the geological distribution were dated in the Groningen laboratory where the samples were assayed using a technique called isotopic enrichment of ^{14}C[80] designed to extend the range of dating using radiocarbon. Once these determinations are removed, the disparity between the two datasets is reduced considerably.

Chappell *et al.* [81] have shown that materials which are close to, or beyond, the radiocarbonlimit tend to cleave asymptotically to a date of *ca.* 40-50 000 BP, due principally to unremoved contamination. They suggest that the oldest dated determinations from archaeological sites in Australia are probably affected by this asymptotic trend. One example of this trend is illustrated in the dating of kauri (*Agathis australis*) tree logs from coastal sand

barriers in northern New South Wales. The sand barriers within which the logs were collected were estimated on geomorphological grounds and $^{230}Th/^{234}U$ dating of corals, to be between 120 and 130,000 years old. Sixteen radiocarbon ages on wood fractions, including resins, humates, humic acids and cellulose ranged from *ca.* 11000 BP to 43000 BP, with only two registering results determined to be beyond background and two yielding minimum or 'greater than' ages (Figure 7). There are lessons from this not just for Australian archaeological radiocarbon dating, but also for dating in other late Quaternary contexts, where the age of archaeological sites approaches the potential limit of the ^{14}C technique.

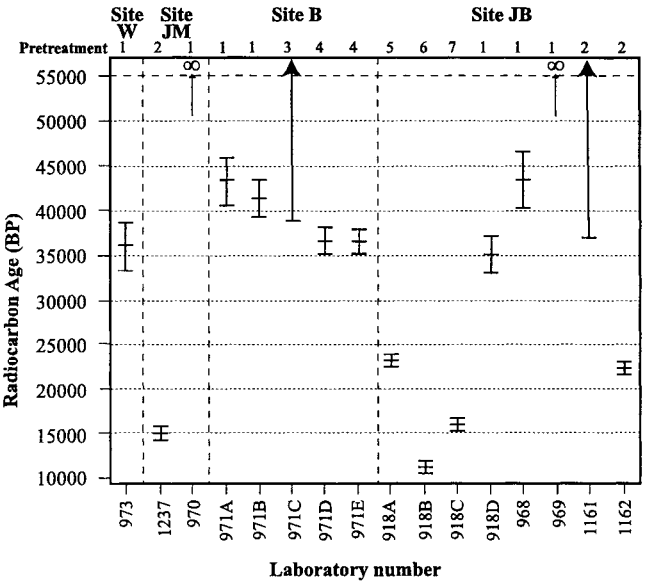

Figure 7: Radiocarbon determinations of kauri (*Agathis australis*) from four sites on coastal dunes in NSW, Australia, whose age is greater than 60 000 years. Ages are given with ± 1 σ error bars. Numbers refer to dated fractions of the wood. 1: cellulose (these ought to be most reliable); 2: humate; 3: humic; 4: wood residue; 5: 'as is' wood (i.e. unpretreated); 6: resin; 7: humic and fulvic acid. All determinations from the Australian National University Radiocarbon Laboratory, Canberra. Only two determinations are background (denoted ∞) age. Two others yielded 'greater than...' ages (ANU-1161 & 971C- denoted →). Data reproduced from Chappell *et al.* [82].

8.3 Testing the reliability of novel sample types

Whilst the ubiquity of carbon in the biosphere ensures a range of possible dating materials, it is necessary to ensure that novel materials are reliable prior to routine ^{14}C determinations being assayed. First, it is important to consider whether the organism

originates from a reservoir which is in equilibrium with atmospheric ^{14}C, or not, and to ascertain whether it is susceptible to post-depositional contamination. This can be achieved by comparison with reliable sample types from identical stratigraphic contexts or by some other independent means of dating[83]. In addition, a potential radiocarbon material must be shown to give reproducible radiocarbon results. Reproducibility is demonstrated when multiple ^{14}C assays of a novel type, as a group, produce results which are statistically indistinguishable.

An investigation into the reliability of dating snapper fish bone (*Pagrus auratus*) from New Zealand archaeological sites demonstrates this need for careful evaluation of novel sample types. In New Zealand, the earliest archaeological sites date from the mid-13th century AD. Many of these Archaic phase sites were, however, dated in the late 50s and early 60s. Since then, advances in the dating of routine sample materials have led to the re-evaluation of many determinations. At sites such as Shag River Mouth[84] and Wairau Bar[85] in the South Island, for instance, re-dating has suggested that both were brief prehistoric occupations (< 50 yr) rather than extensive occupations covering centuries. Unfortunately, many of these key sites cannot be reexcavated and any attempt at re-dating relies heavily on archived material and therefore a limited choice of sample type. For three of these early sites; Houhora[86] and Twilight Beach (northern North Island), and Rotokura (northern South Island)[87], large amounts of snapper bone, which had been initially collected for faunal analysis, was available for dating.

The ability to date fishbone is beneficial for archaeologists because it is common in many archaeological coastal midden sites and it is directly correlated with an identifiable archaeological event, in this instance fishing. The reliability of this sample type for radiocarbon dating had been questioned, however, because of earlier erroneous fishbone determinations and the possibility that some species incorporate carbon from the deep ocean [88]. Snapper do not, however, extend significantly into ^{14}C depleted waters which exist below 200m[89][90] and none of the archaeological snapper populations were located in areas where old ^{14}C–depleted water upwells[91]. Moreover, radiocarbon results of otoliths from modern and historic snapper collected on the eastern North Island coast compare favourably to radiocarbon determinations of surface water, modern shellfish and historic shell[92].

Enough well-preserved snapper bone was isolated from each of the sites to produce three to four radiocarbon determinations. The ^{14}C results of the bone gelatin were compared to assess reproducibility, and the calibrated results compared to radiocarbon determinations on identified charcoal and shell from the same contexts.

Radiocarbon determinations of snapper from all three sites were indistinguishable from one another, supporting the requirement of reproducibility of determinations from this novel sample type (Figure 8). At Houhora and Twilight Beach, the reservoir-corrected snapper gelatin pooled results overlapped with pooled charcoal and shell determinations and yielded acceptable 14th and late 14th to early 15th century dates respectively. The single shell determination for Rotokura (1300—1340 Cal AD at 1 σ), however, was statistically different to the pooled charcoal and shell results for the site. It is thought likely that the shell sample was from a sub-fossil source. The late 14th to early 15th century result for charcoal and fish bone gelatin is an acceptable estimated time for the deposition of Layer 4 at Rotokura on the basis of artefactual and economic evidence[93]. Overall, the preliminary results suggest that snapper bone gelatin is a reliable radiocarbon sample type, while the radiocarbon

determinations for all three sites support the developing scenario of a rapid phase of early exploration and colonisation in New Zealand[94].

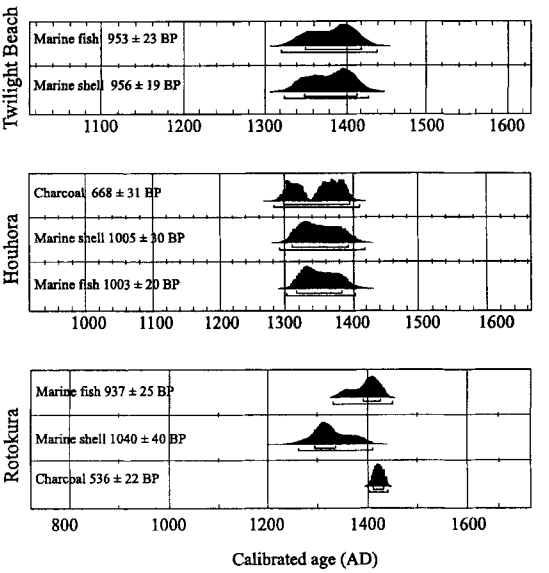

Figure 8: Calibrated radiocarbon determinations of snapper bone gelatin from three archaeological sites in New Zealand. The radiocarbon determinations were calibrated using OxCal, with the INTCAL 98 calibration curves.

8.4 Determining the presence of contamination : The Cuello case.

Bone collagen is subject to alteration following the death of the animal via a combination of chemical, physical and biological processes. The decay process involves the breakdown of soft tissue, which is manifested as a loss of collagen and a corresponding increase in susceptibility to humic and non-humic contaminants. Many of these contaminants do not interact chemically with the sample and can be removed physically or chemically. Unfortunately, some do react with the fraction to be dated and may affect the radiocarbon age.

The general problem of radiocarbon dating bone, particularly in more extreme circumstances (i.e. both reduced collagen content and contaminated bone) is the subject of much active research[95][96]. One avenue involves monitoring the effect of sample pretreatment combined with careful analytical assessment of the bone prior to dating. This relies on the assumption that contamination can be detected and if necessary, the sample rejected. Law *et al.*[97], for example, attempted to obtain a reliable radiocarbon chronology from the Mayan site of Cuello, in Belize by using infra-red spectroscopy combined with a

selective pretreatment regime to isolate a representative protein/peptide fraction from highly degraded, contaminated bone.

A number of charcoal ^{14}C dates from Preclassic contexts at Cuello had supported a "long" chronology, with the Preclassic spanning *ca.* 2500 BC—AD 250. This contradicted the conventional ceramic chronology which, on stylistic grounds, suggested a Middle Preclassic (*ca.* 300 BC—600 BC) date for the ceramics from the earliest deposits. A subsequent set of charcoal determinations produced a short chronology spanning 750 BC—AD 250. No satisfactory explanation could be given as to why radiocarbon determinations from adjoining excavations with visibly contiguous stratigraphy should yield such contrasting results[98].

A fresh approach was to date carefully selected short-lived material from the relevant layers where the contemporeneity of the samples with the archaeological context was assured. Initial attempts to date bone were unsuccessful[99]. A number of reasons were suggested for these initial bone dates being in error, including:

- low collagenous protein remaining;
- high bone degradation and/or environmental contamination resulting from deposition in a tropical environment;
- possible contamination by PVA/PV-OH, used to consolidate fragile bone after excavation.

Four additional human bone samples were therefore selected for dating. To monitor the effectiveness of different pretreatments on such contaminated bone, four fractions were isolated from each; total acid-insoluble, NaOH leached fraction ("crude collagen"); crude gelatin; ion exchange purified gelatin ("ion-exchanged gelatin"); and amino acids from hydrolyzed ion-exchanged gelatin[100]. The progressive cleanup of the sample was monitored by comparison of infra-red spectrographs of control samples ("finger print" spectra of PVA/PV-OH (Figure 9 B1) and modern hydrolysed collagen (Figure 9 B2)) with archaeological human bone samples. Amino acids were also isolated from unconsolidated animal bone to test whether this pretreatment method could provide satisfactory radiocarbon determinations for unconserved samples from this site.

The infra-red analysis confirmed that the crude collagen fraction retained considerable proportions of contaminants. The pretreatment method used on the original bone determinations from Cuello (ion-exchange purification of a collagen hydrolysate) would therefore have left soil-derived amino acid contaminants. Gelatinisation before ion-exchange removed more of these contaminants. Gelatinisation of the protein fraction also resulted in the removal of infra-red peaks associated with the consolidant from most of the samples except the heavily contaminated Burial 62. The spectrum of the gelatinisation residue from Burial 62 (Figure 9 A2) was similar to that for PV-OH (Figure 9 B1), though the lack of definition indicated that additional environmental contaminants were also present. Generally, the similarity of most archaeological spectra from the site (for example Figure 9 A3) to that of partially hydrolysised modern collagen (Figure 9 B2), suggested that there had been breakdown of the archaeological proteins, possibly caused by diagenesis, or as a result of the gelatinisation procedure. An absence of contamination could not be guaranteed, however.

It was hypothesized that ion exchange purification of the gelatin, prior to subsequent hydrolysis and separation of total amino acids, would remove an even greater proportion of

soil contaminants and improve the reliability of radiocarbon determinations. Confirmation that the cleanup of these samples had been successful was demonstrated when the 1725cm^{-1} and 1220cm^{-1} absorption peaks associated with carboxylic acid (-COOH) disappeared and the -COO^{-} peak at *ca.* 1400cm^{-1} appeared following the ion-exchange procedure (Figure 9 A1). This occurs when ammonium salts (-COO^{-}NH$_4^{+}$) are formed, a reaction that would have exposed any masked contamination peaks.

Acceptable ^{14}C determinations were obtained from the unconsolidated control samples and the purified amino-acid fractions isolated from the consolidated samples. Radiocarbon results of the intermediate fractions (crude gelatin, and crude collagen) improved as the degree of purification increased. For the better preserved samples the ^{14}C determinations were fairly uniform throughout the pretreatment process. The largest discrepancy in the determinations was yielded from the gelatinisation residue from Burial 62, demonstrating the effect of contamination by the consolidant and possibly also from humic materials.

Overall, the amino acid radiocarbon determinations of the human burial remains from Cuello supported an occupation beginning in the late second millennium BC. This is over one millennium shorter than the radiocarbon chronology initially determined for the site, but several centuries older than that indicated by the "short" chronology[101]. Recent re-evaluations of the ceramic chronology advanced by Andrews and Hammond[102] have lent support to these conclusions.

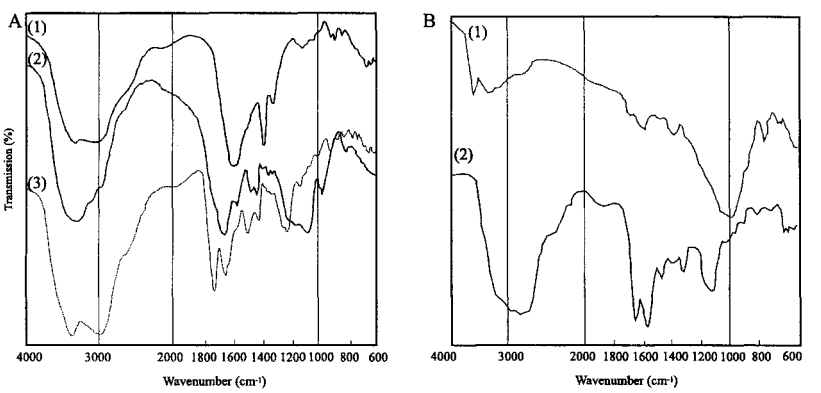

Figure 9: Infra-red spectra from the site of Cuello, Belize. A: prehistoric human bone (1): NH^{4+} form from Burial 7, after ion exchange (2): crude gelatin from Burial 62. (3) peptized gelatin extracts from Burial 7. B: standards; (1): PV-OH. (2): Modern bovine collagen after partial hydrolysis.

9. CONCLUSIONS

The chronological range of ^{14}C covers a span of time covering about 60 000 years. During this time, modern humans expanded throughout the Old and New Worlds, and

agriculture and more complex forms of social organisation become discernible in the archaeological record. Although it began as a method devised by physicists and chemists, the successful application of radiocarbon dating in archaeology depends upon rigorous attention to sample provenance and stratigraphy in order to determine the age of dated events, coupled with an ongoing liaison with the radiocarbon laboratory to produce results which are both accurate and precise.

Avenues of further research which will continue to enhance the application of the radiocarbon method include the development of more optimized measurement methods, such as GC -AMS[103], the development of a new generation of smaller sized AMS facilities[104], as well as improved sample pretreatment methods[105] and the extension of the calibration curve beyond 24 ka. Novel sample types also continue to be introduced for more routine dating applications due principally to the enhanced sensitivities of AMS systems (e.g. pollen and carbon from rock art sites[106]). The second fifty years of radiocarbon dating promises to be as exciting and stimulating as the first.

10. ACKNOWLEDGEMENTS

We are grateful to Dr Caitlin Buck (Department of History and Archaeology, University of Cardiff) and Dr Alan Hogg (Radiocarbon Dating Laboratory, University of Waikato) for their useful comments and suggestions.

REFERENCE

[1] In, Trigger, B.G. 1989. *A History of Archaeological Thought.* Cambridge University Press, Cambridge. pp 71.

[2] Oakley, K.P. 1979. In Honour of Willard Frank Libby. In, *Radiocarbon Dating. Proceedings of the Ninth International Conference, Los Angeles and La Jolla, 1976.* R. Berger and H.E Suess (eds.). University of California Press, Los Angeles.

[3] Clark, J.D. 1979. Radiocarbon Dating and African Prehistory. In, *Radiocarbon Dating. Proceedings of the Ninth International Conference, Los Angeles and La Jolla, 1976.* R. Berger and H.E Suess (eds.). University of California Press, Los Angeles. pp. 7-31.

[4] Movius, H. L Jr. 1960. Radiocarbon dates and Upper Paleolithic Archaeology in Central and Western Europe. *Current Anthropology* 1 (5-6):355-92.

[5] Taylor, R.E. 1987. *Radiocarbon Dating: An Archaeological Perspective.* Academic Press, Orlando.

[6] Aitken, M.J. 1990. *Science-based Dating in Archaeology.* Longman, England.

[7] Arnold, J.R. and Libby, W.F. 1949. Age determinations by radiocarbon content: checks with samples of known age. *Science* 110: 678-680.

[8] Libby, W.F. 1952. *Radiocarbon Dating.* University of Chicago Press, Chicago. 124 pp.

[9] Stuiver, M. and Polach, H.A. 1977. Discussion: Reporting of ^{14}C data. *Radiocarbon* 19: 355-63.

[10] Libby, W.F., Anderson, E.C. and Arnold, J.R. 1949. Age determination by Radiocarbon content: world-wide assay of natural radiocarbon. *Science* 109:227-28.

[11] Coplen, T.B. 1994. Reporting of stable hydrogen, carbon and oxygen isotopic adundances. *Pure and Applied Chemistry* 66:273-276.

[12] Mann W. 1983. An International Reference Material for Radiocarbon Dating. *Radiocarbon* 25(2): 519-527.

[13] Stuiver, M. and Polach, H.A. 1977. Discussion: Reporting of ^{14}C data. *Radiocarbon* 19: 355-63.

[14] Pearson, G.W. 1983. *The development of high-precision ^{14}C measurement and its* University of Belfast, Northern Ireland.

[15] Higham, T.F.G. 1993. "Radiocarbon Dating the Prehistory of New Zealand". Unpublished D.Phil thesis, University of Waikato.

[16] Stuiver, M., Pearson, G.W and Braziunas, T.F. 1986. Radiocarbon age calibration of marine samples back to 9000 Cal Yr BP. *Radiocarbon* 28(2B):980-1021.

[17] Rubin, M., Lockwood, J.P and Friedman, I. 1987. Effects of volcanic emanations on carbon-isotope content of modern plants near Kilauea Volcano. In, *Volcanism in Hawaii* (Eds); Decker, R.W., Wright, T.L. and Stauffer, P.H.USGS Professional paper 1350, US Government Printing office, Washington. pp 209-11.

[18] Dye, T. 1994. Apparent ages of marine marine shells: Implications for archaeological dating in Hawai'i. *Radiocarbon* 36(1): 51-57.

[19] Suess, H.E. 1955. Radiocarbon content in modern wood. *Science*.122:415-17.

[20] de Vries, H. 1958. Atom bomb effect: variations of radiocarbon in plants, shells, snails in the past 4 years. *Science* 128:250-251.

[21] Gupta, S.K. and Polach, H.A. 1985. Radiocarbon Dating Practices at ANU. Handbook, Radiocarbon Dating Laboratory, Research School of Pacific Studies, Australian National University, Canberra.

[22] Peng, T-H., Key, R.M and Östlund, H.G. 1998. Temporal variations of bomb radiocarbon inventory in the Pacific Ocean. *Marine Chemistry* 60(1-2): 3-13.

[23] Horrocks, D.L. 1974. *Applications of Liquid Scintillation Counting*. Academic Press, New York.

[24] Kromer, B and Munnich, K.O. 1994. CO_2 Gas Proportional Counting in radiocarbon dating—Review and Perspective. In, *Radiocarbon Dating after Four Decades: an Interdisciplinary Perspective*. R.E Taylor, A. Long and R.S Kra (eds.). Co-publication with *Radiocarbon*. Springer-Verlag, NY. Pp. 184-197.

[25] Kromer, B and Munnich, K.O. 1994. CO_2 Gas Proportional Counting in radiocarbon dating—Review and Perspective. In, *Radiocarbon Dating after Four Decades: an Interdisciplinary Perspective*. R.E Taylor, A. Long and R.S Kra (eds.). Co-publication with Radicarbon. Springer-Verlag, NY. Pp. 184-197.

[26] Tuniz, C., Bird, J.R., Fink, D. and Herzog, G.F. 1998. *Accelerator Mass Spectrometry: Ultrasensitive analysis for global science*. CRC Press, Boca Raton.

[27] Wohlfarth, B., Skog, G., Possnert, G and Homquist, B. 1998. Pitfalls in the AMS radiocarbon-dating of terrestrial macrofossils. *Journal of Quaternary Science* 13(2): 137-145.

[28] Gove, H.E. 1994. The History of AMS, its advantages over decay counting: Applications and prospects. In, *Radiocarbon Dating after Four Decades: An Interdisciplinary Perspective*. R.E Taylor, A. Long and R.S Kra (eds.). Co-publication with Radiocarbon. Springer-Verlag, NY. Pp. 214-229.

[29] Broecker, W. 1998. In, A Tribute to Minze Stuiver upon his retirement. *Radiocarbon* 40(3): iii-x.

[30] Otlet, R.L., Walker, A.J., Hewson, A.D and Burleigh, R. 1980. ^{14}C interlaboratory comparison in the UK: Experiment design, preparation and preliminary results. *Radiocarbon* 22(3): 936-947.

[31] Scott, E.M., Long, A. and Kra, R (eds.). 1990. Proceedings of the International Workshop on Intercomparison of Radiocarbon Laboratories. *Radiocarbon* 32(3):253-397.

[32] IAEA-International Atomic Energy Agency.

[33] Rozanski, K., Stichler, W., Gonfiantini, R., Scott, E.M., Beukens, R.P., Kromer, B. and Van Der Plicht, J. 1992. The IAEA ^{14}C Intercomparison Exercise 1990. *Proceedings of the 14th International ^{14}C Conference* (eds) A. Long and R. Kra. *Radiocarbon* 34(3):506-519.

[34] TIRI-Third International Radiocarbon Intercomparison.

[35] Scott, E.M, Aitchison, T.C., Baxter, M.S., Cook, G.T. and Harkness, D.D. 1990. ^{14}C Cross Check. International Collaborative Study Report. University of Glasgow.

[36] Gulliksen, S. and Scott, E.M. 1995. Report of the the TIRI workshop, Saturday 13 August 1994. *Proceedings of the 15th International ^{14}C Conference* (eds) D.D Harkness, B.F Miller and E.M Scott. *Radiocarbon* 37(2):820-21.

[37] Schiffer, M.B. 1987. *Formation Processes of the Archaeological Record*. University of New Mexico Press, Albuquerque.

[38] Mook, W.G., and H.T. Waterbolk, 1985. *Handbooks for Archaeologists No. 3. Radiocarbon dating*. European Science Foundation Publication, Strasbourg.

[39] Ashmore, P.J. 1999. Radiocarbon dating: Avoiding errors by avoiding mixed samples. *Antiquity* 73(279): 124-130.

[40] McFadgen, B.G. 1982. Dating New Zealand archaeology by radiocarbon. *New Zealand Journal of Science* 25:379-92.

[41] McFadgen, B.G, Knox, F.B and Cole, T.R.L. 1994. Radiocarbon calibration curve variations and their implications for the interpretation of New Zealand prehistory. *Radiocarbon* 36(2):221-236.

[42] Kuzmin, Y.V and Tankersley, K.B. 1996. The colonization of Eastern Siberia: An evaluation of the Palaeolithic radiocarbon dates. *Journal of Archaeological Science* 23: 577-585.

[43] Caughley, G., 1988. The colonisation of New Zealand by the Polynesians. *Journal of the Royal Society of New Zealand,* 18: 245-270.

[44] Olsson, I.U. 1979. The importance of the pretreatment of wood and charcoal samples. In, *Radiocarbon Dating. Proceedings of the Ninth International Conference, Los Angeles and La Jolla, 1976.* R. Berger and H.E Suess (eds.). University of California Press, Los Angeles.

[45] Van Klinken, G.J and Hedges, R.E.M. 1998. Chemistry strategies for organic ^{14}C samples. *Radiocarbon* 40(1): 51-56.

[46] Stuiver, M., Reimer, P.J., Bard, E., Beck, J.W., Burr, G.S., Hughen, K.A., Kromer, B., McCormac, F.G., v.d. Plicht, J. & Spurk, M. 1998. INTCAL98 Radiocarbon age calibration, 24 000 – 0 Cal AD. *Radiocarbon* 40, 1041-1083.

[47] Vries, H. de. 1958 Variations in concentration of radiocarbon with time and location on earth. *Proceedings, Nederlandsche Akademie van Wetenschappen*, Series B61:1.

[48] Renfrew, C. 1973. *Before Civilization. The Radiocarbon Revolution and Prehistoric Europe*. Penguin, England.

[49] Stuiver, M. and Braziunas, T.F. 1989. Atmospheric ^{14}C and century-scale solar oscillations. *Nature* 338:405-8

[50] Pilcher, J.R., Baillie, M.G.L., Schmidt, B. and Becker, B. 1984. A 7272-year tree-ring chronology for western Europe. *Nature* 312: 150-152.

[51] Becker, B. 1993. An 11000-year old German oak and pine dendrochronology for radiocarbon calibration. 1993 Calibration edition (eds) Stuiver, M., Long, A and Kra, R. *Radiocarbon* 35(1):201-213.

[52] Stuiver, M., Reimer, P.J., Bard, E., Beck, J.W., Burr, G.S., Hughen, K.A., Kromer, B., McCormac, F.G., v.d. Plicht, J. & Spurk, M. 1998. INTCAL98 Radiocarbon age calibration, 24 000 – 0 Cal AD. *Radiocarbon* 40, 1041-1083.

[53] Bard, E., Hamelin, B., Fairbanks, R.G. and Zindler, A. 1990. Calibration of the ^{14}C timescale over the past 30 000 years using mass spectrometric U-Th ages from Barbados corals. *Nature* 345:405-9.

[54] Burr, G.S., Beck, J.W., Taylor, F.W., Récy, J., Edwards, R.L., Cabioch, G., Corrège, T., Donahue, D.J and O'Malley, J.M. 1998. A High-resolution radiocarbon calibration between 11700 and 12400 calendar years BP derived from Th^{230} ages of corals from Espiritu Santo Island, Vanuatu. *Radiocarbon* 40(3): 1093-1105.

[55] Stuiver, M., Reimer, P.J., Bard, E., Beck, J.W., Burr, G.S., Hughen, K.A., Kromer, B., McCormac, F.G., v.d. Plicht, J. & Spurk, M. 1998. INTCAL98 Radiocarbon age calibration, 24 000 – 0 Cal AD. *Radiocarbon* 40, 1041-1083.

[56] Kitagawa, H., and van der Plicht, J. 1998. Atmospheric radiocarbon calibration to 45000 yr BP: late glacial fluctuations and comsogenic isotope production. *Science*, 279:1187-1190.

[57] Stuiver, M., Reimer, P.J., Bard, E., Beck, J.W., Burr, G.S., Hughen, K.A., Kromer, B., McCormac, F.G., v.d. Plicht, J. & Spurk, M. 1998. INTCAL98 Radiocarbon age calibration, 24 000 – 0 Cal AD. *Radiocarbon* 40, 1041-1083.

[58] Stuiver, M., Pearson, G.W and Braziunas, T.F. 1986. Radiocarbon age calibration of marine samples back to 9000 Cal Yr BP. *Radiocarbon* 28(2B):980-1021.

[59] Stuiver, M., Reimer, P.J and Braziunas, T.F. 1998. High-precision radiocarbon age calibration for terrestrial and marine samples. *Radiocarbon* 40(3): 1127-1151.

[60] Buck, C.E., Litton, C.D and Smith, A.F.M. 1992. Calibration of radiocarbon results pertaining to related archaeological events. *Journal of Archaeological Science* 19:497-512.

[61] Buck, C.E., Litton, C.D and, Scott, E.M, 1994. Making the most of radiocarbon dating: some statistical consideration. *Antiquity*, 68:252-63.

[62] Bronk Ramsey, C. (1995). Radiocarbon Calibration and Analysis of Stratigraphy: The OxCal Program. *Radiocarbon* **37**, 425-430.
[63] http://car.ant.auckland.ac.nz/dating/manual.html
[64] http://www.bcal.ac.uk.
See also, Buck, C.E., Christen, J.A and James, G.N. 1999. BCal: an on-line Bayesian radiocarbon calibration tool. *Internet Archaeology* 7 http://intarch.ac.uk/journal/issue7/buck/.
[65] Polach, H.A. 1976. Radiocarbon as a research tool in archaeology - hopes and limitations. In. *Proceedings of the Symposium on Scientific Methods in the Study of Ancient Chinese Bronzes and Southeast Asian Metal and other Archaeological Artefacts*. N. Barnard (ed.). National Gallery of Victoria, Melbourne, Australia. pp. 255-98.
[66] Flannery, T.F. 1999. Debating Extinction. *Science* 283:182-3.
[67] Roberts, R.G,Jones, R. and Smith, M.A. 1994. Beyond the radiocarbon barrier in Australian prehistory. *Antiquity* 68: 611-16.
[68] Allen, J. 1989. When did humans first colonize Australia? *Search* 20:149-54.
[69] Barbetti, M. and Allen, H. 1972. Prehistoric man at Lake Mungo, Australia by 32 000 years BP. *Nature* 240: 46-8.
[70] Flood, J. 1995. *Archaeology of the Dreamtime. The story of prehistoric Australia and its people*. Angus and Robertson, Sydney. 3rd edition.
[71] Jones, R. 1993. A continental reconnaissance: some observations concerning the discovery of the Pleistocene achaeology of Australia. In, Spriggs, M., Yen, D.E., Ambrose, W., Jones, R., Thorne, A and Andrews, A. (eds). *A Community of Culture: People and Prehistory of the Pacific.* Australian National University Occasional Papers in Prehistory 21. Canberra, Australia. pp 97-122.
[72] Roberts, R.G., Jones, R and Smith, M. 1990. Thermoluminescence dating of a 50 000 year old human occupation site in northern Australia. *Nature* 345: (6271:153-6).
[73] Chappell, J., Head, M.J and Magee, J. 1996. Beyond the radiocarbon limit in Australian archaeology and Quaternary research. *Antiquity* 70:543-52.
[74] Allen, J. 1989. When did humans first colonize Australia? *Search* 20:149-54.
[75] Roberts, R.G., Jones, R and Smith, M. 1990. Thermoluminescence dating of a 50 000 year old human occupation site in northern Australia. *Nature* 345: (6271:153-6).
[76] Roberts, R.G., Jones, R., Spooner, N.A., Head, M.J., Murray, A.S and Smith, M.A. 1994. The Human Colonisation of Australia: Optical dates of 53, 000 and 60, 000 years bracket human arrival at Deaf Adder Gorge, Northern Territory. *Quaternary Geochronology (Quaternary Science Reviews)* 13:575-583.
[77] Allen, J and Holdaway, S. 1995. The contamination of Pleistocene radiocarbon determinations in Australia. *Antiquity* 69:101-12.
[78] Allen, J and Holdaway, S. 1995. The contamination of Pleistocene radiocarbon determinations in Australia. *Antiquity* 69:101-12.
[79] Webb, R.E. 1998. Problems with radiometric "time": Dating the initial human colonisation of Sahul. *Radiocarbon* 40(2): 749-758.

[80] Erlenkeuser, H. 1979. A thermal diffusion plant for radiocarbon isotope enrichment from natural samples. *Radiocarbon Dating. Proceedings of the Ninth International conference Los Angeles and La Jolla 1976.* (Ed. R. berger and H.E. Suess). University of California Press, Los Angeles.

[81] Chappell, J., Head, M.J and Magee, J. 1996. Beyond the radiocarbon limit in Australian archaeology and Quaternary research. *Antiquity* 70:543-52.

[82] Chappell, J., Head, M.J and Magee, J. 1996. Beyond the radiocarbon limit in Australian archaeology and Quaternary research. *Antiquity* 70:543-52.

[83] Higham, T.F.G., 1994. Radiocarbon dating New Zealand prehistory with moa eggshell: some preliminary results. *Quaternary Geochronology (Quaternary Science Reviews),* 13:163-169.

[84] Anderson, A.J., I.W.G. Smith, and T.F.G. Higham, 1996. Radiocarbon Chronology. *In* A.J. Anderson, I.W.G. Smith, and B.J. Allingham (eds), *Shag River Mouth: the Archaeology of an Early Southern Maori Village,* pp. 60-69. Australian National University Research Papers in Archaeology and Natural History 27. ANH Publications, RSPAS, Canberra, Australia.

[85] Higham, T.F.G., A.J. Anderson, and C. Jacomb, 1999. Dating the first New Zealanders: the chronology of Wairau Bar. *Antiquity* 73:420-27.

[86] Petchey, F.J., 2000. Radiocarbon Dating Fish Bone from the Houhora Archaeological Site: Comparison with Multiple Sample Types. In press.

[87] Petchey, F.J., 1998. *Radiocarbon Dating a Novel Sample Type: Snapper and Barracouta Bone from New Zealand Archaeological Sites.* Unpublished Phd thesis, University of Waikato.

[88] Anderson, A.J. 1991. The chronology of colonisation in New Zealand. *Antiquity,* 65:767-795.

[89] Paul, L.J., 1992. The biology of the snapper. *In* S. Mossman (ed.), *All You Want to Know About Snapper,* pp. 3-15. New Zealand Fishing News, Auckland, New Zealand.

[90] Lassey, K.R., M.R Manning, and B.J. O'Brien, 1990. An overview of oceanic radiocarbon: its inventory and dynamics. *Reviews in Aquatic Sciences,* 3(2 and 3):117-146.

[91] Heath, R.A., 1985. A review of the physical oceanography of the seas around New Zealand - 1982. *New Zealand Journal of Marine and Freshwater Research,* 19:79-124.

[92] Higham, T.F.G. and A.G. Hogg, 1995. Radiocarbon dating of prehistoric shell from New Zealand and calculation of the ΔR value using fish otoliths. *Radiocarbon,* 37:409-416

[93] Millar, D.G.L. 1967. Recent archaeological excavations in the northern part of the South Island. *Journal of the Nelson Historical Society,* 2:5-13.

[94] Anderson, A.J., 1991. The chronology of colonisation in New Zealand. *Antiquity,* 65:767-795.

[95] Hedges and van Klinken 1995 van Klinken, G.J., and R.E.M. Hedges, 1995. Experiments on collagen-humic interactions: speed of humic uptake, and effects of diverse chemical treatments. *Journal of Archaeological Science,* 22:263-270.

[96] van Klinken, G.J., 1999. Bone collagen quality indicators for palaeodietary and radiocarbon measurement. *Journal of Archaeological Science* 26:687-695.

[97] Law, I.A., R.A. Housley, N. Hammond, and R.E.M. Hedges, 1991. Cuello: resolving the chronology through direct dating of conserved and low-collagen bone by AMS. *Radiocarbon,* 33:303-315.

[98] Law, I.A., R.A. Housley, N. Hammond, and R.E.M. Hedges, 1991. Cuello: resolving the chronology through direct dating of conserved and low-collagen bone by AMS. *Radiocarbon,* 33:303-315.

[99] Gillespie, R., R.E.M. Hedges, and M.J. Humm, 1986. Routine AMS dating of bone and shell proteins. *Radiocarbon,* 28:451-456.

[100] Law, I.A., and R.E.M. Hedges, 1989. A semi-automated bone pretreatment system and the pretreatment of older and contaminated samples. *Radiocarbon*, 31:247-253.

[101] Law, I.A., R.A. Housley, N. Hammond, and R.E.M. Hedges, 1991. Cuello: resolving the chronology through direct dating of conserved and low-collagen bone by AMS. *Radiocarbon,* 33:303-315.

[102] Andrews, V.E.W. and N. Hammond, 1990. Redefinition of the Swasey phase at Cuello, Belize. *American Antiquity* 55(3):570-584.

[103] GC-AMS; Gas Chromatography – Accelerator Mass Spectrometry. Bronk Ramsey, C, Hedges, R.E.M. 1995. Radiocarbon with Gas Chromatography. *Radiocarbon* 37(2): 711.

[104] Suter, M. 1998. A new generation of small facilities for accelerator mass spectrometry. *Nuclear Instruments and Methods in Physics Research* B 139: 150-157.

[105] Bird, M.I, Ayliffe, L.K, Fifield, LK, Turney, C.S.M, Cresswell, R.G, Barrows, T.T, David B. 1999. Radiocarbon Dating of "Old" Charcoal Using a Wet Oxidation, Stepped-Combustion Procedure. *Radiocarbon* 41(2): 127-140.

[106] Tuniz, C. AMS Radiocarbon dating in Art and Archaeometry. This volume.

Radiation in Art and Archeometry
D.C. Creagh and D.A. Bradley (editors)

X-ray Fluorescence Applications for the Study and Conservation of Cultural Heritage

M. Ferretti [a]

[a] CNR - Istituto per le Tecnologie Appicate ai Beni Culturali
Area della Ricerca di Roma, Via Salaria km 29.300 - CP 10, 00016 Monterotondo St., Italy

X-ray fluorescence has been used for some fifty years in the study and conservation of archaeological and historical objects; yet, given the number of papers that are still published in this field, its capability of stimulating the creativity of scientists, conservators, archaeologists and art-historians is far from being exhausted. This paper aims at reviewing part of the considerable number of papers published so far with a special focus on the relationship between non-destructive and quantitative analysis or, one could say, between the instrument and the object analyzed. The criteria used by scientists to design the investigations are also considered, and examples are shown in which similar objects are approached, from the analytical point of view, in totally different ways.

1. INTRODUCTION

X-ray fluorescence has long been used for the investigation of archaeological and historical materials. Early applications date back to the '50s, when wavelength-dispersive (WD) spectrometers [1] were used for non-destructive investigation of small metal objects [2-4] and materials such as glass [5], jade [6] and pigments [7-11]. The introduction of focusing devices in WD-XRF systems [12] improved the spatial resolution, thus allowing investigation of small details on the object [13] as well as a way to approach complex situations such as the element distribution in cross-sections of paintings [14].

Basically XRF was used in a non-destructive way, though local abrasion on the measurement point was necessary to obtain some quantitative data [15-16]. A fully quantitative, though destructive, approach came later and concerned the analysis of pottery [17]. The samples taken from the objects were crushed and prepared with a rather complex procedure that included glass fusion and pellettization; this is still proving to be one of the most effective and widely used methods for the elemental characterization of pottery and stone materials.

A great step forward was made on the non-destructive side when the resolution of energy-dispersive (ED) spectrometers became sufficiently good to split adjacent elements, in particular when semiconductor detectors came into use [18, 19]. Thanks to the intrinsically compact design of ED systems and to the consequent availability of portable spectrometers, *in situ* investigations became possible and the range of use of XRF was virtually extended to any type of object.

Since then, the methods have not changed much, though new system architectures based on total reflection (TRXRF) [20] and microbeams employing capillaries [21, 22] were introduced. The designers' attention has recently been attracted by Peltier-cooled semiconductor detectors that are becoming competitive with the nitrogen-cooled ones [23] and are producing significant improvements in spectrometer portability [24].

2. PHYSICAL PRINCIPLES AND INSTRUMENTATION

The physical principles of X-ray fluorescence are simple and well known: electronic transitions can be induced in the inner shells of the atoms by electromagnetic radiation - or charged particles - of suitable energy; such transitions result in the emission of X-rays whose energy and intensity are related to the type and abundancy of the atoms concerned. Due to the attenuation of the matter, only the X-rays emitted in the first layers under the surface can reach the detector; Figure 1 shows, for each element in a typical bronze alloy, the part of the sample concerned by the analysis.

If one considers that the surface of archaeological and historical materials is in most cases deteriorated and differs in composition from the bulk, it is apparent that quantitative measurements often require surface abrasion or even sampling, depending on the material; conversely a strictly non-destructive measurement cannot provide reliable quantitative data. For each experimental situation the choice depends on: a) the type and intrinsic value of the object, b) the aim of the investigation, c) the instruments available and, last but not least, d) the scientist's or conservator's personal idea of acceptable damage.

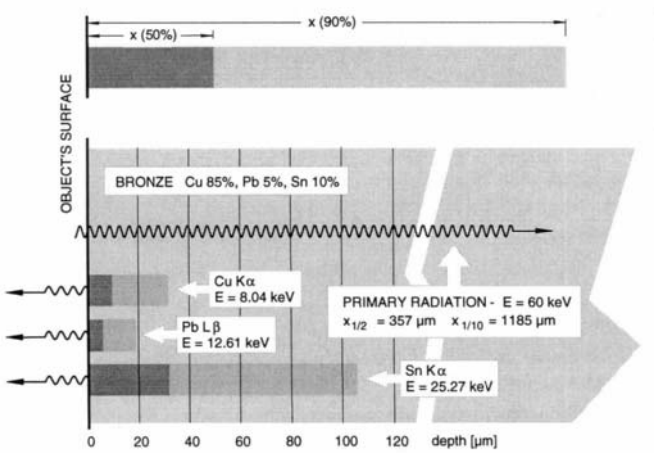

Figure 1. Depth of sample concerned by XRF analysis in a typical bronze alloy; x(50%) and x(90%) are the depths from which 50% and 90% of the emitted X-rays come, respectively.

As regards quantitative analyses, one of the most attractive aspects is that, in principle, the

results can be used by other scientists; in fact this is not always true since the experimental conditions may not be comparable; periodic intercomparisons and standardized procedures [25] have solved the problem but unfortunately, too few laboratories have been involved: indeed, it is still very difficult to use quantitative data from the literature.

Given the above considerations, two main groups of XRF spectrometers will be discussed here:

1) spectrometers for quantitative analysis
2) portable spectrometers.

2.1 Spectrometers for quantitative analysis [26]

These instruments are designed to maximize accuracy, precision and sensitivity: typical figures are 1-10% relative for accuracy, 1% relative for precision and around 10 ppm depending on the element for detection limits [27-30]; this is paid for in terms of weight and dimensions: spectrometers usually have fixed positions in laboratories from which they cannot be moved. The sample, 0.1 – 5 g in weight, has to be crushed and pressed in pellets or fused in glass beads; it is irradiated in a vacuum chamber that allows the detection of light elements down to fluorine (Z=9). Though non-destructive for the specimen itself, the analysis is obviously destructive for the object that has to be sampled. According to whether the wavelength or the energy of the fluorescent radiation is measured, one can have wavelength- or energy-dispersive spectrometers; the layout of both is shown in Figures 2 and 3, respectively.

2.2. Portable spectrometers

These spectrometers are designed for *in situ* non-destructive investigations; the simplification of the system, aimed at reducing weight and dimensions, results in relatively poor precision and detection limits. Usually the primary radiation source is an X-ray tube; if portability is the main requirement, radioisotopic sources can also be used, though with further deterioration of sensitivity. Also among X-ray tubes, one may have different options, obviously affecting the detection limits: low-weight, low-power tubes usually work at relatively low voltages and are therefore unable to excite the K-lines of elements like Ag, Sn, Sb; high-power tubes are heavier and more complex due to the shielding and the cooling system but offer a wider detection range. Table 1 shows typical detection limits for portable spectrometers equipped with X-ray tubes; the one of ref. 19 also has a radioisotopic source, the concerned detection limit for Sn is that of the K line.

As regards detection, Si(Li) and intrinsic planar Ge detectors, cooled by liquid nitrogen, are well established; Figures 4 and 5 show the layout of two portable spectrometers using an X-ray tube and a radioisotopic source, respectively. Peltier-cooled semiconductor detectors have recently achieved comparable energy resolution and will soon be improved in dimensions and intrinsic efficiency. A particular use of portable spectrometers is compositional mapping of the object's surface [31], which clearly relies on large numbers of measurements. For these applications the support system, which has to be easily transportable and provided with the requisite flexibility, becomes a further important component of the XRF spectrometer; Figure 6 shows the layout of the support used by the ENEA research group in Rome, Italy.

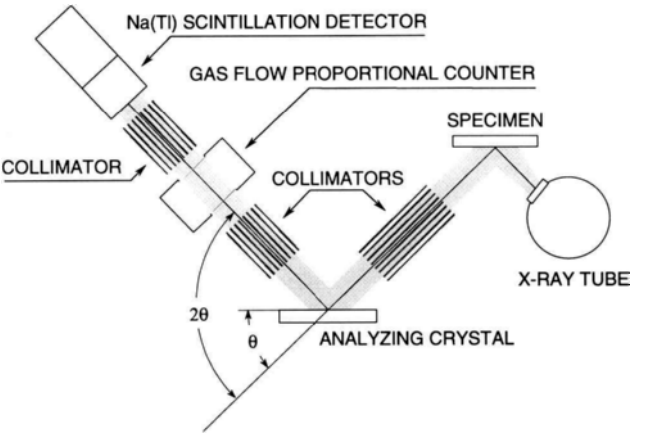

Figure 2. Layout of a wavelength-dispersive XRF spectrometer.

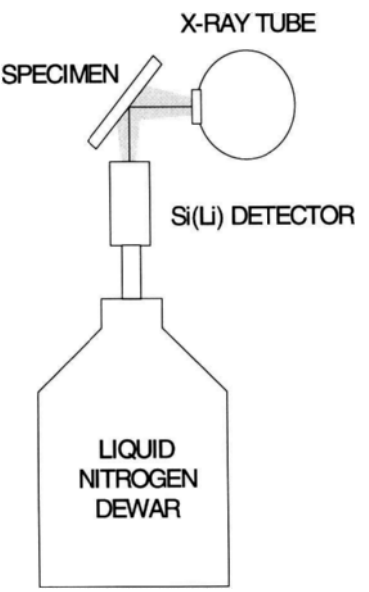

Figure 3. Portable X-ray spectrometer.

Table 1
Detection limits of portable XRF spectrometers [weight %].

Reference	Fe	Ni	Zn	Pb	Ag, Sn, Sb	Notes
Hall *et al.* [19]	0.005	0.03		0.1	0.03 (AgK), 0.01 (AgL), 0.1 (SnK), 1.5 (SnL)	Matrix: Cu alloys Sample: presumably calibration std. X-ray tube operated at 30 kV + Am-241 source
Lutz *et al.* [23]	0.05	0.01	0.5		0.006÷0.01	Matrix: Cu alloys Sample: drill shavings X-ray tube operated at 35 and 50 kV
Ferretti *et al.* [31]			0.5	0.7÷1.0	0.03÷0.07	Matrix: Cu alloys Sample: surface of the object, with no abrasion X-ray tube operated at 60 kV

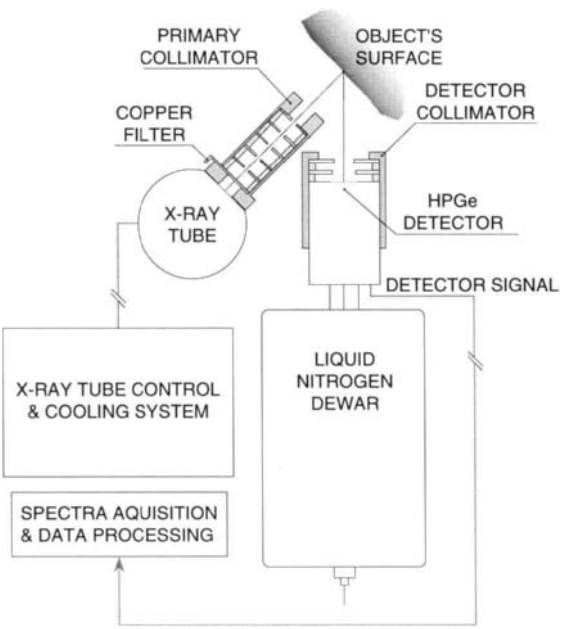

Figure 4. Layout of a portable XRF spectrometer using an X-ray tube as excitation source.

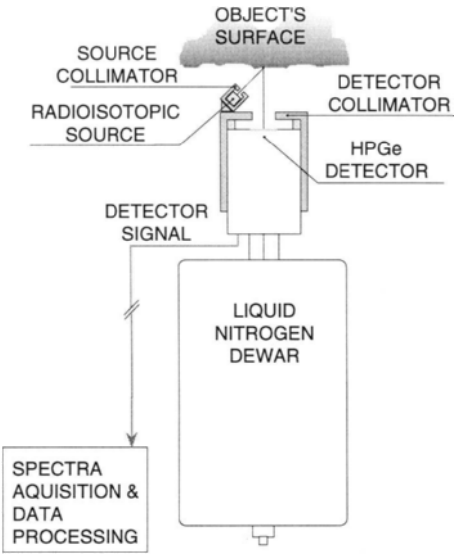

Figure 5. Layout of a portable XRF spectrometer using a radioisotopic souce for excitation.

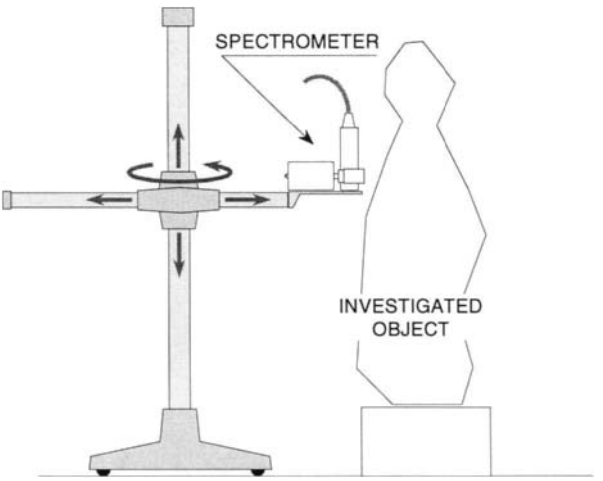

Figure 6. Support system for in situ investigations with the portable spectrometer.

3. CASE STUDIES

This section aims at showing how the investigation of similar objects can be approached in a totally different way; for instance it is surprising how different the feeling of "acceptable extent of destructivity" can be.

3.1 Metals

Brownswords *et al.* [32] sample 10 to 20 mg from pewter objects and analyze the drill shavings in a WD spectrometer; though trace elements are also detected, the study relies on the main components: in particular the amount of tin, which is related to the alloy's quality, is put in relationship to the date and place of manufacturing. It is found that high-quality pewter came from London and adjacent areas, whereas the provinces produced lower-quality alloys.

A "quasi-non-destructive" approach is that of Carter *et al.* [33], who analyze Roman orichalcum coins by comparing seven methods (wet chemistry, various types of XRF, neutron and photon activation, atomic absorption); prior to the XRF analyses, a layer of at least 10-15 microns is removed from the coins' surface. The conclusion is that the reliability of XRF is comparable to that of other techniques, provided the surface of the objects is properly prepared.

A totally non-destructive approach is that of Ferretti *et al.* [34], who use a portable spectrometer to map the surface of a large bronze statue and confirm that some of its parts are not original. If the number of measurements is sufficiently great, it is possible to distinguish different alloys by considering the clustering of the data points; since the differences in major elements are not large and the method is basically qualitative, the capability of detecting trace elements is essential for effective discrimination.

3.2 Pottery

Methods similar to that described in [34] are not unusual for the analysis of pottery: Ballié *et al.* [35] use an ED spectrometer with an X-ray tube working at 22 keV and 0.05 mA in a non-destructive study on the provenance of *terra sigillata*; the discrimination among different production sites is carried out on the basis of Fe/K and Ti/Mn count rate ratios. Similarly Yap [36] uses an ED system with an Am-241 radioisotopic source to distinguish antique porcelains from modern pieces on the basis of Ba and Cs count rates normalized to coherent scattering. Mazo-Gray *et al.* [37] also study Chinese porcelain, but a Cd-109 source is used instead of Am-241; the discrimination is carried out on the basis of Mn/Co, Rb/Sr and Zr/Nb count rate ratios.

Picon *et al.* [38] and Schneider *et al.* [39] prefer absolute but destructive determinations: they analyzed *terra sigillata* by means of a WD spectrometer to derive the compositional fingerprints that characterize artifacts from different areas and workshops. The specimens are prepared from 0.1 to 1.0 g of sample by glass fusion, crushing and pelletization (Picon) or simply by glass fusion (Schneider). In order to distinguish compositional groups, Picon basically considers oxides above 1% in weight, whereas Schneider also considers trace elements such as Zr and Rb.

In a later work, [40] Schneider combines optical microscopy on thin sections and quantitative XRF analysis to study the remains of Phidias' workshop at Olympia; the composition of bricks, crucibles, tuyeres and molds is compared to that of the local clays,

with regard to both the major oxides and the trace elements.

3.3 Glass

A "quasi-non-destructive" approach is that of Cox *et al.*, [41] who use an ED spectrometer to investigate blue soda glass from York. The source is an X-ray tube operated at 15 kV and 0.9 mA and the sample, seemingly a whole piece removed from the stained glass window and polished on one corner, is irradiated in a vacuum chamber; under these conditions the elements detected are Na, Mg, Al, Si, P, K, Ca, Mn, Fe, Cu, Zn and Pb. The multivariate analysis of the data leads to identification of three groups, each characterized by a different way of recycling Roman glass.

Ferretti *et al.* [42] analyze the stained-glass windows of Orvieto Cathedral with a portable non-destructive spectrometer when the panels are removed for restoration; though such major elements as Na, Si and K remain undetected, a purely qualitative comparison among trace elements in glass matrix and colorants is sufficient to distinguish glasses from different workshops and periods. The detection limits are on the order of tens of ppm and hundreds of ppm in glass and lead matrixes, respectively; Table 2 summarizes the results on glasses.

As regards the leads it is not possible to identify a single characteristic *fingerprint* for the original materials; however, used in combination with scanning electron microscopy (SEM), XRF permits study different types of solderings, some of which are localized whereas others are "stretched" along the lead.

Table 2
XRF analyses of the glasses in Orvieto Cathedral stained glass windows.

	Uncolored	Grisailles	Blue	Turquoise	Green	Violet	Red
Original of 1330	Mn (high), Ba (high)	Fe, Cu, Pb	Co, Zn (tr) In (tr)	Cu	Fe (low), Cu (high)		Cu
Late XVth-century restoration	Mn (low)	Fe, Cu, Pb	Co, Ni			Mn	Cu
XVIth - century restoration		Fe, Cu , Pb	Co, Ni		Fe compar. with Cu	Mn	Cu
1905 restoration	Mn (tr)	Co, Cu , Sn, Pb	Cr, Fe, Co, Cu, Pb				Co

Table 3
Identification of pigments by XRF.

Colour	Key element	Class of pigments	Compound	Notes
Yellow Brown Red Green	Fe	Earths, ochres	Minerals composed of iron oxides and silicates	
Blue Green	Cu	Copper-based pigments	Natural compounds (azurite, malachite, atacamite) and artificial compounds (acetates, resinates, chlorides, silicates, sulfates)	
White	Pb	Lead white	Basic lead carbonate $2PbCO_3 \cdot Pb(OH)_2$	
Blue	Co	Smalt	Glass SiO_2 (65-70%), K_20 (10-20%), Al_20_3 (0-8%), CoO (1-18%)	
Red	Hg	Cinnabar (vermilion)	Mercuric sulfide (cinnabar) HgS	
Red	Pb	Red lead	Lead tetroxide Pb_3O_4	
Yellow	As	Orpiment	Arsenic trisulfide As_2O_3	
Dark brown	Mn	Manganese brown	Manganese dioxide MnO_2 (pyrolusite)	
Yellow	Cd	Cadmium yellow	Cadmium sulfide CdS	modern
White	Ti	Titanium dioxide	Titanium dioxide TiO_2	modern

Table 3 (continued)

Identification of pigments by XRF.

Colour	Key element	Class of pigments	Compound	Notes
Yellow	Pb + Sn	Lead-tin yellow, giallolino	Lead-tin oxide Pb_2SnO_4 and $PbSnO_3$	
Yellow	Pb + Sb	Lead antimonate yellow, antimony yellow, Naples yellow	Lead antimonate $Pb_3(SbO_4)_2$	
Brown	Fe + Mn	Umber	Manganese dioxide (8-10%) + iron hydroxide (45-55%)	
Yellow	Pb + Cr	Chrome yellow	Lead chromate $PbCrO_4$	modern
Red	Pb + Cr	Chrome red	Basic lead chromate $PbCrO_4 \cdot Pb(OH)_2$	modern
Green	As + Cu	Emerald green, Scweinfurt green	Copper acetoarsenite $Cu(CH_3COO)_2 \cdot 3Cu(AsO_2)_2$	modern
White	Zn + Ba	Lithopone	Zinc sulfide + barium sulfate $ZnS + BaSO_4$	modern

3.4 Paintings

For XRF, only the non-destructive approach [43] is possible here, due to the difficulties of selective sampling; however, simple qualitative analyses are often sufficient to identify pigments, since many of them are characterized by the presence of one or two detectable elements. Since it is impossible to distinguish among signals coming from the ground and from the different painted layers, the correct interpretation of spectra may require considerable experience and knowledge of painting techniques; Table 3 [44] shows some pigments that can be identified by XRF.

Ferretti *et al.* [45] describe the investigation of an unusual antimony-based pigment used by Correggio; it should be noted that the full identification of the pigment required sampling, yet its recurrence on the three paintings was previously and non-destructively demonstrated by XRF, which also showed the optimum sampling point.

ACKNOWLEDGEMENTS

I am grateful to my former colleagues of ENEA, M. Diana, G. Guidi, M. Massimi, A. Matteja, A. Melchiorri P. Moioli, S. Omarini, F. Persia, A. Sargenti, C. Seccaroni and A. Tognacci for having shared many years of field experience, discussions and arguments with me.

I am very grateful to Mrs. C. Rockwell for her patient and accurate revision of the English.

REFERENCES

1. E.T. Hall, Year Book of the Physical Society, (1958) 22.
2. C.M. Kraay, Archaeometry, 1 (1958) 21.
3. C.H.V. Sutherland and M.R. Harold, Archaeometry, 4 (1961) 56.
4. E.T. Hall and G. Roberts, Archaeometry, 5 (1962) 28-32.
5. M. Banks, N. Elphinstone and E.T. Hall, Archaeometry, 6 (1963) 26.
6. E.T. Hall, M.S. Banks and J.M. Stern, Archaeometry, 7 (1964) 84.
7. R.J. Gettens and E. West Fitzhugh, Studies in Conservation, 11 (1966) 54.
8. J. Plesters, Studies in Conservation, 11 (1966) 62.
9. R.J. Gettens, H. Kuhn and W.T. Chase, Studies in Conservation, 12 (1967) 125.
10. H. Kühn, Studies in Conservation, 13 (1968) 7.
11. B. Mühlethaler and J. Thissen, Studies in Conservation, 14 (1969) 47.
12. M. Banks and E.T. Hall, Archaeometry, 6 (1963) 31.
13. S.C. Hawkes, J.M. Merrick and D.M. Metcalf, Archaeometry, 9 (1966) 98.
14. N. Stolow, J.F. Hanlan and R. Boyer, Studies in Conservation, 14 (1969) 139.
15. E.T. Hall, Archaeometry, 4 (1961) 62.
16. G.F. Carter, Archaeometry, 7 (1964) 106.
17. M. Picon, M. Vichy and E. Meille, Archaeometry, 13 (1971) 191.
18. R. Cesareo, F.V. Frazzoli, C. Mancini, S. Sciuti, M. Marabelli, P. Mora, P. Rotondi and G. Urbani, Archaeometry, 14 (1972) 65.
19. E.T. Hall, F. Schweizer and P.A.Toller, Archaeometry, 15 (1973) 53.
20. W. Devos, L. Moens, A. von Bohlen and R. Klockenkamper, Studies in Conservation, 40 (1995) 153.
21. M. Milazzo and C. Cicardi, Archaeometry, 40 (1998) 351.
22. G. Calvi, F. Di Mauro, L. Pappalardo, F.P. Romano, Proc. of EDXRS98 - European Conference on Energy Dispersive X-Ray Spectrometry, Bologna 7-12 June 1998.
23. J. Lutz and E. Pernicka, Archaeometry, 38 (1996) 313.
24. A. Longoni, C. Fiorini, P. Leutenegger, S. Sciuti, G. Fonterotta, L. Strüder and P. Lechner, Nucl. Instr. and Meth., A 409 (1998) 407.
25. G. Harbottle, Nucl. Instr. and Meth., B 14 (1986) 10.
26. R. Jenkins, R.W. Gould and D. Gedcke, Quantitative X-ray Spectrometry, 2nd ed., Marcel Dekker Inc., New York, 1995.
27. E.B. Buchanan and F.C. Tsai, Anal. Chem., 46 (1974) 1701.
28. J.V. Gilfrich, Prog. Analyt. Spectrosc. 12 (1989) 1.

29. S. Kelley, O. Williams-Thorpe, and R.S. Thorpe, Archaeometry, 36 (1994) 209.
30. K.G. Malmqvist, Nucl. Instr. and Meth., B 14 (1986) 86.
31. M. Ferretti and P. Moioli, Proc. of Metal 98 - International Conference on Metals Conservation, Draguignan 27-29 May 1998, 39.
32. R. Brownswords and E.E.H. Pitt, Archaeometry, 26 (1984) 237.
33. G.F. Carter, E.R. Caley, J.H. Carlson, G.W. Carriveau, M.J. Hughes, K. Rengan and C. Segebade, Archaeometry, 25 (1983) 201.
34. M. Ferretti, L. Miazzo and P. Moioli, Studies in Conservation, 42 (1997) 241.
35. P.J. Ballié and W.B. Stern, Archaeometry, 26 (1984) 62.
36. C.T. Yap, Archaeometry, 28 (1986) 197.
37. V. Mazo-Gray and M. Alvarez, Archaeometry, 34 (1992) 37.
38. M. Picon, C. Carre, M.L. Cordoliani, M. Vichy, J.A. Hernandez and J.L. Mignard, Archaeometry, 17 (1975) 191.
39. G. Schneider, B. Hoffmann and E. Wirz, Archaeo-Physika 10 (1980) 269.
40. G. Schneider, MASCA Res. Pap. Sci. Archaeol. 6 (1989) 17.
41. G.A.Cox and K.J.S. Gillies, Archaeometry, 28 (1986) 57.
42. M. Ferretti, P. Moioli and C. Seccaroni, in press.
43. C. Seccaroni, R. Scafè, P. Moioli, G.F. Guidi and M. Ferretti, I Beni Culturali - Tutela e Valorizzazione, anno II n.6 (1994) 38.
44. P. Moioli and C. Seccaroni, personal communication (1998).
45. M. Ferretti, G. Guidi, P. Moioli, R. Scafè and C. Seccaroni, Studies in Conservation 36 (1991) 235.

Radiation in Art and Archeometry
D.C. Creagh and D.A. Bradley (editors)

A Synchrotron X-ray diffraction study of Egyptian cosmetics

P. Martinetto[a,b], M. Anne[c], E. Dooryhée[b], G. Tsoucaris[a], Ph. Walter[a]

[a]Laboratoire de recherche des musées de France, UMR 171 du C.N.R.S.,
6, rue des Pyramides, F-75041 Paris Cedex 1, France

[b]European Synchrotron Radiation Facility, 6, rue Jules Horowitz, B.P. 220, F-38043
Grenoble Cedex, France

[c]Laboratoire de Cristallographie - CNRS, 25, avenue des Martyrs - BP 166,
F-38042 Grenoble Cedex 9, France

1. INTRODUCTION

1.1. Archaeological background

Visitors of the Egyptian collections are amazed to see the amount and the exceptional preservation of the everyday life artefacts, and note the abundance of the toilet accessories. Unguents, creams, powders and eye-paints were commonly used and kept in receptacles with characteristic shapes (Figure 1), made of stone (alabaster, hematite, and marble), ceramic, wood or reed (Vandier D'abbadie, 1972). These receptacles had been placed in tombs as burial artefacts. Previous studies have shown that the make-up was used since the earlier periods (around 4000 BC for the pre-dynastic times) in relation to its aesthetic, hygienic, therapeutic and religious functions (Lucas and Harris, 1963; Jonckheere, 1952).

Since the time of the Old Kingdom (2700-2200 BC), cosmetics were used in religious ceremonies and can be found on lists of funeral gifts alongside various unguents (Ziegler, 1993). Their role is described in documents concerning religious worship, where the priest can be seen offering to the gods two small purses containing green and black make-up. Their function is respectively to "clean" the god's face and to enable him to "see through Horus's eye" (Moret, 1902; El-Kordy, 1982; Troy, 1993). These documents also describe the symbolic role that the ancient Egyptians attributed to cosmetics in maintaining cosmic order. They believed that the moon's cycle manifested the combat between Horus and Seth, i.e. the combat between light and darkness. According to this myth, Seth injured Horus's eye, thus endangering the return of the full moon. In order to stop the onset of destruction and restore the cosmic order ordained by the gods, the eye had to be cured, that is to say "made complete, rebuilt, given back its various elements". The well being of eyes was therefore assured by the power of cosmetics, whose function was to "make the eyes festive, make them shine, perfect them, make them radiate with life". In the same way that cosmetics filled and restored the eye of Horus and those of the dead, the everyday use of cosmetics had prophylactic and therapeutic functions.

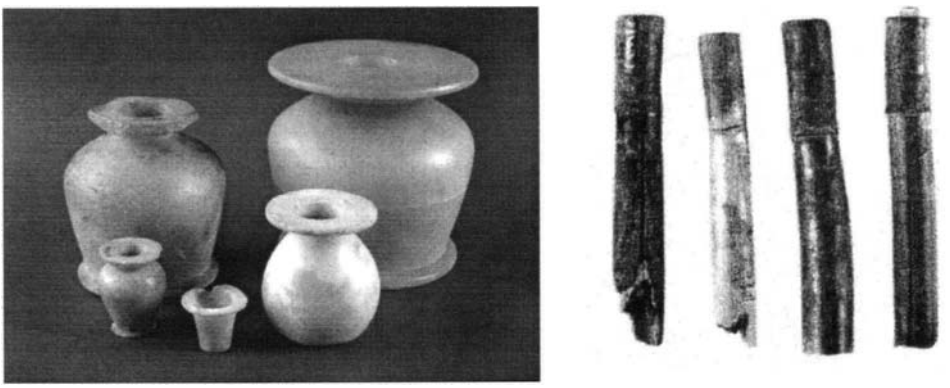

Figure 1. Photographs of make-up vases and reeds at Le Louvre museum

1.2. Description of the cosmetic powders

Analysing cosmetics to uncover their components and the way in which they were made is not a new idea. At the end of the 19th century, several researchers discovered that ancient Egyptians used a wide variety of very complex make-ups, which were very often lead-based compounds. Galena (lead sulphide), cerussite (lead carbonate), pyrolusite (manganese dioxide), chrysocolla (hydrated copper silicate) and malachite (copper carbonate) had also been identified by microscopy and micro-chemical analysis in more than one hundred samples (Lucas and Harris, 1963; Barthoux, 1926).

Our observations have been extended over small volumes of powder taken from 65 artefacts conserved in the Louvre Museum (Paris, France). A representative number of cosmetic mixtures, of different colours (white, grey, green or black) and different textures (hard, powdery or greasy), was examined by electron microscopy and X-ray diffraction. These specimens constitute an outstanding collection dated from the New Kingdom (1552-1070 BC), from the Middle Kingdom (2134-1650 BC), as well as from the Archaic period (3100-2700 BC). Part of the investigated samples come from the French excavations at the end of the 19th century, especially from the tombs near Deir-el Medineh (1550-1300 BC), a craftsmen's village near the Kings and Queens valleys in Middle Egypt. The archaeological context of some objects is well defined: for example, five reed cases (inv. E11048 a,b,c,d,e) were found in the excavations of Lady Touti's tomb at Medinet el-Gorab (Fayoum) in 1900 (Chassinat, 1901). Her death dates back to the 18th dynasty, just before or during Tutankhamun's reign. One reed case bears a column of hieroglyphs written with black ink, which describes the content as being a "3-stars" genuine mesdemet. The word "mesdemet" often refers to galena and the hieroglyph, which stands for "high quality", is here repeated three times. In addition to these boxes, the funerary furniture contained statues of women sitting near a toilet bag containing a mirror, an eye-shadow spoon, unguent boxes and hairpins.

Thus we identified the various as-found materials and worked out their combinations and respective proportions. The ultimate goal is to link the recipes with some possible specific properties and with the historical and archaeological records.

2. EXPERIMENTAL DETAILS

The samples were first observed under a scanning electron microscope (SEM) to observe the morphology and the elementary chemical composition of the grains of the powder (Philips XL30CP microscope equipped with a Si(Li) detector able to detect elements as light as carbon). The analysis by microscopy greatly helped to identify the chemical phases and brought to light the presence of lead compounds of sulphur, carbon, oxygen and chlorine. The various mineral phases were identified using the laboratory diffractometer Brüker D5000 ($\bullet_{CoK\bullet}$ =1,7903 Å) in Bragg-Brentano geometry, the powder being deposited on a flat sample holder made of silicon. The DiffractPlus programme (Socabim, 1998) was used for the qualitative analysis of the phases. The experimental diagram from each archaeological sample was compared with those of the single-phase reference samples available through the database

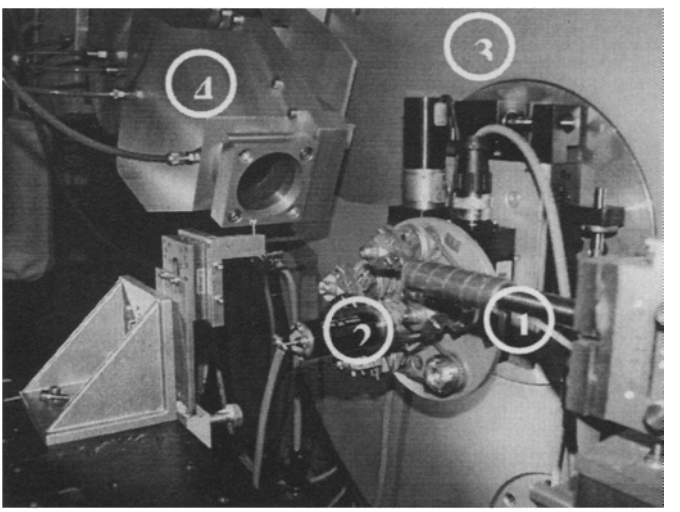

Figure 2. Photograph of the BM16 diffractometer. (1) X-ray beam exit collimator ; (2) goniometer head on sample holder ; (3) ω circle ; (4) detector and analyser crystal assembly.

maintained by the Joint Committee on Powder Diffraction Standards (in 1995, the JCPDS database contained 60,000 references).

Powder diffraction using synchrotron radiation was carried out at the DW22 line in the Laboratoire pour l'Utilisation du Rayonnement Electromagnetique (LURE), Orsay, France, and at the BM16 line at the European Synchrotron Radiation facility (ESRF), Grenoble,

France. The powder was placed in a capillary tube 300• m or 400• m in diameter used in transmission in the Debye-Sherrer geometry. At the beamline BM16, the diffractometer is designed for mounting various detectors and different sample environments (Figure 2). The present set-up used a nine-crystal analyser stage (nine scintillation counters, each fitted with a Ge(111) crystal and offset by ~2° with respect to one another) (Hodeau, 1999). The sample continuously spins on the axis of the diffractometer. Data are collected in a continuous scanning mode. This eliminates the dead time of a conventional step scan. Following data collection, the counts from the nine detectors are summed and normalised, to give the equivalent normalised step scan.

The advantages for this study by synchrotron radiation compared to conventional laboratory diffractometry are:

1) the wavelength is well adapted to the highly absorbing lead-based compounds, off the L-absorption edges of lead (see Table 1 and Figure 3);

Table 1
Linear absorption coefficient of galena (PbS), a major component of archaeological make-up, versus the wavelength used.

		wavelength (Å)	μ_{PbS} (μm^{-1})
D5000	flat plate holder	1.7903	0.233
LURE	capillary ∅400 µm	0.9627	0.0466
ESRF	capillary ∅300 µm	0.3532	0.0129

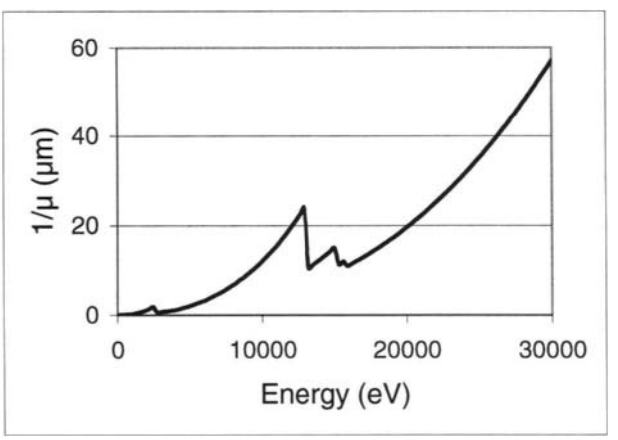

Figure 3. X-ray attenuation length for galena as a function of the photon energy

2) the high photon flux on the specimen ensures high statistics and a good signal-to-noise ratio within a reasonable counting time; at the ESRF, the magnitude of the most intense peak of a major phase can reach up to 30,000 counts in 4 hours (Figure 4). By coupling the

detectors with the analyser crystals, the signal-to-background ratio is improved, and trace compounds can be identified, and sometimes weighed.
3) the parallel beam optics combined with a Si(111) double-crystal monochromator and the post-sample Ge(111) analyser crystals of BM16 reduces the instrumental broadening and the diffraction pattern is immune to common aberrations (2θ error, sample misalignment) (Fitch, 1996). The instrumental contribution to the full width at half maximum (FWHM) around 10° 2θ is of the order of 0.003° 2θ for BM16. The high resolution was needed for interpreting the diagrams of some samples which could contain as many as 10 distinct phases. The high resolution was also advantageous for analysing the pure diffraction line profile after removal of the instrumental function.

3. DATA ANALYSIS

3.1. The Rietveld refinement of powder diffraction patterns

This method is the most efficient way of analysing X-ray and neutron diffraction patterns from powder samples when the crystal structures of the constituent phases are known (Rietveld, 1969). Rather than taking the integrated intensities of a few intense individual Bragg peaks, the full pattern profile is fitted using the instrumental function parameters, the structural parameters (lattice parameters, element scattering form factors, atomic positions and atomic displacement parameters) and the micro-structure parameters defining the sample peak profiles.

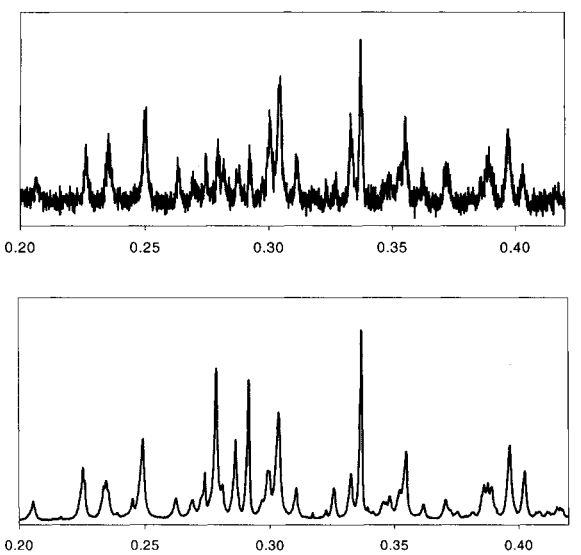

Figure 4. The high photon flux on the specimen ensures high statistics and a good signal-to-noise ratio within a reasonable counting time; at the ESRF, the magnitude of the most intense peak of a major phase can reach up to 30,000 counts in 4 hours

The Rietveld refinement program aims at minimising the following function:

$$M = \sum_i w_i (y_i - y_{ci})^2$$

W_i the weight of the intensity y_i measured over the i^{th} step of the diagram
y_{ci} the corresponding calculated intensity.

M is minimized using either the least-squares (whereby $w_i = \frac{1}{y_i}$) or the maximum-likelihood ($w_i = \frac{1}{y_{ci}}$). The intensity at the step i is calculated by adding the continuous background and the contribution of all the peaks which overlap at that point:

$$y_{ci} = y_{bi} + \sum_{\phi=1}^{N} S_\phi \sum_{k=k1}^{k2} j_{\phi,k} LP_{\phi,k} O_{\phi,k} M |F_{\varphi,k}|^2 \Omega_{i,\varphi,k}$$

y_{bi} the intensity of the continuous background at the position $2\theta_i$, obtained by linear interpolation
S_ϕ the scale factor proportional to the mass fraction of the phase ϕ
j_k the multiplicity of the $k^{ième}$ reflection
LP_k the Lorentz and polarisation factor
O_k the correction term which takes into account a possible preferred orientation, i.e. the difference with respect to an uniform, random orientation distribution of the constituent particles
M the correction term which accounts for any possible absorption and/or micro-absorption effects
$|F_k|$ the structure factor (including the thermal and disorder Debye-Waller terms)
Ω_{ik} the analytical function which best fits the instrument and sample diffraction peak profile

The summation in y_{ci} is carried out over every single crystalline phase present and over all the neighbouring reflections, k_1 to k_2, which contribute into the i^{th} step. The validity or the figure of merit of the profile fitting is estimated through a number of reliability factors R. Figure 5 shows the Rietveld refinement for the archaeological sample E11048e.

3.2. Quantitative analysis by the Rietveld refinement method

The quantitative analyses are based on the fact that the intensity diffracted by a crystalline phase is basically proportional to the quantity of matter irradiated (although in fact absorption effect corrections are required when the mixture contains compounds with highly contrasted absorption coefficients or different grain sizes). Archaeological samples are too precious for the internal standard method to be considered. Another most used method for quantitative analysis is based on the Reference Intensity Ratio (RIR). This consists in comparing the intensity of the most intense Bragg reflection of each of the phases present in the sample with the (113) reflection of corundum. However this technique is extremely

sensitive to systematic errors, especially those due to preferred orientation. On the other hand, using profile refinement techniques makes it possible to minimise the influence of texture, since they apply to the whole pattern and thus provide a more reliable quantitative analysis. In Debye-Scherrer geometry, one shows :

$$S_\phi \infty \frac{m_\phi}{(ZMV_c)_\phi}$$

m. mass of the phase present in the sample
Z. number of formula units per unit cell
M. mass per formula unit (often the molecular mass of the phase $_f$
V_c. *volume of the unit cell*

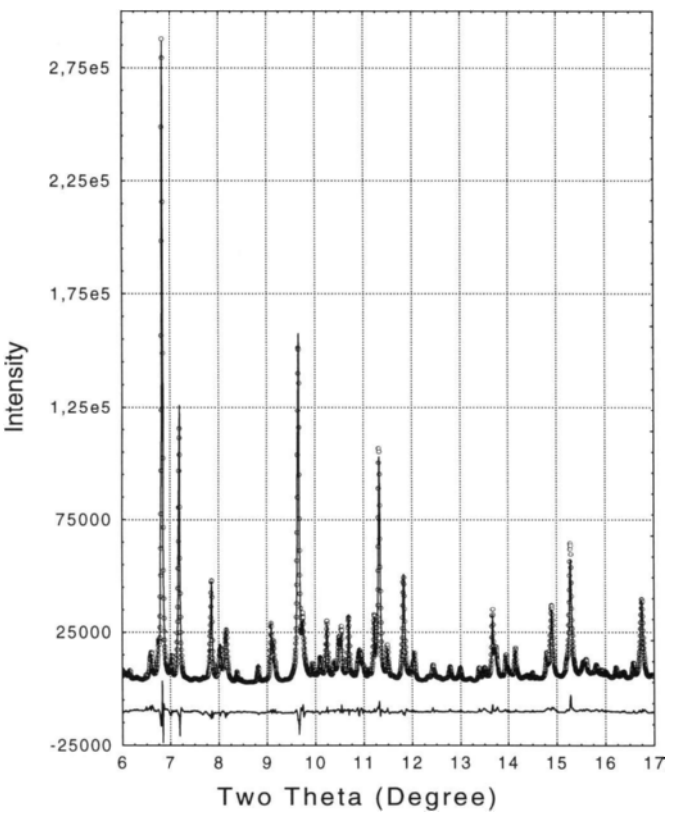

Figure 5. Observed (dots), calculated (solid line) and difference (bottom line) patterns of the archaeological sample E11048e

By constraining the sum of the mass fractions *W.* of all the phases present to be equal to unity, one gets :

$$W_\phi = S_\phi \frac{(ZMV_c)_\phi}{\sum_{\phi=1}^{N} S_\phi (ZMV_c)_\phi}$$

The same result could also be obtained from a measurement in the Bragg-Brentano geometry, given the area of the sample be larger than the beam footprint during the whole acquisition. This condition is not often fulfilled when examining small volumes of archaeological powder. The accuracy of the parameter *S.* (and hence • .) can be estimated from the standard deviation. The applicability and the advantages/limits of the Rietveld procedure were the case of study of the last Round Robin started in 1996 by Madsen, Hill, Groleau and Cranswick. Many Rietveld-type packages are commonly available ; the present study used the Fullprof programme (Rodriguez-Carjaval, 1990). The diffraction peaks were satisfactorily fitted by means of the pseudo-Voigt function convoluted with a correction function which takes into account the low-angle asymmetry caused by the axial divergence of the beam (Finger et al., 1994). Reference mixtures whose composition and granulometry were close to those of the archaeological samples were used to validate our protocol of measurement and our quantitative analysis.

The high resolution patterns collected at the ESRF on géological galena powders show some anisotropy of the peak profile, particularly along the planes h00 et h11 (Martinetto et al., 2000). The anisotropic peak profile was taken into account in the refinement, by using three different sub-sets of pseudo-Voigt function parameters. The preferred orientation along the clivage plane h00 was also often to be corrected.

Each archaeological powder is a mixture of compounds with highly different absorption coefficients (at • = 0.3532• , • can differ by two orders of magnitude). Hence micro-absorption corrections have to be taken into account in the quantitative analysis. These corrections are applied indirectly by dividing by the factor • the molar masses of the unit cell of the phases concerned. • provides for the absorption contrast according to Brindley's model (Brindley, 1945). The validity of these corrections was tested using reference mixtures made of lead compounds (PbOHCl) and alumina (Al_2O_3). The results obtained for the various mixtures, with and without corrections, are given in Table 2.

The effect on the diffracted intensities of the presence of a wide range of grain sizes within a sample was tested using the archaeological sample E20514. This powder contains a considerable quantity of large-grained galena (grain size • 50 • m) while the other phases of the sample have a much smaller grain size (as small as 1-5 • m for the synthesised lead chlorides). A sample of the powder was ground to obtain a homogeneous mixture of fine grains and Table 3 shows the relative results. The mass fractions of galena in the original powder had been under-estimated by roughly 10%, which illustrates that micro-absorption does occur within the powder. For shorter wavelengths, micro-absorption correction analysis shows that the errors induced in the mass fraction of lead compounds are generally small, less than 10%. The mass fractions of non lead-based compounds are liable to induce greater error than this, however such compounds are found only in minute quantities in the mixtures under consideration. In the rest of the present article, micro-absorption corrections will no longer be taken into account for the archaeological samples. The accuracy of the relative mass fractions

of the various compounds in man-made powders would seem sufficient to describe the recipes.

Table 2
Quantitative analysis of reference powder mixtures at $\lambda = 0{,}9627$Å.

	Mass fractions (%) weighed	Mass fractions by Rietveld no correction	Mass fractions corrected	μ (μm^{-1})	Mean grain size (μm)
Galena	50	46	-	0.0466	5
Laurionite	50	54	-	0.0365	2.5
Galena	95	94	-	0.0466	5
Laurionite	5	6	-	0.0365	2.5
Laurionite	80	78	80	0.0365	2.5
Alumina	20	22	20	0.0031	1.5
Laurionite	20	14	16	0.0365	2.5
Alumina	80	86	84	0.0031	1.5

Finally, in order to verify that the sample taken from the powder was representative of the whole container and also to check that the analyses were reproducible, two samples were taken from two different parts of the receptacle E20514 to be analysed and compared. The results, given in Table 3, show good agreement for the two different samples and the different analyses.

Table 3
Mass fractions of 2 samples of one cosmetic powder dated from the New Kingdom, independently measured at the LURE and at the ESRF in distinct capillaries.

# item		λ (Å)	PbS	$PbCO_3$	$Pb_2Cl_2CO_3$	PbOHCl	$PbSO_4$	ZnS	$ZnCO_3$
E20514	LURE	0,9620	73	3	9	1	6	6	2
E20514	ESRF	0,4134	72	2	9	2	4	9	2
E20514 ground	ESRF	0,4134	79	2	7	2	3	6	2

3.3. X-ray diffraction line profile

In complement to the qualitative and quantitative analyses, it is important to gain some information concerning the preparation method of some of the present constituent minerals. Some compounds are expected to differ by their microstructure, since the size and deformation of the grains depend on the processing of the powder. Such information can be inferred from the analysis of the diffraction line broadening, and more generally from the diffraction line profile, combined with SEM observations. The microstructure is essentially governed by two effects (Warren, 1969):

- the finite size of the coherently diffracting domains (also called crystallites) inside the grains ;
- the distortions (or micro-deformations) which cause an inhomogeneous strain of the atomic lattice and local shifts of the atomic positions with respect to the lattice nodes.

A common procedure is to fit the background with a spline or a polynomial function and the diffraction peaks with some adequate analytical functions (Langford et al., 1986). The lorentzian L, gaussian G, Voigt V, or pseudo-Voigt pV profiles are the most often used :

$$V(x) = L(x) * G(x) = \frac{1}{\beta_G} Re\left[erf\left(\frac{\sqrt{\pi}}{\beta_G} x + i \frac{\beta_L}{\beta_{G\sqrt{\pi}}} \right) \right]$$

where β_G et β_L respectively are the gaussian and lorentzian components of the integral breadth β, which is defined as the ratio of the integrated area of the peak over its height.

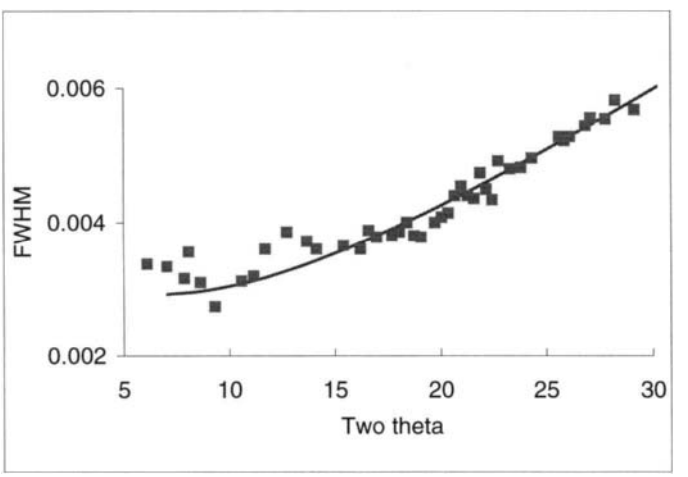

Figure 6. Instrumental Resolution Function of BM16 : Sabine's model (solid line) and FWHM of $Na_2Ca_3Al_2F_{14}$ diffraction lines (data points) at λ = 0.35 Å.

$$pV(x) = \eta L(x) + (1-\eta) G(x) = \eta \left(\frac{2}{\pi H} \frac{1}{1 + \frac{4}{H^2} x^2} \right) + (1-\eta) \left(\frac{2}{H} \sqrt{\frac{\ln 2}{\pi}} \exp\left(\frac{-4 \ln 2}{H^2} x^2 \right) \right)$$

where H is the full width at half maximum (FWHM) of the peak and η the mixing parameter.

Each individual observed peak $h(2\theta)$ was therefore fitted with a pseudo-Voigt function, convoluted with a function which accounts for the asymmetry caused by the axial

divergence of the beam (program PEAKOC, Masson,1998). The integral breadths β of the diffraction peaks, as well as the shape parameter • , and their variations with the Bragg angle are obtained. The parameters β and • , as obtained after refinement, are transformed into the corresponding Voigt parameters β_L and β_G (De Keijser et al., 1983). The instrumental correction of the observed data can then be made by a simple linear or quadratic subtraction of the lorentzian (cauchy) and gaussian widths of the instrumental function $g(2\theta)$ (Langford, 1992; Balzar and Ledbetter, 1993).

The FWHM of the instrumental profile $g(2\theta)$, also called the Instrumental Resolution Function (IRF), was estimated by measuring the diffraction peaks of two reference materials : NIST SRM660 LaB_6 and $Na_2Ca_3Al_2F_{14}$ in experimental conditions analogous with those for the measurement of the archaeological specimens. The sample broadening of the standard $Na_2Ca_3Al_2F_{14}$ is neglegible with respect to the instrumetal broadening. The measured width of g (IRF) can then be compared with the analytical curve given by Sabine (1987), taking into account the vertical divergence and the angular acceptances of the monochromator and analyser crystals (Figure 6). Both the experimental FWHM of the standard peaks and the theoretical curve agree well, and the IRF can be calculated at any 2θ.

The simplified methods of integral breadths use several orders (at least 2) of reflection from one particular family of planes, in order to separate the size and strain effects. . They are based on the principle that:

- the size effect does not depend on the order of reflection
- the lattice strain effect does depend on the order of reflection

Furthermore, the sample-broadened profile f being the convolution of the size and micro-deformation profiles, the type of line profile of each effect must be defined beforehand so that a function linking the integral breadth • to the micro-structural parameters can be established (Klug and Alexander, 1974). One usually assumes that either the size and strain profiles are lorentzian (Cauchy) (L-L), or both are gaussian (G-G) or alternatively the size profile is lorentzian and the strain profile is gaussian (L-G):

$$\beta_f^* = \frac{1}{< D >_v} + 2ed^* \qquad (L-L) \qquad with\ \beta^* = \beta\frac{\cos\theta}{\lambda}$$

$$\beta_f^{*2} = \frac{1}{< D >_v^2} + 4e^2 d^{*2} \qquad (G-G) \qquad d^* = \frac{1}{d} = 2\frac{\sin\theta}{\lambda}$$

$$\beta_f^* = \frac{1}{< D >_v} + 4e^2 \frac{d^{*2}}{\beta^*} \qquad (L-G)$$

The slope and the intercept at zero of the curve • . (d^*) yield respectively the volume-averaged size of the crystallites $<D>_v$ and the upper limit e of the micro-distortion (Williamson and Hall, 1953).

Alternatively some methods make use of the overall peak profile. They are more accurate and do not rely on any assumption as the analytical shape of the profile does. They intrinsically contain some information on the spatial and frequency distribution of the size and strain, but their application often suffers some approximations and are more computer-

demanding (Warren and Averbach, 1950). These methods also are limited whenever the peaks overlap with neighbouring reflections, as is often the case in the diagrams of archaeological powders. If the precise form of the Bragg reflection is needed, the Stokes deconvolution method is usually used (Stokes, 1948). This consists of expanding the instrumental profile g and the observed Bragg peak h into their Fourier series as a function of L, where L is the distance perpendicular to the diffracting planes. The Fourier coefficients of the true profile f are then obtained by the complex division of both coefficients at all L values.

4. RESULTS AND DISCUSSION

4.1. Phase identification

Three quarters of the products contain four lead-based main phases: the black galena and three white products, namely the cerussite PbCO3, the phosgenite Pb2Cl2CO3, and the laurionite PbOHCl (Figure 7). Galena and cerussite are well known lead ores which were abundantly mined in Ancient Egypt from mines situated along the Red Sea coastline (Castel and Soukassian, 1989). Galena being greyish back and cerussite white, various shades of grey could have been obtained simply by mixing them together.

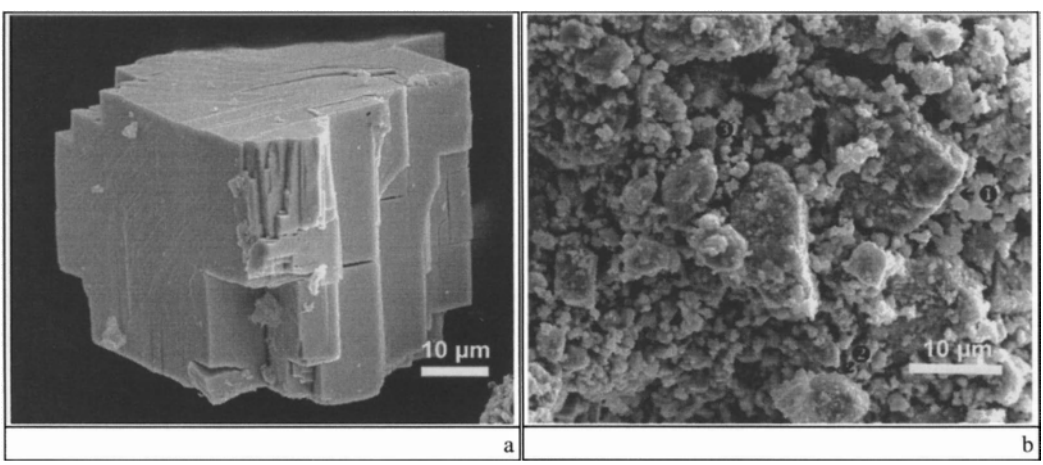

Figure 7. SEM micrographs of major mineral phases of Egyptian makeup powders. (a): Cubic crystal of galena with cleaved faces along (100). (b): Mineral mixture of (1) galena (cubic crystals of 10 to 20 µm long), (2) cerussite (tabular grains about 10 µm long) and (3) phosgenite (ovoid crystals of less than 1 µm long).

Both the phosgenite and the laurionite are white too and therefore cannot have been added to the mixture solely for questions of pigmentation. The on-going analysis brought to light the fact that the two latter chloride compounds could only have been prepared by means of wet chemistry before being incorporated into the mixtures in the form of fine white powders (Walter et al., 1999). Greco-roman authors of the first century AC described the way this

synthesis was carried out, and identified these compounds as health products for eyes and skin and for hair washing (Zehnacker, 1983; Wellman, 1958). These authors explained how the "purified silver foam" (lead monoxide in fact) was ground, then mixed in water with rock salt and sometimes natron (mainly sodium carbonates) and subsequently filtered. This process was repeated daily from one to six weeks. These chemical reactions have been repeated in the laboratory where lead monoxide powders were mixed with sodium chloride and sodium carbonate in water. The pH-pCl-pCO3 stability of the resulting lead-based products was observed at room temperature. Thus it was observed that these recipes give rise to a slow transformation of the weakly-soluble oxide, producing an alkaline solution whose neutrality (pH $\approx$ 7) was approximately maintained by the frequent renewal of the water. Under these conditions, both the laurionite and the phosgenite are formed in proportions which depend on the concentration of dissolved carbonates (Walter, 1999).

The variety of these mixtures and the presence of white synthesised products indicate that the ancient Egyptians deliberately made cosmetics with specific properties. In particular the lead chlorides must have been rather added for their remedial effects, which are in fact described in some ancient Egyptian manuscripts. For example the Ebers medical papyrus, dated around 1550 BC, associates cosmetics and medicine, giving recipes for dying hair, modifying the colour of the skin and beautifying the body (Bardinet, 1995). It gives detailed recipes for eye drops, masks and make-up for the eyes and eyelids which were to be prescribed to cure various ailments. Proportions were given as a percentage of a reference volume, with the relative proportion of some ingredients being as low as 1/64. Ninety-five recipes of cures for eye problems are described in this papyrus with a vocabulary which is usually associated with the application of cosmetics: "Make up the eyes with this ...", "Use this eye make-up in the evening...", "Make-up to improve the eye sight...". A certain amount of information concerning the texture of the mixture to be obtained, its qualitative or quantitative composition and how it is to be used can be obtained from the study of these texts. They all mention galena associated with other mineral and organic substances. It is essential that the translation of these recipes be reviewed. For example, in the translated recipe number 359 of the Ebers papyrus (Bardinet, 1995), the word galena appears three times, but each time the words associated with it are different:

Another (remedy) for eye care : galena :1 ; red ochre (tjerou) : 1 ; djaret-plant : 1 ; gesefen-galena : 1 ; male part of galena : 1. (This) is to be prepared as an homogeneous mass and applied onto the eyes.

In the light of the recent findings and working alongside Egyptologists, it may become possible to better understand the signification of the various modifiers used with galena in the hieroglyphs and thus produce a more accurate translation of the compounds. The same can be said in so far as laurionite and phosgenite are concerned. Neither of these names of minerals are quoted as such in the recipes, but perhaps they should be considered as a possible translation for the 'sia-mineral of the south' and the 'sia-mineral of the north' which are frequently associated with the word galena.

Since not all the seams of galena and cerussite mined were of the same quality, the ancient Egyptians must have sometimes encountered difficulties extracting the required pure compounds from the ore. Thus some traces of lead and zinc compounds, known for being oxidised galena ore, are found in the samples: anglesite $PbSO_4$, suzannite $Pb_4(CO_3)_2PbSO_4(OH)_2$, palmierite $K_2Pb(SO_4)_2$. Other minerals are also found in association with the Pb-Zn ore sources: sphalerite ZnS, smithsonite $ZnCO_3$, hemimorphite

$ZnSi_2O_7(OH)_2H_2O$). Even very tiny quantities of compounds typical of dolomite limestone can be found in the samples, which correspond to the rocks in which seams of lead ores can be found around the Red Sea: gypsum $CaSO_4$ $2H_2O$, dolomite $MgCO_3$, calcite $CaCO_3$ and quartz SiO_2. These elements coincide with data supplied by geological studies of the lead mines worked during the time of the Pharaohs (Castel and Soukassian, 1989). However, it should also be noticed that calcite could have originated from the walls of the receptacle when the sample was being taken, and that some of the quartz could have come from the pestles and mortars used to prepare some of the samples.

Finally, the presence of cotunnite $PbCl_2$ in five of the samples could be associated with the chemical preparation of the two synthesised compounds. Our laboratory experiments mimicking the production of laurionite and phosgenite show that the cotunnite can sometimes form in acid solutions with high levels of chlorine. It may be that this is an unintentional by-product of laurionite and phosgenite making process.

We have also been able to show that various quantities of fatty acids of animal provenance were added to the powders to vary their texture (Comparon et al., 1999). The proportions are fairly similar to the proportions of vegetable fats added to the make-up nowadays, and produce textures ranging from loose face powder, eye shadows to kohl eye pencils.

4.2. Phase proportions

Figure 8 shows the mass fractions of galena, cerussite and synthetic lead compounds (laurionite, phosgenite and contunnite) for 28 different powders on a ternary diagram. The other compounds, present only in minute or even trace quantities, have been ignored. As shown in section 4.1, they provide some information concerning the origin or the elaboration process of the make-up, but they do not seem to have played an important part in the recipes. In fact, the difficulty encountered is to classify each of the ingredients in order to find the typical recipes (if any) for a given period. The wide distribution of the cosmetic compositions is immediately obvious and no single group stands out as representative of a particular recipe or specific use. Some of the difficulty in interpreting the compositions also arises from the fact that the available archaeological corpus, which has been analysed, is not yet considerable enough.

A high percentage of galena is found in most of the mixtures and gives the powder a metallic-grey or black shade. However, in seven of the powders, there is less than 15% of galena and three do not contain any at all. This shows that very light grey or white products were also used alone. Such light colours do not seem appropriate for use as eye make-up and may rather have been used as foundation cream or face powder. The scene on a tombstone kept in the British Museum (BM 1658) which dates from the Middle Kingdom backs up this hypothesis. It shows Lady Ipouet holding a mirror in her left hand and a piece of cloth in her right, with which she seems to be applying make-up onto her face.

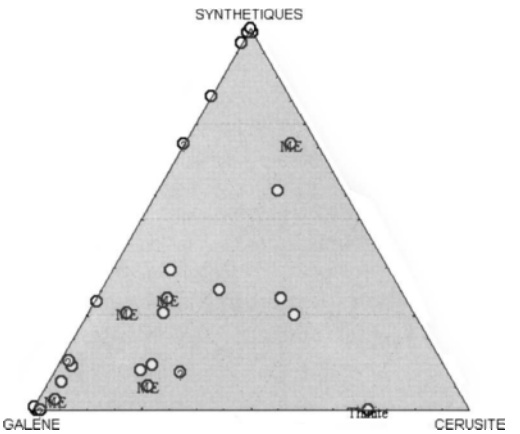

Figure 8. Diagram showing the mass fractions of galena, cerussite and synthetic compounds of 28 make-ups used in Ancient Egypt. The powders dated from the Middle Kingdom (NE) and from the Archaic period (Thinite) are indicated.

It can be seen that the synthetic products probably make their appearance at the time of the Middle Kingdom. They are found in all five samples, which date from that period whereas there is no evidence of these products in the sample from an earlier period. They were very much used since 86% of the powders analysed contains some laurionite and some phosgenite. When exactly these products appeared still has to be dated. The study of objects from the Old Kingdom and the Archaic period would make it clearer what led the Egyptians to prepare such compounds. Unfortunately, the remains of cosmetics from these periods are very rare and it would be most interesting to examine the objects kept in the Egyptian collections of other museums.

4.3. Conditioning of the cosmetic powders

Two minerals are particularly interesting : one is the galena, obtained by manual grinding of the natural ore, and the second one is the laurionite, made of fine grains and obtained by a chemical reaction in solution.

The analysis of the peak profile of archaeological galena (from the make-up numbered E20514) was compared with that of a geological galena powder mined in the United States which had been hand ground with a pestle and mortar, then passed through a 63-125• m mesh. The reflections corresponding to multiplets or overlapping with some reflections of other phases were identified and thus ignored in the analysis of the microstructure. The FWHM variation of the archaeological galena is given in Figure 9, and it is compared with the instrumental resolution function of beamline BM16. It can be seen that the galena is highly crystallised and produces only a very low broadening (of the order of 0.01° 2• FWHM, very close to the instrumental broadening). It is clear that this analysis can only be carried out on an instrument with a very high resolution. For comparison the IRF of a laboratory diffractometer exceeds 0.05° 2• FWHM. Figure 10 shows the integral width • of the

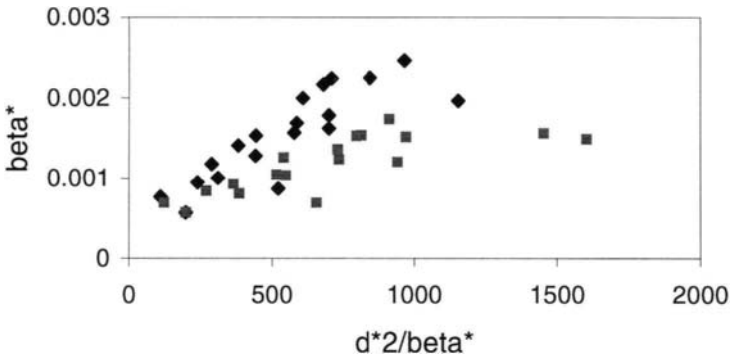

Figure 9. FWHM of archaeological galena (E20514) diffraction peaks, compared with the Instrumental Resolution Function of BM16 (solid line) and D5000 (dotted line).

broadened profiles, corrected for the instrumental contribution, on a Williamson-Hall L-G diagram (Equations in section 3.3).

Figure 10 shows a marked anisotropic broadening of the galena peak profile. This (hkl) dependency has already been mentioned in section 3.2 and was taken into account in the Rietveld refinements by separating the galena reflections into three groups, refined with different profile parameters. This anisotropy could be explained by the presence of a strain field associated with dislocations, and is being modelled by introducing a contrast factor

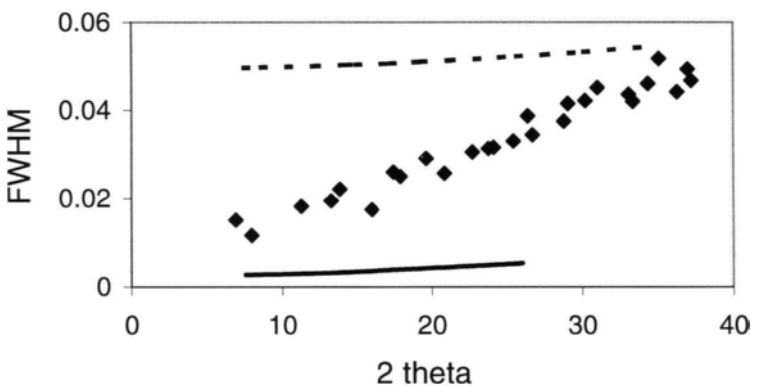

Figure 10. Williamson-hall diagram in reciprocal space (by the method of integral breadth using equation of section 3.3): the FWHM of archaeological (lozenges) and geological (squares) galena powders.

Figure 11. Senynefer and his wife (New Kingdom, 18th dynasty, ~1410 BC.). (H: 68, W:85, Museum Le Louvre E27161). Copyright RMN- Chuzeville

which depends both on hkl and on the elastic constants of the material (Klimanek, Kuzel, 1988; Ungar, Borbély, 1996). Leaving this anisotropy aside, the integral width method, applied to the individual peaks of galena, gives a crystal size of the order of 2000Å for both samples and an upper deformation limit of 0.05% for the geological sample. The archaeological powder shows a greater lattice deformation than the geological powder and therefore it may have been more finely ground. This hypothesis would seem to be confirmed by the SEM observations, which show the E20514 galena sample forming a more heterogeneous assembly of small cubes ranging from 20• m to 150• m long, with a significant fraction of smaller grains. The analysis of other archaeological galena powders show that the galena was more or less finely ground by the Egyptians to obtain either a black mat powder, or grey powders with metallic overtones. The larger the grains of galena, the brighter and the more reflecting they are. The different make-up obtained in this way may have been destined for use on different parts of the eye. It is easy to imagine that the finer mat powders, applied inside the lower eyelid, would adhere thanks to the humidity of the eye itself. The powder made of coarser grains would have to be held by an organic binding agent and would be more likely to be placed in a thick coat on the upper eyelid (Figure 11).

The archaeological laurionite powder AF143 has also been processed and its microstructure compared with that of the newly synthesised powder described in section 4.1 (Figure 12). The mixing parameter • of the pseudo-Voigt function is of the order of 0.8 for the galena powder E20514 and of the order 0.2 for the laurionite powder AF143. Therefore

the origins of the peak broadening are obviously very different for the two minerals. Only the size effect contributes to the peak broadening of the laurionite pattern, whereas both size and strain effects are present in the galena diffraction lines. Both the archaeological and the synthetic laurionite powders have similar behaviour and their crystal size can be evaluated at 1000Å. The scanning electron microscopy study of these powders show that the laurionite is composed of small grains, of about 1µm, which matches the evaluated size. The absence of any significant lattice distortion in the archaeological laurionite and its identical behaviour to that of the synthesised powder reinforces the hypothesis of the chemical process of preparation of this Pb-Cl compound. The synthetic powders, obtained in the form of very fine powders, would simply have had to be mixed with the previously ground mineral powder.

The case of galena and laurionite have illustrated the information which can be obtained from the analysis of diffraction peak broadening. Such analyses should shortly be applied to other compounds found in the cosmetic powders from Ancient Egypt. Furthermore, a more detailed study is being carried out at present, based on the interpretation of the overall peak profile by Fourier analysis.

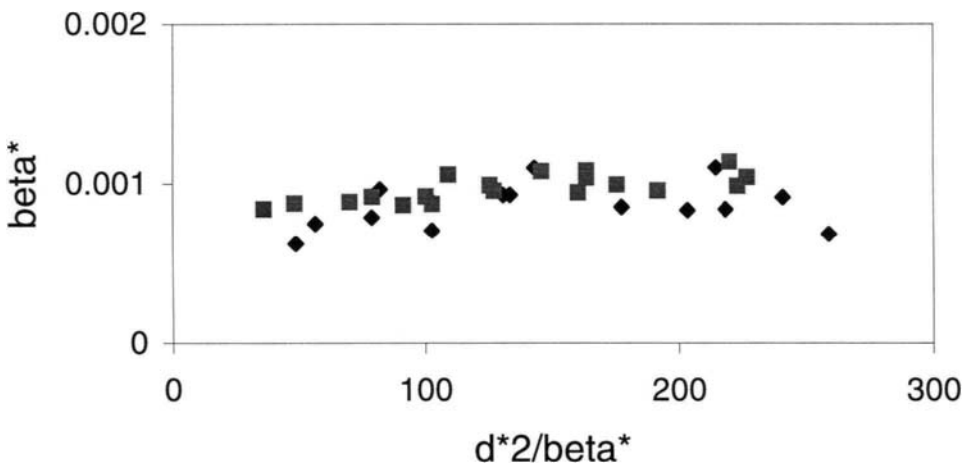

Figure 12. Williamson-hall diagram in reciprocal space (by the method of integral breadth using equation of section 3.3): the FWHM of synthesised (lozenges) and archaeological (squares) laurionite powders.

5. Conclusion

The analysis of cosmetics as used in Ancient Egypt reveals the great variety of compositions using lead compounds and an advanced know-how in chemical synthesis. This shows that 4000 years ago, people already wanted more impact from their use of cosmetics than simply highlighting of the eyes. This work shows the benefits of combining optical and electronic

microscopy methods, X-ray fluorescence measurements and ion beam analysis (Proton-Induced X-ray Emission, Rutherford Backscattering Spectrometry, Nuclear Resonance Analysis) with X-ray diffraction in view of identifying and weighing the crystalline phases in archaeological or artistic objects. The use of X-ray synchrotron radiation enables one to examine small volumes of rare and precious, highly X-ray absorbing powders, without any alteration prior to the analysis. The high resolution and high signal-to-background ratio make it possible to determine the composition of complex mixtures, particularly when the specimen is composed of a large number of phases or when some ingredients are present in extremely small proportions (< 1%). The analysis of the Bragg line profiles could also provide some insight into the micro-structure of some minerals (size and distortions of the grains), in relation with the preparation of the make-up (synthesis, grinding, sieving).

Acknowledgements: this research was carried out in collaboration with L'Oréal Recherche and has benefited from the support of the Département des Antiquités Egyptiennes of Le Louvre museum.

REFERENCES

Balzar D. and Ledbetter H., J. Appl. Cryst., 26 (1993) 97.
Bardinet T., Les papyrus médicaux de l'Egypte pharaonique, Fayard, Paris, 1995.
Barthoux J., Les fards, pommades et couleurs dans l'Antiquité. Congrès Int. de Géog., Le Caire, Avril 1925, No IV (1926) 251.
Brindley G. W., Phil. Mag., 36 (1945) 347.
Castel G. and Soukassian G., Gebel el-Zeit I. Les mines de Galène, Fouilles de l'IFAO, No XXXV, Le Caire, 1989.
Chassinat E., Bull. Inst. Fr. Arch. Orient., 1 (1901) 225.
Comparon C., Bernard T., Manzin V. and Kaba G., J. High Resol. Chromatogr., 22 (1999) 635.
de Keijser T. H., Mittemeijer E. J. and Rozendaal H. C. F., J. Appl. Cryst., 16 (1983) 309.
El-Kordy Z., L'offrande des fards dans les temples ptolémaïques. Annales du service des antiquités de l'Egypte, No LXVIII (1982) 195.
Finger L. W., Cox D. E. and Jephcoat A. P., J. Appl. Cryst., 27 (1994) 892.
Fitch A. N., Mater. Sci. Forum, 219 (1996) 228.
Hodeau J-L., Bordet P., Anne M., Prat A., Fitch A.N., Dooryhée E, Vaughan G., Freund A., SPIE Conference on Crystal and Multilayer Optics - San Diego,1998. Proceedings SPIE, 3448 (1998) 353.
Jonckheere F., Histoire de la médecine, 7 (1952) 2.
Klimanek P. and Kuzel Jr. R., J. Appl. Cryst., 22 (1988) 299.
Klug H. P. and Alexander L. E., X-ray Diffraction Procedures for Polycrystalline and Amorphous Materials 2nd ed, Wiley, New York, 1974.
Langford J. I., Accuracy in Powder Diffraction, NIST Spec. Pub. No 846 (1992) 110.
Lucas A., Harris J.R., Ancient Egyptian Materials and Industries, Edward Arnold Ldt., London, 1963.
Martinetto P., Anne M., Dooryhée E. and Walter P., Mater. Sci. Forum, 321-324 (2000) 1062.
Masson O., Thèse de l'Université de Limoges, France, 1998.
Moret A., Le rituel du culte divin journalier en Egypte, Paris, 1902.

Rietveld H. M., J. Appl. Cryst., 2 (1969) 65.
Rodriguez-Carjaval J., Abst. Satellite Meeting on Powder diffraction of the XVth IUCR Congress, No 127 (1990).
Sabine T.M., J. Appl. Cryst., 20 (1987) 173.
Stokes A. R., Proc. Phys. Soc. Lond., 61 (1948) 382.
Troy L., Bull. D'Egyptologie, No 106/1 (1993) 351.
Ungár T. and Borbély A., Appl. Phys. Lett. 69 (1996) 3173.
Vandier d'Abbadie J., Catalogue des objets de toilette égyptiens du Musée du Louvre, Réunion des Musées Nationaux, Paris, 1972.
Walter P., L'actualité chimique, No Novembre (1999) 134.
Walter P., Martinetto P., Tsoucaris G., Bréniaux R., Lefebvre M.A., Richard G., Talabot J. and Dooryhée E., Nature, 397 (1999) 483.
Warren B. E., X-ray diffraction, Addison-Wesley, New York, 1969.
Warren B. E. and Averbach B. L., J. Appl. Cryst., 21 (1950) 595.
Wellman M., Dioscoridis Pedanii, De Materia Medica, libri quinque, Weidmannsche Verlagsbuchhandlung, Vienna, 1958.
Williamson G. K. and Hall W. H., Acta Metallurgica, 1 (1953) 22.
Zehnacker H., Pline l'Ancien, Histoire naturelle, livre XXXIII, Les Belles Lettres, Paris, 1983.
Ziegler Ch., Le Mastaba d'Akhethetep, une chapelle funéraire de l'Ancien Empire, Réunion des Musées Nationaux, Paris, 1993.

Radiation in Art and Archeometry
D.C. Creagh and D.A. Bradley (editors)

Attribution of antique Chinese blue-and-white porcelains using Energy Dispersive X-Ray Fluorescence (EDXRF)

K.N.Yu

Department of Physics and Materials Science, City University of Hong Kong,
Tat Chee Avenue, Kowloon Tong, Kowloon, Hong Kong, P.R.China.

A brief introduction to antique Chinese blue-and-white porcelains and their attribution using Energy Dispersive X-Ray Fluorescence (EDXRF) were presented. Previous research on attribution of periods using the Mn/Co ratio, Zn, As, Ba contents and other criteria, and on the attribution of geographical origins using Rb, Sr, Y, Zr and Nb contents were summarized. These research has led to many fruitful results. However: there were problems and challenges, some of which were quite fundamental, yet to be investigated and to be handled: (1) the feasibility of using ratios between elemental concentrations for the attribution and the feasibility of using for our criteria some elements characteristic of the colorant (such as Mn and Co) which in theory lies too deep beneath the glaze to be measured; (2) the soundness of calibration sources; (3) the need to use multivariate analysis instead of contents for individual chemical elements; (4) the properties of antique blue and white porcelains other than those of the Qing dynasty, in particular those of the Ming dynasty; (5) the properties of antique blue and white porcelains of the Qing dynasty (separated from the porcelains of the Republic period) and those in different periods of the Qing dynasty, and comparison between Qing and Ming porcelains; (6) properties of antique blue and white porcelains from different main sites of production, including those from the most studied site of Jingdezhen. Discussions on these topics were presented in this article.

1. INTRODUCTION

1.1 Nature of Chinese blue-and-white porcelains

Blue and white porcelains are generally considered the most important among Chinese porcelains produced during the Yuan (1280-1368), Ming (1368-1644) and Qing (1644-1911) dynasties. A chronology of Chinese history from the Yuan dynasty is shown in Table 1 for easy reference. The main sites of production of ancient Chinese blue and white porcelains included Jingdezhen in Jiangxi Province, the Yuxi and Jianshui Kilns of Yunnan Province and the Pinghe Kiln of Fujian Province. Among these sites, Jingdezhen is the utmost important one especially when we consider the imperial-wares, and the most studied blue and white porcelains are the imperial-wares from Jingdezhen.

Blue and white porcelains belong to the underglaze-colored porcelains. The thickness of the glaze is generally in the range of 200 to 500 μm. The various colored decorations are drawn between the glaze and the body of the porcelain using blue colorants containing cobalt

oxide. The thickness of the blue colorant between the glaze and the body of the porcelain is in general about 10 μm (Chen, Kuo and Chang 1978).

Table 1. A chronology of Chinese history from the Yuan dynasty.

	Period (Emperor)	Year (A.D.)
Song dynasty		**960 – 1279**
Yuan dynasty		**1280 – 1368**
Ming dyansty		**1368 – 1644**
	Hongwu	1368 – 1399
	Jianwen	1399 – 1403
	Yongle	1403 – 1424
	Hongxi	1425 – 1426
	Xuande	1426 – 1435
	Zhentong	1436 – 1450
	Jingtai	1450 – 1457
	Tianshun	1457 – 1465
	Chenghua	1465 – 1487
	Hongzhi	1488 – 1505
	Zhengde	1506 – 1521
	Jiajing	1522 – 1566
	Longqing	1567 – 1572
	Wanli	1573 – 1619
	Taichang	1620 – 1621
	Tianqi	1621 – 1627
	Chongzhen	1628 – 1644
Qing dynasty		**1644 – 1912**
	Shunzhi	1644 – 1661
	Kangxi	1662 – 1722
	Yongzheng	1723 – 1735
	Qianlong	1736 – 1795
	Jiaqing	1796 – 1820
	Daoguang	1821 – 1850
	Xianfeng	1851 – 1861
	Tongzhi	1862 – 1874
	Guangxu	1875 – 1908
	Xuantong	1909 – 1912
Republic		**1912 – 1949**
People's Republic of China		**1949 –**

The most important tasks in the research of Chinese blue-and-white porcelains are the attribution of their geographical origins and periods. Related to the attribution of periods is the identification of fake porcelains. Nowadays, a lot of fake porcelains are present in the market. People are eager to look for non-destructive methods for the identification of porcelains.

Currently, there are many scientific analytical methods employed for these purposes. These methods can be broadly divided into two categories. The first one involves absolute measurements. Thermoluminescence dating (TLD) belongs to this category. The period determined for a sample is solely derived from the physical behavior of this sample alone. The second category involves what we call relative measurements. Before testing the sample in which we are interested, samples of known periods or geographical origins should have

been measured to reveal the underlying distribution of chemical compositions with the periods and the geographical origins, against which the results of the tested sample can be subsequently compared. The method adopted for the present investigation belongs to the second category.

Porcelains are valuable and it is essential that they are not damaged during investigations. Therefore, although relative measurements for porcelains have previously been made using destructive methods such as atomic absorption spectrometry (AAS), neutron activation analysis (NAA) and wet chemical analysis, we only focus on the discussion on the studies using the non-destructive Energy Dispersive X-Ray Fluorescence (EDXRF) method. Previous research has made use of EDXRF for studying blue and white porcelains, and has yielded many fruitful results (see Section 1.3 below).

The colorant used for the Jingdezhen imperial-ware blue and white porcelains manufactured during the Ming and Qing dynasties were very complicated (Yu and Miao, 1996a); those typically employed during the Ming dynasty alone have already included the imported "Sumani-Po Blue", "Mohammedan Blue" and the local "Po-Tang Blue". Since these colorants came from different localities, their chemical compositions were different, which were reflected from their EDXRF spectra. The blue color was produced by cobalt derived from minerals such as cobaltite (CoAsS), smaltite ($CoAs_2$) and asbolane (a hydrated manganese mineral). These often contained impurities or associated elements (e.g. Ni, Cu, Mn) which could be used to characterize sources. For discussions on the cobalt mineral types and the analysis on blue colorants on Chinese porcelains, the readers are referred to the works by Taylor (1977), and Zhang and Cowell (1989) respectively. In using EDXRF for the attribution of blue and white porcelains, we have to build a database by systematically investigating large amounts of porcelains from different periods and to establish reliable criteria for the attribution.

Although relative measurements do not directly provide the absolute attribution, they can accurately attribute the porcelains through indirect evidence. It has also got the additional advantage of being able to separate different categories of porcelains which are made in close periods. For example, Yu and Miao (1996c) was able to differentiate between porcelains manufactured in the Jiajing period (1522 – 1566 A.D.) and the Wanli period (1573 – 1619 A.D.) of the Ming dynasty. The essential difference between the Jiajing samples and the Wanli samples (both regarded as samples made in the late Ming dynasty) was that the latter ones used local blue colorants while the former ones used imported colorants, but possibly mixed with various amounts of local colorants. Another example can be cited where Yu and Miao (1996b) found that although the imperial porcelains of the Guangxu period (late Qing dynasty, 1875 – 1908 A.D.), and a contemporary porcelains both came from Jingdezhen of the Jiangxi Province of China, and that the periods of manufacture were separated for less than a century in time, the data (from principal component analysis) were well separated due to the different materials employed. These separations in close periods cannot be achieved using absolute measurement techniques.

The discussions in this article refer to blue-and-white porcelains, but they equally apply to the underglaze blue reign marks or underglaze blue regions in other types of porcelains.

1.2 Energy Dispersive X-ray Fluorescence (EDXRF)

In this Section, the principle behind Energy Dispersive X-ray Fluorescence (EDXRF) will be very briefly introduced in a layman's language. Everything in this world is constructed with atoms. An (over-) simplified model for atoms, i.e., the Bohr model, will be employed for our purposes. An atom is composed of a positively charged nucleus at the center and negatively charged electrons orbiting in fixed orbits (called shells, e.g. the innermost K shell, and then the progressively outer L, M, N, ... shells). At equilibrium, all inner shells are filled up. Electrons are bound by the electrostatic force so energy is required for electrons to go against the force from an inner shell to any outer shell, and conversely, energy is released for electrons to go from an outer shell to any inner shell. Therefore, the energy difference between shells is different for different elements.

When an electron absorbs enough energy, it can leave the atom. Therefore, when an atom is bombarded by external X-ray photons (coming either from radioactive sources or X-ray tubes, depending on the type of the XRF machine), electrons will leave the atom and leave vacancies. An outer shell electron will eventually fall into that inner shell, thereby emitting a photon with the energy equal to the energy difference between the two shells; this is the basic idea of fluorescence, and therefore the technique is called X-Ray Fluorescence (XRF).

When a K shell electron is ejected, electrons in the L, M, N shells, etc., can take up the vacancy and emit photons (K series). The photon energy corresponding to the transition from the nearest (higher) shell is called the α line, that from the second nearest shell the β line, and so on. In the case of K series, the energy corresponding to the transition from the L shell is called Kα line while that from the M shell the Kβ line. The nomenclature is similar for the L series and M series etc. In general, the K series is the most important one. Sometimes, even finer levels are assigned to a particular shell, e.g., I, II, III, levels, so the $K\alpha_1$ line originates from an electron transition from the L III level to the K shell.

Fluorescent photons will have different energies for different elements. More abundant elements will result in more fluorescent photons characteristic of the elements. The XRF spectrometer records a spectrum, with the x-axis representing the energy and the y-axis the photon number. Therefore, the spectrum simultaneously give information on (1) the chemical elements present in the sample; and (2) the amount of the chemical elements. In XRF analyses, the chemical elements in the sample are excited all at once and different methods can be employed to separately measure (disperse) the fluorescent photons from individual elements. The two commonest methods employ respectively selective diffraction using different crystals (called Wavelength Dispersive X-Ray Fluorescence or WDXRF) and selective counting using electronics (called Energy Dispersive X-Ray Fluorescence or EDXRF). In this article, all the discussions are based on EDXRF, but they equally apply to WDXRF.

Some discussions on the X-ray spectrum may also involve coherently or incoherently scattered lines from the X-ray source. Incoherent scatter, the incident X-rays cause the electrons in the sample to emit X-rays at the same energy, but in all directions. Coherent scatter increases with the atomic number of the sample because the number of electrons present in the sample increases with the atomic number. Incoherent scattering always corresponds to the Compton scattering. Here, the incident X-ray photon collides with a loosely bound electron in an outer orbit of an atom. The electron recoils and some energy of

the photon is carried away by the atom. The X-ray photon is therefore deflected with a loss of energy. Refer to the Chapter by Farquharson for further discussion of X-ray scattering.

1.3 Past research on attribution of antique Chinese blue-and-white porcelains using EDXRF

As mentioned in Section 1.1, the most important tasks in the research of antique porcelains are the attribution of their geographical origins and periods. The method using EDXRF is in general to quantitatively analyze the compositions of some chemical elements in the porcelains, which reflect their geographical origins and periods. This research has provided very useful and convenient methods for solving the problem of attribution of Chinese porcelains.

1.3.1 Attribution of periods

Mn/Co ratio

The most extensively studied criterion for attribution of periods of Chinese blue-and-white porcelains using EDXRF is the Mn/Co concentration ratio. Sir Harry Garner (1954) was the first to indicate that the amount of Mn present in Co blue colorant might be a guide to the source of the ore from which the colorant was derived.

Young (1956) observed that porcelain samples made before 1400 A.D. (before around the Yongle period in the early Ming dynasty) had concentration ratios of Mn/Co < 0.5. And those made in the period 1600 to 1900 A.D. (from around the Wanli period in the late Ming dynasty to around the Guangxu period in the late Qing dynasty) had Mn/Co > 3. Banks and Merrick (1967) showed that the concentration ratio of Mn/Co < 0.5 for porcelain samples before 1425 (before Xuande period in the early Ming dynasty) and Mn/Co > 2 around early Qing dynasty. Yap and Tang (1984b) found that Qing and Republic porcelains had concentration ratios of Mn/Co > 2.5, whereas modern pieces had Mn/Co < 0.07. Yap (1987b) found that Qing and Republic porcelains had concentration ratios of Mn/Co between 2 and 4, whereas modern pieces had Mn/Co < 0.07. Yap (1988) found that Qing and Republic porcelains had concentration ratios of Mn/Co > 2.3, whereas modern pieces had very small Mn/Co ratios, most of them having Mn/Co $\cong$ 0; those modern pieces with slightly larger Mn/Co ratios had comparatively larger As/Co ratios. In summary, porcelain samples before early Ming dynasty (around Xuande period) and modern samples (after Word War II) have small Mn/Co (< 0.5), while porcelain samples from early Ming dynasty, Qing dynasty and Republic periods have large Mn/Co (> 2).

Zn and As contents

Yap and Tang (1984a) observed that porcelains made in Jingdezhen prior to World War II contained very little or no Zn and As, whereas modern porcelains from Jingdezhen tend to contain Zn and, to a smaller extent, As. As Yap and Tang (1985c) found that the Zn Kα/Rb Kβ ratio was smaller than 0.12 ± 0.03 for all porcelains made before World War II and greater than this value for porcelains made after World War II. Yap (1987a) found that Jingdezhen porcelains from late Ming to Republic period had very small amounts of Zn (< 70 ppm) and essentially no As, and porcelains made after World War II could have large concentrations of Zn and/or As. Yu and Miao (1999a) showed that a modern Jingdezhen blue and white porcelain had a much more prominent ZnKα peak that that of a Jingdezhen blue and white porcelain of the Hongzhi period.

Ba contents

Yap and Tang (1985a) observed that the ratios of the intensity of Ba Kα line to that of the incoherently scattered gamma ray of 59.75 keV from the Am-241 source were between 5×10^{-3} and 7×10^{-3} for all Qing and Republic porcelains, while the ratios could be outside this range for modern porcelains. Yap (1986b) found similar results. Yap and Tang (1985b) found that porcelains from Jangxi period of Qing dynasty up to World War II had Ba contents between 100 and 130 ppm, and those made after World War II had Ba contents between 60 and 7000 ppm. Yu and Miao (1999a) showed that a modern Jingdezhen blue and white porcelain had a much more prominent BaLα peak that that of a Jingdezhen blue and white porcelain of the Hongzhi period.

Other criteria

Yap (1987b) demonstrated that a plot of the ratio of the intensity of K Kα1 to that of the coherently scattered Mn Kα from the Fe-55 source versus the ratio of the intensity of the Fe Kα1 to that of the coherently scattered Ag Kβ from the Cd-109 source showed that all Qing and Republic porcelains clustered together, and were quite distinctive from the modern porcelains.

Leung and Luo (1999) revealed the possibility of using functions of concentration ratios for dating Jindezhen blue and white procelains from the Yuan, Ming and Qing dynasties: Yuan dynasty, (Cr/Rb > 0.3 and Zr/Rb > 0.72) for folk kilns and (Cr/Rb > 0.3 and Zr/Rb < 0.58) for imperial kilns; Qing dynasty, Cr/Rb < 0.3; Ming dynasty, most of the porcelains (~ 90%) had 0.58 < Zr/Rb < 0.72). They also demonstrated the discrimination of the period of 960 – 1368 A.D. (Song to Yuan dynasties) from the period of 1368 – 1644 A.D. (Ming dynasty) for Dehau white porcelains: Ming dynasty, Rb/Y – 1.81 Zr/Y < 0.82; Song to Yuan dynasties, Rb/Y – 1.81 Zr/Y > 0.82.

1.3.2 Attribution of geographical origins

Yap and Tang (1984a) discovered that porcelains from the Kangxi period of the Qing dynasty to Republic period had little variation in their EDXRF spectra. As well, all had the common characteristic feature in the Rb-Sr-Zr-Nb K-lines region: a giant Rb Kα peak followed by three dwarf peaks (Sr Kα line, Rb Kβ line, and the Zr Kα + Sr Kβ composite line) which are of almost the same height; these dwarf peaks were followed by a baby Nb Kα peak.

Yap (1987c) observed that the elemental concentration of Rb, Sr, Y, Zr and Nb for Jingdezhen porcelains from late Ming to the Republic period lied within narrow ranges:

200 ppm	≤ Rb	≤ 430 ppm
60 ppm	≤ Sr	≤ 140 ppm
10 ppm	≤ Y	≤ 23 ppm
35 ppm	≤ Zr	≤ 55 ppm
11 ppm	≤ Nb	≤ 20 ppm

Non-Jingdezhen porcelains were in general quite different.

Yap, Saligan and Leenanupan (1987) found that a triangular plot using the concentrations of Rb, Sr and Zr as axes successfully separated the data for porcelains coming from Jingdezhen of China, Tang Shan of China, Liling of China, and England.

Yap (1992) demonstrated in a Principal Component Analysis (PCA) of the five elements Rb, Sr, Y, Zr and Nb to identify the Jingdezhen porcelains of the Qing dynasty from other porcelains.

Leung et al . (1998) used PCA of major and trace elements, viz., Ma, Mg, Al, Si, K, Ca, Cr, Mn, Fe, Ni, Cu, Zn, Sr, Y, Zr and Ba to prove that Linjinag porcelains belonged to the Jizhou kiln system. Leung and Luo (1999) also described the possibility of using functions of concentration ratios to identify the geographical origins of Chinese white porcelains: Hebei, $Zr/Rb > 1.29$; Jingdezhen, $Zr/Rb < 1.29$ and $0.79Rb/Y + Zr/Y > 6.00$; and Dehua, $0.79Rb/Y + Zr/Y < 6.00$. For white porcelains from Xing, Ding and Cizou in the Hebei Province: $Zr/Y + 16.0Cu/Y > 32.0$ for Ding and otherwise for Xing and Cizou; and then $Zr/Y - 1.7Rb/Y < 2.3$ for Xing and $Zr/Y - 1.7Rb/Y > 2.3$ for Cizou.

1.4 Recent Progress and Improvements

As shown in Section 1.3, research into the attribution of Chinese porcelains using EDXRF has led to many fruitful results. However, there were problems and challenges, some of which were quite fundamental, yet to be investigated and to be handled.

The first problem concerns the feasibility of using ratios between elemental concentrations for the attribution. As mentioned in Section 1.3, the most extensively studied criterion for attribution of periods of Chinese blue-and-white porcelains using EDXRF is the Mn/Co concentration ratio. Other studied ratios involved the Zn Kα/Rb Kβ ratio (Yap and Tang 1985c), and ratios of Cr/Rb, Zr/Rb, Rb/Y, Zr/Y and Cu/Y (Leung and Luo 1999). The questions whether or why these ratios were meaningful and what ratios were not meaningful have not been looked into carefully. The second problem concerns the feasibility of using for our criteria some elements characteristic of the colorant (such as Mn and Co) which in theory lies too deep beneath the glaze to be measured. These two problems will be addressed in Section 2.

In quantitative investigations by the EDXRF, the need for good calibration sources are critical in terms of their physical and chemical conditions. The criteria for a sound calibration source have been rarely discussed. In Section 3, the use of real antique porcelain shards as calibration sources is described.

Most current methods to attribute porcelains rely on compositional analysis of chemical elements (see Section 1.3). However, contents of individual chemical elements may not be totally reliable due to large probabilities for chance coincidence. The two commonest multivariate analysis method, namely, principal component analysis (PCA) and discrimination analysis (DA) will be discussed in Section 4. Examples will be cited to demonstrate the usefulness of the methods.

Antique blue and white porcelains studied using EDXRF have been mostly those of the Qing dynasty and contemporary ones. Despite that blue and white porcelains of the Ming dynasty are also regarded as the most important porcelains, these are rarely studied. It is also known that the colorants used for typical Jingdezhen blue and white imperial porcelains of the Ming dynasty were very diversified, including imported and local colorants, and it is known that different colorants were employed in different periods of Ming dynasty. In Section 5, blue and white porcelains of different periods of the Ming dynasty will be

investigated. Special discussions will also be made on porcelains of the Xuande period, which are always described as the best porcelains of the Ming dynasty.

Among most EDXRF studies of blue and white porcelains of the Qing dynasty, the majority grouped porcelains of the Qing dynasty and those made in the Republic period together under the same category (see Section 1.3). In Section 6, we will describe the attempts to find out whether different materials were employed for the Qing porcelains made in different periods and to compare the data for Qing porcelains with those for Ming porcelains.

The main sites of production of ancient Chinese blue and white porcelains included Jingdezhen in Jiangxi Province, the Yuxi and Jianshui Kilns of Yunnan Province and the Pinghe Kiln of Fujian Province. However, porcelains other than those from Jingdezhen have rarely been studied. In Section 7, we describe the studies on blue and white porcelains from these less-studied geographical origins. The differences between the porcelains from Jingdezhen and those from outside China are also discussed.

2. FEASIBILITY OF USING EDXRF FOR THE ATTRIBUTION OF BLUE AND WHITE PORCELAINS

Before any experimental attempts to identify criteria for attributing porcelains using the EDXRF method, the appropriateness of setting up these criteria should be assessed. Here two main points are considered. First, as many of these criteria involve ratios between elemental concentrations, we have to know which ratios between elements and why these are meaningful and required. The second question arises as it is well known that, in an EDXRF analysis, only a very thin layer at the sample surface will contribute to fluorescent X-rays. Therefore, the concentrations of the elements Mn, Fe, Co, Ni, Ti, Cu, Zn, Ga, Pb, As, Sr, Y, Zr, Ba and La measured in blue and white porcelains should reflect those in the glaze layer, although calculations of half value thickness show that some elements in the body of the porcelain also make contributions (Yu and Miao 1999a). The question is why we can use information on the elements such as Mn and Co for the attribution even they are known to be characteristic of the colorant.

2.1 Ratios between elements

The EDXRF data from a piece of porcelain are in fact the combination of information from the glaze, the colorant and the body. Since the distribution of the blue colorant on the porcelain is irregular, this causes an inhomogeneous distribution of chemical elements on the surface of the porcelain. In other words, those chemical elements with different EDXRF intensities at different positions of the porcelains are essentially those characteristic of the blue colorant. Accordingly, the elements characteristic of the colorant should be expressed as relevant ratios instead of absolute intensities.

Here we discuss the assignment of elements characteristic of the colorant based on the examination of typical EDXRF spectra for porcelains from different periods. Yu and Miao (1996a) examined two positions on the same Kangxi (Qing dynasty) blue and white porcelain sample using EDXRF; one comprising glaze, colorant and the body while the other comprising only the glaze and the body. The two measured spectra are overlaid in Figure 1

for comparisons. From Figure 1, the intensities of Mn, Co and Ni for the two spectra differed significantly, which implied that these elements essentially came from the colorant.

Similarly, Yu and Miao (1999a) examined positions on Hongzhi (Ming dynasty) and modern porcelain samples. The two measured EDXRF spectra are shown in Figures 2 and 3, respectively. From Figures 2 and 3, it can be seen that Mn, Co and Ni essentially come from the colorant. These elements are defined to be the elements characteristic of the blue colorant. There are also substantial amounts of Fe recorded for the areas with the colorant as well as those without the colorant. The elements As and Cu have similar behavior in some porcelains, e.g., see the behavior of As as shown in Figure2.

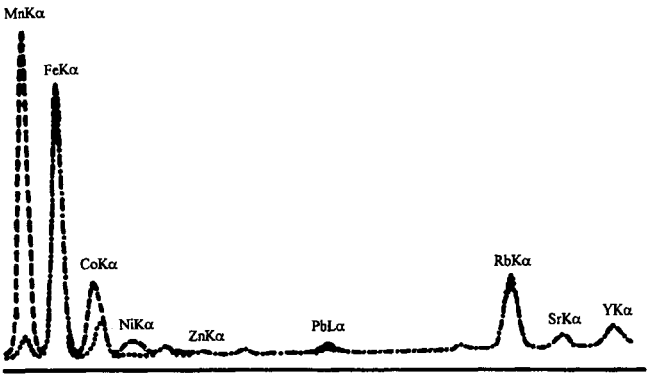

Figure 1. The overlay of the spectra from two different positions on the same porcelain sample (a Kangxi blue and white porcelain). The dashed line refers to a position comprising glaze, colorant and the body; the dotted line refers to that comprising only the glaze and the body; and the dot-dashed line indicates the overlap of the dashed line and the dotted line. (from Yu and Miao, 1996a)

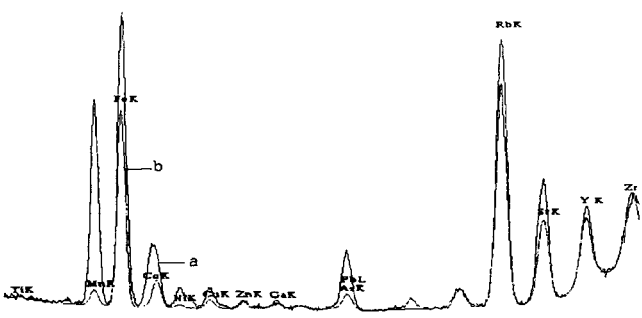

Fig. 2. EDXRF spectra of a blue and white porcelain of the Hongzhi period (mid-Ming dynasty). a: from an area including the glaze, colorant and the body; b: from an area including only the glaze and the body. (from Yu and Miao 1999a)

To study quantitatively the magnitude of variation of these 3 elements, Yu and Miao (1996a) performed the following experiment. Samples of thickness of 1 mm were sliced off from the surface of certain porcelain samples. These were divided into two groups, viz. (a) those comprising glaze, colorant and body and (b) those comprising glaze and body only. These were ground into uniform powder by agate-ball milling and were then analyzed using Inductively Coupled Plasma – Atomic Emission Spectrometry (ICP–AES), the results of which are shown in Table 2. These confirmed that the 3 elements varied significantly from an area comprising the colorant to an area without the colorant.

Table 2.
The ICP–AES results of the two groups of sliced samples (Units are in ppm): (A) those comprising glaze, colorant and body and (B) those comprising glaze and body only (from Yu and Miao, 1996a)

		Mn	Co	Ni
Jiajing	A	1992.00	1028.00	30.06
	B	351.50	2.01	5.64
Kangxi	A	4732.00	994.90	69.67
	B	504.40	<1.00	6.63
Yongzheng	A	7898.00	1782.00	34.65
	B	686.00	2.34	5.72

The above results were commensurate with previous research (Young 1956; Banks and Merrick 1967), which also showed that the elements characteristic of the colorant were Mn, Co and Ni.

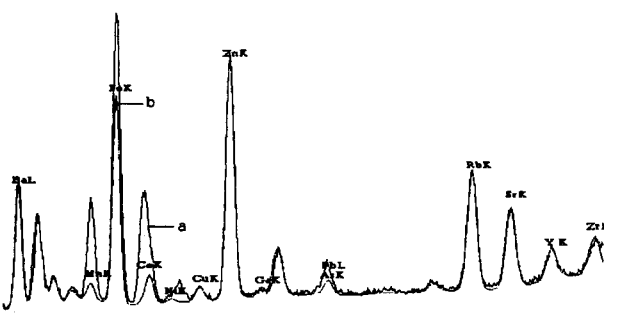

Figure 3. EDXRF spectra of a modern blue and white porcelain. a: from an area including the glaze, colorant and the body; b: from an area including only the glaze and the body. (from Yu and Miao 1999a)

Yu and Yang (1992) described that most imperial-ware blue and white porcelains of the Xuande period of the Ming dynasty employed imported Co blue materials. It was also

established that imported Co materials had lower Mn and higher Fe contents when compared to the native ones (Yu and Yang 1992). Therefore, when we come to discuss the porcelains of the Ming dynasty in Section 5, in particular those of the Xuande period, we will also consider Fe as an element characteristic of the colorant.

As mentioned above, the abundance of elements characteristic of the blue colorant changes with the density of colors on the porcelains. In this way, absolute values for their concentrations are not meaningful. Instead, Yu and Miao (1999a) showed that ratios between their concentrations were unique for a piece of porcelain. Therefore, these ratios have objective and practical values, and are required for meaningful analyses. On the other hand, the ratios between elements which are and are not characteristic of colorants should be variable and cannot be used for the identification of the attribution or geographical origin of the porcelain.

2.2 Elements at great depths

We go on to give an answer to the second question. It is well known that EDXRF analysis mainly gives results for a very thin layer at the sample surface. When the fluorescent X-ray passes through a thickness equal to the half value thickness, its intensity will decrease to half its original value. According to the Lambert law, the half value thickness $t_{1/2}$ for different elements in the porcelain samples can be calculated as follows. The intensity I recorded for an analytical line with an original intensity I_o at a depth t (cm) from the sample surface is given by

$$I=I_o \exp(-\mu_{mz}\rho t) \tag{1}$$

where ρ (in g.cm^{-3}) is the density of the sample, μ_{mz} (in cm^2.g^{-1}) is the total mass absorption coefficient for the element with atomic number Z contributed by 11 essential oxides in the porcelain samples, i.e.,

$$\mu_{mz} = \mu_{z1}w_1 + \mu_{z2}w_2 + \mu_{z3}w_3 + \cdots = \sum_{i=1}^{11} \mu_{zi}w_i \tag{2}$$

μ_{zi} is the mass absorption coefficient for the element with atomic number Z contributed by the i-th oxide and w_i is the concentration percentage of the i-th oxide in the sample. The 11 oxides, namely, SiO_2, Al_2O_3, TiO_2, CaO, Fe_2O_3, MgO, CoO, K_2O, Na_2O, P_2O_5, MnO_2, are taken as the basic components of the glaze layer of the blue and white porcelains. Their average contents in the glaze layer and the blue colorant in porcelains of the Yuan, Ming and Qing dynasties were determined according to Chen, Kuo and Chang (1978), which are respectively 69.61, 14.70, 0.15, 5.38, 1.03, 0.26, 0.31, 2.60, 1.96, 0.18 and 1.62%, summing up to 97.8%.

The average density for porcelains was determined experimentally by Yu and Miao (1999a) as described in the following. A total of 16 pieces of porcelain shards of the Ming and Qing dynasties were employed. Circular discs with a diameter of 4 cm were cut from the shards on areas with small curvature. The volumes were measured using vernier micrometer and the masses were measured using an electronic-optical analytical balance. The average density for porcelains was determined to be 2.337 g.cm^{-3}. From Eq. (1), the half value thickness $t_{1/2}$ can be expressed as

$$t_{1/2} = \frac{0.693 \sin 45^o}{\mu_m \rho} \tag{3}$$

where $I = 0.5I_o$, and the emergent angle of the fluorescent X-ray photons to reach the detector is 45°. Using Eq. (3), the half value thickness for 23 elements, namely, Mg, Al, Si, P, K, Ca, Ti, V, Cr, Mn, Fe, Co, Ni, Cu, Zn, Ga, As, Rb, Sr, Y, Zr, Ba, Pb (which were probable elements to be involved in the EDXRF analysis of porcelains) were calculated, and are shown in Table 3.

The intensity of the fluorescent X-ray will drop by half when it traverses one half value thickness, so effectively, the X-ray cannot penetrate a critical thickness defined by 6 to 7 half value thickness for detection. Investigations (Chen, Kuo and Chang, 1978; Yu and Miao 1999a) showed that the thickness of the glaze layer was in general 200 to 500 μm. Thus, from Table 3, the fluorescent X-rays mainly come from the glaze layer except for the elements Rb, Sr, Y and Zr (these four elements in the body will also contribute to the EDXRF results).

To answer the question why we can use information on the elements such as Mn and Co for the attribution even they are known to be characteristic of the colorant, Yu and Miao (1999a) employed two methods to reveal the behavior of these elements in the glaze and the colorant. The first method was based on ICP–AES and Nuclear Activation Analysis (NAA) methods. Layers with a thickness of 1 mm were sliced off from the surface of porcelain samples and separated into two types: A, those comprising the glaze, colorant and the body; B: those including only the glaze and the body.

Table 3
Half value thickness of elements in blue and white porcelains.
(from Yu and Miao 1999a)

Atomic number	Element	Analytical line	Half value thickness (μm)
12	Mg	Kα	1.1
13	Al	Kα	1.8
14	Si	Kα	2.3
15	P	Kα	1.3
19	K	Kα	5.8
20	Ca	Kα	6.5
22	Ti	Kα	9.3
23	V	Kα	12.7
24	Cr	Kα	15.9
25	Mn	Kα	20.8
26	Fe	Kα	25.9
27	Co	Kα	31
28	Ni	Kα	36
29	Cu	Kα	45
30	Zn	Kα	54.4
31	Ga	Kα	66.6
33	As	Kα	95.2
37	Rb	Kα	183
38	Sr	Kα	217.4
39	Y	Kα	284
40	Zr	Kα	309
56	Ba	Lα	9.1
82	Pb	Lα	95.5

These were then ball-milled and homogenized. The results from the analyses are shown in Table 4. These results show that:

(1) the abundance of the elements Mn and Co differ drastically for areas with and without the colorant (which was discussed in Section 2.1 above);

(2) some of these characteristic elements have somehow diffused from the colorant into the glaze layer during the high temperature firing process.

The second method was based on the electron probe microanalysis (EPMA). The surface glaze layer, colorant, together with 4 layers from the colorant to the surface glaze layer with equal thickness were analyzed using EPMA. The results are illustrated in Figure 4, which show that there are no abrupt changes in the composition between the colorant and the glaze; instead, there are gradients of element concentrations resulted from the diffusion of colorant elements into the glaze layer during the firing process. Therefore, the glaze layer also contains information of the colorant, and this explains why elements characteristic of the colorant can also contribute to the EDXRF results.

Table 4
The concentration (ppm) of various elements analyzed for two types of samples using ICP–AES and NAA. A: comprising the glaze, colorant and the body; B: including only the glaze and the body. (from Yu and Miao 1999a)

Blue and white porcelain	Type	Mn	Co	Ni	As	Method
Hongzhi	A	6406	886	157	—	ICP–AES
(mid-Ming dynasty)	B	525	6	10	—	ICP–AES
	A	—	1030	—	141	NAA
	B	—	9	—	0	NAA
Jiajing	A	1992	1028	30	—	ICP–AES
(late Ming dynasty)	B	352	2	6	—	ICP–AES
	A	—	1120	—	24	NAA
	B	—	3	—	2	NAA
Kangxi	A	4732	995	70	—	ICP–AES
(Qing dynasty)	B	504	1	7	—	ICP–AES
	A	—	1130	—	35	NAA
	B	—	1	—	2	NAA
Yongzheng	A	7898	1782	35	—	ICP–AES
(Qing dynasty)	B	686	2	6	—	ICP–AES
	A	—	2060	—	11	NAA
	B	—	3	—	1	NAA

3. CALIBRATION AND QUANTITATIVE ANALYSIS

As mentioned before, the idea behind relative measurements is to study the distribution of chemical elements in order to identify the difference caused by materials used for porcelains in different periods and from different geographical origins. Accurate quantitative investigations are essential to give realistic relative contents of the elements in different porcelain samples under the same measurement conditions.

In quantitative investigations by EDXRF, the accuracy of results is most affected by the difference between the matrix conditions of the calibration source and the samples. The reasons for the difference are mainly two fold. The first one is the physical condition, i.e., the grain size, density and the structure of the glaze. The second is the chemical composition. Therefore, a sound fabrication of the calibration source is critical. Traditional procedures comprise of the grinding of porcelains into powder, to which specific chemical elements are then added according to certain ratios, and the compression of the mixture to a pellet, which is used as the calibration source (Yap, 1987a, 1988; Yap, Saligan, and Leenanupan 1987; Yap and Tang 1985b). However, the calibration source thus made might have grain size, density and surface condition much different from those of the samples.

To overcome the problems mentioned above, i.e., to minimize the matrix effects and to enhance the accuracy of the quantitative analysis, Yu and Miao (1996b) directly employed porcelain shards of the Ming and Qing dynasties as calibration sources. In this way, the calibration sources automatically had the same grain size, density and surface structure of the samples. Circular discs were cut out for EDXRF measurements. Surface layers of thickness of 1 mm were sliced off from the remnant of the porcelain samples, which comprised the glaze, blue colorant and the body. These layers were ground into uniform powder by agate-ball milling. The powder was then analyzed using ICP–AES. The results from EDXRF and ICP–AES were then input into the "Delta-I" model, which was described by Russ, Shen and Jenkins (1978) as

$$C_i = I_i\left(K_i + \sum_j K_{ij} I_j\right) + B_i + \sum_{j \neq i} B_{ij} I_j \tag{4}$$

where C_i and I_i were the concentration and the EDXRF intensity of the i-th element respectively; and K_i, K_{ij}, B_i and B_{ij} were coefficients. The calibration curves for the trace elements could thus be plotted.

4. MULTIVARIATE ANALYSIS

Most current scientific methods utilized for attribution of porcelains rely on compositional analysis of chemical elements (see Section 1.3). While it is both simple and convenient to determine contents of individual chemical elements, it is recognized that these may not be totally reliable due to the large probabilities for chance coincidence in attribution of porcelains. When the chemical contents are jointly and systematically studied using multivariate analysis, the underlying patterns of the variables can be revealed more clearly.

With advances in computer technology, multivariate analysis no longer represents a major data handling problem. Here, the two commonest multivariate analysis method, namely, principal component analysis (PCA) and discrimination analysis (DA) will be discussed.

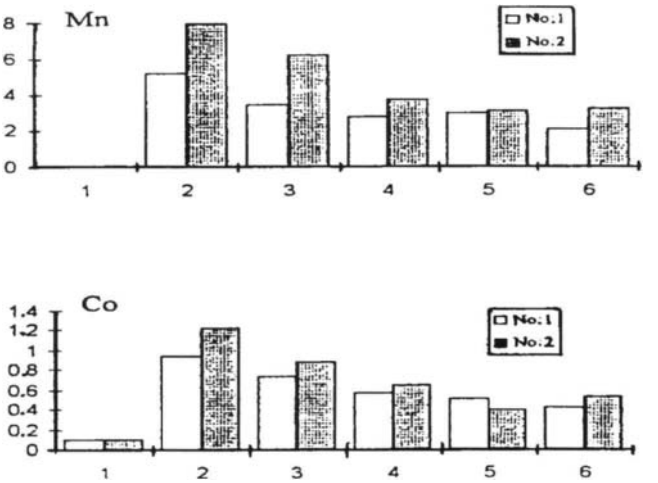

Figure 4. The distribution of Mn and Co in the glaze and the colorant of the porcelains. No.1: blue and white porcelains of the Qianlong period (Qing dynasty); No.2: blue and white porcelains of the Chenghua and Hongzhi periods (Ming dynasty). The y-axis is the relative concentration. The x-axis represents the layers of glaze and colorant. 1: surface glaze layer; 2: blue colorant; 3 to 6: 4 layers from the colorant to the surface glaze layer with equal thickness, which is about 68μm for sample No.1 and 99μm for sample No.2. (from Yu and Miao 1999a)

4.1 Principal component analysis (PCA)

The idea behind the PCA is the reduction of the number of variables (elemental concentrations in our case of attribution of porcelains) to a smaller number of variables called principal components (PCs). These are linear combinations of the original variables, whilst at the same time yielding as much information as possible from the data. This reduction in the number of variables is possible because the original variables might have significant redundancy and large inter-correlations since they are measuring similar things. By definition, the first PC has the largest variance, the second PC the second largest variance, and so on.

Different categories of data will have different distributions of elemental concentrations and thus different values for the PCs. The reduced number of variables can be plotted (in 2D or 3D plots) for a visually comprehensible identification of clustering of data (Kendall 1980). The number of PCs (whether two or three) which are to be used for the final analysis is an important issue (Fang 1989). Under normal circumstances, in order to retain as much as possible the information contained in the original variables, the number of PCs should give an accumulated contribution rate above ~70 % (Fang 1989).

The most convenient use of PCA has been to produce a 2D plot of the first and second PCs to seek out clusterings of data (Yap and Hua 1992, 1994). However, for common data structures, the accumulated contribution rate of the first and the second PCs is generally found to be less than 60%. Therefore, on some occasions (e.g., Yu and Miao, 1997), to

minimize loss of information, use has been made of the first, second and the third PCs and these have been plotted in a 3D plot.

As a demonstration of the usefulness of the method, the applications in Yu and Miao (1996c) and Yu and Miao (1998) will be used here as examples.

As mentioned in Section 1.3, contemporary porcelains can be identified in general by analyzing the relationship between MnKα and CoKα intensities, or the intensities of the ZnKα, As Kα and PbLα characteristic lines from the EDXRF spectra. However, Yu and Miao (1996c) found an exceptional case for a particular contemporary porcelain, which did not have the characteristics of contemporary porcelains, but had an EDXRF spectrum close to those of the Ming dynasty. EDXRF spectra of a Jiajing porcelain and that contemporary porcelain are shown in Figures 5 and 6, respectively, for a comparison. Therefore, it is sometimes difficult to date a piece of porcelain solely from a qualitative study of the EDXRF spectrum, especially when the imitation is deliberately made to have an EDXRF spectrum similar to those of genuine porcelains.

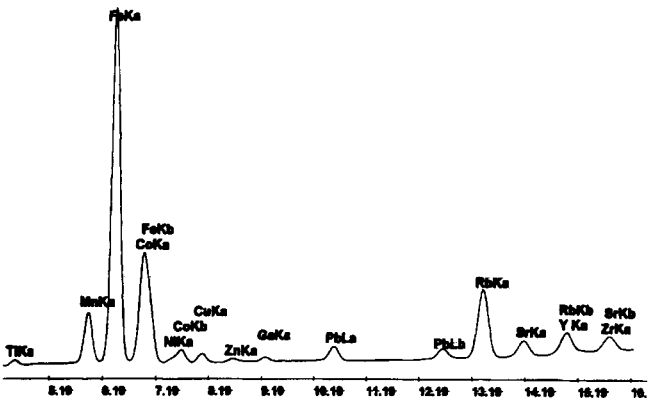

Figure 5. The EDXRF spectrum of a Jiajing porcelain. (from Yu and Miao 1996c)

Yu and Miao (1996c) performed PCA on the data of this contemporary porcelain and also blue and white porcelains of the Ming dynasty (including those of the Yongle, Xuande, Chenghua, Jiajing and Wanli periods). The contents of 13 chemical elements, namely, Ti, Mn, Fe, Co, Ni, Cu, Zn, Ga, Pb, Rb, Sr, Y and Zr, of the surface of porcelain samples determined by the EDXRF technique were used. Figure 7 shows the PCA results of the contemporary porcelain and other porcelains of the Ming dynasty, from which we can see that the contemporary porcelain cannot be incorporated into any clusters. This demonstrates that consideration of all the elements, taken together, is more reliable for attributing the provenance of porcelains.

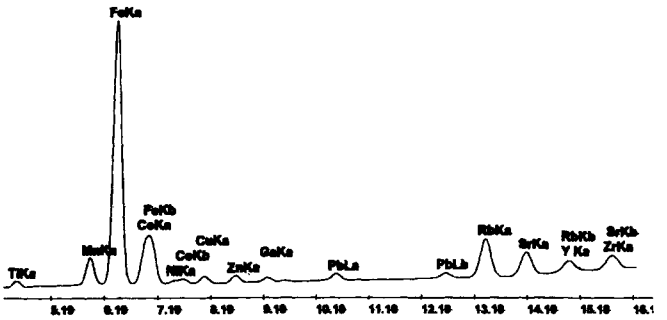

Figure 6. The EDXRF spectrum of the contemporary porcelain. (from Yu and Miao 1996c)

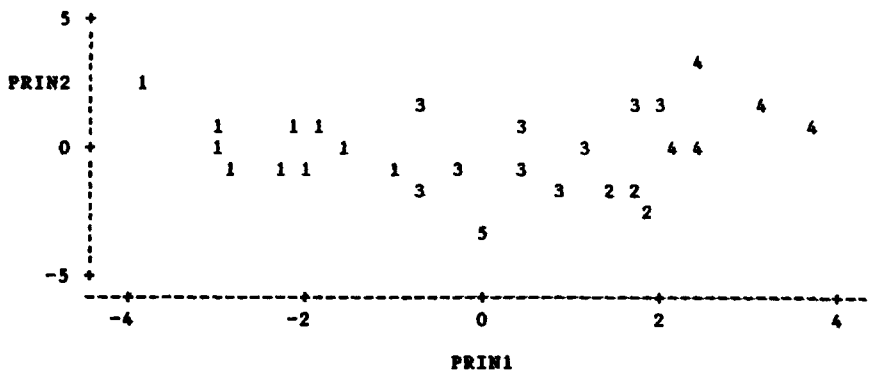

Figure 7. Results from principal component analysis of porcelains of the Ming dynasty and a contemporary porcelain. 1: Yongle and Xuande periods; 2: Chenghua period; 3: Jiajing period; 4: Wanli period; 5: Contemporary. (from Yu and Miao 1996c)

As well, Yu and Miao (1998) performed PCA on the data of blue and white porcelains of the early Qing dynasty and modern blue and white porcelains, both from Jingdezhen. Again, the contents of the above 13 chemical elements were used. Figure 8 shows the 3D scatter plots for the three PCs of the PCA results. It can be seen that the porcelains of the Kangxi, Yongzheng and Qianlong periods did not separate into three distinct clusters, which occurred because the raw materials used did not necessarily change with the change of the emperors (Feng 1994).

To locate the geographical origins of porcelains, Yu and Miao (1998) also performed PCA on the data of blue and white porcelains of Qing dynasty from Jingdezhen of Jiangxi Province, Ming dynasty from Pinghe Kiln of Fujian Province, Ming dynasty from Jianshui, and Yuxi Kilns of Yunnan Province and Qing dynasty from Wun Yiu (or known as Wanyao) of Hong Kong. Again, the contents of the above 13 chemical elements were used. Figure 9

shows the 3D scatter plots for the three PCs of the PCA results. It is seen that the porcelains from the Yuxi and Jianshui Kilns did not separate into two clusters, but overlapped with each other in a single one. This illustrates that the chemical compositions of the porcelains from the two kilns are close to each other. Relevant literature (Ge 1992; Chen et al 1992) gave support to this assertion.

4.2 Discrimination analysis (DA)

The objectives for discrimination analysis (DA) and PCA are different. For the samples to be studied by PCA, the clustering behavior are unknown and are to be identified by the PCA itself. For samples with already known clustering behavior, the DA can establish discrimination functions (DFs) which can then be employed for discrimination of future unknown samples.

Before carrying out the appropriate PCA, direct use of clusters separated by geographical origins or periods for the DA will lead to incorrect results because the chemical composition of the porcelains can not necessarily separated by these geographical origins or periods. Therefore, before the DA, PCA should be used to identify the underlying "true" clusterings, which should then be cross-checked with geographical considerations, historical backgrounds and relevant literature for the decision of the final clusterings used for the DA.

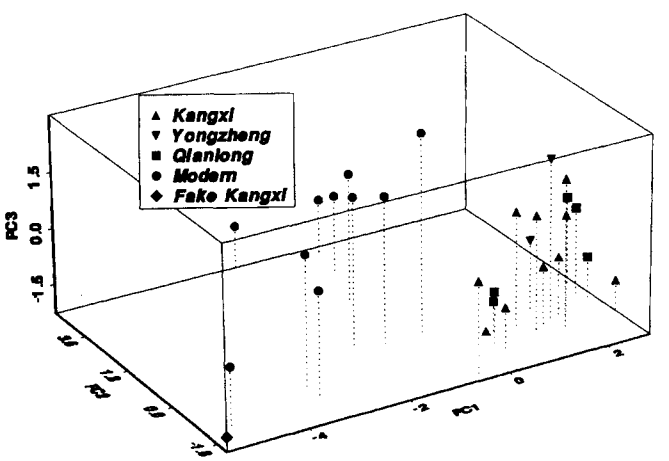

Figure 8. 3D scatter plot of principal components 1, 2 and 3 for blue and white porcelains of the Kangxi, Yongzheng, Qianlong and modern periods (including one modern imitation of a Kangxi blue and white porcelain). (from Yu and Miao 1998)

When the true clusters within the samples have been identified (e.g., by the PCA mentioned above), DA can be performed to pick the variables which can most effectively reveal the differences among the clusters and to establish a discrimination function (DF) for

this purpose. Any future sample whose associated cluster is unknown can then be determined using the DF.

As a demonstration of the method, the application in Yu and Miao (1998) will be used here as an example. As mentioned before, Yu and Miao (1998) studied porcelain samples with known periods and geographical origins. Based on the results of PCA by Yu and Miao (1998) as described above, DA was performed on the data, and two DFs were established by Yu and Miao (1998), one for discriminating blue and white porcelains of Jingdezhen imperial wares of the early Qing dynasty from those of the contemporary period, and the other for discriminating among the main geographical origins of antique blue and white porcelains. When establishing the DF for the periods, the data for Kangxi, Yongzheng and Qianlong were grouped together to form one group to represent porcelains of the early Qing dynasty.

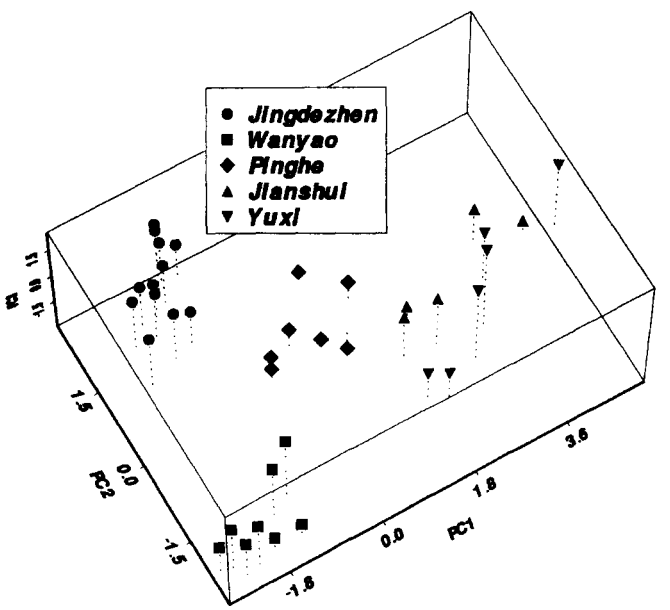

Figure 9. 3D scatter plot of principal components 1, 2 and 3 for blue and white porcelains from Jingdezhen, Wanyao, Pinghe, Jianshui and Yuxi. (from Yu and Miao 1998)

When establishing the DF for the geographical origins, the data for Yuxi and Jianshui Kilns were grouped together to form one group called Yunnan Kilns.

For discrimination between blue and white imperial porcelains of the early Qing dynasty and modern blue and white porcelains, both from Jingdezhen, the concentrations of Ti, Cu, Zn, Sr and Y were observed for the DA. In contrast, for discrimination of the geographical origins of the blue and white porcelains, the concentrations of Ti, Rb, Sr and Y were picked (Yu and Miao 1998). Through the Bayes discrimination, the following linear DFs were established (Yu and Miao 1998):

Discrimination of periods:

$$G_n = A_1Ti + A_2Cu + A_3Zn + A_4Sr + A_5Y + C_n \quad (5)$$

where n refers to imperial wares of early Qing dynasty and to modern blue and white porcelains of Jingdezhen.

Discrimination among geographical origins:

$$G_n = A_1Ti + A_2Rb + A_3Sr + A_4Y + C_n \quad (6)$$

where n refers to Jingdezhen, Pinghe Kiln, Wun Yiu (Wanyao), and Yunnan Kilns (incorporating Yuxi and Jianshui Kilns). In Eqs. (5) and (6), A_i's are coefficients of the chemical concentrations, and C_n are constants, which are shown in Tables 5 and 6.

Table 5
Coefficients and constants in the discrimination function for periods. (from Yu and Miao 1998)

Period	A_1	A_2	A_3	A_4	A_5	C_n
Early Qing	0.06742	0.11266	-0.02633	0.08901	3.56551	-52.87665
Modern	0.07040	-0.02732	0.00197	0.10738	1.39543	-26.54784

Table 6
Coefficients and constants in the discrimination function for geographical origins. (from Yu and Miao 1998)

Geographical origin	A_1	A_2	A_3	A_4	C_n
Jingdezhen	0.05507	0.21790	-0.00775	-0.46351	-41.44011
Pinghe Kiln	0.06564	0.08968	0.00459	-0.09313	-21.31957
Wun Yiu	-0.03440	0.07451	0.18826	0.62757	-63.21508
Yunnan Kilns	0.19665	0.05823	-0.07454	-0.46830	-86.62676

Based on the Bayes discrimination technique, the sample should belong to the cluster whose DF has a larger value (Dong 1993). After the establishment of the DFs, the data for the original samples were inserted into the DFs for cross-checking (Yu and Miao 1998). For the discrimination among geographical origins, the success rates for Pinghe Kiln, Wun Yiu (Wanyao) and Yunnan Kilns were all 100%, while that for Jingdezhen was 91.67%. For the discrimination of periods, both the success rates were 100%.

The modern imitation of a Kangxi blue and white porcelain (shown in Figure 8) had a form, decoration and reign mark closely resembling those of a genuine one. However, in the scatter plot of the PCs shown in Figure 8, it was located far away from the porcelains of the Kangxi period. According to the clustering, it fell into the category of modern porcelains. Substituting its chemical contents into the DF in Eq. (5), G(Qing dynasty) = -6.4232 and

G(modern) = 6.2680. The value of the DF for the modern category was greater than that for the Qing dynasty category, so this sample belonged to the former category. This was consistent with the fact and the PCA results (Yu and Miao 1998).

5. BLUE AND WHITE PORCELAINS OF THE MING DYNASTY

Antique blue and white porcelains studied using EDXRF have been mostly those of the Qing dynasty (1644 – 1912 A.D.) and contemporary ones (after 1912 A.D.) (see Section 1.3 and references therein). Although blue and white porcelains of the Ming dynasty (1368-1644 A.D.) are also regarded as the most important porcelains, these are rarely studied, which might be due to difficulties in obtaining appropriate samples.

The colorant used for typical Jingdezhen blue and white imperial porcelains of the Ming dynasty can be separated into 3 stages.

1. "Sumani-Po Blue" was used for the periods of Yongle and Xuande (early Ming dynasty),
2. "Po-Tang Blue" for the periods of Chenghua, Hongzhi, Zhengde, (mid Ming dynasty),
3. "Mohammedan Blue" for the periods of Jiajing, Longqing, Wanli (late Ming dynasty).

According to Geng (1993), "Po-Tang Blue" is produced in the Leping prefecture of the Jiangxi Province of China, while the other two blue colorants come from countries other than China itself.

Chen, Kuo and Chang (1978) analyzed Jingdezhen blue and white imperial porcelains of the Ming Dynasty using chemical methods, and some fruitful results were obtained. Yu and Miao (1996c) used EDXRF to analyze quantitatively and non-destructively the trace element concentrations in porcelains of the Ming dynasty. Through the EDXRF, quantitative results for the 13 trace elements, viz., Ti, Mn, Fe, Co, Ni, Cu, Zn, Ga, Pb, Rb, Sr, Y and Zr, of 39 porcelain samples were obtained. The idea was to look for difference in the distribution pattern of these elements in Ming porcelains, which was based on the fact that different blue colorants came from different localities. The data were analyzed by PCA and their final results have been reproduced in Figure 7. Among these 13 trace elements, some came from the blue colorant whilst others were characteristic of the glaze and the body.

Since different blue colorants were employed for the blue and white porcelains during the early, mid and late periods of the Ming dynasty, the typical porcelains of different periods should have different characteristics. However, during the early and the late periods, mixtures of imported and local colorants, or even pure local colorants were used as well. From the PCA results shown in Figure 7, typical porcelains of the Ming dynasty can be well separated into 3 categories, viz. early Ming dynasty (represented by Yongle and Xuande samples), mid-Ming dynasty (represented by Chenghua samples) and late Ming dynasty (represented by Jiajing and Wanli samples). Nevertheless, the data for the early and the late periods are fairly scattered. According to the idea behind the PCA, the scatter arises from the non-uniformity of the blue colorants used.

The essential difference between the Jiajing samples and the Wanli samples (both regarded as samples made in the late Ming dynasty) was that the latter ones used local blue colorants while the former ones used imported colorants, but possibly mixed with various amounts of local colorants. The mixing of colorants increased the similarity between porcelains of the two periods. If the glaze and the body materials were the same, the porcelains should have similarities in addition to the expected differences. The results in

Figure7 also objectively reflected the relatively small difference between porcelains of the Jiajing and Wanli periods.

When we come to discuss the porcelains of the Ming dynasty, those of the Xuande period (1426 to 1435 A.D.) deserve special attention. The Jingdezhen imperial-ware blue and white porcelains of the Xuande period are highly valued for their tone and charm, and are always said to be the best porcelains of the Ming dynasty. They are also famous for the unique style of having naturally-formed black specks in the blue colorants. The Co blue materials used for Jingdezhen imperial-ware blue and white porcelains of the Xuande period were so special that no accurate imitations could be produced in succeeding periods and dynasties (Geng 1993).

As mentioned before, the colorant used for typical Jingdezhen blue and white imperial porcelains of the Ming dynasty included the imported "Sumani-Po Blue", "Mohammedan Blue", the native "Po-Tang Blue" and the mixture of imported and native Co (Geng 1993). Yu and Yang (1992) described that most imperial-ware blue and white porcelains of the Xuande period employed imported Co blue materials. Colorants from different localities had different chemical compositions. In particular, it was established that imported Co materials had lower Mn and higher Fe contents when compared to the native ones (Yu and Yang 1992). As regards the analyses of colorants using these two elements, previous research were only confined to the ratio between intensities of Mn and Co (or Mn/Co ratio) (see Section 1.3) and the Fe/Co ratio (Zhang and Cowell 1989). It was surprising that no research was carried out on the Mn/Fe ratio despite its importance.

Yu and Miao (1999b) used EDXRF to identify the source of Co materials used in porcelains of the Xuande period by analysing the ratio of intensity of the MnKα peak to that of the FeKα peak (MnKα/FeKα). In addition, porcelains of the Kangxi, Yongzheng and Qianlong periods of the Qing dynasty were also examined for comparisons. A typical EDXRF spectrum of an imperial-ware blue and white porcelains of the Xuande period of the Ming dynasty is shown in Figure 10, and that of an imperial-ware blue and white porcelains of the Kangxi period of the Qing dynasty is shown in Figure 11.

The intensity of the MnKα line was significantly smaller than that of the FeKα line in the EDXRF spectrum shown in Figure 10, while the two were close to each other in the EDXRF spectrum shown Figure 11. It was therefore straightforward to use the ratio between their intensities (MnKα/FeKα) as a criterion to separate a porcelain sample of the Xuande period from one of the Kangxi period (see also Section 2.1 for the discussion on the feasibility of such a ratio). The numerical ratios for all their samples are shown in Figure 12. From Figure 12, it was clear that a line for MnKα/FeKα = 0.35 separated the porcelains of the Xuande period (lower ratios) from those of the Kangxi, Yongzheng and Qianlong periods (higher ratios). This observed difference agreed with the findings of Yu and Yang (1992) that most imperial-ware blue and white porcelains of the Xuande period employed imported Co materials and that imported Co materials had lower Mn and higher Fe contents when compared to the native ones.

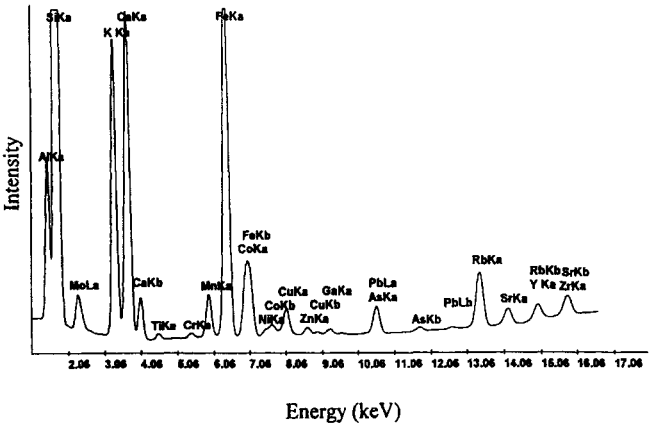

Figure 10. A typical EDXRF spectrum of an imperial-ware blue and white porcelains of the Xuande period (1426 to 1435 A.D.) of the Ming dynasty. (from Yu and Miao 1999b)

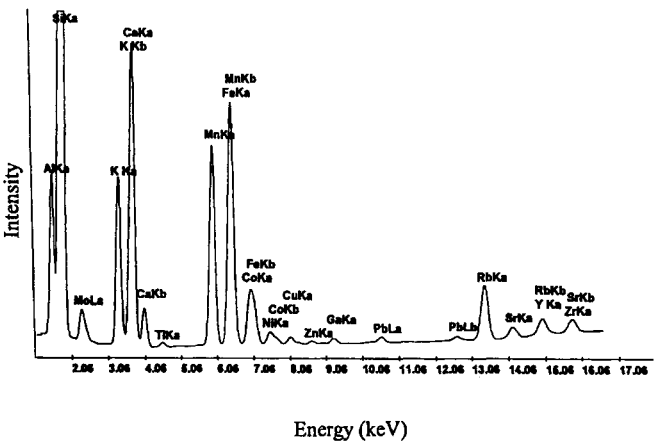

Figure 11. A typical EDXRF spectrum of an imperial-ware blue and white porcelains of the Kangxi period (1662-1722 A.D.) of the Qing dynasty. (from Yu and Miao 1999b)

Despite the above results on the Xuande blue-and-white porcelains, it is also noted that a recent investigation on Xuande porcelains showed contrary results. Li et al. (1999) showed from five Xuande blue-and-white porcelain samples that the colorant employed had high Mn and low Fe contents, and concluded that the colorant was local. More studies seem necessary to clarify the situation, and it is possible that both local and imported colorants were used in the Xuande period.

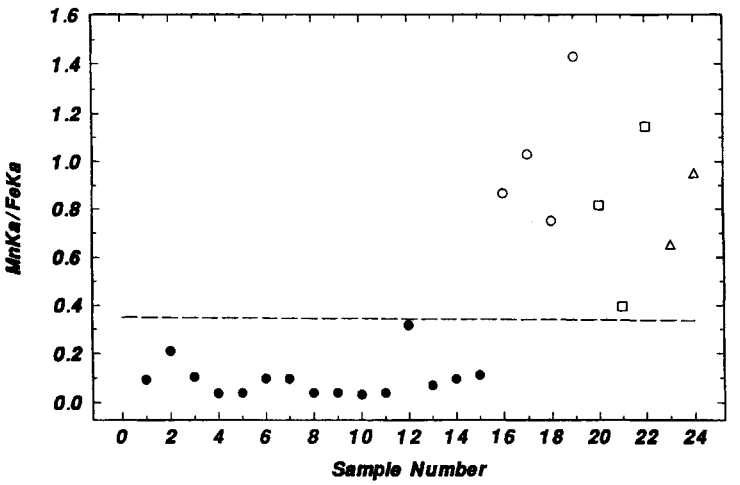

Figure 12. Ratios (MnKα/FeKα) between the intensities of the MnKα line and the FeKα line for porcelain samples. Samples 1 to 15 (solid circles): Xuande period of the Ming dynasty; Samples 16 to 19 (outlined circles): Kangxi period of the Qing dynasty; Samples 20 to 22 (outlined squares): Yongzheng period of the Qing dynasty; Samples 23 to 24 (outlined triangles): Qianlong period of the Qing dynasty. The horizontal broken line refers to MnKα/FeKα = 0.35. (from Yu and Miao 1999b)

6. JINGDEZHEN IMPERIAL BLUE AND WHITE PORCELAINS

As mentioned before, antique blue and white porcelains studied using EDXRF have been mostly those of the Qing dynasty (1644 – 1912 A.D.) and contemporary ones (after 1912 A.D.). However, the majority of these studies considered the porcelains of the Qing dynasty and those made in the Republic period (1912 – 1949) together under a single category (see Section 1.3 and references therein). It is of interest to study porcelains of the Qing dynasty on their own and, if possible, to see whether different materials were employed for the Qing porcelains made in different periods (e.g. those made in early and those made in late Qing dynasty). In Section 5, we discussed on blue and white porcelains of the Ming dynasty. It is also of interest to compare the data for Qing porcelains with those for Ming porcelains.

Jingdezhen imperial blue and white porcelain samples of the Kangxi period (early Qing dynasty, 1662 – 1722 A.D.) and the Guangxu period (late Qing dynasty, 1875 – 1908 A.D.) were studied by Yu and Miao (1996b). The quantitative results for the trace elements were analyzed by PCA. The results are shown in Figures 13. From Figure 13, porcelains of the Kangxi and the Guangxu periods are distinctively separated into two clusters, which reflects the different materials employed for the porcelains of the two periods.

Yu and Miao (1996a) systematically examined blue and white porcelains of the Ming and Qing dynasties. The samples of the Ming and Qing dynasties for their investigation included:

(1) Yongle and Xuande of the early Ming dynasty (1403-1435): colorant is imported "Sumani-Po Blue";
(2) Chenghua of the mid Ming dynasty (1465-1487): colorant is "Po-Tang Blue";
(3) Jiajing of the late Ming dynasty (1522-1566): colorant is "Mohammedan Blue";
(4) Wanli of the late Ming dynasty (1573-1619): colorant is local;
(5) Qing dynasty - Kangxi (1662-1722), Yongzheng (1723-1735), Qianlong (1736-1795), Jiaqing (1796-1820), Daoguang (1821-1850), Guangxu (1875-1908): colorant is local;
(6) Republic (1912-1949): colorant is "Foreign Blue";
(7) Modern (1995): colorant with unknown origin.

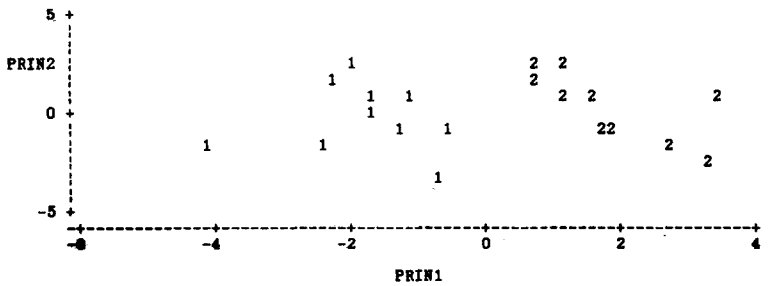

Figure 13. Results from principal component analysis of porcelains of the Qing dynasty. 1: Kangxi period; 2: Guangxu period. (from Yu and Miao 1996b)

Table 7. The XRF intensities of characteristic elements from typical spectra. (from Yu and Miao, 1996a)

	MnKα	CoKα	NiKα	FeKα	ZnKα	PbLα	MnKα/CoKα	CoKα/NiKα
Yongle,Xuande (Ming)	24.24	139.01	4.54	725.33	5.38	44.17	0.17	30.62
Chenghua (Ming)	49.05	9.42	13.81	276.34	4.26	9.88	5.21	0.68
Jiajing (Ming)	84.61	90.83	20.16	403.97	8.31	15.7	0.93	4.51
Wanli (Ming)	131.17	27.86	12.13	328.99	6.56	11.16	4.71	2.3
Kangxi (Qing)	473.07	120.92	13.76	295.59	4.94	12.98	3.91	8.79
Guangxu (Qing)	207.42	50.15	7.22	381.81	5.44	11.18	4.14	6.95
Republic	136.15	231.79	8.55	444.54	6.01	28.71	0.59	27.11
Modern	26.74	31.65	2.99	323.03	147.33	7.91	0.84	10.58

The distribution pattern of the EDXRF intensities of the 6 characteristic elements for these porcelains manufactured at different times were investigated. For porcelains of different periods of the Ming dynasty, the EDXRF spectra varied to a greater extent; those of Yongle, Xuande, Chenghua, Jiajing and Wanli, had 4 forms of elemental distribution (see also Section

5). The EDXRF spectra for porcelains of different periods of the Qing dynasty were difficult to differentiate; those of Kangxi to Guangxu had only 2 forms of elemental distribution in their spectra. It was easy to differentiate between the distributions of Ming and Qing porcelains, and between those of Republic and modern porcelains. It was also obvious that the differences among the spectra arise mainly from the 6 elements Mn, Co, Ni, Fe, Zn and Pb, the intensities and the distribution of which can be see from Table 7 and Figure 14. As mentioned in Section 2.1, when dealing with the intensities of different elements, the elements characteristic of the colorant should be expressed as relevant ratios instead of absolute intensities.

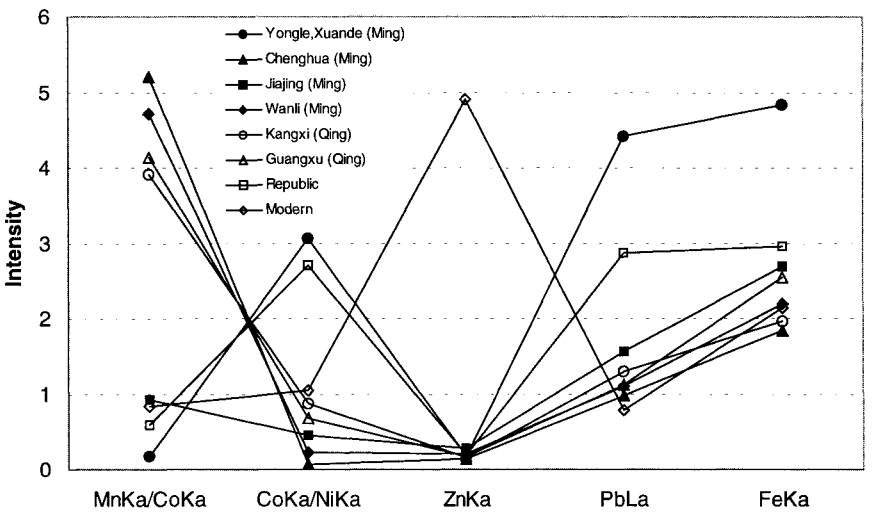

Figure 14. The distribution of intensities of characteristic elements in typical EDXRF spectra. The intensities have been normalized to fit on the same range, i.e., (ZnKα)/30, (CoKα/NiKα)/10, (PbLα)/10 and (FeKα)/150. (from Yu and Miao, 1996a)

From Figure 14: those porcelains having employed imported colorant have MnKα/CoKα < 1 (these include the porcelains of the Yongle, Xuande and Jiajing of the Ming dynasty and the Republic porcelains), whilst those having employed local colorant have MnKα/CoKα ≥ 3.9 (the modern porcelains where the originality of the blue colorant is unknown has not been considered here); the intensity of ZnKα differs significantly for the modern and pre-Republic porcelains; and that the intensities of FeKα and PbLα are highest for the Yongle and Xuande periods, which are far greater than those of other porcelains.

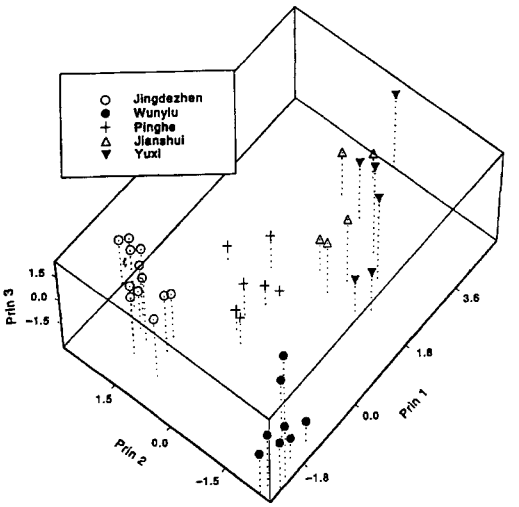

Figure 15. 3D scatter plot of principal components 1, 2 and 3 for blue and white porcelains from Jingdezhen, Wanyao, Pinghe, Jianshui and Yuxi. (from Yu and Miao 1997)

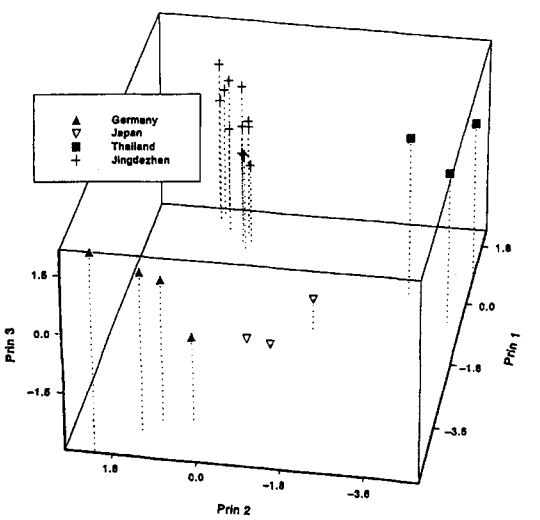

Figure 16. 3D scatter plot of principal components 1, 2 and 3 for blue and white porcelains from Jingdezhen, Germany, Thailand and Japan. (from Yu and Miao 1997)

7. LOCATING GEOGRAPHICAL ORIGINS OF BLUE AND WHITE PORCELAINS

Among the main sites of production of ancient Chinese blue and white porcelains can be included Jingdezhen in Jiangxi Province, the Yuxi and Jianshui Kilns of Yunnan Province and the Pinghe Kiln of Fujian Province. Nevertheless, porcelains other than those from Jiingdezhen have rarely been studied.

Yu and Miao (1997) studied blue and white porcelains from a number of geographical origins. These included: samples of Qing dynasty porcelain from Jingdezhen folk kilns in Jiangxi Province, samples of Ming dynasty porcelain from the Yuxi folk kiln of Yunnan Province, samples of Ming dynasty porcelain from the Jianshui folk kiln of Yunnan Province, samples of late Ming dynasty porcelain from the Pinghe folk kiln of Fujian Province, samples of Qing dynasty porcelain from Wun Yiu (also known as Wanyao) folk kiln of Hong Kong, and modern samples of porcelain from Germany, Japan and Thailand.

The concentrations of 13 chemical elements, namely, Ti, Mn, Fe, Co, Ni, Cu, Zn, Ga, Pb, Rb, Sr, Y and Zr, were analyzed by PCA. The 3D plots for the first, second and third PCs are shown in Figures 15 and 16, in which clustering of data, which aids in locating different geographical origins of porcelain, are clearly identified.

The distribution of chemical elements is distinctly different for blue and white porcelains from the different main geographical origins of ancient blue and white porcelains in China. In Figure 15, some overlaps could be observed between the data for porcelains from the Yuxi and Jianshui Kilns of Yunnan Province. Chen et al (1992) showed that the chemical compositions of the glaze and body of blue and white porcelains from Yuxi and Jianshui Kilns were closely similar, with only minor difference being observed. It was also noted that the cobalt minerals used in both of these two kilns typically had higher contents of MnO and Fe_2O_3 than for sites elsewhere in this study. The proximity of the geographical positions of the two kilns largely accounts for such outcome.

REFERENCES

Banks, M.S. and Merrick, J.M., 1967, "Further analysis of Chinese Blue-and-White", Archaeometry, 10, 101-103.

Chen, Y.C., Kuo, Y.Y., and Chang, T.G., 1978, "Investigation of colorants of blue and white porcelains of different periods", Journal of Chinese Ceramics Society, 6(4), 225-240. (in Chinese)

Chen, Y.C., et al, 1992, in "Study of the blue and white porcelain on Yuxi and Jianshui Kilns", Proceedings of 1989 International Symposium on Ancient Ceramics, (Shanghai Science and Technology Press: Shanghai), 162.

Dong, D.J., 1993, "Introduction to the applications of the SAS® statistical analysis software", (Electronic Industries Publishing: Beijing)

Fang, K.T., 1989, "Practical Multivariate Analysis", (Huadong Normal University Press: Shanghai), 291.

Feng, X.M., 1994, "Chinese Pottery and Porcelains", (Shanghai Antique Books Publishing: Shanghai).

Garner, H, 1954, *Oriental Blue and White*, (Faber and Faber).

Ge, J.F., 1992, "Antique colorant and blue and white porcelains of Yunnan", Jiangxi Relics, 2, 23.

Geng, B.C., "Identification of porcelains of the Ming and Qing dynasties", (Forbidden City Publishing House and Woods Publishing Company: China) (1993). (in Chinese)

Kendall, M.G., 1980, "Multivariate Analysis", 2nd Ed. (Griffin: London).

Leung, P.L., Stokes, M.J., Li, M.T.W., Peng, Z.C., and Wu, S.C., 1998, "EDXRF studies on the chemical composition of ancient porcelain bodies from Linjinag, Jiangxi, China", X-ray Spectrometry, 27, 11-16.

Leung, P.L., and Luo, H., 1999, "A study of provenance and dating of ancient Chinese porcelain by X-ray fluorescence spectrometry", X-ray Spectrometry, 28, in press.

Li, J, Zhang, Z., Deng, Z, Chen, S., 1999, "Three examples of the studies on science and technology of ancient ceramics in scientific and technological archaeology", Sciences of Conservation and Archaeology, 11(2), 1-6.

Russ, J.C., Shen, R.B., and Jenkins, R., 1978, "EXAM: Principles & Experiments", Publication No. 111-0-E-1277, Part No. 80-01201-00, EDAX International, Inc., 62.

Taylor, J.R., 1977, "The origin and use of cobalt compounds as blue pigments", Science and Archaeology, 19, 3-15.

Yap, C.T., 1986a, "A non-destructive scientific technique of detecting modern fake reproduction porcelains", Oriental Art, 32, 48-50.

Yap, C.T., 1986b, "XRF Analysis of Nonya Wares Using an Annular Americium Source", Archaeometry, 28 (1986b), 197-201.

Yap, C.T., 1987a, "X-ray Fluorescence Determination of Trace Element Concentrations of Zinc and Arsenic and Their Relation to Ceramic Attribution", X-ray Spectrometry, 16, 229-231.

Yap, C.T., 1987b, "X-ray fluorescence studies on low-Z elements of Straits Chinese porcelains using Fe-55 and Cd-109 annular sources", X-ray Spectrometry, 16, 55-56.

Yap, C.T., 1987c, "Non-destructive Spectrometric Determination of Trace Element Concentration of Rubidium, Strontium, Yttrium, Zirconium and Niobium in Ceramics", Z. Naturforsch, 42a, 1253-1256.

Yap, C.T., 1988 "A quantitative spectrometric analysis of trace concentrations of manganese and cobalt in ceramics and the significance of As/Co and Mn/Co ratios", Journal of Archaeological Science, 15, 173-177.

Yap, C.T., 1992, "Multi-Variate Analysis of Trace Elements from XRF Studies for Classification According to Origin", Applied Spectroscopy, 46, 843-847.

Yap, C.T. and Hua, Y., 1992, Applied Spectroscopy, 46, 1488

Yap, C.T. and Hua, Y., 1994, Archaeometry, 36, 63

Yap, C.T., Saligan, P.P., and Leenanupan, V., 1987, "A Rapid EDXRF Method of Simultaneous Quantitative Elemental Analysis Using an Annular Cd-109 Source", Applied Spectroscopy, 41, 906-908.

Yap, C.T., and Tang, S.M., 1984a, "X-ray fluorescence analysis of Chinese porcelains from K'ang Hsi to modern times using Cd-109 source", Applied Spectroscopy, 38, 527-529.

Yap, C.T., and Tang, S.M., 1984b, "X-ray fluorescence analysis of modern and recent Chinese porcelains", Archaeometry, 26, 78-81.

Yap, C.T., and Tang, S.M., 1985a, "Energy dispersive X-ray fluorescence analysis of Chinese ceramic glazes using Am-241", Archaeometry, 27, 61-63.

Yap, C.T. and Tang, S.M., 1985b, "Quantitative XRF Analysis of Trace Barium in Porcelains by Source Excitation", Applied Spectroscopy, 39, 1040-1042.

Yap, C.T. and Tang, S.M., 1985c, "Zn Kα/Rb Kβ Ratio of Ch'ing, Republic and Modern Chinese Porcelains", X-ray Spectrometry, 14, 157-158.

Young, S., 1956, "An analysis of Chinese blue-and-white", Oriental Art, 2, 43-47.

Yu, J. and Yang, Y., 1992, "Ancient Chinese Porcelain Appreciation Companion", (Xinhua Publishing: Beijing). (in Chinese)

Yu, K.N. and Miao, J.M., "Non-destructive analysis of Jingdezhen blue and white porcelains", 1996a, Archaeometry, 38, 2, 257-262.

Yu, K.N. and Miao, J.M., "Non-destructive and quantitative investigation of Jingdezhen blue and white porcelains Using EDXRF", 1996b, Journal of X-ray Science and Technology, 6, 167-171.

Yu, K.N. and Miao, J.M., "Non-destructive analysis of Jingdezhen blue and white porcelains of the Ming Dynasty Using EDXRF", 1996c, X-ray Spectrometry, Vol. 25, 281-285.

Yu, K.N. and Miao, J.M., "Locating the origins of blue and white porcelains using EDXRF", 1997, Applied Radiation and Isotopes, 48, 959-963.

Yu, K.N. and Miao, J.M., "Multivariate analysis of the Energy Dispersive X-Ray Fluorescence results from blue and white Chinese porcelains", 1998, Archaeometry, 40, 331-339.

Yu, K.N. and Miao, J.M., "Retrospective study on the feasibility of using EDXRF for the attribution of blue and white porcelains", 1999a, X-ray Spectrometry, 28, 19-23.

Yu, K.N. and Miao, J.M., "Characterization of blue and white porcelains using the Mn/Fe ratio from EDXRF, with particular reference to porcelains of the Xuande Period (1426 to 1435 A.D.)", 1999b, Applied Radiation and Isotopes, 51, 279-283.

Zhang, Fukang and Cowell, M., 1989, "The sources of cobalt blue pigment in ancient China", Sciences of Conservation and Archaeology, 1, 23-27. (in Chinese)

Radiation in Art and Archeometry
D.C. Creagh and D.A. Bradley (editors)

Neutron and synchrotron radiation studies of archaeological objects

W. Kockelmann[a,b], E. Pantos[c], and A. Kirfel[a]

[a]Mineralogisch-Petrologisches Institut, Universität Bonn,
D-53115 Bonn, Germany

[b]ISIS Facility, Rutherford Appleton Laboratory,
Chilton, Didcot, OX11 0QX, UK

[c]SRS Facility, Daresbury Laboratory,
Keckwick Lane, Warrington, WA4 4AD, UK

Time-of-flight neutron and synchrotron X-ray diffraction were used for fingerprint determinations and quantitative mineral phase analyses of archaeological objects. Both neutron and X-ray diffraction techniques have their advantages and drawbacks when used in archaeological research. Neutron diffraction allows non-destructive analysis of complete and unprepared objects. Synchrotron X-ray diffraction can be used for fast and high-resolution data collection on small amounts of powder samples, surfaces or thin sections. This paper concentrates on the introduction of the white-beam neutron diffraction technique applied on archaeological pottery. X-ray diffraction results from both laboratory and synchrotron sources are given for comparison.

1. INTRODUCTION

X-ray and neutron diffraction are well known experimental methods for investigating minerals or other inorganic and organic materials wherever their crystal structures are of interest in the wide field of material science and industrial applications. The knowledge of the crystal structure of a material or the abundance of different known phases in a multi-phase mixture of minerals are not only fundamental for the understanding of the physical and chemical properties of the material but can also help to fingerprint the origin of objects of archaeological interest.

In the archaeological context, powder diffraction methods are ideal for characterising pottery finds which are of fundamental importance to archaeologists for dating excavations sites and/or for revealing trading pattern associated with cultural and technological exchange between peoples and countries [1,2].

Ancient ceramic fragments are found in large quantities but in order for ceramics to be used as markers they have to be characterised first. Provenance and approximate dating of pottery is often possible on the basis of stylistic attributes. However, this is difficult for archaeologically important plain pottery, in particular if prehistoric artefacts are found in areas where archaeological records are scant. Element and/or mineral identification techniques such as microprobe analysis, Mössbauer spectroscopy and neutron activation analysis have been utilised with considerable success to characterise archaeological finds [2]. Diffraction methods are also important characterising tools, ideal for studying the mineral phase composition of pottery, the crystal structure details of the constituent minerals themselves and the characteristic distribution of crystallites in the material. Different types of radiation, such as neutrons, X-rays and electrons, can be used for the characterisation of ceramics taking advantage of the fact that each crystalline phase in the material exhibits a unique diffraction pattern. As the observed material pattern is the superposition of the single phase patterns it may well be characteristic enough to identify the provenance of a find, for example, to help discern locally manufactured from imported pottery or for distinguishing ancient from modern objects. Moreover, quantitative evaluation of the data allows the determination of the mineral phase abundance in clay and pottery products and, hence, it may yield information about the making of the pottery, in particular about firing processes which are accompanied by mineral transformations or phase transitions during the heat treatment.

Whether or not a diffraction experiment is a reasonable option, and if so with which kind of radiation, depends on the underlying diffraction physics. Due to the very different interactions of neutrons and X-ray photons with matter, the absorption of the respective radiation differs by orders of magnitude. Electron and X-ray diffraction can be applied to the sample surfaces and thin sample sections. X-rays are also used with powder specimens which have to be extracted from the object under study. In particular, high intensity X-ray radiation produced at a synchrotron source requires only very small amounts of sample material for the study. This means that only a minimum quantity of material has to be removed from the object. Nevertheless, the possibility that the extracted material may not be representative for the sample as a whole, as well as the prospect of damaging a possibly unique and precious object, may often be the reason for refraining from such diffraction experiments. In this case neutrons may well be more useful because they penetrate large volumes of bulk material without substantial loss of intensity.

X-ray diffraction using laboratory sources is commonly applied for characterisation of archaeological ceramics [2], in particular for mineral phase identification, and to a lesser extent, for quantitative analysis of the weight or volume phase fractions. X-ray diffractometers at synchrotron radiation (SR) sources are also increasingly used for quantitative analysis [3] taking advantage of the wavelength tunability, the low natural divergence as well as the high intensity and brilliance of SR beams. Neutron diffraction on the other hand, has hardly been used so far for quantitative studies of the material properties of archaeological artefacts. Neutron diffraction can be particularly useful in archaeometric research., The experimental set-up is simple, the sample does not need to be moved, and large objects can be accommodated. This applies to energy-dispersive rather than angle-dispersive diffractometry which employs well established diffraction methods at neutron and SR sources, i.e. experimental techniques, data reduction procedures, and data analysis software are well developed and ready to use.

The aim of this paper is to show how archaeological objects can be studied on existing diffraction instruments at neutron and synchrotron sources using white radiation in energy-dispersive and monochromatic radiation in angle-dispersive mode. Examples include medieval 13-15th century German Rhenish stoneware and earthenware pottery, Neolithic potsherds

from Central Russia dating from 7000-4000 BP (years before present) and Attic potsherds dating from 6^{th}-3^{rd} century BC. The main emphasis is on the non-destructive diffraction analysis of original and unprepared archaeometric finds on the white-beam time-of-flight (TOF) neutron powder diffractometer ROTAX at the pulsed source ISIS [4] at the Rutherford Appleton Laboratory, United Kingdom. Neutron results are compared to powder diffraction results obtained at the SRS synchrotron facility [5] at the Daresbury Laboratory, United Kingdom, collected in angle-dispersive mode. The studies are further complemented by conventional laboratory X-ray (CuK_α) powder diffraction data.

2. QUANTITATIVE DIFFRACTION ANALYSIS OF ARCHAEOLOGICAL OBJECTS

This section gives an overview how to analyse diffraction patterns quantitatively. This survey is naturally limited to powder diffraction analysis, since most archaeological objects, such as pottery, are of polycrystalline nature.

2.1. Diffraction pattern as a fingerprint

In a powder diffraction experiment, radiation is coherently scattered by periodic arrangements of scattering centres, such as atoms in a crystal. The scattered radiation occurs and is reinforced only under characteristic diffraction angles so that a diffraction pattern is produced. Usually this pattern shows rotation symmetry with respect to the incident beam. The radiation used can be electromagnetic, as in the case of X-rays, or can consist of particles like neutrons or electrons. The only prerequisite for the diffraction process is that the radiation has a wavelength comparable in magnitude with the spacings between atoms in a crystal structure. The resulting pattern of diffraction peaks is a characteristic fingerprint in the form of intensity versus diffraction angle (angle-dispersive) or intensity versus radiation energy (energy-dispersive). In this way, the fingerprint is characteristic for the whole assembly of crystalline phases in the sample.

Both angle- and energy-dispersive modes obey Bragg's law:

$$\ddot{e} = 2 \cdot d_{hkl} \cdot \sin\grave{e} \qquad (1)$$

In the angle-dispersive mode using monochromatic radiation, i.e. at a constant wavelength λ, one obtains diffraction peaks at varying scattering angles 2θ, depending on the distribution of the lattice plane spacings d_{hkl}. In the second case, the energy-dispersive mode, white radiation with a broad range of wavelengths, scattered at a fixed angle 2θ, gives rise to a reflection whenever a combination of wavelength and d-spacing meets Bragg's law. Thus, one obtains intensity peaks at varying energies. In both modes, the measured pattern of Bragg reflections exhibits peak positions and peak intensities being characteristic for one or more mineral phases in the sample. This fingerprint may therefore identify archaeological objects like a bar-code line-pattern identifies a supermarket product, provided that the experimental pattern has been collected reproducibly and from a powder sample representative of the object.

2.2. The information in the fingerprint

For a single phase sample, e.g. quartz, the reflection pattern provides information in terms of peak positions and peak intensities. According to Bragg's law, the former are directly related to the crystal lattice dimensions of the phase, i.e. to its unit cell. Apart from experimental factors, the peak intensities are determined by the characteristic atomic arrangement in the unit cell of the phase. The intensity distribution of the pattern is therefore characteristic of a known structure, or vice versa, the structure can be determined from the diffraction intensities. Given the unit cell dimensions, Bragg's law also implies that the abundance of reflections in a powder pattern is determined by the symmetry of the crystal structure because reflections from different, but equally spaced lattice planes superimpose. This means that the higher the crystal symmetry, the lower the number of reflections in the pattern. Moreover, the line shapes and integrated intensities can also contain information about the microstructure of the sample, e.g. the size and orientation distribution of the crystallites in the sample.

Since the pattern of a multiphase material can be considered as a fraction-weighted superposition of individual phase patterns, all this information can naturally be severely obscured by peak overlapping giving rise to a complex diffraction pattern which is not easy to unravel. This applies in general to pottery or clay samples which typically contain minerals of low symmetry, such as feldspars and clay minerals. The diffraction patterns of the latter can often be identified by their broad reflection profiles due to very small particle sizes ($<0.2\mu m$). Under these circumstances it is evident that high resolution diffraction is required. The fingerprint also depends on the type of radiation used: X-rays, neutrons, and electrons produce different reflection intensities due to their distinctly different interactions with matter. Finally, experimental conditions such as type of radiation source, primary beam divergence, wavelength, sample geometry, and detector system influence the appearance of the diffraction fingerprint. Time-of-flight neutron diffraction patterns collected at a pulsed spallation source, for example, exhibit reflection peak shapes which are very characteristic for this kind of source.

2.3. Qualitative and quantitative analysis of the diffraction pattern

The first step in the analysis is reflection indexing in order to determine the combination of phases present in the sample. Association of measured peak positions with calculated or observed positions of pure single-phase fingerprints can be made using database search-match routines. Once the phases are identified, the subsequent step is quantitative phase analysis which assesses the amount of each phase in the sample material, either as volume or weight fraction assuming that: (e.g. [6])

(i) each phase exhibits a unique set of diffraction peaks

(ii) the intensities belonging to each phase fraction are proportional to the phase content in the mixture

A full diffraction analysis can, in addition to the phase fraction determination, include the refinement of structure parameters of individual mineral phases, such as lattice parameters and/or atom positions in the unit cell.

A well established technique of quantitative phase analysis from powder diffraction patterns is the full-pattern Rietveld refinement [7,8]. The Rietveld method allows the refinement of phase specific structure parameters along with experiment specific profile parameters by fitting

a calculated model pattern to the entire observed diffraction pattern using the least-squares algorithm which minimises the quantity:

$$D = \sum_i g_i (y_i^{obs} - y_i^{calc})^2 \qquad (2)$$

The summation index i runs over all observed intensities y_i^{obs}. The weights g_i are taken from the counting statistics. y_i^{calc} are the calculated model intensities defined by instrumental and structural parameters, the latter including weight fractions in a multiphase refinement. By refinement of reflection profile parameters, crystallite size and microstrain effects can be studied. The Rietveld routine calculates figures of merit which indicate the quality of the fit of the entire model pattern to the entire observed diffraction pattern. A meaningful criterion is the weighted profile R-value R_{wp}:

$$R_{wp} = \left\{ \frac{\sum g_i (y_i^{obs} - y_i^{calc})^2}{\sum g_i (y_i^{obs})^2} \right\}^{1/2} \qquad (3)$$

which should converge to a minimum. There are a number of programs available, many of them public domain, which can be used for X-ray as well as for neutron diffraction data analysis, e.g. the GSAS General Structure Analysis System [9] or FULLPROF [10]. The quantitative phase information is obtained assuming that the weight fraction W_p of the p-th phase in a mixture is given by the normalised product: [6]

$$W_p = S_p Z_p M_p V_p / \sum_i S_i Z_i M_i V_i \qquad (4)$$

where S_p, M_p, Z_p, V_p are the refined Rietveld scale factor, the mass of the formula unit (e.g. SiO_2), the number of formula units per unit cell and the unit cell volume, respectively, of that phase p. The summation in the denominator accounts for all crystalline phases. Thus, in the case where not all crystalline components can be identified or in the presence of amorphous phases, the Rietveld analysis yields relative phase fractions only with respect to the crystalline phases contained in the model. The main advantages of quantitative phase analysis by the Rietveld method are that:

(i) no internal standard is required;

(ii) crystal structure models are included explicitly. Structure parameters can be refined along with weight fractions of mineral phases.

(iii) Overlapping peaks and even peak clusters are handled without difficulty.

(iv) Preferred orientation of crystallites can be considered in the model.

It may happen that one or more phases have been identified using reflection positions and extinction rules (yielding space group and lattice parameters), but structure models do not fit the experimental data because, for instance, powder grains are not statistically distributed in the object or simply because there are no complete structure models available, as it is the case for some clay minerals like illite. With a program like GSAS, Rietveld analysis of modelled phases can be concurrently performed with a so-called LeBail refinement of 'unmodelled' phases. This full-pattern LeBail fit uses space group and lattice parameters as constraints but does not explicitly

refer to crystal structure models and, consequently, does not yield phase fraction values for those phases.

2.4. Determination of the amorphous content

Archaeological objects such as pottery may also contain a vitreous component, which is often silica glass being characterised by an irregular network of SiO_4 tetrahedra. Extraction of the amorphous silica content can be an important part of the characterisation of pottery because vitrification is dependent on firing temperature and firing duration. In general, amorphous structures cannot be Rietveld refined like crystalline ones. For the case of amorphous silica glass, however, it was shown that the Rietveld method can be applied to estimate the amorphous phase fraction in a ceramic [11]. This application is based on a simple "nanocrystalline" model as satisfactory approximation for the vitreous component, which means that the calculated diffraction spectrum reproduces the experimental one. A silica glass phase fraction is refined along with the crystalline phase fractions. It should be noted, however, that the results are to be taken cautiously and rather be considered only as phase fraction estimates since the calculated glass pattern depends on the type of Rietveld background function used. In principle, the method is not limited to silica glass, however, other types of amorphous structures can only be treated in the same way after constructing appropriate nanocrystalline models.

Table 1
Properties of neutrons and X-ray photons

	neutron	X-ray photon
mass	1.675×10^{-27} kg	0
charge	0	0
spin	½	0
interaction with	nuclei and magnetic moments	electron distributions
scattering cross section	small, irregular dependence on element number	high, increasing with element number
absorption	generally low	considerable

2.5. Interactions of neutrons and X-rays with matter

The process of diffraction by a crystal with respect to geometrical diffraction conditions and systematic reflection extinctions caused by crystal symmetry, is the same for electrons and neutrons (elementary particles with a deBroglie wavelength) and photons (X-ray radiation). For the latter two, also the principles of data collection and data analysis techniques are very similar. However, the interaction mechanisms with matter are fundamentally different for the two probes which are therefore able to provide partially complementary information.

The different interactions not only shape the diffraction fingerprints in a characteristic manner, but also determine the range of possible applications. Table 1 contains some properties of neutrons and X-rays which are of relevance in the context of material research with diffraction methods. One major difference between neutrons and X-rays is that neutrons

are scattered by the nuclei whereas X-ray photons are scattered by the atomic electron distributions. Thus, the neutron probe 'sees' the structure as an arrangement of point scattering centres with scattering powers (neutron scattering lengths), that are momentum transfer independent but depend on the nature of the nuclei. As a result, neutron scattering lengths vary between different isotopes and randomly through the periodic system. In contrast, X-ray radiation 'sees' an atom as an extended electron density distribution whose diffraction power (form factor) depends on the momentum transfer and is proportional to the atomic number Z of the element.

The neutron-nucleus interaction, and hence absorption, is usually weak in neutron diffraction experiments. Compared to X-ray photons, absorption coefficients for neutrons are some three orders of magnitude smaller and, consequently, much larger amounts of sample are needed for neutron scattering measurements. While this may be a drawback on one hand, it is of great advantage on the other hand, because due to their ability to penetrate matter, neutrons are well suited for the analysis of the bulk of a thick sample several centimetres in diameter, be it a powder sample or a solid piece of material. In comparison, X-rays have a penetration depth depending on their energies. Conventional CuK_{α} source X-rays are absorbed within approximately 40 microns of the surface of the object [12]. Bulk analysis with X-rays can therefore only be done on small amounts of powdered sample extracted from the interior of the object, but glazes and coatings of objects can be studied non-destructively to a depth determined by the value of the wavelength.

2.6. Summary

Standard diffraction analysis techniques can be used in archaeological research to quantitatively determine phase fractions, refine crystal structure parameters and estimate amorphous phase contents. Neutron and X-ray diffraction yield both similar and complementary information with respect to mineral phase structure details, but are distinctly different considering the range of applications: Neutrons are well suited for bulk measurements whereas X-rays are appropriate for surface and/or powder studies.

3. INSTRUMENTAL AND EXPERIMENTAL REQUIREMENTS

This section describes the experimental requirements for recording diffraction fingerprints of archaeological objects. As already implied, Bragg's equation suggests both angle-dispersive and energy-dispersive instrumental configu-rations may be used for neutrons and X-rays.

3.1. Neutron radiation sources

Thermal neutrons for research purposes are traditionally produced by nuclear fission in nuclear reactors which are usually operated as continuous neutron sources. A more recent development of neutron production are accelerator based pulsed sources which generate neutrons in a totally different manner [13]: Protons are accelerated to high energies and directed onto a metal target. Hitting the target nuclei the protons produce neutrons by a spallation (or splintering) process. These initially fast neutrons are then slowed down in a moderator and guided to experiment stations. ISIS, a pulsed neutron source at the Rutherford Appleton Laboratory in the United Kingdom, is a 50 Hertz source producing 50 sharp neutron

pulses every second. This time structure of a neutron beam is an important feature of the spallation source, allowing both most efficient use of the neutrons produced and the performance of energy-dispersive, time-of-flight measurements as a natural consequence.

3.2. X-ray radiation sources

X-rays are generated either in the laboratory (X-ray tubes or rotating anode devices) or at synchrotron radiation (SR) sources. X-ray radiation produced with conventional laboratory equipment is characteristically monochromatic (e.g. CuK_α, λ=1.514 Å), hardly polarised and of moderate intensity; it is the fluorescence radiation of the anode material. In contrast, SR sources are based on electrons or protons accelerated to high energy [14] which emit radiation over a wide spectrum from infrared to hard X-rays. The main (intrinsic) properties of SR are high intensity (several orders of magnitude more than laboratory sources) , low vertical divergence, horizontal linear polarisation, wavelength tunability and a well defined time structure. These properties make SR beams attractive tools for diffraction experiments on condensed matter, e.g. on archaeological material, because beam cross sections as small as 0.1 micrometers [15], very high angular resolution and fast data collection times can be achieved.

3.3. Angle-dispersive neutron and SR diffractometers

Using monochromatic radiation, polycrystalline archaeological material can be studied on angle-dispersive neutron and SR diffractometers. The sample material must be extracted from the archaeological object, powdered and mounted on the diffractometer, either in a capillary or on a flat sample holder. Both kinds of sample holders are often rotated in order to increase the radiation acceptance or to reduce preferred orientation effects on the powder intensities. Neutron diffraction generally requires large sample quantities (several mm^3) in comparison to SR diffractometers which can cope with much smaller amounts. The diffracted neutrons or X-rays are counted as a function of the scattering angle using either a movable single detector or position sensitive detector devices (PSD) such as a multi-wire proportional counter, a CCD camera or an image plate. PSD's can be movable or stationary, but in any case they simultaneously record all reflections that are accessible within a certain 2θ range.

3.4. Energy-dispersive neutron and SR diffractometers

Powder material of archaeological interest can also be studied with energy-dispersive neutron and X-ray instruments using a polychromatic primary beam. The scattered radiation intensity is measured as a function of energy at a fixed angle 2θ so that, in principle, only a single energy-resolving detector is needed. Since, in the neutron case, the energy is related to the neutron velocity, the energy dispersion can be expressed on a time scale, i.e. by measuring the (energy dependent) time-of-flight a neutron needs to hit the detector. The energy-dispersive set-up is stationary and allows the investigation of samples other than powders, even solid pieces of material or whole objects. This is because the detector records all accessible Bragg reflections whilst 'looking' along a single scattering direction with respect to the same surface/volume element of the sample. White-beam diffraction stations are often equipped with more than one detector. Even whole banks of detectors, position-sensitive linear or area detectors are positioned at different scattering angles, i.e. the scattered radiation is recorded as a function of both energy and scattering angle. This 'multibank', angle-and-energy-dispersive set-up permits an enormous reduction of data collection times, and, since

detectors at different angles cover different d-spacing regions, a wider range of reflections is then recorded at the same time.

3.5. Method of choice for diffraction analysis of archaeological material

Which kind of instrumentation is useful for the diffraction analysis depends on the specific archaeological problem to be addressed. In many cases, when conservation of the object is not paramount, a sufficient (small) amount of powder material may be extracted from an object for conventional X-ray phase analysis. If there is only a small quantity of material available, or if identification of trace minerals is required, high resolution and high intensity angle-dispersive SR might be taken into consideration. A white highly collimated SR beam allows for the non-destructive study of surface layers of objects. Both local details or variations of mineral composition as a function of position can be studied. Applications of an energy-dispersive multi-detector set-up using hard X-rays for imaging a crystalline phase distribution inside ancient artifacts are described elsewhere in this volume [16].

The neutron time-of-flight technique (TOF), on the other hand, is the method of choice if the average mineral phase composition of the interior/bulk of an object is of archaeological interest, and even more so, if it is important not to impair a precious object by material extraction or X-ray radiation damage. A stationary, non-destructive, energy-dispersive neutron diffraction experiment on, for example, an intact pitcher, is as simple as shown in Figure 1. A large volume of the object's wall is illuminated and neither object nor detector need to be moved during data collection. The neutrons easily penetrate through a painted, glazed or corroded surface and are scattered by the bulk volume. Most primary beam neutrons pass through the object's front wall without interaction. In order to prevent unwanted scattering signals from the back of the pitcher, a secondary collimating device between object and detector or an especially high neutron absorber (such as boron carbide) inside the object can be used (Figure 1). This completely stationary experimental set-up is easy to realize and the sample object is not in danger of being accidentally damaged from any diffractometer or sample holder movements. Thus, TOF-diffraction is a new tool in archaeometry which should be taken into consideration when size and shape, uniqueness, value, but also chemical composition of the object, e.g. metallic objects such as coins, preclude the application of more conventional diffraction methods.

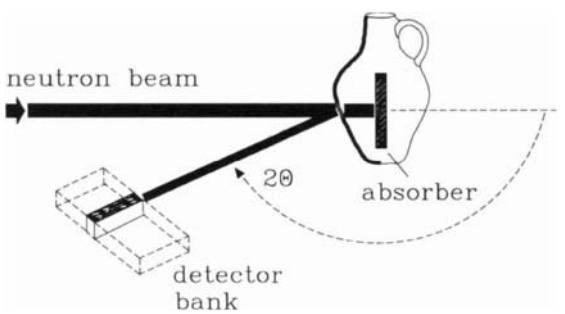

Figure 1.
Schematic TOF neutron diffraction experiment on an archaeological object. One detector tube (channel) of a multi-detector bank is indicated.

Table 2
Properties and application range of time-of-flight (TOF) neutron diffraction and angle-dispersive SR diffraction.

TOF neutron diffraction	SR X-ray diffraction
low primary intensity	high primary intensity
low absorption	high absorption
medium d-resolution	high d-resolution
low spatial resolution	high spatial resolution
stationary, fixed sample & detectors	moving sample & detector(s) or stationary area detector
large powder samples	small powder samples
bulk of thick samples	surface of thick samples at long λ, internal volume at very short λ
non-destructive	destructive for powder diffraction, non-destructive for surfaces

A summary of the properties and the application range of neutron TOF-diffraction as compared to angle-dispersive SR-diffraction is given in Table 2 and details of the TOF-technique and its realisation on the diffractometer ROTAX [17] at ISIS, operated by the University of Bonn, Germany, are outlined in the following section.

4. TOF-ND: Time-of-flight neutron diffraction at ROTAX

Diffraction instruments at spallation sources always use the time-of-flight technique. On ROTAX, neutron wavelengths in the range λ=0.5 to 5 Å relate to neutron velocities v=8000 to 800 meters per second by the de Broglie equation

$$\lambda = h / m_n v \tag{5}$$

h denotes Planck's constant, m_n the neutron mass. For a given total flight path L from source to detector, the neutron velocity and thus its kinetic energy is obtained by the measurement of the flight time t assuming that the neutron was elastically scattered by the sample:

$$v = L / t \tag{6}$$

On ROTAX, the flight path L is about 15 m, therefore time-of-flights are in the range $2 < t <$ 20 milliseconds. Combining (5) and (6) with Bragg's equation (1) yields a direct relation between time-of-flight and crystallographic d-spacing d_{hkl}:

$$d_{hkl} = t/505.56\, L \sin\theta \tag{7}$$

in which t is measured in microseconds, L in meters, and d_{hkl} in Å. Thus, for a given path L and any single detector tube (or detector channel) at a scattering angle 2θ (Figure 1) the TOF measurements yield a diffraction pattern in form of intensities versus d-spacing which can, in principle, be transformed into the usual intensity versus 2θ representation.

The instrument's efficiency is significantly increased by using multiple-detector devices,

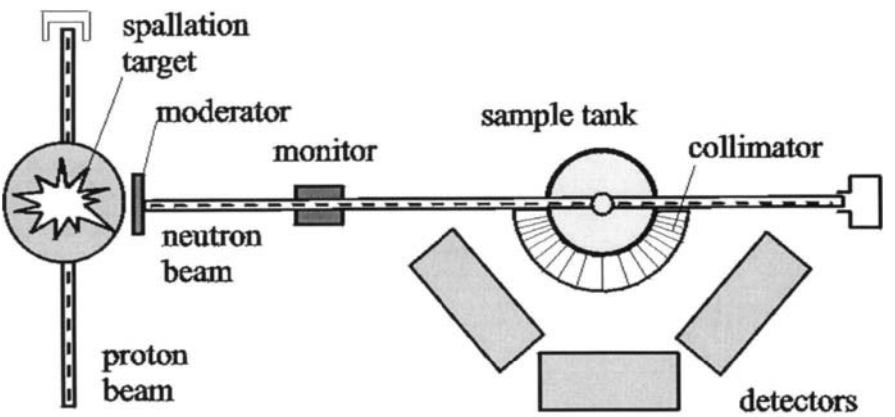

Figure 2. Schematic set-up of the ROTAX diffractometer

or even better, position-sensitive detector (PSD) banks at different 2θ-angles. ROTAX is currently equipped with three linear position-sensitive strip detectors in a distance of about 1 m from the sample (Figure 2). Each of the detectors registers the scattered neutrons with respect to both time-of-flight (t) and position (2θ). The initial result, the raw data, is a two dimensional position-time array of counts which must be normalised to the monitored spectral distribution of the primary beam. Each detector features 256 position channels, in each of which a full TOF pattern (as obtained by a single counter tube) is accumulated according to equation (7) with θ_i and total flight path L_i for channel (i). All these different detector channels, which cover different d-value regimes, can be individually analysed, for example, to check for texture effects or grain distributions. In practice, however, all neutron counts assigned to the same d-spacing are combined ('focused') to generate a one-dimensional TOF diffraction pattern for each detector bank. Figure 3 shows diffraction patterns typical for a two-PSD set-up on ROTAX, one detector bank at forward scattering position to cover larger d-spacings between 1 and 15 Å, the other in backscattering position to cover smaller d-spacings between 0.3 and 3 Å.

At ROTAX, the standard incident beam cross section is 20 x 50 mm. Thus, depending on the sample thickness the investigated sample volume amounts to several thousand mm^3 which is in general representative for the whole sample. To reduce background from air scattering the sample is usually mounted in an evacuated sample tank of about 40 cm diameter and 60 cm height. The flight paths from source to sample (14.0 m - 16.0 m) and from sample to detectors (0.5 m - 1.6 m), respectively, are variable. Accessible 2θ-detector angles are between 3° and 175°. A radial collimator between sample tank and detector banks prevents neutrons which are diffracted by scattering centers outside a 90 mm radius around the sample position from being registered.

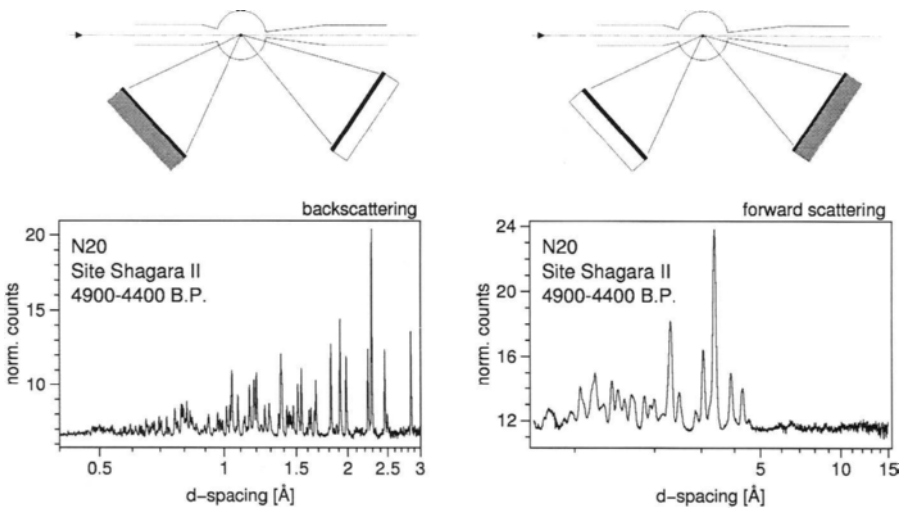

Figure 3. Experimental set-up on ROTAX with two position-sensitive detectors. Examples of TOF diffraction patterns from Russian ceramics (left: backscattering detector; right: forward scattering detector).

Due to its modular design and large sample tank, ROTAX is especially suited for the investigation of 'difficult' samples with respect to size and shape. A large archaeometric object, e.g. a ceramic pitcher, is simply aligned on a laboratory table with the material to be irradiated at the centre of the sample tank. Smaller potsherds or fragments can also be contained in pockets of vanadium foil and suspended from a sample stick. In the case of an intact vessel, scattering from the opposite wall is avoided by the radial collimator if that wall is outside a 90mm radius about the sample tank centre. Alternatively, the neutron beam can be completely absorbed inside the object by absorbing boron carbide (see Figure 1) which is available as slabs or powder. In this case forward scattering from the sample position itself is, of course, also restricted due to absorption. After evacuation of the sample tank, data collection (typically 5 hours) and data reduction (normalisation, focusing) are performed in a

fully automated procedure. The diffraction patterns are ready for separate or combined analysis by a TOF Rietveld refinement program that is able to handle the special TOF reflection peak profiles. Examples are GSAS [9] or FULLPROF [10] which refine phase weight fractions and/or structure parameters.

Summary

TOF neutron diffraction is a non-destructive tool for phase examination of complete, intact archaeological artefacts. The method lacks spatial resolution and consequently gives phase information which is averaged over an extended sample volume. TOF diffraction is well suited for accurate quantitative phase analysis and structure refinement.

5. DIFFRACTION STUDIES ON GERMAN MEDIEVAL EARTHENWARE AND STONEWARE CERAMICS. A FEASIBILITY STUDY.

Several medieval stoneware and earthenware pottery fragments from the Rhineland have been analysed to examine the potential of TOF neutron diffraction for archaeological research [18]. Highly fired ceramics are well suited because their phase contents are generally simple and crystal structures of the phases are known, i.e. the diffraction patterns are clear. For stoneware production, clay and temper are fired up to about 1400 °C to make the bodies very hard and impervious to water [19]. Up to these temperatures, some of the source material minerals undergo partial or complete transformations and new vitreous and/or crystalline phases are produced, the latter including mullite and cristobalite, whose abundance may help elucidate details of the heat treatment.

The chosen material is also well suited because there are plenty of finds available. There is hardly any other class of archaeological artefact that has such a wide geographical and social distribution over northern Europe [19]. During the 13^{th} to 19^{th} centuries, Rhenish ceramics were mass-produced and products as well as manufacturing knowledge were spread around Europe. Excavated waster heaps at the prominent pottery sites in the Rhineland provide many artefacts from the stoneware development period 13^{th} to 15^{th} century. Its different development stages are expected to be reflected in the mineral phase compositions of early proto-stoneware finds. The present study focuses on the differentiation of stoneware types by their mineral compositions.

In order to evaluate TOF neutron diffraction as a new non-destructive archaeometric method, we analysed the mineral phase abundance and silica glass fractions of several medieval pottery fragments excavated at Rhenish pottery centres in Siegburg and Brühl (Figure 4). Provenance and dating information of the objects of known archaeological classification are given in Table 3. Five representative 13 - 15th century fragments, excavated from a 'sherd mountain' (Scherbenhügel) in Siegburg by B. Beckmann in the 1960's [20], were investigated. Siegburg ceramics have been studied extensively before, by neutron activation analysis [21], light microscopy and X-ray diffraction [22]. Between the 13th to 16th century, Siegburg, a town east of the river Rhine, was one of the main pottery production centres and was involved in the development of stoneware technology in Europe [19]. The manufacturing of stoneware required refined material composition and highly developed firing techniques in order to achieve the necessary kiln temperatures for over a long time. To a smaller extent, stoneware was also produced and excavated in Brühl, a town close to Siegburg on the opposite side of the

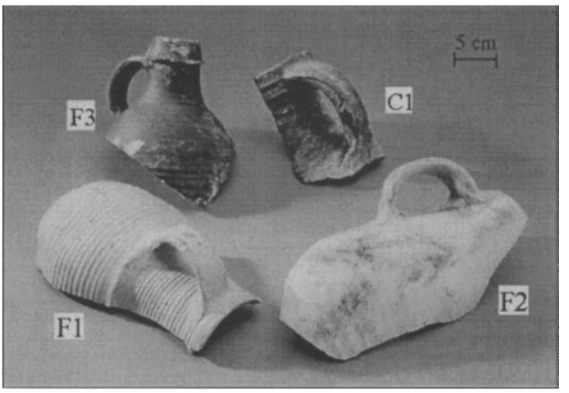

Rhine. Brühl was not as prominent as Siegburg, but plain and ordinary ceramics for every day life purposes were made. Two stoneware fragments from Brühl were selected from a series of

Figure 4. Rhenish pottery sherds.

'experimental' pottery, which was produced within a time period of 50 years in the 13th century, and studied with neutrons on ROTAX, SR radiation at Daresbury Laboratory and laboratory X-rays. The latter diffraction experiments are part of a study to uncover the process for making the characteristic purple-violet engobe of the Brühl stoneware ceramics [23].

The TOF neutron measurements on the Siegburg and Brühl samples were designed to answer two questions:

1. Is the quality of scattering information from a large, penetrated sample equivalent to that from a powder sample bathing in the beam, i.e. is a set-up using a large fragment (Figure 1) allowed?
2. Do the non-destructively measured data provide useful information fit to compare with and complement other available information, e.g. from X-ray diffraction studies?

5.1. Data collection and analysis

Preparation dependent TOF experiments on ROTAX were designed to find out whether or not samples, not fully bathing in the beam, yield data that are considerably compromised by systematic errors. To this purpose different preparations of the same Siegburg stoneware fragment F1 (see Table 3) were studied using a neutron beam of 20x50 mm cross section and:

a) a fine ground powder sample, extracted from F1, contained in a cylindrical vanadium can of 10 mm diameter and 70 mm height, bathed in the beam (standard set-up for powder diffraction analysis)

b) a small chip of F1, 10x40 mm, fully bathed in the beam

c) the large remaining fragment F1 (Figure 4), illuminated by the beam.

Each of the three samples was exposed for about 12 hours using exactly the same experimental set-up with two detectors banks in forward and backscattering position, respectively. The Rietveld fitted diagrams are shown in Figure 5.

The remaining ceramic sherds listed in Table 3 were measured on ROTAX as received, i.e. without any prior sample preparation, for about 5 hours each. Powder samples of the Siegburg fragment were also analysed on an X-ray, Siemens D5000, diffractometer with CuK_α radiation. A thin slice of one of the Brühl samples (B1) was also studied on the high intensity SR X-ray protein crystallography station 9.6 at Daresbury Laboratory in order to analyse microstructural variations and identify phases. Conventional diffractometry of powders extracted from the body and the engobe was also carried out.

Structure refinements using the neutron and X-ray CuK_α data were carried out using the program GSAS [9]. Figure 6 shows Rietveld analysed forward scattering neutron patterns of two of the sherds. The starting refinement model was based on the presence of quartz, mullite and cristobalite, according to earlier X-ray diffraction studies on comparable Siegburg pottery [22]. The structure parameters of quartz [24], mullite [25] and cristobalite [26] were taken from the Inorganic Crystal Structure Database [27]. Refined parameters were: phase fractions, overall temperature parameters for the abundant components quartz and mullite, and atom positions of mullite due to the less certain structure data. Phase fractions of vitreous silica components indicated by more or less pronounced background modulations of the diffraction patterns were refined using the method proposed by LeBail [11] (see paragraph 2.4). Table 4 contains refined weight fractions as well as ratios M/Q=w(mullite)/w(quartz) as characteristic indicators of the crystalline material. Realistic estimates of the relative weight fraction uncertainties are about 2% for all inspected samples. Consequently, the refined weight fractions of cristobalite in the Siegburg samples are hardly significant.

Table 3
List of pottery fragments from the Rhineland, investigated on ROTAX. The samples were kindly provided by E. Hähnel, Freilichtmuseum Kommern (Siegburg samples) and H. Kutzke, Mineralogical-Petrological Institute, Bonn University (Brühl samples from the Museum für Alltagsgeschichte Brühl, Germany).

no	excavation site	date	description
F1	Siegburg F	About 1300	near-stoneware (Faststeinzeug) fragment of a jug, corrugated surface
F2	Siegburg F	15th century	real stoneware (Steinzeug) fragment of jug
F3	Siegburg F	15th century	earthenware (Irdenware) fragment of single-handled bottle
C1	Siegburg C	13th century	upper piece of earthenware (Irdenware) jar, brown coloured surface
G1	Siegburg G		early-stoneware (Frühsteinzeug) rim fragment of jar
B1	Brühl	13th century	stoneware (Steinzeug) , jar bottom fragment purple-violet engobe
B2	Brühl	13th century	stoneware (Steinzeug), jar bottom fragment purple-violet engobe

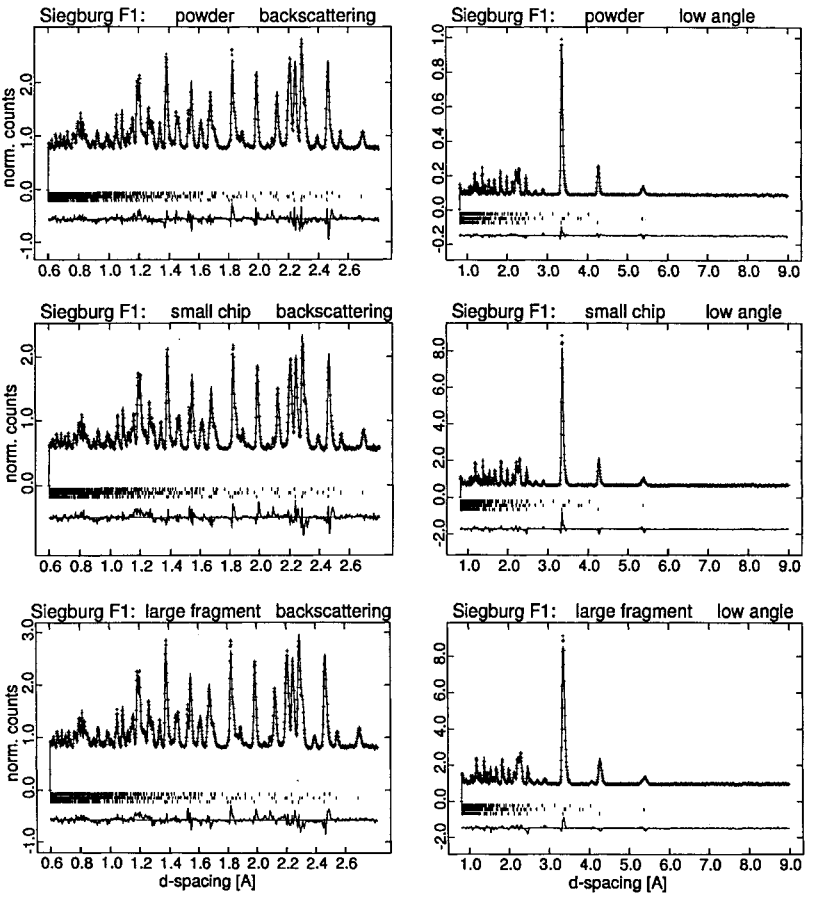

Figure 5. Analysed backscattering (left) and forward scattering (right) diffraction patterns obtained from three different preparations of the stoneware fragment F1: a powder specimen (top), a small fragment (middle) and a large fragment (bottom) (for details see text). Background modulations subtracted.

5.2. Results of the TOF feasibility study

Inspection of the neutron diffraction patterns obtained for the early stoneware fragment F1 (Figure 5) and the ensuing refined phase weight fractions (Table 4), shows no obvious differences between powder sample and large fragment results. No significant systematic differences in the diagrams of Figure 5 can be recognised. Within error limits the results agree independent of the sample preparations and thus imply that whole, intact and unprepared objects

can well be analysed non-destructively. The remaining spread in the phase fraction values can also be due to mineral inhomogenieties of the original fragment from which powder and chip had been removed. Texture in this ceramic can be neglected because preferred orientation of crystallites or grain distribution effects would have been easily recognised by inspection of the raw data of the different position-sensitive detector banks, thus the results obtained for F1 show that the large fragment neutron illumination technique can be applied successfully.

5.3. Classification of Rhenish stoneware and earthenware pottery by TOF neutron diffraction

All samples except C1 show clearly interpretable diffraction patterns exhibiting quartz (Q), mullite (M) and cristobalite (C) as crystalline phases, together with significant amounts of silica glass (g). Fragment C1 which had been classified as early 13^{th} century earthenware contains an additional, yet unidentified crystalline phase, probably present in temper inclusions not fully fused in the ceramic fabric. Quartz, which is the predominant mineral in all samples, was definitely present in the source material whereas mullite and cristobalite are products of firing processes. The mineral transformations and phase transitions leading to these high temperature products are complicated because admixtures of various clay minerals are involved. Therefore, it is not possible to reconstruct the firing processes in detail, but general conclusions can be drawn:

1. There are no clay minerals or typical clay ingredients present such as muscovite/illite, calcite or diopside.
   ⇒ Firing temperatures must have been above approx. 950 °C [28].
2. The high temperature silicate and alumino-silicate phases, cristobalite and mullite, have been crystallised:
   ⇒ Firing temperatures must have been at least 1000 °C. (Temperatures of formation of mullite depend strongly on the phases present in the source material. For example in the system kaolinite-feldspars-quartz cristobalite is formed from quartz at temperatures well above 1200 °C).
3. Considerable amount of vitreous phases are present in stoneware samples:
   ⇒ Firing temperatures must have been considerably above 1000 °C.

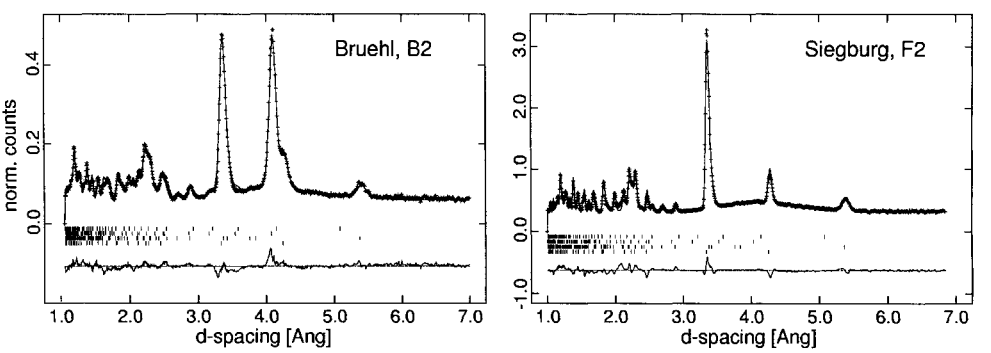

Figure 6. Observed, calculated and difference diagrams of B2 (left) and F2 (right).

Comparison of the different fragments from Siegburg and Brühl shows both differences and agreements (Table 4). In Figure 8 the mullite-to-quartz weight fraction ratio (M/Q) is plotted versus the weight fraction ratio (g+C)/(Q+M) assuming that silica glass and cristobalite are formed from the same 'quartz reservoir' at high temperatures. For the samples C1 and F3, both being classified as earthenware, although they differ by three centuries, almost identical weight fractions are found. The low M/Q ratio is in accordance with a comparatively low firing temperature typical for the production of earthenware. In the early stoneware fragment F1 the mullite weight fraction is found increased at the expense of the quartz fraction indicating higher firing temperature or a longer firing duration. Following this trend, it is not surprising to find an even higher mullite content in the early stoneware potsherd G1 and in the real-stoneware jar fragment F2. The observed M/Q-value of nearly 1.0 for F2 is in fair agreement with the corresponding stoneware M/Q-values which were calculated from the weight fractions reported by Kilb & Hennicke [22]. Siegburg near-stoneware or early-stoneware was fired at a temperature of 1050/1150-1200 °C, kiln temperatures for real stoneware production were between 1200-1400 °C [19]. None of the five Siegburg pottery fragments contains a significant amount of cristobalite, in contrast to 11 wt per cent (B1) and 20 wt per cent (B2) cristobalite in the Brühl samples.

A trend towards higher firing of stoneware compared to earthenware samples is not only indicated by high mullite/quartz (M/Q) ratios but also supported by the observation of a significant amount of amorphous silica glass or cristobalite. Both glass+cristobalite amount and mullite fraction are expected to rise with firing temperature. High ratios (g+C)/(Q+M) correlate with high M/Q ratios (Figure 7), and the early-stoneware and near-stoneware samples are clearly discerned from real stoneware samples. These results show that classification is possible on the basis of neutron diffraction data which were non-destructively obtained.

Table 4
Relative weight fractions w (in percent) of quartz (Q), mullite (M), cristobalite (C) and glass (g) in Rhenish stoneware and earthenware ceramics as analysed by Rietveld refinement. Weight fraction ratios of mullite/quartz (M/Q), glass+cristobalite/quartz+mullite (g+C)/(Q+M) are given. R_{wp} denotes the Rietveld profile R value (in percent).

	w(Q)	w(M)	w(C)	w(g)	M/Q	(g+C)/ (Q+M)	R_{wp}
F1: powder	47.2	32.5	0.2	20.1	0.69	0.25	5.1
F1: chip	48.0	31.8	0.3	19.9	0.66	0.25	6.5
F1: large fragment	49.4	29.9	0.3	20.4	0.61	0.26	5.2
G1	42.7	32.5	0.1	24.7	0.76	0.33	4.9
F2	35.5	34.8	0.1	29.6	0.98	0.42	6.6
F3	60.2	22.3	0.1	17.4	0.37	0.21	6.1
C1	61.4	21.8	0.2	16.6	0.37	0.20	6.7
B1	35.7	35.6	11.4	17.3	1.0	0.40	6.0
B2	33.1	30.9	19.8	16.2	0.93	0.56	6.6

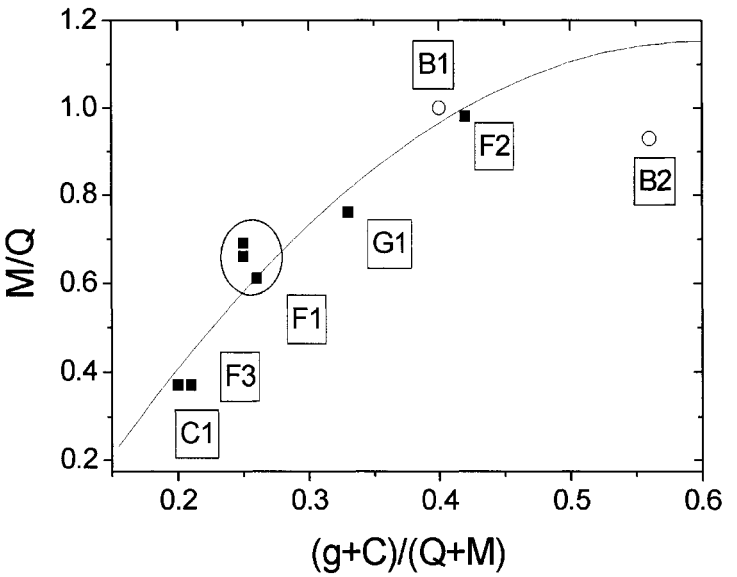

Figure 7. Classification of pottery fragments using mineral phase fractions. Encircled points result from different preparations (powder, small/large fragment). The dotted line is a guide to eye.

It seems that the Siegburg and Brühl samples group onto the same branch in Figure 7, but the number of samples studied is too small to draw conclusions. It is the high cristobalite content that distinguishes the Brühl from the Siegburg samples (see cristobalite peak at about 4 Å in Figure 6a). The roughly equal shares of quartz and mullite (M/Q ≈1) in the Brühl fragments suggest, however, similar firing conditions as for the Siegburg stoneware sherd F2. The glass contents of the Brühl stoneware are similar to those of the Siegburg earthenware samples but adding the cristobalite to the silica glass fractions, i.e. using g+C as indicator of high firing temperatures, brings the Brühl samples more in line with the Siegburg stoneware samples. It must be remembered, however, that the formation of vitreous phases is not only critically dependent on temperature but also on the presence of fluxes (oxides of for example Na, K, Ca, Fe) in the potter's clay which may lower the temperature at which vitreous phases appear [2].

5.4. Comparison with X-ray analyses

Figure 8 compares the neutron results with M/Q values obtained from the laboratory X-ray powder data. There is a reasonable overall agreement between the neutron and X-ray results, keeping in mind, that a perfect match cannot be expected because the object may not be homogeneous in its mineral composition, i.e. mullite and glass fractions may vary through the ceramic. The general trend, however, is the same. It is fair to assume that neutron data,

obtained non-destructively from fragments without prior preparation, are more representative and also more reliable than the X-ray powder data because of a wider d-spacing range, which generally ensures stable Rietveld refinements. Extraction of information about the glass phase from the X-ray data was not possible.

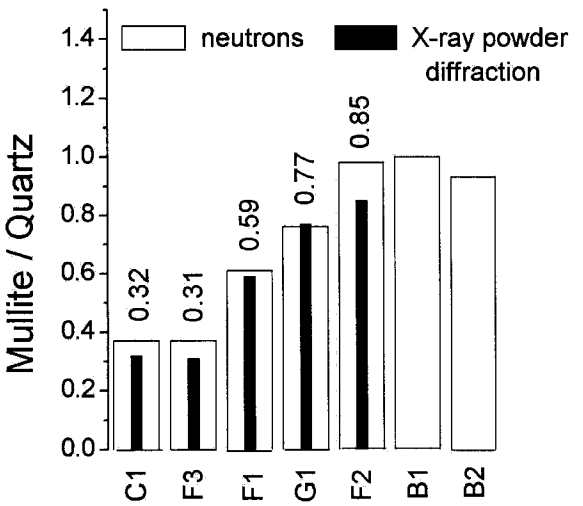

Figure 8. Comparison of laboratory X-ray with neutron results. M/Q values above columns are from X-ray refinements.

The SR data from the body of sample B1 from Brühl show the same phases as identified in the neutron patterns, i.e. quartz, mullite and cristobalite. A quantitative Rietveld refinement of the SR radiation data, however, was not attempted because of preferred orientation effects and local texture variations. The diffraction patterns from some sample zones reveal distinctly different, but yet unidentified minor minerals. Conventional X-ray diffraction from the engobe powder sample shows the presence of hematite, which is not detected in the neutron patterns. This demonstrates that SR experiments are surface sensitive whereas surface phases do not contaminate the neutron patterns.

5.5. Summary

The experiments have shown the potential of stationary TOF neutron diffraction for providing reliable information from large archaeological ceramics without prior sample preparation. TOF yields the abundance of crystalline phases and relative phase fractions of material and allows the estimate of silica glass contents. The results of mineral composition analyses on German Rhenish ceramics show a clear correlation between mullite and silica weight fractions which can be used for a classification of the objects. Since the neutron diffraction information stems from the bulk material, it is not contaminated by ceramics coatings and engobes which, on the other hand, can be studied using X-rays.

6. Mineral phase studies of ancient pottery

This last section summarises first results of neutron and SR radiation studies on some selected potsherds from Neolithic sites in Middle Russia and from the Athenian Agora. In addition, SR radiation data collected from a whole museum piece are presented in order to demonstrate the usefulness of short X-ray wavelengths for non-destructive fingerprinting.

6.1. Neolithic ceramics from Central Russia

The transition from the Mesolithic to Neolithic in Central Russia is marked by the emergence of the earliest pottery about 7100 BP (before present: radiocarbon years before AD 1950). Pottery is usually found in large numbers in Neolithic peat excavation sites in Middle Russia [29,30]. Representative potsherds N1-N5, N19 (Figure 9) and N20, excavated from different cultural layers of Neolithic sites (Table 5), have been studied with TOF neutron diffraction on ROTAX, and with high resolution SR powder diffraction on station 2.3 at Daresbury using a wavelength of 1.2 Å. One Bronze Age pottery fragment (N21, Figure 9) was analysed for comparison. The fabric of potsherds N1-N5 is generally coarse-grained and brittle, whereas the sherds N19-N21 are fairly hard. For the TOF measurements the 'complete' fragments were used. For the SR measurements small quantities were scraped off the sherds. Figure 10 shows the forward scattering neutron diffraction patterns.

Table 5
List of pottery fragments of large hand-made vessels from Central Russia. Datings from uncalibrated C-14. The sherds were kindly provided by M.G. Zhilin (N1, N3, N4, N5) and A. Emelyanov (N19, N20, N21), Institute of Archaeology, Academy of Sciences, Moscow.

no	excavation site	date (BP)	
N1	Ozerki 5, Tver region	6900-6500	Early stage of Upper Volga culture
N3	Ozerki 5, Tver region	6300-6000	Late stage of Upper Volga culture
N4	Stanovoye 4, Ivanovo region	7000	Earliest stage of Upper Volga Culture
N5	Stanovoye 4, Ivanovo region	7000	Earliest stage of Upper Volga Culture
N19	Shagara II, Ryazan region	5500-5100	Second half of Lyalovo culture
N20	Shagara II, Ryazan region	4900-4400	Volosovo culture
N21	Shagara II, Ryazan region	Bronze Age	Fatyanovo culture

In comparison to stoneware ceramics the mineral composition of this low fired pottery is more complex, being generally characterised by the presence of feldspars and clay minerals. The additional presence of illite/muscovite implies firing temperatures well below 900 °C [28]. Illite is difficult to model in a Rietveld refinement because the structure information is poor and non-statistical distribution of crystallites (preferred orientation) is possible. Models of the phases identified in the Russian sherds are taken from the ICSD database [27]:

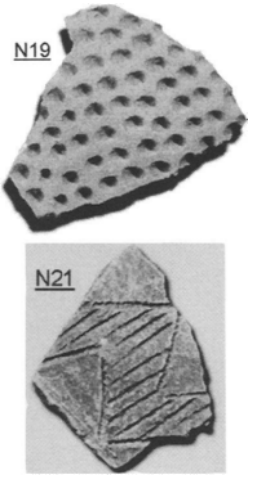

Figure 9. Russian potsherds N19 and N21 (about 5 cm in diameter).

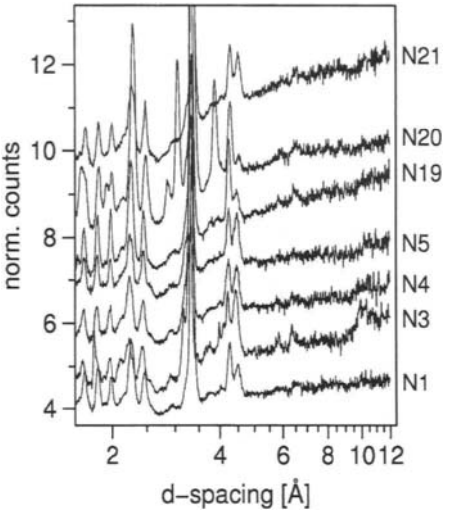

Figure 10. Forward scattering neutron fingerprints of Russian potsherds. The patterns are shifted vertically for clarity.

Table 6
Neutron results on Russian sherds. Relative weight fractions w (in percent) of quartz (Q), orthoclase (O), plagioclase (P), calcite (Ca). Q/F=wQ)/(w(O)+w(P)) is the weight fraction ratio quartz/feldspars. Strength of reflection intensities at d=4.5 Å (I: illite) and 10 Å (M: muscovite) is indicated by (0: zero), (+: weak), (++: medium), (+++: strong). Values in parentheses from SR experiments. Profile R_{wp} values in [%].

	w(Q)	W(O)	w(P)	W(Ca)	Q/F	I	M	R_{wp}
N1	83	11	6	0	4.9	+	0	2.0
	(73)	(15)	(12)	0	(2.7)	+		(9.5)
N3	47	26	27	0	0.9	+++	+++	2.0
N4	65	11	24	0	1.9	++	+	1.5
N5	63	17	20	0	1.8	++	+	1.7
N19	84	11	5	0	4.7	+	0	1.5
N20	59	7	8	26	3.9	+	0	1.6
N21	83	12	5	0	4.9	++	0	1.0

quartz (Q: ICSD 18172 [24]), calcite (Ca: ICSD 80869 [31]), orthoclase (O: ICSD 10270 [32]), a calcium rich plagioclase, e.g. bytownite (P: ICSD 30933 [33]). The feldspar identification presents some problems: (1) despite the presence of significant phase fractions the diffraction intensities are low due to large unit cells: (2) there is not much scattering

contrast between Na, K, Ca, (i.e. it is difficult to discern between albite (Na-rich) and anorthite (Ca-rich) both of which belong to the plagioclase family); (3) there is considerable correlation between orthoclase and plagioclase phase fractions (due to peak coincidences). Nevertheless, the refinement results are quite stable with respect to the total feldspar content.

Reflections in the neutron patterns at about 4.5 Å and 10 Å are attributed to illite and mica (probably muscovite) minerals. Illite and muscovite are structurally related and, thus, display similar reflection positions in the diffraction patterns. Since there is no illite structure model (atom co-ordinates) available, it was not possible to fit the respective peaks in a Rietveld refinement. The muscovite model does not fit very well either, probably because of strong preferred orientation and overlap of muscovite with illite reflections. The illite/muscovite peaks were fitted using the LeBail full-pattern procedure (see section 2.3) along with the Rietveld refinement of quartz, calcite and feldspar phases. The LeBail fit does not yield weight fractions but confirms or refutes the lattice parameters and the space group symmetries of the assumed phases. The danger of the combined Rietveld/LeBail fit is that deficiencies in the Rietveld modelling may be compensated by 'LeBail phases' if there is considerable peak overlap. Figure 11 shows fitted neutron and SR diagrams using this method. Refined phase fractions and ratios Q/F=w(Q)/(w(O)+w(P)) of all sherds are given in Table 6 which also indicates intensities of the illite/muscovite peaks in the diagrams.

Both neutron and high resolution SR data of N1 (Figure 11) yield a high quartz-to-feldspar ratio. However, the fractions obtained from the SR data are noticeably different compared to the neutron results (Table 6), probably because the latter represent an average over a large volume. By zooming into the SR diagram well resolved feldspar peaks become visible (Figure 11d). The high angular resolution enables remaining discrepancies between observed and calculated patterns to be disclosed.

The refined weight fractions in Table 6 show that the samples fall into distinctly different groups. The seemingly K-rich (orthoclase) samples N1, N19, N21 display high ratios Q/F, the seemingly Ca-rich (bytownite/anorthite) samples N4, N5 medium Q/F because F is increased at the expense of Q. N3 is characterised by almost equal shares of quartz and feldspar, in accordance with the visible observation of granite inclusions. Sample N20, which contains visible admixtures of ground shell and organic material, is completely different exhibiting a large fraction of calcite.

6.2. Attic potsherds from the Athenian Agora

Pottery fragments excavated from the Athenian Agora by the American School of Classical Studies [34] and kept at The Manchester Museum for scientific investigations were also studied. These fragments are characterised by typical black gloss Athenian style of decoration and clay/gloss colour. The list of sherds analysed is given in Table 7. Table 8 contains the refined fractions using the procedure described in the previous section except that a hematite phase (H: ICSD 15840 [35]) has been included in the model. The Athenian sherd results are compared to data obtained from a complete miniature olpe (wine jug, accession number 1963.110) (Figure 12) of a shape used all over the Greek world in the 4th century BC. It came to the museum in 1963 as part of a private collection; its provenance was given as Clusium (Chiusi) in Etruria, which was by then very much in the Greek sphere of influence, but the evidence for this attribution is not known, and it may be no more than a fine-sounding name given by a dealer to make the piece more attractive to a potential purchaser. In other words, the provenance of the olpe is not certain.

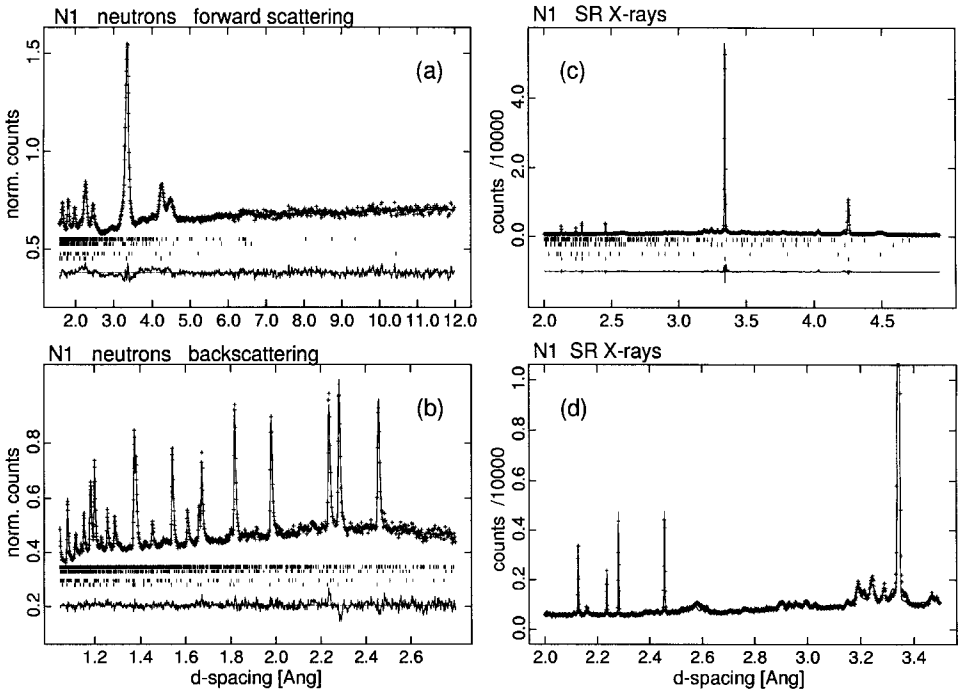

Figure 11. Profile fitted neutron and SR diffraction patterns of N1.

The Attic sherds have, in general, lower Q/F ratios than the Russian samples. Refined calcite fractions of 2% for some of the sherds are not significant. Two fragments (A4, A6) contain small amounts of hematite. Phase fractions from SR measurements have not been refined yet, but it should be noted that the SR powder measurements indicate hematite in every sherd. The neutron diffraction results of the intact olpe are not conclusive. Phase fractions of the olpe are close to those of A6 (Table 8), but also similar to those of the Russian sherd N3 (Table 6). Likewise, it is possible to relate sherd A25 (kados fragment) to Russian sherds N1 and N19. This illustrates that it is impossible to draw unambiguous conclusions with respect to the provenance of an object if only the composition of main mineral phases is considered. Quartz and feldspars dominate the patterns, and in fact it is, at present, impossible to be definitive about the precise type of feldspar. The result of the Rietveld fit is dependent on the choice of phases selected as appropriate candidates. It may well be that differences in significant details (e.g. trace mineral contents) make two ceramics different. Nevertheless, a reliable analysis of the abundance of the main minerals in pottery may well support or undermine a provenance hypothesis.

Table 7
Attic Black Gloss pottery from the Athenian Agora. Datings on stylistic grounds. The sherds were kindly provided by Dr. A.J.N.W. Prag, The Manchester Museum.

	description	date	accession no.
A4	cup fragment	late 6cBC	1999.4
A6	bolsal fragment	last quarter 5cBC	1999.6
A10	fragment from large vase	late 6cBC or early 5cBC	1999.10
A11	Bell-krater fragment	late 5cBC or early 4cBC	1999.11
A13	Bell-krater fragment	4cBC	1999.13
A25	wall fragment, probably from a kados	late 7cBC or early 6cBC	1999.25

Table 8
Neutron results on Attic sherds and the intact Clusium olpe. Relative weight fractions w (in percent) of quartz (Q), orthoclase (O), plagioclase (P), calcite (Ca) and hematite (H). Strength of reflection intensities at d=4.5 Å (I: illite) and 10 Å (M: muscovite) indicated by (0), (+), (++), (+++). R_{wp} in [%].

	w(Q)	w(O)	W(P)	w(Ca)	w(H)	Q/F	I	M	R_{wp}
A4	45	19	29	2	5	0.9	++	+++	4.9
A6	53	20	21	2	4	1.3	+++	++	3.0
A10	59	21	18	2	0	1.5	++	+	2.1
A11	69	15	12	4	0	2.6	+++	0	2.1
A13	51	16	13	20	0	1.8	++	0	1.4
A25	74	7	10	9	0	4.4	++	0	2.3
Olpe	53	22	20	1	0	1.3	+	0	2.6

6.3. Non-destructive SR X-ray diffraction using a short X-ray wavelength

SR diffraction data from a thymiaterion (incense burner, accession number 37325) (Figure 14) from The Manchester Museum, was collected non-destructively on station 16.2 at Daresbury using a short X-ray wavelength of λ=0.52 Å. At this wavelength, the attenuation length for a typical ceramic elemental composition is about 1200 microns [36]. The X-ray beam (20 microns vertically by 1 mm horizontally) strikes the stationary object at a grazing angle (3-5°) and the diffracted X-rays are then received from within 100 microns of the surface.

SR patterns from the stem and the bowl of the thymiaterion were collected to investigate whether the same clay was used for both. It was identified as Apulian, made in the Greek colonies in south-eastern Italy in the late 4th century BC. There was a neat repair, joining the bowl to the stem, probably made before it was donated to the Whitworth Art Gallery in 1894

whence it was transferred to the Manchester Museum in the 1970's. Stylistic differences in the painting of the bowl and stem, the fact that bowl and stem "rang" differently when tapped gently, had a different feel to the touch, coupled with the fact that there appeared to be no ancient parallels for the shape of the bowl, gave us reason to suspect that this is a 19th century pastiche: a fake bowl set upon a genuine ancient stem.

Figure 12. Complete olpe (wine jug), (height: approx. 7 cm).

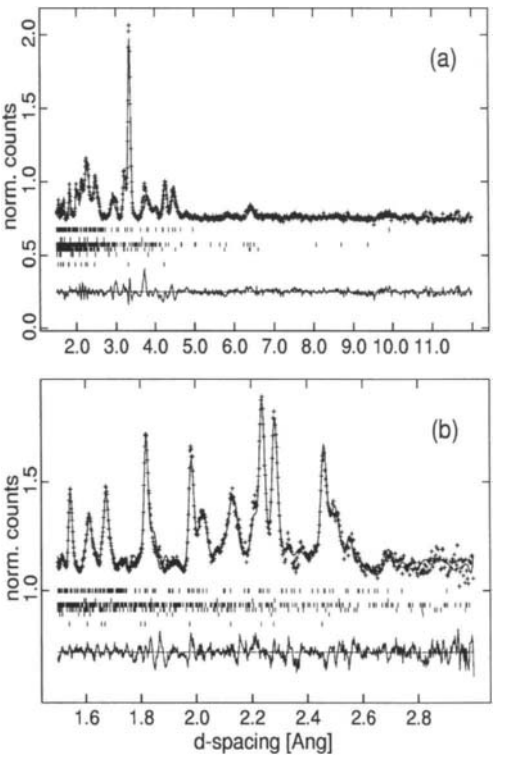

Figure 13. Profile fitted neutron forward (a) and backscattering (b) patterns of the olpe.

Figure 15 shows the diagrams taken from stem and bowl on station 16.2. There are striking similarities between the two diffraction patterns, but also notable discrepancies. However, SR patterns taken from 20 mg powder samples, collected from the unglazeded base of the bowl and the base of the stem in a spinning capillary on the high resolution station 9.1 [37], are in good agreement. This indicates a high probability of the two parts having being made from the same clay: i.e. it is likely that stem and bowl belong to the same original object. The comparison with the powder diffraction measurements indicates, that the non-destructively collected SR patterns are probably strongly influenced by grain orientation effects as diffraction arises from a fixed volume of the stationary object. A significant improvement in the data collection strategy would be the collection of high angular resolution, two-dimensional diffraction data where orientation effects as well as identification of minor phases are easier to interpret.

6.4. Summary

Measurements on ancient ceramics give further evidence that neutron as well as SR diffraction can be applied for fingerprinting and mineral phase studies of archaeological ceramics including intact objects. The quantitative Rietveld analysis comes to its limits if clay minerals are to be quantified or if phase identification is ambiguous. Sample provenancing cannot be based on the composition of major phases alone and, in the case of SR, orientation effects from grains in small volumes of stationary objects may give rise to ambiguities.

Figure 14. Thymiaterion (incense burner) (height approx. 30 cm)

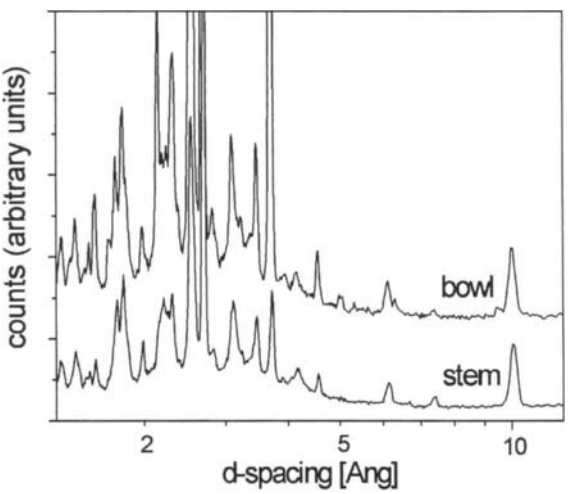

Figure 15. Comparison of diagrams from stem and bowl of the thymiaterion (upper diagram scaled and shifted).

7. Conclusions

Neutron and SR X-ray radiation is capable of providing high quality diffraction fingerprints of archaeological ceramics. This paper is deliberately confined to diffraction methods, since the interpretation of neutron and SR diffraction patterns in terms of mineral phases and their abundance is well established. Both neutron and SR diffraction can offer more than just 'fancy' types of diffraction patterns in comparison to conventional X-ray data because they may well be indispensable for providing information that cannot be obtained with conventional X-ray equipment. This is the case, for example, if big objects have to be dealt with (neutron, SR), non-destructiveness is paramount (neutrons, SR for glazes using long λ, internal volume using short λ), or high primary beam intensities are needed (SR). Moreover, neutron and SR facilities have a lot more to offer to archaeological science than mineral phase analysis by diffraction, for example, Small Angle Neutron/X-ray Scattering (SANS, SAXS) for porosity characterisation [38]. SR beams can be used for chemical speciation using Extended X-ray Absorption Fine Structure (EXAFS) measurements and molecular (non-crystalline) species identification using Fourier Transform InfraRed analysis (FTIR) [39] or fibre degradation analysis using Wide Angle X-ray Scattering (WAXS) [40].

It has been shown that quantitative mineral phase analysis of archaeological ceramics is useful for revealing correlations between phase fractions. These correlations may be used to classify an unknown piece within a collection. Having investigated only a few different ceramics series from different locations and time periods, the mineral phase compositions give limited information about the origin (firing and provenance) of the pottery, which can be used, however, in combination with results from other archaeometric methods. The quantitative phase analysis method employed here, the Rietveld method, uses crystal structure models of the minerals as strong constraints. Although this approach is limited by the availability of structural models for the particular phases, accurate measurements of the diffraction profiles themselves can often be a sufficient characteristic fingerprint for comparison purposes.

TOF neutron diffraction is a new method for the characterisation of archaeological objects. TOF-ND provides additional or complementary information about constituent phase components of archaeological ceramics and other objects. No preparation of objects is needed as they can be measured as they are. Thus, the method is truly non-destructive, which is an important consideration if objects are not to be damaged by cutting, drilling, scraping etc. Data can be collected from large and complete objects. The technique is suited to quantify average mineral phase fractions, including amorphous silica, from the bulk of an object. Neutrons do not see thin coatings or glazes, or other surface material which might be affected by corrosion or conservation treatment. That is to say, neutron diffraction is very suitable for obtaining an overview of the bulk phase composition and good sampling of large volumes. A further advantage is that TOF neutron Rietveld refinements are very stable. The method has some problems, though, if unknown phases are to be identified because database automated search-match routines are generally based on X-ray intensities. Another, not so severe, drawback is that samples are activated in the neutron beam. The rate at which the radioactive activation decays depends on the element composition of the material and the neutron flux. On ROTAX, decay times are in the negligible order of minutes for most ceramics ingredients, and only a few hours for certain metals like manganese.

SR diffraction can address several aspects of archaeological science problems by taking advantage of the unique SR properties. High angular resolution measurements can provide

accurate phase identification and quantitative fingerprinting of archaeological ceramics. Fast data collection made possible by the high intensity and efficient detecting systems enable both position-sensitive X-ray measurements for detailed studies of the fabric of ceramics as well as fast survey of dozens of samples per hour. High primary intensity can also be used for identification and analysis of trace minerals. Limitations of SR in comparison to neutron diffraction are clearly the problem of preferred orientation and of localised sampling of the mineral composition. On the other hand, these very problems may be turned into a unique advantage when mineral and area specificity is the objective.

In this study we have concentrated on ceramic objects. The potential of neutron diffraction is further enhanced by the ability to investigate also metal objects, for example coins. First test measurements on contemporary coins on ROTAX show surprisingly little texture. In general, texture is a case study of its own and may be an important characteristic of an archaeological, mechanically treated, metallic object. ROTAX has already shown its potential with respect to quantitative volume texture analysis of metallurgical and geological samples [41]. Another untapped potential for neutron applications in experimental archaeology is the ability of neutrons to easily penetrate the walls of a container, for instance a furnace, an interesting objects might be in. This allows to simulate firing conditions and, thus, to study in situ phase transformations of clay samples in a kiln-type set-up.

Acknowledgements

We wish to thank E. Hähnel, Freilichtmuseum Kommern, H. Kutzke, Mineralogical-Petrological Institute, Bonn University, Dr. A.J.N.W. Prag, The Manchester Museum, University of Manchester, Dr. M.G. Zhilin and Dr. A. Emelyanov, Institute of Archaeology, Academy of Sciences, Moscow for providing materials and archaeological background. We thank B. Barbier, Mineralogical-Petrological Institute, Bonn University, for the collection of X-ray diffraction patterns and assistance with the mineral structure data bases. We thank Drs M.Z. Papiz, S.E. Girdwood, C.C. Tang, M.A. Roberts, G.F. Clark for feasibility measurements taken at stations 9.6, 2.3, 9.1, and 16.2 of the SRS, and R.L. Jones and his staff for sample preparation facilities. The neutron diffraction work was funded by the German Bundesminister für Bildung und Forschung, BMBF, under contract no KI5BO3.

REFERENCES

1. P.M. Rice, Pottery Analysis, a Sourcebook, University of Chicago Press, Chicago, 1987.
2. R.E. Jones, Greek and Cypriot pottery: A review of scientific studies. The British School at Athens, Fitch Laboratory. Occasional Paper 1, 1986, pp. 1-949.
3. P. Walters, P. Martinetto, G. Tsoucaris, R. Bréniaux, M.A. Lefebvre, G. Richard, J. Talabot, E. Dooryhee, Nature 397 (1999) 483.
4. ISIS 99, The Rutherford Appleton Laboratory, ISIS Facility Annual Report 1998-99, RAL-TR-1999-50, 1999 (availble at: http://www.isis.rl.ac.uk).
5. Synchrotron Radiation Department, Annual Report 1998-99, CLRC Daresbury Laboratory (http://www.srs.dl.ac.uk).
6. R.J. Hill, C.J. Howard, J. Appl. Cryst. 20 (1987) 467.
7. H.M. Rietveld, Acta Cryst. 22 (1967) 151.
8. R.A. Young (Ed.), The Rietveld Method, International Union of Crystallography, Oxford University Press, 1993.

9. A.C. Larson, R.B. Von Dreele, GSAS: General Structure Analysis System, Report LAUR 86-748, Los Alamos Laboratory, Los Alamos, NM, USA, 1986.
10. J. Rodriguez-Carvajal, Physica B 192 (1993) 55.
11. A. LeBail, J. Non-Cryst. Solids 183 (1995) 39.
12. G. Brown, G.W. Brindley, in: G.W. Brindley and G. Brown, (Eds.): Crystal Structures of Clay Minerals and their X-ray Identification, Mineralogical Society Monograph No 5, Chapter 5, 1980.
13. U. Steigenberger (Ed.), European Spallation Source, ESS Council, Report ESS 97-62-M, 1997.
14. I.H. Munro, Journal of Synchrotron Radiation 4 (1997) 344.
15. C. Riekel, Rep. Prog. Phys (2000) in print.
16. S. Colston, A. Jupe, P. Barnes, this volume
17. W. Kockelmann, M. Weißer, H. Heinen, A. Kirfel, W. Schäfer, Materials Science Forum 321-324 (1999) 332.
18. W. Kockelmann, A. Kirfel, E. Hähnel, Zeitschrift für Kristallographie, Suppl Issue 16 (1999) 164.
19. D. Gaimster, German Stoneware 1200-1900, British Museum Press, 1997.
20. B. Beckmann, Rheinische Ausgrabungen 16, Rheinisches Landesmuseum Bonn (1975) 340.
21. H. Mommsen, Th. Beier, D. Heimermann, A. Hein, E. Hähnel, Th. Ruppel, Denkmalpflege und Forschung in Westfalen 32 (1995) 101.
22. L. Kilb, H.W. Hennicke, Keramische Zeitschrift 9 (1980) 509.
23. H. Kutzke, Mineralogical Institute, Bonn University, private communication.
24. W.H. Zachariasen, H.A. Plettinger, Acta. Cryst. 18 (1965) 710.
25. R.J. Angel, C.T. Prewitt, American Mineralogist 71 (1986) 1476.
26. J.B. Parise, A. Yeganeh-Haeri, D.J. Weidner, J.D. Jorgensen, M. A. Saltzberg, J. Appl. Phys. 75 (1994) 1361.
27. ICSD, Inorganic Crystal Structure Database, Fachinformationszentrum Karlsruhe (National Institute of Standards and Technology, USA) 1999.
28. M. Maggetti, in M.J. Hughes (Ed.), Scientific Studies in Ancient Ceramics, British Museum Ocassional paper no 19, British Museum Research Laboratory, 1981, pp. 31-49.
29. M.G. Zhilin, in I.N. Chernyh (Ed.): Tverskoy Arheologicheskyi Sbornik, Tver, 1994, pp. 47-52.
30. M.G. Zhilin, European Journal of Archaeology 1 (1998) 149.
31. E.N. Maslen, V.A. Streltsov, N.R. Streltsova, N. Ishizawa, Acta Cryst. B51 (1995) 929.
32. E. Prince, G. Donnay, R.F. Martin, Acta Cryst 14 (1961) 443.
33. D.L. Bish, Clays and Clay Minerals 41 (1993) 738.
34. B.A. Sparkes, L. Talcott, Black and Plain Pottery of the Sixth, Fifith and Fourth Centuries B.C. The Athenian Agora XII, Princeton: American School of Classical Studies at Athens, 1970.
35. R.L. Blake, R.E. Hessevick, T. Zoltai, L.W. Finger, American Mineralogist 51 (1966) 123.
36. W.D. Kingery, Archaeomaterials 5 (1991) 47.
37. M.A. Roberts, private communication.
38. G.J. Grossmann, E. Pantos, D.T. Clarke, O. Byron, C. Ackerman, N. Terrill, G.R. Mant, G. Diakun, S. King, H. Kutzke, M.G. Zhilin, K. Prag, A.J.N.W. Prag, Proc. EMAC99, 5th European Meeting on Ancient Ceramics, October 1999 in Athens, accepted.

39. E. Pantos, C.C. Tang, E.J. MacLean, K.C. Cheung, R.W. Strange, P.J. Rizkallah, M.Z. Papiz, S.L. Colston, M.A. Roberts, B.M. Murphy, S.P. Collins, D.T. Clark, M.J. Tobin, M.G. Zhilin, K. Prag, A.J.N.W. Prag, Proc. EMAC99, 5th European Meeting on Ancient Ceramics, October 1999 in Athens, accepted.
40. T.J. Wess, K. Nielsen, O. Paris, P. Fratzl, M. Collins, private communications.
41. E. Jansen, W. Schäfer, W. Kockelmann, G. Will, Textures and Microstructures 26-27 (1996) 11.

Radiation in Art and Archeometry
D.C. Creagh and D.A. Bradley (editors)

The study of the characterisation and provenance of coins and other metalwork using XRF, PIXE and Activation Analysis

Maria Filomena Guerra

C.N.R.S. – I.R.A.M.A.T. (Centre Ernest-Babelon)
3d, rue de la Férollerie
45071 Orléans Cédex France
e-mail : guerra@cnrs-orleans.fr

The aim of this work is to give a general description of how radiation techniques can be used for determining the provenance of metals and understanding the manufacture technology of metallic objects. The main properties and differences for the most in use techniques are given. Some, used to complement radiation techniques and used in the later examples, are also considered.

I give several examples, most of them on coinage, for the most important non-ferrous metals and alloys used in the Past. These cover a large but far from complete number of fields of research. It is demonstrated that provenance may sometimes be determined by using trace elements patterns. However, for more accurate results a good knowledge of trace elements present as well the geological context is required. To understand the fabrication of an object we need in general to couple both analytical and metallurgical data.

A large number of examples illustrate the questions posed for metalwork. For each main metal, after some geological, smelting and purification considerations, application of the radiation techniques to the manufacture technology and the provenance of the ores were considered to answer a number of particular historical questions.

1. INTRODUCTION

The demonstration of status is one of the oldest preoccupations of mankind and has taken many forms over time [1]. One of the best-known demonstrations of the status of a society is through the value it gives to particular metals. Thus the history of metals is somehow the history of Man in society[1] [2].

The study of metals may take several forms, but most of the questions posed in actual times can be regrouped in two main groups: the manufacturing technology of the objects and the source of the raw materials. To understand the way objects were done in the past and where the metals came from, we must incorporate in the same study the knowledge of a

[1] « Je ferai entrer ce tiers dans le feu; je les épurerai comme on épure l'argent, je les éprouverai comme on éprouve l'or ». I will make this third enter into fire ; I will purify them as silver is purified, I will assay them as gold is assayed. Zacharie 13, 9.

metallurgist, of a physicist, of a chemist, of an historian, of a geologist, and so on. In fact, from the ore to the fabricated object many stages have to be passed through. And each stage has a meaning, depending not only on the ability of Man to refine and fabricate, but also on the religion, the economy, the politics and other societal factors.

During certain periods specific countries have had access to certain mines: for example, the gold from South Africa in present times. So objects were manufactured with a certain type of ore. At a certain period man had the technology only to process certain ores to use, and to make alloys of. These alloys have different colours and could later be gilded or silvered by surface treatment.

The first metal used by Man was certainly gold. This metal exists in Nature in its native form and can be found as dust and nuggets in alluvial deposits and obtained by simple panning and washing. Shining like the sun, untarnishable, and very malleable, gold can be beaten to make jewels, alloyed to silver and/or copper to produce very different work and colours[2] and also be soldered by varying the melting point of the alloys.

The other precious metal used in the past is silver. The scarcity of this metal in its native form compelled to the exploitation of silver-base ores and forced the use of a more sophisticated metallurgy[3]. We can cite electrum, a native gold-silver alloy very used in the past and several lead ores containing silver like galena and cerrussite. In order to obtain pure silver a separation of the different metals had to be done through the extraction of silver required the smelting of the ore, followed by a purification of the silver.

The third precious metal is platinum which only reached Europe through Spain after the conquest of the New World[4]. This metal, that could be found there in alluvial deposits and panned as gold, was widely used by the Indians. As platinum melting point is 1775°C, objects were made with sintered alloys of platinum and gold and then hammered. Examples of the use of platinum were found in the site of Esmeraldas and Las Tolitas [4].

The most important metal associated with the precious metals is copper. Like gold, copper is present in Nature under its native form but to such an extent that its price is lower. Very important metals are tin and zinc, much used to produce two copper-base alloys: bronze and brass. Lead plays an important role in the manufacture of those alloys as well as on others like pewter and is also used as a single metal.

The determination of the composition of archaeological object gives an immediate indication of the alloy used by the smith and the changes of its properties and difference in details like soldering indicates the skill of the smith. The evolution of the composition, the way the object was made, the identification of the origin of the metals are all questions that can in some circumstances be elucidated by their analysis. The aim of this work is to give a general idea about the possibilities and limitations of non-destructive radiation base techniques to solve questions posed by ancient metalwork.

---

[2] Agricola (Book V) [3] thought that minerals had different colours. A description of the different minerals and their colours is given in note 22 of pages 108-115.

[3] In Egypt the price of silver was higher than the price of gold till the Ptolemaic period.

[4] It occurs in its native form with iron, which sometimes is replaced by copper and nickel.

2. THE DEVELOPMENT OF THE RADIATION-BASED ANALYTICAL TECHNIQUES

Most of the techniques we present here are based in bombarding the object and the measurement of the radiation emitted by the atoms excited by the particles. Depending on the bombarding and emitted particle or radiation and their energy the experimental system is different. But all the techniques are based on the induction of an atomic or nuclear transmutation which gives rise to the emission of energy under the form of gamma-rays, X-rays, electrons, alpha-particles, and so on. These emissions can be identified and measured. Each transmutation for each chemical element gives rise to the emission of characteristic spectra from which we can deduce the concentration of the element in the object.

The development of the analysis of art and archaeological objects followed the development of each technique, but one of the most important for those concerning this work was the development of solid state detectors coupled to multi-channel analysers in the 1960s allowing multi-element determination by using the emitted X-ray or gamma spectra.

Amongst the most common techniques used for the non destructive determination of the composition of art and archaeological objects are XRF (X-ray fluorescence spectroscopy), PIXE (proton induced X-ray spectroscopy), and NAA (activation analysis using neutrons) and (AMS) charged particles. The main differences between these techniques are the incident beam used, the number of elements that can be simultaneously detected, the analysed depth and the limits of detection. Depending on the number of elements and the quantities measured we use different techniques to solve different problems. The analysis of trace elements of specific atomic number has the advantage of giving information with respect to the provenance of the raw material, giving access to the study of the commercial routes in earlier times. Activation analysis has been widely used for trace element studies of ancient metalwork.

Irradiation of artefacts in nuclear reactors was the first application in Archaeometry[5]. It was done either by irradiation of the whole object and so analysis could be carried out in a non-destructive way, or by means of a small sampling. The first reported work, performed by activation analysis dates from 1953, was done by Ambrosinus and Pindrus [6], and concerns the analysis of Gaulish coins. The use of neutrons generated by a cyclotron was undertaken for the first time in 1956 in a single experiment by Emoto [7] to analyse a gold foil attached to a sword. However: the entire development of the technique of fast neutron production in a cyclotron by means of deuteron beams to analyse copper alloy coins together with the development of the charged particles activation in a cyclotron to analyse gold and silver coins was performed in 1968 by P. Meyers [8,9,10].

The use of techniques based on the measurement of X-rays started in the 1960s with the development by Hall first of the milliprobe [11] and in 1973 of the isoprobe [12]. If the use of protons to produce X-ray spectra was suggested in 1964 by Birk et al. [13], the first actual experiment performed using an accelerator of van de Graaff type dates from 1970 and was performed by Johansson and Johansson [14]. Its application to metalwork dates from the

[5] The first step of the use of activation analysis in the study of metalwork can be found in the paper of Sayre and Meyers [5].

middle of the 70s [15,16]. Later, the use of other particles [17] and higher energies [18] and also external beams and of μ-beams [19,20] became available.

However, we must be aware of the heterogeneity of the ancient alloys very often buried during a long period and subject, in particular, to phenomena like segregation, corrosion and preferential removals in time of certain metals, like copper from gold. The use of surface techniques like XRF and PIXE, analysing the first μm of the samples, may so give a composition which does not correspond to the bulk one. Several authors have published work in this field [21,22,23], but one of the first showing the difference observed for the concentration of several elements by surface and bulk techniques was done in 1964 by Condamin and Picon [24] on silver coins and later on bronze, brass and bullion (silver-copper alloy with low silver) coins [25].

3. SOME CHARACTERISATION TECHNIQUES OF ANCIENT METALS

The most widely spread techniques used to analyse metalwork can be easily found in the literature [26, 27]. The choice of analytical technique depends on the questions posed by the object. For example: many fast and inexpensive techniques measure the main components of an alloy, and if the object does not present a patina, or if the patina is very thin, can give useable results. Even surface techniques like XRF may be used directly on the object [28,29]. Of course we must always consider the possibility of performing chemical or physical cleaning on the region of the analysis in order to remove the patina [30,31]. PIXE is also widely used, giving better results for lighter elements and allowing the analysis of very small details by using μm-sized beams. In this chapter our aim is giving some of the most important details about the most in use techniques, but in reference [26] an explanation of many techniques and their applications to the analysis of coins is presented.

X-ray fluorescence is perhaps the most versatile technique at our disposal. It uses either an X-ray tube (XRF) or a radioactive source (γXRF) to provide the primary radiation. This radiation excites the atoms of the sample giving rise to the emission of a characteristic X-ray spectrum of the elements contained in the sample. The identification of the elements can be made by dispersion of the X-rays spectrum either in energy (faster and easier to apply, using solid state detectors) or in wavelength (better sensitivity and resolution, using Bragg reflection form analyzing crystals). The limits of detection enable us to measure both major and minor atomic constituents, but, depending on the element, the matrix in which the emitting element is embedded, and the count time, the limit of detection can be as low as some hundreds of parts per million (ppm).

Techniques developed around van de Graaff accelerators known as IBA techniques are very often used in Archaeometry. (Examples of applications in Archaeometry and references can be found in Bird et al. [32, 33]). To determine the composition of the objects PIXE, PIGE and RBS (Rutherford Back Scatter) can be used, the latter for analysis of very thin surface layers.

PIXE in most cases is performed with proton beams from 1 to 4 MeV and the strong interaction of the proton with the material under examination makes this a technique for studying surface compositions. Its detection limits may attain a factor of 5 to 10 better then XRF. The use of that loss of proton energy and the production of (p,γ) nuclear reactions in the

sample allows the determination, by direct gamma ray spectrometry of the major elements distribution profile in a layers of about 15 μm depth.

Electron microscopy has been used since the 1950s either as electron probe microanalysis (EPMA) when coupled to an the X-ray detector (nowadays energy dispersive) or as scanning electron microscope (SEM) for imaging facilities. A beam of electrons, generated by heating a filament under a potential difference, is focused by a complex system of lenses in a column in the base of which the sample is positioned. The electrons produced by the primary beam interaction with the sample are transformed into electrical signals and displayed in a screen. The X-rays produced by the impact of the electron beam on the sample can also be detected for composition analysis. Coupling both detection systems we can obtain the composition of very small details, inclusions and so on as well as images showing details of the fabrication of the object. Depending on the element and on the matrix the limits of detection range from 100 ppm to 0.2%.

Although destructive, and only allowing the measurement of a single element by run, a technique which has been widely used in Archaeometry since the 1960s is atomic absorption spectrometry. The emission spectrum of the element passes through an absorption cell containing the sample in an atomised state. The atoms in the cell absorb the light at their characteristic wavelengths and re-emit it giving rise to a decrease in the beam intensity, the attenuation of the wavelength being measured. Limits of detection depend on elements and range from 0.001 to 1 μg/ml in solution

If we intend to look for the origin of the raw material we must determine trace elements and/or isotopic ratios. Depending on the geological formation of the ores, trace elements present patterns that may be used as "fingerprinting". Thus we require all possible elements be detected and that the equipment is set to operate to provide the lowest limit of detection for the determination of the provenance of a material. Few techniques allow the determination of important trace elements[6] in metals to very low detection levels. Two highly sensitive techniques are activation analysis and ICP-MS.

Activation techniques are all based in the irradiation of the sample in fluxes of neutrons or charged particles. The capture by the nuclei of the incident particle or neutron produces a radioactive isotope that decays by emission of particles and gamma rays. The gamma ray spectra of each element can be identified and easily measured. It is possible to undertake direct gamma spectrometry on the sample, or to perform a chemical separation after irradiation in order to measure some specific elements at very low concentration levels, and eventually increase their number of measure elements. The limits of detection depend on the matrix, the element, the incident particle, its energy and can easily attain 1 ppm. With chemical separation the detection limit can reach down to the ppb level. The most used activation technique is based on neutron activation produced in nuclear reactors (NAA). This can be used to measure only about 60 elements, but this can be increased if activation using accelerators can also be performed. Fast neutron activation analysis (FNAA) is usually based on neutron generators, but for numismatics, deuteron beams have been used to produce a neutron flux by impinging on a thick Be target [8, 34]. This type of neutrons has the advantage of crossing the sample without attenuation, and this makes analysis easier. The

[6] Many techniques allow the determination of several trace elements in metals. However, considering the process of smelting, purification and manufacture through which the raw material passes till the final object, many elements are lost and only few may be considered as representatives of the initial ore.

analysis is a bulk one but the number of elements determined in routine analysis is lower than for NAA. Charged particles beams are used to determine specific elements in specific matrices. Their use is limited because of the attenuation of the particle's energy during the penetration of the sample which reduces the thickness of the analyzed layer which can be analyzed. One technique that has been used for the analysis of trace elements in gold and silver coins consists on the use of proton beams of high energy produced in a cyclotron (PAA) allowing the analysis of a layer of some hundreds of μm [8,10,35].

Inductively coupled plasma-atomic emission spectrometry, ICP-AES, has been widely used since the 1970s. The technique is based on the measure of the atomic spectra of the elements but recently it has been replaced by Inductively Coupled Plasma-Mass Spectrometry (ICP-MS) as a tool for trace element analysis. ICP-MS is used to determine a very wide range of trace elements at very low levels either in solutions or in solid samples, the latter by using a laser ablation system. The sample reaches the plasma as an aerosol and is ionised in it. Then the ions are extracted and enter the mass spectrometer by a decrease in pressure and are separated by mass. Although this technique allows the determination of a large number of elements simultaneously, the performance of several measurements increases the precision. We must also be aware of major and minor elements which give rise to interference with certain trace elements (like ion $CuAr^+$ on Rh [36]). Also some volatile elements may be lost during the sample preparation or during the interaction laser/matter and transportation to plasma. Deposition of elements like Hg in the tubes and glasses inhibits their determination in low concentration. This technique can be considered as virtually non-destructive and has been applied in Archaeometry [36,37,38,39,40]. We developed a technique of solid analysis for gold with an UV laser that produces craters of 40μm diameter and 130 μm depth, sampling of about 1μg per crater with limits of detection from 10 ppb to 1 ppm [36,41,42]. Also for liquid gold samples we obtain limits of detection of the same order of magnitude by using about 2 mg of the object[7].

One main technique used for provenancing is based on isotope analysis, usually measured by thermal ionisation mass spectrometry (TIMS) and sometimes by ICP-MS, determining the atomic abundance ratio of two or more isotopes of the same element which carry information about the age of a geological sample [43]. The isotopic composition of Pb were different in different ore deposits as three of the its isotopes come from the radioactive decay of U and Th present in most ore deposits. The three-dimensional cloud of data of the ratios 208Pb/206Pb, 207Pb/206Pb, 206Pb/204Pb differentiate the ores provenance. The hardest step is the preparation of the sample consisting on the separation of the element of interest but the new chemical techniques for separating lead allow 100 ng samples of lead to be measured to ±0.1% at 95% confidence level [44,45].

4. CHARACTERISATION OF COINS AND OTHER METALWORK

In this chapter we present by type of metal some applications of the radiation techniques to the analysis of metalwork [46], mostly for monetary metals and their alloys.

[7] This technique has been developed by A. Gondonneau and M. F. Guerra together with M. Cowell from the British Museum and will be published soon.

4.1 Gold

Gold occurs in Nature under a small variety of geological forms among which the native one. The erosion of rocks (mainly auriferous quartz) during a long period gives rise to placer deposits. Because of its density gold tends to settle down and form either sedimentary buried deposits or, if the gold falls in a river, to form nuggets in the water currents. If gold is nowadays obtained by mining of veins in quartz rocks, and recovery by pulverisation and purification, gold mining in ancient times was essentially a surface or near to surface activity.

The heavy minerals are concentrated in the placers and relative proportions of detrital placer minerals are in general related. For example: the log/log coefficients of correlation between gold and uranium seem to be characteristic for each placer [47]. Other metals are found in gold placers like silver and mercury (1 to 5 % Hg in gold from South Africa), sometimes with a complex heterogeneity of the composition [47]. Nearly all gold in nature is gold/silver, with a wide range of silver concentration till 40-50% and copper below 1% and quite frequently iron [48]. The presence of Pt in gold is more difficult to use in determining provenance as its presence has been observed in objects but not in minerals from the same region [49]. In primary deposits gold is frequently associated with tellurium, bismuth and silver, and less frequently with antimony, selenium and copper (pyrite and arsenopyrite). Typical minerals are calaverite $AuTe_2$, nagyagite $Pb_5Au(Te,Sb)_4S_{5\text{-}8}$, petzite Ag_3AuTe_2, sylvanite $(Au,Ag)_2Te_4$, kostovite $CuAuTe_4$ [50].

Gold is as almost soft as lead and very ductile and malleable. It can be hammered when cold to produce very thin sheets or very long wires. Jewellery in primitive societies often is made from gold in the form of wire. In more sophisticated societies gold dust was put into crucibles and melted in a charcoal fire under a temperature of at least 1063°C. To refine native gold the first step was cupellation to get rid of the base metals by oxidation. The second step was the separation of gold and silver by the reacting the silver with salt or sulphur to leave behind refined gold [51]. However, in some cases coins and objects were made by compacting powder by sintering. This may explain the cracks on Celtic coins, as only a partial melting and sintering of blanks occurred because the low heat conductivity of the metal[48]. As well, the alloying of copper and gold was widely practised in the prehistoric civilisations of Central and South America to create tumbaga. During finishing these objects were treated with a corrosive preparation that dissolved copper from the surface [51,52].

4.1.1 Fineness and debasement

One of the most important attributes of precious metals alloys are their quality, called the fineness. For example: the quantity of gold in gold alloys[8]. The increase of one or two lower price metals in the alloys is called debasement. For coinages this is related to the political and economical state of society.

The non-destructive analysis of gold in a gold alloy is quite easy when using techniques based on X-rays emission and activation analysis. In Figure 1 we present the gold content obtained by PAA for a group of dinars[9] issued in the Iberian Peninsula from the

[8] See Agricola (Book VII) [3] for the assay of coins by the touchstone.
[9] Muslim gold coins are called dinars.

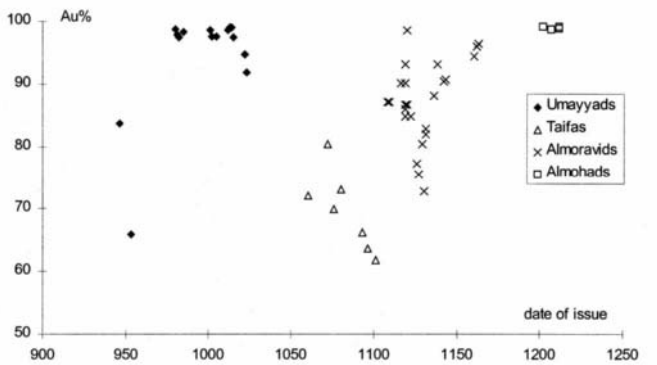

Figure 1. Evolution of the gold contents with the date of issue for the Muslim coins struck in the Iberian Peninsula. We can observe a debasement under the Taifas and a smaller one under the Almoravids.

arrival of the Muslims till the Almoravids [53,54,36]. This Figure shows clearly the hard economical situation in al-Andaluz under the Taifas when the fineness fell below 62% and the reestablishment of a central power under the Almoravids when the gold content reached 98.5%. A small number of coins struck by the Visigothic kings Erwig, Egica and Egica and Wittiza[10], who reigned in Spain before the Muslim caliphates, show in Figure 2 significant debasement with a gold content as low as 36%. If we consider in Figure 3 the concentration of Ag as a function of the contents in Cu for all these coins we observe that for the Visigoths the debasement was obtained by increasing mainly the concentration of silver to about 59% (Cu is only about 4%). For the coinage of the Taifas the debasement was obtained by the increase of both metals, Cu attaining about 15% and Ag about 30%. For those positioned in the line we could consider that their contents are correlated so that the alloy eventually added would have about 80% Ag and 20% Cu. A few dirhems[11] struck from 960 to 1020 showed a content of Cu of about 21% and could be use to debase the gold coins, however many others have a Cu content of about 5% [40].

As suggested by many authors in the 1970s such as Hartmann [56] and Antweiller and Sutton [57] the debasement of coins by an increase of the silver amount may be obtained either by addition of silver or by less (or non) purification of placer gold. For the latter the concentration of lead in the coin would come only from cupellation while for silver obtained from lead ores the concentrations of Pb and Bi would increase and be correlated to the amount of silver present in the gold alloy[12].

[10] For the fineness of the Visigothic gold coins see [55].
[11] A dirhem is a Muslim coin minted with silver.
[12] Some gold globules obtained from melting sherds in Lydia showed Pb and Bi inclusions [59].

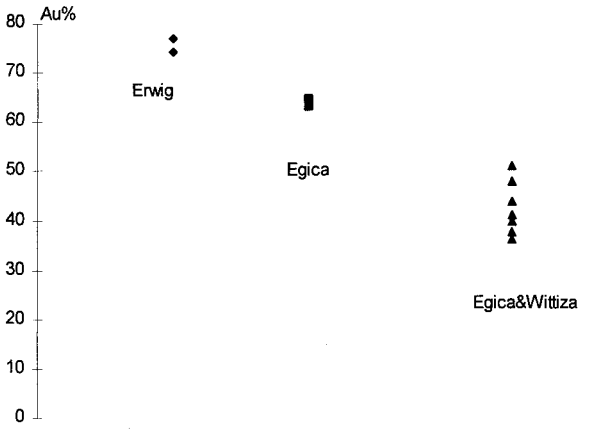

Figure 2. Evolution of the gold contents for the coins struck by three Visigothic kings. The enormous debasement shows the poor state of the economy in those times.

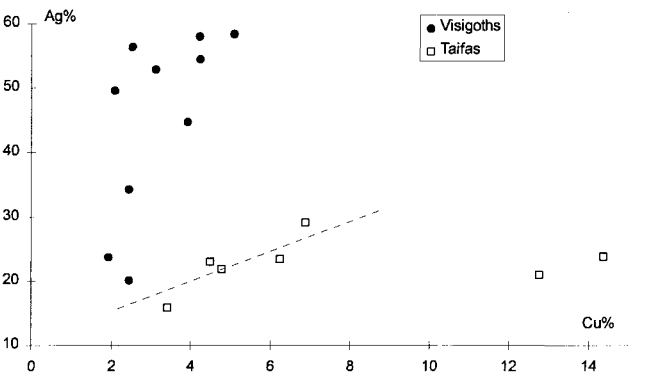

Figure 3. Copper in function of the silver contents for the coins struck by the Taifas and by the Visigoths showing that the debasement is due either to an increase of silver only or to an increase of both metals.

In Figure 4 we have plotted the concentration of Pb in function of the amount of Ag for the gold coins struck in the Iberian Peninsula. Some of the coins on line A seem to present a correlation between silver and lead but coins in square B, with very high contents of Ag, have a Pb content of under 500 ppm. Addition of silver obtained from other than lead ores is also quite possible.

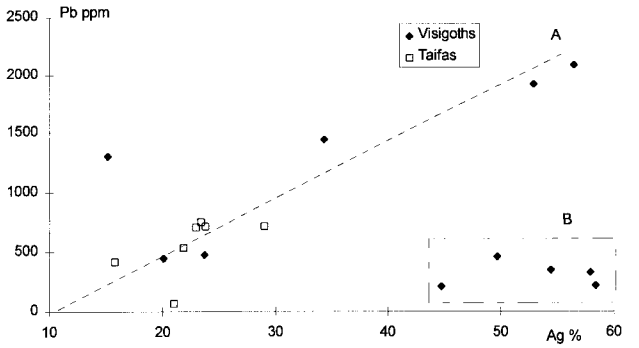

Figure 4. Lead in function of silver contents for the coins struck by the Taifas and the Visigoths.

If some coins could have been debased by addition of silver extracted from a lead ore, others have suffered debasement by other techniques. A very interesting case of gold coins debasement was shown for the gold coins struck in Persia known as double-darics analysed by PAA [58]. The first coins struck in Lydia by Croesus as well as the following ones called darics have 96.5 to 99.5 % Au, but the double-darics only showed to have 71 to 94 % Au with a lead content lower than 200 ppm. Figure 5 shows that this debasement corresponds to an increase of Cu and Ag, these elements being correlated. All the silver coins struck and used in Persia at that time had a very good silver content[13] that may attain 99% for the tetradrachms, so they were not directly used to debase the double-darics. According to Forbes [51] and Joannès [62] the refining techniques were carefully controlled in the Ancient Near East and, depending on the type of object, the fineness was well controlled, indicating that this debasement could be related with a different manufacture. We must notice that the analysis performed by N. Hughes [63] on a gold earring from the Babylon treasure (4th century BC) revealed a composition very similar to the double-darics.

4.1.2 Provenance of the ore

To trace metals back to the ore deposits or to the mines supplying the metals used for the manufacture of objects by means of their chemical composition we need to establish a pattern by means of the trace elements concentrations [64]. This is not easy to determine even if the ore deposits were themselves homogeneous. In fact during and cupellation smelting fluxing metals are added to the ore, the temperature and the atmosphere of the furnace are variables and corrosion can change the original composition. Melting experiments under oxidising and reducing conditions showed that elements like copper and tellurium were affected [65] and metals are often melted down for re-use.

[13] Sigloi were analysed by Cowell [60] giving 96.5 to 98% silver (see also [61]). Several tetradrachms were analysed to check for their composition. We obtained 90 to 97% for lion and elephant type and 99 to 99.7% for Alexander type [58].

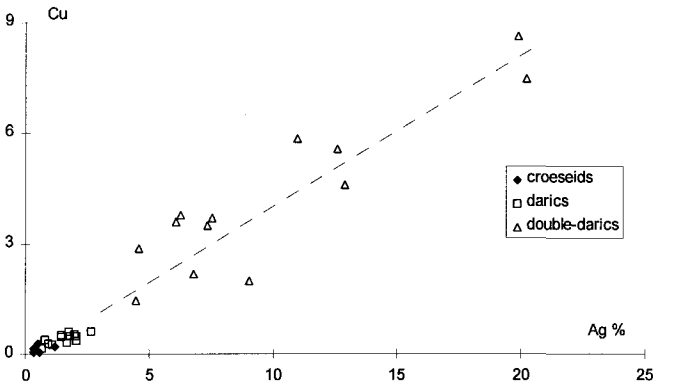

Figure 5. Copper in function of the silver contents for coins struck in Anatolia. The debasement of the double-darics was made by addition of the two metals.

The change in the quantities of certain trace elements gives important information to numismatists [66]. If we examine the staters struck in Macedonia (exploitation of Mt. Pangaeus in southern Thrace) by Philips II, his son Alexander the Great and his successors, and plot in Figure 6 the results (on the first two axes that account for 41% of the proportion of inertia) of a principal component factor analysis on several trace elements taken relative to the concentration on Au we can observe two groups [58]: one characterised by very low contents of Pt, Pd and Sn, corresponding to the coins struck after the death of Alexander the Great, and another rich in Pt an Sn, corresponding to the coins struck before his death. If these results only suggest a change on the exploited deposit maybe from placer to vein gold[14] they are very useful to date the posthumous coins.

An example showing the importance of the trace elements patterns to define changes in the ores supplies is given by the analysis by PAA and LA-ICP-MS of gold coinage struck in the North of Africa and Spain by the Muslims during the expansion of their empire [36, 53]. The analysis of Byzantine and Arab/Latin solidi minted in Carthage as well as Ifriqiyan dinars struck by several Muslim dynasties shows in Figure 7 that the Umayyads re-cycled the ancient gold. This has been characterised by a correlation between Pt and Ir and shows that a new gold ore source became active under the Aghlabids. Principal component factor analysis performed on the dinars shows (Figure 8) several data clouds corresponding to different gold types: one used by the Aghlabids which have high Ga contents, and certainly comes from a small source in the North of Africa; another used by the Almoravids, certainly corresponds to the gold from ancient Sudan[15] because this dynasty controlled the gold routes of West Africa. Fatimid dinars are spread from the Aghlabids to the Almoravids, but we must remember that after 1050/51 AD the Fatimids lost control of the western routes and took the control of the

[14] We must notice that Hartmann [42] suggested that the gold used to strike Celtic coins was gold from the Rhein as it contains high contents of Pt and Sn. In fact those elements come together with gold during panning and washing operations as already suggested by Agricola (Book VIII) [2] and explained by Healy [67].
[15] Ancient Sudan includes Mali, Ghana, Niger, ...

eastern ones. Therefore gold from Nubia could also be used to mint the dinars. The same type of phenomenon is observed in Spain. The first dinars were struck using Visigothic gold from the southern mints and another source of gold becomes active under the Umayyads.

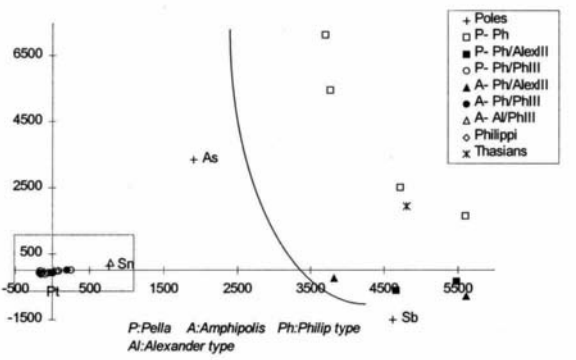

Figure 6. Component factor analysis separating in two groups the coins struck in Macedonia from Philips II to the successors of Alexander III.

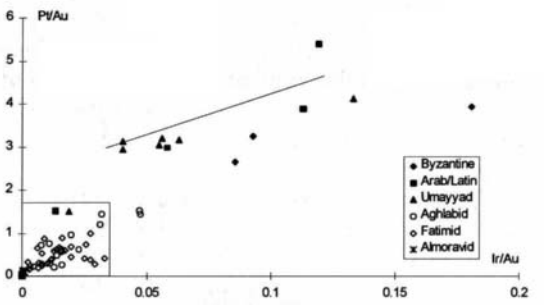

Figure 7. The contents on platinum group elements of coins minted in the North of Africa before and after the Muslim conquest show a change in the gold supply under the Aghlabids.

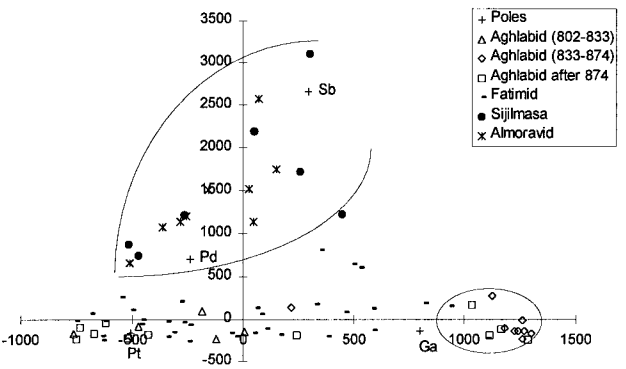

Figure 8. The component factor analysis for the Muslim coins struck in Africa shows different sources of gold ores.

4.1.3 Manufacturing technology

When dealing with metalwork the study of manufacture technology is of great significance[16]. One of the most interesting possibilities of the use of radiation techniques concerns the use of microbeams and external beams. The use of an external PIXE beam allowed the analysis of every jewel, soldering included, from the Eauze's treasure (Gers, France, 3rd century AD) and this gave us an understanding of the manufacturing technology of the goldsmiths of the time [69]. The jewels compositions are 85<Au<99%, 1<Ag<14% and 0.2<Cu<2.3%. In Figure 9 we can see a double distribution showing that most of the objects were made with native gold and that objects from the same typological groups do not have the same composition. Certain parts of the objects have a higher concentration of copper, for example, the loop points. Deliberate addition of copper increases the hardness and lowers the melting point. The analysis of soldering on all objects shows a small increase in copper with the silver concentration remaining constant. This is a typical case of soldering by copper diffusion (addition of copper compounds).

The variation of the incident proton beams energy may be used to make non destructive depth profile analysis [70] (as well as the use of the ratio L lines/K lines by EDXRF). One technique associates DP-PIXE and alpha-IXE together with RBS to determine the depth distribution profile of Au, Ag and Cu allowing to study the surface gilding treatments [71,72]. Figure 10 taken from the work of Ruvalcaba-Sil [71] shows the profiles obtained, and demonstrates the gold surface enrichment typical of a tumbaga treatment (see Forbes [51]) for a Tairona style anthropomorphic pendant made in the North of Colombia in 600-1500 AD. Also DP-PIGE is another technique for the determination of the composition of both surface and substrate of gilded objects [73]. Fire or mercury gilding is peformed [74] either (i) by the application of a gold amalgam to the surface of the object and then by heating

[16] For gold coins see Lerhberger and Raub [68] : several techniques are used to determine the composition and the manufacture technologies and Celtic coins. Identification of inclusions, micro-structures, micro-hardness, ...

the object causing mercury to evaporate, (ii) by rubbing clean mercury over the surface of the object and then laying gold leaf on top.

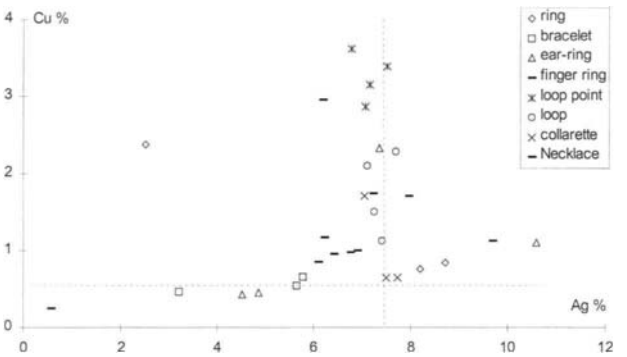

Figure 9. Copper in function of the silver contents for the jewels of the Euze's treasure. Soldering was made by the copper diffusion technique [69].

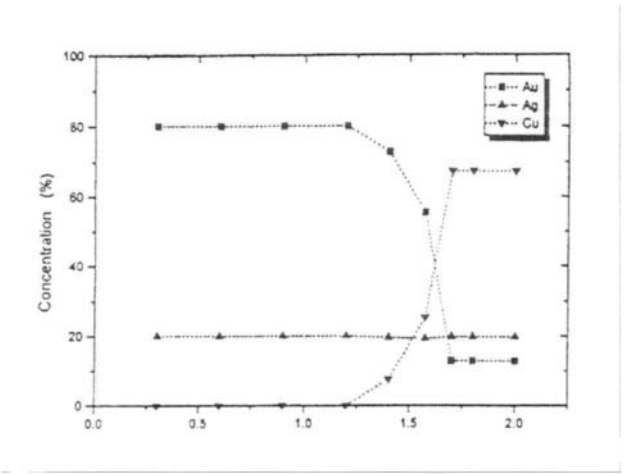

Figure 10. Concentration profiles for Cu, Ag and Au of an anthropomorphic pendant of Tairona style made in the North of Colombia in 600-1500 AD, showing a typical tumbaga treatment [71,72].

The gold dissolves in mercury and several layers are added[17]. The analysis of Roman (4th century) and Merovingian (5th to 7th century) gilded brooches by PIXE and RBS showed the same technology as silver and copper concentrations are very diversified for each typological group and that the ratio Hg/Au is the same for both periods [78,79]. However, the analysis of the substrate by DP-PIGE (plating thickness reaching 11 μm) showed that, contrary to the complete gilding of bronzes made by the Romans, the Merovingian goldsmiths used a silver/gold colouring effect by partial gilding. (Figure 11 shows the profiles obtained for a Roman brooch by DP-PIGE [79].).

4.2 Silver

The silver smelting and refining technology was certainly very closed to that of lead because the most important silver ores were intermixed with lead ores. Silver occurs very rarely in the native state, in deep veins and is also frequently obtained by separation from natural alloys with gold. The most important ore of silver is galena (PbS) with 0.03 to 1% Ag but copper ores like chalcopyrite may also contain silver, and secondary lead minerals cerrussite ($PbCO_3$)and anglesite ($PbSO_4$) are also important. Some rare ores like argentite (Ag_2S) and cerargyrite (AgCl) could be easily used to produce silver, but it is also possible to use embolite, kerargite, polybasite, stephanite [67,50].

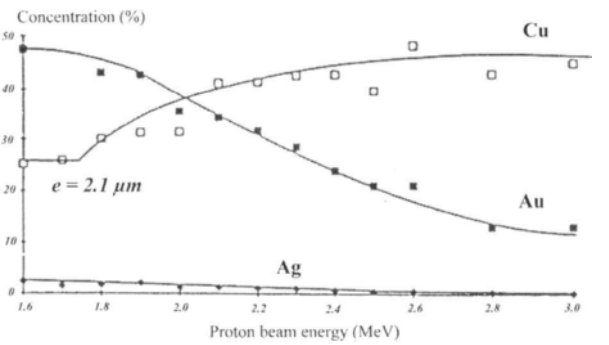

Figure 11. Concentration profiles for Cu, Ag and Au of a Roman brooch by DP-PIGE with a gilded layer of 2.1 μm thickness [79].

Silver is produced[18] by cupellation from ores like cerrussite. The ore is melted with lead, and the liquid lead together with the other impurities oxides are separated from the

[17] For plating techniques and see also [75, 76,77].
[18] Good description of refining and smelting of silver ores in Forbes [51].

metallic silver by absorption on a cupel. If sulphidic ore like galena is used a first roast is made to remove the sulphur followed by a reduction by charcoal to oxide (oxidation of lead to litharge) is made to obtain lead metal. (An extra roast step may be necessary to remove sphalerite[19] [80,67]). Finally cupellation is performed to separate silver. For other ores silver may be separated from copper by granulation of silver in water, mixing it with common salt and clay and placing in a furnace with charcoal. The silver is converted to silver chloride and absorbed by the clay and the gold is unchanged and washed out. The silver mixture is then mixed with lead and cupelled.

Cupellation leaves traces of Cu, Au, Pb, Zn, Ni, Sb, Te, As and Bi in silver, and the content of bismuth depends on the process conditions because it behaves like lead [51,67]. For trace elements, depending on the cupellation conditions several results can be obtained for the same ores. A description of the techniques used for the de-silvering of Roman lead has been given by a number of authors. A comprehensive discussion can be found in Tylecote [81] (see also [82]); Healy [67] gives 0.02% of silver in Greek lead and 0.01 to 0.002% Roman one and Forbes [51] gives 0.002-0.008% for Roman lead pigs.

Several of the technological problems are similar to those discussed for gold. Soldering silver is based on the fact that alloys of copper and silver have melting points below those for the pure metals. Silver objects have melting points in the range 890-900°C while for the solders the lowest melting point is 778°C for an alloy of 72% silver and 28% copper [83]. Silver coins may also be plated. In this technique a thin core of sheet copper is covered with two thin sheets of fine silver welded to the copper, except at the edges where the silver layers are joined with a silver-copper solder [81][20]. For copper and silver alloys mercury (or fire) gilding can also be used. In Figure 12 we can observe a section of a forgery of a Celtic silver coin of Epaticus obtained by Cowell and La Niece [75] where the corroded copper core was coated with a continuous layer of copper-silver alloy. This process could also be made with molten tin on copper alloys for decorative purposes [74]. A very common coating technique in the Middle Ages was blanching, in which there was selective removal of copper at the surface (surface enrichment in silver) leaving a very thin high purity silver coating[21].

4.2.1 Debasement and manufacture technology

The reasons for the debasement of silver coinage and objects are the same as for gold. A few examples of use of radiation techniques for analysis will now be outlined.

Silver coins can be used to debase gold coins. The problem of re-melting coins to produce debased ones of higher monetary value is discussed in some detail in the work of Sarthre [84] on Gaulish coins. The high Pb and Sn contents found in a group of gold coins of the "trident" type analysed by PAA suggested the addition of silver coins of the same or preceding periods to debase the gold ones [85]. The average theoretical composition of the silver coins was estimated to 58.8% Ag, 0.35% Pb and 40.6% Cu. The silver coins of the

[19] Sphalerite (ZnS) is a zinc ore occurring in general with galena [67].

[20] Tylecote [81] gives a description of the production and composition of coins in Britain including production of dies and striking.

[21] A good description of forgeries can be found in [76]

"cavalier ailé" type showed a composition of 54.9% Ag, 0.92% Pb and 39.2% Cu which means that they could have been used to debase the gold coins [86].

The debasement of silver coins is in general done by progressive addition of copper or of a copper base alloy. A group of 122 billion[22] coins called "dinheiros" issued from the reign of Afonso I to that of Fernando I (1128-1383) were analysed by EDXRF for their major and minor elements and by FNAA [87]. Figure 13 shows the comparison for silver concentrations obtained by both methods and we can observe that, if we except 1 coin, the results fit quite well. The debasement was obtained by addition of Cu to the alloy. If we consider (Figure 14) the evolution of the fineness we can see a progressive debasement from 25% silver to almost pure copper, with the main debasements initially from Afonso I to Sancho I[23], and later from Afonso II to Sancho II. Finally, under Fernando I the silver had vanished, which is unexpected, given the legal value implied by the coinage.

The high quantity of tin obtained by XRF compared with FNAA suggested the use of tinning rather than silvering, although it was demonstrated that the coating of ancient coins is always silver [74]. In order to test this possibility two coins were cut and analysed by SEM to determine the Sn, Ag and Cu depth profiles. This study revealed that silver is distributed in form of precipitates (white spots in Figure 15) dispersed all over the coin, and also as a surface layer of 1 to 2 μm thick. This showed that the silvered aspect was done by a silver coating and not a tin one.

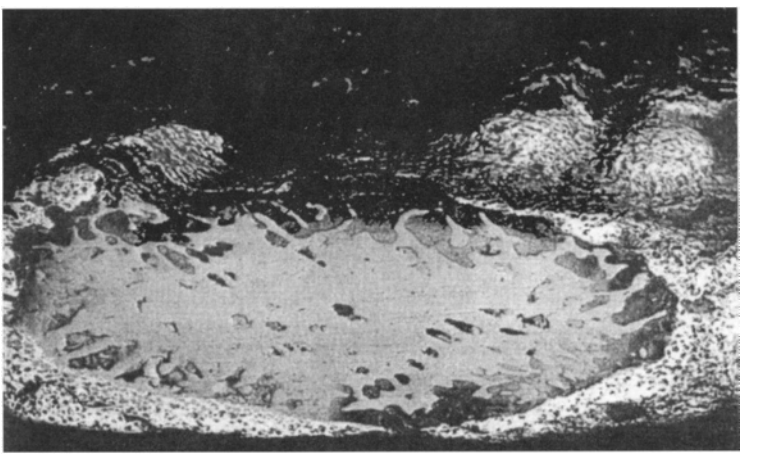

Figure 12 : Section of a contemporary forgery of a silver-copper coated Celtic silver coin of Epaticus obtained by Cowell and La Niece [75].

[22] Billion is an alloy of copper and silver which, in the case of the dinheiros, is silvered.

[23] The coins struck under Sancho I are separated in two groups. The explanation can be found in chapter 4.2.2

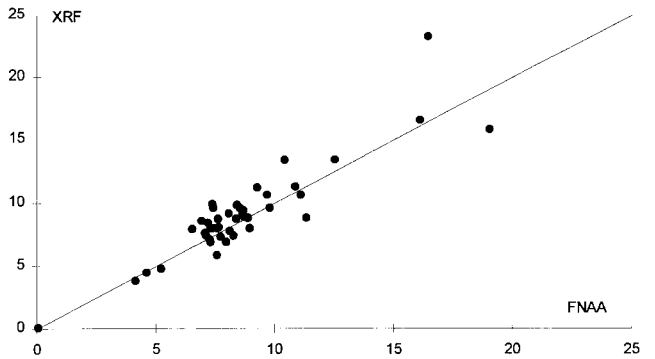

Figure 13. Comparison between the results obtained by XRF and by FNAA for the Mediaeval billion silvered coins dinheiros.

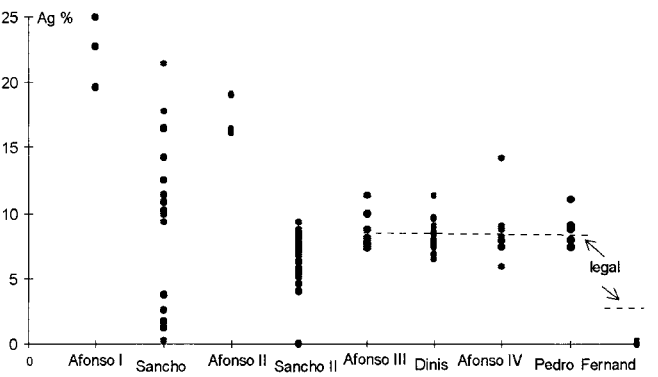

Figure 14. Evolution of the silver content of minted dinheiros. Legal values correspond to those obtained by analysis except for the last reign.

We can also mention the use of Zn to debase silver coins in the Middle Ages, as referred by in England [88]and in France [89]. At the 11th century this debasement was probably done by addition of brass. As well, the zinc content decreases with re-melts (see 4.3 for Zn properties). The increasing and decreasing of the Zn contents observed in England [90] is also observed in France as shown for a small set of French coins in Figure 16 [91], suggesting that the quantity of Zn could be used to roughly date hitherto non-datable coins.

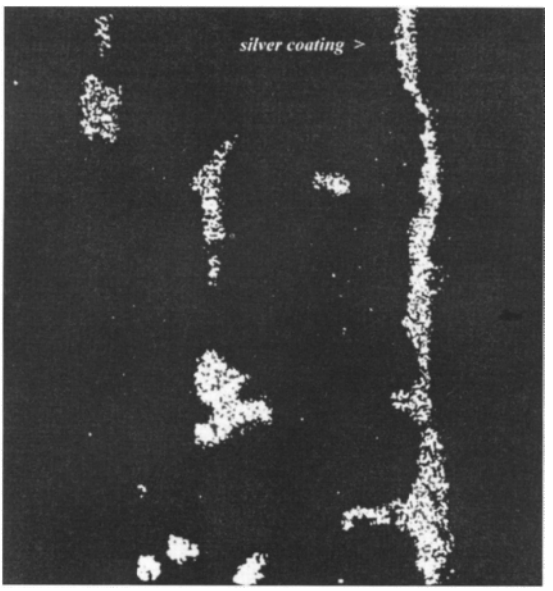

Figure 15. Silver distribution profile on a section of one dinheiro showing that the coated layer was made by selective removal of copper on the coin's surface.

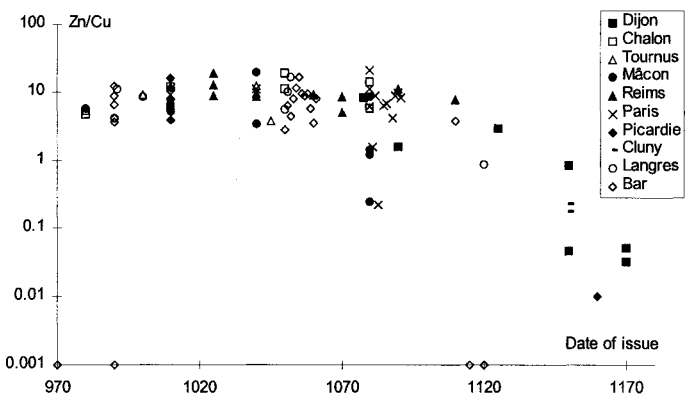

Figure 16. The evolution of the ratio zinc to copper in function of the date of issue for the French zinc-debased coins give criteria for dating the coins.

4.2.2 The provenance of the ore

Determining the provenance of silver is more difficult than for gold because most trace elements are easily separated from silver, and their concentration may not be representative of the ore [92]. Also silver is in general mixed with copper ores which have the same impurities. Only gold and in some particular cases other platinum group elements are not affected by smelting and cupellation and are characteristic of a certain ore. If silver has less than 0.1% Au it was probably produced from galena but if the gold content is higher the silver could come for other lead ores like cerussite. If the amount of lead in the silver artefact is less than 0.05% it shows that silver was not produced by cupellation [67, 80].

Sometimes the study of trace elements may give an indication on the change in the source of the ore supplies. This is the reason for the two groups of coins of Figure 14 for Sancho I. In Figure 17 the contents of silver in function of the ratio As/Cu measured by FNAA [93] show that two types of ores were used. As the copper ores from the south of Portugal have high quantities of arsenic the plot suggests that there was a change in the ore supplies. If we consider the typological groups we can observe that coins included in the group of low arsenic content belong to the era of the first kings and were struck in the northern mint, while the second group was struck in the centre and southern mints. The H group belonging to Sancho I is separated in group H1 produced with northern ores and H2 produced with southern ores. This suggests that group H2 was minted by Sancho II rather than Sancho I.

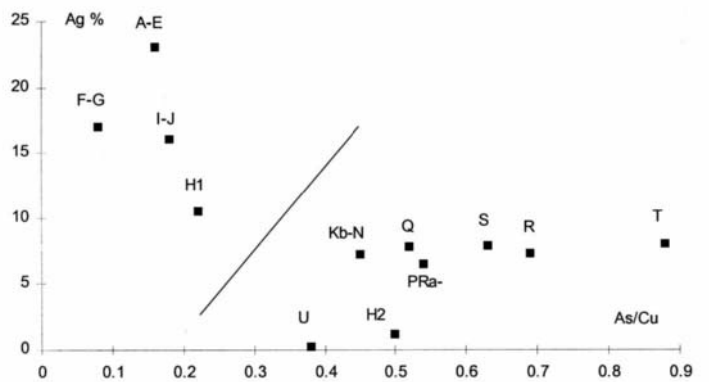

Figure 17. For silver, the ratio of arsenic to copper for the dinheiros shows that the northern mint has a different ore supply from that of the southern mint.

In the last example the change in ore supplies to the silver mint can be indicated by characteristic elements of copper if the geological context is known. As well, a small number of examples exist in the literature in which the provenance of silver ores has been determined by trace elements present. Using Au together with Ir Meyers showed that good results could be found for several types of Eastern silver [94]. The analysis by NAA, followed by chemical

separation of Au, Ag and Cu on drilled samples of 200-1000μg from Sasanian silver objects, enabled the determination of nineteen major, minor and trace elements, amongst which are Au and Ir which are the characteristic traces considered to be typical of the "Central Sasanian" period [95][24]. The same elements were detected by NAA on 0.5mg samples of Byzantine silver objects. Discriminant analysis, based on Au, Ir, Zn, Sb, Co and Hg impurities, was used to distinguish in Figure 18, 7th century stamped from 6th century unstamped silver objects. This showed that the stamped silver was alloyed in one location and stamped in another [80].

The knowledge of the geological content of a certain silver ore is of much help to find a trace element patterns, as shown for the silver deposits of Potosi in the south of Bolivia which are characterised by the presence of indium and germanium [97]. The presence of gold together with indium and germanium fingerprints the ore. As germanium is very hard to be measured non-destructively in silver, we have developed a technique of activation analysis based on the production and the moderation of neutrons produced in a cyclotron by a 20 MeV HH+ beam to measure indium and gold at very low quantities in silver [98].

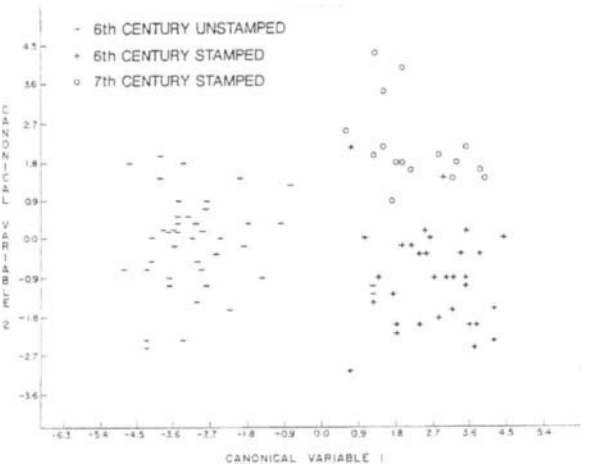

Figure 18. Discriminant analysis differentiates 7th century stamped from 6th century unstamped Byzantine silver objects obtained by Meyers [80].

[24] We must recognize the great work performed by A. Gordus using micro-drillings of coins analysed by the Howitzer and by NAA. For Sasanian silver, the 1000 coins analysed in [96] showed by their gold contents that modern fakes can be identified. In the same reference and also using the quantity of gold but in the Umayyad dirhems he set out the different ores supplies for different mints and different periods.

A large amount of money was sent by the Spanish Kings to the Flanders to pay for the war first by sea, then through France, and after that through Barcelona to Genoa whence the money was sent to Antwerp. The evolution of the ratio In/Ag in function of the date of issue for Spanish and Potosian silver coinages is shown in Figure 19. We can see that the Andean silver arrived in Spain under Philip II in such large quantities that no re-melt of the preceding coins was performed[25]. But this silver supply did not last long because there is a dilution of another ore, certainly the Mexican one, considering the registered production of the Mexican and the Potosian mines. The arrival of this silver in the Spanish coinages was estimated around 1570, which corresponds to the introduction in Peru in 1570-72 of the more productive technique for silver extraction by mercury amalgamation. The same behaviour was found in other European countries [99], for example, France, were coins were marked with their date of issue.

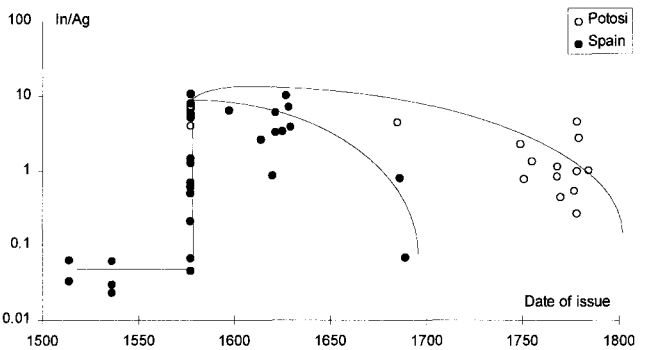

Figure 19. The evolution of the indium contents taken to silver in function of the coin's date of issue shows the arrival of the silver from Potosi into Spain under Philip II.

We plot in Figure 20 the ratio In/Ag as a function of the coins' date of issue. It can be seen that Potosian silver arrives in France in large quantity in 1575[26]. During the 1580s most of the coins were struck with almost pure Potosian silver, and this decreases in the 1640s [100].

4.3 Copper and other base metals

In the main, metallic objects were fabricated from a wide variety of alloys of gold, silver, copper, arsenic, tin, antimony and zinc. The introduction of other metals in certain alloys changes the properties of the alloy, as, for example, the addition of lead to bronze increases the fluidity and lowers the melting point. Both are desirable properties from the

[25] Usually old coins are re-melted to strike new ones. However we observe here for the new coins the same ratio of In/Ag as for pure Potosian coins. This shows that no mixture of metals was made.
[26] This date corresponds to the monetary reform of Henry III and the creation of the silver franc.

point pf view of pouring the alloy into moulds. The evolution of processing is well shown by the chronological development of the non-ferrous metals and alloys in Ancient Egypt.

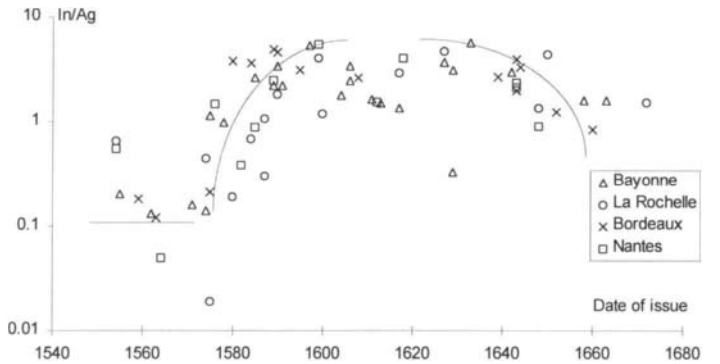

Figure 20. The evolution of the indium contents taken to silver in function of the coin's date of issue shows the arrival of the silver from Potosi into France in 1575.

In Figure 21 Cowell [75] presents the results for the analysis of tools and weapons, particularly axes found in datable excavation contexts. We can see a gradual replacement of four copper-based metals or alloys from the 3rd millennium BC to the 1st millennium: pure copper, arsenic copper (up to 6% As), tin bronze or lead tin bronze, and iron.

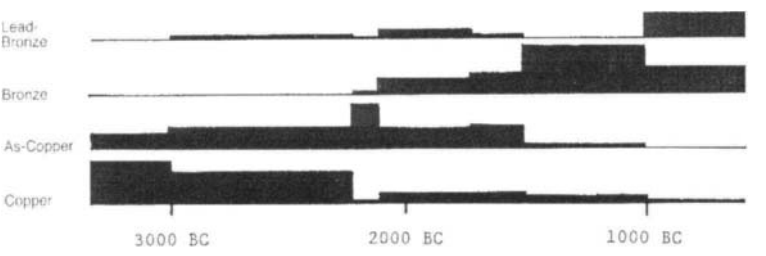

Figure 21. Chronological development of the metals and alloys in Egypt obtained by Cowell and La Niece, for tools and weapons [75].

Like gold, copper and brass are ductile and can be beaten into foils, drawn into wires, and forged [101]. Copper alloys have colours ranging from red to golden yellow. Objects can be produced by soldering and casting. The different copper-based alloys are demonstrated by

Baley [102] in Figure 22 for Roman Britain metalwork: brass with zinc from 10 to 25%, bronze with tin from 5 to 16%, gunmetal with tin and zinc in %. Leaded alloys may contain from 4 to 20 % of lead.

The processing of copper and the other base metals can be found in Forbes [38], Tylecote [81], Healy [67] and Craddock [101,103]. Native copper is quite pure, with low contents of Au, Ag, Fe, Sb, and can be found either as small grains or laminated masses. Copper may obtained either from oxides, carbonates and silicates associated with native copper or from deep vein sulphides. The oxidised ores are malachite, chrysocolla or cuprite and sulphide ores are chalcocite or chalcopyrite ($CuFeS_2$), the principal primary copper mineral. Refined copper has in general the following impurities : As, Pb, Zn, Sb, Ni, S [67].

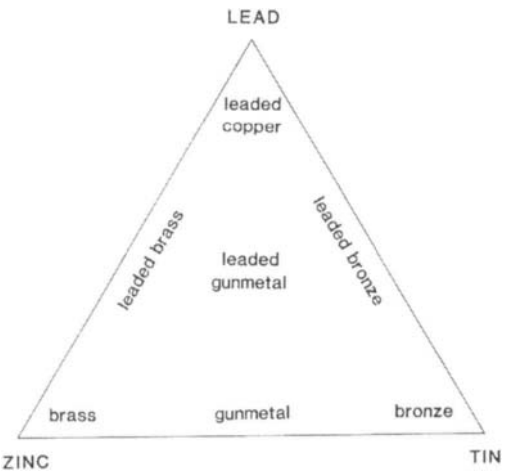

Figure 22. The different copper-based alloys as defined by Baley [102] for Roman Britain metalwork.

Forbes [104] describes the smelting and refining steps of copper. The first step for oxides-carbonates-silicates was refinement by heating and reduction of the ore with charcoal. For sulphides, an extra refinement was performed to remove impurities like Sb and As. An initial roasting consisting of calcination of the ore was followed by the smelting of the roasted ore with charcoal. This was sometimes followed by a second and third smelting to take away any iron oxides leaving pure copper with variable amounts of Au, Ag, Fe, Pb, As, Sb, Ni, Co, Zn and Sn. The removal of those impurities needs an extra refining step requiring considerable skill. If precious metals are present in worthwhile ampouns liquation is performed with lead in which the impurities are soluble.

The first element alloyed to copper was ***arsenic*** (Figure 21), which improves the properties of copper. Arsenopyrite (FeAsS) is the most common mineral containing As, occurs with Sn and W ores, and is associated with Ag, Pb, Cu, Sb and Au; also realgar (AsS)

may be found with veins of Pb, Ag and Au and Sb. Because arsenic ores occur mixed with copper and iron ores its presence in copper and bronze can readily be explained [67].

The new alloy was formed by the addition of ***tin*** to copper to produce ***bronze***. In fact, as referred by Shepherd [105], small increases in the amount of tin increases the hardness values: copper 87; 9-31 % tin-bronze has a hardness of 136 and 10-34 % tin-bronze has a hardness of 171 (using the Vickers scale). The main ores of tin are : cassiterite (SnO_2), forming often by erosion placer deposits with gold and other heavy elements, called stream tin, and stannite (Cu_2FeSnS_4) associated as inclusions with cassiterite, chalcopyrite, tetrahedrite and pyrite [67]. Tin is present in alloys of bronze, pewter and solders, but was also used to produce for example tin ingots.

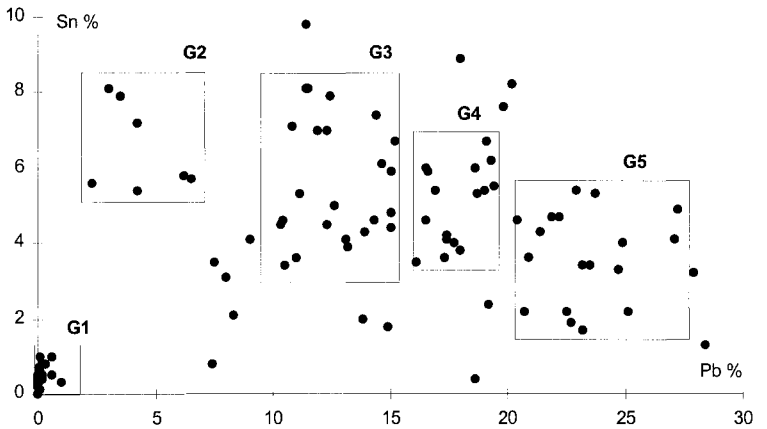

Figure 23. The evolution of tin as a function of lead content shows the gradual replacement of the more expensive by the less expensive metal in the horse-type Iberian coins.

Another important copper alloy is ***brass***. Although much used in Roman times to produce coins and jewels[27], it was only recognised as an alloy of copper and zinc in the 18th century. ***Zinc*** occurs frequently as sphalerite (ZnS) - with galena -, smithonite ($ZnCO_3$) and calamine. It is always associated with Pb, Ag, Cu, Sb, As, Fe ores and oxides are obtained as by-product during the treatments of those ores [67].

Pure ***zinc*** is extremely volatile and cannot be smelted: its melting point is 419°C and its boiling point 907°C, which is low compared with the 1000°C required to reduce the ores. Until the 18th century brass was made by mixing finely divided copper metal with calamine and charcoal in a closed crucible. When heated zinc is reduced to metal and diffuse into copper. Under reducing conditions the Romans obtained till about 28% of zinc in brass [103].

The last base metal, as lead was considered in the silver chapter, is ***antimony***. This metal can be found mainly in stibnite (Sb_2S_3) and as a by-product of other ores of copper, lead and iron. The high quantities observed in bronzes come from the copper ores [67].

[27] But used in preceding periods and other regions [106].

4.3.1 Debasement and Provenance

We may consider that copper or bronze coins are debased by the addition of less expensive metals like Pb. In antiquity a large number of coinages took this option during difficult periods in their economies. (For example: Greek coins from Thasos and Macedonian mints [107] and minted and casted bronze Celtic coins [108,109]). One particular example is shown in Figure 23 for the Iberian horse type coins struck in the IInd-Ist century BC. Here group 1 contains almost pure copper coins, but group 2 is already a bronze and contains 7% Sn and 4% Pb. The following groups progressively reach 4% Sn and more than 20% Pb in the case of group 5 [97]. The compositions of the last group suggest that the coins were minted during and after the war with the Romans.

Fingerprinting of copper ores is necessary to determine the geological sources of the artefacts, but the attribution of a certain composition to a certain type of ore is difficult since the impurities present depend also on the smelting and refining techniques. Several papers discuss research on trace elements [110,111,112], in particular the paper by Berthoud [113][28]. But, even when the geological context is known, determining the provenance is difficult. This fact is demonstrated by the work performed on copper pre-Colombian bells by Palmer et al. [114]. The analysis performed by Mauk and Hancock [115] using NAA of native copper samples from veins, sheet and disseminated grains from White Pine mine in the USA showed the variability in its trace element geochemistry, but it is possible to separate it from European trade copper and other native copper. For the twenty-two determined elements only those presented in Table 1 gave important information and form a pattern for each type of metal. Using the same technique Hancock et al. [116] analysed copper-based metal kettles from the 16th century European-Amerindian tradeware found in Ontario. He could separate the fifty-two brass samples into five geo-chemical groups by using Au and As, and as well Sn and In compositions (Figure 24).

Table 1.
The results obtained by Mauk and Hancock [115] for several copper samples from White Pine mine in the USA show that this source of copper is different from the European sources.

Element	*Disseminated*	*Sheet*	*Vein*	*European*	*Native*
ppm Ag	370 ± 150	610 ± 580	580 ± 520	850 ± 320	170 ± 81
ppm Hg	≤6.4 ± 6.0	≤10 ± 11	≤9.6 ± 7.6	≤4.2 ± 2.1	11 ± 11
ppm As	1600 ± 880	310 ± 440	140 ± 250	1200 ± 1300	35 ± 120
ppb Au	≤18 ± 10	≤39 ± 78	≤23 ± 37	23000 ± 11000	≤29 ± 24
ppm Co	2.2 ± 0.4	2.2 ± 0.3	2.2 ± 0.5	34 ± 58	≤2.2 ± 0.8
ppm Sb	4.5 ± 2.6	3.4 ± 3.2	5.9 ± 4.7	1300 ± 970	≤1.0 ± 1.7
ppm Sc	0.25 ± 0.39	≤0.028 ± 0.019	≤0.033 ± 0.017	≤0.064 ± 0.039	0.28 ± 0.64
ppm Na	≤260 ± 380	≤59 ± 20	≤51 ± 23	1900 ± 1400	450 ± 960

We can show evidence of the use of trace elements to define changes on ores supplies for the Portuguese coins called ceitis struck from the 15th to the 16th centuries [117]. The analysis by FNAA allowed the determination of several impurities, the proportions of which

[28] This author compared one series of 40 elements data on copper ores and another and of 49 elements on copper objects.

were subject to a principal component factor analysis. These gave the clouds represented on Figure 25. We could observe that each reign issued one or two groups of coins with different compositions, corresponding to several ore supplies. The coins from Afonso V with the monetary letter L, corresponding to the Lisbon's mint, are in group G1while those struck under the same king and with monetary letter P, for Porto mint, are all in group G2.

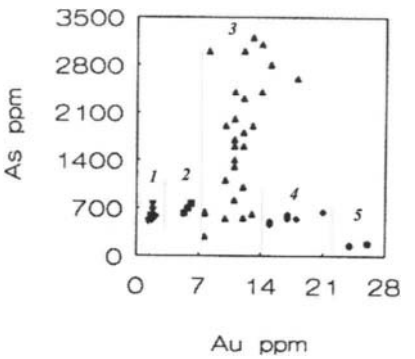

Figure 24. Brass kettles from the 16th century found in Ontario are separated by Hancock et al. [116] in 5 geo-chemical groups.

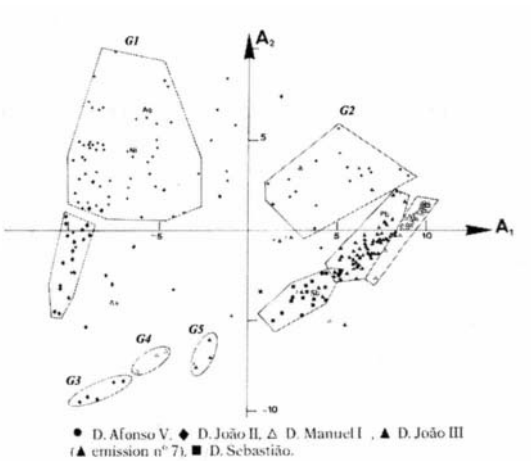

Figure 25. Principal component factor analysis for the composition of the ceitis shows that Oporto and Lisbon mints have different ores supplies and that coins with C have the same composition as those from Lisbon.

The coins having a monetary letter C, which are supposed to indicate Ceuta, fit into the Lisbon group. This confirms the fact that the archival documents never referred the existence of this North African mint. For João II coins were struck with a metal similar to the Lisbon one. However some coins in group G3 have high contents in As which suggests the use of a southern copper. For Manuel I, João III and Sebastião we observe the same phenomena in groups G4 and G5 but with main groups that are closer to the northern metal used in Porto mint.

As well, tin can be fingerprinted as Grant has shown[118]. The determination of Co, Fe, Sb, As, Au by NAA in artefacts and ingots from Roiberg in South Africa showed the same pattern for the ingots and three artefacts. The contents of Fe and As in one of the artefacts showed refining before casting, whilst the contents of Th and In in another one showed another source of tin ore.

4.3.2 Manufacturing technology

Manufacturing technology is certainly a most interesting field of work in the case of base metals[29]. Analyses by the various techniques add to our understanding of the development of the production and processing of metal through the ages. A good discussion of the different techniques that are currently used can be found in Northover and Rychner [120,121]. Also much work was done on smelting: for example [122,123].

For the study of surface treatments IBA techniques are very important for precious metals, as shown by the work of Chen et al [124]. They used 3 MeV protons external PIXE beam to analyse two copper swords from about 600 BC. These were still bright, rust-free and sharp. Analysis showed that, contrary to normal Chinese copper objects, these swords have low levels of Pb and Fe and the high contents in S. This is associated with an ancient surface treatment called sulphuring.

Several problems associated with base metals are of concern to numismatists. One concerns the study of the composition of lead Byzantine seals of several types, including modern forgeries [125]. The result of analysis by TFNAA and FNAA is given in a principal component factor analysis on Sb, Ag, Fe, Au, Zn, As, Mn and Ni shown on Figure 26. Here one clear group containing the seals with high contents of Sn and In appears. These were made in Syria and the one fake (L VI) has very high contents of Sb. All the copies and the imperial seals are very pure which suggests that lead could be a by-product of another ore processing like silver.

To show the importance of the use of complementary techniques when dealing with base metals, we consider the analysis made by Sarthre [108] using FNAA of the Francueil and Fondettes treasures from the collection of the Hôtel Gouïn (Tours, France). These are composed of a large number of cast bronze coins called potins of the "taureau cornupète" style. Figure 27 shows that a Sn content of over 20% in early examples is progressively substituted by lead. Some coins present high contents of Sb and high contents of lead and/or Sn[30]..

[29] Benvenuto Cellini, born in 1500, wrote a treatise on metalwork and sculpture considering the problems of melting copper base metals. See also [119]

[30] This problem was already referred by Northover for ingots [126] and coins [127].

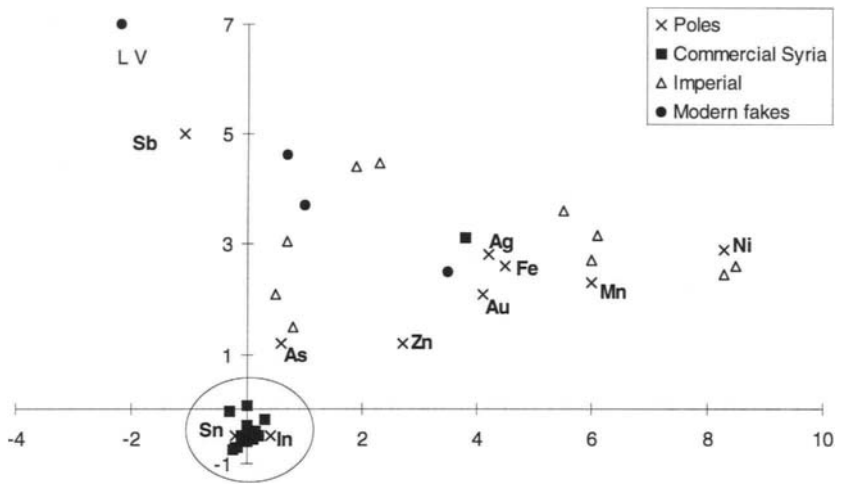

Figure 26. Principal component factor analysis for the Byzantine lead seals shows one group containing the Syrian specimens.

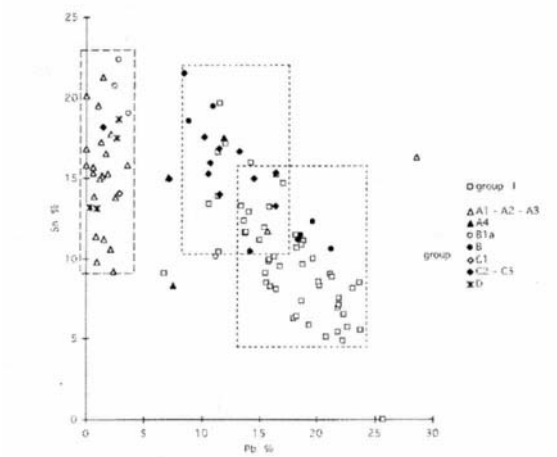

Figure 27. Lead contents in function of tin shows that this latter elements is progressively replaced by lead in the potins made by the Turons obtained by Sarthre [108].

We could consider the use of grey copper if we were to consider the analysis of two samples by Marechal [128]: As 17%, Sb 13%, Pb 19-16%.

A high tin content makes bronze brittle which means closer to the alloys used for the production of Chinese mirrors are different from those used for the production of coins'[31]. As several of the coins analysed were highly corroded, the analysis of the remaining metal might give an erroneous impression of the bulk composition. To observe the phase composition of the alloy several potins were cut to allow structural analysis by optical metallography [129]. This analysis as well as SEM in the core showed a high tin content[32], but others showed problems related to the corrosion of lead. Lead occurs in bronzes in separate phase in the form of globules of different size and irregularly distributed throughout the mass of metal [52]. With time, the initial lead grain could be replaced by copper, as shown in Figure 28 for the potin TD10 made by the Turons. We obtained 19.8% Sn and no Pb by FNNA but the Pb content could have been 5-10% in the initial alloy. As well, a set of foundry and laboratory simulations of the ancient alloys have been done[33] to understand the manufacturing technology as well as the use of such a wide variety of alloys for the same coins[34] especially those having different colours.

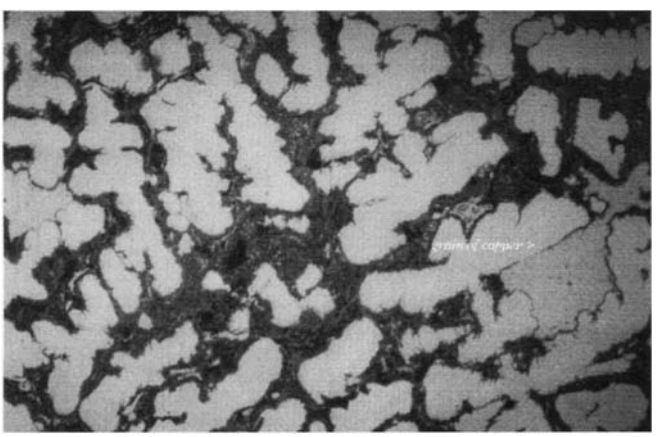

Figure 28. Optical microscope image (x 500) of a section of a potin made by the Turons showing that due to corrosion the grains of lead were completely replaced by copper (note 32).

[31] Caley [52] gives some analysis of Chinese mirrors : Sn 23-30%, Pb 1-10%, Sb 0.3-4.5%.

[32] For potin D18 made by the Suessions the compositions found are: Pb 2.1%, Sn 25.3% by FNAA and Pb 2.1%, Sn 27.5% by SEM. The SEM and optical metallography analyses were made in Oxford with P. Northover.

[33] Work done by C. Sarthre and M. F. Guerra in collaboration with D. Griffith and A. Lacey, forthcoming.

[34] The analysis of some potins made by the Pictons showed a wide variety of bronzes and leaded bronzes as well as some brasses [83]

4. CONCLUSION

The aim of this work was to give a general idea about the possibilities offered by the radiation techniques for provenancing metals and understand the manufacture technology of metallic objects. The main properties and differences for the most in use techniques were given, some, used as complementary to radiation techniques and used in the later examples, were also considered.

Several examples, most of them on coinage, for the most important non-ferrous metals and alloys used in the Past and covering a large but far from complete number of fields of research, were considered. We showed that provenance could sometimes be determined by using trace elements patterns. However, a good knowledge of trace elements present as well the geological context is required. For the questions concerning the fabrication of an object we need in general to couple both analytical and metallurgical data. A large number of examples illustrate the questions posed for metalwork.

For each main metal, after some geological, smelting and purification considerations, application of the radiation techniques to the manufacture technology and the provenance of the ores were considered for several precise historical questions.

ACKNOWLEDGEMENTS

This work recounts many examples from the PhD studies of A. Gondonneau, C. Roux and C. Sarthre. The work done for copper base alloys is included in a common program with D. Griffiths, J. P. Northover and A. Lacey. I am indebted to P. meyers for extensive discussions on the topic of silver. All the work on the Portuguese coinages is done in collaboration with F. C. Magro, and many coins come from C. Costa's collection. Almost all the coins come from the Bibliothèque Nationale de France. Most of the work done between 1985 and 1989 had the support of the Calouste Gulbenkian Foundation.

REFERENCES

1. G. Carr, Symbols of Excellence: precious material as expressions of status, Cambridge University Press (1986).
2. C. H. V. Sutherland, Gold, its beauty power and allure. Thames and Hudson London (1959).
3. G. Agricola, De Re Metallica, translated by H. C. Hoover and L. H. Hoover, Dover Publications, Inc. (1950) New York.
4. D. A. Scott and W. Bray, Pre-Hispanic Platinum Alloys: Their Composition and Use in Ecuador and Colombia. p. 285-322, in Archaeometry of Pre-Columbian Sites and Artifacts, D. A. Scott and P. Meyers (eds), The J. Paul Getty Trust, (1994).
5. E. V. Sayre and P. Meyers, Nuclear activation applied to materials of Art and Archaeology. AATA, vol. 8, n°4 (1971) 115-150.

6. G. Ambrosino and P. Pindrus, Non destructive analysis of ancient metal objects. Rev. Metall., 50 (1953) 136-138.
7. Y. Emoto, Application of radio-activation analysis to antiques and art crafts, Scient. Papers Japan, Antiques, 13 (1956) 37-41.
8. Meyers P., Non-destructive activation analysis of ancient coins using charged particles and fast neutrons. Archaeometry 11 (1969) 67-84.
9. P. Meyers, Non-destructive analysis of ancient coins using charged particle and fast neutrons, National Bureau of Standards, 189-206, Gaitherburg, Maryland, 1968.
10. P. Meyers, Activation analysis methods applied to coins : a review. E.T. Hall, D.M. Metcalf (eds), Methods of Chemical and Metallurgical Investigation of Ancient Coinage, 183-193, Royal Numismatic Society, S.P. 8, London 1972.
11. M. Banks and E. T. Hall, X-ray fluorescence analysis in archaeology ; the 'Milliprobe' Archaeometry 6, (1963) 31-36.
12. E. T. Hall, F. Schweizer and P.A. Toller, X-ray fluorescence analysis of museum objects : a new instrument Archaeometry 15,1 (1973) 53-78.
13. R. Cesareo and F. W. von Hase, Analisi di ori Etruschi del VII sec. A.C. con uno strumento portatile che impiega la tecnica dell fluorescenza X eccitata da radioisotopi, Applicazione dei metodi nucleari nel campo delle opere d'arte, Atti dei Convegni Lincei 11, 257-296, Accademia Nazionale dei Lincei, Roma, 1976
14. S. A. E. Johansson and T. B. Johansson, Analytical application of particle induced X-ray emission Nucl. Instrum. Meth. 37 (1976) 473-516.
15. G. Demortier, Characterization of Gold Jewellery Items by NRA, PIGE PIXE and PISXRF in Non-Vacuum Milliprobe and Vacuum Milliprobe Assemblies,. New paths in the use of Nuclear techniques for art and archaeology, G. Furlan, P. C. Guida, C. Tuniz (eds.), 48-64AISA-ISSA, World Scientific Publishing CO Pte Ltd., 1986.
16. Guerra M.F., The analysis of archaeological metals. The place of XRF and PIXE in the determination of technology and provenance. X-ray Spectrometry 27 (1998) 73-80.
17. H. Mommsen and T. Schmittinger, Test analysis of ancient Au and Ag coins using high energy PIXE Archaeom. 23, 1 (1981) 71-76.
18. A. Denker and K. H. Maier, High-energy PIXE using 68 MeV protons, Nucl. Instrum. Meth. B150 (1999) 118-123.
19. J. Weber, Th Beier, U. Diehl, D. Lambrecht, H. Mommsen, F. J. Pantenburg, A PIXE mini-beam set-up at the Bonn cyclotron for archaeometric analyses, Nucl. Instrum. Meth. B 50 (1990) 221-225.
20. F. Watt and G. W. Grime (eds.), Principles and Applications of High Energy Ion Microbeams, Adam Hilger, Bristol, IOP Publishing Limited, 1986
21. J. A. Charles, Heterogeneity in metals, Archaeometry 15, 1 (1973) 105-114.
22. E. T. Hall, Surface enrichment of buried metals, Archaeometry 4 (1961) 62-66.
23. F.Beauchesne, J.-N. Barrandon, L. Alves, F. B. Gil, M.F. Guerra, Ion beam analysis of copper and copper alloy coins. Archaeometry 30,2 (1988) 187-197.
24. J. Condamin and M. Picon, The influence of corrosion and diffusion of the percentage of silver in Roman denarii, Archaeometry 7 (1964) 98.
25. J. Condamin and M. Picon Changes, Changes suffered by coins in the course of time and the influence of these on the results of different method of analysis In: Methods of

Chemical and Metallurgical Investigation of Ancient Coinage Royal Numismatic Society ed., London, Special Publication n°8, 49-66 (1972)
26. W. A. Oddy and M. Cowell (eds.), Metallurgy in Numismatics, vol. 4, Royal Numismatic Society, SP. N°10, London 1998
27. A. M. Evans, Ore Geology and Industrial Minerals. An Introduction. Blackwell Science Ltd, 1980
28. F.B. Gil, G. Barreira, M.F. Guerra, L.C. Alves, Quantitative elemental analysis of thick samples by XRF and PIXE. X-Ray Spect., 18 (1989) 157-164
29. G. Ferreira, F.B. Gil, Elemental analysis of gold coins by PIXE, Archaeometry 23,2 (1981) 189-199.
30. G. F. Carter, Prepâration of ancient coins for X-ray fluorescence analysis Archaeometry 7 (1964) 106-113.
31. G. F. Carter, E. R. Caley, J. H. Carlson, G. W. Caniveau, M. J. Hughes, K. Rengan and C. Segebade, Comparison of analyses of eight Roman orichalcum coin fragments by seven methods Archaeometry 25,2 (1983)201-213.
32. J. R. Bird, P. Duerden and D. J. Wilson, Ion beam techniques in Archaeology and the Arts Nuclear Science Applications 1 (1983) 357-516.
33. J. R. Bird, E. Clayton, P. Duerden The problems and potential of ion beam techniques in Archaeology and Art: nuclear reaction analysis, Nuclear Instruments and Methods, B14 (1986) 127-132
34. F. Beauchesne, J.-N. Barrandon, Analyse globale et non destructive des objets archéologiques cuivreux par activation avec des neutrons rapides de cyclotron. Rev. d'Archéométrie, 10 (1986) 75-85
35. J.-N. Barrandon, J.-L. Debrun and M. Hours. Application des réactions nucléaires induites par des protons de moyenne énergie à la caractérisation des ors anciens, 77-85, Accademia Nazionale dei Lincei, Roma 1976.
36. A. Gondonneau, M. F. Guerra, The analysis of gold by ICP-MS with an UV laser. Application to the study of the gold currency of the Muslim West Africa. Proceedings of the conference Metals in Antiquity, pp. 262-270 S. M. M. Young, A. M. Pollard, P. Budd and R. A. Ixer editors, BAR International Series 792, 1999.
37. R. J. Watling, H. K Herbert., D. Delev, and I. D. Abell, Gold fingerprinting by laser ablation-inductively coupled plasma-mass spectrometry. Spectrochimica Acta 49B (2) (1994) 205-219.
38. W. Devos, Ch. Moor and P. Lienemann, Determination of impurities in antique silver objects for autentification by laser ablation inductevely coupled plasma mass spectrometry (LA-ICP-MS) Journal of Analytical Atomic Spectrometry, 14 (1999) 621-626.
39. Tykot, R. H. & S. M. M. Young. Archaeological applications of inductively coupled plasma-mass spectrometry. Archaeological Chemistry: organic, inorganic and biochemical analysis, M. V. Orna ed., American Chemical Society (1996) 116-130
40. B. Grigorova, S. Anderson, J. de Bruyn, W. Smith, K. Stülpner, A. Barzev, The AARL gold fingerprinting technology, Gold Bulletin, 31, 1 (1998) 26-29
41. M. F. Guerra, C.-O. Sarthre, A . Gondonneau, J.-N. Barrandon, Precious metals and provenance enquiries using LA-ICP-MS Journal of Archaeological Science 26 (1999) 1101-1110

42. Gondonneau, A., M. F. Guerra, & J.-N. Barrandon. Sur les traces de l'or monnayé: recherche de provenances par LA-ICP-MS. Revue d'Archéométrie 20 (1996) 23-32.
43. N. H. Gale, The isotopic composition of tin in some ancient metals and the recycling problem in metal provenancing, Archaeometry 39, 1 (1997) 71-82.
44. G. A. Wagner, N. Gentner, H. Gropengiesses and N. H. Gale, Early Bronze Age lead-silver mining and metallurgy in the Aegean: The ancient work of Siphnos, p-63-86. Occ Papers N° 20 Scientific studies in Early Mining and extractive metallurgy, ed. P. T. Craddock, British Museum occasional papers, The Trustees of the British Museum, 1980
45. Lead Isotope Studies in the Aegean, N. H. Gale and Z. A. Stos-Gale, p. 63-108. New developments in Archaeological Science ed. A. M. Pollard, Oxford University Press, The British Academy 1992
46. H. Moesta and P. R. Franke, Antike Metallurgie und Münzprägung. Ein Beitrag zur Technikgeschichte, Birkhäuser Verlag, Basel 1995
47. W. E. L. Minter, Ancient placer gold deposits. In Gold metallogeny and exploration, 283-308 R. P. Foster, Chapman and Hall (eds.), 1993.
48. Ch. J. Raub, The metallurgy of gold and silver in prehistoric times pp. 243-260. Prehistoric Gold in Europe, ed. G. Morteani and J. P. Northover, Kluwer Academic Publishers 1995
49. G. Weisgerber and E. Pernicka Ore mining in prehistoric Europe: an overview. Prehistoric Gold in Europe, 159-182, G. Morteani and J. P. Northover (eds.), Kluwer Academic Publishers 1995.
50. G. Morteani, Mineral economics mineralogy, geochemistry and structure of gold deposits. Prehistoric Gold in Europe, 97-113, G. Morteani and J. P. Northover (eds.), Kluwer Academic Publishers 1995.
51. Forbes, R. J. Studies in Ancient Technology. Volume VII. E. J. Brill (ed.), Leiden, Netherlands, 1971.
52. E. Caley, Analysis of ancient metals, International series of monographs on Analytical Chemistry, vol 19, R. Belcher and L. Gordon editors, Pergamon Press 1964
53. C. Roux and M. F. Guerra, A moeda almorávida : estudo do título e caracterização do metal, 145-168, F. A. Magro (ed.), Associação Numismática de Portugal, Actas do IV Congresso Nacional de Numismática, Lisboa, 1998
54. M. F. Guerra and A. Gondonneau, As technologias de fabrico das ligas amoedáveis e a proveniência dos metais utilizados : perspectivas abertas pelas novas técnicas de análise elementar, 369-402, F. A. Magro (ed.), Associação Numismática de Portugal, Actas do IV Congresso Nacional de Numismática, Lisboa, 1998
55. J. M. P. Cabral, M. G. Marques, M. F. Araújo and J. R. Marinho, Application of XRF spectrometry to the study of Visigothic coinage, 472-482 Metallurgy in Numismatics, vol. 4 W. A. Oddy and M. Cowell (eds.), Royal Numismatic Society, SP. N°10, London 1998
56. A. Hartmann and E. Nau, Über die spektralanalytische Untersuchung einiger griechischer Philipp- und Alexander-Statere sowie deren keltischer Nachprägungen, 7-34, Beiträge zur Süddeutschen Münzgeschichte, Selbstvervag, Stuttgart 1976. See also A. Hartmann, Prähistorisch Goldfuns aus Europa. Studie zu den Anfängen der Metallurgie, Berlin. Vol.3 – 5, 1970 - 1982.
57. J. C. Antweiler and A. L. Sutton, Spectrochemical analyses of native gold samples, U.S.G.S. Report GD-70-00.3 (1970) 1-28

58. A. Gondonneau, H. Nicolet-Pierre and M. F. Guerra, The Persian and Macedonian gold. From Croesus to Alexander the Great, Proceendigs of the Archaeometry'98, BAR forthcoming.
59. N. D. Meeks, P. T. Craddock, D. R. Hook, A. P. Middleton, A. E. Geçkinli, A. Ramage, The scientific study of the refractory remains and gold particles from Lydian gold refinery at Sardis, 461-482, Archaeometry 94, S. Demirci, A. M. Özer and G. D. Summers (eds.), Tübitak 1994.
60. Cowell M. R., Preliminary notes on the analysis of sigloi in a hoard found at Babylon, Iran vol. XXIV (1986) 89-91.
61. M. R. Cowell, K. Hyne, N. D. Meeks and P. Craddock, Analysis of Lydian electrum, gold and silver coinages, p. 526-538. Metallurgy in Numismatics, vol. 4 W. A. Oddy and M. Cowell (eds.), Royal Numismatic Society, SP. N°10, London 1998
62. Joannès F., Métaux précieux et moyens de paiment en Babylonie achéménide et hellénistique, Trans. 8, (1994) 137-144.
63. Hughes M. J., Analysis of silver and gold items in a hoard found at Babylon, Iran vol. XXIV (1986) 87-88
64. Guerra M.F., Gondonneau A., Barrandon J.-N., South American precious metals and the European economy. A scientific adventure in the Discoveries time. Nucl. Inst. Meth. B 136-138 (1998) 875-879
65. A. Hauptmann, Th. Reheren and E. Pernicka, The composition of gold from the ancient mining district of Verespatak/Rosia Montana, Romania, 369-381. Prehistoric Gold in Europe, G. Morteani and J. P. Northover (eds.), Kluwer Academic Publishers 1995
66. H. G. Bachmann, A. Burkhardt, R. Dehn, W. B. Stern, New aspects of Celtic gold coinage production in Europe, Gold Bulletin, 32, 1 (1999) 24-29
67. J. F. Healy Mining and Metallurgy in the Greek and Roman World. Thames and Hudson London 1978
68. G. Lehrberger and Ch. J. Raub, A look into the interior of Celtic gold coins, 341-355. Prehistoric Gold in Europe, G. Morteani and J. P. Northover (eds.), Kluwer Academic Publishers 1995
69. L. Beck, Développement de méthodes nucléaires par faisceaux d'ions de basse énergie pour la caractérisation d'objets archéologiques composites, PhD Université d'Orléans, France 1991
70. M. Ahlberg, Simple depth profile determination by proto-induced X-ray emission Nucl. Instrum. Method. 131 (1975) 381-384.
71. J. L. Ruvalcaba Sil and G. Demortier, Elemental concentration profile in ancient gold artifacts by ion beam scattering, Nucl. Instrum. Meth. B 5803 (1996).
72. J.-L. Ruvalcaba Sil, Analyse non destructive par faisceaux d'ions de bijoux anciens d'Amérique, PhD Facultés Universitaires Notre-Dame de la Paix, Namur, Belgique 1997.
73. Beck L., Barrandon J.-N., Non destructive depth profiling using the PIGE technique. Nucl. Inst. Meth. B 61 (1991) 100-105
74. W. A. Oddy, Gilding and tinning in Anglo-Saxon England. Occ Papers N° 17 Aspects of Early Mining, 129-134, W. A. Oddy (ed.), British Museum occasional papers, The Trustees of the British Museum, 1991
75. M. Cowell and S. La Niece Metalwork: artifice and artistry In Science and the Past, 74-98 S. Bowman (ed.), The Trustees of the British Museum, 1991.

76. S. La Niece, Silver plating on copper, bronze and brass, The Antiquaries Journal 70, 1 (1990) 102-114 and Metallography in numismatics. In Metallurgy in Numismatics, 114-133, vol. 4, W. A. Oddy and M. Cowell (eds.), Royal Numismatic Society, SP. N°10, London 1998
77. L. H. Cope, Surface-silvered ancient coins. E.T. Hall, D.M. Metcalf (eds), Methods of Chemical and Metallurgical Investigation of Ancient Coinage, 261-278, Royal Numismatic Society, S.P. 8, London 1972.
78. L. Beck, J.N. Barrandon and B. Gratuze, A non destructive method of the characterisation of plating: depth profiles using PIGE Technique, p.1-10 Archaeometry'90, E. Pernicka, G.A. Wagner (eds.), Birkhäuser Verlag Basel 1991.
79. L. Beck, F. Beck, Ch. Eluère and F. Vallet, Etudes de dorures gallo-romaines et mérovingiennes. Antiquités Nationales 22/23 (1990/91) 95-110
80. P. Meyers, Elemental composition of the Sion Treasure and other Byzantine silver objects in Ecclesiastical silver plate in sixth-century Byzantium, S. A. Boyd and M. M. Mango editors, Dumbarton Oaks Research Library and Collection, Washington D.C. 1998
81. R. F. Tylecote, Metallurgy in Archaeology, Edward Arnold publishers Ltd., London 1962
82. M. J. Hughes, The analysis of Roman Tin and Pewter Ingots. Occ Papers N° 17 Aspects of Early Mining, 41-50, W. A. Oddy (ed.), British Museum occasional papers, The Trustees of the British Museum, 1991
83. Joining techniques, J. Lang and M. J. Hughes. Occ Papers N° 17 Aspects of Early Mining, 169-178, W. A. Oddy (ed.), British Museum occasional papers, The Trustees of the British Museum, 1991
84. C. Sarthre PhD, Université de Poitiers, France, forthcoming
85. J.-N. Barrandon, G. Aubin, J. Benusiglio, J. Hiernard, D. Nony, S. Scheers. L'or gaulois : le trésor de Chevanceaux et les monnayages de la façade atlantique. Cahiers Ernest-Babelon 6, CNRS (ed.) 1994
86. C. Sarthre, M. F. Guerra M.F., J.-N. Barrandon, J. Hiernard, Les monnaies d'argent du Centre-Ouest de la Gaule. Rev. Numismatique, volume 151 (1996) 7-27.
87. J.-N. Barrandon, M. F. Guerra, F. A. Magro, Chemical compositions of Portuguese dinheiros. Problems of medieval coinage in the iberian area 3, 343-372 M.G. Marques and D.M. Metcalf (eds.), Santarém, 1988.
88. H. McKerrel, R. B. K. Stevenson, Some analyses of Anglo-Saxon and associated Oriental silver coinage, In E.T. Hall, D.M. Metcalf (eds), Methods of Chemical and Metallurgical Investigation of Ancient Coinage, 195-209, Royal Numismatic Society, S.P. 8, London 1972.
89. F. Dumas , Le trésor de Fécamp et le monnayage en Francie occidentale dans la seconde moitié du Xe siècle, 303, 40-45, Paris 1971, analyses by A. A. Gordus.
90. D. M. Metcalf, J. P. Northover, Interpreting the alloy of the later Anglo-Saxon coinage, Britain Numismatic Journal, 56 (1986) 35-63
91. M. Bompaire et M. F. Guerra, Analyses de monnaies françaises du XIe siècle, le problème du zinc, Proceedings of the Numismatic Symposium, Berlin 1997, forthcoming.
92. M.F. Guerra, Elemental analysis of coins and glasses. Appl. Radiat. Isot. 46, 6/7 (1995) 583-588.
93. M. F. Guerra, J.-N. Barrandon, F. A. Magro, F.B. Gil, Analyse de "dinheiros" de la 1ère dynastie du Portugal: Nouvelles approches. Rev. d'Archéométrie 13 (1989) 31-41.

94. P. Meyers, L. van Zelst, E. V. Sayre, Major and Trace elements in Sasanian silver. Archaeological Chemistry, C. W. Beck (ed.), advances in Chemistry series 138, 22-33 American Chemical Society 1974.
95. Gordus A. A.: Neutron activation analysis of coins and coin-streaks, In E.T. Hall, D.M. Metcalf (eds), Methods of Chemical and Metallurgical Investigation of Ancient Coinage, 127-148, Royal Numismatic Society, S.P. 8, London 1972.
96. M. F. Guerra, Da caracterização dos arqueometais. Análise quantitativa pot métodos nucleares e perinucleares, PhD Universidade Nova de Lisboa, Portugal 1990.
97. M. F. Guerra, J.-N. Barrandon, Thermal neutron activation analysis of archaeological artifacts using a cyclotron. In : Proceedings of Archaeometry 88. The Archaeometry Laboratory, 262-268, Univ. of Toronto (ed.), 1988
98. J.-N. Barrandon, M. F. Guerra, E. Le Roy Ladurie, C. Morrisson, B. Collin, La diffusion de l'argent du Potosi dans le monnayage européen à partir du XVIe siècle. Le circuit méditerranéen. Gaceta Numismatica 197 (1992) 15-22.
99. M. F. Guerra, J.-N. Barrandon, E. Le Roy Ladurie, C. Morrisson, B. Collin, The diffusion of the silver from Potosi in the XVI century European coinage. Archaeometry 90, 11-18, Birkhäuser Verlag Basel (ed.), 1991.
100. P. Craddock, Mining and Smelting in Antiquity Science and the Past, 57-73, S. Bowman (ed.), The Trustees of the British Museum, 1991.
101. J. Bailey, The production of brass in Antiquity with particular reference to Roman Britain, 7-26, Occasional Pappers N° 50: 2000 years of zinc and brass, P. T. Craddock (ed.), 1998
102. Occasional Pappers N° 50: 2000 years of zinc and brass, P. T. Craddock (ed.), 1998
103. Forbes, R. J., Studies in Ancient Technology. Volume IX. E. J. Brill ed., Leiden, Netherlands 1972.
104. R. Shepherd, Prehistoric Mining and Allied Industries, Academic Press Inc., London 1980
105. T. Rehren, A Roman zinc tablet from Bern, Switzerland: reconstruction of the manufacture, Archaeometry' 94, 35-45., S. Demirci, A. M. Özer and G. D. Summers (eds.), Tübitak and the authors 1994
106. M. F. Guerra and O. Picard, L'alliage des monnaies de bronze (Amphipolis, Thasos, Maronée, Thasos matières premières et technologie de la préhistoire à nos jours, 195-206, A. Muller (ed.), 1999,
107. C. Sarthre, Monnaies gauloises de l'Hôtel Gouïn et de la Société archéologique de Touraine, Société archéologique de Touraine, France 1998
108. C.-O. Sarthre L'apport des analyses de monnaies découvertes au Gué-de-Sciaux (Antigny, Vienne) à la compréhension des monnayages pictons. Proceedings of the Symposium of Antigny 1998, forthcoming
109. G. R. Gilmore and B. S. Ottaway, Micromethod for the determination of trace elements in copper-based metal artifacts Journal of Archaeological Science 7 (1980) 241-254
110. E. Pernicka, F. Begemann, S. Schmitt-Strecker, H. Todorova and I. Kuleff, Prehistoric copper in Bulgaria, Eurasia Antiqua, Zeitschrift für Archäollogie Eurasiens, band 3, pp. 41-180, Schriftleitung Berlin 1997

111. J. Lutz and E. Pernicka, Energy dispersive X-ray fluorescence analysis of ancient alloys : empirical values for precision and accuracy Archaeometry 38, 2 (1996) 313-323.
112. Th. Bertoud, S. Bonnefous, M. Dechoux and J. Françaix, Data analysis: Towards a model of chemical modification of copper from ores to metals, Occ Papers N° 20: Scientific studies in Early Mining and extractive metallurgy, 87-102, P. T. Craddock (ed.), The Trustees of the British Museum, 1980
113. J. W. Palmer, M. G. Hollander, P. S. Z. Rogers, T. M. Benjamin, C. F. Duffy, J. B. Lambert, J. A. Brown, Pre-Colombian metallurgy: technology, manufacture and microprobe analyses of copper bells from the Greater Southwest. Archaeometry 40, 2 (1988) 361-382.
114. J. L. Mauk and R. G. V. Hancock, Trace element geochemistry of native copper from the White Pine mine, Michigan (USA): implications for sourcing artefacts. Archaeometry 40, 1 (1998) 97-107
115. R. G. V. Hancock, L. A. Pavlish, W. A. Fox and M. A. Latta, Chemical analysis of copper alloy trade metal from a post-contact Huron site in Ontario, Canada. Archaeometry 37, 2 (1995) 339-350
116. F. A. Magro, M. F. Guerra, J.-N. Barrandon, Les ceitis portugais (XVe-XVIe siècles) : composition des alliages utilisés et problèmes numismatiques, pp. 199-219 Revue de Numismatique VIe série, Tome XXXVI, 1994
117. M. R. Grant, Trace elements in Southern African artefact tins using NAA. Archaeometry'90, 165-172, E. Pernicka and G. A. Wagner (eds.), Birkhäuser Verlag Basel 1991
118. Metalwork and enamelling, H. Maryon, Dover Publications, inc. New York 1971.
119. J. P. Northover and V. Rychner, Bronze analysis : experience of a comparative programme. L'atelier du Bronzier en Europe du XXe au VIIIe siècle avant notre ère, Tome I, 19-39, C. Mordant, M. Pernot and V. Rychner (eds.), Paris 1998
120. Comparative Analysis of Archaeological Bronzes, W. T. Chase. Archaeological Chemistry, 148-185, C. W. Beck (ed.), advances in Chemistry series 138, American Chemical Society 1974.
121. A. Hauptmann, H.G. Bachmann, R. Maddin. Chalcolitic copper smelting: new evidence from excavations at Feinan, Jordan, Archaeometry' 94, 3-10, S. Demirci, A. M. Özer and G. D. Summers (eds.), Tübitak and the authors 1994
122. F. F. Miranda, M. D. F. Posse, C. Martin, I. Montero and S. Rovira Changes in Bronze Age metallurgy as depicted by laboratory analysis: the "La Mancha" model, Spain Archaeometry' 94, 23-34, S. Demirci, A. M. Özer and G. D. Summers editors, Tübitak and the authors 1994
123. J-X Chen, H-K Li, C-G Ren G-H Tang, X-D Wang, F-C Yang, H-Y Yao, PIXE research with an external beam, Nuclear instruments and Methods, 168 (1980) 437-440
124. C. Morrisson, M. F. Guerra, J.-N. Barrandon, Premières analyses des plombs byzantins : perspectives et impasses des recherches sur leur composition métallique. Studies in Byzantine Sigillography 3, 1-17, Dumbarton Oaks Trustees for Harvard University, Washington, 1993.
125. P. Northover, Analysis of copper alloy metalwork from Arbedo TI, In Der Depotfund von Arbedo TI und die Bronzedepotfunde des Alpenraums vom 6. bis zum Beginn des 4.

Jh. v.Chr., M. P. Schindler (ed.), Antigua 30, 289-310, Verlag Schweizerische, Basel 1998.

126. P. Northover, Metallkundliche Untersuchungen, In Üetliberg, Uto-Kulm, Berichte der Zürcher Denkmalpflege, Archäologische Monographien 9, 239-251, Orell Füssli Verlag Zürich 1991

127. J. R. Marechal, Methods of ore roasting and the furnaces used, Occasional Paper n°48, Furnaces and Smelting Technology in Antiquity, 29-42, P. T. Craddock and M. J. Hughes (eds.) 1985

128. D. A. Scott, Metallography and microstructure of ancient and historic metals, The J. Paul Getty Trust, 1991

Radiation in Art and Archeometry
D.C. Creagh and D.A. Bradley (editors)

The use of Mössbauer Spectroscopy in studies of archaeological ceramics

U. Wagner[a], F.E. Wagner[a], W. Häusler[a] and I. Shimada[b]

[a]Physics Department, Technical University of Munich, D-85747 Garching, Germany

[b]Southern Illinois University, Carbondale, IL 62907, USA

After a brief introduction to Mössbauer spectroscopy, the physical, chemical and mineralogical aspects of the use of this technique in studies of clay-based ceramics are described. The Mössbauer spectra of pottery fired under oxidizing, reducing, and changing conditions are explained. Finally, the possibilities of deriving information on the firing temperatures and the kiln atmosphere during firing in antiquity from Mössbauer spectra are discussed and illustrated by recent results on finds from the Batán Grande region on the north coast of Peru.

1. INTRODUCTION

Mössbauer spectroscopy makes use of low energy γ-rays emitted by nuclei for studying the properties of solids. In Mössbauer studies of works of art and archaeological ceramics, the 14.4 keV γ-rays of ^{57}Fe are used in most cases, although other Mössbauer isotopes, like ^{119}Sn and ^{121}Sb, can also be used, for instance, for studies of bronzes [1] or glazes containing tin or antimony, while ^{197}Au has recently been used for studying Celtic gold coins [2]. In this paper, only ^{57}Fe Mössbauer spectroscopy and its application to studies of ceramics will be discussed. Ceramics in this context will be mainly pottery, but also building materials like fired bricks and tiles as well as parts of kilns and furnaces or even soil or mudplaster heated in fires. In this field, Mössbauer spectroscopy has a well established place, with over a hundred papers published [3] since the first suggestion by Cousins and Dharmawardena about thirty years ago [4]. Other closely related applications of ^{57}Fe Mössbauer spectroscopy, for instance in studies of pigments used for painting [5], will not be considered in any detail, although the technical and mineralogical aspects are largely the same as those in studies of ceramics.

The wide applicability of ^{57}Fe Mössbauer spectroscopy for investigations of clay-based ceramics arises from the fact that practically all clays contain iron, usually in concentrations between 1 and 10 weight percent. Natural iron contains only about 2 % of the ^{57}Fe isotope used in Mössbauer spectroscopy, but this is sufficient for measuring good Mössbauer spectra of most clay-based ceramics.

The primary information that can be derived from Mössbauer spectra is mainly on the hyperfine interactions between the Mössbauer nuclei and their solid state environments. Mössbauer spectroscopy thus primarily provides information on the chemical state of the iron, for instance on its oxidation state and on the magnetic properties of the iron bearing compounds. This enables one to tell which iron bearing compounds or minerals are present in the ceramics. Even though iron is only a minor constituent of ceramics, the physical and chemical transformations of the iron during the firing are manifold and depend strongly on the firing conditions. A knowledge of the state of the iron in fired ceramics therefore often permits conclusions as to the conditions under which the ceramics were fired, like the firing temperature, the oxidizing or reducing character of the kiln atmosphere, and even the sequence of reducing and oxidizing firing periods. Such knowledge is frequently of interest from the point of view of archaeology or anthropology, since it permits an assessment of the technical skills of ancient potters and hence on the cultural achievements of ancient civilizations. Another interesting application of Mössbauer spectroscopy is in the classification of pottery. Since the Mössbauer spectra of fired ceramics depend on both the raw material used and the manner in which it was fired, pottery finds can be partitioned into groups on the basis of their Mössbauer patterns. Such groupings may be combined with information from other methods such as trace element analysis and used to assign individual sherds to certain production sites or workshops, or distinguish between locally produced and imported pottery [6].

To get a complete picture of the state of ceramics, it is often useful to combine Mössbauer spectroscopy with other methods, like X-ray diffraction, optical thin section microscopy or electron micrography. X-ray diffraction and Mössbauer spectroscopy complement each other particularly well because the former yields information on the major minerals in the pottery clays and fired ceramics, while Mössbauer spectroscopy looks selectively at the iron compounds which often cannot be observed by X-rays because of the minute iron content.

In this overview we shall focus on Mössbauer spectroscopy. We will first give an outline of the Mössbauer method and the hyperfine interactions that are the primary source of information. In this introduction to the method, we shall emphasize the aspects important in studies of ceramics. For a more detailed description of the method, the reader may consult a multitude of introductory texts [e. g., 7-10]. We shall then briefly describe the Mössbauer spectra of the different minerals found in ceramics and the changes these components undergo during firing under different conditions. Finally, procedures that have been found useful for extracting information on the manufacture of ceramics from Mössbauer spectroscopy will be discussed and illustrated by a few results on finds of Formative ceramics from the region of Batán Grande on the north coast of Peru [11,12].

2. MÖSSBAUER SPECTROSCOPY

2.1 Principle

Gamma quanta emitted when nuclei undergo transitions from an excited state to the groundstate have the right energy to be resonantly absorbed by nuclei of the same isotope, causing these to undergo transitions from the groundstate to the excited state. In ^{57}Fe Mössbauer spectroscopy, one uses sources of radioactive ^{57}Co, which decays to ^{57}Fe by electron capture with a half life of 270 days. In this process the 14.4 keV first excited state of ^{57}Fe is populated and decays to the groundstate by emission of a 14.4 keV γ ray. These γ-rays

can excite the ^{57}Fe nuclei in an absorber. The source is usually ^{57}Co incorporated into a matrix of metallic Rh. The emission line of such a source has virtually the energy width resulting from the lifetime of the 14.4 keV state, τ = 141 ns, and Heisenberg's uncertainty relation. The Mössbauer resonance in the absorber, however, may be shifted and split by the hyperfine interactions between the nuclei and their solid state environment. It is these shifts and splittings that furnish information on the physical and chemical state of the iron. To scan the hyperfine spectrum of the absorber, one usually shifts the energy of the γ quanta emitted by the source using the Doppler effect. To this end, one has to move the source with velocities of a few millimeters per second. A Mössbauer spectrum is thus measured by recording the count rate in a detector located behind the absorber as a function of the source velocity. For such transmission experiments the source is usually mounted on an electromechanical velocity drive and vibrated with a frequency of a few tens of cycles per second. The whole velocity range of interest is scanned within each cycle of motion and the counts are stored as a function of the velocity in a multichannel analyzer. To gather enough counts for the desired statistical accuracy, the data acquired during many velocity cycles are added. The measurement of a spectrum with sufficient statistical accuracy usually takes one or several days, depending on the iron content of the absorber. When the absorber needs to be cooled, one uses either bath or gas flow cryostats. For standard absorption experiments one uses about 200 mg of powdered ceramics in absorbers having an area of about 2 cm^2. Measurements with smaller amounts of material are possible by reducing the diameter of the absorber at the expense of the count rate.

Mössbauer spectra of the 14.4 keV γ-rays of ^{57}Fe can also be obtained in experiments where the resonance absorption is detected by observing resonantly scattered γ-rays, X-rays emitted after resonant absorption and subsequent internal conversion, or conversion electrons emitted after resonant absorption (Conversion Electron Mössbauer Spectroscopy, or CEMS). These methods are, at least in principle, non-destructive, i.e., one can study the backscattering from whole objects without the need to take samples. Gamma ray backscattering has, for instance, been used to study pigments in paintings [5] and surfaces of sherds of ceramics [13-15]. Because of the limited range of the radiation, such scattering experiments probe only a thin surface layer of the material. For γ-ray and X-ray backscatterig experiments, the probing depth is of the order of ten micrometers, while with conversion electrons one probes only the uppermost 100 or 200 nm because of the short range of the low energy conversion electrons. This surface sensitivity may have advantages when surface features like slips or glazes on ceramics are to be studied [15]. In this overview, we shall, however, focus on the standard transmission experiments, although the hyperfine patterns and their interpretation would be the same in scattering experiments.

2.2 Lamb-Mössbauer Factor

For the Mössbauer effect to be observed, the source and absorber must be solids. In gases or liquids the γ-ray recoil and thermal motion broaden the lines so much that the resonance effect becomes unobservable. Even in solids, energy may be gained from or lost to lattice vibrations (phonons) during the emission or absorption of γ-rays. Only processes without phonon creation or annihilation contribute to the Mössbauer spectrum. The probability for such "recoil free" processes is called the Lamb-Mössbauer factor, or f-factor. Notably, the solid containing the Mössbauer nuclei need not be crystalline. Recoil free processes also take

place in amorphous solids like silicate glasses. Therefore, iron in vitrified parts of ceramics is detected as well as iron in crystalline components.

By definition, the Lamb-Mössbauer factor is smaller than unity. It decreases with increasing temperature and γ-ray energy and is the larger the more rigid the lattice is. Owing to the relatively low γ-ray energy of 14.4 keV, the f-factor in many iron compounds is close to unity already at ambient temperature and hence will not increase much at cryogenic temperatures [16]. For instance, the f-factor for a ^{57}Co:Rh source is f = 0.78 at 300 K and f = 0.88 at 4.2 K [17]. Thus, the f-factors for iron in oxides and silicates should have similar values, although exact values are not known in most cases.

Because of their expected small variability, it is a good approximation to assume that the f-factors of all components in pottery clays and ceramics are the same. Then the relative intensities of the individual components in the Mössbauer patterns represent the relative amounts of iron in the respective phases. There are indications [18] that the f-factors of individual components in ceramics may change on firing at certain temperatures. This could be of interest in characterizing ceramics, but as yet this aspect has not been given much attention.

2.3 Evaluation of Mössbauer Spectra

The individual Mössbauer resonance lines are expected to have a Lorentzian shape, at least when the absorbers are sufficiently thin [7-10]. For thick absorbers the lineshape becomes distorted by saturation effects, and the proper lineshape must be calculated numerically as a so called "transmission integral" [7-10,19]. In most measurements on ceramics the absorbers are, however, sufficiently thin for the use of superpositions of Lorentzian lines to be a reasonably good approximation. In order to extract meaningful information on the relative intensities and the hyperfine interactions of the individual constituents, the Lorentzian lines are grouped into appropriate hyperfine patterns that can be described by physically meaningful parameters, which are fitted to the data by a least squares procedure. Often one finds that the hyperfine parameters, e.g., magnetic hyperfine fields or electric quadrupole splittings, are distributed quasi-continuously. The evaluation of such spectra has been given much attention in the Mössbauer literature. One can derive the distribution function without a priori assumptions on its shape directly from the Mössbauer patterns [20,21] or one makes certain assumptions on the shape of the distribution function, which is then described by one or more parameters. Often the assumption of gaussian distributions of Lorentzian lines (Voigt profiles) leads to satisfactory results [22,23]. Simply fitting broadened Lorentzian lines is the physically least satisfying approach [24], but is often used because of its simplicity.

3. HYPERFINE INTERACTIONS

There are three types of hyperfine interactions of the Mössbauer nuclei with their environment in a solid that lead to shifts and splittings of the Mössbauer line. Hyperfine interaction energies are always the product of a nuclear quantity, which is typical for a given Mössbauer resonance and usually known with sufficient accuracy, with an electronic quantity which contains the information on the solid under study.

3.1 Isomer Shift

The isomer shift is proportional to the product of the electron density at the site of the ^{57}Fe nuclei and the change of the nuclear charge radius during the Mössbauer transition. The isomer shift causes a displacement of the whole Mössbauer pattern on the velocity scale, but no splitting. It must be given with respect to a suitable reference material. ^{57}Fe isomer shifts are often referred to metallic α-iron. Alternatively, one may use the source as the reference; then the isomer shifts can be given directly as obtained from the spectra. In this work, we refer all shifts to the ^{57}Co:Rh source. Metallic α-Fe has a shift of –0.11 mm/s with respect to a ^{57}Co source. Thus 0.11 mm/s must be added to the shifts given in this paper to refer them to α-Fe.

In the iron compounds occurring in clays and ceramics, the electron density at the iron nuclei and hence the isomer shift depend mainly on the oxidation state of the iron. For Fe^{3+}, the shift is between about -0.1 and 0.4 mm/s, while for Fe^{2+} one finds shifts between 0.8 and 1.2 mm/s. The isomer shift thus already allows an unambiguous determination of the oxidation state of the iron. The covalency of the iron bonds also affects the isomer shift. As a rule, the more covalent the bonds become, the smaller the isomer shifts are. For instance, iron that is tetrahedrally surrounded by four oxygen ligands is more covalent than iron octahedrally surrounded by six ligands. This explains the difference in isomer shift mentioned above.

3.2 Electric Quadrupole Splitting

The electric quadrupole interaction represents the orientational energy of non-spherical nuclei in the electrostatic field produced by the electrons and ions in a solid. The latter is described by the tensor of the electric field gradient (EFG). For sites of cubic point symmetry, all components of the EFG tensor vanish and no electric quadrupole interaction is observed.

The electric quadrupole interaction leaves the groundstate of ^{57}Fe with spin I = 1/2 unsplit and splits the I = 3/2 excited state into two substates. As a consequence, the Mössbauer line splits into a doublet whose separation is called the electric quadrupole splitting. In isotropic polycrystalline absorbers the two components of the quadrupole doublet have the same intensity. For such symmetric quadrupole doublets, which are the rule in pottery clays and ceramics, only the magnitude but not the sign of the electric quadrupole interaction can be determined.

The quadrupole splitting in iron compounds is different for Fe^{3+} and Fe^{2+} and can therefore be used, together with the isomer shift, to distinguish between the two oxidation states. The half filled $3d^5$ shell of Fe^{3+} ions is spherical and hence does not contribute to the EFG, which is thus produced only by the charge distribution caused by the neighbors in the lattice. For this reason the EFG is relatively small, but rather sensitive to distortions of the environment of the Fe^{3+} ions. The corresponding splittings are usually below 0.8 mm/s in oxides and silicates, but for strongly distorted sites, e.g., in dehydroxilized clays, they may be as big as 1.6 mm/s. The $3d^6$ electron configuration of Fe^{2+} ions makes a large contribution to the EFG. The splittings for Fe^{2+} therefore lie usually between 0.8 and about 3.0 mm/s range, although in rare cases, like that of the cubic FeO (wüstite), the splittings may be smaller or even vanish [25, 26].

3.3 Magnetic Hyperfine Interaction

The interaction between the nuclear magnetic dipole moment and the magnetic hyperfine field produced by the electrons at the site of the nucleus leads to the Zeeman splitting of both

the groundstate and the excited state of the nucleus. Such a magnetic hyperfine fields exist at the iron nuclei in magnetically ordered materials, i. e., in ferro-, antiferro-, or ferrimagnets or in spin glasses. In paramagnetic substances, the magnetic hyperfine interaction normally vanishes because the spins of the magnetic ions change orientation so rapidly that the nucleus senses only a vanishing time average of the magnetic hyperfine interaction.

With the excited nuclear state (I = 3/2) splitting into four and the groundstate (I = 1/2) splitting into two substates, a magnetically split ^{57}Fe Mössbauer pattern should consist of eight lines, but only six are allowed because of the magnetic dipole character of the 14.4 keV transition. The relative positions of the six lines are determined by the ratio of the magnetic moments of the excited state and the groundstate, and the relative intensities of the six lines are expected to have a 3:2:1:1:2:3 ratio [7-10]. The magnetic hyperfine pattern thus depends only on a single solid state parameter, the magnetic hyperfine field B_{hf}. In α-iron the magnetic hyperfine field is B_{hf} = 33 Tesla. For the $3d^5$ electron configuration of Fe^{3+}, the hyperfine field arises from core polarization only. It is usually above 45 T and can have values up to about 55 T at low temperatures. For the $3d^6$ electron configuration of Fe^{2+}, there is also an orbital contribution to the hyperfine field, which is opposite to the core polarization field, whence the hyperfine fields are often quite small.

A further complication arises when the magnetic dipole and the electric quadrupole interaction are present simultaneously in non-cubic, magnetically ordered compounds. The Mössbauer patterns then generally consist of eight lines whose positions and intensities are obtained by numerical diagonalization of the joint Hamiltonian. Such cases are the rule for magnetic Fe^{2+} compounds, where the electric quadrupole and magnetic dipole interaction often have about the same magnitude. For Fe^{3+}, the electric quadrupole splittings are usually small and the hyperfine fields are large. The quadrupole interaction can then be treated as a small perturbation of the magnetic interaction. The result is a so called quadrupole shift of the magnetic hyperfine lines. For a positive quadrupole interaction, the two outermost lines of the magnetic sextets shift towards positive velocities, while the four inner lines shift towards negative ones, for a negative quadrupole interaction, the quadrupole shifts are in the opposite direction. In such cases one therefore obtains information on both the magnitude and the sign of the electric quadrupole interaction.

4. MÖSSBAUER SPECTRA OF CLAYS AND CERAMICS

Iron occurs in pottery clays and fired ceramics in a variety of forms. Pottery clays consist of clay minerals proper and of other materials present in the exploited clay deposits or added intentionally as temper. The clay fraction is often a mixture of different clay minerals. Clay minerals usually contain several percent of iron as so called structural iron, i.e., iron substituting for major elements like Al or Mg in the structure of the layer silicates. In addition to the clay minerals, quartz and feldspars are often present in pottery clays, either because they were already present in the raw clay used by the potters, or because they were added as a temper to give the clay the desired consistency. These additions usually do not contain much iron and therefore do not contribute much to the Mössbauer spectra. The same is true for most other materials added as temper, like calcite from ground shells of marine animals or marble. The occasional use of ground, fired pottery as temper, however, is a source of iron that may seriously affect the Mössbauer spectra of ceramics.

More often than not, iron is also present in pottery clays in the form of oxides or oxyhydroxides. These may adhere to clay mineral particles even in rather pure clays. They would usually be present in the soil of the clay deposits exploited by the ancient potters and they may have been present in the added temper.

The individual iron bearing compounds in pottery clays can be analyzed by their Mössbauer spectra, although often only when measurements are made not only at room temperature but also at temperatures down to that of liquid helium (4.2 K). Temperatures below 4.2 K have but rarely been used in studies of clays and ceramics [27-30] because they are difficult to reach and may not even yield useful additional information. Mössbauer measurements at temperatures above room temperature might yield information worth the while to obtain, but have not been used in studies of ceramics so far.

4.1 Mössbauer Spectra of Clay Minerals

The Mössbauer spectra of clay minerals have been studied in a multitude of papers, which are well documented by the Mössbauer Effect Data Center [3,31,32] and have been reviewed repeatedly [33-36].

(i) Electric quadrupole interactions and isomer shifts

The layered aluminosilicate structure of clay minerals [37] is made up of octahedral layers, where the Al^{3+} and the metals substituting for it (Fe^{3+}, Fe^{2+}, Mg^{2+}) are surrounded by four O^{2-} and two OH^- neighbors, and layers of SiO_4 tetrahedra, in which the silicon may be replaced by Al^{3+} and Fe^{3+}. Iron may thus be present as octahedral Fe^{3+} or Fe^{2+} and tetrahedral Fe^{3+}. These three types of iron can be distinguished by their isomer shifts and quadrupole splittings (cf. Section 3.1 and 3.2) even though the distinction between tetrahedral and octahedral Fe^{3+} by the isomer shift may not always be unambiguous. Even in pure clay minerals, one usually observes several ill resolved and often broadened quadrupole doublets for octahedral Fe^{3+} and Fe^{2+}. There are several possible reasons for this. One is that the four O^{2-} and two OH^- neighbors of octahedral iron may be arranged in a cis and a trans configuration. This may give rise to different quadrupole splittings and, possibly, isomer shifts [38,39]. It is not certain, however, that the cis and trans (or M1 and M2) sites can be distinguished in the Mössbauer patterns. This arises because there are other causes for the variability of the quadrupole splitting and, to a lesser extent, the isomer shift [40-42], like the distribution of the nearest metal ions (Al^{3+}, Fe^{3+}, Fe^{2+}, Mg^{2+}) around a given iron site. In pottery clays, one faces the additional difficulty that the clay fraction often consists of several different clay minerals.

As a consequence, the Mössbauer patterns for each oxidation state of the clay fraction will usually consist of several ill resolved quadrupole doublets. The standard way of evaluating such patterns is to fit them with a superposition of several quadrupole doublets with different quadrupole splittings and isomer shifts. The relative areas of Fe^{3+} and Fe^{2+} can usually be obtained in this way with good accuracy, but a unique fit of the Fe^{3+} fraction by several quadrupole doublets is often impossible, the same being true for the Fe^{2+} components. The empirical rule that the isomer shifts of individual components of the same oxidation state often differ less than the quadrupole splittings may help, but often some ambiguity remains in the unraveling of the complex patterns, particularly because the left components of the Fe^{3+} and Fe^{2+} doublets usually overlap. The spectra of clays are therefore often fitted by suitable superpositions of broadened Lorentzian quadrupole doublets or – and this is certainly the better choice – by suitable Voigt profiles (cf. Section 3.2).

(ii) Magnetic Hyperfine Interactions

At room temperature, clays are usually not magnetically ordered because the iron concentration is too low. At 4.2 K magnetic ordering is sometimes observed when the iron content is sufficiently high [27-30]. Even then, part of the sample often remains paramagnetic while the rest is magnetically ordered. This is probably so because the iron is inhomogeneously distributed or because the clay is a mixture of different clay minerals. Not much is known about the type of magnetic order in clay minerals; presumably is of the spin glass type rather than simply antiferro- or ferrimagnetic. As is typical for spin glasses, the Mössbauer spectra often reveal a rather wide distribution of hyperfine fields which for Fe^{3+} may reach from a few Tesla to about 50 T. The spectra of Fe^{2+} in magnetically ordered clays are particularly complicated [27-30], since they are distributions of octet patterns (cf. Section 3.3). Typical Fe^{2+} hyperfine fields in clay minerals are between 10 and 20 T.

Magnetic order will occur in clays with a high iron content. When the iron concentration is low, however, the relaxation of the iron spins may, particularly at low temperatures, become so slow that even in the paramagnetic state magnetic hyperfine interactions occur in the Mössbauer spectra [43,44]. The theoretical treatment of such paramagnetic relaxation patterns is difficult even in well-crystallised compounds [45]. In crystallographically complicated, impure systems like clays, no viable theoretical approach exists. Such relaxation spectra can, however, often be fitted reasonably well, though in the physical sense incorrectly, by superpositions of magnetic sextet patterns corresponding to distributions of magnetic hyperfine fields. It is, in fact, difficult or even impossible to decide whether a magnetically split low temperature Mössbauer pattern of a clay is due to magnetic ordering or to slow paramagnetic relaxations of the structural iron.

4.2 Mössbauer Spectra of Iron Oxides or Oxihydroxides

Iron oxides and oxihydroxides and their Mössbauer spectra have been described in detail in several comprehensive papers [46,47]. Those found in soils and hence in pottery clays are mainly hematite (α-Fe_2O_3), goethite (α-FeOOH) and, more rarely, ferrihydrite ($Fe_5HO_8.4H_2O$). Magnetite (Fe_3O_4) and maghemite (γ-Fe_2O_3) are rare in soils, and so are the oxihydroxides akaganeite, lepidocrocite and ferroxyhite. For this reason, we shall consider here only hematite, goethite and ferrihydrite.

(i) Hematite

Hematite is weakly ferromagnetic below its Curie temperature of 955 K. The weak ferromagnetism is caused by a slight canting of the antiferromagnetically ordered Fe^{3+} spins. The Mössbauer spectra of hematite show a large magnetic hyperfine splitting, with a hyperfine field of about 52 T at 300 K. Since the magnetic moments in the weakly ferromagnetic state are aligned perpendicular to the crystallographic c-axis, and hence perpendicular to the axis of the tensor of the electric filed gradient, the observed quadrupole shift of about -0.20 mm/s represents the corresponding projection of the quadrupole interaction on the direction of the hyperfine field.

Below about 250 K, well-crystallised hematite undergoes the Morin transition, during which the iron spins flip into the direction parallel to the c axis and the compound becomes antiferromagnetic. In the Mössbauer spectra this leads to a slight increase of the hyperfine field, and, more conspicuously, to a change of the quadrupole shift from -0.20 mm/s to +0.41

mm/s, since now the hyperfine field is aligned in the direction of the axis of the EFG tensor. At 4.2 K, the hyperfine field of antiferromagnetic hematite is about 54 T.

Impurities like Al or Si, bad crystallinity or small particle size, which often occur in natural hematites, tend to lower the Morin transition temperature as well as the hyperfine field [48]. Often the Morin transition is completely suppressed and the hematite remains weakly antiferromagnetic even at 4.2 K. This can be seen in the Mössbauer spectra from the sign of the quadrupole shift and goes along with a slightly reduced hyperfine field, which may become as low as 52 T at 4.2 K.

The accessory hematite in clays and the hematite formed in ceramics during firing usually are of the non-Morin type, but in some ceramics Morin type hematite has been observed and shown to be due to specific firing conditions [49,50] which, however, are not well understood.

The small hematite particles in ceramics often exhibit the phenomenon called superparamagnetism [51-54]: Owing to thermal excitation, small ferro- or antiferromagnetic particles, which usually consist of only a single magnetic domain, may spontaneously change the direction in which the spins are aligned. When the corresponding changes of the direction of the hyperfine field are sufficiently fast, the nuclei sense only a time-averaged hyperfine field, which is usually zero. The magnetic hyperfine splitting of the Mössbauer spectra then collapses and one observes merely a quadrupole doublet. In ^{57}Fe Mössbauer spectroscopy, the relaxation rates at which the collapse of the hyperfine splitting occurs are about 10^9 s^{-1} [51-54]. The relaxation rate depends on particle size and shape and increases exponentially with decreasing particle size. For a given particle size and shape, the collapse of the magnetic splitting of the Mössbauer spectra occurs in a rather narrow temperature range. Hematite particles smaller than about 10 nm will show superparamagnetic behavior in their Mössbauer spectra at 300 K [51-54].

In clays and ceramics there is usually a distribution of sizes and shapes of the particles. Therefore part of the hematite may be blocked and part may be superparamagnetic at a given temperature. The superparamagnetic behavior may then be used to obtain some information on the particle size distribution in ceramics [54]. The superparamagnetic fraction in the Mössbauer patterns is practically indistinguishable from paramagnetic structural Fe^{3+} in the clay minerals. A distinction requires measurements at liquid helium temperature, where the superparamagnetism is expected to be blocked. Even there, however, the interpretation of the Mössbauer spectra may be ambiguous, because, on the one hand particles may be so small that they are still superparamagnetic, whilst on the other the iron in the clays may order magnetically at very low temperatures or show magnetic hyperfine patterns because of slow paramagnetic relaxation (cf. Section 3.3).

(ii) Goethite

Well crystallised goethite orders antiferromagnetically at about 400 K [46,47]. One then observes a magnetic hyperfine splitting at room temperature with a hyperfine field of about 38 T and a quadrupole shift of –0.26 mm/s. At 4.2 K the hyperfine field is 50.6 T, which renders goethite distinguishable from hematite, for which one has $B_{hf} > 52$ T. When goethite is not well crystallised or impure, it shows a broadened magnetic sextet pattern at room temperature. Small goethite particles may also exhibit superparamagnetism at room temperature. The quadrupole doublet with a splitting of about 0.5 mm/s is then difficult to distinguish from that of superparamagnetic hematite or from structural Fe^{3+} in clays. In fact, this situation is often encountered in soils and raw pottery clays.

(iii) Ferrihydrite

Ferrihydrite is a poorly crystallised hydroxihydrate of iron that gives rise to only a few broad X-ray diffraction peaks [46,47,55]. It is paramagnetic at room temperature, and exhibits a broadened quadrupole doublet with IS ≈ 0.24 mm/s, and a mean quadrupole splitting Q ≈ 0.6 mm/s. This makes ferrihydrite difficult to distinguish from structural iron in the clays and from superparamagnetic hematite or goethite on the basis or room temperature Mössbauer spectra.

Between 120 and 25 K, ferrihydrites begin to show magnetic hyperfine interactions, either because magnetic order sets in or because superparamagnetism becomes blocked. At 4.2 K all ferrihydrites exhibit a sextet Mössbauer pattern with broadened lines, nearly no quadrupole shift and mean hyperfine fields between 50 and 47 T, depending on the quality of the material.

4.3 Mössbauer spectra of raw pottery clays

Raw, i.e., unfired pottery clays contain iron in the clay fraction and in varying amounts of accessory iron oxides and oxihydroxides [56]. The relative amounts of the different iron bearing constituents can usually be determined from Mössbauer spectra taken at Room Temperature (RT) and 4.2 K, but sometimes even from such data unambiguous conclusions may be difficult or impossible to draw. Even when one cannot identify the individual minerals contributing to the different features of the Mössbauer spectra, it is usually possible to determine the relative spectral area arising from Fe^{2+} (A_{Fe2+}) and the relative area of the magnetically split components, often briefly called the magnetic area (A_m). Conversely, the relative area of all components that are not magnetically split, or nonmagnetic area (A_{nm}), is often given. Since these areas do not refer to specific minerals, they usually change with the temperature at which the Mössbauer spectra are measured, for instance when superparamagnetism gets blocked. In such cases, the chemical extraction of the oxides and oxihydroxides may help to distinguish between the clay and the oxide fraction. Extraction of the oxidic phases by bicarbonate buffered dithionite, $Na_2S_2O_4$ (DCB extraction) is often used to this end [57] and should leave only the structural iron in the silicates. One could also arrive at definite conclusions by carefully measuring the temperature dependence of the Mössbauer spectra, but this is a time consuming procedure that may not even yield unambiguous results. Figure 1 shows the Mössbauer spectra of a pottery clay from Batán Grande, Peru [58-62] measured at 300 K and 4.2 K before and after DCB extraction of the oxides. The clay fraction of this material consists mainly of kaolinite and illite, and about 40 % of the iron are bound in hematite and goethite. Before extraction, the 300 K Mössbauer spectrum shows the presence of some magnetically ordered hematite, of some structural Fe^{2+} in the clay fraction, and a dominant, broad Fe^{3+} doublet, to which the structural Fe^{3+} in the clay as well as superparamagnetic hematite or goethite may contribute. At 4.2 K one can distinguish the magnetic sextet patterns of hematite (B_{hf} = 53.4 T) and goethite (B_{hf} = 50.1 T). After DCB extraction, the room temperature spectrum exhibits only the clay pattern, with a higher fraction of Fe^{2+} and two distinguishable broadened Fe^{3+} doublets. The 4.2 K pattern of the extracted sample reveals a broad background with little structure that has been fitted by a wide distribution of magnetic hyperfine fields. This component is only just visible in the 4.2 K pattern of the unextracted material, where it could easily pass unnoticed because of its low relative intensity. The broad magnetic pattern can arise either from magnetic ordering of part

of the clay mineral fraction, or to slow paramagnetic relaxation of some of the Fe^{3+} in the clay.

4.4 The Firing of Ceramics as Reflected by Mössbauer Spectroscopy

The firing of pottery clays leads to physical and chemical changes in the clay fraction and in the iron oxides and oxihydroxides. These changes are reflected in typical changes of the Mössbauer spectra that can be used to obtain information on the firing process. In pottery kilns, the firing may occur under different conditions, i.e., in oxidizing or reducing atmospheres, whose composition may even change in the course of the firing cycle. Moreover, the temperature changes during kiln firing may be more complicated than a simple rise to a certain temperature, which would then be maintained for some time, and a final cooling phase. The question is to what extent one can draw conclusions on the ancient firing conditions from the Mössbauer spectra of ceramic finds. To find an answer to this, one has to resort to laboratory firing experiments that are designed to emulate the firing conditions in a kiln as well as possible but can be performed with some scientific rigor. Another source of information would be test firings in replica kilns or furnaces with temperature monitoring [63,64] or even in excavated ancient kilns [58-62]. Such test firings can yield interesting information on the ancient procedures, but they cannot replace laboratory firing experiments, both because the conditions are difficult to control and because they are more laborious to perform.

In laboratory firing experiments, the question about the best firing time arises. In most studies, the temperature was raised quickly to the desired value, and this temperature was then maintained for the same time at all temperatures (isochronal annealing). Then the samples were then cooled to room temperature by either taking them out of the furnace, or by letting them cool in the switched-off furnace. The times at maximum temperature were chosen between 1 hour and 2 days. The dependence of the Mössbauer spectra of fired clays on the firing time has been studied in some detail [61,62]. It turned out that at temperatures above 500 °C a quasi-equilibrium state is reached already after about 2 hours or even less, while at lower temperatures the reactions are more sluggish and the firing time may seriously affect the state of the iron in the fired material. Another question concerns the time it takes the temperature in the interior of a ceramic sherd to reach the temperature at the surface through heat conduction. Studies of the thermal conduction in fired clays show that this takes less than about five minutes for sherds of centimeter thickness [58,60,61].

Firing pottery clays in an oxidizing atmosphere is relatively straightforward. One will usually do it in air using an electric furnace. Firing in a reducing atmosphere is more demanding. In the pottery kiln reducing atmospheres will arise when not enough air is admitted to completely oxidize the fuel. The kiln atmosphere will then contain carbon monoxide, which can reduce the trivalent iron to the divalent state or even to metallic iron if the temperature exceeds 900 °C [62-64]. The presence of divalent iron in pottery can therefore be considered as showing that ceramics were fired under reducing kiln conditions. To emulate reducing firing in the laboratory, one must choose a furnace atmosphere that resembles the situation in a kiln, which, however, is not clearly defined. Two procedures have been used in most cases: one is to fire the samples in a stream of a CO/CO_2 gas mixture containing a few percent of CO[65]; the other is to put the samples into a closed vessel together with charcoal or other fuels like sawdust, taking care that the clay sample does not have direct contact with the charcoal [58-62,66]. In the beginning, the vessel would thus contain air, charcoal, and the

clay sample. Only when the furnace temperature exceeds about 400 °C, does the charcoal begin to react with the oxygen, and CO is formed which then acts as the reducing agent. In this arrangement, the oxygen fugacity will depend on the furnace temperature, but the whole arrangement may emulate the situation in a pottery kiln better than the use of CO/CO_2 gas mixtures. In any case, one should keep in mind that the results of reducing laboratory firing may depend on the experimental procedure, whence results obtained by different groups may be difficult to compare.

(i) Firing under oxidizing conditions

The results of oxidizing firing of clays are relatively straightforward. Different clay minerals will behave differently as far as the temperatures of certain reactions are concerned, but basically all appear to behave in the same manner. Some spectra obtained at room temperature after firing the clay from Batán Grande [11,12,58-62] (Figure1) are shown in Figure 2. The whole series of spectra obtained after firing this clay at temperatures up to 1000 °C in temperature intervals of 50 °C are shown in Figure 3 in a three-dimensional representation. The firing behavior of many clay minerals and pottery clays has been measured. Examples can, for instance, be found in [56,58-64,67-69].

At firing temperatures up to about 200 °C first the pore water and then the water that may be contained in the interlayer spaces of the layer silicates will be driven off. These processes usually do not cause noticeable changes in the Mössbauer spectra of clays.

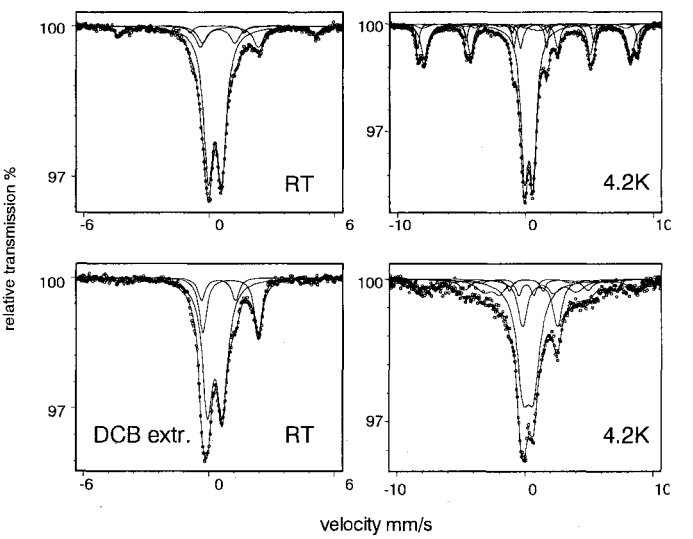

Figure 1. Room temperature (left) and 4.2 K (right) Mössbauer spectra of a pottery clay from Batán Grande, Peru, taken with a source of ^{57}Co in Rh which was at the same temperature as the absorber. The upper row represents spectra taken before DCB extraction, the lower one the corresponding ones obtained after extraction of the oxidic iron. Note that the velocity scales for the room temperature spectra is different from that for the 4.2 K patterns. In the room temperature spectrum of the unextracted material, the outermost lines of hematite are outside the scanned velocity range.

At about 200 °C the structural Fe^{2+} in the clay begins to be oxidized to Fe^{3+}, a process that is concluded at about 450 °C in most cases. Between about 300 and 500 °C dehydroxilation of the octahedral layers of most clay minerals takes place. This involves the evolvement of water according to $2OH^- \rightarrow O^{2-} + H_2O\uparrow$. As a consequence, the number of ligands of the octahedral iron is reduced from six to five. This reduction of the site symmetry causes an increase of the electric quadrupole splitting of the structural Fe^{3+} from about 0.7 mm/s in fresh clay to about 1.4 mm/s on firing the Batán Grande clay at 700 °C. When the dehydroxilation is completed, the quadrupole splitting of Fe^{3+} reaches a plateau that may be more than 100 °C wide and extends up to about 800 °C in most cases, but is not very pronounced in the Batán Grande clay.

Between 700 and 900 °C the layer structure of the clays will break down altogether. The structural iron contained in the clays then mainly forms hematite, while the silica and alumina recrystallize as cristobalite (SiO_2) and mullite ($Al_6Si_2O_{13}$) at higher temperatures. The formation of hematite is seen in the Mössbauer spectra as an increase of the magnetic or, conversely, as a decrease of the nonmagnetic area of the Mössbauer spectra [56,58-64,67-69].

The large quadrupole splitting of the dehydroxilized clays disappears when the clay structure breaks down and consequently the quadrupole splitting of the Fe^{3+} doublet decreases again.Above about 1000 °C vitrification may take place and an increasing amount of hematite may dissolve in the silicate glass phase. This goes along with another slight increase of the Fe^{3+} quadrupole splitting and an increase of the nonmagnetic fraction in the Mössbauer spectra. Figure 4 shows the dependence of the most significant Mössbauer parameter, the quadrupole splitting of the Fe^{3+} doublet, Q_{Fe3+}, and the nonmagnetic fraction, A_{nm}, for the Batán Grande clay. In this case the described features are rather washed out. A clay with very sharp transitions and a wide plateau with $Q_{Fe3+} \approx 1.6$ mm/s extending from 450 to 900 °C is a Kaolin from Brazil [56,67,68]. The Fe^{3+} isomer shift usually shows no or very little dependence on the firing temperature (Figure 4).

In clays containing percent amounts of calcium, minerals of the melilite group will form at or above about 900 °C [70], in particular gehlenite ($Ca_2Al_2SiO_7$), into which varying amounts of Fe^{3+} can be incorporated up to the composition of ferrigehlenite ($Ca_2Fe_2SiO_7$) [71-73]. These minerals can easily be recognized in the Mössbauer spectra of ceramics owing to their large quadrupole splittings ($1.1 \leq Q \leq 1.9$ mm/s) and their small isomer shifts ($0.0 \leq IS \leq 0.1$ mm/s). Their formation may be an important indicator for both the assessment of the firing temperature and the classification of ceramics by Mössbauer spectroscopy.

Hematite is stable under oxidizing firing, but at elevated temperatures, perhaps beginning at 600 C, small hematite particles may coalesce into larger ones. This may gradually suppress room temperature superparamagnetism and hence lead to a steady decrease of the nonmagnetic fraction in the RT Mössbauer spectra [56,58-64,67-69]. Under suitable conditions, hematite may convert from the non-Morin type which remains weakly ferromagnetic at all temperatures into the better crystallised Morin type (cf. Section 4.2) which becomes antiferromagnetic below room temperature. The presence of Morin type hematite ceramics in cases where it is absent in the raw pottery clay is therefore an interesting feature [49,50]. Unfortunately, the conditions under which this conversion may take place have not yet been studied in detail.

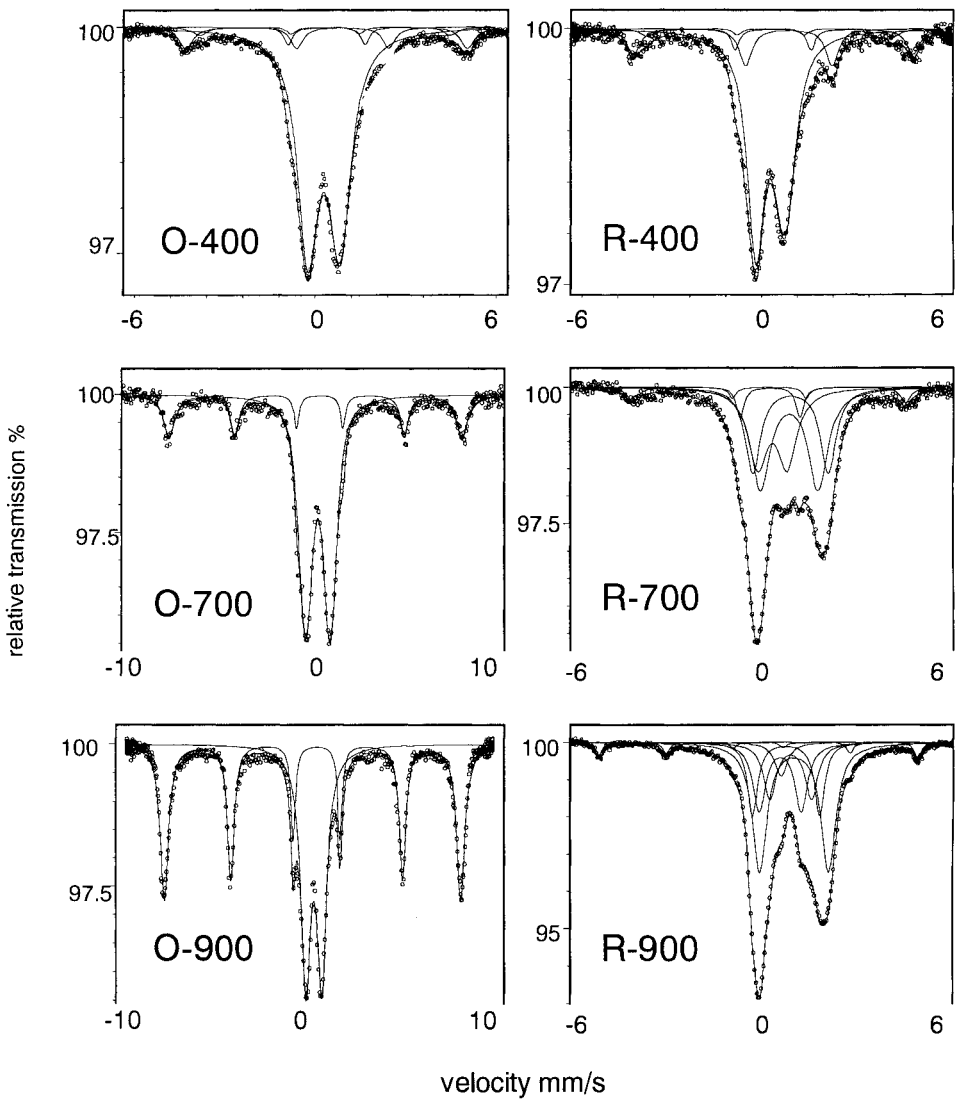

Figure 2. Room temperature Mössbauer spectra of the clay from Batán Grande fired in air for 48 hours (left) and in a reducing atmosphere produced with charcoal for 3 hours (right) at 400, 700, and 900 °C. Note the different velocity scales.

Goethite and ferrihydrite convert into hematite at temperatures between about 200 and 400 °C. In this temperature range, maghemite may form as an intermediary phase, but it would eventually also convert to hematite at about 400 °C. It would also be difficult to distinguish maghemite, a spinel phase containing only Fe^{3+}, from hematite in the Mössbauer spectra of mixtures [74]. The conversion of oxihydroxides into hematite is reflected as a rather sudden

decrease of A_{nm} in the temperature range between 200 and 400 °C [56,58-64,67-69]. In fired ceramics no iron oxihydroxides should persist. If they are found, this is a strong indication of weathering or precipitation from iron bearing fluids during burial.

(ii) Firing under reducing conditions

Under reducing conditions, the firing behavior of clays is largely different and less well understood than under oxidizing conditions. To illustrate the differences, selected spectra of the clay from Batán Grande [58-62] fired under reducing conditions are shown in Figure 2 together with the spectra for the same clay fired in air. In Figure 3 a three-dimensional representation of the behaviour of this clay under reducing firing is given. Instead of an oxidation of the Fe^{2+} present in the raw clay, a reduction of the structural Fe^{3+} takes place, beginning at around 500 °C. The onset of reduction during firing with charcoal as a reducing agent may, in fact, be due to the onset of the reaction of the carbon with air. The iron oxides also become oxidized, and the Fe^{2+} content rises until, at about 800 °C, practically all the iron has become reduced. The Fe^{2+} spectra are usually more complicated than those of the original clays, i.e., they have more components which, however, cannot easily be attributed to specific chemical compounds. The mean quadrupole splittings of Fe^{2+} do not show an increase analogous to that exhibited by the Fe^{3+} splittings during oxidizing firing. Some spectra of the Batán Grande clay fired reducingly with charcoal were shown in Figure 2.

Above 800 °C, whatever remains of the layer structure of the clays will break down and the iron will be set free. It may form wustite (FeO), which is not very stable and therefore rarely seen in Mössbauer spectra of reducingly fired clays. Magnetite (Fe_3O_4), a ferrimagnetic spinel containing both Fe^{2+} and Fe^{3+} [46,47], is also rarely found in fired clays. It is easily recognizable by its Mössbauer spectra, because it is already ferrimagnetic at room temperature (T_c = 850 °C) and exhibits two sextets with hyperfine fields of 49.2 and 46.1 T at room temperature [46,47].

The most common products seem to be ferroan spinel phases related to hercynite ($FeAl_2O_4$), but probably containing impurities like Mg that render the Mössbauer spectra even more complicated [75,76] than those of pure hercynites [77,78]. As other Fe^{2+} bearing mineral phases that may form [76] when clays are fired reducingly are olivines ($(Fe,Mg)_2SiO_4$), pyroxenes ($(Fe,Mg)SiO_3$), ferrous mullite and feldspars, which all have rather similar spectra. For this reason a detailed interpretation of the Mössbauer patterns of reducingly fired ceramics in terms of the formed compounds is difficult .

Some of the Fe^{2+} bearing phases order magnetically at 4.2 K. For instance, pure hercynite orders magnetically at about 15 K with a hyperfine field of about 15 T, probably as a spin glass [78]. Consequently, the low temperature Mössbauer spectra of reducingly fired ceramics often show magnetic ordering of part of the Fe^{2+}, but these spectra are complicated and often cannot be unraveled in a satisfactory manner [6].

Above about 900 C, the iron begins to be reduced to the metallic state. The stable crystal structure of metallic iron at these temperatures is that of the fcc austenite phase. On cooling, however, austenite normally converts to the low temperature bcc ferrite phase (α-iron), which is ferromagnetic with a hyperfine field of 33 T at room temperature and thus easily recognizable as a sextet in the Mössbauer spectra of fired clays [63,64,79]. In rare cases, however, the austenite is in part retained on cooling the samples to room temperature. Being paramagnetic, austenite gives rise to a single line with an isomer shift of about –0.2 mm/s,

which can also be easily recognized [79]. In archaeological ceramics, metallic iron is but rarely observed, probably because is has oxidized in most cases during burial.

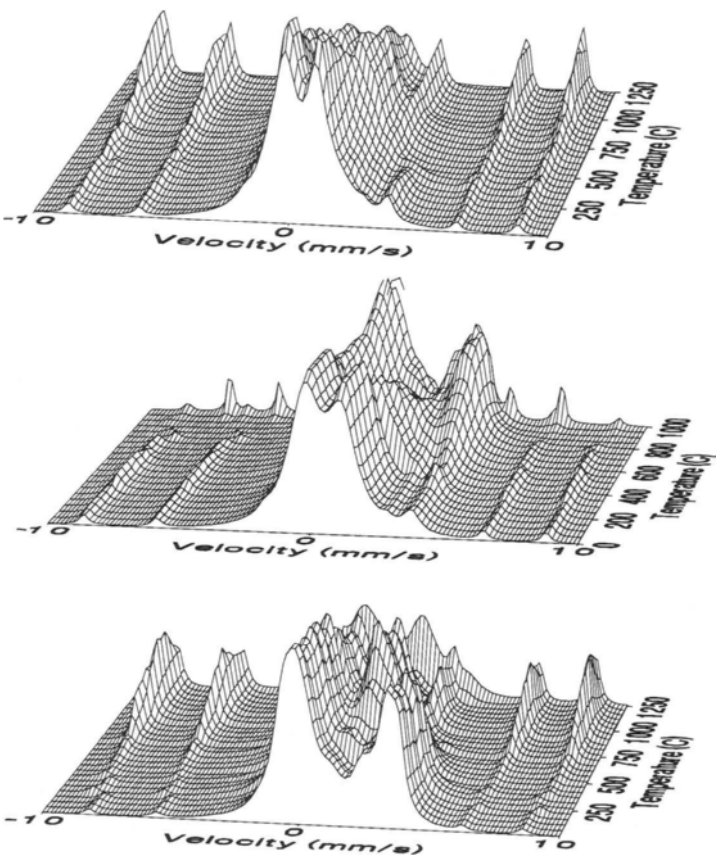

Figure 3. Three-dimensional representation of the room temperature Mössbauer spectra of the clay from Batán Grande fired at temperatures up to 1250 °C for 48 hours. The data points are omitted for the sake of clarity. From top to bottom the figure shows firing in air, firing under reducing conditions produced with charcoal, and refiring in air for 48 hours of samples first reduced with charcoal at 800 °C for three hours.

There are, however, cases where the iron is conserved, perhaps because it is protected in a vitreous matrix [79].

Like in pottery fired in an oxidizing atmosphere, the presence of calcium in the clay may also affect the state of the iron in reducingly fired pottery [66], apparently because Fe^{3+} in gehlenite forms easily and is sufficiently stable against reduction to persist even at temperatures around 1000 °C, where metallic iron already forms.

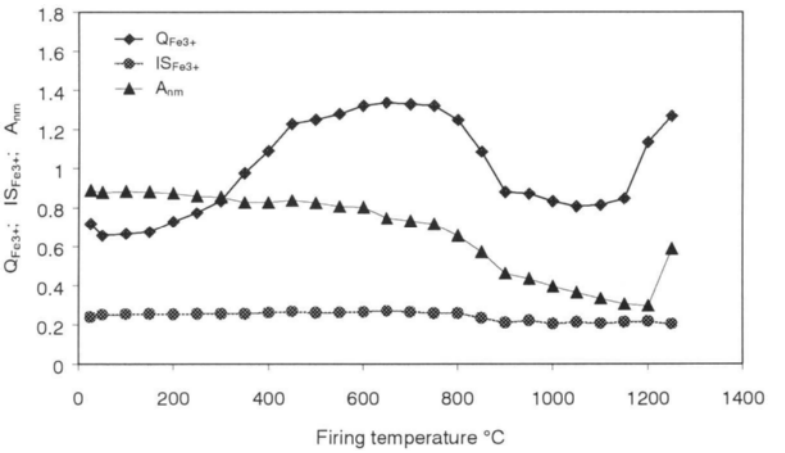

Figure 4. Dependence of selected room temperature Mössbauer parameters on the firing temperature for firing in air for 48 hours. Q_{Fe3+} and IS_{Fe3+} (in mm/s) are the mean quadrupole splitting and isomer shift of the trivalent iron that does not show a magnetic hyperfine splitting. A_{nm} is the nonmagnetic fraction, i. e., the relative area of all components in the Mössbauer spectra that do not exhibit a magnetic hyperfine splitting.

(iii) Firing under changing conditions

In pottery kilns, not only the firing temperature but also the kiln atmosphere may change in a complicated way in the course of the firing cycle, for instance when more or less air is admitted or when more fresh fuel is added. One may ask how such changing conditions affect the final product, and in particular its Mössbauer spectra. This also prompts the question to which extent ancient ceramics retain information on such changing firing cycles, and whether such information can be extracted by Mössbauer experiments.

Quite generally, when the kiln temperature changes during firing, the Mössbauer spectra of the pottery will correspond to the highest temperature reached, even if this temperature is maintained only briefly [61,62]. Any changes in the state of the iron induced at a certain temperature cannot be reversed subsequently at a lower temperature, for instance during the cooling phase, as long as the kiln atmosphere does not change. Complicated time dependencies of the firing temperature are therefore of little importance for the final outcome. When the composition of the atmosphere, i.e., the oxygen fugacity changes during firing, matters become more involved.

A substantial body of laboratory data exists for clays first fired under reducing conditions, e. g., at 800 °C, and then refired in an oxidizing atmosphere at different temperatures. This type of procedure is of interest because potters often first fire under reducing conditions for effective use of the fuel, and then, towards the end of the firing cycle, admit more air, either to achieve a red color of the ceramics, or because they inadvertently open the kiln before it has cooled sufficiently.

When previously reduced material is heated again in air, the Fe^{2+} is oxidized to Fe^{3+} between about 450 and 600 °C. Figure 5 shows this for spectra of the Batán Grande first fired

reducingly at 800 °C with charcoal and then refired in air at 400 and 500 °C. The full dependence of the Mössbauer spectra on the temperature at which the material is refired is shown in Figure 3. Since the Fe^{3+} formed during reoxidation is no longer structural iron in sheet silicates but mainly superparamagnetic small particle hematite, one does not observe the increase of the quadrupole splitting of the nonmagnetic Fe^{3+} observed when fresh clays are fired in air (Figure 4). One can make use of this to distinguish between ceramics that were oxidized after being fired under reducing conditions and ceramics that were fired under oxidizing conditions only [58-62].

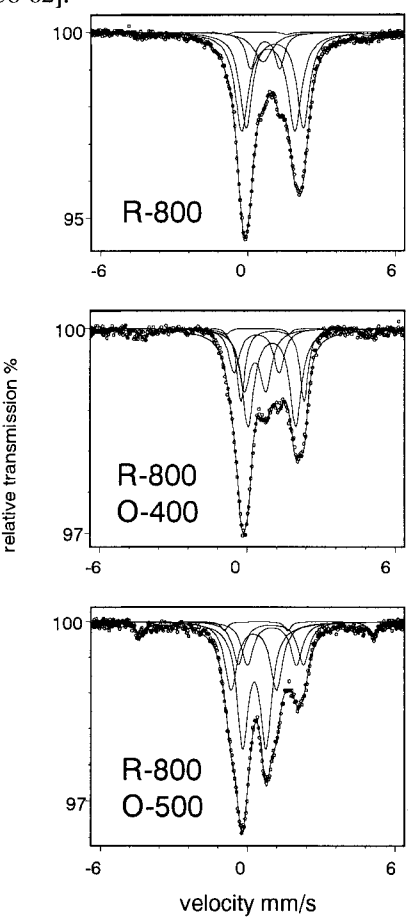

Figure 5. Room temperature Mössbauer spectra of the clay from Batán Grande fired in a reducing atmosphere produced by charcoal for 3 hours (top) and then refired in air at 400 °C (middle) and 500 °C (bottom) for 48 hours

When ceramics in which the Fe^{2+} bearing phases (section 4.2) formed during reducing firing has been oxidized are again fired in a reducing atmosphere between 600 and 900 °C, the Fe^{2+} bearing phases form again. In fact, this transformation has been found to be reversible

repeatedly [80]. Pottery would thus be expected to record the last firing atmosphere, i.e., the last atmosphere in which it was still hot enough for oxidation or reduction to take place.

5. DETERMINATION OF THE FIRING CONDITIONS OF POTTERY

Conclusions drawn from Mössbauer spectra concerning original firing conditions, be they on the firing temperature or on the kiln atmosphere, imply that the pottery has not undergone any alteration during burial. Chemical changes may result from weathering, which could, for instance, cause dehydroxilized clays to rehydroxilizse, or hematite to convert back into oxyhydroxides with the effect that the size of the hematite particles could shrink. Such processes seem to be rare since hematite is very stable, rehydroxilation seems to be a slow process, and once the sheet silicate structure is destroyed it will not form again under the conditions of burial. Nevertheless, signs of weathering of pottery detected by Mössbauer spectroscopy have been reported [81-84] and one should always be wary of this possibility. It has also been discussed whether exposure to environmental ionizing radiation could influence the Mössbauer spectra of ceramics [85], but one can dismiss this idea at least for the doses of the order of tens of gray be absorbed naturally by archaeological ceramics.

5.1 Pottery fired under oxidizing conditions

Pottery fired in oxidizing kiln atmospheres at temperatures above about 500 °C will show no Fe^{2+} in its Mössbauer spectra. Assuming that one does not have a case in which the material has first been fired reducingly and then oxidized (cf. Section 4.4), the main information that can be extracted from the Mössbauer data will be the firing temperature. The room temperature Mössbauer parameters that change most sensitively during the oxidizing firing of pottery clays are the quadrupole splitting of the trivalent iron, Q_{Fe3+}, and the nonmagnetic fraction, A_{nm}. While Q_{Fe3+} exhibits a typical increase on firing between 400 and 700 °C and a decrease above 800 °C, A_{nm} decreases first when the oxyhydroxides are converted to magnetically split hematite between 200 and 400 °C, and again when structural iron is set free and becomes hematite between 800 and 900 °C. Another cause of the decrease of A_{nm} with the firing temperature is the growth of hematite particles, which may thus be no longer superparamagnetic at room temperature. These features (Figure 4) can be exploited for the determination of the firing temperature of ancient pottery.

One way of doing this is to compare the Mössbauer spectra of pottery finds with those of reference materials fired in the laboratory under controlled conditions. This requires clay of the type used by ancient potters for the laboratory experiments. Such clay may sometimes be available, for instance when pottery workshops are excavated in which unfired clay is found, or when one can identify the clay deposits that were exploited by the ancient potters. One can then compare the spectra of pottery finds with those of the laboratory fired materials. The firing temperature of pottery will be the one for which the spectra of the laboratory fired material and the pottery finds agree best. The comparison can be made visually by comparing the whole Mössbauer spectra, or by comparing sensitive fit parameters like Q_{Fe3+} and A_{nm}. It is obvious that this method permits rather accurate determinations in temperature regions where the Mössbauer spectra change sensitively with the firing temperature, while in regions where little or no change occurs one can deduce the firing temperatures only within wider limits. Comparing spectra obtained at different temperatures, for instance at room temperature and 4.2 K, may help to avoid ambiguities. The comparison with spectra of laboratory fired

authentic clay is suitable for determining the firing temperatures of large numbers of sherds, since for each of them only one spectrum (or a few at different temperatures) need be measured.

As an example, Figure 6 shows Mössbauer and X-ray diffraction patterns of the lining of a pre-Hispanic copper-arsenic alloy furnace from Batán Grande on the northern coast of Peru, where a large number of such furnaces have been excavated [11,12]. These furnaces are dug into the ground and the walls of the chamber is lined with regional clay of the type described in Section 4. The studied piece of furnace lining (Figure 6) is about 7 cm thick. On the surface directed towards the chamber there is a dark reddish brown layer with a violet tinge (a) of about 1 cm thickness. Below this surface layer, a bright brown or brick-colored layer (b) of about the same thickness follows, below which the color is the dull brown of the raw clay. Figure 6 shows room temperature Mössbauer spectra and X-ray diffraction diagrams of samples from layers (a) and (b) and from spot (c) about 5 cm below the surface. In the spectrum of layer (a) the quadrupole splitting of the trivalent iron is rather small, $Q_{Fe3+} = 0.74$ mm/s. According to the reference curve for this clay (Figure 4), this shows that the material has reached a temperature between 900 and 1150 °C. This is compatible with the amount of magnetically split iron and with the X-ray diffraction diagrams, which show no more mica and amphiboles, which disintegrate around 950 and 1000 °C, respectively. One can therefore conclude that the uppermost layer of the furnace lining has reached a temperature between 1000 and 1150 °C. For layer (b) one finds $Q_{Fe3+} = 1.16$ mm/s. According to Figure 4 this corresponds to a temperature of 830 °C. This temperature is one at which Q_{Fe3+} depends very sensitively on the firing temperature, suggesting very narrow error limits of about ±10 °C. An additional uncertainty arising from the unknown firing time also is small in this temperature region [59], whence a temperature of 830±30 °C seems to be a fair estimate. Again X-ray diffraction confirms this result, though only crudely, since the presence of mica shows that this layer has always remained below 950 °C. Finally, the Mössbauer spectrum of sample (c) still shows the presence of Fe^{2+}, which should have disappeared at 350 °C (Figure 3) and $Q_{Fe3+} = 0.62$ mm/s. This shows that this sample has practically not been heated at all and has certainly not become hotter than 250 °C. The X-ray diffraction pattern confirms this, albeit again with less accuracy, by still showing the presence of sheet silicates with a 14 Å separation of the basal planes (mainly vermiculite) and of kaolinite, which will both decompose above 500 °C. The conclusions to be drawn from this series of measurements would thus be that the inner surface of the furnace lining did get very hot, indeed, but that already a few centimeters inside the material the temperature rise was only very moderate.

When no original clay is available, one can refire pottery samples in the laboratory at different temperatures and record Mössbauer spectra after each firing step. As long as only oxidizing firing is considered, the physical and chemical transformations taking place in pottery clays during firing cannot be reversed by firing again below the original firing temperature. One therefore expects no changes in the Mössbauer spectra to occur on refiring below the original firing temperature; only when this temperature is exceeded will changes take place. The original firing temperature should then be just below the temperature at which the first changes occur in refired samples.

Figure 6. X-ray diffraction patterns recorded with Co K_α radiation (left) and room temperature Mössbauer patterns of three layers of the inner lining of a pre-Hispanic copper alloy furnace from Batán Grande, Peru. The 7 cm thick piece of the lining from which the samples were taken is also shown. The spectra show that the studied layers reached the temperatures given with the Mössbauer patterns (see text).

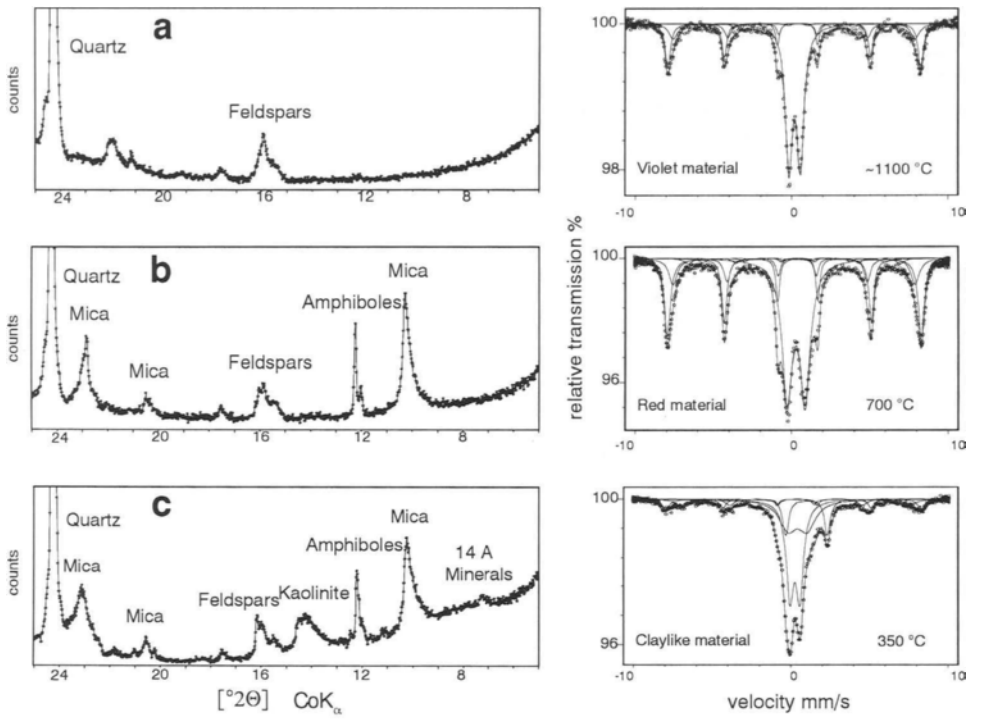

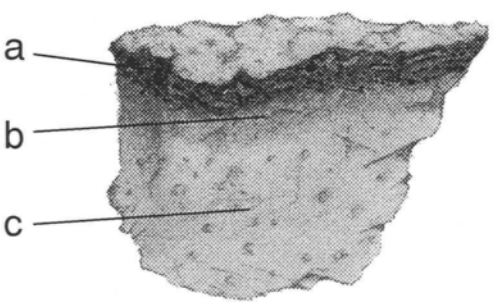

This method will again be most accurate when the Mössbauer spectra change sensitively in the region of the original firing temperature. When no or only minor changes occur near the original firing temperature, this method may become rather inaccurate and, depending on the circumstances, only an upper limit for the firing temperature may be obtained. The method may also become inaccurate or inapplicable when alterations have taken place during burial or when divalent iron is present [84].

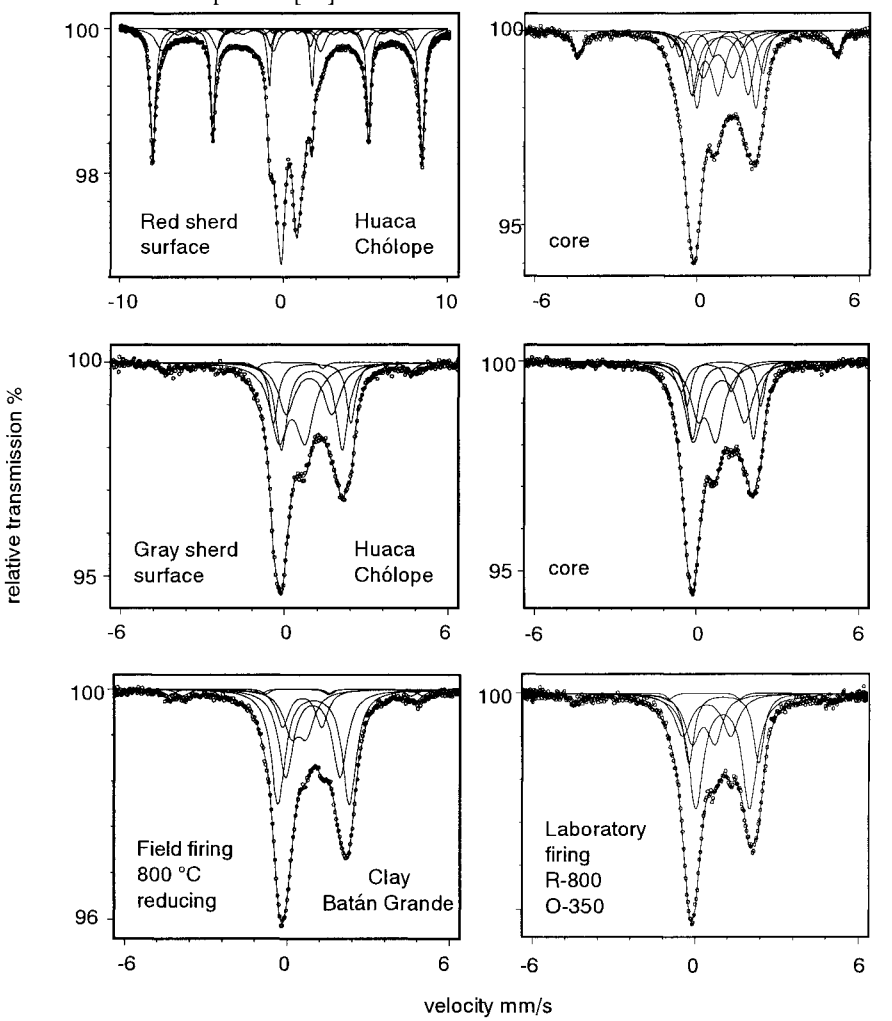

Figure 7. Room temperature Mössbauer spectra of ceramics fired under reducing and changing conditions. In the top row spectra of the red surface layer and the gray core of a sherd from Huaca Chólope are shown. The middle row shows spectra of a Huaca Chólope sherd that is gray throughout, and the bottom row similar spectra obtained for field fired and laboratory fired specimens of clay from Batán Grande.

5.2 Pottery fired under reducing and changing conditions

The firing behavior under reducing or even changing conditions is not understood as well as that under oxidizing conditions, mainly because there are many parameters that can be varied in experiments. The presence of Fe^{2+} in ceramics that have been fired at temperatures above about 500 °C shows that the kiln atmosphere must have been reducing, since under oxidizing conditions any Fe^{2+} present in the raw clay would have been oxidized. This, however, still allows for a wide range of oxygen fugacities. It is therefore difficult to determine the firing temperature using the methods applicable after oxidizing firing, since the atmosphere of the original kiln cannot be emulated reliably. Moreover, the composition of the kiln atmosphere may have changed during firing. For reducing kiln atmospheres resembling those obtained in the laboratory in closed vessels with charcoal, one expects to find no or very little Fe^{3+} when the firing temperature has exceeded 700 °C (Figure 3 and, e.g., ref. [58-62]), as it would have in most cases. The presence of Fe^{3+} then is a strong indication that either the kiln atmosphere was not sufficiently reducing to convert all iron to Fe^{2+}, or that, after all iron had been converted to Fe^{2+} during the reducing firing step, a reoxidation took place due to the admission of air into the kiln at the end of the firing cycle. An exception would be calcareous clays, in which rather stable Fe^{3+} compounds may form [66].

Such reoxidation processes can result in a colorful layer structure of the sherds, with a red or violet layer near the oxidized surface of the sherd and a gray, reduced core [44,45]. The layer near the surface is then more strongly oxidized than the interior of the sherd, the red or violet color being due to hematite particles of various sizes. However, even in cases where the color gives no clue to such a reoxidation at the end of the firing cycle, the Mössbauer patterns may show differences when measured separately for the surface and the core of a sherd [58-62]. A separation into layers may therefore be interesting even for apparently homogeneous sherds.

Grey or black coring of sherds can also arise from the presence of organic material in the raw pottery clay. On heating, the organic material will act as a reducing agent, and may also be carbonized and thus contribute to the dark color. The surface of such sherds may be oxidized during firing under oxidizing conditions, and when the clay body is sufficiently dense to prevent the ready permeation of oxygen, the core may remain reduced while the surface is oxidized [76].

As an example spectra of a sherd from Huaca Chólope, Peru, [58-62] with a red surface layer and a gray core are shown in the top row of Figure 7. The red surface layer contains no Fe^{2+} at all, while the iron in the core is nearly all divalent, with only a minor contribution of paramagnetic Fe^{3+} and magnetically split hematite. Spectra like that of the core of this sherd are frequently observed, both in the cores and on the surfaces of sherds. An example of a sherd that is gray throughout and has nearly the same spectrum for the core and the surface is shown in the second row of Figure 7, while the third row of Figure 7 shows two rather similar spectra obtained by firing in an authentic kiln [58-62] and in the laboratory. Spectra like those observed in the gray sherd or the core of the sherd with the red surface may be obtained by different firing cycles. One would be direct firing of the clay under reducing conditions at temperatures between 600 and 650 °C, at which a small amount of Fe^{3+} is still left. The other is an initial firing at a higher temperature in a strongly reducing atmosphere and a mild reoxidation at the end of the firing cycle. A reoxidation at about 400 °C after a reducing firing at 800 °C, for instance, will yield (Figure 5) spectra just like those found in many ceramics (Figure 7). By refiring such material in the laboratory under oxidizing conditions, however,

one can distinguish between the two possibilities. The reason for this is that the Fe^{3+} formed in material previously reduced near 800 °C will not exhibit the large Q_{Fe3+} values found after mere oxidizing firing (Figure 4) at temperatures between about 400 and 800 °C. But in material fired in a reducing atmosphere near 600 °C only, the sheet silicate structure is still largely intact and therefore the Fe^{3+} formed when such pottery is oxidized again will exhibit the large Q_{Fe3+} values. *This shows that the pottery retains a memory of details of certain features of the firing process.* Such details are still not very well understood, but they show that Mössbauer spectroscopy may eventually become quite useful for the determination of the firing conditions of ceramics in changing kiln atmospheres.

REFERENCES

1. M. Takeda, H. Mabuchi and T. Tominaga, Radiochem. Radioanal. Letters 29 (1977) 191.
2. J. Friedl, A. Füssel, R. Gebhard, A. Kyek, G. Lehrberger, T. Kobayashi, M. Regen and F.E.Wagner, in: I. Ortalli (ed.), Conference Proceedings Vol. 50, International Conference on the Applications of the Mössbauer Effect, Rimini, Italy, 10-16 September 1995. Italian Physical Society, Bologna, 1996, p. 773.
3. A listing of the Mössbauer papers on pottery and related subjects may be obtained by accessing the data base of the Mössbauer Effect Data Center, University of North Carolina at Asheville, NC (www.unca.edu/medc).
4. D.R. Cousins and K. G. Dharmawardena, Nature 223 (1969) 732.
5. B. Keisch, Nucl. Instr. Methods 104 (1972) 237; Archaeometry 15 (1973) 79; J. Physique Colloq. 35-C6 (1974) 151.
6. R. Gebhard, W. Ihra, F.E. Wagner, U. Wagner, H. Bischof, J. Riederer und A.M. Wippern, in: R.M. Farquhar, R.G.V. Hancock and L.A.Pavlish (eds.), Proceedings of the 26th International Archaeometry Symposium, Toronto, Canada, May 16-20, 1988. The Archaeometry Laboratory, University of Toronto, 1988, p. 196.
7. N.N. Greenwood and T.C. Gibb, Mössbauer Spectroscopy. Chapman and Hall, London, 1971.
8. G.J. Long (ed.), Mössbauer Spectroscopy Applied to Inorganic Chemistry, Vol. 1. Plenum, New York, 198 4.
9. Ph. Gütlich, R. Link and A. Trautwein, Mössbauer Spectroscopy and Transition MetalChemistry. Springer-Verlag, Berlin, 197 8.
10. D.P.E. Dickson and F.J. Berry, eds., Mössbauer Spectroscopy. Cambridge University Press, Cambridge, 1986.
11. Shimada and J.F. Merkel, Scientific American 265 (July 1991) 80.
12. Shimada, V. Chang, U. Wagner, R. Gebhard, H. Neff, M. Glascock and D. Killick, in: I. Shimada (ed.), Andean Ceramics: Technology, Organization and Approaches, MASCA Research Papers in Science and Archaeology, Supplement to Vol. 1 5. University of Pennsylvania Museum of Archaeology and Anthropology, Philadelphia, 1998, p. 2 3.
13. G. Longworth and M.S. Tite, J. Physique Colloq. 40-C2 (1979) 46 0.
14. U. Wagner, F.E. Wagner, B. Marticorena and R. Salazar, R. Schwabe and J. Riederer, Hyperfine Interactions 29 (1986) 1117.

15. I.N. Makundi, A. Waern-Sperber and T. Ericsson, Archaeometry 31 (1989) 54.
16. W. Meisel and G. Kreysa, Z. anorg. allg. Chem. 395 (1973) 31.
17. Z.M. Stadnik, in: J.W.Robinson (ed.), CRC Handbook of Spectroscopy, Vol. 3. CRC Press Inc., 1983, p. 41 5.
18. Ch. Janot and P. Delcroix, J. Physique Colloq. 35-C6 (1974) 557.
19. T.-M. Lin and R.S. Preston, in: C.W. Seidel and D. K.Dieterly (eds.), Mössbauer Effect Methodology, Vol. 9. Plenum, New York, 1974, p. 205.
20. J. Hesse and A. Rübartsch, J. Phys. E 7 (1974) 526.
21. G. Le Caër and J.M. Dubois, J. Phys. E 12 (1979)
22. J.Y. Ping, D.G. Rancourt and Z.M. Stadnik, Hyperfine Interactions 69 (1991) 49 6.
23. D.G. Rancourt and J.Y. Ping, Nucl. Instr. Methods Phys. Res. B 58 (1991) 85.
24. D.G. Rancourt, Phys. Chem. Minerals 21 (1994) 244.
25. N.N. Greenwood and A.T. Howe, J. Chem. Soc. Dalton Trans. (1972) 110.
26. C. Wilkinson, A.K. Cheetham, G.J. Long P.D. Battle, and D.H.O. Hope, Inorg. Chem. 23 (1984)
27. J.M.D. Coey, O. Ballet, A. Moukarika and J.L. Soubeyroux, Phys. Chem. Minerals 7 (1981) 141.
28. O. Ballet and J.M.D. Coey, Phys. Chem. Minerals 8 (1982) 218.
29. M.G. Townsend, G. Longworth and H. Kodama, Can. Mineralogist 24 (1986) 10 5.
30. D.P.E. Dickson and C.M. Cardile, Clays Clay Minerals 34 (1986) 103.
31. J.G. Stevens, A. Khasanov, J.W. Miller, H. Pollak and Zh. Lee, Hyperfine Interactions 117 (1998) 71.
32. J.G. Stevens, A.M. Khasanov, J.W. Miller, H. Pollak and Z. Lee (eds.) Mössbauer Mineral Handbook. Mössbauer Effect Data Center, Asheville, 1998.
33. J.M.D.Coey, Atomic Energy Review 18 (1980) 73.
34. J.M.D.Coey, in G.J. Long (ed.), Mössbauer Spectroscopy Applied to Inorganic Chemistry, Vol.I, ed. G.J. Long (Plenum, New York 1984) p. 44 3.
35. E. Murad, Hyperfine Interactions 111 (1998) 251.
36. D.G. Rancourt, Hyperfine Interactions 117 (1998) 3.
37. R.E. Grim, Clay Mineralogy (McGraw Hill, New York 1968).
38. Rozenson, E.R. Bauminger and L. Heller-Kallai, American Mineralogist 64 (1979) 893.
39. L. Heller-Kallai and I. Rozenson, Phys. Chem. Minerals 7 (1981) 223.
40. V.A. Drits, L.G. Dayniak, F. Muller, G. Besson and a. Manceau, Clay Minerals 32 (1997) 153
41. D.G. Rancourt, Phys. Chem. Minerals 21 (1994) 250.
42. D.G.Rancourt, J.Y.Ping and R.G. Berman, Phys. Chem. Minerals 21 (1984) 258.
43. E. Murad and U. Wagner, Clay Minerals 29 (1994) 1.
44. E. Murad and U. Wagner, Hyperfine Interactions 91 (1994) 685.

45. G.R. Hoy, in: Mössbauer Spectroscopy Applied to Inorganic Chemistry, Vol. 1, G.J. Long (ed.). Plenum, New York, 1984, p. 195.

46. E. Murad and J.H.Johnston, in: Mössbauer Spectroscopy Applied to Inorganic Chemistry, Vol. 2, G.J. Long (ed.). Plenum, New York, 1987, p. 507.

47. R.M. Cornell and U. Schwertmann, The Iron Oxides. Verlag Chemie, Weinheim, 1996.

48. E. Murad and U. Schwertmann, Clays Clay Minerals 34 (1986) 1.

49. J. Riederer, U. Wagner and F.E. Wagner, Radiochem. Radioanal. Letters 40 (1979) 319.

50. J. Riederer, U. Wagner and F.E. Wagner, J. Physique Colloq. 40-C2 (1979) 487.

51. S. Mørup, in: G.J. Long (ed.), Mössbauer Spectroscopy Applied to Inorganic Chemistry, Vol. 2, Plenum, New York, 1987, p. 89.

52. W. Kündig, H. Boemmel, G. Konstabaris and R.H. Lindquist, Phys. Rev. 142 (1966) 327.

53. A.M. van der Kraan, Phys. Stat. Solidi a 18 (1973) 215.

54. N.H. Gangas, A. Simopoulos and K. Kostikas, N.J. Yassoglu and S. Filippakis, Clays Clay Minerals 21 (1973) 151.

55. J.L. Jambor and J.E.Dutrizac, Chem. Rev. 98 (1998) 2549.

56. E. Murad and U.Wagner, Hyperfine Interactions 45 (1989) 161.

57. O.P. Mehra and M.L.Jackson, Clays Clay Minerals 7 (1960) 317.

58. U. Wagner, R. Gebhard, E. Murad, G. Grosse, J. Riederer, I. Shimada and F.E. Wagner, Hyperfine Interactions 110 (1997) 165.

59. U. Wagner, R. Gebhard, E. Murad, J. Riederer, I. Shimada, C. Ulbert and F.E. Wagner, in: I. Shimada (ed.), Andean Ceramics: Technology, Organization and Approaches, MASCA Research Papers in Science and Archaeology, Supplement to Vol. 1 5. University of Pennsylvania Museum of Archaeology and Anthropology, Philadelphia 1998, p. 17 3.

60. U. Wagner, R. Gebhard, E. Murad, G. Grosse, J. Riederer, I. Shimada and .E. Wagner, Hyperfine Interactions 110 (1997) 165.

61. U. Wagner, R. Gebhard, G. Grosse, T. Hutzelmann, E. Murad, I. Riederer, I. Shimada and F.E. Wagner, Hyperfine Interactions 117 (1998) 323.

62. U. Wagner, R. Gebhard, W. Häusler, T. Hutzelmann, J. Riederer, I. Shimada, J. Sosa and F .E. Wagner, Hyperfine Interactions 122 (1999) 163.

63. R. Gebhard, G. Lehrberger, G. Morteani, Ch. Raub, F.E. Wagner and U. Wagner, in: G. Morteani and J.P. Northover (eds.), Prehistoric Gold in EuropeMines, Metallurgy and Manufacture, Proceedings of the NATO Advanced Research Workshop on Prehistoric Gold in Europe, Seeon, Germany, September 27 – October 1, 1993, NATO ISI Series E: Applied Sciences, Vol 28 0. Kluwer Academic Publishers, Dordrecht, 1965, p. 27 3.

64. R. Gebhard, G. Große, G. Lehrberger, J. Riederer, F.E. Wagner and U. Wagner, in: I. Ortalli (ed.), Conference Proceedings Vol. 50, International Conference on the Applications of the Mössbauer Effect, Rimini, Italy, 10-16 Septamber 199 5. Italian Physical Society, Bologna, 1996, p.781.

65. R. Chevalier, J.M.D. Coey and R. Bouchez, J. Physique Colloq. C6 (1976) 86 1.

66. Y. Maniatis, A. Simopoulos and A. Kostikas and V. Perdikatsis, J. Amer. Ceram. Soc. 66 (1983) 773.

67. E. Murad and U. Wagner, Neues Jahrb. Miner. Abh. 162 (1991) 281.
68. E. Murad and U. Wagner, Hyperfine Interactions 117 (1998) 337.
69. Quin Guangyong, Pan Xianjia and Li Shi, Archaeometry 31 (1989) 3.
70. Y. Maniatis, A. Simopoulos ans A. Kostikas, J. Am. Ceram. Soc. 64 (1981) 26 3.
71. M. Akasaka and H. Ohashi, Phys. Chem. Minerals 12 (1985) 13.
72. M. Akasaka, H. Ohashi and I. Shinno, Phys. Chem. Minerals 13 (1986) 152.
73. D. Barb, S. Constantinescu, D. Tarina, I.S. Lyubutin, B.V. Mill, V.G. Terziev, T.D. Dimitrieva and A.V.Butashin, Hyperfine Interactions 50 (1989) 64 5.
74. G.Longworth and M.S.Tite, Archaeometry 19 (1977) 3.
75. U. Russo, S. Carbonin and A. della Giusta, in: G.J. Long and F. Grandjean (eds.), Mössbauer Spectroscopy Applied to Magnetism and Materials Science, Vol. 2, Plenum, New York, 1996, p. 20 7.
76. K.J.D. McKenzie and C.M. Cardile, J. Mater. Sci. 25 (1990) 2937.
77. L. Larsson, H. St. C. O'Neill and H. Annersten, Eur. J. Mineral. 6 (1994) 39.
78. J.L. Dormann, M. Seqqat, D. Fiorani, M. Noguès, J.L. Soubeyroux, S.C. Bhargava and P. Renaudin, Hyperfine Interactions 54 (1990) 503.
79. M. Bertelle, S. Calogero, G. Leotta, R. Salerno, R. Segnan and L. Stievano, to be published.
80. R.D. Bott, R. Gebhard, F.E. Wagner and U. Wagner, Hyperfine Interactions 91 (1994) 639.
81. Kostikas, A. Simopoulos and N.H. Gangas, Physique Colloq,. 35-C6 (1974) 536.
82. J. Danon, C.R.Enriquez, E. Mattievich, M. da C. de M. Coutinho Beltrão, J. Physique Colloq,. 37-C6 (1976) 866.
83. N.H.J. Gangas, I. Sigalas and A. Moukarika, J. Physique Colloq,. 37-C6 (1976) 867.
84. U. Wagner, F.E. Wagner and J. Riederer, Radiochem. Radioanal. Letters 51 (1982) 244.
85. N.A. Eissa, H.A.Sallam and N.H. Morcy, J. Physique Colloq,. 40-C2 (1979) 46 2.

Radiation in Art and Archeometry
D.C. Creagh and D.A. Bradley (editors)

AMS dating in archaeology, history and art

C. Tuniz [a *], U. Zoppi[a] and M. Barbetti [b]

[a]Australian Nuclear Science & Technology Organisation, Physics Division, PMB 1, Menai NSW 2234, Australia

[b]The NWG Macintosh Centre for Quaternary Dating, Madsen Bldg F09, University of Sydney, NSW 2006, Australia

Radiocarbon (^{14}C) dating provides an absolute time scale for human history over the last 50,000 years. Accelerator Mass Spectrometry (AMS), with its capacity to analyse ^{14}C in sub-milligram carbon samples, has expanded enormously the applicability of this dating method. Specific molecular compounds extracted from ancient bones, single seeds and other microscopic carbon-bearing substances of archaeological significance can now be dated, increasing the sensibility and reliability of the chronological determination. Thanks to the very limited invasiveness of AMS, rare artefacts can be sampled for dating without undue damage. The state of the art in AMS dating of objects significant for archaeology, history and art is reviewed with examples from some recent applications.

1. INTRODUCTION

One of the main objectives of archaeology is to chronologically order past events by studying material remains that reflect human behaviour. A versatile array of dating methods is nowadays available. Relative chronologies can be deduced from circumstantial evidence, such as change of style and manufacturing technique. Relative chronological information can also be obtained using methods based on time-dependent geological and chemical changes (eg stratigraphy, sedimentation rate, weathering, hydration, magnetism). Certain kinds of annual phenomena, such as tree rings or varves, will yield very precise chronologies if stringent precautions are followed. Finally, many methods providing absolute chronologies are based on time-dependent phenomena related to natural radioactivity, and include:

1. exponential decay of long-lived cosmogenic radionuclides, as in the radiocarbon method;
2. exponential in-situ production by secondary cosmic rays of long-lived radionuclides, such as ^{10}Be, ^{26}Al and ^{36}Cl, which can be used for dating rock surfaces and stone artefacts;

* Present address: Australian Permanent Mission to the United Nations, Mattiellistrasse 2-4/III A-1040 Vienna, Austria

3. linear build-up of radiation exposure effects, in thermoluminescence (TL), optically stimulated luminescence (OSL), electron spin resonance (ESR) and fission track dating;
4. exponential build-up of a radiogenic daughter from a primordial radionuclide, in K-Ar, Ar-Ar and U-series dating.

^{14}C is the most widely used of these chronometers. In the late 1940s, the development of radiocarbon dating by detection of the ^{14}C residual activity (Libby, 1946; Arnold and Libby, 1949) revolutionised archaeology providing a precise and direct measurement of the time scale for the development of human activities during the late Quaternary. In particular, radiocarbon dating had a strong impact on the understanding of European prehistory, previously dated only by correlation with the historical chronology of the Near East (Renfrew, 1973)

In the late 1970s (Muller, 1977; Bennett *et al.*, 1977; Nelson *et al.*, 1977), the development of direct atom counting by AMS enhanced more than a million-fold the sensitivity of ^{14}C analysis. Extensive AMS work followed, particularly in the analysis of radiocarbon and other cosmogenic radionuclides for archaeological, geological and environmental applications (Tuniz *et al.*, 1998; Fifield, 1999). Through the non-invasive analysis of famous artefacts and findings such as the Shroud of Turin (see Figure 1; Damon *et al.*, 1989), the Ice Man (Prinoth-Fornwagner and Niklaus, 1994) and the Dead Sea Scrolls (Bonani *et al.*, 1992), AMS has gained widespread public recognition as a dating technique.

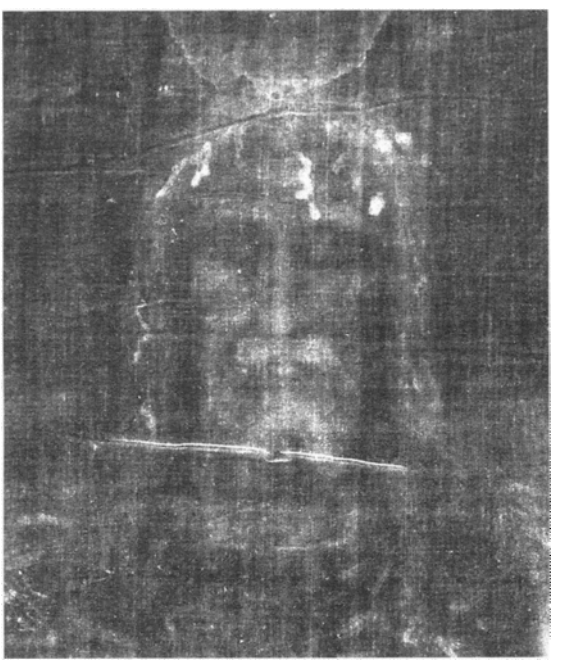

Figure 1. Close up of the facial image of the Shroud of Turin as it appears on a photographic negative (photo: © 1978 Barrie M. Schwortz).

Radiocarbon dating must be applied with due consideration for contamination, bioturbation, natural isotopic fractionation and many other factors that can influence its accuracy. Appropriate procedures to correct for these effects have been established. In the following, AMS dating will be reviewed with some illustrations that draw on the special advantages of this method to determine a precise chronology for human prehistory. The application of AMS dating to authenticate objects and materials of historical and artistic significance will be also discussed.

2. PRINCIPLES OF RADIOCARBON DATING

^{14}C is formed in the atmosphere by nuclear reactions of secondary cosmic neutrons with nitrogen (78 % of the atmosphere consists of N_2) and is quickly distributed throughout the atmosphere as $^{14}CO_2$. In pre-industrial times, the atmospheric isotopic ratio $^{14}C/^{12}C$ was about 1.2×10^{-12}. In a simplified model, which is not strictly correct (see sections 4. and 5.) but is often used to introduce the basic idea, we may argue that living organisms participating to the carbon cycle via metabolic processes are characterised by this radiocarbon concentration. When a living organism dies, the carbon exchange stops. Hence, by measuring the residual ^{14}C concentration in organic samples, if they have not been contaminated by younger material (eg via bacterial action, soil organic acids) or older material (eg geologic calcium carbonate), it is possible to calculate the time elapsed since the material was originally formed. Ages up to about 50,000 BP can be determined by radiocarbon dating.

2.1. Radiocarbon: a gift of nature

The functioning of radiocarbon as a precise natural chronometer in archaeology is due to a number of favourable circumstances. Firstly, the ^{14}C half-life of 5730 years is ideal for studies in the temporal scale characterising the development of human civilisation. Furthermore, the rather rapid and homogeneous mixing in the atmosphere of the freshly produced $^{14}CO_2$ gas attenuates production variations. Hence, the *time zero* point of the chronometer (the initial isotopic ratio in living organisms) is fairly uniform in space and time. Finally, incorporation of ^{14}C within organic molecules permits the extraction of material for dating which is directly derived from the original living organism.

In principle, other natural long-lived radioisotopes could be useful to extend the datable time span in archaeology. In particular, the cosmogenic isotope ^{41}Ca was measured by AMS in modern bones and other terrestrial materials to test the possibility of directly dating archaeological findings with ages of 10^5 - 10^6 years (Middleton *et al.*, 1989). Unfortunately, the variability of the $^{41}Ca/^{40}Ca$ ratio in contemporary materials makes it difficult to establish the *time zero* point for this chronometer.

3. AMS: COUNTING ATOMS RATHER THAN DECAYS

AMS is the analytical technique of choice for the detection of long-lived radionuclides in samples which cannot be practically analysed with decay counting or conventional mass

spectrometry (MS). Its advantage is that the ambiguities in ion identification are practically removed, enabling the analysis of isotopic ratios as low as 10^{-15}, a factor 10^5 lower than in most MS systems. Since the atoms and not the radiation resulting from their decay are directly counted, the sensitivity of AMS is unaffected by the half-life of the isotope being measured and detection limits at the level of 10^6 atoms are possible. Compared to the decay counting technique, the efficiency of AMS in detecting long-lived radionuclides is 10^5 – 10^9 times higher, the size of the sample required for analysis can be 10^3 - 10^6 times smaller and the measurement can be performed 100 to 1000 times faster. For example, samples having as little as 20 • g carbon are analysed in 30 minutes at the ANTARES AMS centre (see Figure 2). To highlight the difference between decay counting and atom concentration analysis, consider 1 g of modern carbon containing 6 x 10^{10} atoms of ^{14}C, which can be measured by decay counting with 1% precision (10^4 decays detected) in 1000 minutes hours. With a high-intensity ion source, AMS can count 10^4 ^{14}C atoms in one minute, consuming only 100 • g of the source material.

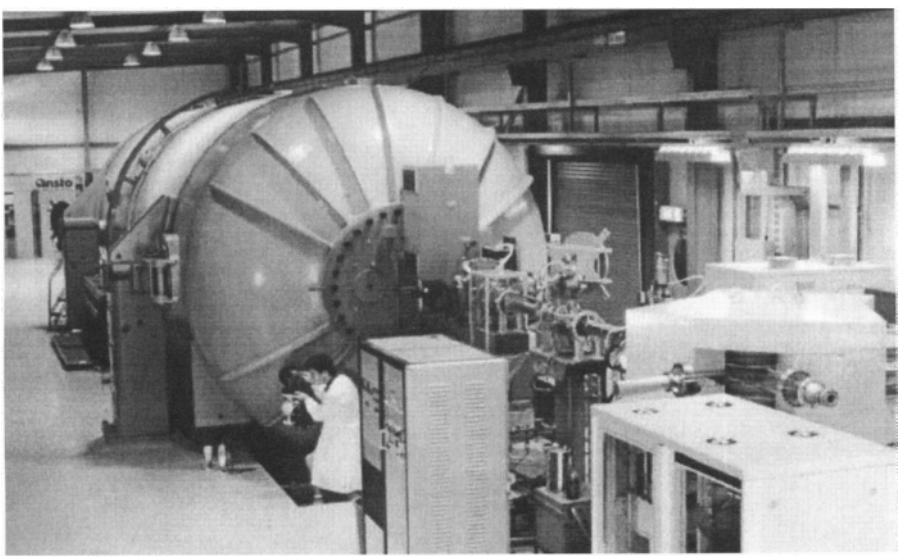

Figure 2. The Tandem Accelerator in use at the ANTARES AMS centre (Australian Nuclear Science and Technology Organisation, Sydney; Tuniz *et al.*, 1995).

3.1. Choice of accelerator

In AMS, the intrinsic analytical properties of ion accelerators are exploited to perform ultra-sensitive isotopic analyses.

Van de Graaff tandem electrostatic accelerators are the optimum choice for a variety of AMS applications. Tandem accelerators working between 0.5 - 3 MV have been specifically designed for ^{14}C analysis (Purser, 1994; Suter, 1999). Large tandem accelerators, originally

developed for nuclear physics research, are also used to analyse a variety of rare radionuclides (Tuniz *et al.*, 1995) with the advantage of allowing higher energies and a more effective separation of isobaric interferences.

Other accelerators, such as cyclotrons, were unsuccessfully used in early attempts to measure long-lived cosmogenic radioisotopes at natural ^{14}C levels. Only recently, an AMS system based on a small cyclotron has been developed to detect ^{14}C at natural abundances (Chen *et al.*, 1999). However, its practical use is limited and further developments will be required to allow precise measurements of isotopic ratios.

3.2. Radiocarbon analysis with tandem Van de Graaff accelerators

A typical AMS set-up is shown in Figure 3. Negative carbon ions are produced in the caesium sputter ion source and, after low-energy mass analysis, are injected into the tandem accelerator. In the case of ^{14}C, isobaric interferences are completely eliminated because ^{14}N does not form stable negative ions. High precision AMS measurements are carried out either by using simultaneous injection or by rapid sequential injection of the isotopes ^{12}C, ^{13}C and ^{14}C. Negative ions are attracted to the positive voltage on the terminal and thereby accelerated to energies between 0.5 - 15 MeV, at which point they pass through a low pressure gas or a thin carbon foil and are stripped of some of their electrons. Multi-charged positive ions are then further accelerated away from the same positive terminal voltage. The stripping process is used to destroy molecular interference which is the main limitation for conventional mass spectrometry. After the acceleration stage, a magnet selects the most probable charge state (typically 3^+ or 4^+, depending on ion energy). Velocity or energy analysers provide additional filtering to remove residual background. Finally, identification of the ^{14}C ions is performed in an ion detector. The isotopic ratio $^{14}C/^{12}C$ (or $^{14}C/^{13}C$) is derived from the ^{14}C counting rate in the detector and the ^{12}C and ^{13}C beam currents measured in Faraday cups. A similar methodology is used to analyse other rare cosmogenic radionuclides, such as ^{10}Be, ^{26}Al, etc.

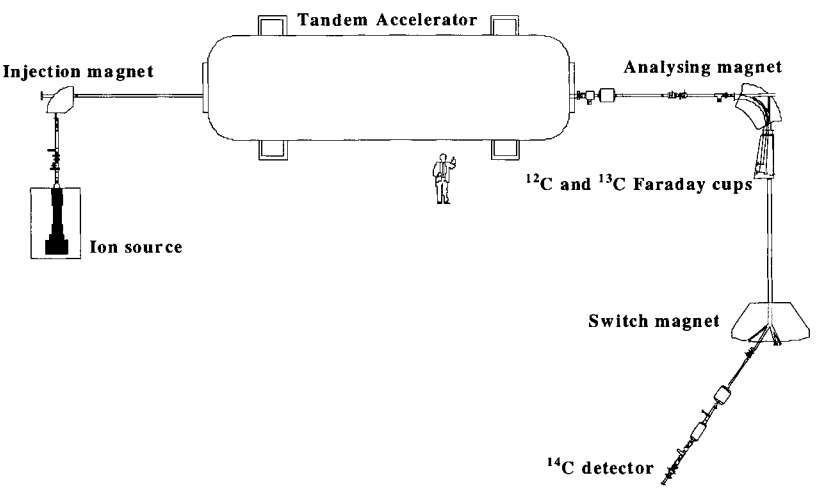

Figure 3. Scheme of the ANTARES AMS facility as used for ^{14}C AMS (Tuniz *et al.*,

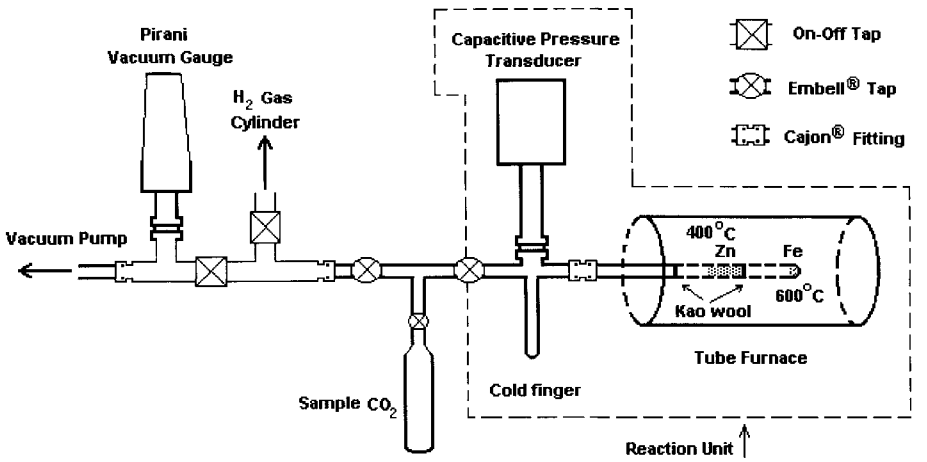

Figure 4. Scheme of the graphitisation line using the Zn/Fe method.

4. SAMPLES FOR AMS ^{14}C ANALYSIS

Organic samples to be analysed by AMS need to be purified and transformed into a graphite target for the ion source. Most samples require treatment to remove extraneous carbon or to extract fractions containing only original carbon compounds. CO_2 is obtained from the purified sample either by combustion or hydrolysis. Finally, CO_2 is reduced to graphite via a catalytic process with Fe or Co in the presence of Zn (see Figure 4) and/or hydrogen (Jull et al., 1986; Jacobsen *et al.*, 1997). CO_2 rather than graphite can be also used, eliminating the need of converting gas to graphite (Bronk-Ramsey and Hedges, 1997). However, only low ion currents are achievable, considerably limiting the analytical throughput.

4.1. What is being dated?

The degree to which AMS dated samples are representative of a specific past event is crucial to the satisfactory interpretation of the results. Some of the archaeological materials that have been studied illustrate the importance of the small sample capability. In particular

1. individual amino acids extracted from bone or blood can sometimes provide a better basis for radiocarbon dating than the use of all organic material;
2. individual seeds can be directly dated instead of using neighbouring pieces of charcoal;
3. tiny pieces of charcoal, extracted from inclusions in ceramics can directly date the object of interest;
4. a small number of foraminifera shells (or pollen grains) of one species can be selected under a microscope and used to date sediment layers with good time resolution

The interpretation of ^{14}C measurements, including the potential for contamination, depends on the molecular species that are extracted and used to date the original sample. The

small sample capability of AMS increases the need for careful study of the material used for dating and provides the means for making detailed assessments of the differences in ^{14}C content of various molecular species present in a sample.

An important example is the radiocarbon dating of bones. Buried bones are easily contaminated by carbonates from the surrounding soil. A simple extraction of the original organic components such as collagen may not be sufficient, as complex molecules, including proteins present in ground-waters and various soluble carbonaceous materials, may also penetrate the bone. To limit this kind of contamination, methods based on the isolation of carbon atoms forming intact peptide bonds in bone proteins have been developed (Nelson, 1991).

A simpler approach is to date all organic carbon whilst avoiding any inorganic components. For example Russ *et al.* (1990) have developed a method for using a low-temperature (100 °C), low-pressure (4 torr) oxygen plasma to selectively oxidise the organic carbon in small samples of pigments from prehistoric rock paintings to CO_2 for AMS dating.

Nelson *et al.* (1986) reported the use of AMS to obtain radiocarbon dates for blood residues on prehistoric stone tools. In one case, involving blood from a snowshoe hare, the ^{14}C date (1010 ± 90 BP) was in good agreement with measurements on charcoal from a closely associated hearth (1060 ± 160 BP). Only 50 μg of carbon, extracted from high molecular weight proteins, was obtained in the second case of human blood from a chert tool and this proved sufficient to obtain a date (2180 ± 160 BP) compatible with expectations.

Another important issue to consider is the biological aging process. The ^{14}C concentration of living tissues is fixed as it is formed. Thereafter the cells and bone carbonate in animals are renewed very slowly by the metabolic processes, while radioactive decay of the fixed ^{14}C is continuously lowering the initial level. The net result is that the ^{14}C content lags the atmosphere by up to a few decades. In the case of growing trees, cells formation happens only in a narrow zone under the bark, so the innermost wood may already be centuries old before the tree dies. In some but not all species, there is a clear ring boundary corresponding to each year. This forms the basis of dendrochronology and explains why wood is so widely employed for radiocarbon calibration studies.

5. PERFORMANCE AND LIMITATIONS OF AMS ^{14}C DATING

The attributes of AMS ^{14}C dating which are most significant for archaeological applications are sample size, datable time span and dating accuracy.

Table 1. Typical sample size required for ^{14}C dating of archaeologically significant materials.

Material	Quantity*	Material	Quantity*
Wood	5	Shell, Carbonates	10
Bone	500	Paper, textiles	5 – 10
Charcoal	3 – 5	Grass, seeds, leaves, grains	5 – 10
Beeswax	1 – 2	Hair, skin	5 – 7
Pollen	1	Teeth, tusk, ivory	500 – 700

* milligrams for AMS, grams for decay counting

5.1. Sample size

Sample sizes required for AMS, as reported in Table 1 for some archaeologically significant carbonaceous materials, are generally 1000 times smaller than those required for decay counting and samples as small as 20 μg carbon can be processed. While the use of small samples greatly extends the applicability of ^{14}C dating, contamination in the field and during chemistry processing may limit both accuracy and datable time span.

5.2. Datable time span

Oxidation and graphitisation processes are responsible for a background equivalent to about 1 μg modern carbon. This sets an equivalent age limit of about 50,000 BP for 1 mg specimens. On the other hand, measurements carried out with geological (*i.e.* ^{14}C-free) unprocessed graphite give results equivalent to an age of 60,000 to 70,000 BP, and accelerator background (with no sample) is equivalent to an age of 80,000 to 90,000 BP. Hence, the datable time span by AMS ^{14}C could, in principle, be extended beyond the present limits. This extension would be very valuable for studying early activities of *Homo sapiens sapiens* in order to corroborate results from other dating techniques such as OSL and U-series dating (for a comparison of the datable time span for different dating techniques see Figure 5). Recent studies suggest that the use of a stepped combustion technique could further reduce the contamination (Bird *et al.*, 1999). Pre-treatment of the glassware by baking it under streaming oxygen also showed a beneficial effect (Lawson *et al.*, 1999).

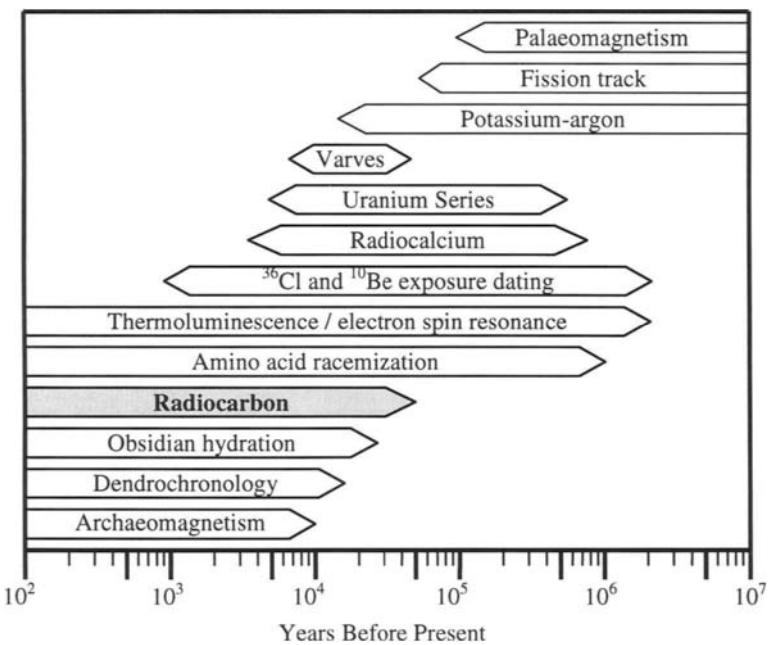

Figure 5. Comparison of the datable time span of different dating techniques.

5.3. Precision and accuracy

The precision of AMS radiocarbon measurements is usually dominated by statistical error. A minimum mass of about 20 μg is necessary to date recent (< 5000 BP) specimens with an error of 1% (~ 80 *a*). With the use of multiple graphite targets obtained from the same material, AMS has demonstrated the capability to provide a precision of 0.2 % (< 20 *a*) for the radiocarbon analysis of modern samples. However, there are a number of systematic effects which must be considered to obtain an accurate age. These effects are briefly discussed in the following.

5.3.1. Contamination

As mentioned above, due to the small mass of material used in AMS measurements, the oxidation and graphitisation processes inevitably lead to contamination by modern CO_2. It is essential to assess the contamination level introduced by each type of procedure by processing a blank material (*eg* coal, graphite, marble etc.). A correction can then be applied (see Figure 6). For contamination of modern origin, the correction is small for recent samples and large for older samples. It ultimately limits the maximum age of the materials which can be dated.

5.3.2. Fractionation

Natural chemical or physical processes can mass fractionate the carbon isotopes during carbon uptake and alter the $^{13}C/^{12}C$ and $^{14}C/^{12}C$ isotopic ratios. Natural mass fractionation is expressed in terms of $\delta^{13}C$ which is a measure (in parts per thousand) of the deviation of the isotope ratio $^{13}C/^{12}C$ from a standard material referred to as PDB, a Cretaceous belemnite, *Belemnitella americana*, from the Pee Dee formation of South Carolina (Olsson, 1970). Typical $\delta^{13}C$ values for environmental materials can vary between +2 permil (eg marine

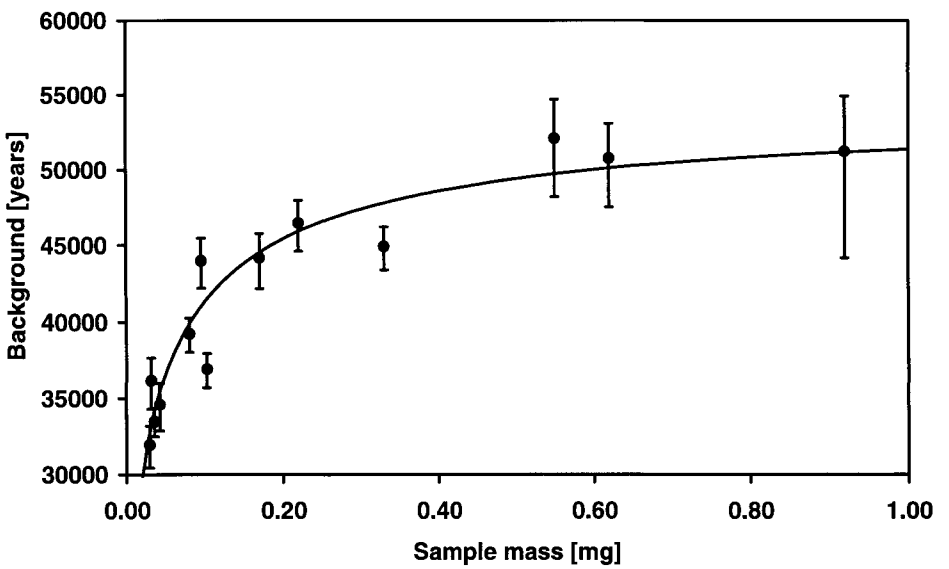

Figure 6. A typical background corresponding to the contamination introduced by the chemical procedures.

carbonate) to -27 permil (eg some kinds of wood). This effect is significant and must be taken into account to obtain accurate ages. The $\delta^{13}C$ value for a material to be radiocarbon dated must be known to correct for the fractionation affecting the ^{14}C isotopic ratio. Additional fractionation may be introduced by chemistry processing of AMS samples (*eg* incomplete graphitisation) and during AMS analysis (*eg* ion sputtering and stripping processes). In general, these effects are corrected by processing and measuring standard materials of known isotopic ratio such as the oxalic acid HOxI (Stuiver, 1983).

5.3.3. Reservoir effects

Organic specimens drawing carbon from reservoirs other than the atmosphere may yield incorrect ages. In the case of marine shells deriving their carbon from seawater, a system not in equilibrium with the atmosphere, the reservoir effect leads to age differences of up to 1000 years (Stuiver *et al.*, 1998b). This difference can be reflected in bones of animals or humans consuming fish. High apparent ages can be found in plants near volcanoes erupting ^{14}C-depleted CO_2. Other small age shifts arise from differences in atmospheric mixing between northern and southern hemispheres, and regional air-sea exchange of CO_2.

5.3.4. Variation in ^{14}C production rate (calibration)

Conventional radiocarbon ages are reported in years before present (BP), where present is 1950 AD, and are calculated using the "Libby" half-life of 5568 years on the assumption that the production of ^{14}C in the past has been constant (Donahue *et al.*, 1990). The difference between conventional radiocarbon ages and calendar ages (*calibrated* ages) has been determined with high precision for all of the Holocene by radiocarbon measurements on tree ring samples (see Figure 7; Stuiver *et al.*, 1998a), which are independently and precisely dated by dendrochronology. Part of this difference derives from the use of the conventional

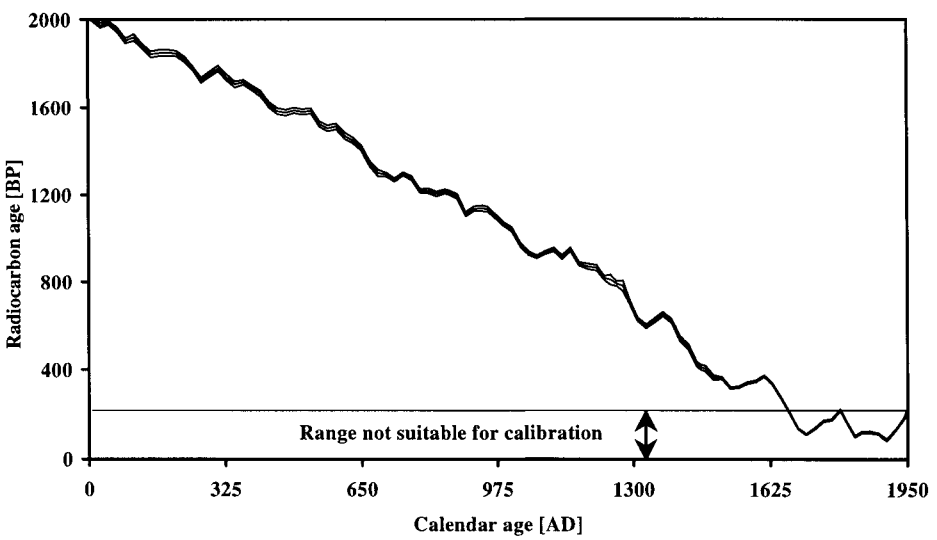

Figure 7. The calibration curve for the last two millennia (Stuiver *et al.*, 1998a).

half-life, which is known to be 3% too small. The remaining difference derives from secular variations of ^{14}C production rate in the atmosphere due to geo- and helio-magnetic effects and global variations in the parameters of the carbon cycle. In the range 1650 – 1950 AD calibrated ages are ambiguous due to fluctuations in atmospheric ^{14}C concentration. Samples with conventional radiocarbon ages of 200 years or less are often reported as 'modern' (Stuiver and Polach, 1977). A radiocarbon calibration for the late Pleistocene has been obtained by comparing radiocarbon results to ages obtained by Uranium/Thorium (Bard *et al.*, 1998) and varve (lacustrine annual sedimentary layers) chronology (Kitagawa and van der Plicht, 1998; Hughen *et al.*, 1998). Radiocarbon ages are younger than calendar ages during the late Pleistocene, with a difference of 1000-2000 years between 15,000 and 10,000 BP.

6. THE *IN SITU* METHOD

Long-lived radioisotopes such as ^{14}C, ^{10}Be (1.50 Ma half-life), ^{26}Al (720 ka), ^{36}Cl (310 ka) and ^{41}Ca (103 ka) are produced *in situ* in the shallow horizons of the Earth by interaction of secondary cosmic rays (mainly neutrons and muons) with suitable target nuclides in rocks and soil. Typical production rates at sea level and high latitudes are discussed in Tuniz *et al.* (1998). AMS is used to determine the radioisotope concentration and subsequently estimate the exposure age of the rock surface. The in-situ method works best on the time period from 5 ka to 5 Ma. The lower limit is set by the sensitivity of AMS. In principle, this method could be used to set an upper limit to the age of rock carvings or paintings. However, the practical limits are determined by the strong dependence on geographic location (latitude and altitude), on shielding conditions and on erosion rates. The analysis of the depth profile of a radionuclide or the measurement of the concentration of two radionuclides with different half lives can be used to determine erosion rate, exposure age and history of a surface.

One of the first archaeological applications of the *in situ* method was the determination of a limit age of the petroglyphs found in the Côa Valley in Portugal (Phillips *et al.*, 1997). ^{36}Cl exposure ages showed that the rock panels were available for engraving during the Palaeolithic, supporting the Palaeolithic origin inferred by the archaeologists (Zilhão, 1995). The *in situ* method was also applied to the dating of the Tabun Cave, Mt. Carmel in Israel (Boaretto *et al.*, 1999). The sediments in the cave are of aeolian origin and are rich in quartz. To study the burial history, ^{26}Al and ^{10}Be concentrations were measured in sediment samples and flint tools.

7. AMS ^{14}C DATING IN PREHISTORY

Radiocarbon dates are the main source of the time perspective in prehistory. Although AMS ^{14}C dating cannot access the earliest human developments occurring at the order of 100,000 BP and beyond, it can reach a highly significant era in human prehistory. It was during the last 50,000 years that *Homo sapiens sapiens*, or modern humans, colonised large habitable parts of our planet. In the following we briefly discuss the contribution of AMS ^{14}C dating to the construction of a chronology for the spread of modern humans, including the

early manifestations of civilisation, *viz.* the capacity of representing and interpreting the reality through rock pictographs.

7.1. Early human migrations

When *Homo sapiens sapiens* colonised America, Europe and Australia is a matter for controversy at present.

The study of human bones in North American sites originally provided a wide range of dates from less than 20,000 BP up to 70,000 BP, with many of these results obtained by amino-acid racemisation and ^{14}C decay counting. It must be noted that radiocarbon dating of ancient bones is unreliable unless specific amino acids are extracted. AMS dating of such minute components extracted from the same bones gave results around 11,000 BP at the oldest (Taylor, 1987). This strengthened the common view that the north American continent was populated not much before the Holocene period, when an ice-free land corridor was opened across the Bering Strait at the end of the last ice age. More work is needed to support these theories as the validity of AMS ^{14}C dates on poorly preserved fossil bones remains questioned (Stafford *et al.*, 1990). In recent years, the debate has been re-opened and many archaeologists now accept the date 12,500 BP for the far southern site of Monte Verde in Chile (Adovasio and Pedler, 1997).

Palaeoanthropologists are interested in the origins of *Homo sapiens sapiens* in Europe and its relation to the hominids of Neanderthal type. AMS has been used to date bones from the Upper Pleistocene to reconstruct the human evolution in this part of the world (Stringer, 1986). The Mousterian - Aurignacian boundary has been dated at about 37,000 BP in Spain (Bischoff *et al.*, 1994) by AMS ^{14}C analysis of charcoal fragments. These dates are at the fringes of the radiocarbon method but they have been confirmed by U-series dating on the enclosing carbonate. The latter method yields a date of about 43,000 BP, a difference which may be partly explained by ^{14}C production variations due to geomagnetic field fluctuations and climatic changes. The evolutionary fate of the Neanderthals and the spread *of Homo sapiens sapiens* has been recently reviewed by Pettitt *et al.* (1999).

Concerning the first colonisation of Australia, many archaeologists agree on the idea that the first humans entered via the north of the continent, Cape York, Arnhem Land or the Kimberley. Much less agreement exists on the time frame of this colonisation. Until recently, the most ancient radiocarbon dates for the human presence in Australia corresponded to less than 40,000 BP, as shown by AMS dates from the Kimberley region (O'Connor, 1995) and from Chillagoe in the Cape York peninsula (David *et al.*, 1997). On the other hand, optically stimulated luminescence yields dates corresponding to 50,000-60,000 BP for sites in the Northern Territory (Roberts *et al.*, 1994). In addition, ESR and U-series dating investigations on the Lake Mungo 3 human skeleton yielded a date of 62,000 ± 6000 BP, in good agreement with OSL age estimates on the sediments into which the skeleton was buried (61,000 ± 2000 BP) (Thorne *et al.*, 1999). This is arguably the earliest known human presence in Australia. The difference between the dates inferred by radiocarbon and other dating methods for the earliest presence of humans in Australia is too large and it cannot be explained by astrophysical or environmental effects on ^{14}C concentration in the atmosphere during the late Pleistocene. Various theories have been advanced to explain this discrepancy, including the hypothesis that Australia was colonised in two or more separate human migrations (Allen and Holdaway, 1995). The association between rising seas in the Austral region, around 60,000,

80,000 and 100,000 years ago, and human occupation of the Australian continent, have also been considered (Chappell, 1993). Recent ^{14}C AMS dates show that the Devil's Lair site in South Western Australia was occupied by aboriginal people 48-49 ka BP, supporting the hypothesis of an early human colonisation of Australia (Turney *et al.*, 2000).

7.2. Prehistoric rock art

Dating rock art is essential to building archaeological models describing the evolution of prehistoric civilisation. The antiquity of European cave paintings was qualitatively established since last century. Relative chronologies were developed using stylistic criteria and the status of the pigments or the presence of Figures, such as extinct fauna, of known antiquity. Some indirect chronological information was then obtained by radiocarbon dating of human occupation remains found near the paintings. However, the real test was to date actual pigments or, better still, organic components of pigments which are likely to have derived from the painters or other contemporary carbon. However, location and extraction of material that has not been contaminated since its original application, which carries a radiocarbon signature unique to that moment, and which has not become part of a complex sequence of updates or overpainting is an enormous challenge. Only recently, direct dating of the charcoal used for the drawings was possible thanks to the sensitivity of AMS ^{14}C dating.

Dates in the range 12,900 - 14,000 BP (Valladas *et al.*, 1992) were obtained for pictures of bison in the Spanish caves of Altamira and El Castillo and in the French Pyrenean cave of Niaux. On the other hand, remains of human occupation in the same caves range approximately from 5,000 to 18,000 BP.

Some very sophisticated Palaeolithic paintings were discovered in 1994 in the Ardèche Valley in France (Chauvet-Pont d'Arc cave). Between 300 and 400 animals are depicted with advanced techniques (including the use of perspective), such as rhinoceros, lions, mammoths, horses and bison. AMS radiocarbon dating using microscopic samples of charcoal from the paintings yield a consistent age of about 31,000 BP for several of these animals (Clottes *et al.*, 1995). Pieces of charcoal found on the ground in the cave yield dates of 22,000 - 29,000 BP, suggesting human incursions for extended periods of time. The radiocarbon dates obtained are the oldest found for prehistoric rock art and confirm that *Homo sapiens sapiens* created elaborate forms of art long before the Upper Palaeolithic.

7.2.1. Australian rock art

The Australian program in AMS dating of rock art includes research into the probable age of the rock art of Chillagoe and Laura (North Queensland), the Kimberley (Western Australia) and Olary District (South Australia). A variety of materials is being analysed, including pigments, oxalate minerals, silica coatings, plant fibres, carbonised plant matter, fatty acids, beeswax and mud-wasp nests. Different sample processing techniques are being explored, including low-pressure plasma techniques and laser extraction methods. Laser-induced combustion and AMS have been used to date single laminae in 2 mm thick rock surface accretions, a very useful method to study prehistoric paintings and engravings (Campbell *et al.*, 1996). AMS dating on charcoal drawings from Chillagoe yield ages of less than 1000 years, supporting the hypothesis of population increase and intensified use of this region during the late Holocene (David *et al.*, 1999).

7.2.1.1. Bradshaw rock art

The Bradshaws are Australian Aboriginal rock paintings with a unique style characterised by elegant and graceful Figures with many ornaments and accoutrements. An example is shown in Figure 8. Paintings of this style are found in the Kimberley region in the north west of the state of Western Australia. The paint colour is usually a light mauve or mulberry. These Figures were first reported by early explorer Joseph Bradshaw who, accompanied by his brother, surveyed this region in 1891. The paintings are so unusual and distinctive that there has been much speculation and debate concerning their origins and meanings. Some researchers have gone as far as to suggest origins other than the ancestors of modern indigenous Australians.

Despite the considerable interest no scientific attempts to date the paintings were made until 1997, primarily because of the difficulties inherent in dating rock paintings. The ANTARES AMS team was involved in two separate investigations. Watchman *et al.* (1997) dated carbon-bearing material scraped from on or near paintings. The conclusion was that the Bradshaw paintings are at least 4,000 years old.

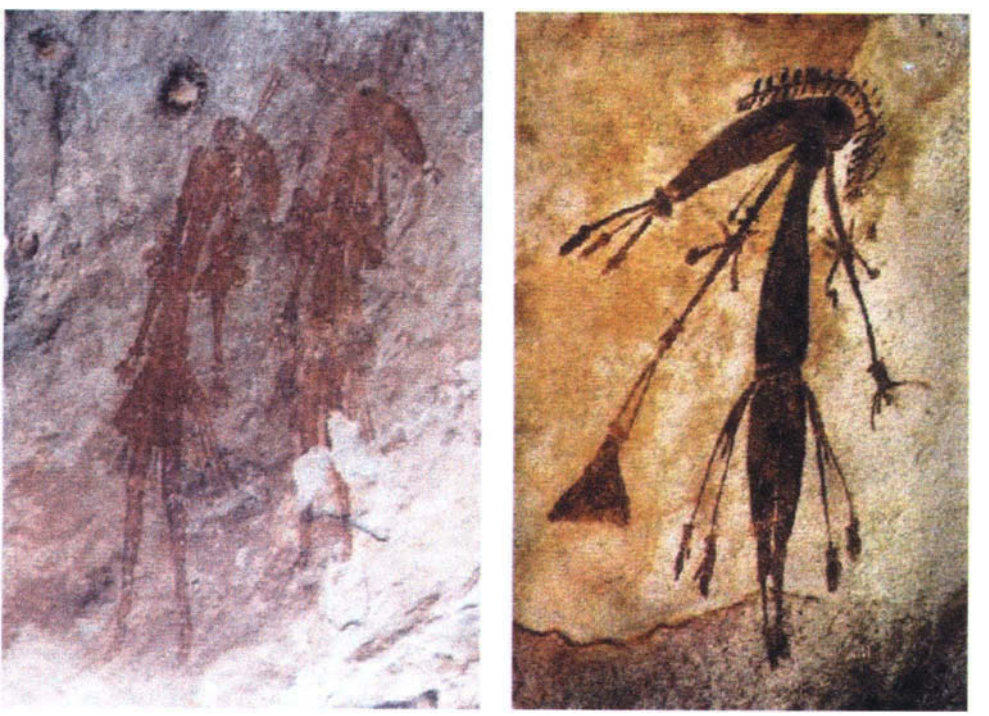

Figure 8. Computer enhanced "Tassel" Bradshaw Figures showing their ornate form of dress with rear triple tassels, bangles, elbow bands, cummerbund waistbands with pubic aprons and complicated head-dresses. A mud-wasp nest can be seen on the rock face just above the left hand Figure. Photo: courtesy of Graham Walsh, Takarakka Rock Art Research Centre.

These dates are somewhat at odds with the findings of the second investigation in which Roberts *et al.*, (1997) made use of the nests of mud-wasps to provide a limit for the age of a Bradshaw painting. Two measurement techniques were involved in this investigation – radiocarbon AMS and OSL. The investigators found a minimum age of 17,000 BP. So the origins of the Bradshaw paintings are still unknown and further (perhaps many) measurements to establish their ages will be required.

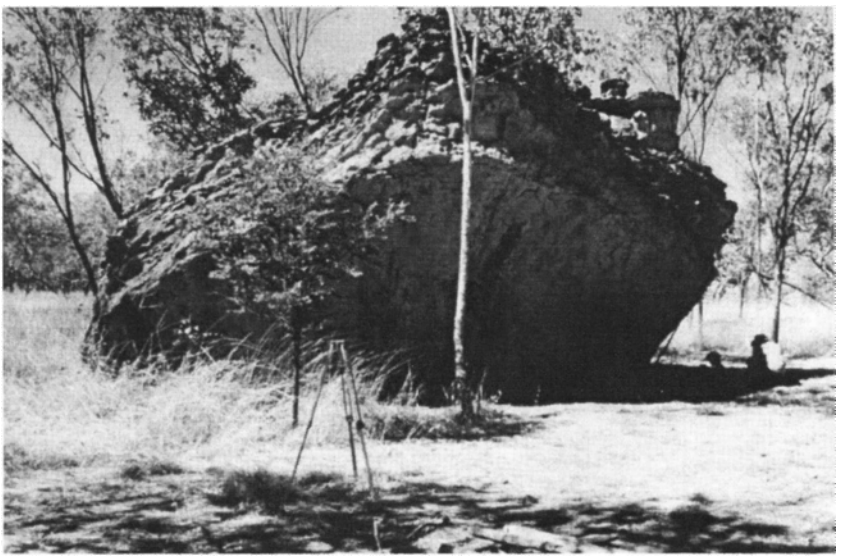

Fig. 9. The Jinmium rock shelter. Photo: courtesy of Richard Roberts, La Trobe University.

7.2.1.2. Jinmium

The Jinmium rock shelter is located in the northern region of Australia under a tilted block of sandstone (see Figure 9). Circular engravings (pecked cupules) have been carved by the early inhabitants of this remote area. Thermoluminescent dating provided ages of 50,000 – 70,000 BP for the quartz sand associated with the buried engravings. Dates between 116,000 and 176,000 BP were provided by TL for the quartz sands of the artefact bearing sedimentary deposits near the rock shelter (Fullagar *et al.*,1996).

These results were subsequently contradicted using other dating techniques. Optically Stimulated Luminescence (OSL) applied to single sand grains indicated that the Jinmium deposits are younger than 10,000 BP. AMS ^{14}C dating of the carbon fragments in the deposits provided similarly young ages (Roberts *et al.*, 1998).

7.3. The ice man

The mummy of a human body (see Figure 10) was discovered in September 1991 in a glacier, at 3210 m on the Ötzal Alps, Alto Adige Region, Italy. The find is now displayed at the South Tyrol Museum of Archeology (Bozen, Italy) and includes shoes, clothes, a copper axe and a quiver of arrows. AMS was used to date a variety of samples from this find, including grass from the shoes and tissue specimens from the body. Results obtained at a number of laboratories concord on a radiocarbon age of 4546 ± 17 BP (Prinoth-Fornwagner and Niklaus, 1994), corresponding to a calendar age between 3100 and 3350 BC. This result and the style of the artefacts found with the body support the hypothesis that the Ice Man belonged to the Remedello culture present in the northern part of the Italian peninsula during this period.

Figure 10. The mummified corpse discovered in 1991. (photo: Marco Samadelli; © South Tyrol Museum of Archaeology, Bozen, Italy)

8. AMS IN HISTORY AND ART

8.1. The Shroud of Turin

The shroud of Turin (Figure 1), held in a church in Turin (Italy), is an object of devotion for many Catholics. The image of a crucified man appears on the textile, considered by the believers to be the burial cloth of Jesus Christ. In 1988, a 10 mm by 70 mm strip of linen was cut, divided in three postage stamp-size samples and distributed to the AMS laboratories in Zurich, Oxford and the University of Arizona in Tucson. The results from the three laboratories agreed on a medieval date, 1290 – 1360 AD, at 90% confidence (Damon *et al.*, 1989). This is close to 1353, the first appearance of the Shroud in historical records. The possibility that the AMS ^{14}C date does not reflect the true age of the Shroud is still being debated. A number of causes, including the 1500s fire and the effect of bacteria and microorganisms, have been considered to explain the younger age. The historical details on the AMS dating of the Shroud of Turin have been given by Gove (1996).

8.2. The Dead Sea Scrolls

The Dead Sea Scrolls are a collection of 1200 parchment and papyrus manuscripts found in 1947 in cave locations close to the Dead Sea. It is believed that they have been written by the Essenes, a religious group belonging to Judaism who lived in the Quman site until the occupation by the Romans in 68 AD. Several manuscripts were dated by means of the ^{14}C AMS technique (Bonani *et al.*, 1992; Jull *et al.*, 1995). The measured ages were in good agreement with the dates on the manuscripts (when present) and/or the ages derived by means of palaeographic estimates.

8.3. The Venafro chessmen

The Venafro chessmen, discovered in 1932 in the southern Italian necropolis of Venafro, are among the most controversial chess-related archaeological finds of this century. For more than 60 years, archaeologists have formulated a variety of hypotheses to explain how bone chess pieces of Arabic shape were discovered in a tomb of Roman age. Some scholars claimed that the chessmen were indeed of Roman origin. The chess pieces are preserved in the Archaeological museum of Naples, where a bone fragment of 2 grams was collected for AMS analysis. Radiocarbon measurements carried out at the ANTARES AMS Centre yielded a calibrated age of 885-1017 AD (68 % confidence level) (Terrasi *et al.*, 1994), supporting the view that this game was introduced to Central Italy during the Saracen invasions of the 10th century AD.

8.4. Charlemagne's crown

The Iron Crown (see Figure 11) of the first Holy Roman Emperor, Charlemagne, is held in the Cathedral at Monza, near Milan in Italy. The origin and age of the crown, later used to crown Napoleon Bonaparte, are uncertain. Historical records place its origin between the Roman and Middle Ages, a spread of several centuries. In 1996, it was discovered that the precious stones were held in place by a mixture of clay and beeswax, which provided enough carbon for AMS radiocarbon dating. The analysis performed at ANTARES yielded an age between 700 and 780 AD (Milazzo *et al.*, 1997), consistent with the historical date for the crowning of Charlemagne, 800 AD, on Christmas Night.

8.5. Donatello's glue

The Annunciazione Cavalcanti (Cathedral of Santa Croce, Florence) is one of the best known creations of the Italian sculptor Donatello (1386-1466 AD). The sculpture is decorated with a group of terra-cotta cherubs. The base of one of these Figures has large cracks that had been subsequently repaired with a resin glue. It is not known when the accident occurred. The ANSTO results for the glue, 1331-1429 AD (68 % confidence level), proved that the restoration had been performed during the lifetime of the artist. The breakage and repair may therefore have happened when the work of art was created. Italian scholars believe that the cherub cracked because it was not hollowed out before firing and that the repair was carried out by Donatello himself, after damaging the statue in the kiln.

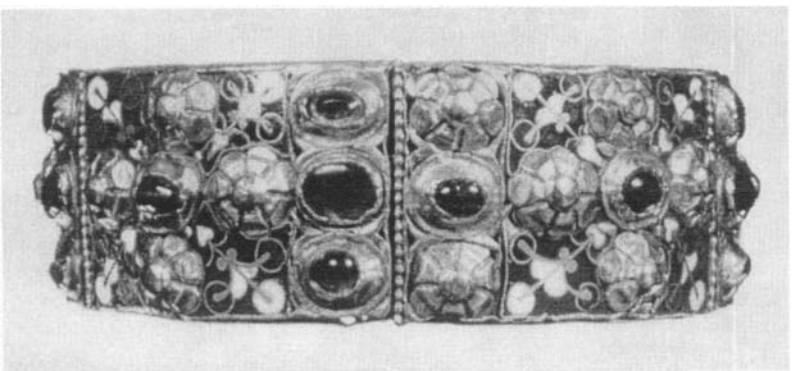

Figure 11. Charlemange's Crown.

8.6. The conquest of Peru

The manuscripts "*Historia et Rudimenta Linguae Piruanorum*" and "*Exsul Immeritus Blas Valera populo suo*", which were found in the family papers of Neapolitan historian Clara Miccinelli, are commonly known as the "Miccinelli documents". They discuss events and people associated with the Spanish conquest of Peru (see Figure 12).

As well as containing details about reading literary *quipus* (documents which were written using a combination of textile ideograms and knots) "*Historia et Rudimenta Linguae Piruanorum*" (History and Rudiments of the Language of the Peruvians; Laurencich Minelli *et al.*, 1995) makes the incredible claims that Pizarro conquered the region after having Inca generals poisoned with arsenic-tainted wine and then condemned the Inca emperor, Atahuallpa, to death instead of granting him an audience with the King of Spain. The account departs markedly from the long-held version of the event - that Atahuallpa was put to death for ordering the execution of his brother and rival. Furthermore, the manuscript suggests that the chronicler Guamán Poma de Ayala (1538?-1620?), author of one of the most important works on Inca Peru, the "*Nueva*

Corónica y Buen Gobierno" (New Chronicle and Good Government) written sometimes before 1618, merely lent his name to a work actually written by the Jesuit priest Blas Valera.

Fig. 12. Pizarro on his way to Peru, as portrayed in one of the scenes of a painted panorama in the frieze of the Rotunda of the U.S. Capitol Building (Washington DC).

Valera is also believed to be the author of the manuscript "*Exsul Immeritus Blas Valera populo suo*", an account of his own actions. According to this document dated May 10, 1618, Valera was forced to fake his own death in 1597 and, under a false name, was able to live in Peru between 1599 and 1618 and write the "*Nueva Corónica y Buen Gobierno*". Attached to "*Exsul Immeritus Blas Valera populo suo*" there were:

1. a letter from Francisco de Chaves (Laurencich Minelli *et al.*, 1998), a *conquistador* and chronicler on Pizarro's expedition; (the letter, dated August 5, 1533, was addressed to Charles V, King of Spain, and is the source of the accusations already suggested in "*Historia et Rudimenta Linguae Piruanorum*" and "*Exsul Immeritus Blas Valera populo suo*");
2. a wax box containing a fragment of a letter from Columbus and the contract between Guamán Poma de Ayala and Blas Valera; (under the agreement, Ayala lent his name to Valera after payment of a horse and a chariot);
3. a few literary *quipus*.

The historical significance of the discovered material is immense and historians considered it to be of primary importance to verify the authenticity. As a part of a worldwide research collaboration ANSTO performed the radiocarbon dating of five samples associated with the Miccinelli documents (Zoppi *et al.*, 1999). The results showed that, with a high degree of confidence, the wax used to seal the letter to the King of Spain originated earlier than 1533 (see Figure 13), the date on the letter. Similarly, the wax used for the box containing the

agreement allowing Valera to write "*Nueva Corónica y Buen Gobierno*" under a false name, most probably originated before 1618, the accepted completion date of this document.

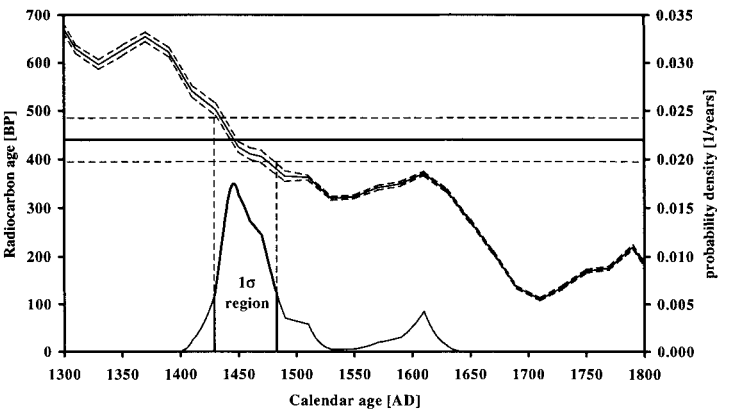

Fig. 13. The calibration of the wax sample from the seal of the letter to the King of Spain.

9. DATING WITH THE BOMB PULSE

Atmospheric nuclear weapons tests during the 1950s and early 1960s produced a rapid increase in ^{14}C. In the northern hemisphere, the 1963-1964 ^{14}C concentration reached a level nearly 100% higher than the pre-bomb level (see Figure 14). Since the Nuclear Test Ban Treaty came into effect in 1963, the atmospheric ^{14}C concentration has been decreasing due to exchange with the biosphere and the oceans (with minor perturbations due to sporadic nuclear tests). Presently, the ^{14}C level has declined to about 110 percent of the pre-bomb level. The shape and intensity of this *bomb pulse* has been determined by measuring ^{14}C in atmospheric CO_2 (Levin *et al.*, 1994; Manning and Melhuish, 1994) tree rings (Hua *et al.*, 1999a&b) and ice cores (Levchenko *et al.*, 1997). The decrease of atmospheric ^{14}C is presently about 80 times faster than radioactive decay.

This well determined temporal change of ^{14}C provides a clock for dating biological materials formed since 1955 AD, and leads to interest in forensic applications. For example, it was shown that it is possible to determine the time of death of humans by using the lipid fraction of bones, which is the most suitable component for dating purposes, thanks to its fast turnover (Wild *et al.*, 1998).

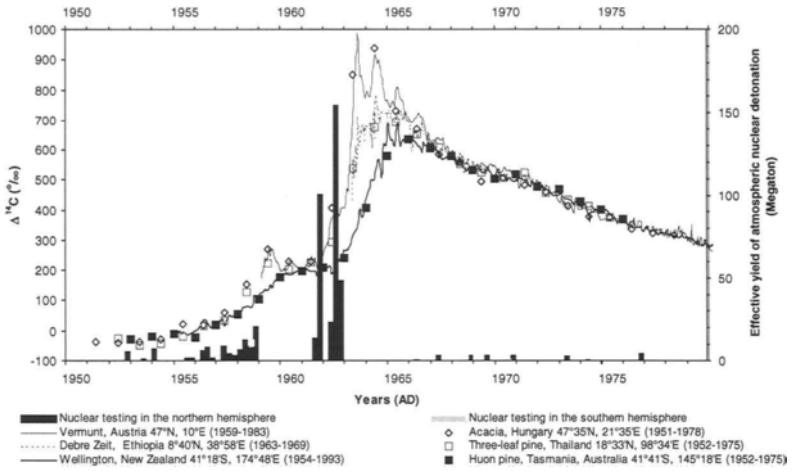

Fig. 14. ^{14}C in tree rings (points) vs atmospheric radiocarbon records (lines) at similar latitudes. Bars represent the magnitude of atmospheric nuclear detonation for 3 month periods. For a review of radiocarbon data from atmospheric and tree-ring samples for the period 1945-1997 AD see Hua *et al.* (1999a&b).

10. CONCLUSIONS

AMS ^{14}C dating is having a tremendous impact on studies in prehistory thanks to a 1000-fold reduction in sample size. Accurate dating is possible by extracting only the most reliable fraction or by minimising sample contamination. Presently, the age limit is around 45,000 - 50,000 BP, with potential for an extension to 60,000 BP. AMS ^{14}C can play an important role in the verification of other dating techniques, such as optically stimulated luminescence and U-series dating, which allow a further extension of the datable time span. Alternative AMS radionuclides with longer half-lives have been considered for archaeological dating but ^{14}C remains a unique chronometer to reconstruct the sequence of prehistoric events.

AKNOWLEDGMENTS

We thank Ewan Lawson, Quan Hua and Cheryl Jones for suggestions and many valuable discussions.

REFERENCES

Adovasio J.M. and Pedler, D.R. (1997) Monte Verde and the antiquity of humankind in the Americas, Antiquity 71, 573-580.

Allen J. and Holdaway S. (1995) The contamination of Pleistocene radiocarbon determinations in Australia, Antiquity 69, 101-112.

Arnold J.R. and Libby W.F. (1949) Age determinations by radiocarbon content: checks with samples of known age, Science 110, 678-680.

Bard E., Arnold M., Hamelin B., Tisnerat-Laborde N. and Cabioch G. (1998) Radiocarbon Calibration by Means of Mass Spectrometric $^{230}Th/^{234}U$ and ^{14}C ages of Corals: An Updated Database Including Samples from Barbados, Mururoa and Tahiti, Radiocarbon 40 (3), 1085-1092.

Bennett C.L., Beukens R.P., Clover M.R., Gove H.E., Lievert R.B., Litherland A.E., Purser K.H. and Sondheim W.E. (1977) Radiocarbon dating using accelerators; negative ions provide the key, Science 198, 508-509.

Bird M.I., Ayliffe L.K., Fifield L.K., Turney C.S.M., Cresswell R.G., Barrows T.T. and David B. (1999) Radiocarbon dating of "old" charcoal using a wet oxidation, stepped-combustion procedure, Radiocarbon 41(2), 127-140.

Bischoff J.L., Ludwig K., Garcia J.F., Carbonell E., Vaquero M., Stafford T.W., Jull A.J.T. (1994) Dating of the Basal Aurignacian sandwich at Abric Romani (Catalunya, Spain) by Radiocarbon and Uranium-series, Journal of Archaeological Science 21, 541-551.

Boaretto E., Berkovits D., Hass M., Hui S.K., Kaufman A., Paul M. and Weiner S. (1999) Dating of prehistoric cave sediments and flints using ^{10}Be and ^{26}Al in quartz from Tabun Cave, Israel, in: Conference Compendium of the 8th International Conference on Accelerator Mass Spectrometry, 6-10 September 1999, Vienna, p. 176, to be published in Nuclear Instruments and Methods in Physics Research B.

Bonani G., Ivy S., Wölfli W., Broshi M., Carmi I. and Strugnell J. (1992) Radiocarbon Dating of Fourteen Dead Sea Scrolls, Radiocarbon 34 (3), 843-849.

Bronk-Ramsey C. and Hedges R.E.M. (1997), Hybrid ion sources: radiocarbon measurements from microgram to milligram, Nuclear Instruments and Methods in Physics Research B 123, 539-545.

Campbell J., Cole N., Hatte E., Tuniz C. and Watchman A, (1996) Dating of rock surface accretions with Aboriginal paintings and engravings in North Queensland, Tempus 6, 231-239.

Chappell, J. (1993) Late Pleistocene coasts and human migrations in the Austral region, Department of Prehistory, Research School of Pacific Studies, The Australian National University, Occasional Papers in Prehistory 21, 43-48.

Chen M., Lu X., Li D., Liu Y. and Zhou W. (1999) Mini-cyclotron based accelerator mass spectrometry and real ^{14}C measurements, in: Conference Compendium of the 8th International Conference on Accelerator Mass Spectrometry, 6-10 September 1999, Vienna, p. 64, to be published in Nuclear Instruments and Methods in Physics Research B.

Clottes J., Chauvet J.M., Brunel-Deschamps E., Hillaire C., Daugas J.-P., Arnold M., Cachier H., Evin J., Fortin P., Oberlin C., Tisnerat N. and Valladas H. (1995) The Palaeolithic paintings of the Chauvet-Pont-D'Arc cave, at Vallon-Pont D'Arc (Ardèche, France): direct and indirect radiocarbon dating, C.R. Acad. Sci. Paris 320, 1133-1140.

Damon P.E., Donahue D.J., Gore B.H., Hatheway A.L., Jull A.J.T., Linick T.W., Sercel P.J., Toolin L.J., Bronk C.R., Hall E.T., Hedges R.E.M., Housley R., Law I.A., Perry C., Bonani G., Trumbore S., Wölfli W., Ambers J.C., Bowman S.G.E., Leese M.N. and Tite M.S. (1989) Radiocarbon dating of the Shroud of Turin, Nature 337, 611-615.

David B., Roberts R., Tuniz C., Jones R. and Head J. (1997). New optical and radiocarbon dates from Ngarrabulgan Cave, a Pleistocene archaeological site in Australia: implications for the comparability of time clocks and for the human colonisation of Australia, Antiquity 71, 183.

David B., Tuniz C., Lawson E.M., Hua Q., Jacobsen G.E., Head J. and Rowe M. (1999) New AMS determinations for Chillagoe rock art, Australia, and their implications for Northern Australian prehistory, in: D. Seglie (ed.), NEWS95 - International Rock Art Congress, Proceedings CD ROM, Centro Studi e Museo d'Arte Preistorica, Pinerolo (Italy).

Donahue D.J., Linick T.W. and Jull A.J.T. (1990) Isotope-ratio and background corrections for accelerator mass spectrometry radiocarbon measurements, Radiocarbon 32 (2), 135-142.

Fifield L.K. (1999) Accelerator mass spectrometry and its applications, Rep. Prog. Phys 62, 1223-1274.

Fullagar R.L.K., Price D.M. and Head L.M. (1996) Early human occupation of northern Australia: archaeology and thermoluminescence dating of Jinmium rock-shelter, Northern Territory, Antiquity 70, 751-773.

Gove H.E., (1996) Relic, Icon or Hoax: Carbon Dating the Turin Shroud, Institute of Physics Publishing, London.

Hua Q., Barbetti M., Worbes M., Head J. and Levchenko V.A. (1999a) Review of radiocarbon data from atmospheric and tree-ring samples for the period 1945-1997 AD, IAWA Journal 20 (3), 261-283.

Hua Q., Barbetti M., Jacobsen G.E., Zoppi U and Lawson E.M. (1999b) Radiocarbon in annual tree rings from Thailand and Tasmania for the period AD 1952-1975, in: Conference Compendium of the 8th International Conference on Accelerator Mass Spectrometry, 6-10 September 1999, Vienna, p. 90, to be published in Nuclear Instruments and Methods in Physics Research B.

Hughen K.A., Overpeck J.T., Lehman S.J., Kashgarian M., Southon J.R. and Peterson L.C. (1998) A new 14C calibration data set for the last deglaciation based on marine varves, Radiocarbon 40 (1), 483-494.

Jacobsen G.E., Hua Q., Tarshishi J., Fink D., Hotchkis M.A.C., Lawson E.M., Smith A.M. and Tuniz C. (1997) AMS radiocarbon analysis of microsamples, in: Handbook of The Sixth Australian Archaeometry Conference, 10-13 Februrary 1997, Sydney, Australia, p. 36.

Jull A.J.T., Donahue D.J., Hatheway A.L., Linick T.W. and Toolin L.J. (1986) Production of Graphite Targets by Deposition from CO/H_2 for Precision Accelerator ^{14}C Measurements, Radiocarbon 28 (2A), 191-197.

Jull A.J.T., Donahue D.J., Broshi M. and Tov E. (1995) Radiocarbon Dating of Scrolls and Linen Fragments from the Judean Desert, Radiocarbon 37 (1), 11-20.

Kitagawa H. and van der Plicht J. (1998) Atmospheric Radiocarbon Calibration to 45,000 yr B.P.: Late Glacial Fluctuations and Cosmogenic Isotope Production, Science 279, 1187-1191.

Laurencich Minelli L., Miccinelli C. and Animato C. (1995) Il documento seicentesco "Historia et Rudimenta Linguae Piruanorum", Studi e Materiali di Storia delle Religioni 61, 363-413.

Laurencich Minelli L., Miccinelli C., Animato C. (1998) Lettera di Francisco de Chaves alla Sacra Cesarea Maestà: un inedito del sec. XVI., Studi e Materiali di Storia delle Religioni 64, 57-91.

Lawson E.M., Elliott G., Fallon J., Fink D., Hotchkis M.A.C., Hua Q., Jacobsen G.E, Lee P., Smith A.M., Tuniz C., Tyler P., Williams A. and Zoppi U. (1999) AMS at ANTARES – the first 10 years, in: Conference Compendium of the 8th International Conference on Accelerator Mass Spectrometry, 6-10 September 1999, Vienna, p. 49, to be published in Nuclear Instruments and Methods in Physics Research B.

Levchenko V.A., Etheridge D.M., Francey R.J., Trudinger C., Tuniz C., Lawson E.M., Smith A.M., Jacobsen G.E., Hua Q., Hotchkis M.A.C., Fink D., Morgan V. and Head J. (1997) Measurement of the $^{14}CO_2$ bomb pulse in firn and ice at Law Dome, Antarctica, Nuclear Instruments and Methods in Physics Research B 123, 290-295.

Levin I., Kromer B., Schoch-Fischer H., Bruns M., Munich M., Berdau D., Vogel J.C. and Munich K.O. (1994) $\Delta^{14}CO_2$ records from two sites in Central Europe, in: Boden T.A., Kaiser D.P., Sepanski R.J. and Stoss F.W. (eds.), Trends 93 - A compendium of data on global change, Carbon Dioxide Information Analysis Centre. Oak Ridge National Laboratory, Oak Ridge, 203-222.

Libby W.F. (1946) Atmospheric Helium Three and radiocarbon from cosmic radiation, The Physical Review 69, 671-672.

Manning M.R. and Melhuish W.H. (1994) $\Delta^{14}CO_2$ record from Wellington, in: Boden T.A., Kaiser D.P., Sepanski R.J., and Stoss F.W. (eds.), Trends 93 - A compendium of data on global change, Carbon Dioxide Information Analysis Centre. Oak Ridge National Laboratory, Oak Ridge, 173-202.

Middleton R., Fink D., Klein J. and Sharma P. (1989) ^{41}Ca concentrations in modern bone and their implications for dating, Radiocarbon 31, 305-310.

Milazzo M., Cicardi C., Mannoni T. and Tuniz C. (1997) Non destructive measurements for characterisation of materials and datation of *Corona Ferrea* of Monza, in: Handbook of The Sixth Australian Archaeometry Conference, 10-13 Februrary 1997, Sydney, Australia, p. 39.

Muller R.A. (1977) Radioisotope dating with a cyclotron, Science 196, 489-494.

Nelson D.E., Korteling R.G. and Stott W.R. (1977) Carbon-14: direct detection at natural concentrations, Science 198, 507-508.

Nelson D.E., Loy T.H., Vogel J.S. and Southon J.R. (1986) Radiocarbon dating blood residues on prehistoric stone tools, Radiocarbon 28,170-174.

Nelson D.E. (1991) A new method for carbon isotopic analysis of protein, Science 251, 552-554

O'Connor S. (1995) 40,000 years of Aboriginal occupation in the Napier Ranges, Kimberley, W.A., Australian Archaeology 41, 58.

Olsson U.I. (1970) The use of Oxalic acid as a standard, in: Olsson I.U. ed, Radiocarbon variations and absolute chronology, Nobel symposium, 12th Proc., John Wiley & Sons, New York, p 17.

Pettitt, P.B., Bronk-Ramsey C., Hedges R.E.M. and Hodgins G.W.L. (1999) AMS radiocarbon dating at Oxford and its contribution to issues of the extinction of Neanderthals and the spread of Homo sapiens sapiens across Eurasia, in: Conference Compendium of the 8th International Conference on Accelerator Mass Spectrometry, 6-10 September 1999, Vienna, p. 171, to be published in Nuclear Instruments and Methods in Physics Research B.

Phillips F.M., Flinsch M., Elmore D. and Sharma P. (1997) Maximum ages of the Côa valley (Portugal) engravings measured with Chlorine-36, Antiquity 71, 100-104.

Prinoth-Fornwagner R. and Niklaus Th.R. (1994) The man in the ice: results from radiocarbon dating, Nuclear Instruments and Methods in Physics Research B 92, 282-290.

Purser K.H. (1994) A future AMS / chromatography instrument for biochemical and environmental measurements, Nuclear Instruments and Methods in Physics Research B 92, 201-206.

Renfrew, C. (1973). Before civilisation, the radiocarbon revolution and prehistoric Europe, Jonathan Cape, London.

Roberts R.G., Jones R., Spooner N.A., Head M.J., Murray A.S. and Smith M.A. (1994), The human colonisation of Australia: optical dates of 53,000 and 60,000 years bracket human arrival at the Deaf Adder Gorge (Northern Territory), Quaternary Geochronology 13, 575-583.

Roberts R., Walsh G., Murray A., Olley J., Jones R., Morwood M., Tuniz C., Lawson E., Macphail M., Bowdery D. and Naumann I. (1997) Luminescence dating of rock art and past environments using mud-wasp nests in northern Australia, Nature 387, 696-699.

Roberts R., Bird M., Olley J.,Galbraith R., Lawson E., Laslett G., Yoshida H., Jones R. Fullagar R., Jacobsen G. and Hua Q. (1998) Optical and radiocarbon dating at Jinmium rock shelter in northern Australia, Nature 393, 358-362.

Russ J., Hyman M., Shafer H.J. and Rowe M.W. (1990) Radiocarbon dating of prehistoric rock paintings by selective oxidation of organic carbon, Nature 348, 710-711.

Stringer C.B. (1986) Direct dates for the fossil hominid record, in: Archaeological results from accelerator dating (ed. Gowlett J.A.J. and Hedges R.E.M.), Oxford University Committee for Archaeology Monogr. Ser. no.11, 45-50.

Stafford T.W., Hare P.E., Currie L., Jull A.J.T. and Donahue, D. (1990) Accuracy of north American human skeleton ages, Quaternary Research 34, 111-120.

Stuiver M. and Polach H.A. (1977) Discussion: reporting of ^{14}C data, Radiocarbon 19 (3), 355-363.

Stuiver M. (1983) International Agreements and the Use of the New Oxalic Acid Standards, Radiocarbon 25 (2), 793-797.

Stuiver M., Reimer P.J., Bard E., Beck J.W., Burr G.S., Hughen K.A., Kromer B., McCormac G., van der Plicht J. and Spurk M. (1998a) INTCAL98 radiocarbon age calibration, 24,000-0 cal BP, Radiocarbon 40 (3), 1041-1083.

Stuiver M., Reimer P.J. and Braziunas Th.F. (1998b) High-Precision Radiocarbon Age Calibration for Terrestrial and Marine Samples, Radiocarbon 40 (3), 1127-1152.

Suter M. (1999) Tandem AMS at sub-MeV energies – status and prospects, in: Conference Compendium of the 8th International Conference on Accelerator Mass Spectrometry, 6-10 September 1999, Vienna, p. 59, to be published in Nuclear Instruments and Methods in Physics Research B.

Taylor, R.E. (1987) Dating techniques in archaeology and paleoanthropology, Anal. Chem. 59, 317-331.

Terrasi F., Campajola L., Petrazzuolo F., Brondi A., Cipriano A., D'Onofrio M., Hua Q., Roca V., Romano M., Romoli M., Tuniz C. and Lawson E. (1994) L'Italia Scacchistica 1064, 48-60.

Thorne A., Grün R., Mortimer G., Spooner N.A., Simpson J.J., McCulloch M., Taylor L. and Curnoe D. (1999) Australia's oldest human remains: age of the Lake Mungo 3 skeleton, Journal of Human Evolution 36, 591-612.

Tuniz C., Fink D., Hotchkis M., Jacobsen G., Lawson E., Smith A., Hua Q., Peter D., Lee P., Levchenko V., Bird R., Boldeman J., Barbetti M., Taylor G. and Head J. (1995) The Antares AMS Centre: A Status Report, Radiocarbon 37 (2), 663-674.

Tuniz C., Bird J.R., Fink D. and Herzog G.F. (1998) Accelerator Mass Spectrometry (Ultrasensitive Analysis for Global Science), CRC Press, Boca Raton (Florida).

Turney C.S.M., Bird M.I. Fifield L.K., Roberts R.G., Smith M.A., Dortch C.E., Grün R., Lawson E., Miller G.H., Dortch J., Cresswell R.G. and Ayliffe L.K. (2000) Breaking the radiocarbon barrier and early human occupation at Devil's Lair, southwestern Australia, submitted for publication to Nature.

Valladas H., Cachier H., Maurice P., Bernaldo de Quiros F., Clottes J., Cabrera Valdez V., Uzquiano P., Arnold M. (1992) Direct radiocarbon dates for prehistoric paintings at the Altamira, El Castillo and Niaux Caves, Nature 357, 68-69.

Wachman A.L., Walsh G.L., Morwood M.J. and Tuniz, C. (1997) AMS radiocarbon age estimates for early rock paintings in the Kimberley, N.W. Australia: preliminary results, Rock Art Research 14, 18-26.

Wild E., Golser R., Hille P., Kutschera W., Priller A., Puchegger S., Rom W., Steier P. and Vycudilik W. (1998) First ^{14}C Results from Archaeological and Forensic Studies at the Vienna Environmental Research Accelerator, Radiocarbon 40(1), 273-282.

Zilhão J. (1995) The age of the Côa valley (Portugal) rock art; validation of archaeological dating to the Palaeolithic and refutation of 'scientific' dating to historic or proto-historic times, Antiquity 69, 883-901.

Zoppi U., Hua Q., Jacobsen G., Lawson E.M., Sarkissian G., Petitti P., Vargiu R. and Laurencich Minelli L. (1999) Controversies in European history: two significant examples, in: Conference Compendium of the 8th International Conference on Accelerator Mass Spectrometry, 6-10 September 1999, Vienna, p. 173, to be published in Nuclear Instruments and Methods in Physics Research B.

Radiation in Art and Archeometry
D.C. Creagh and D.A. Bradley (editors)

Dating beyond the radiocarbon barrier using U-series isotopes and trapped charges

Rainer Grün

Research School of Earth Sciences
The Australian National University
Canberra ACT 0200, Australia

U-series and trapped charge dating are methods that can be applied to establish chronologies well beyond the range of radiocarbon dating. This paper gives a short introduction into these methods and their potential is illustrated with the dating of the Lake Mungo 3 skeleton.

1. INTRODUCTION

Since the introduction of radiocarbon dating in the late 1940's [1,2], archaeology underwent a revolution by being able to obtain absolute chronologies [3]. Using the most sophisticated equipment, AMS accelerators, and sample pretreatment techniques (e.g. [4]), radiocarbon is limited to the dating materials that are younger than 60,000 years and in most cases younger than 40,000 years (e.g. [5]). The theoretical basis for K/Ar (and Ar/Ar) dating was also introduced in the late 1940's [6] and has found wide application since the mid 1960's. The method provides chronologies for most of the Earth's history, but reliable dates can only be obtained from *in situ* volcanic material [7] and until recently was not suited for the timescale of less than about 200,000 years. For a long time there was a significant chronological gap for which it was difficult to obtain numerical age estimates.

The last two decades have seen the increased application of U-series as well as trapped charge dating in archaeology. These methods have made considerable impacts, for example, on our understanding of modern human evolution. They have demonstrated that modern humans lived in the Levant at about 100,000 years ago, nearly 60,000 years earlier than when they first arrived in Europe [8]. A recent dating study showed that anatomically fully modern humans arrived in Australia at about 60,000 years [9] (see section 4).

2. U-SERIES DATING

The element U has two naturally occurring decay chains, the parent isotopes being ^{238}U and ^{235}U (see Figure 1). U-series dating is based on the different geochemical behaviour of uranium (U), thorium (Th) and protactinium (Pa). U^{6+} is water-soluble, whereas Th and Pa are in practical terms water- insoluble. Natural waters therefore contain traces of U, but are virtually free of Th and Pa.

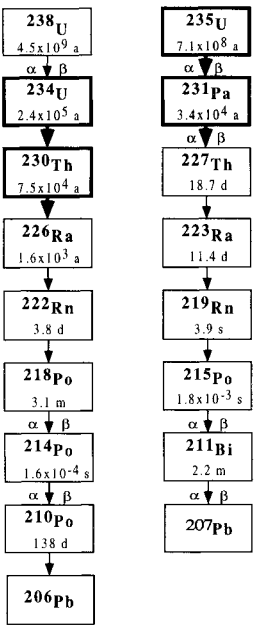

Figure 1: (from [10]) The ^{238}U and ^{235}U decay chains. For simplification only the alpha decays are shown. The bold boxes indicate the isotope pairs that are used for U-series dating in archaeological contexts. (α and β indicate a series of an alpha decay combined with one or two beta decays).

Minerals precipitated from water, such as carbonates (speleothems, travertines, shells, corals etc.), contain uranium, but no Th and Pa. Therefore, the $^{230}Th/^{234}U$ activity ratio in the ^{238}U decay chain as well as the $^{231}Pa/^{235}U$ activity ratio of the ^{235}U decay chain are zero at the time of formation (t=0). With time, isotopes of the decay chains grow into secular equilibrium where all activity ratios are practically 1. The dating range is determined by the instrumental ability to measure activity ratios of < 1 and is in practical terms about 500,000 years (Th/U) and 200,000 years (Pa/U). U-series dating was recently comprehensively reviewed [11].

2.1. Basic principles

The basic principles of Pa/U and Th/U dating were recently described [12]: the activity of a radioactive isotope, A, is defined as the number of atoms decaying per time unit. If N is the number of atoms present, A is expressed by:

$$A = \lambda N \tag{1}$$

If initially no atoms of a daughter isotope are present (e.g., the daughter isotopes were isolated from the parent through chemical separation), the daughter's activity, A_d, increases with time, t:

$$A_d = A_p(1 - e^{(-\lambda_d t)}) \tag{2}$$

where A_p is the parent activity and λ_d the decay constant of the daughter ($\lambda_d = \ln(2)/T_{1/2}$; $T_{1/2}$ is the half life of the daughter).

If $t \gg 1 / \lambda_d$ secular equilibrium is achieved (for practical purposes, $t \approx 7\ T_{1/2}$, $A_d = A_p$). In old materials, all members of the decay chains are in equilibrium with each other. The ^{231}Pa activity is (in the equations to follow, the isotope name stands for its activity):

$$^{231}Pa = {}^{235}U\ (1 - e^{(-\lambda_{231}\ t)}) \tag{3}$$

The activity of ^{230}Th is expressed by:

$$\begin{aligned} {}^{230}Th &= {}^{234}U\ (1 - e^{(-\lambda_{230}\ t)}) \\ &= {}^{238}U\ (1 - e^{(-\lambda_{230}\ t)}) \end{aligned} \tag{4}$$

Equation (4) requires that ^{234}U and ^{238}U are in secular equilibrium at t=0 (i.e. when the uranium is incorporated into the sample). This is usually not the case because most natural waters have an excess of ^{234}U over ^{238}U [11]. This is due to the fact that ^{234}U is produced by α-decay of ^{238}U: when an alpha particle is emitted, the decaying atom recoils leading to a weakening of its lattice position. Dissolution of minerals starts preferentially at weakened lattice sites, as a consequence, these solutions are enriched with ^{234}U. Because of its long half-life ($T_{1/2}$ = 245.4 ka), the excess ^{234}U activity has to be taken into account:

$$\frac{^{230}Th}{^{238}U} = (1 - e^{-\lambda_{230}\ t}) + \frac{\lambda_{230}}{(\lambda_{230} - \lambda_{234})} \left(\frac{^{234}U}{^{238}U} - 1 \right) (1 - e^{-(\lambda_{230} - \lambda_{234})\ t}) \tag{5}$$

where λ_{230} and λ_{234} are the decay constants of ^{230}Th and ^{234}U, respectively. When ^{234}U excess occurs, the present ^{234}U/^{238}U activity ratio can be greater than 1. Equation (5) reduces to equation (4) for ^{234}U/^{238}U = 1.

2.2. Measurement

Before measurement, U is chemically separated from Th and Pa. Until the mid-1980's, the isotopes for U-series dating had been measured by alpha spectrometry. Similar to the advances in radiocarbon dating achieved by accelerator mass spectrometry [13,14], thermal ionisation mass spectrometry (TIMS) has lead to a breakthrough in U-series, particularly Th/U dating [15]. TIMS allows the measurement of significantly smaller samples (by a factor of 30 to 100) with greatly improved precision. Whilst the upper dating limit of alpha counting is about 350,000 years, TIMS allows the measurement of the Th/U ratio that are distinctively different from unity for samples older than 500,000 years. At the other end of the dating range, samples as young as 200 years were measured with uncertainties of about 5 years which is more precise than radiocarbon dating [16]. TIMS Pa/U age determinations require a radioactive Pa standard [17], and have so far rarely been carried out on archaeological samples.

Th/U and Pa/U ratios can also be measured by gamma spectrometry (see [12,18] for details). The advantages of this technique are that no pretreatment of the sample is required and is completely non-destructive. The disadvantage lies in the much lower detection limits of high

resolution gamma counters compared with alpha or mass spectrometry. Therefore gamma spectrometry is associated with larger errors (about 5 to 15% in the 100,000 years range).

To be suited for U-series dating samples must fulfil the following criteria:

- it must have been formed at a well-defined event;
- it must contain measurable amounts of uranium;
- after formation, it remained a closed system;
- it must not contain any ^{230}Th or ^{231}Pa at the time of formation, or the amount of ^{230}Th or ^{231}Pa at the time of formation is measurable.

The only materials that comply with these conditions are speleothems and corals. These are only rarely found in archaeological contexts. Initial ^{230}Th and ^{231}Pa, often introduced into the sample by clay minerals, can be measured using isochrons (see Figure 10, section 4.1). Recently, there have been advances in the dating of bones. Bones are open systems for uranium, but several diffusion models have been developed to account for this [19-26], see also section 4.2..

3. TRAPPED CHARGE DATING

Trapped charge dating, TCD, covers a range of techniques: electron spin resonance (ESR), thermoluminescence (TL) and optically stimulated luminescence (OSL). Most archaeological ESR dating studies have been carried out on tooth enamel, TL on burnt flint and OSL on sediments. TL and ESR dating demonstrated successfully the early occurrence of modern humans in Israel at about 100,000 years ago [8,27,28]. OSL can be used for dating sediments that were exposed to dim sunlight for short periods of time. OSL dating is not yet routinely applied in archaeological studies but one can expect that this technique will lead to a breakthrough of knowledge similar to the radiocarbon dating revolution in the 1950's and 1960's [3]. ESR and luminescence dating applications in archaeology have recently been reviewed [29-32].

3.1. Basic Principles

The trapped charge dating methods are based on the same principles, namely the time dependent accumulation of electrons and holes in the crystal lattice of some common minerals. In that way, the minerals act as natural dosimeters. Radiation induced centers are created by the exposure of the sample to high energy particles (e.g., α-, β-, or γ-particles originated by the radioactive decay; nucleons and muons in cosmic rays, neutrons as well as laboratory produced X-rays). A *point defect* is any position in the crystal structure which violates the notion of an 'ideal crystal'. Point defects are anion and cation vacancies, interstitial atoms and molecules, impurity ions, disorder of the crystal lattice, vacancy and impurity aggregates. A defect denotes a local charge deficit of both positive (cation vacancy) and negative charge (anion vacancy). By trapping holes or electrons a *center* is created leading to the reestablishment of electrical neutrality. An electron centre can be created by the following scheme [33]:

$$L^+ \longrightarrow I^{2+} \longrightarrow I^{2+} + e^- \longrightarrow I^+$$

substitution irradiation trapping

The lattice cation L is replaced by an impurity cation I with a greater charge which can then trap an electron produced by irradiation. The trapping of a hole center by a negative charged site is not completely symmetric:

$$L^{4+} + O^{2-} \longrightarrow I^{3+} + O^{2-} \longrightarrow I^{3+} + O^{2-} + e^{+} \longrightarrow I^{3+} + O^{-}$$

If a cation is substituted by one with a lower charge (e.g., Si^{4+} by Al^{3+} in quartz) irradiation removes the surplus electron and the electron deficit (hole-center) is then placed at the neighbouring oxygen site. *Free radicals* are e.g, produced by the following scheme of irradiation of a CO_3^{2-}-radical:

$$CO_3^{2-} \xrightarrow{\text{irradiation}} \begin{cases} e^{+} \xrightarrow{\text{trapping}} CO_3^{-} \\ e^{-} \xrightarrow{\text{trapping}} CO_3^{3-} \end{cases}$$

By trapping a hole or an electron the CO_3^{2-}-radical becomes a free radical. In radicals the electron or the hole is not trapped by a specific ion but as the whole radical. The branch of the trapping scheme is dependent on the sort of substitution at the cation site. The existence of a free CO_3^{3-}-radical in calcite demonstrates the existence of a substitution at the cation site (with a positive or negative surplus charge) which then stabilizes the respective free radical (e.g., Y^{3+} replacing Ca^{2+} stabilizes the CO_3^{3-} free radical). A Ca^{2+} substitution by an M^{+}-ion leads to the stabilization of CO_3^{-}.

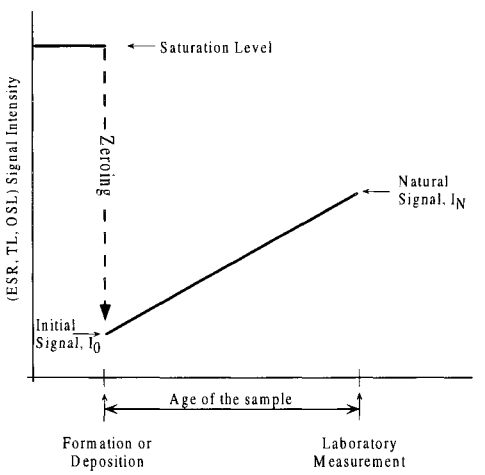

Figure 2 (from [34], after [31]): a zeroing event dissociates defects and electrons. The corresponding TCD signal is set to zero, or to a small, measurable, initial signal, I_0. Natural radiation generates new centres, thus the TCD signal intensity increases continuously until the sample is measured. The signal of the sample is called *natural intensity*, I_N. For the measurement of the dose that the sample was exposed to, the dose response of the sample is established with a series of laboratory irradiations. The measured signal intensities are plotted versus the defined laboratory doses and these data points are used to extrapolate to I_0, which, in most cases, is practically zero. The intersection with I_0 yields the equivalent dose, D_E, the sample has received in the past.

Paramagnetic centres give rise to an characteristic ESR signal and can be detected with an ESR spectrometer. For the measurement of a luminescence signal, the trapped electrons have to be either thermally (by heating) or optically (by light exposure) activated. The electrons recombine with the holes. If such holes are luminescence centres, light emission (luminescence) is observed.

Figure 2 shows the basic principle of the dating process. A TCD age, T, is derived from the simple relationship:

$$D_E = \int_0^T D(t)dt\,, \tag{6}$$

If the dose rate, D(t) or $\dot{D}$, is constant, equation (6) is reduced to:

$$T = \frac{D_E}{\dot{D}}\,. \tag{7}$$

The D_E value is determined by ESR/TL/OSL measurement. The dose rate is calculated from the analysis of the radioactive elements (Th, U, and K, other contributions are usually negligible) in the sample and its surroundings; their U, Th and K concentrations are converted into dose rates by published tables (see Table 1 in section 3.5).

3.2. ESR measurement

ESR measurements are made with an ESR spectrometer. The sample is placed into a microwave cavity which is located in a strong external magnetic field. Paramagnetic centers have a permanent magnetic moment (μ_s) which is generated by the self-rotation (spin) of an unpaired electron, specifically by its negative charge. This magnetic moment can be expressed by:

$$\vec{\mu}_s = -\frac{g\mu_B}{\hbar}\vec{s} \tag{8}$$

where μ_s is magnetic moment, μ_B the Bohr magneton (9.274078 10^{-24} J T^{-1}), g the Landé factor (henceforth g-value), ħ Planck constant (6.626176 10^{-34} J s^{-1}) divided by 2π and s the spin quantum number.

When brought into an external magnetic field (Figure 3A), the component of the magnetic moment in direction of the magnetic field (μ_z) is:

$$\mu_z = \frac{g\mu_B}{\hbar}(\pm 1/2\hbar) = \pm 1/2\, g\mu_B = g\mu_B M_s \tag{9}$$

where M_s is magnetic quantum number of the spin s. The effect of the external magnetic field on the magnetic moment of the electron causes a splitting of the initial energy level (E_0) into two discrete energy levels E_+ and E_- (Zeeman energies, see Figure 3B).

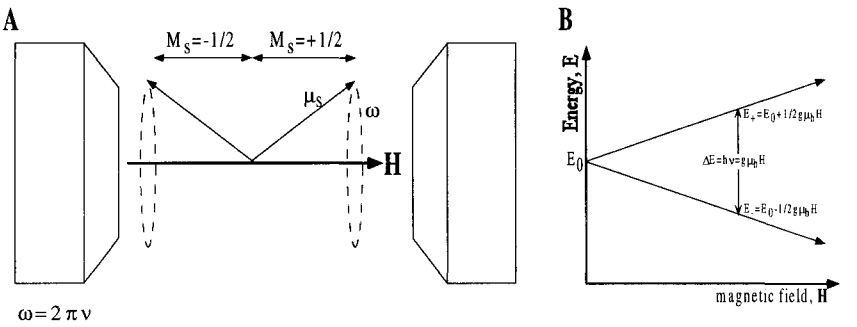

Figure 3: (A) Orientation of the magnetic moment of an electron in an external magnetic field. (B) Zeeman splitting of the energy of a free electron

The energy difference between these levels, ΔE, is:

$$\Delta E = g\mu_B H \tag{10}$$

A transfer from the lower to the higher energy level can be induced by microwaves with the frequency, ν, if $\nu = \omega/2\pi$, where ω is the precession frequency of μ_s. It follows the resonance condition:

$$h\nu = g\mu_B H \tag{11}$$

i.e. a transfer of electrons from the lower to the higher energy level can be induced by absorption of radiation (in this case of electromagnetic waves) with the frequency ν; on the other hand a transfer from the higher to the lower level emits energy of the same magnitude.

In principle, after absorption of microwave energy the two electron populations would equalize and no further absorption could be observed. The fact that an electron transfer from the lower to the higher level can be induced continuously is due to the fact that the transition from the higher to the lower energy level is not connected with emission of microwave energy but rather the energy is transferred to the crystal-lattice by phonons.

The ESR spectrometer has basically three components: a strong magnet whose field strength can be linearly varied, a microwave generator (Gunn diode or klystron), and an electronic processing unit. The sample is located in a cavity between the pole shoes of the magnet. The cavity is connected to the microwave generator via waveguides. As can be seen from the resonance condition, equation (11), an ESR spectrum could be recorded by either varying the microwave frequency or the magnetic field strength. Because the dimensions of the waveguide and especially the cavity are very dependent on the microwave frequency, the magnetic field is varied linearly for an ESR measurement. For the most used frequency of around 9GHz (X-band) a magnetic field strength of about .35 Tesla (T) is required to record a signal with the g-value of a free electron (g around 2). If higher resolution is required, samples are recorded with a Q-band (35 GHz) ESR spectrometer where a magnetic field strength of more than 1 T must be generated.

To optimise the signal-to-noise ratio, ESR signals are recorded as derivatives using field modulation. For more details on ESR spectroscopy in dating applications see [35-37].

3.3. Luminescence measurement

For a TL measurement, the sample is deposited on a small steel disk which in turn is placed on a heating element (Figure 4, left). At elevated temperatures electrons and defects dissociate and if electron recombine with a hole that is a luminescence centre, light emission occurs. The photons pass through some colour filters, are detected and converted into an electrical signal by a photo-multiplier. The amount of light emission is recorded versus the heating temperature, resulting in a *glow curve*. For more details on the basic principles of luminescence see [38].

The basic OSL reader is very similar to the TL instrument. For OSL measurements (Figure 4, right), the sample is exposed to a light source which emits light in a narrow frequency spectrum (lasers; Xe or halogen lamps with appropriate colour filters). Feldspars are particularly sensitive to infrared stimulation (resulting in the acronym IRSL: infrared stimulated luminescence) and quartz to green light (GLSL: green light stimulated luminescence). The light that is shone onto the sample activates the trapped electrons and on recombination with luminescence centres, light emission is observed. The colour filters under the photo-multiplier must suppress the light frequencies of the light source completely. In most cases, the light emission used for dating lies in the ultra violet range, but other colours have also been investigated [39]. The equipment records the light emission versus the time after the light source was switched on, resulting in a *shine-down curve*. For more details on OSL measurements see [31].

Because TL and OSL readers are very similar, many OSL readers started their lives as TL instruments. The combination of TL and OSL in one piece of equipment has the advantage that OSL measurements can be carried out at elevated temperatures [40,41]. For more details on luminescence instrumentation see [31, 42].

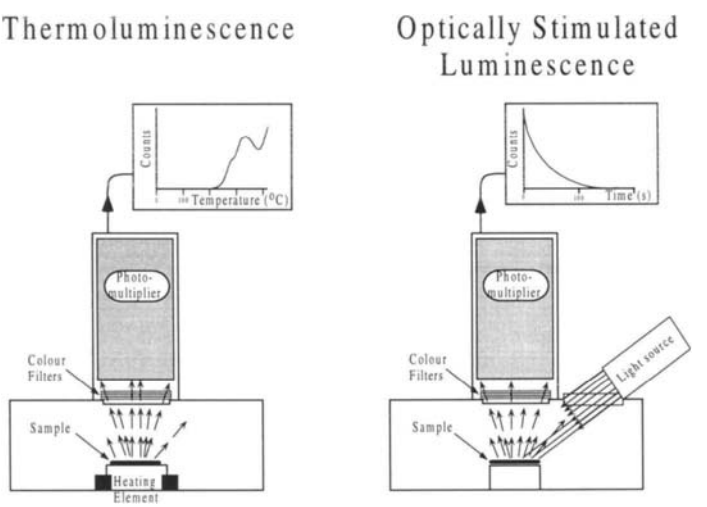

Figure 4 (from [34], after [31] and [43]): Luminescence readers.

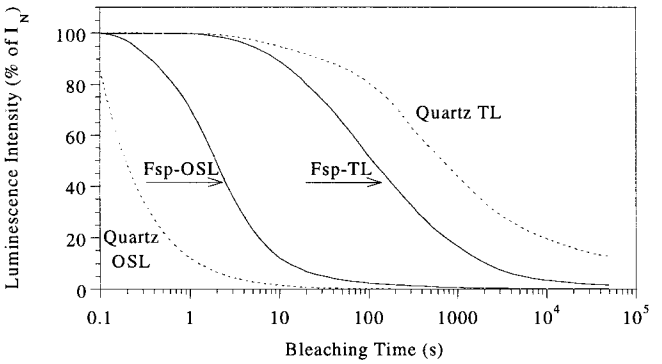

Figure 5 (from [34] using data of [44]): Comparison of TL and OSL bleaching characteristics. The OSL signals are virtually completely reset after a very short time of light exposure. The TL signals which are composites of a range of centres, bleach significantly slower to a non-zero residual level.

When quartz and feldspar sediment grains are exposed to sunlight, certain centres are reset whilst others are partly or not at all reset. TL records the effect of light on all of these centres whilst OSL only measures the light sensitive centres. This has the consequence that the TL signal is only rarely completely reset. Furthermore, because of thermal quenching [45, 46], TL measurements are far less efficient for the measurement of luminescence (see Figure 5). Because the OSL measurement simulates the actual resetting mechanism for sediments and targets only the light sensitive centres, which are practically completely reset after a short time of light exposure, this method is now preferred for the dating of sediments. On the other hand, for the dating of burnt flint [28], where heating causes the resetting, TL is the preferred method.

3.4. Determination of the dose value, D_E

In order to provide reliable results, the measured TCD signal must have the following properties:

- When the sample is reset it contains an initial signal that can either experimentally be determined or assumed to be zero.
- The signal intensity grows in proportion to the dose received.
- The signals must have a thermal stability which is at least one order of magnitude higher than the age of the sample.
- The number of traps is constant or changes in a predictable manner. Recrystallisation, crystal growth or phase transitions must not have occurred.
- The signals should not show anomalous fading [47,48].
- The signal is not influenced by sample preparation (grinding, exposure to laboratory light etc.).

Laboratory irradiations are carried out with mono-energetic β or γ sources whereas the dose the sample has received in the past is the sum of multi-energetic α, β, γ and cosmic rays (see below). Therefore, the experimentally determined dose value is the β or γ equivalent of the naturally received dose and is called *equivalent dose*, D_E.

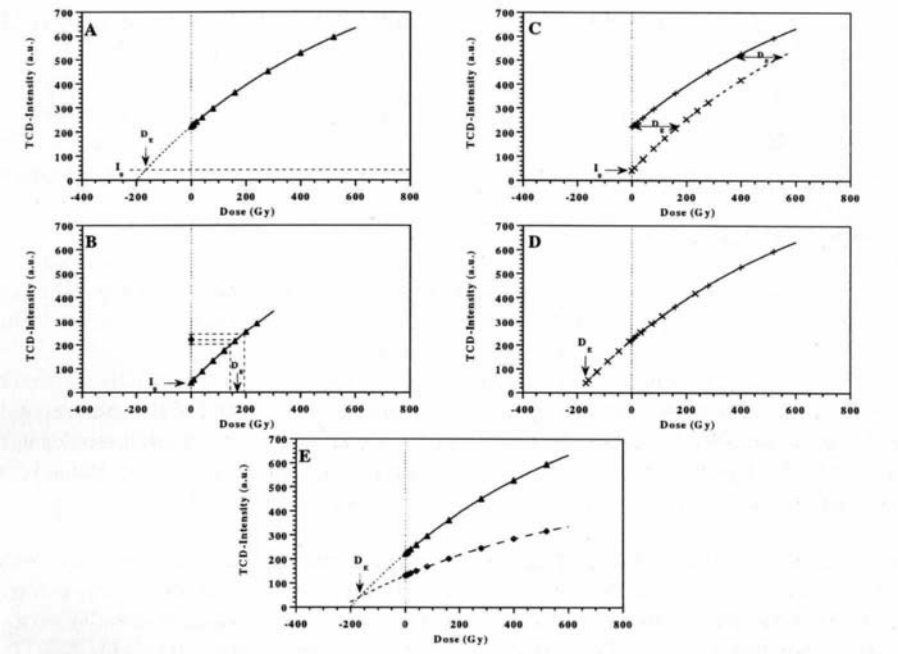

Figure 6 (from [49]): Methods for dose estimation. A: additive dose; B: regeneration; C and D: slide; E: partial bleach

There are four basic techniques for the determination of the D_E value (see Figure 6). The additive dose method is most widely used (Figure 6A): the natural signal intensity of the sample, I_N, is measured and further aliquots are irradiated with defined doses. The plot of intensity versus laboratory dose, the *dose response* and is used for extrapolation to the initial intensity, I_0. I_0 is often demonstrably zero or assumed to be zero. However, in TL studies of sediments, I_0 is often a significant percentage of I_N (see Figure 6) and has to be determined experimentally. I_0 is either determined with a sunlight simulator [43] or a surface sample is collected and its natural intensity is used as I_0 for the archaeological samples in the vicinity [50]. In ESR studies, the additive dose method is nearly exclusively used. For the fitting of the data points, the dose response curve has to be mathematically described. For a single centre, the data points are usually best fitted by a single saturating function. The magnitude of errors involved in the extrapolation procedures and reproducibility has been investigated by [51-53]. However, many samples show different dose responses, such as a saturating plus linear function [54,55] or inflexion points [56].The application of an inappropriate model for curve fitting leads to erroneous D_E-values.

The regeneration technique is an alternative for D_E estimation (Figure 6B). I_N is measured first, the subsequent aliquots are reset to I_0. These aliquots are then irradiated and the projection of I_N onto the regenerated dose response curve yields D_E. The regeneration method has the advantage of involving smaller errors than the additive dose method and furthermore, the D_E result is little dependent on the mathematical model used for the fitting of the data points (in contrast to the additive and partial bleach techniques [49]). However, some samples show sensitivity changes

after resetting, and as a consequence, the regeneration D_E-value differs from the additive D_E value. This problem is addressed in the slide technique (Figure 6C,D; see [57]): the natural and reset aliquots are irradiated so that the additive dose response curve overlaps significantly with the regenerated dose response curve. The D_E-value is given by the horizontal distance between the two curves. The overlapping parts of the two dose response curves are used for the recognition of sensitivity changes. If necessary, re-scaling of the regenerated dose response curve can be carried out.

The partial bleach technique is used in TL studies of sediments where insufficient light bleaching is suspected (i.e. it is not possible to determine I_0). First, a conventional additive dose response curve is established, then irradiated aliquots are exposed to light for a relative short time and a second dose response curve is produced (Figure 6E). The intersection of both curves yields the D_E value.

ESR spectra and TL glow curves may contain components which are not thermally stable, i.e. the use of such D_E values would lead to age underestimations. ESR spectra may contain signals that are not radiation sensitive at all and TL glow curves may contain peaks that are not light sensitive. For the recognition of such areas, plateau tests were introduced in early TL studies and later adopted in ESR and OSL. Rather than determining a single value, D_E-values are continuously determined of the whole spectrum range (Figure 7) and thermally unstable or radiation insensitive components can be recognised (Figure 7B,D).

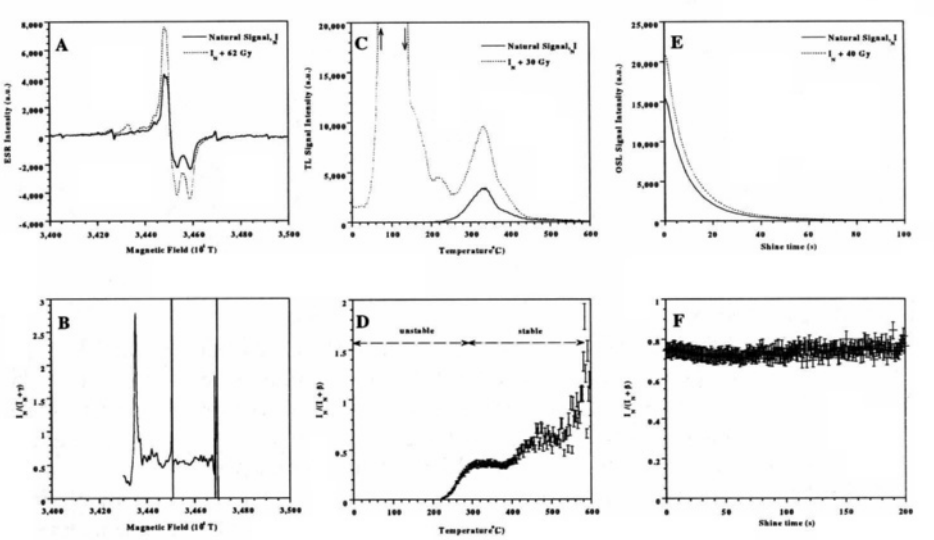

Figure 7 (from [34]): ESR spectra (A), TL glow curves (C) and OSL shine down curves (E) of a natural geological sample and the same sample with an additional dose. Plateau tests (continuous dose determinations) allow the recognition of stable and unstable regions for ESR and TL (B and D). The dose versus light emission time for the OSL measurement is partly related to the kinetics and partly to the occurrence of signals with different bleachability [58].

3.5. Determination of the dose rate, $\dot{D}$

The dose rate is calculated from the concentrations of radioactive elements in the sample and its surroundings (only the U and Th decay chains and the ^{40}K-decay are of relevance; a minor contribution comes from ^{87}Rb in the sediment) plus a component of cosmic rays. There are three different ionising rays which are emitted from the radioactive elements (Figure 8). In sediment:

- gamma rays have a range of about 30 cm;
- beta rays (electrons) have a range of about 2 mm;
- alpha rays have only a very short range of between20 and 40 μm because of the large size of the particles. Alpha particles are not as efficient in producing centres as are beta and gamma rays (due to local saturation along the alpha tracks). This requires the determination of the alpha efficiency, which is usually in the range of 0.05 to 0.2 [43].

The concentrations of radioactive elements in the sample and its environment are usually different. Therefore, *internal dose rates* and *external dose rates* have to be assessed separately. Furthermore, it is necessary to estimate the cosmic dose rate which is about 300 μGy/a at sea-level and decreases with depth below ground and is also dependent on altitude as well as geographic latitude [59,60].

The conversion of the elemental analysis into dose rates are shown in Table 1. Dose rate calculations become more complicated when disequilibrium in the U-decay chains or attenuation factors have to be considered (see [35, 43]for details). Typical errors in the estimation of the total dose rate are in the range of 4 - 7%.

Table 1: Dose rates for the U and Th decay chains and K [61]:

	$\dot{D}_\alpha$	$\dot{D}_\beta$	$\dot{D}_\gamma$	
1 ppm ^{238}U + ^{235}U	2780	146	113	μGy/a
1 ppm ^{232}Th	732	27	48	μGy/a
1 % K		782	243	μGy/a

3.5.1. External Dose Rate

The calculation of the external dose rate is dependent on the size of the samples. The removal of the outer 50 μm of the sample eliminates the volume that received an external alpha dose. If the outer 2 mm can be removed, the external beta dose is eliminated and the external dose rate consists of gamma and cosmic rays only. If the samples are smaller, they receive external beta radiation which decreases with depth and therefore attenuation factors have to be considered (see [35, 43]for more details). The external beta dose rate has to be calculated separately from the external gamma dose rate because the beta dose rate is generated from the sediment immediately attached to the sample, whereas the gamma dose rate originates from all sediment that is within a radius of about 30 cm around the sample (see Figure 8). The beta dose rate from the sediment is derived from the chemical analysis of U, Th, and K.

The gamma dose rate can normally not be deduced from laboratory analyses but has to be measured *in situ* with a portable, calibrated gamma spectrometer or TL dosimeters. *In situ* measurements have the advantage to include the present-day water contents. Water absorbs some ß and γ rays and its presence in the surrounding sediment has to be considered in the calculation of the beta and gamma dose rate [62,63].

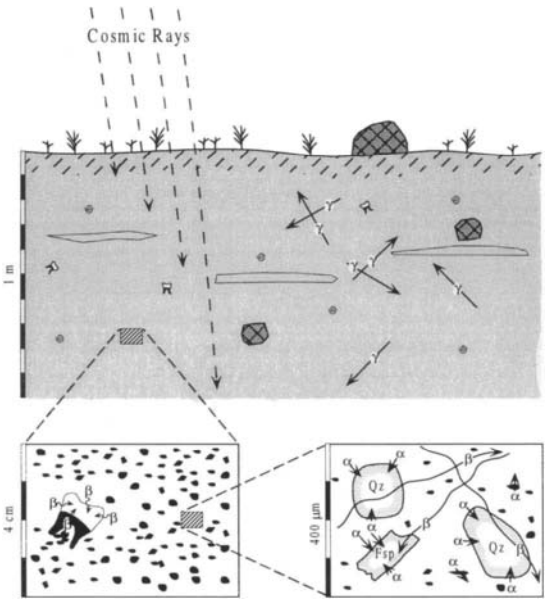

Figure 8 (from [34], after[31]): Sources of external radiation. Gamma radiation originates up to 30 cm around the sample. Because of sediment inhomogeneity, the gamma dose rate has to be measured *in situ*.

3.5.2. Internal Dose Rate

This parameter is mainly generated by alpha and beta rays emitted from elements in the sample. In luminescence studies, it is often assumed that quartz is free of radioactive elements. This assumption will cause only small errors if the external dose rate is relatively high. However, in low dose rate environments, e.g. quartz sand dunes [64], the internal dose rate originated by small amounts of radioactive elements may constitute a significant part of the total dose rate. Feldspars contain K but are usually free of U and Th. Quaternary calcitic samples, including speleothems, shells and corals, but also enamel and dentine of teeth, display disequilibrium in the U-decay chains which is actually the basis for U-series dating. U-series disequilibrium affects the average dose rates and has to be taken into account mathematically [35].

Alpha efficiencies range from 0.13 (ESR of tooth enamel [65]) to 0.03 (OSL of quartz [66]). Note that alpha efficiencies can not only change from sample to sample but also from technique to technique on the same samples [67]. Alpha efficiencies can be routinely measured in luminescence studies whereas the size requirements for ESR measurements make its assessment difficult [65]. If the samples are small, the internal alpha and beta dose rates are not 100% absorbed and a self-absorption factors have to be calculated (which is 1 minus the external attenuation factors).

The dose rate can be measured with a precision of about 5%. The overall uncertainty of a trapped charge dating result may be as low as 6 to 7%.

4. APPLICATION OF U-SERIES AND TRAPPED CHARGE DATING FOR THE ESTABLISHMENT OF THE AGE OF THE LAKE MUNGO 3 SKELETON

The dating of the Lake Mungo 3 skeleton, LM3, is an example how U-series and trapped charge dating can be used for the age assessment of important archaeological material whose age may be well beyond the radiocarbon dating range (see [9] for more details on this dating study).

LM3 is a complete skeleton which was found in the lunette of the now dry Lake Mungo (western NSW; Figure 9A). Detailed sedimentological studies concluded that the burial was carried out before the development of the soil horizon on the Lower Mungo unit [68] (see Figure 9B, C). Radiocarbon dating places the age of the skeleton to about 42,000 years [69]. However, numerous studies have shown that material with radiocarbon ages of such antiquity may well be considerably older [5].

For the assessment of the age of LM3, the following dating was carried out: TIMS Th/U dating on four bone fragments of LM3 as well as the encrusting soil carbonates, gamma spectrometric Th/U and Pa/U dating on the whole skull, ESR dating of a tooth fragment and OSL dating of sediments found immediately under the Lower Mungo soil horizon (see Figure 9C).

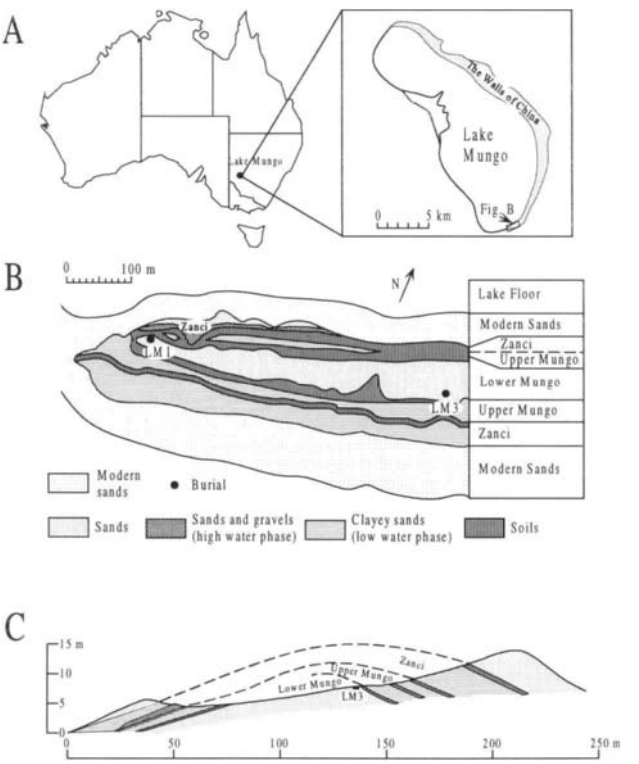

Figure 9 (from [9], after [70]): (A) Location of Lake Mungo in Western New South Wales; (B)Stratigraphic map; (C) cross section through the dune.

4.1. Dating results on the calcitic matrix and embedding sediment

Figures 10A and B show the isochron plots of the mass spectrometric U-series data on the calcitic fraction of the matrix. These calcitic samples contain significant amounts of detrital material (e.g. clay minerals) in which the U-decay chain are in equilibrium. During chemical preparation Th and U is not only derived from the calcite, but also from the detrital material. Thus, the basic assumption that at t=0 the sample does not contain any ^{230}Th is not valid. However, clay also contains ^{232}Th which is not present in the calcite. Because the chemical behaviour of the two Th isotopes is identical, ^{232}Th can be used to estimate the amount of initial ^{230}Th in the sample. This is done by isochrons (for details see [71-73]): The sample is partly dissolved with acids of increasing concentrations. This leads to a varying amounts of leached ^{232}Th (and detrital ^{230}Th) in chemical separate that is later measured. Normalisation on ^{232}Th leads to the estimation of the ^{230}Th/^{234}U (Figure 10A) and ^{234}U/^{238}U ratios (Figure 9B). The slope on the plot of ^{230}Th/^{232}Th versus ^{234}U/^{232}Th (Figure 10A) yield the age of the sample and the Y-intersection the initial ^{230}Th/^{232}Th ratio.

The fitted ^{230}Th/^{234}U and ^{234}U/^{238}U values result in an isochron age of 81±21 ka using the *Isoplot* program of K. Ludwig for data fitting and age calculation [74]. The large uncertainty in the age estimate is caused by the low U-concentrations and consequently low ^{230}Th count rates as well as the relatively small spread in the ^{230}Th/^{232}Th isotope ratios.

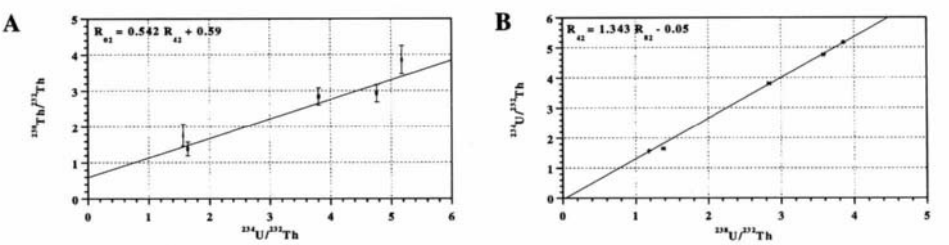

Figure 10 (after [9]): Isochron plots for five soil carbonate samples which encrusted the Mungo 3 skeleton. The slopes of the isochron diagrams yield the age of the calcite precipitation: 82,000±21,000 years.

The OSL age estimates of the two samples, 59±3 and 63±4 ka, result in a weighted mean of 61±2 ka. This age estimate should in principle provide a maximum age for the LM3 specimen because the deposition of the sediment took place before the burial of the skeleton.

4.2. Dating results on the bones and teeth

When dating bones and teeth with U-series or ESR it has to be realised that these are open systems for uranium. In short, modern bones and teeth fossil teeth contain only very small amounts of U (< 1 to 50 ppb) whereas archaeological specimens may contain several hundreds of ppm U. For dating, the temporal uptake of uranium has to be considered. When the organic constituents of bone and teeth decompose these form a reducing chemical environment where the water soluble U^{6+} is reduced into in-soluble U^{4+}. It is often assumed that the chemical decomposition and the accompanying U-accumulation is a fast process compared with the age of the sample. Here, closed system age calculations will give reasonable results. However, it has been shown at a range of sites that U-uptake can be greatly delayed [19,23]. Recently, a variety

of U-uptake models for bones have been investigated. The model of Millard [23, 26] requires the knowledge of U-distribution in a cross section of a bone. Unfortunately, this was not possible to measure on the LM3 bones. The model of Grün et al. [19] requires the simultaneous measurement of ESR and U-series and solves such for age, T, and a one parameter uptake equation of the form:

$$U(t) = U_m\,(t/T)^{P+1} \tag{12}$$

where U(t) is the uranium concentration at the time t, U_m the measured present day U-concentration, T the age of the sample and p the uptake parameter.

4.2.1. Mass spectrometric U-series dating

Figure 11A shows the mass spectrometric results on the bone samples. Given the undisputed contemporaneity of the samples, the range in the mass spectrometric Th/U ages clearly displays the effect of uranium mobilisation. The samples with the higher U-concentrations (samples BC, BD) have lower apparent U-series ages than those with lower U-concentrations (BA, BB).

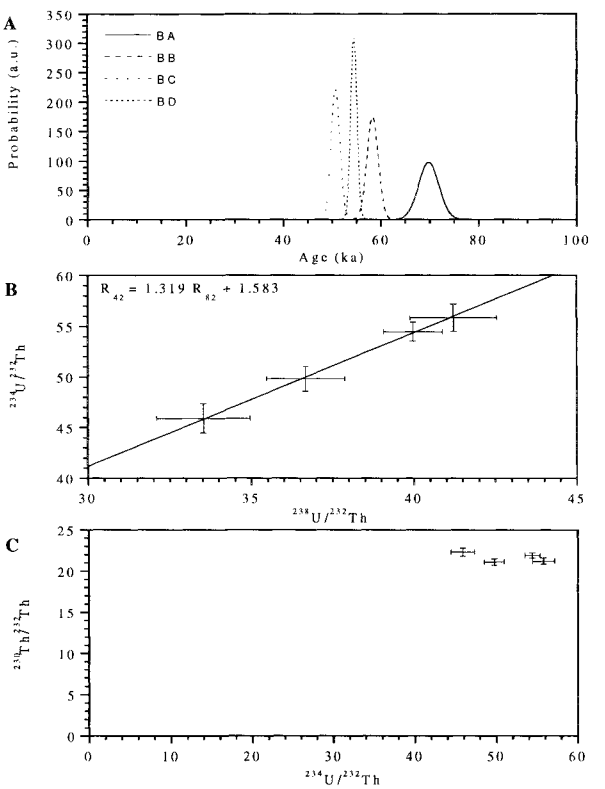

Figure 11 (after [9]): (A) Apparent TIMS U-series ages on bone shavings. The $^{234}U/^{232}Th$ versus $^{238}U/^{232}Th$ plot shows that the $^{234}U/^{238}U$ ratio mobilised in the sediment was constant irrespectively of U-mobilisation. The plot of $^{230}Th/^{232}Th$ versus $^{234}U/^{232}Th$ (C) shows that the different samples have experienced U-mobilisation. As a consequence no isochron age can be calculated.

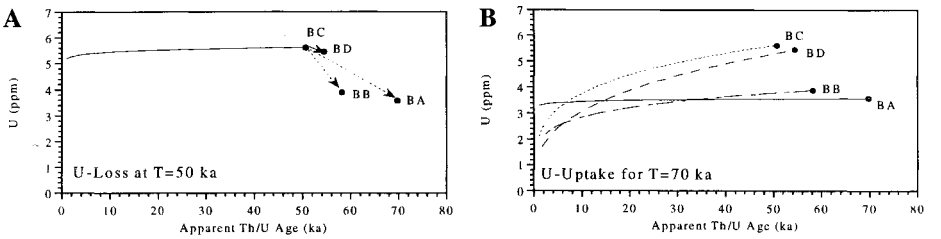

Figure 12: The mass spectrometric data can be explained by either U-loss (A) where the sample is 50,000 years old and U was leached relatively recently, resulting in older apparent U-series ages; or varying U-uptake rates (B) where the sample is 70,000 years old but the delayed U-uptake causes younger apparent U-series ages.

The sequence of ages can be explained by both delayed U-uptake and recent U-loss (Figure 12). On the one hand, the bones may have experienced a relatively fast uptake of about 3 to 3.5 ppm of uranium at about 70 ka ago, samples BB, BC and BD continued to accumulate uranium up to about 5.5 ppm, thus yielding apparently younger U-series ages than sample BA (Figure 12A). Of course, all samples may have experienced delayed U-uptake and the correct age of LM3 is older than 70 ka. Alternatively, all samples may have accumulated about 5.5 ppm uranium about 50 ka ago and along with the relatively recent deflation of the lunette, uranium was oxidised and removed from the bones. The more uranium that is lost from the bones, the older their apparent U-series ages become. Again, all sub-samples may have experienced recent U-loss and the correct age of the sample may be younger than 50 ka (Figure 12B).

The $^{234}U/^{232}Th$ versus $^{238}U/^{232}Th$ plot (Figure 11B) shows that the $^{234}U/^{238}U$ ratio in the four bone samples was not affected by uranium mobilisation. Indeed the $^{234}U/^{238}U$ ratio of the bones, 1.319 is closely similar to the corresponding value in the calcitic matrix, 1.343 (Figure 10B). This means that all the uranium that was mobilised in the upper part of the Lower Mungo Unit had closely similar $^{234}U/^{238}U$ ratios. All bone samples show some detrital ^{232}Th with $^{230}Th/^{232}Th$ ratios close to 22. Unfortunately, the isochron data cannot be used to estimate an initial $^{230}Th/^{232}Th$ ratio. If we assume that the initial $^{230}Th/^{232}Th$ ratio is in the range of 1 to 1.5 (as often assumed in U-series studies of speleothems[75], the U-series results would become younger by about 5 to 7%. This has to be regarded as a maximum correction, because the sediments, with considerably higher detrital contaminations, have an initial $^{230}Th/^{232}Th$ of about 0.55 (Figure 10A).

To summarise, the mass spectrometric U-series data on the bones show that the four different bone samples have closely agreeing $^{234}U/^{238}U$ ratios, but their apparent ages range from 50 to 70 ka. This age range may reflect different histories of U-mobilisation such as delayed U-uptake, recent U-loss or a combination of these processes. The mass spectrometric data alone do not enable us to distinguish between these two uranium mobilisation processes.

4.2.2. Gamma spectrometric U-series dating

The skull was measured twice for a 50 day period. The average closed system Th/U age was 69,500±2,900 years (using the mass spectrometric $^{234}U/^{238}U$ ratio) and the Pa/U age 74,000±7,000 years. The somewhat larger Pa/U indicates that some U-leaching might have taken place. However, the skull also contained significant amounts of ^{232}Th, correcting for detrital Th and Pa results in ages are 64,100±3,700 (Th/U) and 60,000±5,000 years (Pa/U).

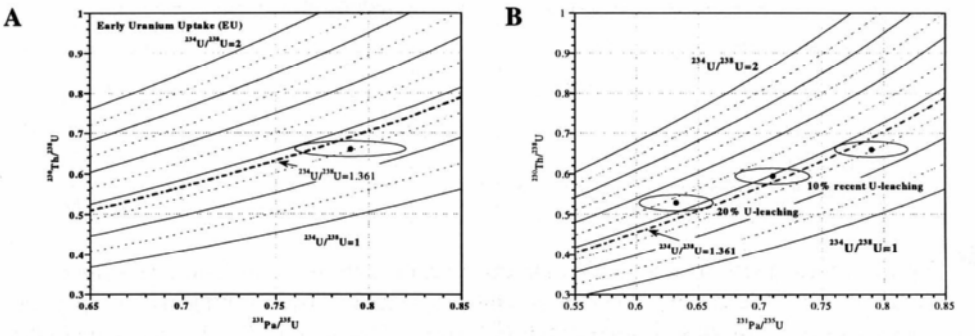

Figure 13 (from [9]): Concordance diagrams of the measured gamma spectrometric Th/U and Pa/U ratios. The data point lies below the iso-$^{234}U/^{238}U$ line (average value of bone shavings) (A) indicating that some recent U-leaching might have taken place (B). However, the Pa/U and Th/U ratios are not corrected for detrital ^{231}Pa and ^{230}Th.

4.2.3. ESR Dating

ESR dating yielded a closed system age estimate of 63,000±6,000 years.

4.2.4 Open system modelling

The Th/U and Pa/U data can be used for open system modelling. Figure 13 shows a concordance plot of the Th/U and Pa/U data. In a perfectly closed system the data point would lie on the iso-$^{234}U/^{238}U$-line (and within error it does). The offset towards higher Pa/U ratios can be explained by some recent U-leaching, which would result in apparent U-series ages which are too old. When modelling for recent U-leaching, the corrected data points move towards lower Th/U and Pa/U values. The modelling suggests that an average recent leaching of 7% may have occurred.

When correcting for detrital ^{230}Th, the data point lies above the iso-$^{234}U/^{238}U$-line (Figure 14). This can be explained by U-uptake. Modelling according to equation (12) yields a p-value of -0.72 and the corresponding mean age is 86,000 years.

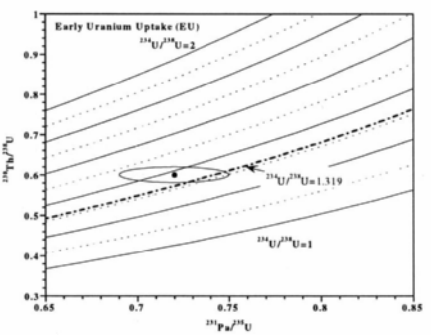

Figure 14: Concordance diagram for Pa/U and Th/U ratios corrected for detrital ^{231}Pa and ^{230}Th. The data point lies now above the iso-$^{234}U/^{238}U$ ratio (from Figure 10B) indicating that delayed U-uptake might have taken place [12].

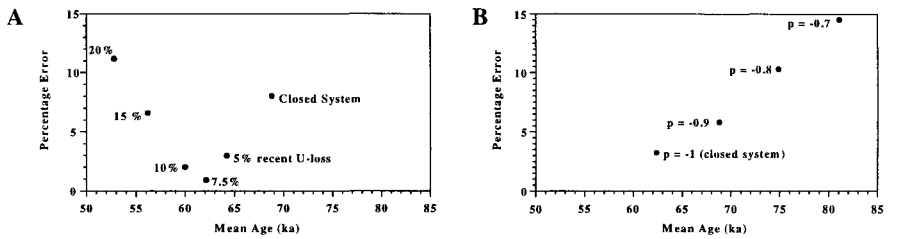

Figure 15 (from [9]): Modelling of U-mobilisation using Th/U, Pa/U and ESR results. (A) no correction for detrital ^{230}Th and ^{231}Pa (B) correction for detrital ^{230}Th and ^{231}Pa. Both models converge for the same age, 62,000 years.

Rather than using the U-series results alone, U-mobilisation can be derived from the combination of U-series and ESR. The components of the tooth (dentine, enamel) should have experienced similar U mobilisation as the skull. In order to assess the possible effect of U-mobilisation, U-series and ESR results are combined. Considering the mathematical complexity of open system modelling for combining U-series and ESR age estimates [19], the error of the mean is used as convergence criterion in Figure 15. Figure 15A (no detrital Th and Pa) shows the mean and standard deviation (expressed as percentage error of the mean) of the Th/U, Pa/U and ESR age estimates for a variety of recent U-losses. The age estimates converge for a recent U-loss of 7.5% (corresponding to a mean age of 62.1±0.6 ka). The individual errors of the modelled Th/U, Pa/U and ESR age estimates overlap in the range of 0 to 15% U-loss, corresponding to a mean age range of between 56 and 68 ka. If the initial ^{230}Th/^{232}Th is assumed to be 1.5, Figure 15B shows that the age estimates converge for the closed system age (62.4±2.0 ka). The individual errors of the modelled Th/U, Pa/U and ESR age estimates overlap in the range of p=-1 to p=-.9, corresponding to a mean age range of between 62 and 69 ka.

Surprisingly, the different scenarios give very robust age estimates for the skeletal remains. This lies in the fact, that ESR age estimates are significantly less influenced by U-mobilisation than the U-series results. Considering all uncertainties of the modelling, the best age estimate for the skeleton is 62±6 ka.

4.2.5. Discussion of the results

The age result on the human skeleton, 62±6 ka, is in good agreement with the OSL age estimate of 61±2 ka as well as with the U-series result on the calcitic matrix of 82±21 ka. On a 1-σ-error basis, the combination of all results would suggest that the skeleton is younger than the OSL date (i.e., < 63 ka) and older than 56 ka as estimated age of the skeleton. The dating results on LM3 have been met with serious criticism [69,76] and the readers are invited to entertain themselves by this controversy [69, 76, 77].

This dating study demonstrates (i) that it is essential to analyse hominid fossils directly, particularly when their age is beyond the practical limits of radiocarbon dating and (ii) the importance of combining mass spectrometric and gamma spectrometric measurements because only the combination of gamma spectrometric ^{230}Th/^{238}U, ^{226}Ra/^{230}Th and ^{231}Pa/^{235}U ratios and mass spectrometric ^{234}U/^{238}U and ^{230}Th/^{238}U values allows the recognition of open systems. The best strategy to solve the open system problem for the dating of human remains is the combination of U-series data with ESR analyses of dental material.

4.2.6 Implications

We know from a series of dating studies that modern humans occurred in Israel around 100,000 years, however, it took about another 60,000 years before modern humans could completely replace the Neanderthals occupying Europe (summarised in [8]). It now seems that some modern humans turned to the east and arrived in Australia earlier than their cousins in Europe. In other words, the Aboriginals in Australia are more ancient people in their environment than Europeans in theirs.

5. CONCLUSIONS

The direct dating analysis on human fossils using U-series isotopes and ESR will allow the establishment of chronologies for many sites that were excavated a long time ago and where the association of human fossils to other material is uncertain and for sites where humans were buried. We can expect many new results from these dating techniques in the near future. When the archeologists finally overcome their hesitation to accept OSL dating results - after all, the only thing that can be dated with OSL is dirt [78] - this method will revolutionise the archaeology of the pre-carbon dating times.

Acknowledgment

I thank F.M. Grün for corrections.

REFERENCES

1. J.R. Arnold and W.F. Libby, Science, 110 (1949) 678.
2. W.F. Libby et al., Science, 109 (1949) 227.
3. C. Renfrew, Before civilization: the radiocarbon revolution and prehistoric Europe, Cape, London (1973).
4. M.I. Bird et al., Radiocarbon, 41 (1999) 127.
5. J. Chappell et al., Antiquity, 70 (1996) 543.
6. L.T. Aldrich and A.O. Nier, Phys. Rev., 74 (1948) 876.
7. I. McDougall and T.M. Harrison, Geochronology and thermochronology by the $^{40}Ar/^{39}Ar$ method. Oxford University Press, Oxford (1999).
8. R. Grün and C.B. Stringer, Archaeometry, 33 (1991) 153.
9. A. Thorne et al., J. Hum. Evol., 36 (1999) 591
10. R. Grün, In: L. Ellis (ed.), Archaeological Method and Theory: An Encyclopedia, Garland, New York (2000) 645.
11. M. Ivanovich and R.S. Harmon (eds.), Uranium series disequilibrium: applications to environmental problems. Oxford University Press, Oxford (1992).
12. J.J. Simpson and R. Grün, Quat. Geochronol. (Quat. Sci. Rev.), 17 (1998) 1009.
13. T. Higham and F. Petchey, this volume.
14. C. Tuniz et al., this volume.
15. R.L. Edwards et al., Earth. Plan. Sci. Let., 81 (1987) 175.
16. R.L. Edwards et al., Science, 236 (1987) 1547.
17. R.L. Edwards et al., Science, 276 (1997) 782.

18. Y. Yokoyama and H.V. Nguyen, Isotope Marine Chemistry, 1980 (1980) 259.
19. R. Grün et al., Nucl. Tracks Radiat. Meas., 14 (1988) 237.
20. R. Grün and F. McDermott, Quat. Geochronol. (Quat. Sci Rev.), 13 (1994) 121.
21. F. McDermott et al., Nature, 363 (1993) 252.
22. R. Grün et al., J. Arch. Sci., 26 (1999) 1301.
23. A.R. Millard, Diagenesis of archaeological bone: the case of uranium uptake. DPhil. Thesis. University of Oxford, Oxford (1993).
24. R.E.M. Hedges and A.R. Millard, J. Arch. Sci., 22 (1995) 155.
25. A.R. Millard and R.E.M. Hedges, J. Arch. Sci., 22 (1995) 239.
26. A.R. Millard and R.E.M. Hedges, Geochim. Cosmochim. Acta, 60 (1996) 2139.
27. H. Valladas et al., Nature 331 (1988) 614.
28. N. Mercier et al. Quat. Geochronol. (Quat. Sci. Rev.), 14 (1995) 351.
29. W.J. Rink. Radiat. Meas., 27 (1997) 975.
30. R. Grün, In: R.E. Taylor and M.J. Aitken (eds) Chronometric and Allied Dating in Archaeology, Plenum, New York. (1997) 217.
31. M.J. Aitken, Optical dating. Oxford University Press, Oxford (1998).
32. R.G. Roberts, Radiat. Meas., 27 (1997) 819.
33. A.S. Marfunin, Spectroscopy, luminescence and radiation centers in minerals, Springer, Berlin (1979).
34. R. Grün, In M. Pollard and D. Brothwell (eds.), Introduction to Archaeological Sciences. Wiley, London, (in press).
35. R. Grün, Quat. Internat. 1 (1989) 65.
36. M. Ikeya, New applications of electron spin resonance - dating, dosimetry and microscopy. World Scientific, Singapore (1993).
37. M. Jonas, Radiat. Meas., 27 (1997) 943.
38. S.W.S. McKeever and R. Chen, Radiat. Meas., 27 (1997) 625.
39. M. Krbetschek et al., Radiat. Meas., 27 (1997) 695.
40. A. Murray and R.G. Roberts, Radiat. Meas., 29 (1998) 503.
41. A. Murray and A.G. Wintle, Radiat. Meas., 32 (2000) 57.
42. L. Bøtter-Jensen, Radiat. Meas., 27 (1997) 749.
43. M.J. Aitken, Thermoluminescence dating, Academic Press, New York (1985).
44. D. Godfrey-Smith et al., Quat. Sci. Rev., 7 (1988) 373.
45. N.A. Spooner, The validity of optical dating based on feldspar. Unpublished DPhil thesis, Oxford University, Oxford (1993).
46. N.A. Spooner, Radiat. Meas., 23 (1994) 593.
47. A.G. Wintle, J. Luminescence, 15 (1977) 385.
48. S. Tyler and S.W.S. McKeever, Nucl. Tracks Radiat. Meas., 14 (1988) 149.
49. R. Grün, Radiat. Meas., 23 (1994) 175.
50. M.L. Readhead, Quat Sci. Rev., 7 (1988) 257.
51. R. Grün and S. Brumby, Radiat. Meas., 23 (1994) 307.
52. R. Grün, Radiat. Meas., 29 (1998) 177.
53. R. Grün, Radiat. Meas., in press.
54. G.W. Berger, Ancient TL, 8 (1990) 23.
55. R. Grün, Ancient TL, 8 (1990) 20.
56. O. Katzenberger and N. Willems, Quat. Sci. Rev., 7 (1988) 485.
57. J.R. Prescott et al., Ancient TL, 11 (1993) 1.

58. R.M. Bailey, The form of the optically stimulated luminescence signal in quartz: implications for dating. Unpublished PhD thesis, Royal Holloway, London (1998).
59. J.R. Prescott and J.T. Hutton, Radiat. Meas., 14 (1988) 223.
60. J.R. Prescott and J.T. Hutton, Radiat. Meas., 23 (1994) 497.
61. G. Adamiec and M.J. Aitken, Ancient TL, 16 (1998) 37.
62. S.G.E. Bowman, Thermoluminescence dating, the evaluation of radiation dosage. Unpublished DPhil. thesis, University of Oxford, Oxford (1976).
63. M.J. Aitken and J. Xie, Ancient TL, 8 (1990) 6.
64. J.R. Prescott and J.T. Hutton, Quat. Geochronol. (Quat. Sci. Rev.), 14 (1995) 439.
65. R. Grün and O. Katzenberger-Apel, Ancient TL, 12 (1994) 35.
66. J. Rees-Jones and M. Tite, Archaeometry, 39 (1997) 177.
67. A. Lang and G.A. Wagner Archaeometry, 38 (1996) 129.
68. J.M. Bowler, Archaeol. Oceania, 33 (1998) 120.
69. R. Gillespie and R.G. Roberts, J. Hum. Evol., in press.
70. J.M. Bowler and A.G. Thorne, In R.L. Kirk and A.G. Thorne (eds.) The origin of the Australians. Australian Institute of Aboriginal Studies, Canberra (1976) 127.
71. T.L. Ku and Z.C. Liang, Nucl. Instr. Meth. Phys. Res., 223 (1984) 563.
72. H.P. Schwarcz and A.G. Latham, Chem. Geol. (Isot. Geosci. Sect.), 80 (1989) 35.
73. W. Przybylowicz et al., Chem. Geol. (Isot. Geosci. Sect.), 86 (1991) 161.
74. K.R. Ludwig and D.M. Titterington, Geochim. Cosmochim. Acta, 58 (1994) 555.
75. H.P. Schwarcz, Archaeometry, 22 (1980) 3.
76. J.M. Bowler and J. Magee, J. Hum. Evol., in press.
77. R. Grün et al., J. Hum. Evol., in press.
78. M.J. Aitken, pers. comm.

This Page Intentionally Left Blank

AUTHOR INDEX

This Page Intentionally Left Blank

SUBJECT INDEX